Nanoscale Libraries and Novel Drug Modalities for Targeting RNA Methyltransferases



Dissertation

Zur Erlangung des Grades

„Doktor der Naturwissenschaften (Dr. rer. nat.)“

im Promotionsfach Pharmazeutische und Medizinische Chemie

am Fachbereich Chemie, Pharmazie, Geographie & Geowissenschaften

der Johannes Gutenberg-Universität Mainz

Ariane Hübner

geb. Frey

Master of Science, geb. in Wiesbaden

Januar 2026

Submitted at the Faculty of Chemistry, Pharmacy, Geography, and Geoscience.

Dean: PROF. DR. EVA RENTSCHLER

Name of the 1st reviewer and supervisor: [redacted]

Name of the 2nd reviewer: [redacted]

Name of the 2nd supervisor: DR. FABIAN BARTHELS

Date of the doctoral examination: 17.04.2026

Lizenz: CC-BY-ND-4.0
D77 (Dissertation Universität Mainz)

Eigenständigkeitserklärung

Hiermit erkläre ich, Ariane Felicitas Hübner, dass ich die vorliegende Arbeit mit dem Titel: „*Nanoscale Libraries and Novel Drug Modalities for Targeting RNA Methyltransferases*“ selbstständig verfasst und keine anderen als die angegebenen Quellen und Hilfsmittel (dazu zählen auch KI-basierte Anwendungen oder Werkzeuge) benutzt habe. Sämtliche wörtlichen oder sinngemäßen Übernahmen und Zitate sind kenntlich gemacht und nachgewiesen (dies gilt auch für Texte, die durch generative KI, wie ChatGPT erzeugt wurden). Ich versichere, dass ich keine Hilfsmittel verwendet habe, deren Nutzung die Prüferin oder der Prüfer explizit ausgeschlossen hat. Im Anhang „Nutzung KI-Tools“ habe ich die verwendeten KI-Tools dokumentiert. Mit Abgabe der vorliegenden Leistung übernehme ich die Verantwortung für das eingereichte Gesamtprodukt. Ich verantworte damit auch jegliche KI-generierten Inhalte, die ich in meine Arbeit übernommen habe. Die Richtigkeit übernommener (KI-generierter) Aussagen und Inhalte habe ich nach bestem Wissen und Gewissen geprüft. Mir ist bekannt, dass ein Verstoß gegen die genannten Punkte prüfungsrechtliche Konsequenzen hat und insbesondere dazu führen kann, dass die Promotionsleistung als mit „nicht bestanden“ bewertet wird. Die Einschreibung kann für bis zu zwei Jahre widerrufen werden, wenn Studierende zweimal oder häufiger bei Prüfungsleistungen täuschen (§ 69 Abs. 4 und 5 HochSchG).

Anhang: Nutzung KI-Tools

Tool	**Verwendung**	
Grammarly free version	Korrektur von einzelnen Wörtern und Grammatik	Über die gesamte Arbeit hinweg
DeepL translate	Übersetzung einzelner Wörter	Über die gesamte Arbeit hinweg
ChatGPT	Sprachunterstützung für amerikanisches Englisch: Korrektur einzelner Wörter und Sätze	Über die gesamte Arbeit hinweg

Mainz, 22.04.2026 AHübner

Ort, Datum und Unterschrift

Abstract

In recent years, epitranscriptomics has emerged as a rapidly evolving field of significant relevance to biomedical research. The research primarily concerns the methylation of ribonucleic acid (RNA), a process catalyzed by RNA methyltransferases (Mtases). Members of this enzyme family have been implicated in a wide range of pathological conditions, including cancer, making them promising targets for medicinal chemistry. This dissertation focused on developing and applying innovative strategies to identify novel inhibitors of RNA Mtases. The results are divided into three distinct projects.

Project 1: Direct-to-Biology (D2B). In the first project, the D2B strategy, originally described in 2021, was applied to two distinct subprojects. The first subproject aimed to identify fluorescent tracers suitable for high-throughput screening (HTS) of disease-associated RNA Mtases. Two novel fluorescent tracers were developed for a variety of RNA Mtases using a copper(I)-catalyzed azide-alkyne cycloaddition (CuAAC) synthesis strategy. This approach enabled an HTS campaign against methyltransferase-like 1 (METTL1), resulting in the identification of (*S*)-crizotinib as a first-in-class inhibitor. In the second subproject, inhibitors of *Staphylococcus aureus* tRNA methyltransferase D (TrmD) were identified. The fluorescent tracer developed in the first subproject served as a starting point for a D2B-based strategy targeting *S. aureus* TrmD. A CuAAC-based D2B approach led to the discovery of five promising hit compounds. Moreover, a carbamate prodrug design was employed, yielding the first prodrug targeting TrmD, which effectively inhibited the growth of *S. aureus*. Lastly, the first crystal structure of *S. aureus* TrmD in complex with the active inhibitor was elucidated.

Project 2: DNA-Encoded-Library (DEL) Screening. In the second project, DEL technology was employed to identify inhibitors of deoxyribonucleic acid (DNA) methyltransferase 2 (DNMT2) with novel chemotypes. This approach resulted in the identification of five selective DNMT2 binders, featuring triazin- and peptidomimetic-based core structures. Among these, only the peptidomimetic compounds demonstrated inhibitory activity, prompting subsequent X-ray crystallographic analysis. Structural characterization revealed an allosteric inhibition mechanism for the lead compound, which guided a structure-activity relationship (SAR) study conducted via solid-phase peptide synthesis. The optimized compound from this study exhibited not only enhanced binding affinity but also, as a distinguishing feature, permeability in a parallel artificial membrane permeability assay (PAMPA). Follow-up cellular assays confirmed that the compound effectively reduced m^5C levels in tRNA and exhibited synergistic effects in MOLM-13 cells when combined with doxorubicin.

Project 3: Novel Modalities for Medicinal Chemistry of RNA and RNA Methyltransferases. In the third project, two novel strategies were explored to expand the repertoire of tools for targeting RNA Mtases. The first approach focused on the degradation of METTL3 using a proteolysis-targeting chimera (PROTAC) strategy, employing the known METTL3 inhibitor STM2457 as a recruiter ligand. Iterative optimization across four generations led to the development of AF 151, a potent and selective METTL3 degrader. A second, conceptually distinct strategy was conducted to enable the characterization of RNA-binding ligands and RNA modifications. This approach utilizes a mix-and-measure assay with non-covalent RNA dyes, which facilitates the quantification of various RNA modifications, including m^6A, mediated by the METTL3/14 complex, among other applications

Zusammenfassung

In den vergangenen Jahren hat sich die Epitranskriptomik zu einem stark wachsenden Forschungsfeld mit hoher Relevanz für die biomedizinische Forschung entwickelt. Ein zentraler Aspekt ist die Untersuchung von RNA-Methylierungen, die durch RNA-Methyltransferasen (Mtasen) katalysiert werden. Diese Enzyme sind mit verschiedenen pathologischen Zuständen, darunter Krebs, assoziiert und stellen somit interessante Zielstrukturen für die medizinische Chemie dar. Die vorliegende Dissertation widmet sich der Entwicklung und Anwendung innovativer Strategien zur Identifizierung neuartiger RNA-Mtase-Inhibitoren. Die Arbeit gliedert sich in drei Projekte.

Projekt 1: *Direct-to-Biology* (D2B). Im Rahmen des ersten Projekts wurde die 2021 erstmals beschriebene D2B-Strategie in zwei unterschiedlichen Teilprojekten angewendet. Das erste Teilprojekt zielte auf die Entwicklung fluoreszierender Sonden für Hochdurchsatz-*Screenings* (HTS) medizinisch relevanter RNA-Methyltransferasen (Mtasen) ab. Zwei neuartige Sonden wurden mittels einer Kupfer(I)-katalysierten Alkin-Azid-Cycloaddition (CuAAC)-Synthesestrategie für eine Vielzahl unterschiedlicher RNA-Methyltransferasen entwickelt. Dieser Ansatz ermöglichte ein HTS einer Wirkstoffbibliothek unter Verwendung der *Methyltransferase-like 1* (METTL1) und führte zur Identifizierung von (*S*)-Crizotinib als erstem Inhibitor seiner Klasse. Im zweiten Teilprojekt wurden Inhibitoren gegen die tRNA-Methyltransferase D (TrmD) von *Staphylococcus aureus* (*S. aureus*) identifiziert. Eine im ersten Teilprojekt entwickelte fluoreszierende Sonde diente dabei als Ausgangspunkt für die Anwendung der D2B-Strategie gegen *S. aureus* TrmD. Der CuAAC-basierte Ansatz führte zur Entdeckung von fünf Inhibitoren. Ein Carbamat-*Prodrug*-Derivat eines dieser Inhibitoren reduzierte das Wachstum von *S. aureus* signifikant und stellt somit das erste antibakteriell aktive *Prodrug* gegen *S. aureus* TrmD dar. Darüber hinaus wurde die Kristallstruktur des aktiven Inhibitorkomplexes gelöst.

Projekt 2: ***DNA-Encoded Library* (DEL) Screening.** Ziel war die Entwicklung neuartiger DNA-Methyltransferase-2 (DNMT2)-Inhibitoren durch ein DEL-Screening. Fünf selektive Liganden mit Triazin- bzw. peptidomimetischer Kernstruktur wurden identifiziert, wobei nur die peptidomimetischen Verbindungen inhibitorisch wirkten. Kristallstrukturanalysen belegten einen allosterischen Bindungsmodus. Eine darauf basierende Struktur-Aktivitäts-Beziehungsstudie (SAR) mittels Festphasen-Peptidsynthese führte zu einer Verbindung mit deutlich gesteigerter Affinität und als Alleinstellungsmerkmal Zellpermeabilität in einem *Parallel Artificial Membrane Permeability Assay* (PAMPA). In MOLM-13-Zellen reduzierte diese Verbindung das tRNA-m^5C-Level und zeigte Synergie mit Doxorubicin.

Projekt 3: Neue Modalitäten in der medizinischen Chemie von RNA und RNA-Mtasen. In diesem Projekt wurden zwei neue Ansätze zur Adressierung von RNA-Mtasen und RNA entwickelt. Erstens wurden *Proteolysis Targeting Chimeras* (PROTACs), aufbauend auf dem bekannten Inhibitor STM2457 zur gezielten Degradation von METTL3 konzipiert. Sukzessive Optimierung über vier PROTAC-Generationen führte zur Identifizierung von AF 151 als potentem METTL3-*Degrader*. Der zweite, konzeptuell andere Ansatz zielte auf die Beschleunigung der Charakterisierung von RNA-Liganden oder -Modifikationen ab. Hier wurde ein „*mix-and-measure*"-Protokoll auf Basis nicht-kovalenter RNA-Farbstoffe etabliert, das unter anderem die Quantifizierung von METTL3/14-vermittelten m^6A-Modifikationen ermöglicht.

.

Acknowledgment

I would like to use this section of my thesis to take the opportunity to thank the many people who supported and guided me during my dissertation. First, I would like to thank my supervisors, **Dr. Fabian Barthels** and [redacted]. I would like to thank **Dr. Fabian Barthels** for his continuous effort, motivation, and support, as well as for the constant exchange of ideas and his never-ending enthusiasm for research and science projects. I am especially grateful not only for his role as my supervisor, but also for being my lab partner and a constant source of research inspiration. I am deeply grateful to [redacted] for giving me the opportunity to work in the fascinating field of Medicinal Chemistry, for her constant support, insightful discussions, and for acting as the first reviewer of this thesis.

Furthermore, I would like to extend my thanks to [redacted] for serving as the second reviewer of this thesis and for the valuable collaborations with him and his research group throughout my doctoral studies.

Special thanks go to my lab partners [redacted], [redacted], and [redacted] for the friendly and supportive working atmosphere. I also thank the assistants of the first-semester practical course, [redacted], [redacted], and [redacted], for the productive collaboration. I would also like to thank the members of the Barthels working group – [redacted], [redacted], [redacted], and [redacted] – as well as the previously unmentioned colleagues from the [redacted] group: [redacted], [redacted], [redacted], [redacted], [redacted], [redacted], [redacted], [redacted], and [redacted] for sharing their expertise and knowledge and for their collaborations. Furthermore, I would like to thank the former members of the [redacted] group – [redacted], [redacted], [redacted], [redacted], and [redacted] – for their support during our work together. I am grateful to the students I supervised during my doctoral studies [redacted], [redacted], [redacted] and [redacted] for their motivation and dedication to their projects.

Moreover, I would like to thank from the [redacted] and [redacted] groups [redacted], [redacted], and [redacted] for the excellent cooperation on various projects, as well as [redacted], [redacted], and [redacted] for their reliable coordination and support in the isotope laboratory. I would like to express my gratitude to my collaborators in Heidelberg: [redacted], [redacted], and [redacted]. I would also like to thank my collaborators in Würzburg: [redacted], [redacted] and [redacted].

Last but not least, I would like to thank my family and friends for always supporting me, not only during my dissertation but also throughout my studies since 2015. Special thanks go to my parents, who made this long educational journey possible and have always supported me financially and emotionally. My deepest gratitude goes to [redacted], who has been incredibly patient with me during long workdays and has been the best support and rock I could have imagined over the past eight years. Finally, I would like to thank [redacted] for proofreading my thesis and for the many conversations that have repeatedly given me new motivation and insights.

Table of Contents

Eigenständigkeitserklärung ..... **I**

Abstract ..... **II**

Zusammenfassung ..... **IV**

Acknowledgment ..... **VI**

Table of Contents ..... **VIII**

List of Abbreviations ..... **X**

1 Introduction **1**

1.1 RNA Methyltransferases *1*

1.1.1 DNA Methyltransferase 2 (DNMT2) 3

1.1.2 tRNA Methyltransferase D (TrmD) 6

1.1.3 Methyltransferase-like (METTL) Family 10

1.2 Limitations and New Modalities in Medicinal Chemistry *17*

1.2.1 Limitations and Challenges in Targeting RNA Mtases 18

1.2.2 New Approaches in Medicinal Chemistry 20

Review: Direct-to-Biology (D2B) Strategies 22

2 Project Overview **43**

2.1 Project 1: Direct-to-Biology Strategies *43*

2.2 Project 2: DNA-Encoded Library Screening *45*

2.3 Project 3: Novel Modalities for Medicinal Chemistry of RNA and RNA Methyltransferases *46*

2.4 Publications Beyond this Doctoral Thesis *47*

3 Project 1: Direct-to-Biology Strategies **48**

3.1 Nanomole Scale Screening of Fluorescent RNA-Methyltransferase Probes Enables the Discovery of METTL1 Inhibitors. *48*

3.1.1 Context and Project Summary 48

3.1.2 Contributions 49

3.1.3 Publication 50

3.1.4 Supporting Information 57

3.2 Nanoscale Direct-to-Biology Optimization and Structural Insights into Selective S. aureus TrmD Inhibitors ... *92*
3.2.1 Context and Project Summary ... 92
3.2.2 Contributions ... 93
3.2.3 Publication ... 94
3.2.4 Supporting Information ... 111

4 Project 2: DNA-Encoded Library Screening ... 129

4.1 DNA-Encoded Library Screening Uncovers Potent DNMT2 Inhibitors Targeting a Cryptic Allosteric Binding Site ... *129*
4.1.1 Context and Project Summary ... 129
4.1.2 Contributions ... 130
4.1.3 Publication ... 131
4.1.4 Supporting Information ... 172

5 Project 3: Novel Modalities for Medicinal Chemistry of RNA and RNA Methyltransferases 199

5.1 Structure-Guided Design of a Methyltransferase-like 3 (METTL3) Proteolysis Targeting Chimera (PROTAC) Incorporating an Indole–Nicotinamide Chemotype ... *199*
5.1.1 Context and Project Summary ... 199
5.1.2 Contributions ... 200
5.1.3 Publication ... 201
5.1.4 Supporting Information ... 215

5.2 Non-covalent Dyes in Microscale Thermophoresis for Studying RNA Ligand Interactions and Modifications ... *276*
5.2.1 Context and Project Summary ... 276
5.2.2 Contributions ... 277
5.2.3 Publication ... 278
5.2.4 Supporting Information ... 289

6 Summary & Outlook ... 298

7 Bibliography ... 301

8 Curriculum Vitae ... 319

List of Abbreviations

A	Adenine
A site	Aminoacyl site
A. baumannii	*Acinetobacter baumannii*
aaRS	Aminoacyl-tRNA synthetase
ADP	Adenosine diphosphate
AI	Artificial intelligence
AKT	Protein kinase B
Ala	Alanine
AML	Acute myeloid leukemia
Arg	Arginine
Asn	Asparagine
Asp	Aspartic acid
ATAD2	ATPase family AAA-domain containing protein 2
AURKA	Aurora kinase A
BAX	Bcl-2-associated X protein
Bcl2	B-cell lymphoma 2
BMP4	Bone morphogenetic protein 4
Boc	*tert*-Butyloxycarbonyl
BRD4	Bromodomain-containing protein 4
BTK	Bruton's tyrosine kinase
C	Cytosine
CA	Carbonic anhydrase
Cas3	Caspase 3
Cbz	Benzyloxycarbonyl
CC_{50}	Half-maximal cytotoxicity concentration
CDK	Cyclin-dependent kinase
cIAP1	Cellular inhibitor of apoptosis proteins 1
c-MET	Mesenchymal-epithelial transition factor
Cpd	Compound
CRBN	Cereblon
CuAAC	Copper(I)-alkyne-azide cycloaddition
Cy5TAD	Cy5-triazolyl-adenosyl-diaminobutyric acid
Cy5TPD	Cy5-thienopyrimidine
CycE	Cyclin E
Cys	Cysteine
D2B	Direct-to-Biology
DC_{50}	Half-maximal degradation concentration
DEL	DNA-encoded library
DNA	Deoxyribonucleic acid
DNMT	DNA methyltransferase

DOT1L	Disruptor of telomeric silencing 1-like
E3	E3-ligase
E site	Exit site
E. coli	*Escherichia coli*
eIF4E	Eukaryotic translation initiation factor 4E
ERRα	Estrogen-related receptor α
ESC	Embryonic stem cell
Phe	Phenylalanine
FAM	Carboxyfluorescein
FDA	U.S. Food and Drug Administration
FGF2	Fibroblast growth factor 2
F_{norm}	Normalized fluorescence
FP	Fluorescence polarization
FRET	Förster resonance energy transfer
FTAD	5-FAM-triazolyl-adenosyl-diaminobutyric acid
G	Guanine
GBB	Groebke-Blackburn-Bienaymé
GCS	Glucosylceramide synthase
Gln	Glutamine
Glu	Glutamic acid
Gly	Glycine
GNMT	Glycine *N*-methyltransferase
GP	Glycoprotein
GSK3	Glycogen synthase kinase 3
H. influenzae	*Haemophilus influenzae*
H3K79	Histone H3 at lysine 79
HA	Hemagglutinin
HCC	Hepatocellular carcinoma
HDAC2	Histone deacetylase 2
His	Histidine
hiPSC	Human-induced pluripotent stem cell
HIV	Human immunodeficiency virus
HPLC	High-performance liquid chromatography
HTRF	Homogeneous time-resolved fluorescence
HTS	High-throughput screening
IC_{50}	Half maximal inhibitory concentration
Ile	Isoleucine
InhA	Enoyl-ACP reductase
ITC	Isothermal titration calorimetry
JAK	Janus kinase
k_{cat}	Catalytic turnover
K_D	Dissociation constant

K_I	Inhibition constant
K_M	Michaelis-Menten constant
LC	Liquid chromatography
Leu	Leucine
m^1A	N^1-methyladenosine
m^1G	N^1-methlyguanosine
m^3C	3-methylcytidine
m^4C	4-methylcytidine
m^5C	5-methylcytosine
m^6A	N^6-methyladenosine
m^7G	N^7-methylguanosine
MAP	Mitogen-activated protein
MAPK	Mitogen-activated protein kinase
MCE	Mitotic clonal expansion
MDM2	Mouse double minute 2 homolog
Met	Methionine
METTL	Methyltransferase-like
miRNA	micro-RNA
MKK7	MAP kinase kinase 7
MLL	Mixed lineage leukemia
MMTV	Mouse mammary tumor virus
M^{Pro}	Main protease
mRNA	Messenger RNA
MRSA	Methicillin-resistant *S. aureus*
MS	Mass spectrometry
MST	Microscale thermophoresis
Mtase	Methyltransferase
mTOR	Mammalian target of rapamycin
NF-κB	Nuclear factor κB
NNMT	Nicotinamide *N*-methyltransferase
NonO	Non-POU domain-containing octamer-binding protein
NSD2	Nuclear receptor-binding SET domain 2
Nsp	Non-structural protein
NSUN	NOL1/NOP2/Sun family
OCT4	Octamer-binding transcription factor 4
P site	Peptidyl site
PAMPA	Parallel artificial membrane permeability assay
PARPi	Poly-ADP-ribose polymerase inhibitors
PDB	Protein Data Bank
PhABit	PhotoAffinity Bit
PHIP(2)	Pleckstrin-homology domain interacting protein
PI3K	Phosphoinositide-3-kinase

PNMT	Phenylethanolamine *N*-methyltransferase
POI	Protein of interest
PRMT1	Protein arginine methyltransferase 1
Pro	Proline
PROTAC	Proteolysis-targeting chimera
RCC	Renal cell carcinoma
RF	Reactive fragment
RIP1	Receptor-interacting serine/threonine-protein kinase 1
RIPK2	Receptor-interacting serine/threonine-protein kinase 2
RNA	Ribonucleic acid
rRNA	Ribosomal RNA
S. aureus	*Staphylococcus aureus*
SAH	*S*-adensoly-L-homocysteine
SAM	*S*-adensoyl-L-methionine
SAR	Structure-activity relationship
SARS-CoV-2	Severe acute respiratory syndrome coronavirus 2
sEH	Soluble epoxide hydrolase
Ser	Serine
SFG	Sinefungin
SHP2	Src homology region 2 tyrosine phosphatase 2
SI	Supporting information
S_N2	Nucleophilic substitution 2
S_NAr	Aromatic nucleophilic substitution
sncRNA	Small non-coding RNA
SOCS2	Suppressor of cytokine signaling 2
SOX2	Sex-determining region Y-box 2
SPOUT	SpoU-TrmD
SPR	Surface plasmon resonance
STAT	Signal transducers and activators of transcription
SuFEx	Sulfur (VI) fluoride exchange
T	Thymine
TAK1	TGF-β-activated kinase 1
TAMRA	Carboxytetramethylrhodamine
Thr	Threonine
tRF	tRNA fragment
TRIM25	Tripartite motif-containing protein 25
TrmD	tRNA methyltransferase D
Trm(t)	tRNA methyltransferase
tRNA	Transfer RNA
Tyr	Tyrosine
U	Uracil
Ub	Ubiquitin

Val	Valine
VHL	Von Hippel-Lindau
WDR	WD-repeat domain
Wnt	Wingless Int-1
WNT2	Wingless-type MMTV integration site family, member 2
WRN	Werner syndrome helicase
WTAP	Wilms' tumor 1-associating protein
YTHDF2	YTH N^6-methyladenosine RNA binding protein 2
ZFP217	Zinc finger protein 217

1 Introduction

1.1 RNA Methyltransferases

Recently, the field of epitranscriptomics, describing ribonucleic acid (RNA) modifications, has received increasing scientific attention.[1,2] RNA modifications are introduced post- or co-transcriptionally by diverse enzymes.[3–5] To date, more than 170 distinct RNA modifications have been identified.[4] Representative examples include pseudouridylation[6,7], 3'-terminal uridylation[8], and adenosine-to-inosine conversion.[9,10] Among the smallest molecular modifications, RNA methylation exerts a significant functional impact. RNA methylation is catalyzed by RNA methyltransferases (Mtases), and its downstream effects are implicated in numerous biological processes such as cell differentiation and stress response.[3,11–13] Nearly all RNA Mtases utilize *S*-adenosyl-L-methionine (SAM) as a cofactor and methyl group donor.[3,14,15] During the catalytic reaction, SAM is converted to *S*-adenosyl-L-homocysteine (SAH), which acts as a product inhibitor and a broad-spectrum inhibitor of methyltransferases. (Figure 1).[3,14]

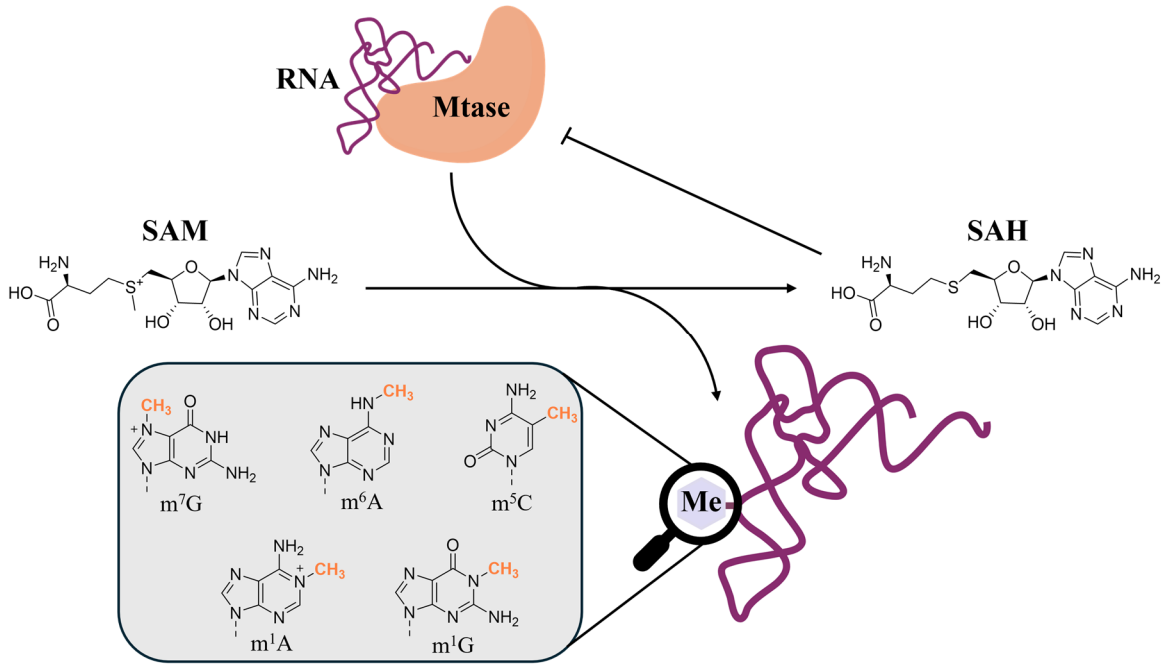


Figure 1. Enzymatic conversion of SAM to the product inhibitor SAH by Mtases. SAM is converted to SAH, acting as a methyl group donor. The figure illustrates a selection of RNA methylation patterns resulting from Mtase activity.

Methylations are catalyzed by distinct Mtases, which are classified into five major classes, each defined by unique structural characteristics.[3] Class I Mtases represent the largest and most prevalent class.[3,14] These enzymes feature a Rossmann fold, typically composed of a seven-stranded β-sheet, flanked by α-helices (Figure 2A).[3,14,16–19] Notably, the first β-strand comprises a glycine-rich motif, while the second β-strand contains a conserved acidic residue at its end.[3,14,16] Both motifs play a critical role in SAM binding.[14] Class II significantly differs from class I Mtases in their topology. They are characterized by a central, extended antiparallel β-sheet surrounded by clusters of α-helices (Figure 2B).[16,20,21] The SAM binding site is located at a solvent-exposed edge of the β-sheet containing a conserved RxxxGY motif.[14,16,20,21] Class III Mtases are characterized by an extensive SAM binding pocket, in which SAM binds in a folded conformation.[16] This structural configuration is formed by two αβα-domains, each comprising five β-strands and four helices (Figure 2C).[3,16,22] Class IV Mtases possess a characteristic SpoU-TrmD (SPOUT) domain, containing a variable N-terminal subdomain with an α/β fold, and a conserved C-terminal trefoil knot (Figure 2D).[16,20,23,24] This knotted region contains a parallel β-sheet composed of five strands.[20,23,24] The SAM binding site is located within the trefoil knot, where SAM binds in a bent conformation that is unique to this class.[20,23,24] Class V Mtases correspond to the SET domain proteins, which are composed of a series of β-strands, including a C-terminal knot distinct from that of class IV enzymes (Figure 2E).[14,16,20] SAM binds near the C-terminus at the enzyme surface in a kinked conformation.[20,25]

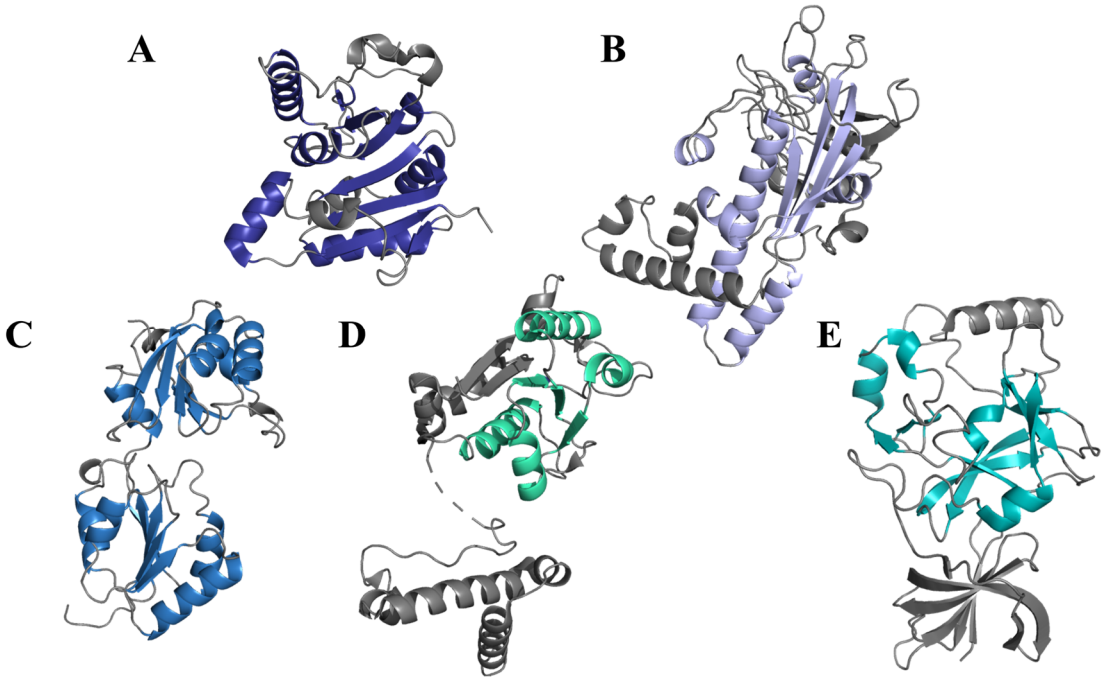


Figure 2. Structural overview of representative Mtase classes I–V. (**A**) Class I Mtase exemplified by METTL1 (PDB: 8CTH), highlighting the canonical Rossmann-like fold (dark blue). (**B**) Class II Mtase represented by methionine synthase (PDB: 1MSK), featuring a central β-sheet flanked by α-helices (light blue). (**C**) Class III Mtase illustrated by cobalt precorrin-4 methyltransferase (PDB: 1CBF), comprising two domains, each formed by five β-strands and four α-helices (blue). (**D**) Class IV Mtase exemplified by TrmD (PDB: 1UAL), characterized by the distinctive trefoil knot motif (green). (**E**) Class V Mtase represented by SET7/9 (PDB: 1O9S), highlighting the conserved SET domain (teal).

At least as diverse as the Mtase architecture itself are the methylation patterns generated by this enzyme class (Figure 1). Examples of widespread RNA methylations include 5-methylcytosine (m^5C), N^6-methyladenosine (m^6A), N^1-methyladenosine (m^1A), N^7-methylguanosine (m^7G), and N^1-methylguanosine (m^1G). Most of these modifications contribute to RNA stability and structure, transcription, and translation, and thus, also through additional mechanisms of action, to protein biosynthesis and gene expression.[11,26–44] Numerous studies have indicated a close association between dysregulation of RNA methylation and cancer metabolism; however, the precise mechanisms linking RNA modification to cancer metabolism remain poorly understood.[2,11] Methylation modifications exert substantial influence on various biological processes and regulatory pathways, which explains why RNA methylations and their respective Mtases have emerged as promising targets in medicinal research.[2,3] Methylation of tRNA has been demonstrated to influence disease development – this observation aligns with its essential function in protein biosynthesis.[2,45]

Notably, STC-15 (Figure 14, **10**), a methyltransferase-like 3/14 (METTL3/14)-targeting compound developed by Storm Therapeutics, represents an RNA Mtase inhibitor recently entering clinical trials, underscoring the therapeutic potential, medicinal relevance, and druggability of this enzyme class.[46,47] For this reason, the following sections highlight a selection of exceptional Mtases that are of special interest for current medicinal research.

1.1.1 DNA Methyltransferase 2 (DNMT2)

A remarkable representative of RNA Mtases is DNMT2, which introduces the m^5C38 modification in tRNA.[48] Its misleading designation as a DNA Mtase originates from its structural similarity to the DNA Mtases DNMT1 and DNMT3. Its actual function as an RNA Mtase was only discovered in 2006 by Goll *et al.*.[48] DNMT2 is conserved across both eukaryotes and prokaryotes, and its tRNA substrate specificity varies between species, targeting $tRNA^{Gly}$, $tRNA^{Val}$, $tRNA^{Glu}$, or $tRNA^{Asp}$.[49–53] The first crystal structure of DNMT2, reported by Dong *et al.* in 2001, revealed that DNMT2 belongs to the class I Mtases, characterized by the class-defining Rossmann fold (Figure 2A, 3A).[17]

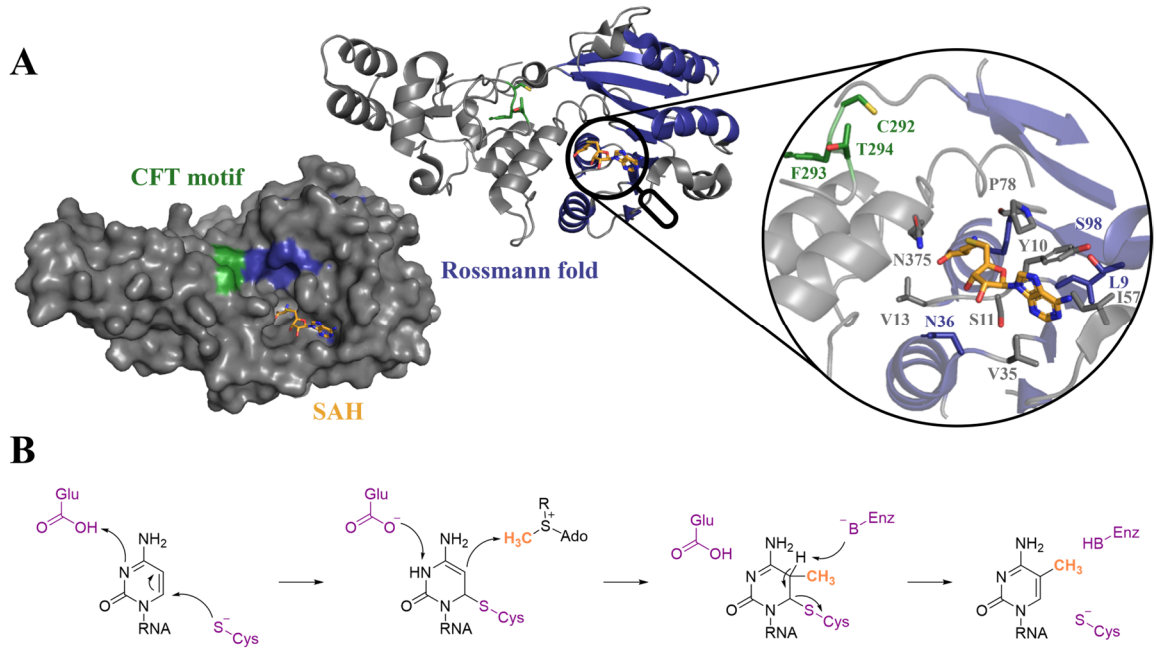


Figure 3. (**A**) DNTM2 crystal structure by Dong *et al.* (PDB: 1G55).[17] The characteristic CFT motif is highlighted in dark green, and elements contributing to the canonical Rossmann fold typical of class I Mtase are shown in dark blue. The pan-Mtase inhibitor SAH is depicted in orange. (**B**) Catalytic mechanism of DNMT2 (amino acids in purple) utilizing SAM as a methyl group donor. The mechanism is initiated by the activation of the cytosine C^5 carbon by a catalytic cysteine, which attacks the C^6 position, while a glutamate residue protonates the N^3 nitrogen. The activated C^5 then attacks the methyl group of SAM and is subsequently deprotonated by an unknown base, leading to the elimination of cysteine and the release of methylated cytosine.[52,54,55]

Compared to DNMT1 and DNMT3, DNMT2 is relatively small (~400 amino acids), as it lacks the regulatory domains found in DNMT1 and DNMT3 and consists solely of a catalytic domain.[17,56] The catalytic domain itself contains a cysteine-phenylalanine-threonine (CFT) motif, which is unique among DNMTs (Figure 3A, highlighted in dark green).[17,56] The catalytic mechanism follows the DNMT-type pathway, as originally described by Santi *et al*., rather than the mechanism characteristic of m^5C RNA Mtases (Figure 3B).[55] Prior to methylation, cytosine requires activation. In DNMT2, the catalytic cysteine of the proline-cysteine-glutamine (PCQ) motif attacks the C^6 of cytosine.[52,54,55] This process is facilitated by the protonation of the N^3 nitrogen by the catalytic glutamate residue and results in the formation of a covalent protein-RNA intermediate with an activated C^5 carbon.[52,54,55] The C^5 carbon then functions as a nucleophile, attacking the methyl group of SAM.[52,54,55] Subsequent deprotonation of C^5 enables the elimination of the catalytic cysteine, leading to re-aromatization of the cytosine base.[52,54,55] Lastly, SAH and the methylated RNA are released (Figure 3B).[52,54,55]

DNMT2 is located in the cytoplasm and nuclear compartments, which is unique among DNMTs.[31,57] The localization of DNMT2 is associated with cellular stress response.[31] Part of this response is tRNA fragmentation by the endonuclease angiogenin, generating tRNA fragments (tRFs).[58,59] Notably, tRNAs lacking DNMT2-mediated m^5C38 methylation show increased cleavage rates, indicating that DNMT2 contributes to the regulation of tRNA stability and degradation and therefore protein biosynthesis (Figure 4A).[27,31] In addition, tRFs exert regulatory functions, such as the repression of protein translation.[60–62] tRNA stability is not the only factor influencing protein biosynthesis; the proximity of the m^5C38 modification to the anticodon loop already hints at the crucial role in translation. A double knockout of NOL1/NOP2/Sun 2 (NSUN2, which also introduces m^5C38) and DNMT2 has been shown to reduce protein translation.[27] Moreover, the presence of m^5C38 improves codon discrimination, particularly between aspartate and glutamate codons, thereby enhancing translational accuracy and efficacy (Figure 4C).[63] Another functional consequence of the m^5C38 modification is its impact on aminoacylation efficiency. It enhances the affinity of $tRNA^{Asp}$ to aminoacyl-tRNA synthetase (aaRS), resulting in a higher rate of aminoacylation of $tRNA^{Asp}$ (Figure 4B).[64] In the absence of m^5C38, reduced aminoacylation impairs the synthesis of polyaspartate-containing proteins, underscoring the role of DNMT2 in the regulation of protein biosynthesis.[64]

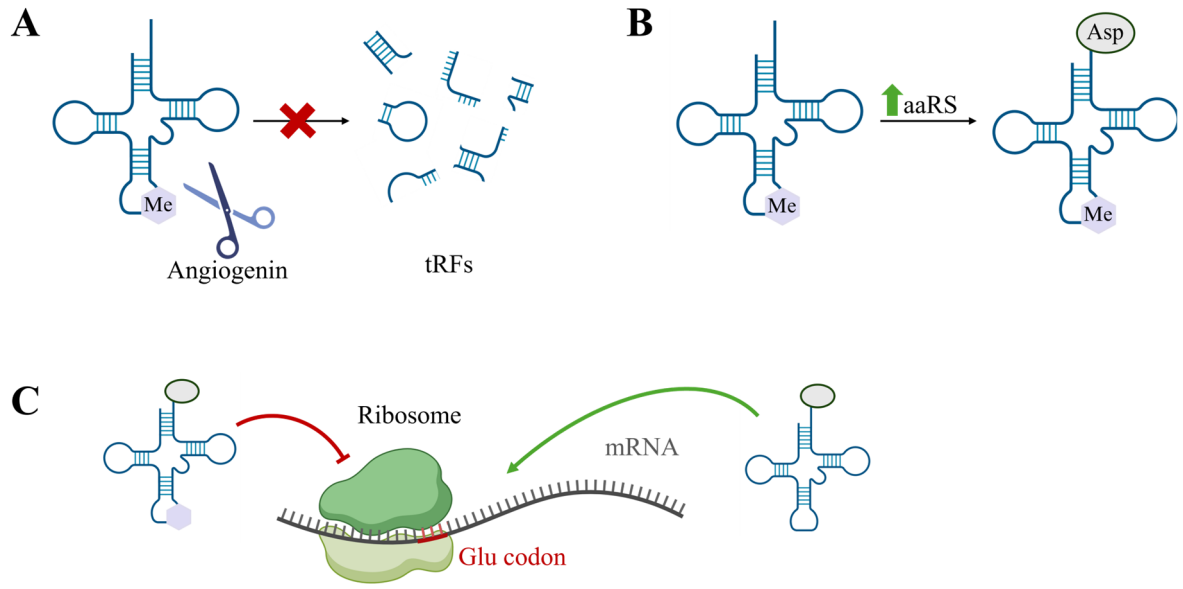
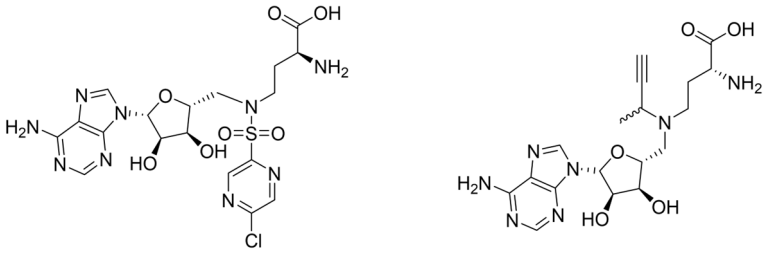


Figure 4. Biological functions of DNMT2. (**A**) The DNMT2-mediated m^5C38 modification leads to a decrease in the tRNA cleavage by angiogenin. (**B**) The m^5C38 modification enhances the affinity of $tRNA^{Asp}$ to the aaRS. Therefore, the aminoacylation is increased. (**C**) m^5C38 improves codon discrimination between aspartate and glutamate, and the accuracy of protein biosynthesis.

Given the diverse biological functions of DNMT2, its dysregulation has been associated with a range of pathological conditions. Upregulation of DNMT2 has been associated with several cancer types, including lymph node metastases, liver cancer, ovarian cancer, and leukemia.[65–67] Knockout of the

DNMT2 gene has been shown to sensitize various cancer cell types to radiotherapy, chemotherapy, and other targeted anticancer agents.[67,68] For example, DNMT2 silencing sensitized tumor cells to poly-ADP-ribose polymerase inhibitors (PARPi), cisplatin, or doxorubicin.[68–70] Additionally, DNMT2 suppression has been associated with the upregulation of tumor-suppressive microRNAs (miRNAs).[71] Elevated m^5C levels in small non-coding RNAs (sncRNAs), catalyzed by DNMT2, have been implicated in the intergenerational transmission of metabolic disorders induced by a high-fat diet and mediated by sperm-derived sncRNAs.[72,73] A knock-out of *Dnmt2* in mice attenuates the epigenetic inheritance of these diet-induced phenotypes.[72,73]

Despite its involvement in diverse pathological conditions, DNMT2 remains a significant challenge as a target for drug development campaigns.[76] Efforts to develop DNMT2 inhibitors have primarily focused on SAH analogs (**1** & **2**, Figure 5).[3,74,75] Although some compounds display selectivity within the NSUN family (which is also responsible for m^5C modifications in tRNA), none of them demonstrated selective inhibition of DNMT2 over DNMT3.[75] Moreover, existing inhibitors failed to inhibit DNMT2 within cellular assays, likely due to the low membrane permeability of zwitterionic SAH derivatives.[75] Notably, the most potent DNMT2 inhibitors reported to date exhibit enzymatic IC_{50} values (half maximal inhibitory concentration) in the range of 1.1 µM, indicating potential for further optimization of selectivity, permeability, and affinity.[74]



1
IC_{50} = 1.1 µM

2
IC_{50} = 12.9 µM

Figure 5. Inhibitors developed by Schwickert *et al.* for DNMT2.[74,75] Compound **1** is a covalent SAH-analogue, while compound **2** shows selectivity for DNMT2 over NSUN2 and NSUN6, though not against DNMT3. Owing to its high intrinsic reactivity, compound **1** forms covalent adducts not only with the catalytic cysteine but also with an additional cysteine residue of DNMT2.[74]

1.1.2 tRNA Methyltransferase D (TrmD)

Within the bacterial domain, TrmD represents a highly conserved tRNA Mtase present in Gram-positive and Gram-negative bacteria.[77,78] By contrast, TrmD is not found in eukaryotic or archaeal cells, in which its functional analogue is tRNA methyltransferase 5 (Trm5).[78] TrmD catalyzes the methyl group transfer from SAM to the N^1 nitrogen of guanosine at position 37 in tRNA, introducing the m^1G37 modification.[79] TrmD belongs to class IV Mtases, characterized by the typical SPOUT fold, and functions as a homodimer (Figure 6A, chain A in light green and chain B in grey).[80–82] A characteristic feature of this class is the presence of a trefoil knot formed in TrmD by three β-strands within the central

β-sheet (highlighted in dark blue and light blue in Figure 6A).[80–83] Crystallographic investigations revealed that each TrmD monomer comprises three distinct regions: an N-terminal domain (residues 1–160), a C-terminal domain (residues 169–246), and an interdomain linker (residues 161–168).[81–84] Both monomers are capable of binding SAM to the deep cleft of a trefoil knot in a bent conformation typical for SPOUT Mtases (Figure 6A).[80–83] However, only chain B is capable of binding tRNA by positioning the G37 base within its flexible linker region, which undergoes a conformational transition into a helical structure.[81,83] The interaction involves the knot of chain A, the N-terminal domains of both subunits, and the adjacent C-terminal domain of chain B.[81]

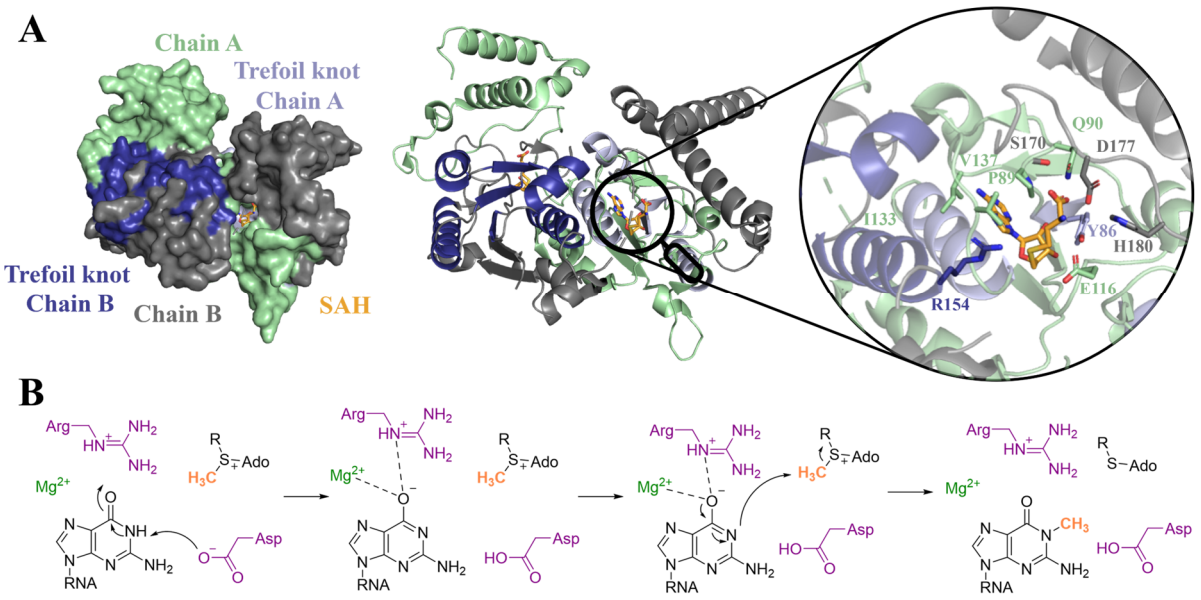


Figure 6. (**A**) *Haemophilus influenzae* TrmD crystal structure by Ahn *et al.* (PDB: 1UAL).[82] The two subunits are shown in light green (chain A) and grey (chain B). In each chain, the characteristic trefoil knot is highlighted – light blue in chain A and dark blue in chain B. SAH, shown in orange, binds in a bent conformation typical for SPOUT-class Mtases. (**B**) Catalytic mechanism of m^1G37 formation catalyzed by TrmD. The side chain of Asp169 in monomer B functions as a general base, activating the N^1 position of guanine for nucleophilic attack on the methyl group of SAM. The resulting transition state is stabilized by Arg154 and a coordinated Mg^{2+} ion.

Mutational analysis demonstrated that the knot is essential not only for SAM binding but also for the catalytic activity of TrmD.[84] Further studies revealed that substitution of Arg154 and Asp169 against alanine abolishes the enzymatic function of TrmD, and that Mg^{2+} is required for the methyl group transfer.[81,85] Based on these findings, a catalytic mechanism has been proposed, as illustrated in Figure 6B. The negatively charged side chain of Asp169 in monomer B acts as a general base, deprotonating the N^1 position of the guanine.[81] This results in a negative charge at the O^6 position, which is stabilized by the guanidine group of Arg154, also in monomer B, and by a coordinating Mg^{2+} ion.[81] The activated N^1 then performs a nucleophilic attack on the methyl group of SAM, leading to the formation of the m^1G37 modification.[81]

The m^{1}G37 modification introduced by TrmD plays a crucial role during translation. Translation is an essential step in protein biosynthesis, during which the ribosome decodes each set of three messenger RNA (mRNA) nucleotides into a single amino acid.[86] This process involves the stepwise translocation of tRNA molecules loaded with the respective amino acid from the aminoacyl (A) site to the peptidyl (P) site, and ultimately to the exit (E) site.[86] During elongation, so-called frameshifts can occur, wherein the ribosome shifts by one nucleotide relative to the mRNA. A shift in the 5′ direction results in a −1 frameshift, moving the ribosome backward, while a shift in the 3′ direction produces a +1 frameshift, advancing it forward (Figure 7).[83]

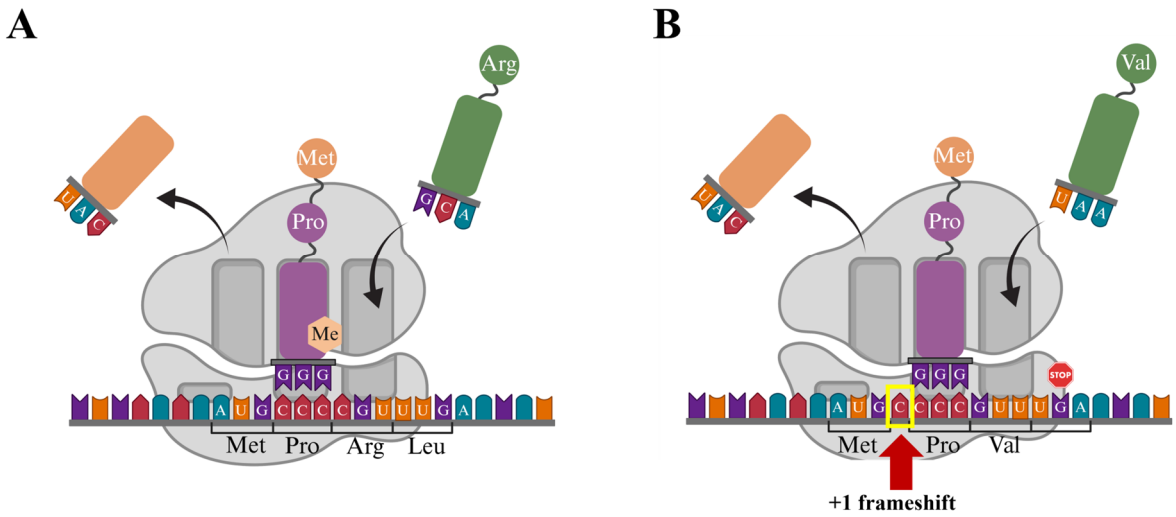


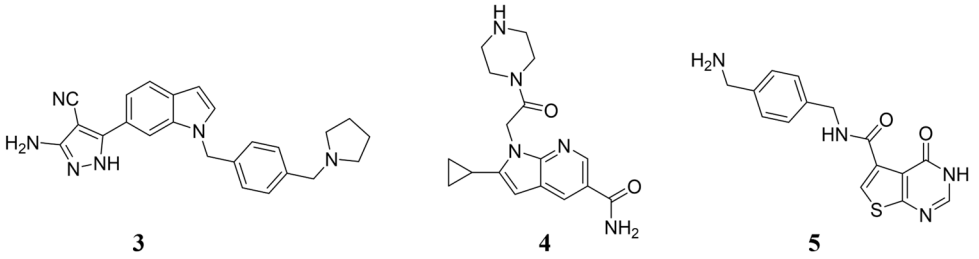
Figure 7. Translation in the absence (**A**) and the presence (**B**) of a +1 frameshift on the slippery mRNA sequence of CCC-C (proline codon). (**A**) In the presence of m^{1}G37 modification on tRNA^{Pro}, no frameshift occurs, allowing translation to proceed in the correct reading frame. (**B**) In the absence of m^{1}G37 modification, a +1 frameshift is induced, shifting the reading frame. This results in an altered amino acid sequence (Arg → Val) and in a premature stop codon (UGA).

Such frameshifting events serve as programmed mechanisms for regulating gene expression in bacteria.[83] Non-programmed frameshifts are translational errors that result from the shifting of the tRNA-ribosome complex on slippery mRNA sequences, such as CC[C/U]-[C/U] motifs encoding proline.[83,87] These frameshifting events are deleterious, as they disrupt the correct reading frame and can lead to premature stop codons within the coding sequence (Figure 7).[83,87] The m^{1}G37 modification introduced by TrmD is crucial for maintaining the translational reading frame by preventing frameshifting at the ribosome.[44,88,89] This modification is widely conserved in tRNA^{Pro}, tRNA^{Leu}, and tRNA^{Arg}, each exhibiting a high propensity to shift at slippery mRNA sequences.[44,88,89]

Owing to its key function in maintaining translational fidelity, TrmD is among the few enzymes indispensable for bacterial growth and survival across a broad range of species.[90–93] Its strict conservation among bacteria, essentiality for proliferation, and marked structural and mechanistic divergence from the human homolog Trm5 have established TrmD as a high-priority target for

antimicrobial drug development, offering a promising and selective therapeutic strategy with minimal risk of off-target effects.[82,83,94,95] Trm5 belongs to the class I Mtases characterized by the presence of a canonical C-terminal Rossmann fold (Figure 2A) in the active site and a linear binding conformation of SAM.[95]

Building on the promising role of TrmD as a drug target, the enzyme from *Staphylococcus aureus* (*S. aureus*) emerges as a particularly relevant candidate. However, most current knowledge is based on studies from *Escherichia coli* (*E. coli)* and *Haemophilus influenzae* (*H. influenzae*).[81,83,84] *S. aureus* is a widespread bacterial pathogen implicated in a broad spectrum of human infections, ranging from mild skin conditions to severe diseases such as pneumonia and cardiovascular infections.[96–98] The clinical management of *S. aureus* infections is highly challenging due to its multiple resistances to various antibiotics, often occurring in combination.[99,100] Of particular concern is methicillin-resistant *S. aureus* (MRSA), which ranks among the most clinically significant antibiotic-resistant pathogens.[97,100–102] Recent research campaigns have focused on the development of TrmD inhibitors for other bacterial species like *H. influenzae*, *E. coli*, *Mycobacterium abscessus* (*M. abscessus*), and *Mycobacterium tuberculosis* (Figure 8).[103–106] Whitehouse *et al.* focused on the development of *M. abscessus* TrmD inhibitors and identified compound **3** with an IC_{50} value of 27 nM, whereas Wilkinson *et al.* reported a nanomolar inhibitor (**4**) targeting *H. influenzae* TrmD.[103,104] Hill *et al*. focused on TrmD inhibitors targeting *H. influenzae*, identifying primarily thienopyrimidone-based compounds via fragment-based screening.[106] Notably, a compound **5** was identified, demonstrating an IC_{50} value of 7.5 µM against *S. aureus* TrmD, thereby representing a valuable starting point for future drug discovery campaigns.[106]



3 **4** **5**

IC_{50} (*M. abscessus)* = 27 nM IC_{50} (*H. influenzae)* = 13 nM IC_{50} (*S. aureus)* = 7.5 µM

Figure 8. TrmD inhibitors developed to date, with IC_{50} values for the corresponding TrmD enzyme. Compounds **3** and **4** were developed against *M. abscessus* and *H. influenzae* TrmD, respectively.[103,104] The thienopyrimidone-based compound **5** exhibits weak inhibitory activity toward *S. aureus* TrmD but lacks selectivity.[106]

1.1.3 Methyltransferase-like (METTL) Family

The METTL protein family is currently a focus of molecular, medicinal, and biochemical research. Members of this family are characterized by a conserved SAM-binding domain and are capable of modifying various RNA substrates (mRNA, tRNA, microRNA, rRNA, mitochondrial RNA).[107] These enzymes introduce distinct methylation patterns on RNA, such as m^6A (METTL3/14, METTL16, METTL5)[108–110], m^3C (METTL2, METTL6, METTL8)[111,112], m^7G (METTL1)[113], and m^4C (METTL15)[114]. Structurally, METTL proteins share a conserved seven-stranded β-sheet fold.[107,115] Despite these structural similarities, individual METTL family members exhibit divergent substrate specificities and functional roles, reflecting their involvement in a wide range of biological and pathophysiological processes.

METTL1

METTL1 is among the best-characterized members of the METTL protein family and introduces m^7G modifications in tRNA[113,116–118], microRNA[119], and mRNA[120,121]. The catalytic activity of METTL1 requires the presence of its non-catalytic subunit, WD-repeat domain 4 (WDR4), which is essential for the formation of an active Mtase complex.[113]

METTL1 is classified as a class I Mtase and accordingly adopts a conserved Rossmann fold architecture, characterized by a central seven-stranded β-sheet flanked by six α-helices (Figure 9A, highlighted in dark blue).[18] Its binding partner WDR4 exhibits a β-propeller architecture composed of seven blades (B1–B7), of which highly conserved blades B2 to B5 are in proximity to METTL1 (Figure 9A).[18] Notably, B4 mediates the interaction with METTL1, while B3 and B4 contribute to RNA binding (light blue and turquoise in Figure 9A).[18] Structural superposition of WDR4-bound and RNA-bound complexes revealed conformational rearrangements in METTL1 upon tRNA binding.[18] Specifically, four α-helices of METTL1 (α1, α2, α5, and α6) undergo a coordinated shift toward the tRNA molecule.[18] Additionally, a loop segment comprising residues 164–173, which connects α1 to the core of the Rossmann fold, adopts a short 3_{10}-helix conformation that is inserted into the groove of the tRNA elbow region.[18] The conserved N-terminal region of METTL1 (residue 1–33) is predicted to be disordered – complicating structural characterization by crystallography – and plays a critical role in the formation of the SAM binding pocket.[18,122] Li *et al*. demonstrated that, in particular, residues 16–27 are highly conserved and essential for METTL1's catalytic activity.[18] For the catalytic activity, residues Asp163, Glu240, and Arg109 are directly involved in stabilizing RNA (Figure 9).[18]

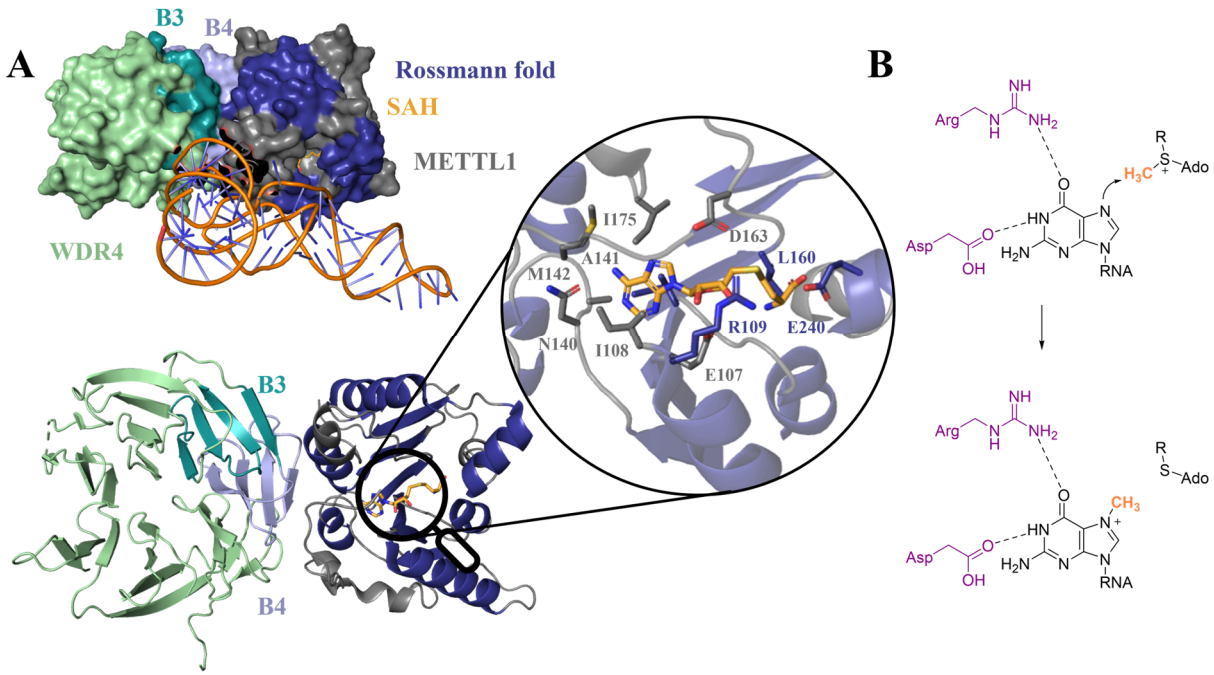


Figure 9. (**A**) Structure of the METTL1/WDR4 complex bound to $tRNA^{Phe}$ and SAH (Li *et al*., PDB: 8CTH).[18] METTL1 is shown in grey, and WDR4 in light green. The canonical Rossmann fold characteristic of class I Mtases is highlighted in dark blue. Two distinct β-propeller blades of WDR4 are involved in critical interactions: blade 4 (B4), engaging with METTL1, is colored light blue, and blade 3 (B3), which interacts with tRNA along with B4, is shown in turquoise. (**B**) Proposed catalytic mechanism of m^7G modification introduced by METTL1/WDR4. Residues Asp163 and Arg109 (purple) contribute to the stabilization of the tRNA, thereby facilitating the methyl transfer reaction.

In humans, the activity of METTL1 is regulated by a protein kinase B (AKT)-mediated Ser27 phosphorylation.[123] Ser27 is located in the N-terminal region and is part of the catalytic pocket.[18,123] Cartlidge *et al*. hypothesize that the phosphorylated Ser27 induces steric hindrance by clashing with the side chain of Arg109 or with the backbone of Ala21.[123] Several studies demonstrate that METTL1 is involved in many biological processes and has regulatory responsibilities in cardiomyocyte proliferation, DNA repair, neurogenesis, angiogenesis, and vitamin D metabolism.[115,124–127] METTL1 is a key regulator of pluripotency and differentiation in human induced pluripotent stem cells (hiPSCs) (Figure 10A).[126] Its function is mediated through m^7G methylation of tRNA and mRNA, which facilitates the efficient translation of essential pluripotency transcription factors such as octamer-binding transcription factor 4 (OCT4), sex-determining region Y-box 2 (SOX2), and Nanog.[115,126] Knockdown of METTL1 leads to a significant reduction in m^7G levels, resulting in impaired translation of these factors. Consequently, mesodermal differentiation is promoted, including the formation of new blood vessels, while neural ectodermal differentiation is inhibited.[115,126] Loss of METTL1 also accelerates the conversion of hiPSCs into endothelial progenitor cells and enhances the proliferation of vascular smooth muscle cells.[126] In addition, METTL1 influences key signalling pathways involved in stem cell maintenance, including bone morphogenetic protein 4 (BMP4), fibroblast growth factor 2 (FGF2), and wingless-type MMTV integration site family member 2 (WNT2), which are significantly downregulated

upon METTL1 depletion.[126] Together, these findings demonstrate that METTL1-mediated methylation plays a central role in maintaining stem cell identity. High METTL1 expression is markedly elevated across a wide range of human cancers, including acute myeloid leukemia (AML), hepatocellular carcinoma[128,129], bladder cancer[130], head and neck squamous cell carcinoma[131], and gastric cancer[132], and is frequently associated with poor patient prognosis and reduced overall survival.[107,133]

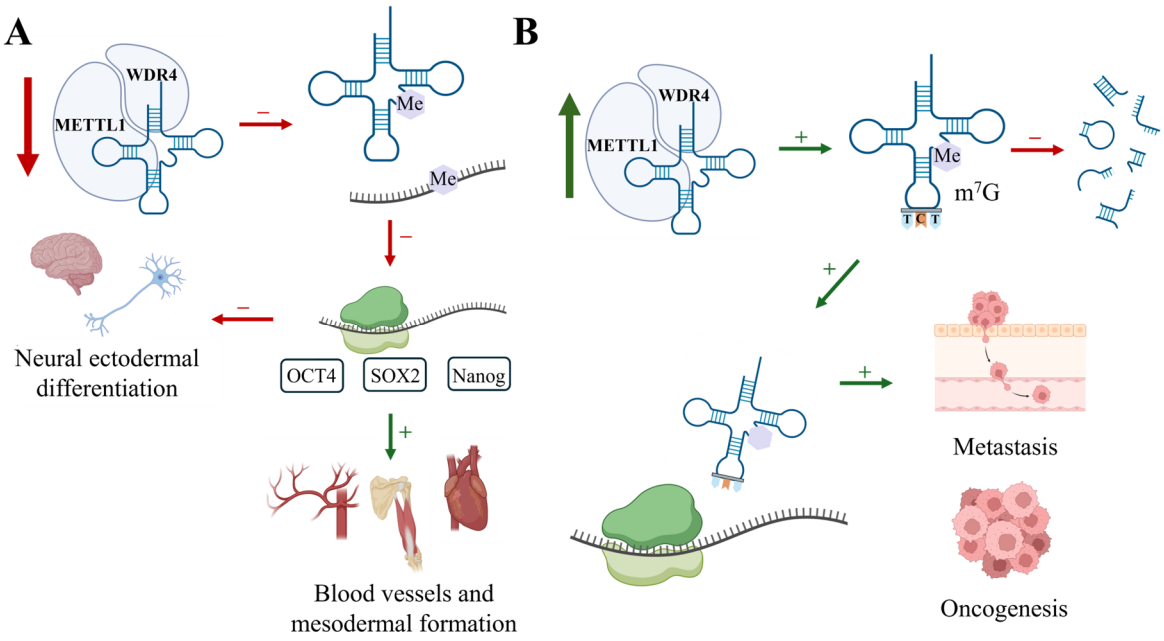
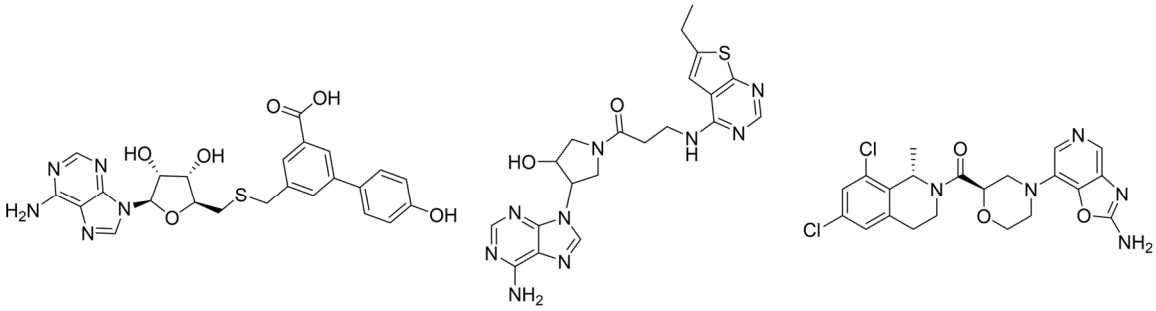


Figure 10. Physiological (**A**) and pathophysiological (**B**) roles of METTL1. (**A**) Regulatory function of METTL1/WDR4 in pluripotency and hiPSCs. Downregulation of METTL1 attenuates neural ectodermal differentiation while promoting blood vessel and mesodermal formation. (**B**) Medicinal relevance of the METTL1/WDR4 complex. The m^7G modification enhances the stability of Arg-TCT tRNA, thereby promoting efficient translation of mRNAs enriched in AGA codons and reshaping the tRNA pool. This translational reprogramming contributes to oncogenic transformation.

Mechanistically, METTL1 drives malignant transformation by catalyzing m^7G methylation on a subset of tRNAs, thereby altering the translational machinery of cancer cells (Figure 10B). Among these tRNAs, Arg-TCT, which decodes the AGA codon for arginine, has emerged as a particularly important contributor to tumor progression.[133] The m^7G modification enhances the structural stability and translational efficiency of Arg-TCT, enabling it to more effectively facilitate the translation of mRNAs with enriched AGA codons – many of which are involved in cell cycle regulation and oncogenic signalling.[133] Loss or knockdown of METTL1 leads to a global reduction in m^7G-modified tRNAs and impairs tumorigenesis in various *in vivo* models.[133] Furthermore, high METTL1 expression has been linked to enhanced tumor cell invasion, metastasis, chemoresistance, immune evasion, and dysregulation of autophagy.[107,128,134] These findings highlight METTL1 as a critical epitranscriptomic regulator of cancer progression.

Given the profound role of METTL1 in tumorigenesis, it is unsurprising that considerable efforts have been directed to develop inhibitors targeting this enzyme (Figure 11). Nai *et al*. conducted high-throughput docking studies using adenine derivatives alongside enzymatic assays with adenosine derivatives (e.g., compound **6**) and adenosine mimetics (e.g., compound **7**).[135] Their investigations identified inhibitors exhibiting IC_{50} values ranging from 41 µM to 277 µM.[135] All identified inhibitors demonstrate weak selectivity profiles; however, there remains considerable scope for improvement in binding affinity and specificity. In contrast, Storm Therapeutics conducted a structure-activity relationship (SAR) study on a series of compounds, among which compound **8** exhibited nanomolar affinity.[136]



6 IC_{50} = 41 µM

7 IC_{50} = 164 µM

8 IC_{50} = 13 nM

Figure 11. Inhibitors of METTL1 identified by Nai *et al*. (**6** and **7**) through high-throughput docking and enzymatic assays.[135] Compound **8** was discovered by Storm Therapeutics, showing nanomolar affinity.

METTL3/14

A Mtase attracting increasing attention in medicinal research is METTL3, the key enzyme responsible for m^6A modification of RNA.[108,137] METTL3 functions as part of a heterodimer with METTL14, which lacks intrinsic Mtase activity.[108,137] Studies suggest that METTL14 contributes to substrate recognition and facilitates RNA binding.[108,137,138] In addition, Wilms' tumor 1-associating protein (WTAP) forms a protein complex with METTL3/14 and is essential for the full catalytic activity of the complex.[139] Although WTAP does not possess catalytic activity, it plays a crucial regulatory role in modulating the function of METTL3/14.[139]

METTL3 and METTL14 form a pseudo-symmetric heterodimer, with each Mtase core adopting the characteristic class I Rossmann fold (Figure 12A highlighted in dark (METTL3) and light (METTL14) blue).[19] This fold comprises an eight-stranded β-sheet flanked by four α-helices.[19,140] METTL3 contains a zinc finger motif within the Mtase domain and two CCCH-type zinc finger motifs in its N-terminal region.[19] The catalytic site of METTL3 is located at the C-terminal ends of β-strands β1, β7, and β8.[19,140] In the binding pocket, SAM is stabilized through multiple hydrogen bonds, formed within two loops: one fully ordered (Arg508–Lys513) and one partially disordered (Asp395–Thr408).[19] The adenine

moiety of SAM is positioned in a hydrophobic pocket formed by Ile378, Pro397, Leu409, and Phe534 (Figure 12A), while hydrogen bonding of Asp377 and the backbone amide of Ile378 further stabilize SAM.[19,141] The ribose hydroxyl groups form hydrogen bonds with Asn549 and Gln550.[19]Although METTL14 adopts a nearly identical fold, it lacks catalytic activity due to steric hindrance preventing proper SAM binding.[19] Specifically, METTL14 does not feature residues capable of hydrogen bonding with the ribose hydroxyl groups of SAM.[19] Instead, METTL14 plays a role in RNA binding.[19,140] The ribose-phosphate backbone of the target RNA binds to a positively charged surface formed cooperatively by METTL3 and METTL14.[19,140]

For methyl group transfer, an interaction between Asp395 and SAM is essential.[19,140,141] Mutation of Asp395 to alanine has been shown to abolish METTL3/14's entire catalytic activity.[19] The carbonyl group of Asp395 forms a hydrogen bond with the N^6 position of the adenosine base in the target RNA, thereby facilitating the nucleophilic attack of N^6 on the methyl group of SAM (Figure 12B).[19]

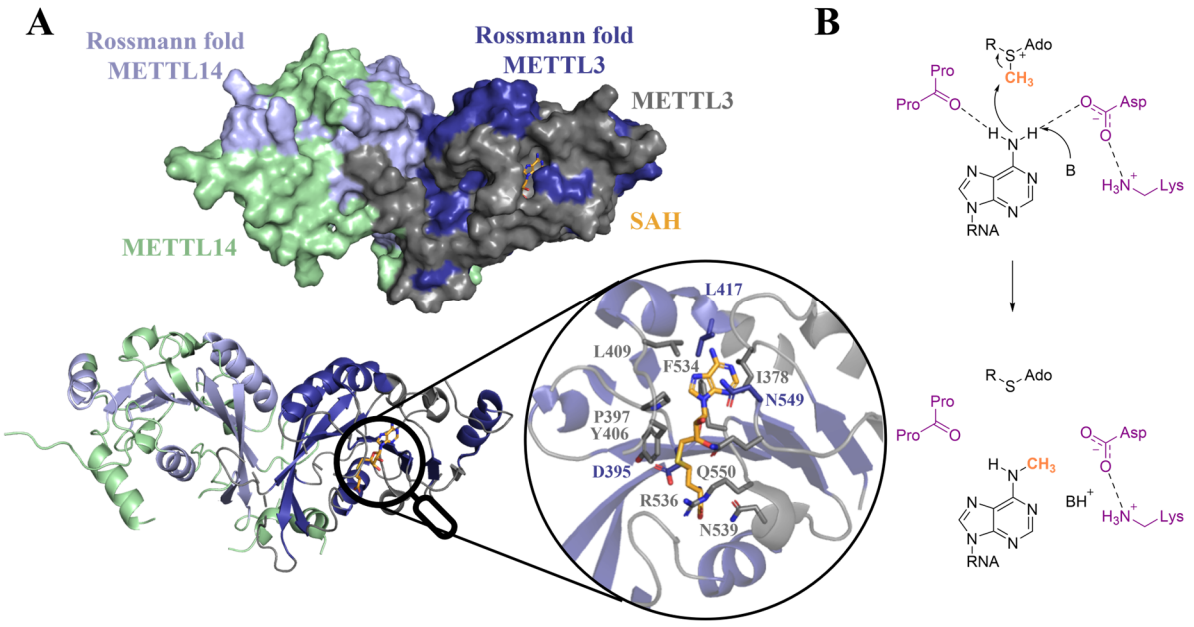


Figure 12. (**A**) Crystal structure of the METTL3/14 heterodimer (Śledź and Jinek, PDB: 5L6D).[19] METTL3 is shown in grey and METTL14 in light green. The respective Rossmann folds are highlighted in dark blue (METTL3) and light blue (METTL14). SAH is depicted in orange. (**B**) Catalytic mechanism of METTL3/14. The RNA is stabilized by Asp395, while the nucleophilic attack of N^6 is enabled by the interaction of the carbonyl group of proline.[19]

Numerous studies have investigated the role of METTL3/14 in biological processes, demonstrating its widespread involvement in diverse cellular functions.[142] The broad functional impact of METTL3/14 primarily originates from its involvement in multiple key signalling pathways, including Janus kinase/signal transducers and activators of transcription (JAK/STAT)[143], phosphoinositide-3-kinase (PI3K)/AKT[144], Wnt/β-catenin[145], and mitogen-activated protein kinase/nuclear factor κB

(MAPK/NF-κB)[146]. Due to their participation in these pathways, METTL3 contributes to a wide range of biological processes, such as adipogenesis[147,148], maintenance of pluripotency[149], brain function[150], and spermatogenesis.[151] Studies investigating the role of METTL3/14 in adipogenesis have shown that a knockout of METTL3/14 or WTAP induces cell cycle arrest during mitotic clonal expansion (MCE), thereby preventing preadipocyte differentiation *in vitro*.[148] Mechanistically, WTAP recruits the METTL3/14 complex to cyclin D1 mRNA, a key regulator of the cell cycle, to facilitate m^6A methylation.[148] The methylated transcript is subsequently recognized by YTH *N*^{6}-methyladenosine RNA binding protein 2 (YTHDF2) and degraded, resulting in cell-cycle arrest and inhibition of adipogenesis.[148] Furthermore, it was found that depletion of zinc finger protein 217 (ZFP217) increases METTL3 levels, enhancing m^6A methylation of cyclin D1 mRNA.[148] The interaction between METTL3/14 and ZFP217 also plays a crucial role in maintaining the pluripotency of stem cells.[149] In this context, ZFP217 modulates METTL3/14 activity and thereby influences the m^6A levels of key pluripotency genes.[149] ZFP217 depletion increases m^6A methylation of mRNAs encoding Nanog, Sox2, and Klf4, promoting their degradation and compromising embryonic stem cell (ESC) self-renewal.[149] Thus, low m^6A levels in ESC-associated transcripts support pluripotency and somatic cell reprogramming.[149] However, the precise mechanisms underlying the interaction between ZFP217 and METTL3/14 remain complex and not yet fully understood.

Given its extensive involvement in diverse cellular processes, it is not unexpected that METTL3 has also been implicated in a range of pathological conditions – most notably, cancer. Although the underlying mechanisms remain poorly understood, METTL3 has been reported to exhibit both upregulation and downregulation across various cancer types, suggesting a context-dependent role in tumorigenesis.[152–160] To illustrate the diverse and context-dependent roles of METTL3 in cancer, several examples are presented below. METTL3 has been identified as essential for the survival of AML cells.[155,161] Depletion of METTL3 induces cellular differentiation, promotes apoptosis, delays leukemic progression, elevates phosphorylated AKT levels, and activates the PI3K/AKT pathway.[161] The latter two have been shown to contribute to the pro-differentiation effects observed upon METTL3 loss.[161] The oncogenic role of METTL3 in human hepatocellular carcinoma (HCC) has been comprehensively investigated by Chen *et al*. (Figure 13, 2).[156] In this context, METTL3 catalyzes m^6A modification of the mRNA encoding suppressor of cytokine signalling 2 (SOCS2), a known negative regulator of the JAK/STAT signalling pathway.[156,162] The m^6A-modified SOCS2 transcript is recognized by the m^6A reader protein YTHDF2, which facilitates its degradation, thereby leading to a substantial reduction in SOCS2 expression.[156] The resulting attenuation of SOCS2 activity promotes hyperactivation of the JAK/STAT pathway, contributing to increased HCC cell proliferation, enhanced migration, and reduced overall patient survival.[156] The functional role of METTL3 in lung cancer was further elucidated by Wei *et al*., who demonstrated that METTL3 knockout in lung cancer cell lines impairs PI3K signalling, leading to reduced phosphorylation of AKT within the PI3K/AKT pathway (Figure 13, 1).[154,163] This

diminished phosphorylation of AKT results in increased expression of the pro-apoptotic protein Bcl-2-associated X protein (BAX) and decreased expression of the anti-apoptotic factor B-cell lymphoma 2 (Bcl2).[154] The resulting shift in the apoptotic balance promotes mitochondrial activation of caspase-3 (Cas3), resulting in suppressed apoptosis.[154] Collectively, these findings indicate that knockout of METTL3 triggers apoptosis via a mitochondria-dependent intrinsic pathway in lung cancer cells.[154] A mechanistically similar pathway was identified by Lin *et al*. in gastric cancer cells.[159]

Notably, METTL3 does not universally promote oncogenesis. Recent studies have demonstrated that METTL3 expression is significantly reduced in renal cell carcinoma (RCC), and higher METTL3 levels correlate with improved patient survival.[160] Upregulation of METTL3 suppresses tumor growth and metastasis.[160] Although the underlying mechanism remains unclear, Li *et al.* reported that METTL3 knockdown alters the expression of key components within the PI3K-AKT-mammalian target of rapamycin (mTOR) signalling pathway, suggesting that the tumor-suppressive effects of METTL3 may be mediated through modulation of this pathway.[160]

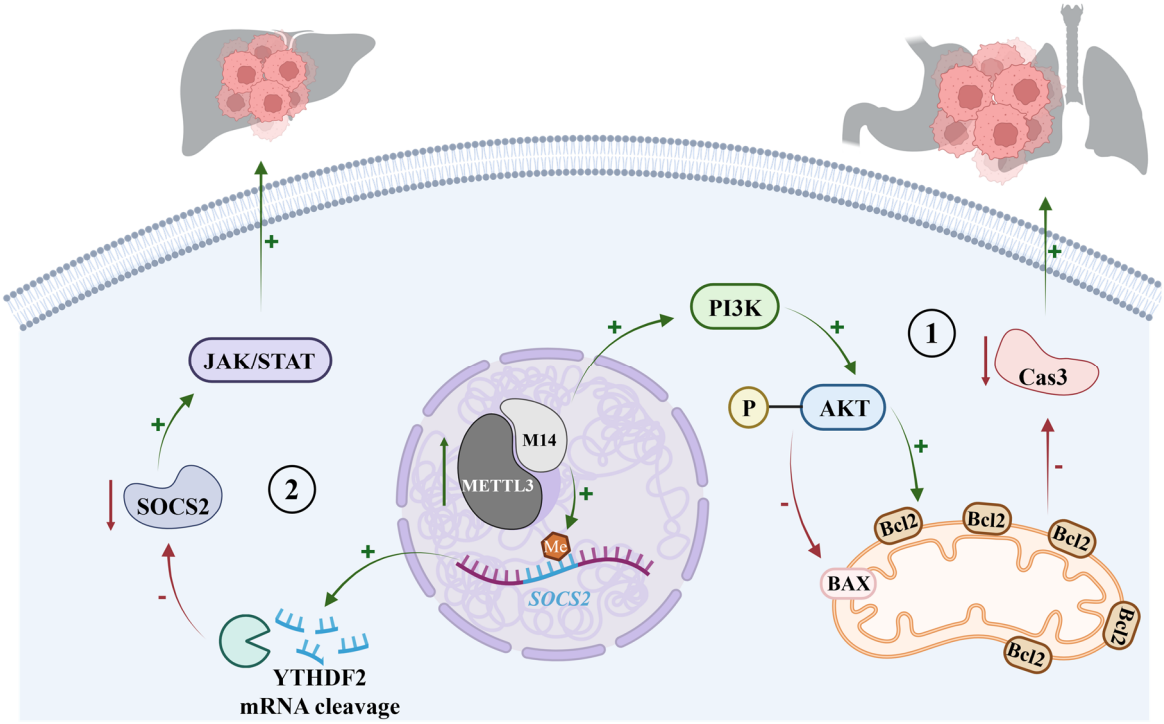


Figure 13. Context-dependent roles of METTL3 in oncogenesis. Two distinct molecular mechanisms by which METTL3 overexpression contributes to tumorigenesis are depicted. (**1**) Overexpression of METTL3 enhances PI3K signaling, resulting in increased phosphorylation of AKT. Activated AKT suppresses BAX and upregulates Bcl2, shifting the apoptotic balance and attenuating caspase-3 activation via the mitochondrial pathway. This promotes the survival of malignant cells.[154,159] (**2**) In the context of HCC, overexpression of METTL3 induces excessive methylation of SOCS2 mRNA. The modified transcript is targeted by the m^{6}A reader YTHDF2, promoting its degradation and thereby reducing SOCS2 protein levels. As SOCS2 normally acts as a negative regulator of the JAK/STAT pathway, its downregulation leads to pathway hyperactivation, resulting in increased proliferation and migratory capacity of HCC cells.[156]

Given the frequent overexpression of METTL3 across various cancer types, numerous drug discovery efforts have focused on inhibiting this RNA Mtase.[164–167] A high affinity and selectivity in this context was achieved by Storm Therapeutics, who initially identified STM1760 (IC_{50} = 51.7 µM) via a high-throughput screen of over 250 000 structurally diverse, drug-like compounds.[166] Subsequent optimization yielded STM2457 (**9**) and STM3006 (**13**), highly potent METTL3 inhibitors with IC_{50} values of 16.9 nM and 5 nM, respectively, and a favorable selectivity profile against 45 RNA-, DNA-, and protein Mtases (Figure 14).[166,168] Further development of Storm Therapeutics discovered STC-15 (**10**), which is currently undergoing clinical trials (Figure 14).[46,47] The Caflisch group screened over 4 000 SAM analogues and identified compound **11** with an IC_{50} of 8.7 µM.[165] A distinct approach of the group yielded UZH2 (compound **12**) through SAR optimization, exhibiting an IC_{50} of 5 nM.[169]

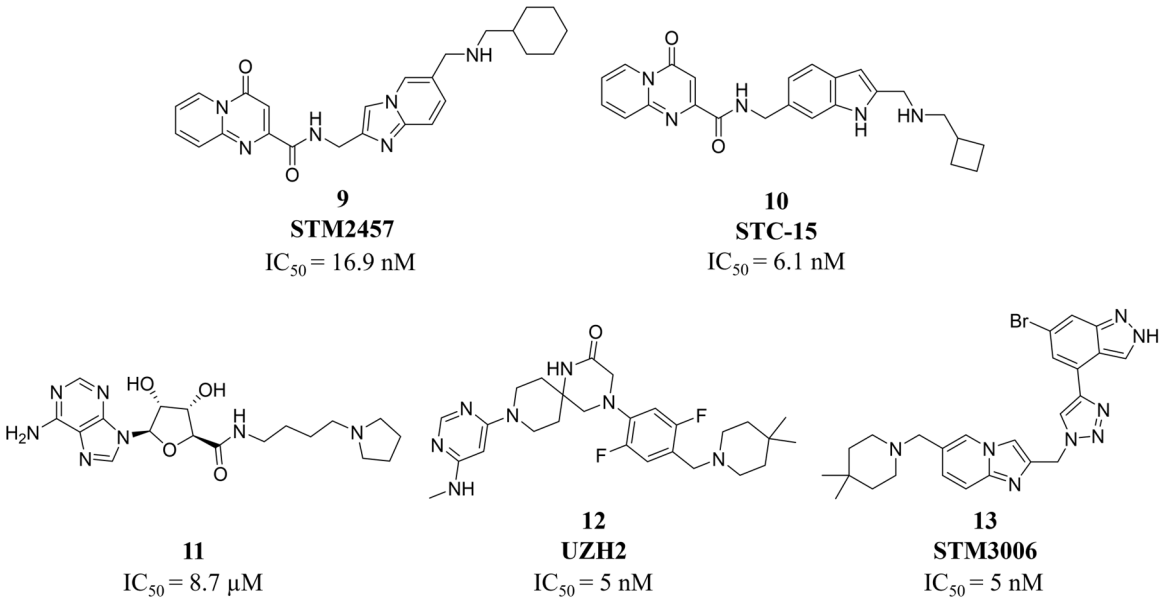


Figure 14. METTL3 inhibitors reported by Storm Therapeutics (STM2457, STM3006, and STC-15), the Caflisch group (UZH2 and compound **11**).

1.2 Limitations and New Modalities in Medicinal Chemistry

In summary, the evidence presented in the preceding sections highlights the widespread involvement of RNA Mtases in various pathological processes, particularly in cancer.[107,115,128,130,133,154,156,159] However, no RNA Mtase inhibitors have yet been approved for clinical use. The following sections explore potential reasons (1.2.1) and novel strategies in medicinal chemistry (1.2.2). Emerging strategies include proteolysis-targeting chimeras (PROTACs), DNA-encoded libraries (DEL), and Direct-to-Biology (D2B) strategies. The latter is presented in the form of a review article that was prepared during the doctoral studies and submitted for publication in *ChemMedChem.*

1.2.1 Limitations and Challenges in Targeting RNA Mtases

Classical medicinal chemistry approaches face inherent limitations in the rational design of Mtase inhibitors. Additionally, the lack of reliable Mtase-specific high-throughput screening platforms has significantly hindered the progress of identifying new inhibitor chemotypes.

Challenges of Classical Medicinal Chemistry

For many years, inhibitor design in classical medicinal chemistry has relied primarily on substrate or transition-state analogues, as well as on the screening of natural products for lead compound identification.[170,171] A prototypical example is the development of protease inhibitors, where rational design approaches such as the truncation of polypeptide substrates, the replacement of cleavable amide bonds with stable isosteres, and the systematic reduction of peptidic character through SAR studies were employed.[170] Structural analogues have played a central role in the development of various enzyme inhibitors, most notably against human immuno-deficiency virus (HIV)-1 protease.[172,173] These principles have also proven effective for other targets such as phosphorylases.[174–176]

The development of Mtase inhibitors is more challenging than it may seem, firstly due to the high intracellular levels of SAM and SAH that inhibitors must compete with.[177–179] The difficulty is further compounded by the fact that over 200 human Mtases utilize SAM, limiting the applicability of classical substrate- or transition-state-based inhibitor design strategies such as mentioned above.[180] This may, among other factors, explain why no SAM-like inhibitor is currently used in clinical practice. Nevertheless, SAM and pan-Mtase inhibitors such as SAH and sinefungin (SFG) have served as starting points for several drug discovery efforts (Figure 15).[181–183] A notable example of a SAM analog is EPZ004777 (**14**), which selectively inhibits the histone Mtase disruptor of telomeric silencing 1-like (DOT1L) with an IC_{50} of 0.4 nM.[184] DOT1L catalyzes methylation of histone H3 at lysine 79 (H3K79), and its inhibition has shown antileukemic activity.[184,185] This approach has also been applied to target the Mtases non-structural protein (Nsp) 14 and Nsp16 of severe acute respiratory syndrome coronavirus 2 (SARS-CoV-2), which methylate the N^7 position of the guanosine cap and the 2′-OH groups of the first two nucleotides of viral mRNA – modifications that prevent viral transcripts from degradation and immune detection (compound **15**, Figure 15).[186–188] However, none of the compounds in the study showed selectivity over the chosen off-target human glycine *N*-methyltransferase (GNMT).[188] Similarly, SAH-like inhibitors (e.g., **16**) have been successfully developed against nicotinamide *N*-methyltransferase (NNMT), which catalyzes the methylation of nicotinamide to 1-methylnicotinamide and is overexpressed in a broad spectrum of diseases (IC_{50} = 1.4 μM).[189–192] This compound displays selectivity over nuclear receptor-binding SET domain 2 (NSD2) and protein arginine methyltransferase 1 (PRMT1). For phenylethanolamine *N*-methyltransferase (PNMT), a transition-state

analogue inhibitor has been identified with nanomolar affinity.[193] PNMT catalyzes the SAM-dependent methylation of noradrenaline to adrenaline in the catecholamine biosynthetic pathway.[194]

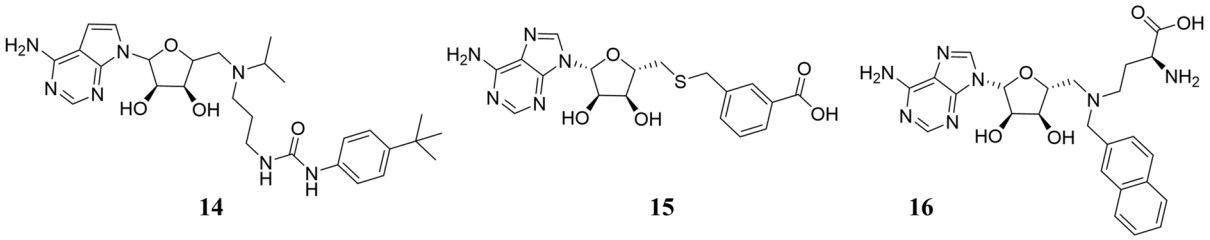


Figure 15. Examples of SAM/SAH-like inhibitors. Compound **14** (EPZ004777) inhibits the histone Mtase DOT1L. Compound **15** targets the viral Mtases Nsp16 (IC_{50} = 4.0 nM) and Nsp14 (IC_{50} = 8.0 nM), while compound **16** inhibits NNMT.

In summary, while the development of high-affinity SAM/SAH-like inhibitors is possible, ensuring selectivity continues to pose significant challenges. Additionally, several SAH/SAM analogs, such as those designed for DNMT2 (chapter 1.1.1), have not demonstrated efficacy in cellular contexts – presumably due to the limited permeability associated with their zwitterionic nature.[75]

Limitations of Conventional Mtase Characterization Methods

Among other challenges, the lack of reliable high-throughput screening (HTS) platforms has significantly impeded progress. Accurate measurement of modified RNA is inherently challenging because methylation causes only minimal changes to the physicochemical properties of the nucleosides, making their detection and quantification difficult. However, a limited number of assays have been reported in the literature for the identification of novel Mtase inhibitors and binders. Isothermal titration calorimetry (ITC) is an efficient method to measure the **binding affinities** of compounds to a Mtase.[195] ITC provides accurate, label-free measurements of the thermodynamics of molecular interactions.[195–197] However, ITC has high sample consumption and is described as low-throughput.[195,196,198] Another widely used strategy utilizes liquid chromatography/mass spectrometry (LC/MS) methods. Established protocols involve enzymatic hydrolysis of RNA and analysis based on retention times, UV absorbance in high-performance liquid chromatography (HPLC), and mass spectra.[199–201] Additionally, tandem MS (LC/MS-MS) techniques offer the opportunity of detecting and quantifying RNA methylation patterns with high sensitivity. A second approach involves the quantification of SAM and SAH by LC/MS[202,203], or via chromatographic separation followed by coulometric electrochemical detection.[204] Nevertheless, despite their analytical robustness, all these methods remain limited by low-throughput constraints due to instrument time requirements. A widely used method for assessing the **activity** of many RNA Mtases – and often referred to as the gold standard – is the tritium (^{3}H) incorporation assay.[3,74,106,205–208] In this approach, the methyl group of SAM is radioactively labeled with tritium and subsequently transferred to the respective RNA, which can be quantified using scintillation counting.[209] While the assay is highly

sensitive and well-established, it presents several drawbacks: it is inherently low-throughput, relies on the use of radioactive material, and is associated with high operational costs.

A more recent approach is the split-aptamer microscale thermophoresis (MST) assay developed by Nidoieva *et al.*.[210] In this method, SAH binds to split aptamers, which are labeled with carboxyfluorescein (FAM) and carboxytetramethylrhodamine (TAMRA) fluorophores, enabling detection via Förster resonance energy transfer (FRET) or MST.[210] Importantly, it enables the determination of enzymatic parameters such as the Michaelis-Menten constant (K_M) and catalytic turnover (k_{cat}), as well as the quantification of inhibitor potency through IC_{50} and K_I.[210] Additionally, an HTS strategy involves displacement experiments using an active-site tracer. The underlying principle of this approach is that increased displacement of the active-site tracer correlates with higher binding affinity of the tested compound. Zimmermann *et al.* have previously invented this method with an application to DNMT2, where the SAH-like tracer 5-FAM-triazolyl-adenosyl-diaminobutyric acid (FTAD) was developed as a fluorescent tracer.[211] This tracer binds selectively to DNMT2, showing minimal affinity for other Mtases.[211] The displacement can be measured using various experimental techniques, such as fluorescence polarization (FP) assays and MST assays.[211] However, this approach has so far been limited to DNTM2, as FTAD remains the only reported tracer.

1.2.2 New Approaches in Medicinal Chemistry

As described in the previous chapters of this thesis, classical drug development of RNA Mtases is hampered by the lack of new lead structures and HTS suitable methods. The following three chapters are dedicated to three new approaches currently gaining increasing scientific attention, including PROTACs, D2B strategies, and DEL technology.

Proteolysis-Targeting Chimeras (PROTACs)

Heterobifunctional degraders such as PROTACs represent a novel modality in medicinal chemistry. PROTACs are composed of two distinct ligands – one that binds the protein of interest (POI) and another that recruits an E3 ubiquitin ligase (E3) – covalently connected by a linker with different chemical properties regarding length, rigidity, and composition.[212–215] These bifunctional molecules hijack the endogenous ubiquitin-proteasome system to induce the degradation of targeted proteins.[212,213] Mechanistically, PROTACs induce the formation of a ternary complex comprising the POI and the E3, thereby positioning the ubiquitination machinery in proximity to the POI.[212,213] This proximity facilitates polyubiquitination of the target, leading to its subsequent recognition and proteolysis by the 26S proteasome (Figure 16A).[212,213] Following substrate degradation, the PROTAC molecule is released and can act catalytically to engage in further degradation cycles.[212,213] In contrast to conventional small-molecule inhibitors, which rely on occupancy-driven pharmacology, PROTACs operate through an event-driven mechanism of action.[212,213] By functioning in a catalytic manner, PROTACs can achieve

target depletion at lower concentrations, thereby potentially minimizing off-target effects and reducing dose-related side effects compared to conventional inhibitors.[216]

In the design of PROTACs, ligands derived from known binders of the POI are frequently employed in combination with various E3 ligase-recruiting moieties. However, the optimization and rational design of PROTACs often remain empirical, characterized by substantial trial and error and limited predictability.[217] Among the E3 ligases exploited to date, cereblon (CRBN) and von Hippel-Lindau (VHL) are the most commonly targeted, although examples involving mouse double minute 2 homolog (MDM2) and cellular inhibitor of apoptosis proteins 1 (cIAP1) have also been reported.[214,218–221] CRBN-recruiting ligands are typically derived from the phthalimide scaffold, including thalidomide and its derivatives lenalidomide and pomalidomide, whereas VHL ligands are commonly based on thiazolidinedione-containing chemotypes.[218,219] Another unpredictable factor in PROTAC design arises from the phenomenon of cooperativity.[213] In this context, favorable or repulsive interactions between the POI and the E3 influence the stability and formation of the ternary complex.[213] Positive cooperativity occurs when interactions between the POI and the E3 promote ternary complex formation. Moreover, the so-called hook effect represents an additional factor impacting PROTAC performance.[222,223] At elevated PROTAC concentrations, excessive formation of unproductive binary complexes (PROTAC-POI or PROTAC-E3) can hinder productive ternary complex formation, thereby reducing overall degradation efficiency.[222] Notably, positive cooperativity can shift the onset of the hook effect to higher concentrations, thereby extending the effective concentration range of the degrader.[222]

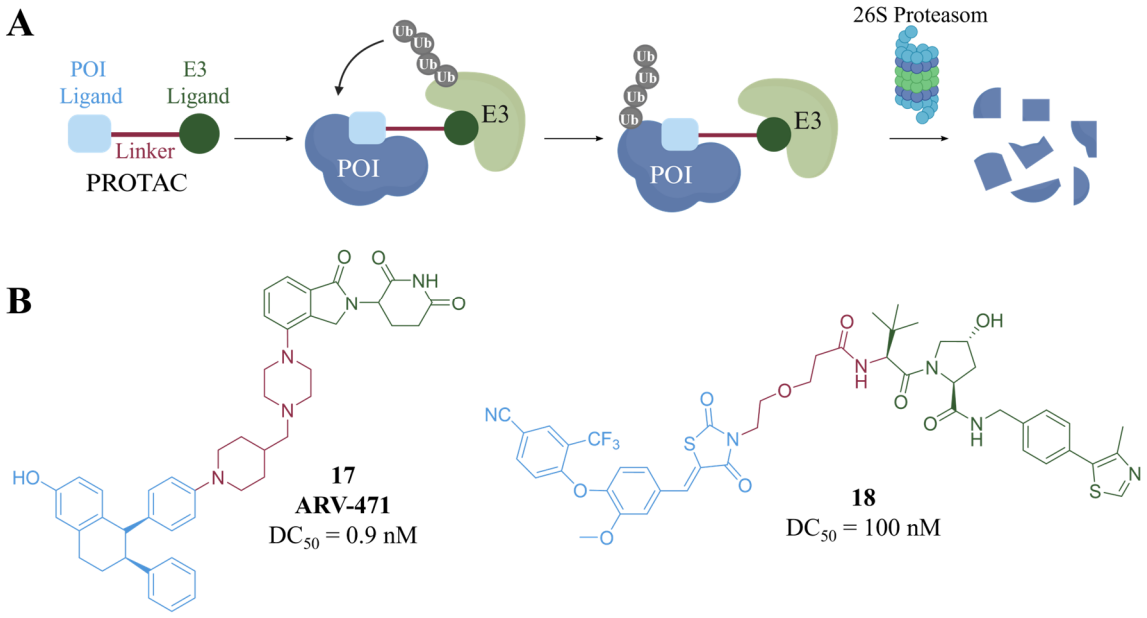


Figure 16. Functional principle and selected examples of PROTACs. (**A**) Mechanism of action of PROTACs. The heterobifunctional molecule comprises a ligand for the POI (light blue) and a ligand for an E3 (dark green), connected by a linker (red). Formation of the ternary complex facilitates E3-mediated ubiquitination (Ub) of the POI, thereby marking it for subsequent degradation by the 26S proteasome. (**B**) Representative PROTAC structures. ARV-471 (**17**) exemplifies a CRBN-recruiting PROTAC, whereas compound **18** incorporates a VHL-binding moiety.

Several examples of PROTACs – particularly those employing VHL or CRBN E3 recruiters – have been reported in the literature. Numerous highly potent CRBN-based PROTACs have been described, including ARV-471 (**17**, vepdegestrant, Figure 16B), which has completed clinical trials.[224–227] ARV-471 targets the estrogen receptor and exhibits picomolar degradation activity across multiple breast cancer cell lines.[224,225] Likewise, a bromodomain-containing protein 4 (BRD4)-targeted PROTAC derived from birabresib, an established BRD4 inhibitor, displays picomolar DC_{50} values.[219] Notably, this molecule exemplifies the catalytic mode of action of PROTACs: despite binding affinities of only 30–90 nM for BRD4 and approximately 3 µM for CRBN, it achieves a DC_{50} smaller than 1 nM.[219]

VHL-recruiting PROTACs have also been developed. For example, a VHL-based PROTAC (e.g., **18**) targeting estrogen-related receptor α (ERRα) exhibits a DC_{50} of 100 nM and induces target degradation in mouse models.[218] Additional VHL-based PROTACs include a receptor-interacting serine/threonine-protein kinase 2 (RIPK2) degrader with a D_{max} of 95% at 10 nM, as well as BRD4-directed degraders based on the known inhibitor JQ1 as POI-ligand.[218,228]

Direct-to-Biology (D2B) Strategies

In D2B workflows, large compound libraries are generated via parallel synthesis, typically in well plate formats. These compounds are not or only minimally purified and are directly evaluated in biological assays. This chapter is incorporated as a review article.

Own contribution: Writing and Figure design of the chapter “Applications of Direct-to-Biology: Target-Specific Insights”.

Contributions from other authors: Writing and Figure design of the chapters “Introduction & History”, ”Current Landscape of Direct-to-Biology Research”, and “Limitations and Outlook of Direct-to-Biology”.

This work has been submitted to *ChemMedChem* (impact factor: 3.4).

The following manuscript quoted within "" from page 23 to page 40 was submitted for publication with *ChemMedChem*. "

Direct-to-Biology: Streamlining the Path from Chemistry to Biology in Drug Discovery

Ariane F. Hübner,[a] and Fabian Barthels*[a]

[a] Ariane F. Hübner, Dr. Fabian Barthels
Institute of Pharmaceutical and Biomedical Sciences (IPBS)
Johannes Gutenberg-University, Mainz
Staudingerweg 5, 55128 Mainz
E-mail: barthels@uni-mainz.de

Abstract: Direct-to-Biology (D2B) has emerged as a transformative concept in early drug discovery, defined by the direct on-target screening of crude reaction mixtures without prior purification. First coined in 2021, the approach builds on advances in nanoscale synthesis platforms and was shaped by seminal studies that demonstrated the feasibility of plate-based microscale chemistry for library generation. Today, D2B is increasingly adopted in academia and industry, with campaigns exploring diverse reaction classes, targeting modalities, and assay platforms. Thus, very recently, the first commercial providers now offer D2B services for ligand optimization, further driving adoption. Yet, despite clear advantages in speed, cost, and sustainability, D2B also faces limitations from assay interference and technical constraints in reaction miniaturization. Looking ahead, integration with AI-driven design and high-content biology promises to expand the scope of D2B and position it as a robust complement to traditional discovery paradigms.

1. Introduction & Origin

Direct-to-biology (D2B) denotes workflows in which newly, in-parallel synthesized compounds, often as crude reaction mixtures or minimally purified products, are tested directly in biological assays, collapsing the traditional make-purify-test cycle into rapid make-test loops. The initial origin of the term is disputed, but it was popularized in a 2021 publication by Bush and co-workers through a GSK pharma-led "D2B-HTC" platform that generated >1,000 molecules in 384-well plates within 24 h and screened them without purification against drug targets, establishing practical feasibility and a vocabulary for the field.[1] Conceptually, D2B rests on advances in nanomole-scale, high-throughput wellplate-based synthesis that matured over the 2010s publications introducing synthetic technologies for high-throughput plate-based synthesis, yet without a dedicated biological confirmation of synthesized molecules.[2–7] From roughly 2014 to the seminal definition of "Direct-to-Biology", the groundwork for a more integrated synthesis-to-screening paradigm was quietly laid by a series of incremental but conceptually aligned studies:
In 2014, an off-rate screening (ORS) by surface plasmon resonance introduced a kinetic hit-to-lead sampling directly from unpurified reaction mixtures, foreshadowing the idea of extracting biologically relevant information from crude products.[8] That same year, the activity-directed synthesis (ADS) concept was introduced by Nelson et al., wherein reaction arrays were screened for function, and only the most promising crude mixtures were scaled up and purified, demonstrating a bioactivity-guided synthesis loop.[9–15] In the following years, several publications with similar concepts were published.[16–22] This trend crystallized in 2018 with Cernak and colleagues' Nature study coupling nanomole-scale reactions to affinity-selection bioassays, thereby ranking drug potency without time-intensive purification.[23] This early-stage concept (first dubbed by Cernak as "nanoSAR" and later as "Direct-to-Biology") demonstrated that chemical and biological readouts can be tightly integrated at a reaction scale, a core D2B tenet.[23] Yet, D2B is distinct from other nanoscale high-throughput library generation methods such as DNA-encoded libraries,[24] bead-based & split-and-pool-derived immobilized libraries,[25] or prefabricated peptide/nucleic acid arrays[26]: whereas these other approaches typically decouple synthesis from screening e.g., by solid-phase or nucleic-acid immobilization, D2B emphasizes on-the-fly synthesis in plate-based layouts with immediate biological readout, enabling fast, iterative design-make-test cycles with minimal material and maximal learning per experiment.

2. Current Landscape of Direct-to-Biology Research

In this review article, we summarize research publications that use the terms “direct-to-biology” or “nanoSAR” in the title or main body, published through November 2025. We analyzed D2B publications, encompassing both peer-reviewed articles, patents, and preprints describing *in situ* synthesis campaigns coupled to immediate biological evaluation (N=41). Publications were annotated across multiple categories and dimensions; hence, a medicinal chemistry-focused analysis of the D2B landscape is depicted in Figure 1.

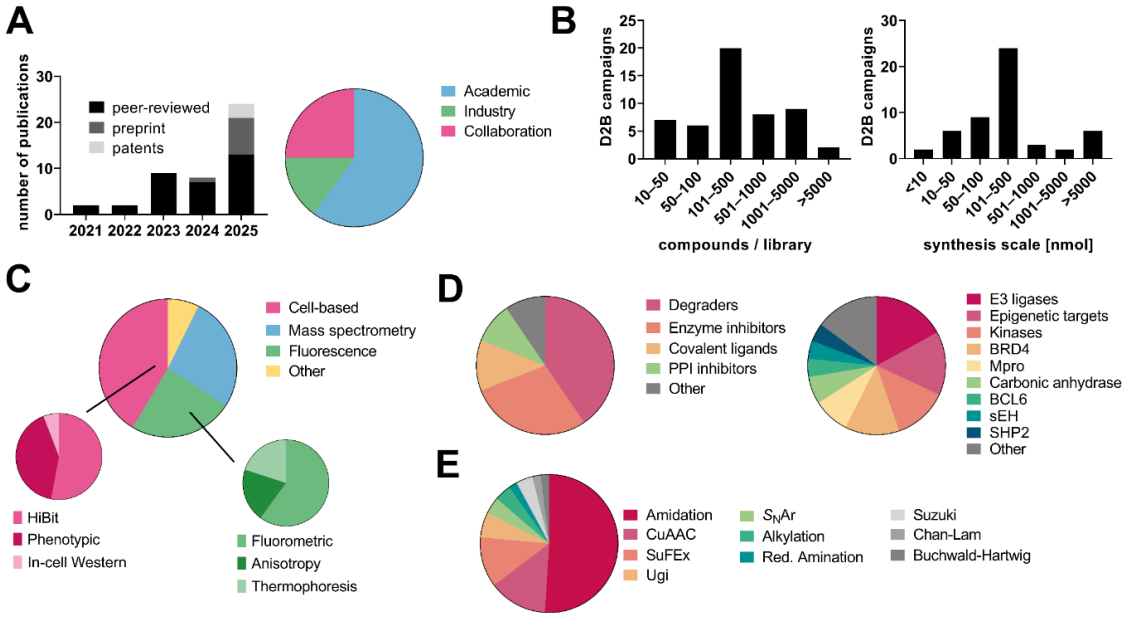


Figure 1. Current landscape and analysis of the direct-to-biology research. (**A**) D2B publication format dynamics and authorship proportions. (**B**) Library size and reaction scales of published D2B campaigns. (**C**) Assay modalities for D2B biological evaluation per screening campaign. (**D**) Target landscape and modalities per screening campaign. (**E**) Reaction chemistry per D2B campaign.

Publication dynamics & authorship. Annual output increased from the first denoted D2B publication in 2021 to ~20 publications/year in 2025. The inflection in 2023/2024 coincides with the very recent adoption of nanoscale synthesis and campaign-style optimization. Industry submissions and mixed academic-industry collaborations account for ~40% of D2B campaigns, highlighting that both academia and pharmaceutical industries are interested in this concept. Yet, so far, no significant differences regarding time-to-data metrics and methodological diversity could be noticed to distinguish academic from industrial D2B campaigns.

Library sizes and reaction scales. Current D2B campaigns span library sizes from min. 50 to >5000 compounds (median 100–500 compounds/library). Reaction scales cluster at the triple-digit nanomole scale for most campaigns, but depending on the application, can be as low as 1 nmol or as high as 10 µmol. Notably, campaigns with library size >500 predominantly operate at ≤500 nmol per reaction, underscoring the coupling between throughput and material economy applicable for 96- or 384-well-based synthesis layouts.

Reaction chemistry. The dominant D2B transformations are currently amide formations (50% of campaigns), copper-catalyzed alkyne-azide click chemistry (CuAAC, 15%), sulfur(VI)fluoride exchange (SuFEx, 12%), and other late-stage diversification chemistries followed by diverse arylation, alkylation, amination, and C-C cross-coupling reactions. Notably, this aligns well with the frequency of reaction types used in conventional medicinal chemistry SAR studies, but still diverges from the frequency of preferred chemotypes found in approved drugs.[27,28]

In general, selection of chemistry reflects the need for (i) biocompatibility with downstream assay technologies, (ii) robustness at the nanomole scale, mostly in well-plates, and (iii) clean conversion profiles suitable for testing minimally purified mixtures. Over the past five years, the field has observed a slight shift toward click-like transformations and an uptick in C-N/C-C cross-couplings enabled by improved microscale synthesis protocols.

Assay modalities. Cell-free assays remain prevalent, with fluorescence-based readouts (25%) and mass spectrometry (30%) dominating early triage; cell-based assays constitute 40%, increasingly used

for PROTAC screening or phenotypic profiling. In more detail, fluorescence-based assays use either fluorometric, anisotropic, or thermophoretic readouts. Meanwhile, cell-based assays mostly characterize biological effects using phenotypic or HiBit screening technologies. Among other assays (5%), luminescence and high-throughput crystallographic screening represent two rarely used assay modalities coupled with in situ D2B synthesis.

Target landscape and modalities. Classical inhibitor campaigns predominate in absolute number (60%) while reversible small molecule ligands only constitute half of those campaigns, and covalent and protein-protein-interface ligands form the other half. Targeted degraders-oriented campaigns (molecular glues and PROTACs) constitute 40% of D2B publications and typically use convergent assembly (e.g., linker diversification, also known as "linkerology") under nanoscale conditions to explore E3/warhead/linker space efficiently. Beyond E3-ligases and BRD4-targeting PROTACs, kinases and epigenetic enzymes account for 14% and 12% of addressed targets, often expanding fragment-like D2B libraries.

Emerging picture. The field is transitioning from demonstration-scale experiments to platformized, iterative D2B workflows: small, robust reaction sets at nanomole scale; rapid, mostly purification-sparing analytics; and assay choices that tolerate residual matrix. Recently, several commercial providers, including Concept Life Sciences, Domainex, WuXi AppTec, and Molecule.one, have begun to offer D2B-based synthesis services specifically for the commercial optimization of existing ligands, further underlining translational traction and the potential for broader adoption in pharmaceutical and academic pipelines.[29–32] Together, these trends point to D2B as a complement to conventional library-based discovery, optimized for fast learning cycles per unit material.

3. Applications of Direct-to-Biology: Target-Specific Insights

3.1. Kinase Inhibitors

Kinases are among the most prominent and well-characterized target families in medicinal chemistry, due to their central role in cellular signaling and druggability for cancer-related diseases, and hence, their biological relevance makes them also attractive targets for D2B strategies.[33,34] Several D2B campaigns have been applied to kinase targets, including Proteolysis targeting chimeras (PROTAC)-based approaches (detailed in chapter 3.3.1. "PROTACs") as well as compound libraries derived from known inhibitors of Mitogen-activated protein kinase kinase 7 (MKK7) and Cyclin-dependent kinase 2/Cyclin E (Cdk2/CycE).[35–40]

In one of the first influential studies coining the term "nanoSAR", Gehrtz et al. used a covalent ibrutinib derivative (1), bearing an acrylamide warhead and alkyne handle, to generate inhibitor analogues via copper(I)-catalyzed azide-alkyne cycloaddition (CuAAC) to target MKK7 (Figure 2A).[35] Using a droplet-ejection system, they coupled 448 commercially available azides in a 384-well format and screened the crude mixtures directly using an in-cell Western assay. CuAAC is particularly suitable for D2B efforts due to its high efficiency, aqueous compatibility, biocompatibility, non-toxic reagents, and the broad commercial availability of azide libraries.[41,42] This MKK7-targeting strategy yielded potent inhibitors with IC_{50} values of 3–4 nM (compound 2) and EC_{50} values of 265–380 nM, which displayed major improvements compared to the parent compound 1 (EC_{50}>10 µM).[35] Furthermore, co-crystal structures with MKK7 were elucidated, providing insights into their binding modes (Figure 2A).

During a second kinase-targeting D2B study, Douthwaite et al. applied this concept to explore Cdk2/CycE inhibitors (Figure 2B).[36] Through a high-throughput combinatorial screen, they coupled six aminopyrazole cores (compound **3** among others, Figure 2B) with 128 carboxylic acids to generate a 768-membered library. To maximize reaction efficiency, they systematically combined different bases (DIPEA, NMI) with coupling reagents (CDI, HATU), achieving a synthetic success rate of 90% using an automated liquid handling system. The crude reactions were tested with ADP-Glo and off-chip Caliper mobility-shift assay, and subsequently were tested orthogonally using an Affinity Selection-Mass Spectrometry assay (ASMS). Notably, during this study, ligand-containing crystal structures could also be obtained directly from crude reaction mixtures (compound **4** in Figure 2B).

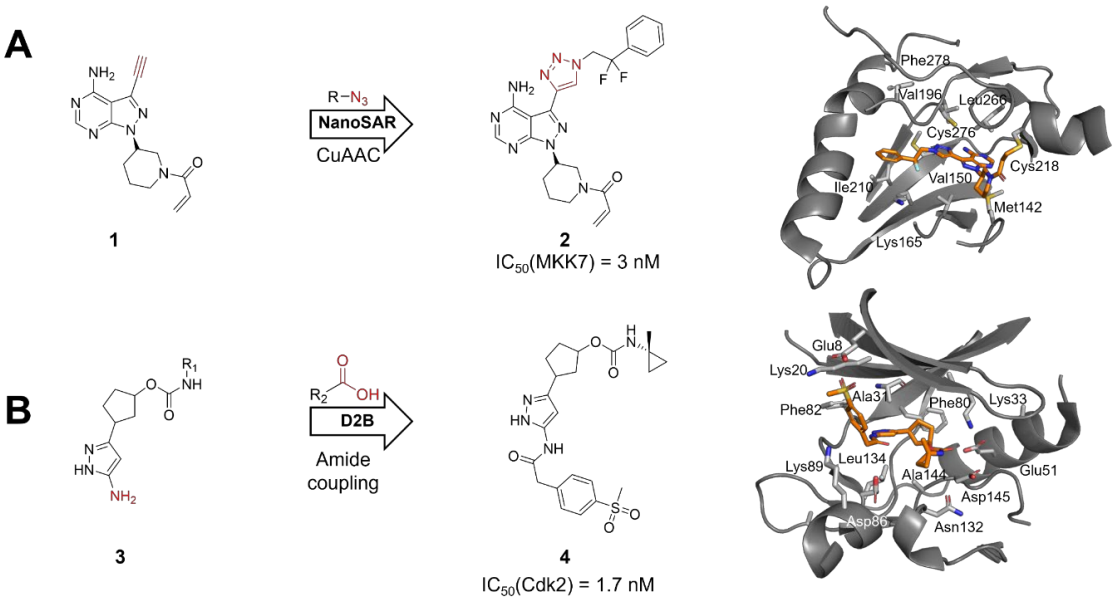


Figure 2. D2B campaigns targeting kinases. (**A**) Optimization scheme and X-ray crystal structure (PDB: 7OVJ) of the CuAAC nanoSAR campaign reported by Gehrtz et al. targeting MKK7.[35] (**B**) D2B campaign conducted by the Cernak group targeting CDK2 via amide diversification, resulting in compound **4** (X-ray crystal structure PDB: 9OB2).[38]

3.2. SARS-CoV-2 Main Protease (M^{pro}) Inhibitors

The COVID-19 pandemic has sparked intense interest in antiviral drug development, particularly targeting the main protease (M^{Pro}) of SARS-CoV-2, which plays an essential role in viral replication.[43,44] Accordingly, multiple D2B approaches have been employed to explore this enzyme as a therapeutic target, while notably, several of these D2B campaigns have employed nanoscale synthesis, which relied on amide coupling reactions to generate libraries of diverse amide derivatives.[45–48]

Recently, Bush and coworkers have applied a distinct D2B strategy starting from cysteine-targeting chloroacetamide reactive fragments (RFs) to identify covalent (Figure 3) and non-covalent (Figure 4) M^{Pro} inhibitors.[48] An initial screen of 219 purified RFs yielded a covalent hit, which was elaborated via a D2B library of 193 amines reacted with the *N*-hydroxysuccinimide ester of chloroacetic acid to form chloroacetamide-decorated inhibitors. Screening of these inhibitor candidates by intact protein LC/MS identified M^{Pro}-targeting compound **5** with an IC_{50} smaller than 39 nM (Figure 3B). It is noteworthy that, beyond M^{Pro}, this covalent inhibitor-focused D2B screening strategy could be harnessed for multiple other targets (including TRIM25, SspH1, BCL6, and WRN) and diverse electrophilic warheads (including chloroacetamides, acrylamides, and sulfonyl fluorides).[48–52] The most potent covalent D2B inhibitors (**5**–**10**) are summarized in Figure 3B and described in detail in the respective chapters 3.3–3.7.

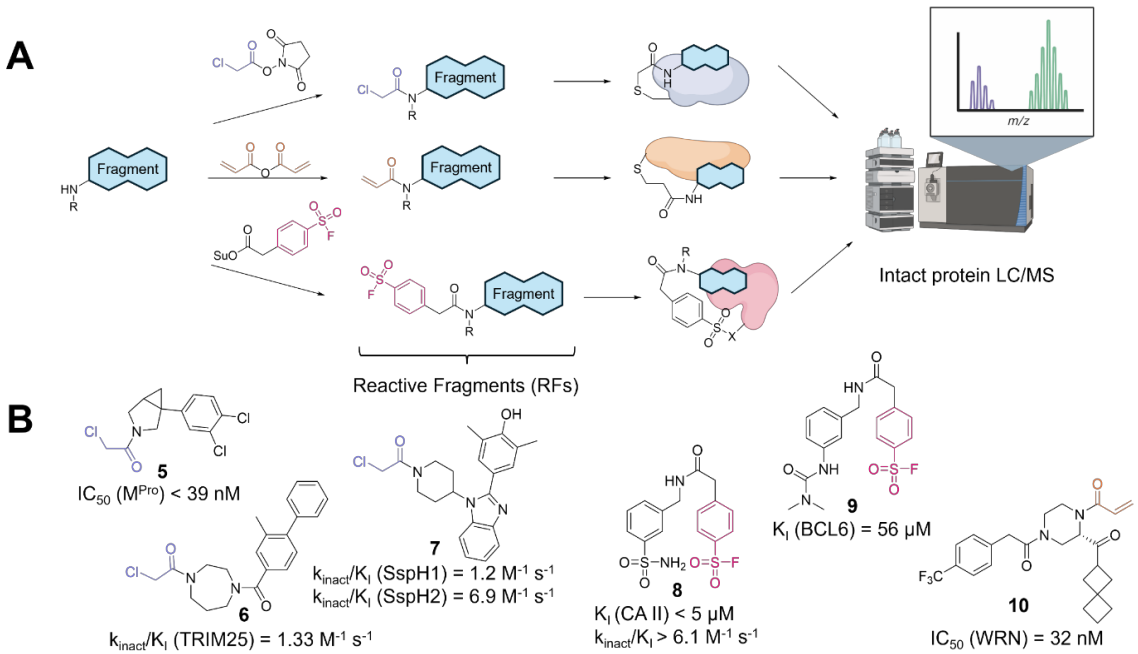


Figure 3. Reactive fragment (RFs) screening strategy introduced by Bush and co-workers. (**A**) Scheme illustrating the workflow of different RF-D2B strategies (chloroacetamides, acrylamides, and sulfur(VI) fluorides). Fragments containing amine groups are reacted with a covalent warhead transfer reagent to form a nanoscale library of the corresponding RF, which is incubated with the target enzyme and analyzed by intact protein LC/MS. (**B**) Covalent D2B inhibitors identified by multiple RF-D2B screenings on different target enzymes.[48–52]

Subsequently, to discover non-covalent M^{Pro} inhibitors, a cascade D2B campaign was performed in which the covalent warhead of the initial hit **5** was replaced, followed by HATU-mediated amide coupling with two iterative carboxylic acid libraries (first 146 diverse building blocks and subsequently 72 focused candidates), ultimately yielding non-covalent inhibitor **12** with a K_I of 110 nM (Figure 4A).[48] In this context, another amidation-focused D2B study of the Cernak group started from a previous *in silico* screening campaign, and, through RapidFire MS-based screening, identified a hit compound with an IC_{50} of 5.06 µM.[45]

Two additional M^{Pro} targeting publications, including the open-science COVID Moonshot initiative and a study led by the King-Smith group, were also utilizing amidation-stirred D2B optimization of M^{Pro} inhibitors.[46,47] These amidation-stirred campaigns yielded compounds with binding affinities in the low nanomolar range, targeting the P3/P5 pocket of M^{Pro} (e.g., compound **17**, IC_{50}=28 nM).[46,47] The COVID Moonshot project not only employed amide coupling but also pioneered another chemically distinct D2B strategy, uniquely applying a Chan-Lam to compound **14** derived from a fragment-based crystallographic screen (compound **13**) (Figure 4B,C).[46] This led to compounds targeting the P4 pocket of M^{Pro}, with the most potent compound **15** exhibiting an IC_{50} of 387 nM (Figure 4B). It is worth noting that the amide coupling reactions were overall more successful than the Chan-Lam reactions, with 151 out of 300 reactions yielding >30% product compared to only 29 out of 300 for the Chan-Lam transformations.

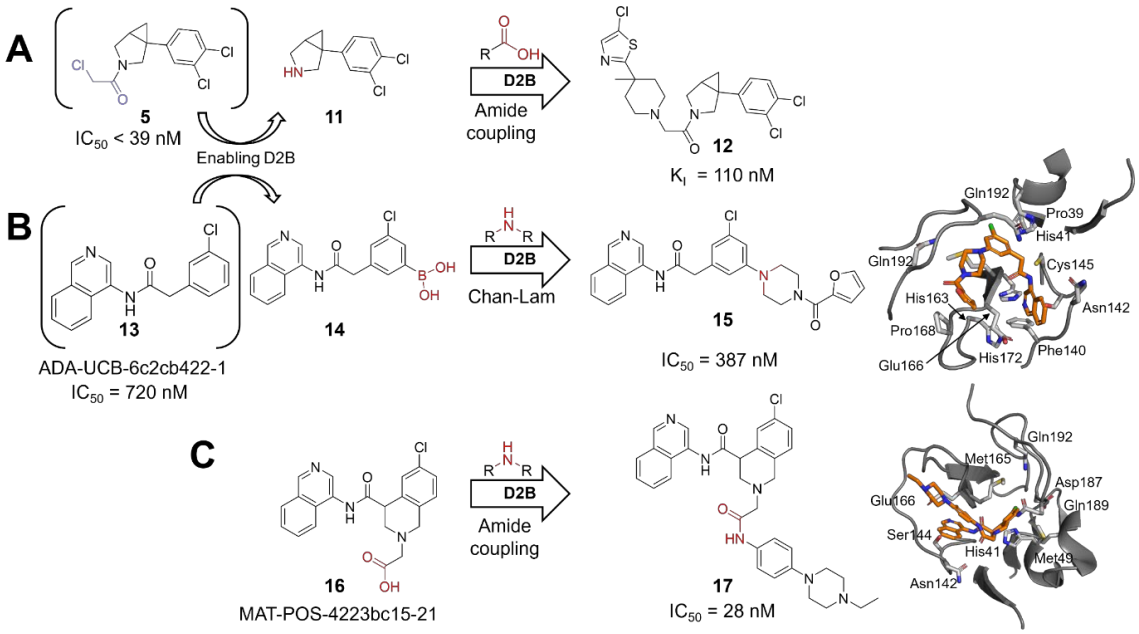


Figure 4. D2B campaigns targeting the SARS-CoV-2 M^{Pro}. (**A**) Scheme illustrating the transformation of reactive fragment **5** into a non-covalent M^{Pro} inhibitor **12** by D2B amidation.[48] (**B**, **C**) D2B campaigns reported by the Moonshot open science initiative, featuring Chan-Lam and amidation D2B to generate M^{pro} inhibitors **15** and **17** (X-ray structures PDB: 7GJZ, 7GNL).[46]

3.3. Epigenetic/Epitranscriptomic Inhibitors

Epigenetic and epitranscriptomic targets have become increasingly relevant due to their key roles in gene regulation and disease progression. Consequently, D2B strategies have enabled the exploitation of the unique features of the epigenetic landscape for accelerated drug discovery.[53,54]

In the context of D2B, multicomponent reactions (MCRs) provide efficient access to large, diverse libraries with drug-like properties, and hence, provide an opportunity for large combinatorial screens.[55,56] In one of the first conceptual D2B publications, Dömling and colleagues applied the Groebcke-Blackburn-Bienaymé reaction (GBB-3CR) to generate 1536 compounds (from a theoretical space of 142,994) and screened crude products via differential scanning fluorimetry assays (DSF) to identify Menin-MLL inhibitors (Figure 5A).[57] From this screening, 22 hits were resynthesized and validated by microscale thermophoresis (MST) assay, with the most potent compound **18** showing a K_D of 2.8 µM.

In a complementary study targeting Histone Deacetylase 2 (HDAC2), a 70-membered compound library was synthesized via amide coupling and Pd-catalyzed Suzuki-Miyaura reactions on literature-reported scaffolds of HDAC inhibitors (Figure 5B). The crude reactions were screened by the Automated Ligand Identification System (ALIS) and microsomal stability assays, which revealed that amide-derived compounds showed better correlation between ACE_{50} and biochemical-assessed IC_{50} values than Suzuki products.[58] During this study, lipophilic Ligand Efficiency (LLE) and Lipophilic Metabolism Efficiency (LipMetE) calculations also supported the selection of D2B candidates with a favorable balance of potency, lipophilicity, and metabolic stability for future drug development. The most potent inhibitor **20** with an IC_{50}-value of 9.06 nM is shown in Figure 5B.

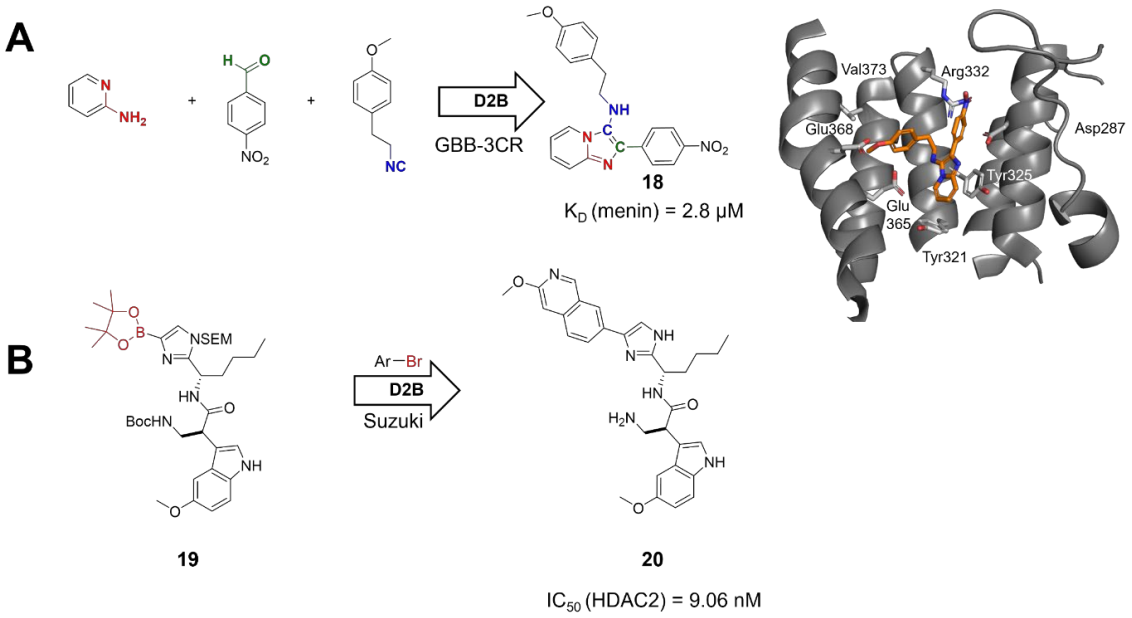


Figure 5. D2B campaigns targeting selected epigenetic drug targets. (**A**) GBB-3CR-based D2B strategy utilizing 38 amidines/aminopyridines, 53 aldehydes, and 71 isocyanides, resulting in menin inhibitor **18** (X-ray structure PDB: 6S2K).[57] (**B**) Suzuki coupling-based D2B campaign yielding HDAC2 inhibitor **20**.[58]

Beyond traditional activity-based screening, advanced D2B platforms have recently combined automated synthesis and structural biology. One such campaign integrated the usage of liquid handlers for synthesis coupled with high-throughput protein crystallography to evaluate 1696 fragment-extended compounds targeting pleckstrin homology domain-interacting protein (PHIP2), yielding 969 diffraction datasets and 29 co-crystal structures.[59] Although the initial fragment showed no activity in solution-based assays, D2B optimization led to a compound with K_D and IC_{50} values of 50.03 and 31.15 µM, respectively. Subsequently, Biggin and colleagues applied the results from this crystallography study in "xSAR" calculations to further evaluate the screening results from this study (see chapter 4, "Computational D2B Technologies").[60]
To support high-throughput screenings (HTS) and D2B approaches of other epigenetic and eptitranscriptomic targets, fluorescent methyltransferase tracers were developed via CuAAC in a "nanoSAR" workflow and tested via MST and Fluorescence Polarization (FP) assays.[61] This led to the identification of novel displacement tracers for multiple epitranscriptomic drug targets, including METTL3/14, METTL1/WDR4, and bacterial methyltransferases.

3.4. Targeted Degraders

D2B has been employed for several discovery campaigns of targeted degraders. In this review, we differentiate between divalent Proteolysis Targeting Chimeras (chapter 3.4.1) and monovalent Molecular Glues (chapter 3.4.2). Due to the synthetic complexity of heterobifunctional degraders and the limited predictive power for the degrader development, structure-activity relationship (SAR) exploration remains largely empirical and resource-intensive.[62,63] In addition to nearly 20 peer-reviewed publications that use D2B for degrader development, three patents employing the D2B technology for degrader development were published in 2025.[64–66]

3.4.1. Proteolysis Targeting Chimeras (PROTACs)

D2B approaches are particularly well-suited for PROTAC discovery, where hit identification typically requires high synthetic effort and offers limited opportunities for rational design, and thus, degrader development is the single most frequent application of recent D2B publications (Figure 1D). A key distinction from classical D2B enzyme inhibitor screening is that unreacted precursors during PROTAC development often retain target or E3 ligase binding activity, potentially contributing to cytotoxicity and influencing degradation readouts. Accordingly, many D2B PROTAC studies evaluate educts in both cytotoxicity and degradation assays, sometimes by mimicking incomplete conjugation.[39,40,67] Most PROTAC-D2B campaigns employ HiBiT assays followed by mechanistic validation, such as western blotting or inhibition of the proteasome or recruited ligase.[37–40,67–72]

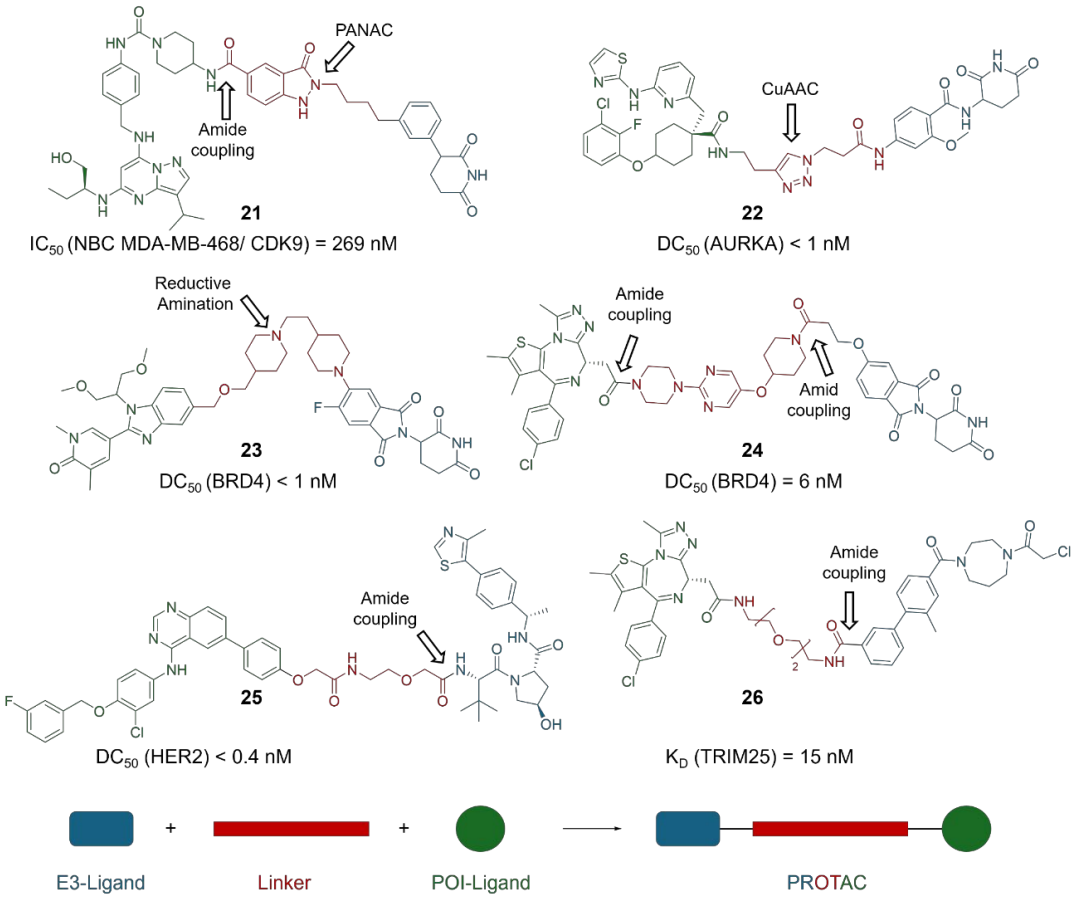


Figure 6. Overview of selected PROTACs synthesized via various D2B strategies.[39,40,49,68,69,73] The recruiting chemotype for the protein of interest (POI) is highlighted in green, the linker in red, and the E3 ligase-binder in blue.

In the current landscape of D2B-PROTACs, Cereblon (CRBN)-recruiting PROTACs have often outperformed von Hippel-Lindau (VHL) ligands,[37,39,69] while several campaigns have employed amidation strategies, for example, for Bromodomain-containing protein 4 (BRD4) targeting PROTACs using mono-*N*-Boc-protected diamines in a coupling-deprotection-coupling workflow for modular assembly (e.g., compound **24**, Figure 6).[68] Similar to many conventional PROTAC development studies, BRD4 remains a common proof-of-concept system for D2B-PROTAC platforms, similar to non-D2B degrader establishment.[39,40,49,67–69,74] For example, JQ1- or I-BET469-based libraries were synthesized via EDC- or HATU-mediated coupling with diverse linkers and ligase ligands.[67,69] In one case, three I-BET469 acid exit vectors were screened and further optimized, yielding picomolar PROTACs (DC_{50}<0.1 nM).[69] Similarly, Human epidermal growth factor receptor 2 (HER2)-directed PROTACs based on lapatinib were synthesized using linker pre-functionalized E3 ligase ligands (Figure 6, compound **25**).[69]

Beyond CRBN and VHL-based E3 ligases, Bush and colleagues employed a fragment-based D2B approach (Figure 3, compound **6**) to identify novel covalent ligands for the E3 ligase tripartite motif containing 25 (TRIM25), in a manner analogous to previous efforts targeting M^{Pro} (chapter 3.2).[49] In this study, TRIM25 binding fragments were linked via NHS esters to chloroacetamides warheads, guided by crystallography data to define the exit vector. Hence, the resulting JQ1-based BRD4 PROTAC **26** of this new type of E3 degrader demonstrated surface plasmon resonance (SPR) affinity in the nanomolar range (Figure 6).[49] In a different D2B-PROTAC strategy, amide coupling was combined with “PANAC” (primary amines and *o*-nitrobenzyl alcohols cyclization) linker chemistry, utilizing amines and bifunctional linkers bearing NHS esters and *o*-nitrobenzyl alcohols.[37] The “PANAC” reaction enables the intramolecular light-induced cyclization of primary amines with *o*-nitrobenzyl alcohols, forming heterocyclic scaffolds via a cyclization followed by dehydration and tautomerization.[73] This modular approach enabled the generation of 580 PROTACs targeting CDK9 in MDA-MB cells, yielding the most potent CDK9 PROTAC **21** with an IC_{50} of 269 nM (Figure 6).

Also, CuAAC chemistry was recently used to generate PROTAC libraries targeting BRD4, Aurora kinase A (AURKA), soluble epoxide hydrolase (sEH), and WD repeat domain 5 (WDR5) inhibitors functionalized with solvent-exposed alkyne-functionalized target recruiters.[39] The subsequent reaction with 48 ligase-binding azides (36 for CRBN, 12 for VHL) yielded 192 PROTACs per target with up to 92% conversion and subnanomolar DC_{50} values for AURKA (compound **22**, Figure 6). In another D2B study, two GSK3 ligands and 7 CRBN binding ligands were similarly linked to 12 CuAAC and S_N2-compatible linkers.[38] At AstraZeneca, D2B researchers explored the development of PROTACs targeting 2′-deoxynucleoside 5′-monophosphate *N*-glycosidase (DNPH1).[72] For this, two D2B synthetic approaches were pursued, each based on a distinct parent compound. The first (with a triazol core), derived from a DNA-encoded chemical library (DECL) hit against DNPH1, was chemically modified to enable amide coupling with various E3 ligase recruiters via different linkers and an amine handle, affording a PROTAC with a DC_{50} of 405 nM.[72] The second (with quinazoline core), originating from a prior HTS campaign, was functionalized with an aldehyde moiety to enable reductive amination with the same E3 recruiter library, yielding a highly potent PROTAC (DC_{50}=28 nM, DC_{max}=100%).[72]
Beyond CuAAC and amid coupling, other D2B-compatible chemistries have occasionally also been explored: A solid-phase Ugi reaction was employed to generate photocleavable BRD4-targeting PROTACs, using linkers of varying length, composition, and rigidity, as well as CRBN ligands with diverse substituents.[70] Furthermore, in another proof-of-concept study, several reaction classes were adapted for D2B assembly of BRD4 PROTACs based on I-BET469.[40] In this regard, reductive amination with picoline borane delivered picomolar degraders, e.g., compound **23** (Figure 6), while a Suzuki-Miyaura cross-coupling was integrated into a three-step sequence (cross-coupling, Boc deprotection, and amidation). Finally, different alkylation strategies were demonstrated for RIPK2-directed PROTACs, yielding both *N*- and *O*-linked variants and further validating this method for D2B synthesis.[40]

3.4.2. Molecular glues

Similar to PROTACs, molecular glues (MGs) are often discovered serendipitously, and rational design remains highly challenging due to the lack of clear structure-activity relationships.[75–78] Consequently, large-scale empirical screening remains a central strategy. Hence, SuFEx (sulfur(VI) fluoride exchange) chemistry has gained traction in MG discovery owing to its robust reactivity and high conversion rates, especially in reactions of aryl fluorosulfates with primary and secondary amines (Figure 7B).[74,75,78] Several MG campaigns have focused on CRBN-recruiting scaffolds, commonly derivatizing CRBN ligands and screening for degradation phenotypes.[70,75–78]

For instance, G1 to S phase transition 1 (GSPT1) degraders were identified via a Ugi-based D2B screen using a pomalidomide-derived isocyanide (Figure 7A, DC_{50}=0.88 nM for compound **27**) or with a SuFEx-based library of 3180 amines coupled to 5′-amino-lenalidomide (Figure 7B, compound **32**), tested across leukemia and neuroblastoma cell lines with HiBiT validation.[75,77] Also, GSPT2 emerged as a hit in a newly established isogenic cell painting assay from a SuFEx screen involving six fluorosulfates (compound **28,** Figure 7B) and 21 aliphatic amines as a proof of concept.[78] In another study, over 20,000 CRBN-based compounds were synthesized via amide formation and Buchwald-Hartwig coupling.[76] The resulting library was screened by ASMS against the lymphocyte-specific tyrosine kinase (LCK), enabling targeted MG identification. In contrast to these E3 ligase-first approaches, some efforts have pursued a “degraded target”-first strategy: For BRD4 and histone acylation reader eleven-nineteen leukemia (ENL), known inhibitors (JQ1 and SR-0813 (**30**), respectively) were functionalized with SuFEx-compatible exit vectors and reacted with 3163 structurally diverse amines (Figure 7B).[74] Screening via HiBiT yielded ENL degraders (e.g., compound **31**) with DC_{50} values from 50 nM to 1.85 µM, while CRISPR/Cas9-mediated knockout of CRBN in MV4;11 cells confirmed that degradation was CRBN-dependent.

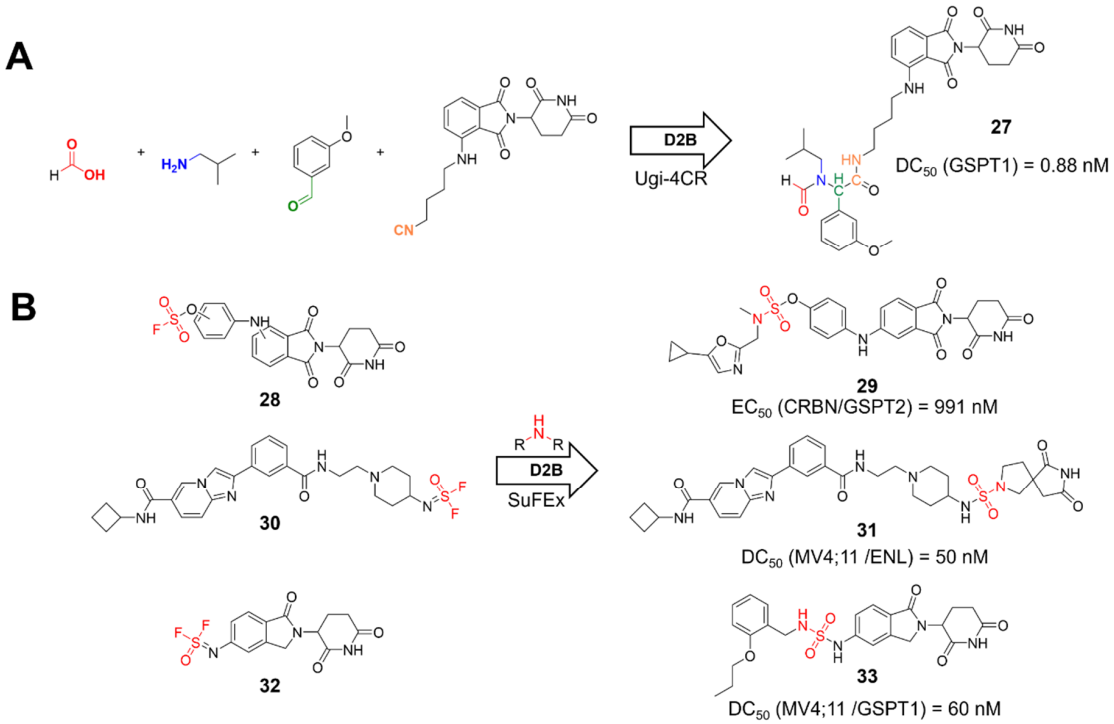


Figure 7. D2B campaigns for the development of molecular glue degraders. (**A**) Ugi-4CR reaction-stirred D2B campaign for the development of GSPT1 degrader **27**.[77] (**B**) SuFEx chemistry was employed in three different D2B campaigns for the discovery of molecular glues **29**–**33**.[74,75,78]

3.5. Carbonic Anhydrase Inhibitors

Carbonic anhydrases (CAs) catalyze the hydration of CO_2 to HCO_3^-, playing a central role in pH regulation.[79] Their inhibitors are utilized in diseases such as glaucoma, macular edema, and cancer.[80] Although carbonic anhydrase inhibitors are not new in the current focus of medicinal chemistry, there are several D2B development campaigns highlighting the model character of carbonic anhydrase for D2B development.

To explore fragment-protein interactions beyond cysteine residues (as described for M^{Pro} above, Figure 3), new platforms for screening of covalent inhibitors were adapted by Bush and coworkers, targeting CAs, among others.[1,50,81] In their first strategy, a 1073-membered alkyl-amine fragment library was functionalized via NHS ester chemistry with a photoreactive alkyl diazirine moiety, enabling initial noncovalent binding followed by UV-induced crosslinking, also dubbed the PhotoAffinity Bits (PhABits) methodology (Figure 8).[1,82] Displacement experiments with ethoxzolamide, a known inhibitor targeting the zinc-binding site, confirmed active-site engagement and yielded five primary sulfonamide-containing hits, and subsequently, a focused library of 100 sulfonamide analogues was synthesized, resulting in several micromolar-affinity binders (e.g, compound **34**).[1] In a second strategy, photoactivatable 2-aryl-5-carboxytetrazoles (ACT)-PhABits targeting Asp/Glu residues were explored via amidation D2B and generated 17 hits for CA I and 16 for CA II (e.g., compound **36**).[81]

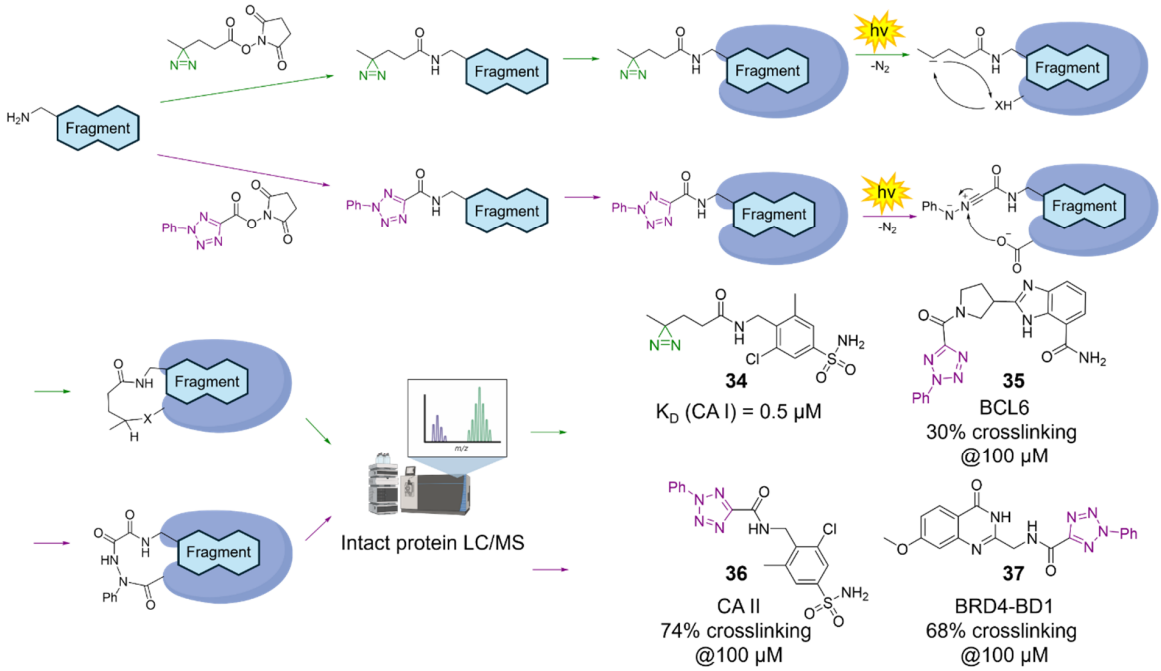


Figure 8. PhABit/D2B methodology introduced by Bush and co-workers. Scheme illustrating two different PhABits containing a diazirine chemotype (green) or 2-aryl-5-carboxytetrazole chemotype (violet). Fragments containing amine groups are reacted with the respective photosensitive transfer reagent, which is then incubated with the target enzyme, irradiated, and analyzed by intact protein LC/MS. This methodology was used for D2B campaigns targeting CA I/II (**34**, **36**) and also BRD4-BD1 (**35**, **37**).[1,81]

In a different CA-targeting campaign, sulfur(VI) fluoride-RFs targeting lysine, tyrosine, and serine yielded four initial hits; although initial k_{inact} values were low, an optimized 96-member analog library achieved higher modification yields and improved selectivity (Figure 3, e.g., compound **8**).[50] Collectively, these studies expand fragment-based covalent ligand discovery beyond traditional cysteine targeting for CA I and CA II.

3.6. Antiviral and Antibacterial Drugs

The emergence of antibiotic resistance drives the search for new antibacterial agents as an ongoing priority in academic and industrial research.[83] Likewise, viral targets remain central to drug discovery efforts, particularly since the COVID-19 pandemic.[84] It is therefore unsurprising that the D2B approach has been applied to both bacterial and viral targets beyond the SARS-CoV-2 main protease.

Two prominent viral targets explored using D2B strategies are the Influenza virus and Ebola virus (EBOV). In the case of Influenza, the stem region of hemagglutinin (HA) was targeted by D2B-derived inhibitors, and thus, building on a previously established high-throughput fluorescence polarization (FP) assay, a fragment-like ligand with an EC_{50} of 1.9 µM could be identified (**38**/**40**, Figure 9A).[85] Subsequent X-ray crystallography revealed three unoccupied regions, which were subsequently derivatized using SuFEx chemistry in a D2B manner.[19,85] This enabled the generation of a 690-membered library via reaction with 230 amines. In parallel, an amide library was synthesized by coupling an amine-modified version of the fragment to 500 carboxylic acids. Both libraries were tested without purification in the FP assay, and the best compounds (**39** and **41**) from each library (SuFEx and amidation) were merged, yielding final compound **42** with sub-nanomolar EC_{50} values across multiple H1 strains, representing the most potent HA stem binder reported to date.[19]

For targeting EBOV, Kitamura and colleagues selected the EBOV glycoprotein (GP) as a potential D2B target.[86] *In silico* docking of tamoxifen to this receptor guided the strategy of derivatization, followed by SuFEx-based modification using thionyl tetrafluoride to introduce a difluoride functionalization handle to yield compound **43**. A library of 2496 amines was subsequently coupled using an automated liquid handling robot, and the crude products were evaluated in a cell-based EBOV entry assay. The top hit (**44**) of this study exhibited a K_D of 0.63 µM; an over 50-fold improvement compared to tamoxifen (K_D=32 µM) and an EC_{50} value of 92 nM in VSV-EBOV-GP (Vero cells).[86]

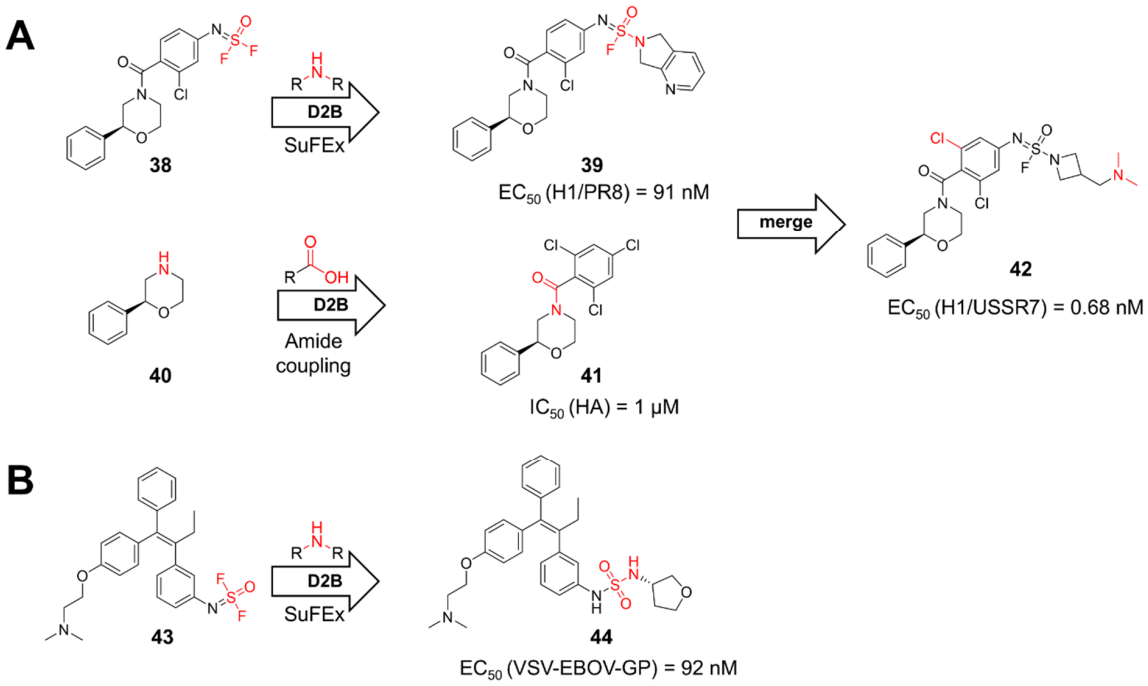


Figure 9. D2B campaigns targeting selected antiviral targets. (**A**) Scheme illustrating the workflow for the development of influenza virus HA inhibitors, combining SuFEx and amide coupling-based D2B approaches to yield compound **42**.[85] (**B**) SuFEx-based D2B strategy targeting EBOV GP, resulting in compound **44**.[86]

For D2B-targeting of bacterial targets, several complementary approaches have been explored. In this regard, covalent fragment-based drug discovery was applied to *Salmonella* and *Shigella* NEL E3 ligases by screening 227 electrophilic fragments bearing chloroacetamide warheads targeting cysteines (similar to the approach used for M^{Pro} and TRIM25 above, Figure 3); while no hits were found for IpaH (*Shigella*), three hits could be identified for SspH (*Salmonella*).[51] A focused D2B library of 430 amines was used for hit expansion via amide coupling to chloroacetamide warheads, yielding compound **7** (Figure 3) that showed significant protein labeling at 6.25 µM and inhibition of PKN1 ubiquitination in a reconstituted ubiquitin enzymatic cascade.[51]
Beyond cysteine targeting inhibition, Wennekes and coworkers investigated the dichlorotriazine (ClTriZ) covalent warhead for lysine targeting and optimized it using a biotin-avidin model system.[87] Its integration into a modular “double-click” (CuAAC and Strain-promoted azide-alkyne click chemistry reaction (SPAAC)) platform enabled sequential ligand and reporter diversification, yielding a panel of functionalized probes for *Photobacterium multocida* sialyltransferase 1 (PmST1) and supporting a D2B approach. This strategy was subsequently applied to generate and screen covalent ClTriZ-based probes targeting *Neisseria gonorrhoeae* lipooligosaccharide sialyltransferase (Ngono Lst), enabling irreversible inhibition in complex lysates without purification.[87] In a separate D2B publication, investigating nitrofuran-based coupling products, 40 derivatives were tested in a nanoscale format, yielding potent MICs (0.8–7.8 µM) against *S. aureus* and *E. coli*.[88] Also, recently, a different antibacterial strategy for peptide nucleic acid (PNA)-based antisense molecules targeting essential bacterial mRNAs, using 1536 sequences and truncation strategies.[89]
One of the most recent studies in the D2B field targets DsbA, a bacterial oxidoreductase essential for the folding and function of virulence factors.[90] This enzyme features two key binding sites (a cryptic pocket and a hydrophobic loop). Starting from a fragment that bound to the cryptic pocket, a D2B strategy generated a library of amino alcohols containing a hydroxyethylamide moiety, crucial for engaging the interface of the cryptic pocket and hydrophobic loop. The crude library (92 members) was coupled to the phenylisoxazole core, which contains an alkyne linker with a carboxylic acid handle. The resulting products were screened using SPR and ASMS, and the most potent hit demonstrated a K_D of 1.5 µM (ITC).

3.7. Other Targets and Inhibitors

Several additional D2B campaigns not categorized by the chapters above were conducted by Bush, Rittinger, and colleagues using reactive fragments (RFs) as previously discussed (Figures 3&8). The ACT-PhABit approach (Figure 8) yielded 17 selective KRAS, 14 BCL6 hits (compound **35**), and BRD4-BD1 (compound **37**), characterized by weak binding affinities, representing starting points for further optimization.[81] Sulfonyl fluorides, also applied in CA II targeting, were used to identify covalent RFs for BCL6, and thus, a focused library of 352 compounds, designed in a D2B manner, revealed meta-substituted benzamides (compound **9**) as preferred covalent chemotypes (Figure 3).[50]
A similar strategy was applied for the development of covalent acrylamide-based inhibitors of the Werner (WRN) helicase (Figure 3).[52] Here, an initial LC/MS screen of 1055 acrylamides yielded two moderately affine hits (IC_{50}=15.8 µM). Hence, two parallel optimization approaches were followed: one coupled 328 Tanimoto-similar amines to the acrylamide electrophile, leading to a best hit with IC_{50}=1 µM, the other employed multistep syntheses including amide coupling and acrylamide formation, resulting in a compound with IC_{50}=251 nM. Structural insights via X-ray crystallography informed a third round of D2B optimization, using 123 amines to generate analogues, culminating in lead compound **10** with IC_{50}=31.6 nM (Figure 3).[52]
Similarly, chloroacetamide-based screenings to identify selective inhibitors of OTU domain-containing protein 7B (OTUD7B), yielding a hit with IC_{50}=3.5 µM.[91] In this study, targets labeled with fragments were identified via biotinylated ubiquitin vinyl sulfone probes and LC/MS from HEK lysates. Subsequently, a 351-membered amine library was then coupled to a chloroacetamid electrophile and screened via intact protein LC/MS to yield the mentioned hit.
In another study, Roecker and co-workers, targeting glucosylceramide synthase (GCS), crucial in Parkinson's disease, identified a diazepane core (**45**) via HTS.[92] Guided by QSAR, they synthesized 1390 diazepane derivatives via HATU coupling and screened them directly in a GCS enzymatic assay, and following scaffold hopping, they identified compound **46** (Figure 10A) with picomolar potency in enzymatic assays and an IC_{50} of 1.7 nM in human iPSC-derived neurons. Further, Ponzi et al. used S_NAr chemistry to attach 160 amines to an imidazopyrazine scaffold (**47**) via automated synthesis, identifying Src homology region 2 tyrosine phosphatase 2 (SHP2) allosteric inhibitors with IC_{50} values of 225 nM and, after further improvement, 88 nM (compound **48**, Figure 10B).[93] Lastly, Chen et al. generated 2720 celastrol derivatives targeting peroxiredoxins (PRDXs).[94] The best compound **50** showed a 4.6-fold improvement over celastrol in PRDX1 inhibition (IC_{50}=42 nM) and selectivity over PRDX2/3/4/6 (Figure 10C).

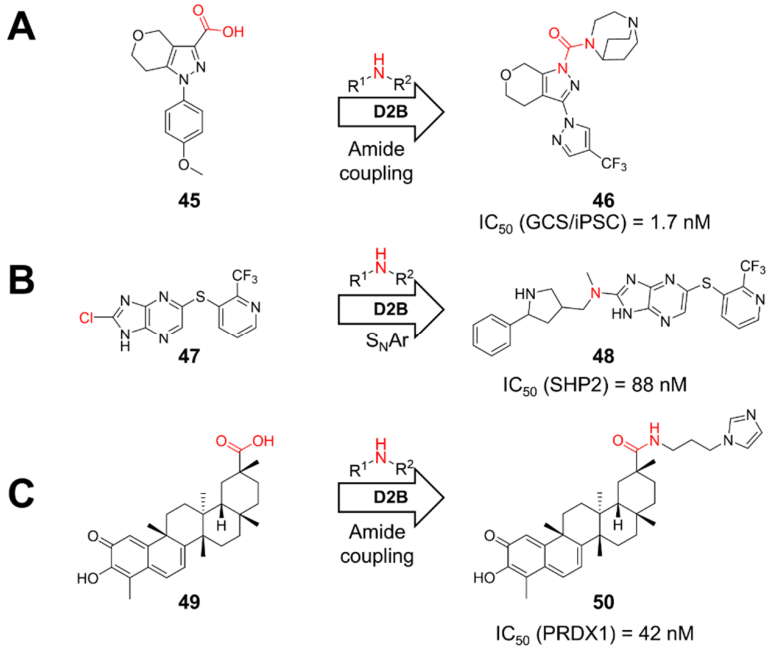


Figure 10. A selection of D2B campaigns targeting various other targets. (**A**) Amidation-based D2B campaign by Roecker and co-workers targeting glucosylceramide synthase (GCS) for the treatment of Parkinson's disease.[92] (**B**) D2B campaign targeting SHP2, leading to the development of compound **48**.[93] (**C**) Identification of calosterol derivative **50** by Xiong et al. via an amidation-based D2B campaign.[94]

4. Computational D2B Technologies

Together with synthetic developments, computational methods have been leveraged to support D2B workflows and the analysis of high-throughput screening data. One such platform is the Cernak laboratory development “phactor”, a software tool designed to automate data handling and streamline reaction array setup and evaluation (Figure 11B).[45] It processes diverse data types, including LC/MS and biochemical assay outputs, and is compatible with widely used instruments and programs by utilizing Excel and Python. Similarly, King-Smith and co-workers employed an M^{Pro} targeting campaign to validate a machine learning (ML)-based “deconfounder” that distinguishes low potency from low synthetic yield, mitigating false negatives.[47] Their “Swiss cheese” method integrates Random Forest and Gaussian Process models to identify consistent SAR patterns within noisy datasets and is extendable to *in silico* screening for novel scaffolds (Figure 11A).
In another publication, transfer learning of known antibiotics was applied to a chemical language model to find new antibacterial compounds *de novo*.[88] This enabled the generation of synthetically feasible, novel antibacterial structures. Subsequent D2B evaluation through amide coupling with 40 amines yielded compounds with promising MIC values against *S. aureus* and *E. coli*. Furthermore, the Biggin group analyzed data from a D2B crystallographic study by von Delft and Spencer using a so-called “xSAR” approach. They extracted features from Morgan fingerprints and calculated positive and negative binding scores (PBS/NBS) based on conserved binding (CBB) and conserved non-binding bits (CNB), ultimately identifying 26 previously classified as non-binder PHIP2 binders.[59,60]

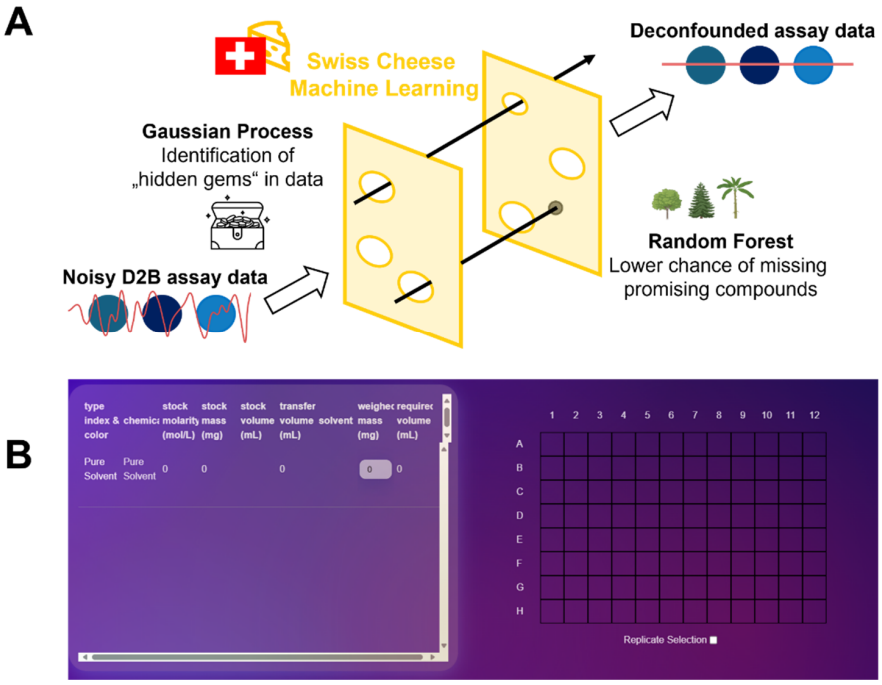


Figure 11. (**A**) The “Swiss Cheese” machine learning based deconfounder, based on Gaussian Process and Random Forest models, to detect false negative results in noisy D2B assay data. Figure adapted from McCorkindale et al.[47] (**B**) Screenshot of the toolkit from phactor.cernaklab.com, designing a grid for D2B experiments.[45]

5. Limitations and Outlook of Direct-to-Biology

Direct-to-Biology (D2B) workflows trade purification for speed and material economy, but that trade introduces specific and consequential limitations. The principal concern is matrix interference in biochemical and cell-based assays.[95–98] Reagents, side products, solvents, and residual catalysts can, in principle, interfere with biological assays, leading to false positives (assay readout driven by an impurity rather than the intended compound) or false negatives (loss of signal due to inhibitory or quenching components). A corollary is assay dependence; fluorescence- and luminescence-based readouts are particularly susceptible to quenching or background signal from reaction components, whereas label-free biophysical methods (e.g., mass spectrometry) are generally less prone to such artefacts. To mitigate matrix-dependent assay interference, some recent studies recommend project-agnostic D2B compatibility tests, in which crude but structurally irrelevant reactions are spiked with

positive controls to probe assay robustness. Nonetheless, such procedures add overhead and may reveal that certain reaction types or assay formats will be simply unsuitable for D2B.

On the chemistry side, D2B currently favors a constrained subset of transformations that are robust, high-yielding, and assay-tolerant (e.g., amide formation, CuAAC, and SuFEx). This selection of chemistry aligns well with the needs of academic and early pharma medicinal chemistry campaigns. However, when comparing the frequency of chemotypes found in approved drugs with the current D2B toolbox, there is a strong need to expand the reaction repertoire to the benefit of C-C/C-N cross-couplings and heterocyclization reactions. Furthermore, attempts to push more sensitive or complex chemistries to nanomole, plate-format conditions expose issues of incomplete conversion, reagent decomposition, and poor mixing (diffusion limits in 384/1536 wells), which can impair hit identification or translatability to batch synthesis.[99]
Analytical throughput and decision-making are further bottlenecks: mass spectrometric profiling and data parsing for hundreds of crude wells is time-consuming and requires semi-automated pipelines and bespoke thresholds for acceptable conversion, thresholds that depend on both assay sensitivity and project context. Finally, because only resynthesized hits are validated, early SAR can be clouded by artefacts in the crude matrix, so D2B is currently best deployed as a filtering strategy that demands rigorous controls, orthogonal confirmatory assays, and conservative interpretation until purified follow-up data are available.
Together, these considerations underscore that D2B is not yet a universal replacement for conventional synthesis-purification-assay pipelines. It is best viewed as a complementary strategy that, when applied with rigorous controls and awareness of its limitations, can substantially accelerate the early discovery cycle while avoiding costly conventional SAR deadends.
Looking forward, D2B is expected to expand both in methodological breadth and translational scope. Continued progress in biocompatible microscale chemistries, including photoredox, late-stage C-H functionalization, and sp^3-sp^3 coupling, will broaden the reaction space accessible to D2B campaigns. At the same time, integration with AI-driven library design promises more intelligent hypothesis-driven compound sets, minimizing wasted synthesis and assay capacity. On the biological side, adoption of label-free and high-content cellular assays should help mitigate artefacts from crude mixtures while generating richer data.
Increasing engagement from commercial providers (for D2B service and for affordable building block libraries) underscores that D2B is moving from proof-of-concept toward a standardized discovery tool. Ultimately, the field will need to demonstrate consistent success across diverse targets and chemistries to solidify its role as a mainstream complement to traditional library-based discovery. To this end, further development and more frequent use of computer-assisted methods for designing and evaluating D2B campaigns will certainly play a major role in the near future.

Keywords: Direct-to-Biology • High-throughput screening • Nanomole synthesis • Drug discovery • Combinatorial chemistry

[1] R. P. Thomas, R. E. Heap, F. Zappacosta, E. K. Grant, P. Pogány, S. Besley, D. J. Fallon, M. M. Hann, D. House, N. C. O. Tomkinson, J. T. Bush, “A direct-to-biology high-throughput chemistry approach to reactive fragment screening” *Chem. Sci.* **2021**, *12*, 12098–12106.
[2] A. McNally, C. K. Prier, D. W. C. MacMillan, “Discovery of an α-Amino C–H Arylation Reaction Using the Strategy of Accelerated Serendipity” *Science* **2011**, *334*, 1114–1117.
[3] D. A. DiRocco, K. Dykstra, S. Krska, P. Vachal, D. V. Conway, M. Tudge, “Late-Stage Functionalization of Biologically Active Heterocycles Through Photoredox Catalysis” *Angew. Chem. Int. Ed.* **2014**, *53*, 4802–4806.
[4] A. Buitrago Santanilla, E. L. Regalado, T. Pereira, M. Shevlin, K. Bateman, L.-C. Campeau, J. Schneeweis, S. Berritt, Z.-C. Shi, P. Nantermet, Y. Liu, R. Helmy, C. J. Welch, P. Vachal, I. W. Davies, T. Cernak, S. D. Dreher, “Nanomole-scale high-throughput chemistry for the synthesis of complex molecules” *Science* **2015**, *347*, 49–53.
[5] S. Lin, S. Dikler, W. D. Blincoe, R. D. Ferguson, R. P. Sheridan, Z. Peng, D. V. Conway, K. Zawatzky, H. Wang, T. Cernak, I. W. Davies, D. A. DiRocco, H. Sheng, C. J. Welch, S. D. Dreher, “Mapping the dark space of chemical reactions with extended nanomole synthesis and MALDI-TOF MS” *Science* **2018**, *361*, eaar6236.
[6] D. Perera, J. W. Tucker, S. Brahmbhatt, C. J. Helal, A. Chong, W. Farrell, P. Richardson, N. W. Sach, “A platform for automated nanomole-scale reaction screening and micromole-scale synthesis in flow” *Science* **2018**, *359*, 429–434.
[7] Y. Wang, S. Shaabani, M. Ahmadianmoghaddam, L. Gao, R. Xu, K. Kurpiewska, J. Kalinowska-Tluscik, J. Olechno, R. Ellson, M. Kossenjans, V. Helan, M. Groves, A. Dömling, “Acoustic Droplet Ejection Enabled Automated Reaction Scouting” *ACS Cent. Sci.* **2019**, *5*, 451–457.
[8] J. B. Murray, S. D. Roughley, N. Matassova, P. A. Brough, “Off-Rate Screening (ORS) By Surface Plasmon Resonance. An Efficient Method to Kinetically Sample Hit to Lead Chemical Space from Unpurified Reaction Products” *J. Med. Chem.* **2014**, *57*, 2845–2850.
[9] G. Karageorgis, S. Warriner, A. Nelson, “Efficient discovery of bioactive scaffolds by activity-directed synthesis” *Nat. Chem.* **2014**, *6*, 872–876.
[10] G. Karageorgis, M. Dow, A. Aimon, S. Warriner, A. Nelson, “Activity-Directed Synthesis with Intermolecular Reactions: Development of a Fragment into a Range of Androgen Receptor Agonists” *Angew. Chem.* **2015**, *127*, 13742–13748.
[11] A. Leggott, J. E. Clarke, S. Chow, S. L. Warriner, A. J. O’Neill, A. Nelson, “Activity-directed expansion of a series of antibacterial agents” *Chem. Commun.* **2020**, *56*, 8047–8050.
[12] G. Karageorgis, S. Liver, A. Nelson, “Activity-Directed Synthesis: A Flexible Approach for Lead Generation” *ChemMedChem* **2020**, *15*, 1776–1782.

[13] A. I. Green, F. Hobor, C. P. Tinworth, S. Warriner, A. J. Wilson, A. Nelson, "Activity-Directed Synthesis of Inhibitors of the p53/hDM2 Protein–Protein Interaction" *Chem. – Eur. J.* **2020**, *26*, 10682–10689.

[14] X. Zhou, Y. Tan, K. Gou, L. Tao, Y. Luo, Y. Zhou, Z. Zuo, Q. Sun, Y. Luo, Y. Zhao, "Discovery of novel inhibitors of human phosphoglycerate dehydrogenase by activity-directed combinatorial chemical synthesis strategy" *Bioorganic Chem.* **2021**, *115*, 105159.

[15] D. Francis, S. Farooque, A. Meager, D. Derks, A. Leggott, S. Warriner, A. J. O'Neill, A. Nelson, "Algorithm-driven activity-directed expansion of a series of antibacterial quinazolinones" *Org. Biomol. Chem.* **2022**, *20*, 9672–9678.

[16] B. Yang, M. L. Lamb, T. Zhang, E. J. Hennessy, G. Grewal, L. Sha, M. Zambrowski, M. H. Block, J. E. Dowling, N. Su, J. Wu, T. Deegan, K. Mikule, W. Wang, R. Kaspera, C. Chuaqui, H. Chen, "Discovery of Potent KIFC1 Inhibitors Using a Method of Integrated High-Throughput Synthesis and Screening" *J. Med. Chem.* **2014**, *57*, 9958–9970.

[17] Z. Liu, J. Li, S. Li, G. Li, K. B. Sharpless, P. Wu, "SuFEx Click Chemistry Enabled Late-Stage Drug Functionalization" *J. Am. Chem. Soc.* **2018**, *140*, 2919–2925.

[18] M. Benz, M. R. Molla, A. Böser, A. Rosenfeld, P. A. Levkin, "Marrying chemistry with biology by combining on-chip solution-based combinatorial synthesis and cellular screening" *Nat. Commun.* **2019**, *10*, 2879.

[19] S. Kitamura, Q. Zheng, J. L. Woehl, A. Solania, E. Chen, N. Dillon, M. V. Hull, M. Kotaniguchi, J. R. Cappiello, S. Kitamura, V. Nizet, K. B. Sharpless, D. W. Wolan, "Sulfur(VI) Fluoride Exchange (SuFEx)-Enabled High-Throughput Medicinal Chemistry" *J. Am. Chem. Soc.* **2020**, *142*, 10899–10904.

[20] L. M. Baker, A. Aimon, J. B. Murray, A. E. Surgenor, N. Matassova, S. D. Roughley, P. M. Collins, T. Krojer, F. von Delft, R. E. Hubbard, "Rapid optimisation of fragments and hits to lead compounds from screening of crude reaction mixtures" *Commun. Chem.* **2020**, *3*, 122.

[21] N. M. Morato, M. T. Le, D. T. Holden, R. Graham Cooks, "Automated High-Throughput System Combining Small-Scale Synthesis with Bioassays and Reaction Screening" *SLAS Technol. Transl. Life Sci. Innov.* **2021**, *26*, 555–571.

[22] F. Sutanto, S. Shaabani, R. Oerlemans, D. Eris, P. Patil, M. Hadian, M. Wang, M. E. Sharpe, M. R. Groves, A. Dömling, "Combining High-Throughput Synthesis and High-Throughput Protein Crystallography for Accelerated Hit Identification" *Angew. Chem. Int. Ed.* **2021**, *60*, 18231–18239.

[23] N. J. Gesmundo, B. Sauvagnat, P. J. Curran, M. P. Richards, C. L. Andrews, P. J. Dandliker, T. Cernak, "Nanoscale synthesis and affinity ranking" *Nature* **2018**, *557*, 228–232.

[24] A. A. Peterson, D. R. Liu, "Small-molecule discovery through DNA-encoded libraries" *Nat. Rev. Drug Discov.* **2023**, *22*, 699–722.

[25] Á. Furka, "Forty years of combinatorial technology" *Drug Discov. Today* **2022**, *27*, 103308.

[26] L. C. Szymczak, H.-Y. Kuo, M. Mrksich, "Peptide Arrays: Development and Application" *Anal. Chem.* **2018**, *90*, 266–282.

[27] S. D. Roughley, A. M. Jordan, "The Medicinal Chemist's Toolbox: An Analysis of Reactions Used in the Pursuit of Drug Candidates" *J. Med. Chem.* **2011**, *54*, 3451–3479.

[28] D. G. Brown, J. Boström, "Analysis of Past and Present Synthetic Methodologies on Medicinal Chemistry: Where Have All the New Reactions Gone?" *J. Med. Chem.* **2016**, *59*, 4443–4458.

[29], "Direct-to-Biology D2B | Drug Discovery | Concept Life Sciences," can be found under https://www.conceptlifesciences.com/services/integrated-drug-discovery/direct-to-biology-d2b(accessed 19 August 2025), **n.d.**

[30], "Direct-to-Biology D2B | Drug Discovery | Domainex," can be found under https://www.domainex.co.uk/services/direct-to-biology-d2b(accessed 19 August 2025), **n.d.**

[31], "Integrated Direct-to-Biology (D2B) Platform | WuXi AppTec," can be found under https://wuxibiology.com/integrated-direct-to-biology-d2b-platform/(accessed 19 August 2025), **2025**.

[32], "molecule.one | D2B," can be found under https://molecule.one/(accessed 19 August 2025), **n.d.**

[33] P. Cohen, D. Cross, P. A. Jänne, "Kinase drug discovery 20 years after imatinib: progress and future directions" *Nat. Rev. Drug Discov.* **2021**, *20*, 551–569.

[34] S. Baldi, N. Long, S. Ma, L. Liu, A. Al-Danakh, Q. Yang, X. Deng, J. Xie, H. Tang, "Advancements in Protein Kinase Inhibitors: From Discovery to Clinical Applications" *Research* **2025**, *8*, 0747.

[35] P. Gehrtz, S. Marom, M. Bührmann, J. Hardick, S. Kleinbölting, A. Shraga, C. Dubiella, R. Gabizon, J. N. Wiese, M. P. Müller, G. Cohen, I. Babaev, K. Shurrush, L. Avram, E. Resnick, H. Barr, D. Rauh, N. London, "Optimization of Covalent MKK7 Inhibitors via Crude Nanomole-Scale Libraries" *J. Med. Chem.* **2022**, *65*, 10341–10356.

[36] J. L. Douthwaite, D. J. Houde, E. H. Pardo, M. S. Moran, J. Baird, S. R. Meyer, B. Mahjour, Q. Zhao, J. F. Larrow, Y.-P. Juang, C. K. Han, B. Kelley, D. R. Dunstan, K. J. Billings, M. M. Mader, A. M. Taylor, J. Z. Sexton, A. A. Boezio, T. Cernak, **2025**, ChemRxiv preprint, DOI: 10.26434/chemrxiv-2025-4fr3l.

[37] K.-N. Yan, Y.-Q. Nie, J.-Y. Wang, G.-L. Yin, Q. Liu, H. Hu, X. Sun, X.-H. Chen, "Accelerating PROTACs Discovery Through a Direct-to-Biology Platform Enabled by Modular Photoclick Chemistry" *Adv. Sci.* **2024**, *11*, 2400594.

[38] A. Holmqvist, N. M. Kocaturk, C. Duncan, J. Riley, S. Baginski, G. Marsh, J. Cresser-Brown, H. Maple, K. Juvonen, N. Morrice, C. Sutherland, K. Read, W. Farnaby, **2025**, ChemRxiv preprint, DOI: 10.26434/chemrxiv-2025-nq14w.

[39] M. Mitrović, F. A. Greco, Y. C. García, A. Lučić, L. Hoffmann, R. Chander, J. Schönfeld, N. Liebisch, M. P. Schwalm, M. Egner, M. Lewandowski, D. Merk, V. Morasch, E. Wolf, S. Müller, T. Hanke, E. Proschak, K. Hiesinger, S. Knapp, **2025**, bioRxiv preprint, DOI: 10.1101/2025.07.29.667383.

[40] R. Stevens, H. J. Shrives, J. Cryan, D. Klimaszewska, P. Stacey, G. A. Burley, J. D. Harling, D. J. Battersby, A. H. Miah, "Expanding the reaction toolbox for nanoscale direct-to-biology PROTAC synthesis and biological evaluation" *RSC Med. Chem.* **2025**, *16*, 1141–1150.

[41] M. Meldal, F. Diness, "Recent Fascinating Aspects of the CuAAC Click Reaction" *Trends Chem.* **2020**, *2*, 569–584.

[42] X. Wang, B. Huang, X. Liu, P. Zhan, "Discovery of bioactive molecules from CuAAC click-chemistry-based combinatorial libraries" *Drug Discov. Today* **2016**, *21*, 118–132.

[43] A. Zagórska, A. Czopek, M. Fryc, J. Jończyk, "Inhibitors of SARS-CoV-2 Main Protease (Mpro) as Anti-Coronavirus Agents" *Biomolecules* **2024**, *14*, 797.

[44] Y. L. Janin, "On the origins of SARS-CoV-2 main protease inhibitors" *RSC Med. Chem.* **2024**, *15*, 81–118.

[45] B. Mahjour, R. Zhang, Y. Shen, A. McGrath, R. Zhao, O. G. Mohamed, Y. Lin, Z. Zhang, J. L. Douthwaite, A. Tripathi, T. Cernak, "Rapid planning and analysis of high-throughput experiment arrays for reaction discovery" *Nat. Commun.* **2023**, *14*, 3924.

[46] M. L. Boby, D. Fearon, M. Ferla, M. Filep, L. Koekemoer, M. C. Robinson, The COVID Moonshot Consortium, J. D. Chodera, A. A. Lee, N. London, A. von Delft, F. von Delft, "Open science discovery of potent noncovalent SARS-CoV-2 main protease inhibitors" *Science* **2023**, *382*, eabo7201.

[47] W. McCorkindale, M. Filep, N. London, A. A. Lee, E. King-Smith, "Deconvoluting low yield from weak potency in direct-to-biology workflows with machine learning" *RSC Med. Chem.* **2024**, *15*, 1015–1021.

[48] H. Wilders, G. Biggs, S. M. Rowe, E. E. Cawood, I. G. Riziotis, A. R. Rendina, E. K. Grant, J. Pettinger, D. J. Fallon, M. Skehel, D. House, N. C. O. Tomkinson, J. T. Bush, "Expedited SARS-CoV-2 Main Protease Inhibitor Discovery through Modular 'Direct-to-Biology' Screening" *Angew. Chem. Int. Ed.* **2025**, *64*, e202418314.

[49] K. A. McPhie, D. Esposito, J. Pettinger, D. Norman, T. Werner, T. Mathieson, J. T. Bush, K. Rittinger, "Discovery and optimisation of a covalent ligand for TRIM25 and its application to targeted protein ubiquitination" *Chem. Sci.* **2025**, *16*, 10432–10443.

[50] A. Aatkar, A. Vuorinen, O. E. Longfield, K. Gilbert, R. Peltier-Heap, C. D. Wagner, F. Zappacosta, K. Rittinger, C. Chung, D. House, N. C. O. Tomkinson, J. T. Bush, "Efficient Ligand Discovery Using Sulfur(VI) Fluoride Reactive Fragments" *ACS Chem. Biol.* **2023**, *18*, 1926–1937.

[51] C. R. Kennedy, K. A. McPhie, A. Vuorinen, J. Dudley-Fraser, D. Esposito, S. Maslen, J. Pettinger, J. M. Skehel, J. Bush, D. House, K. Rittinger, **2025**, ChemRxiv preprint, DOI: 10.26434/chemrxiv-2025-8ppqz.

[52] S. M. Rowe, A. Price, D. J. Murphy, J. Lin, E. N. Nartey, A. Chaikuad, K. Wong, J. E. Cottom, N. O. Concha, R. A. Reid, E. R. Dickinson, M. Jundt, K. Kammerer, M. Steidel, T. Mathieson, T. Werner, E. K. Grant, C. K. Stanborough, M. Rouah, J. Wojno-Picon, P. Pogány, J. Pettinger, D. J. Norman, H. Wilders, F. Rianjongdee, G. Valdes-Garcia, N. Nevins, R. Shenje, R. K. Thalji, C. Chung, H. C. Eberl, G. Neubauer, D. House, Y. Rao, M. P. Martino, J. T. Bush, **2025**, ChemRxiv preprint, DOI: 10.26434/chemrxiv-2025-tvdzn.

[53] P. A. Boriack-Sjodin, S. Ribich, R. A. Copeland, "RNA-modifying proteins as anticancer drug targets" *Nat. Rev. Drug Discov.* **2018**, *17*, 435–453.

[54] T. K. Kelly, D. D. De Carvalho, P. A. Jones, "Epigenetic modifications as therapeutic targets" *Nat. Biotechnol.* **2010**, *28*, 1069–1078.

[55] T. Zarganes-Tzitzikas, A. Dömling, "Modern multicomponent reactions for better drug syntheses" *Org. Chem. Front.* **2014**, *1*, 834–837.

[56] C. S. Graebin, F. V. Ribeiro, K. R. Rogério, A. E. Kümmerle, "Multicomponent Reactions for the Synthesis of Bioactive Compounds: A Review" *Curr. Org. Synth.* **2019**, *16*, 855–899.

[57] K. Gao, S. Shaabani, R. Xu, T. Zarganes-Tzitzikas, L. Gao, M. Ahmadianmoghaddam, M. R. Groves, A. Dömling, "Nanoscale, automated, high throughput synthesis and screening for the accelerated discovery of protein modifiers" *RSC Med. Chem.* **2021**, *12*, 809–818.

[58] S. Tyagarajan, C. L. Andrews, D. C. Beshore, A. V. Buevich, P. J. Curran, P. Dandliker, T. J. Greshock, J. Hoar, A. Kim, P. Karnachi, I. Knemeyer, J. Kozlowski, J. Liu, M. Maletic, R. Myers, V. Rada, D. Sha, B. Sauvagnat, P. Vachal, S. Wolkenberg, W. Yu, Y. Yu, S. W. Krska, "Rapid Affinity and Microsomal Stability Ranking of Crude Mixture Libraries of Histone Deacetylase Inhibitors" *ACS Med. Chem. Lett.* **2024**, *15*, 1787–1794.

[59] H. Grosjean, A. Aimon, S. Hassell-Hart, W. Thompson, L. Koekemoer, J. Bennett, A. Bradley, C. Anderson, C. Wild, W. J. Bradshaw, E. A. FitzGerald, T. Krojer, O. Fedorov, P. C. Biggin, J. Spencer, F. von Delft, "Binding-Site Purification of Actives (B-SPA) Enables Efficient Large-Scale Progression of Fragment Hits by Combining Multi-Step Array Synthesis With HT Crystallography" *Angew. Chem. Int. Ed.* **2025**, *64*, e202424373.

[60] H. Grosjean, K. Fieseler, R. Sanchez-Garcia, W. Thompson, C. M. Deane, F. von Delft, P. C. Biggin, **2025**, ChemRxiv preprint, DOI: 10.26434/chemrxiv-2025-bg2ll.

[61] J. L. Meidner, A. F. Frey, R. A. Zimmermann, M. O. Sabin, Z. Nidoieva, A. C. Weldert, S. N. Hoba, M. W. Krone, F. Barthels, "Nanomole Scale Screening of Fluorescent RNA-Methyltransferase Probes Enables the Discovery of METTL1 Inhibitors" *Angew. Chem. Int. Ed.* **2024**, *63*, e202403792.

[62] Z. Liu, M. Hu, Y. Yang, C. Du, H. Zhou, C. Liu, Y. Chen, L. Fan, H. Ma, Y. Gong, Y. Xie, "An overview of PROTACs: a promising drug discovery paradigm" *Mol. Biomed.* **2022**, *3*, 46.

[63] T. A. Bemis, J. J. La Clair, M. D. Burkart, "Unraveling the Role of Linker Design in Proteolysis Targeting Chimeras" *J. Med. Chem.* **2021**, *64*, 8042–8052.

[64] D. A. Erlanson, K. R. WEBSTER, *High-Throughput Engineering of Molecular Glues*, **2025**, US20250093362A1.

[65] A. CHAMESSIAN, R. GEREAU, *Targeted Protein Degradation Compositions and Methods of Use Thereof for Pain Control*, **2025**, WO2025123001A1.

[66] J. SHAUM, M. A. ERB, E. STEEN, *High Throughput Parallel Synthesis of Small Molecule Degraders*, **2025**, WO2025076501A1.

[67] M. P. Plesniak, E. K. Taylor, F. Eisele, C. M. B. K. Kourra, I. N. Michaelides, A. Oram, J. Wernevik, Z. S. Valencia, H. Rowbottom, N. Mann, L. Fredlund, V. Pivnytska, A. Novén, M. Pirmoradian, T. Lundbäck, R. I. Storer, M. Pettersson, G. M. De Donatis, M. Rehnström, "Rapid PROTAC Discovery Platform: Nanomole-Scale Array Synthesis and Direct Screening of Reaction Mixtures" *ACS Med. Chem. Lett.* **2023**, *14*, 1882–1890.

[68] C. E. Hendrick, J. R. Jorgensen, C. Chaudhry, I. I. Strambeanu, J.-F. Brazeau, J. Schiffer, Z. Shi, J. D. Venable, S. E. Wolkenberg, "Direct-to-Biology Accelerates PROTAC Synthesis and the Evaluation of Linker Effects on Permeability and Degradation" *ACS Med. Chem. Lett.* **2022**, *13*, 1182–1190.

[69] R. Stevens, E. Bendito-Moll, D. J. Battersby, A. H. Miah, N. Wellaway, R. P. Law, P. Stacey, D. Klimaszewska, J. M. Macina, G. A. Burley, J. D. Harling, "Integrated Direct-to-Biology Platform for the Nanoscale Synthesis and Biological Evaluation of PROTACs" *J. Med. Chem.* **2023**, *66*, 15437–15452.

[70] B. Ding, J. Hu, R. Zhang, B. Shou, M. Chen, L. Jiang, M. Yuan, B. Yang, Q. He, J. Cao, C.-L. Zhu, "Solid-Phase Parallel Synthesis of Photocleavable Bifunctional Molecules Enables Efficient Phenotypic Protein Degrader Discovery" *Angew. Chem. Int. Ed.* **2025**, *64*, e202424118.

[71] J. Schönfeld, N. Liebisch, S. Brunst, L. Weizel, S. Knapp, A. Kannt, E. Proschak, K. Hiesinger, "Click chemistry enables rapid development of potent sEH PROTACs using a direct-to-biology approach" *Chem. Commun.* **2025**, *61*, 18108–18111.

[72] N. A. Anderson, B. Barlaam, A. Argyrou, P. C. Astles, H. Bruss, E. B. Cadogan, L. Carlino, L. Alonso-Crisostomo, G. W. Collie, A. J. Edwards, A. Gryniukova, J. Hall, K. Jamal, J. Kent, L. Kitching, C. Kourra, C. Lam, A. G. Milbradt, J. Nikkilä, S. Northall, M. J. O'Connor, J. Overman, C. Pathe, W. Savory, D. Slade, J. A. Spencer, D. Stead, C. J. Stubbs, B. C. Whitehurst, S. Winfield, "Use of Direct-to-Biology Strategies for the Discovery of 2′-Deoxynucleoside 5′-Monophosphate N-Glycosidase (DNPH1) PROTACs" *J. Med. Chem.* **2025**, DOI 10.1021/acs.jmedchem.5c02337.

[73] A.-D. Guo, D. Wei, H.-J. Nie, H. Hu, C. Peng, S.-T. Li, K.-N. Yan, B.-S. Zhou, L. Feng, C. Fang, M. Tan, R. Huang, X.-H. Chen, "Light-induced primary amines and o-nitrobenzyl alcohols cyclization as a versatile photoclick reaction for modular conjugation" *Nat. Commun.* **2020**, *11*, 5472.

[74] J. B. Shaum, M. M. i Ordoño, E. A. Steen, D. V. Wenge, H. Cheong, M. Hunkeler, E. M. Bilotta, Z. Rutter, P. A. Barta, A. M. Thornhill, N. Milosevich, L. M. Hargis, J. Janowski, T. R. Bishop, T. R. Carter, B. da Camara, M. Hinterndorfer, L. Dada, W.-J. He, F. Offensperger, H. Furihata, S. R. Schweber, C. Hatton, Y. Wen, B. F. Cravatt, K. M. Engle, K. A. Donovan, B. Melillo, S. Kitamura, A. Ciulli, S. A. Armstrong, E. S. Fischer, G. E. Winter, M. A. Erb, **2025**, bioRxiv preprint, DOI: 10.1101/2024.09.30.615685.

[75] T. R. Carter, N. Milosevich, L. Dada, J. B. Shaum, K. Barry Sharpless, S. Kitamura, M. A. Erb, "SuFEx-based chemical diversification for the systematic discovery of CRBN molecular glues" *Bioorg. Med. Chem.* **2024**, *104*, 117699.

[76] M. Hu, J. Ochoada, M. Actis, K. McGowan, J. Jarusiewicz, S. Yoshimura, U. Neelakantan, A. Aggarwal, A. Mayasundari, S. Young, L. Yang, Y. Li, S. Mercer, M. Babu, M. Fischer, B. Young, J. Yang, G. Nishiguchi, A. Shelat, D. Blair, **2025**, ChemRxiv preprint, DOI: 10.26434/chemrxiv-2025-4d7nq.

[77] Z. Wang, S. Shaabani, X. Gao, Y. L. D. Ng, V. Sapozhnikova, P. Mertins, J. Krönke, A. Dömling, "Direct-to-biology, automated, nano-scale synthesis, and phenotypic screening-enabled E3 ligase modulator discovery" *Nat. Commun.* **2023**, *14*, 8437.

[78] A. Ng, F. Offensperger, J. A. Cisneros, N. S. Scholes, M. Malik, L. Villanti, A. Rukavina, E. Ferrada, J. T. Hannich, A. Koren, S. Kubicek, G. Superti-Furga, G. E. Winter, "Discovery of Molecular Glue Degraders via Isogenic Morphological Profiling" *ACS Chem. Biol.* **2023**, *18*, 2464–2473.

[79] C. T. Supuran, "Carbonic anhydrase versatility: from pH regulation to CO2 sensing and metabolism" *Front. Mol. Biosci.* **2023**, *10*, DOI 10.3389/fmolb.2023.1326633.

[80] C. T. Supuran, "Carbonic anhydrases: novel therapeutic applications for inhibitors and activators" *Nat. Rev. Drug Discov.* **2008**, *7*, 168–181.

[81] R. P. Thomas, E. K. Grant, E. R. Dickinson, F. Zappacosta, L. J. Edwards, M. M. Hann, D. House, N. C. O. Tomkinson, J. T. Bush, "Reactive fragments targeting carboxylate residues employing direct to biology, high-throughput chemistry" *RSC Med. Chem.* **2023**, *14*, 671–679.

[82] E. K. Grant, D. J. Fallon, M. M. Hann, K. G. M. Fantom, C. Quinn, F. Zappacosta, R. S. Annan, C. Chung, P. Bamborough, D. P. Dixon, P. Stacey, D. House, V. K. Patel, N. C. O. Tomkinson, J. T. Bush, "A Photoaffinity-Based Fragment-Screening Platform for Efficient Identification of Protein Ligands" *Angew. Chem. Int. Ed.* **2020**, *59*, 21096–21105.

[83] H. Sati, E. Carrara, A. Savoldi, P. Hansen, J. Garlasco, E. Campagnaro, S. Boccia, J. A. Castillo-Polo, E. Magrini, P. Garcia-Vello, E. Wool, V. Gigante, E. Duffy, A. Cassini, B. Huttner, P. R. Pardo, M. Naghavi, F. Mirzayev, M. Zignol, A. Cameron, E. Tacconelli, A. Aboderin, M. Al Ghoribi, J. Al-Salman, A. Amir, A. Apisarnthanarak, M. Blaser, A. El-Sharif, S. Essack, S. Harbarth, X. Huang, G. Kapoor, G. Knight, J. C. Muhwa, D. L. Monnet, T. Ousassa, R. Sacsaquispe, J. Severin, M. Sugai, N. Taneja, A. Umubyeyi Nyaruhirira, "The WHO Bacterial Priority Pathogens List 2024: a prioritisation study to guide research, development, and public health strategies against antimicrobial resistance" *Lancet Infect. Dis.* **2025**, *25*, 1033–1043.

[84] A. von Delft, M. D. Hall, A. D. Kwong, L. A. Purcell, K. S. Saikatendu, U. Schmitz, J. A. Tallarico, A. A. Lee, "Accelerating antiviral drug discovery: lessons from COVID-19" *Nat. Rev. Drug Discov.* **2023**, *22*, 585–603.

[85] Y. Yao, R. U. Kadam, C.-C. D. Lee, J. L. Woehl, N. C. Wu, X. Zhu, S. Kitamura, I. A. Wilson, D. W. Wolan, "An influenza A hemagglutinin small-molecule fusion inhibitor identified by a new high-throughput fluorescence polarization screen" *Proc. Natl. Acad. Sci.* **2020**, *117*, 18431–18438.

[86] L. Dada, E. Nagai, S. Agrawal, A. S. Wirchnianski, I. A. Wilson, K. Chandran, S. Kitamura, "SuFEx-enabled high-throughput medicinal chemistry for developing potent tamoxifen analogs as Ebola virus entry inhibitors" *Front. Immunol.* **2025**, *16*, DOI 10.3389/fimmu.2025.1533037.

[87] J. Y. Ong, E. A. Melendez, T. Wennekes, **2025**, ChemRxiv preprint, DOI: 10.26434/chemrxiv-2025-4kzhd.

[88] M. F. Köllen, M. G. Schuh, R. Kretschmer, J. Chen, A. I. Bohne, D. P. Halter, S. A. Sieber, **2025**, ChemRxiv preprint, DOI: 10.26434/chemrxiv-2025-s418c.

[89] G. Danti, L. Popella, J. Vogel, H. M. Maric, "High-Throughput Tiling of Essential mRNAs Increases Potency of Antisense Antibiotics" *Adv. Sci.* **2025**, *12*, 2504284.

[90] Y. Tasdan, G. Balaji, J. Davidson, N. Akhtar, O. Ilyichova, L. Guetzoyan, I. Chandrashekaran, W. Alwan, H. Cobb, M. Gunzburg, A. Hasanzada, S. Roughley, J. Murray, B. Mohanty, B. Capuano, B. Doak, M. Scanlon, **2025**, ChemRxiv preprint, DOI: 10.26434/chemrxiv-2025-hzb0c.

[91] A. Vuorinen, C. R. Kennedy, K. A. McPhie, W. McCarthy, J. Pettinger, J. M. Skehel, D. House, J. T. Bush, K. Rittinger, "Enantioselective OTUD7B fragment discovery through chemoproteomics screening and high-throughput optimisation" *Commun. Chem.* **2025**, *8*, 12.

[92] A. J. Roecker, K. M. Schirripa, H. M. Loughran, L. Tong, T. Liang, K. L. Fillgrove, Y. Kuo, K. Bleasby, H. Collier, M. D. Altman, M. C. Ford, R. E. Drolet, M. Cosden, S. Jinn, N. G. Hatcher, L. Yao, M. Kandebo, J. D. Vardigan, R. B. Flick, X. Liu, C. Minnick, L. A. Price, M. L. Watt, W. Lemaire, C. Burlein, G. C. Adam, L. A. Austin, J. N. Marcus, S. M. Smith, M. E. Fraley, "Pyrazole Ureas as Low Dose, CNS Penetrant Glucosylceramide Synthase Inhibitors for the Treatment of Parkinson's Disease" *ACS Med. Chem. Lett.* **2023**, *14*, 146–155.

[93] S. Ponzi, F. Ferrigno, M. Bisbocci, C. Alli, J. M. Ontoria, A. Petrocchi, C. Toniatti, E. Torrente, "Direct-to-biology platform: From synthesis to biological evaluation of SHP2 allosteric inhibitors" *Bioorg. Med. Chem. Lett.* **2024**, *100*, 129626.

[94] S. Chen, Z. Wang, J. Gao, Y. Wang, J. Liang, Y. Zhu, H. Xu, K. Chen, L. Jin, H. Zhang, H. Xiong, C. Luo, "Rapid Discovery of Celastrol Derivatives as Potent and Selective PRDX1 Inhibitors via Microplate-Based Parallel Compound Library and In Situ Screening" *J. Med. Chem.* **2025**, *68*, 13609–13627.

[95] J. Mason, "D2B or Not D2B?: An Introductory Guide to Direct-to-Biology," can be found under https://www.domainex.co.uk/news/d2b-or-not-d2b-introductory-guide-direct-biology, **2025**.

[96] J. B. Baell, J. W. M. Nissink, "Seven Year Itch: Pan-Assay Interference Compounds (PAINS) in 2017—Utility and Limitations" *ACS Chem. Biol.* **2018**, *13*, 36–44.

[97] J. Baell, M. A. Walters, "Chemistry: Chemical con artists foil drug discovery" *Nat. News* **2014**, *513*, 481.

[98] T. Gerstberger, H. Berger, F. H. Büttner, M. Gmachl, D. Kessler, M. Koegl, S. Lucas, L. J. Martin, M. Mayer, D. B. McConnell, S. Mitzner, G. Scholz, M. Treu, B. Wolkerstorfer, S. Zahn, K. M. Zak, P. A. Jaeger, P. Ettmayer, "Chasing Red Herrings: Palladium Metal Salt Impurities Feigning KRAS Activity in Biochemical Assays" *J. Med. Chem.* **2024**, *67*, 11701–11711.

[99] R. Stevens, H. E. P. Palmer, A. H. Miah, G. A. Burley, "Factors to Consider for Synthesis in 1536-Well Plates─An Amide Coupling Case Study for PROTAC Synthesis" *J. Org. Chem.* **2025**, *90*, 2192–2200.

"

DNA-Encoded Library (DEL) Screening

The concept of DELs was originally postulated by Brenner and Lerner in 1992.[229] Since then, DEL screening has emerged as a powerful and increasingly adopted approach in academic and industrial research. In this strategy, up to billions of small molecules are covalently linked to unique DNA barcodes, collectively constituting a DEL. Standard protocols (Figure 17A) typically involve immobilization of the targeted protein followed by incubation with the library.[230,231] Subsequent washing steps remove non-binding compounds, whereas high-affinity binders are selectively enriched.[230,231] Enriched ligands are then eluted, and DNA sequencing of the associated barcodes enables identification of their chemical structures.[230,231] DEL screenings can be performed under diverse experimental conditions and with different target variants, including enzyme mutants or interaction partners, thereby providing early insights into the binding profiles and potential ligand binding sites. A major advantage of DEL screening over conventional hit-identification methodologies lies in its inherently low selection bias, as compound enrichment is largely independent of user-driven design choices and subjective decision-making.[232] Moreover, the combinatorial nature of DEL synthesis enables the generation of libraries containing billions of compounds through a small number of synthetic steps.[232]

The synthesis of DELs normally follows the split-and-pool protocol (Figure 17B).[231,233] In the split-and-pool synthesis, chemical building blocks are sequentially added and encoded by ligating corresponding DNA tags using T4 ligase.[231,233,234] The resulting conjugates are then “pooled” and randomly redistributed ("split"), and then the next cycle of monomer addition and DNA tagging is performed.[231,233,234] This process can be repeated multiple times, allowing for the stepwise construction of large and diverse molecular libraries. Over time, the scope of compatible chemical transformations has significantly expanded. While early DEL strategies mainly relied on robust reactions such as amide bond formation, heterocycle synthesis, Diels-Alder cycloadditions, nucleophilic aromatic substitution, and reductions, more recent developments have incorporated a broader range of methodologies.[235] These include metal-catalyzed C-C bond formations[236], photoredox chemistry[237,238], enzymatic catalysis[239], and multicomponent condensations[240] – enhancing the structural complexity and diversity of DELs.[241] Numerous DEL screenings have already resulted in successful case studies within the field of inhibitor discovery.[232] Not only has this approach enabled the targeting of previously "undruggable" proteins, but it has also revealed novel and unexpected modes of ligand-protein interaction.[232]

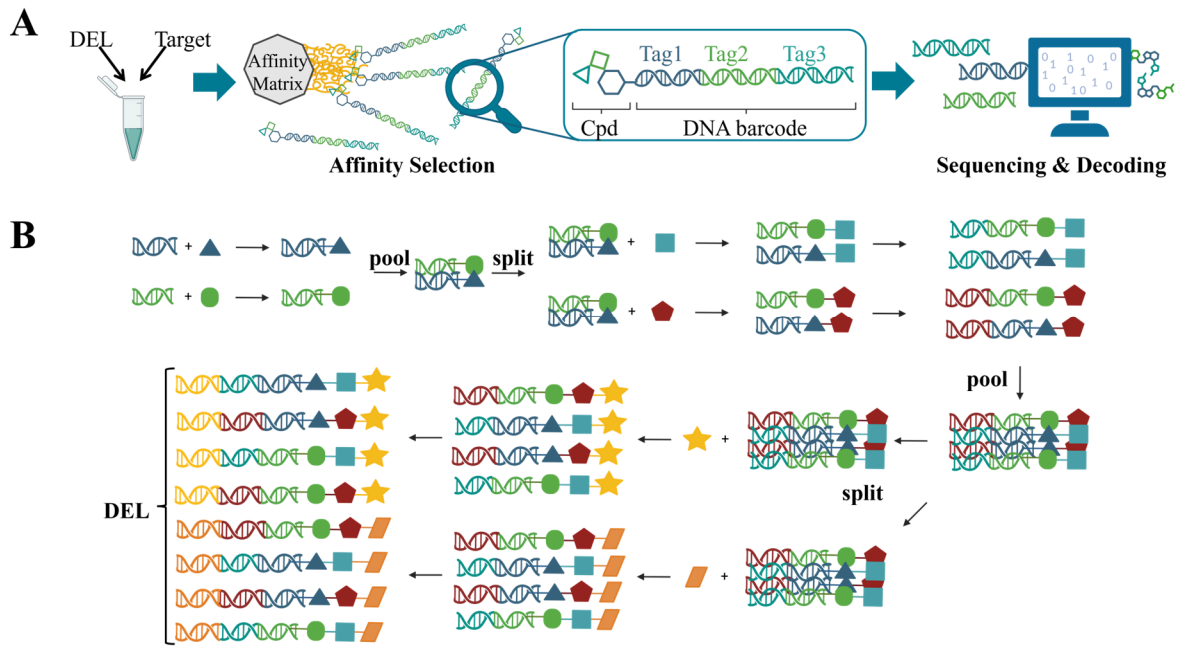


Figure 17. Schematic overview of DEL screening principles. (**A**) General workflow of a DEL screening. The DEL is incubated with the target protein under various conditions. Through iterative rounds of affinity selection, binders are enriched while non-binders are removed. The DNA barcodes of retained molecules are sequenced to identify the corresponding small-molecule structures. (**B**) DEL synthesis via the split-and-pool strategy. Following each synthetic step, in which a distinct building block is incorporated (represented here by various geometric shapes), a unique DNA tag is ligated using T4 ligase. The resulting conjugates are then pooled and redistributed ("split") for the next synthetic cycle, enabling the combinatorial assembly of a highly diverse library.

In some instances, DEL-derived compounds were found to induce conformational changes in target proteins, thereby inhibiting their function through previously unrecognized mechanisms. This was demonstrated, for example, in the case of the mesenchymal-epithelial transition factor (c-MET)[242] and TGF-β-activated kinase 1 (TAK1)[243], where inhibitors exhibited nanomolar IC_{50} values. In addition to these findings, DEL screening has facilitated the identification of novel protein-ligand interactions. Notable examples include Bruton's tyrosine kinase (BTK)[244], receptor-interacting serine/threonine-protein kinase 1 (RIP1)[245], Mer tyrosine kinase[246], autotaxin[247], BRD4[248], and enoyl-ACP reductase (InhA)[249]. All of these have ligands displaying nanomolar to picomolar potency. A particularly striking example is the discovery of a DEL-derived compound that induces dimerization of ATPase family AAA-domain containing protein 2 (ATAD2), achieving inhibition in the nanomolar range.[250] All these examples demonstrate favorable selectivity profiles, likely attributed to their novel binding modes. Taken together, these successful examples demonstrate that DEL technology enables the identification of novel chemotypes for established and previously uncharacterized binding modes. Furthermore, this approach holds potential for addressing enzymes that have traditionally been considered "undruggable".

2 Project Overview

The work presented in this doctoral thesis is primarily structured around two main research projects focusing on diverse libraries (D2B and DEL) for drug discovery targeting RNA Mtases, complemented by studies exploring new modalities in medicinal chemistry targeting RNA and RNA Mtases. The main research projects – D2B and DEL – are two distinct types of nanoscale libraries, each employing different design principles and strategies for molecular diversification.

2.1 Project 1: Direct-to-Biology Strategies

The first project comprised two parts centered on the application of D2B strategies targeting distinct RNA Mtases. The D2B approach involves the direct use of crude, miniaturized reaction mixtures – typically in a well-plate format – within biochemical assays, thereby saving time, resources, and costs (see Chapter 1.2.2).[251]

In the first part of the project, this strategy was employed to discover novel fluorescent tracers for various RNA Mtases via CuAAC chemistry. Crude products were directly assessed using MST and FP assays without further purification. As a starting point, the previously reported tracer FTAD served as a prototype.[211] The newly identified tracers were subsequently utilized in an HTS campaign of a U.S. Food and Drug Administration (FDA)-approved drug library to discover novel inhibitors of METTL1.

In the second part, a triazole library was synthesized via CuAAC-based D2B methodology, using a core scaffold structurally related to a pyrrolopyrimidone motif previously reported by Hill *et al*..[106] The crude reaction mixtures were directly screened in an FP displacement assay targeting *S. aureus* TrmD, employing a newly developed fluorescent tracer. This effort led to the identification of potent and selective TrmD inhibitors. A benzyloxycarbonyl (Cbz)-protected intermediate from a preparative hit compound synthesis represents the first compound with demonstrable antibacterial activity against *S. aureus* via a prodrug strategy.

The following two publications are the results obtained in this project:

*shared first authors

(1) Meidner, J. Laurenz*; **Frey, Ariane F.***; Zimmermann, Robert A.*; Sabin, Mark O.; Nidoieva, Zarina; Weldert, Annabelle C.; Hoba, Sabrina N.; Krone, Mackenzie. W.; Barthels, Fabian; Nanomole Scale Screening of Fluorescent RNA-Methyltransferase Probes Enables the Discovery of METTL1 Inhibitors. *Angew. Chem. Int. Ed Engl.* **2024**, *63* (48), e202403792. https://doi.org/10.1002/anie.202403792.

Own contribution: Synthesis of scaffold alkynes (70%), D2B synthesis of fluorescent tracers, and preparative synthesis of tracer Cy5TPD, ^{3}H-incorporation assay of hit compounds from METTL1 screening, manuscript editing, and SI writing.

Contributions from other authors: Protein expression, FP and MST assay, preparative synthesis of Cy5TAD and SAH-like alkyne, synthesis of scaffold alkynes (30%), METTL1 assays, manuscript writing, SI writing.

(2) **Hübner, Ariane F.***; Weldert, Annabelle C.*; Marciniak, Tessa; Hof, Florian; Beck, Vivien S.; Carien, Samuel; Mulartschyk, Sophie N.; Wolf, Eva; Ziebuhr, Wilma; Barthels, Fabian; Nanoscale Direct-to-Biology Optimization and Structural Insights into Selective S. Aureus TrmD Inhibitors. *J. Med. Chem*. **2025**, *68* (24), 26246–26262. https://doi.org/10.1021/acs.jmedchem.5c02323.

Own contribution: Establishing CuAAC for alkyne scaffold and adaptation for D2B strategy, D2B synthesis of triazole library, establishing FP assay with new tracer, D2B library FP-screening, preparative synthesis (tracer, hit compounds, prodrugs and starting point compounds), validation of hit compounds and prodrugs in FP and ^{3}H-incorporation assay (selectivity and inhibitory efficiency), manuscript and SI writing and editing.

Contributions from other authors: Protein preparation and crystallization, FP selectivity assay, aptamer assay, bacterial growth inhibition assays, Cell Titer Glo cell viability assay, lysate assay, manuscript and SI writing and editing.

2.2 Project 2: DNA-Encoded Library Screening

The second project focused on the identification of novel chemotypes targeting the RNA Mtase DNMT2 through a DEL screening. The goal was to achieve high affinity and selectivity across different Mtases. The DEL technology has shown in the past the capability of discovering unforeseen new chemotypes and binding modes for a variety of enzymes.[232] The DEL utilized in this study was obtained via the DELopen initiative from WuXi AppTec, which provides access to the DEL technology for academic research purposes.

From this screening campaign, five unique hits were identified, comprising two distinct chemotypes. These candidates were subjected to biophysical characterization, revealing that all hit compounds were binders, yet only a few are inhibitors of the DNMT2. X-ray crystallographic investigations of an inhibitory hit compound provided detailed insights into its binding mode. This analysis uncovered an allosteric compound interaction with DNMT2, inducing a conformational rearrangement of a flexible loop blocking the SAH/SAM pocket. This structural insight enabled a subsequent SAR study, ultimately leading to the development of a selective DNMT2 inhibitor. The inhibitor showed synergistic effects with doxorubicin in cancer cells and a cellular decrease in the m^5C modification of tRNA.

The following publication contains the results obtained in this project:

*shared first authors

(3) **Frey, Ariane F.***; Schwan, Merlin*; Weldert, Annabelle C.; Kadenbach, Valerie; Kopp, Jürgen; Nidoieva, Zarina; Zimmermann, Robert A.; Gleue, Lukas; Zimmer, Collin; Jörg, Marko; Friedland, Kristina; Helm, Mark; Sinning, Irmgard; Barthels, Fabian; DNA-Encoded Library Screening Uncovers Potent DNMT2 Inhibitors Targeting a Cryptic Allosteric Binding Site. *iScience* **2025**, *28* (9), 113300. https://doi.org/10.1016/j.isci.2025.113300.

Own contribution: DEL panning, analysis of hit clustering data, hit selection, MST assay, ^3H-incorporation assay, synthesis of compounds and tracers (partly supervision of students Valerie Kadenbach and Hanna Bodenstaff), AS-MS and MST assay (supervision of Valerie Kadenbach and Hanna Bodenstaff), writing and editing manuscript and SI.

Contributions from other authors: Protein expression and purification, protein crystallization, ITC, pull-down assay, tRNA preparation, cell viability assays and tRNA LC/MS assay, PAMPA, and writing and manuscript and SI editing.

2.3 Project 3: Novel Modalities for Medicinal Chemistry of RNA and RNA Methyltransferases

The third project includes two distinct parts: (1) the rational design and development of PROTACs targeting METTL3 for targeted protein degradation in cells, and (2) the establishment of non-covalent RNA-binding dyes for MST assays.

In the first part, four successive generations of PROTACs were synthesized, utilizing the METTL3 inhibitor previously developed by Storm Therapeutics (STM2457 (**9**), Figure 14).[166] These degraders incorporated varying E3 ligase ligands, linker architectures, and METTL3-binding moieties. Their cellular and biochemical activities were evaluated via FP-assays, homogeneous time-resolved fluorescence (HTRF), and Western blot analysis, enabling the optimization of degradation efficiency and affinity.

The second part focused on the development of an MST mix-and-measure protocol using non-covalent RNA-binding dyes from the Sybr and Syto series. This approach enables rapid and cost-effective analysis of RNA-ligand/protein interactions and RNA modifications, eliminating the need for prior RNA labeling and thus accelerating the assay workflow.

The following two publications are part of the results obtained in this project:

(4) Weldert, Annabelle C.; **Frey, Ariane F.**; Krone, Mackenzie W.; Krähe, Franziska; Kuhn, Hannah; Kersten, Christian; Barthels, Fabian; Structure-Guided Design of a Methyltransferase-like 3 (METTL3) Proteolysis Targeting Chimera (PROTAC) Incorporating an Indole–Nicotinamide Chemotype. *RSC Med. Chem.* **2025**, *16* (9), 4194-4207. https://doi.org/10.1039/d5md00359h.

Own contribution: Synthesis of compounds (45%, partly supervision of student Franziska Krähe), SI writing (synthesis and NMR) and editing, and manuscript editing.

Contributions from other authors: Synthesis of compounds (55%), protein preparation, FP-assay, Western Blot analysis, HTRF-assay, cultivation of cells, docking and MD simulations, cell assays, manuscript writing and editing, SI writing and editing.

(5) Kallert, Elisabeth; Behrendt, Malte; **Frey, Ariane**; Kersten, Christian; Barthels, Fabian; Non-Covalent Dyes in Microscale Thermophoresis for Studying RNA Ligand Interactions and Modifications. *Chem. Sci.* **2023**, *14* (36), 9827–9837. https://doi.org/10.1039/d3sc02993j.

Own contribution: ^{3}H-incorporation assay, SI writing.

Contributions from other authors: MST experiments, RNA preparation, PCR, *in vitro* transcription, and manuscript and SI writing and editing.

2.4 Publications Beyond this Doctoral Thesis

(6) Müller, Patrick; Meta, Mergim; Meidner, J. Laurenz; Schwickert, Marvin; Meyr, Jessica; Schwickert, Kevin; Kersten, Christian; Zimmer, Collin; Hammerschmidt, Stefan J.; **Frey, Ariane F.**; Lahu, Albin; De La Hoz-Rodríguez, Sergio; Agost-Beltrán, Laura; Rodríguez, Santiago; Diemer, Kira; Neumann, Wilhelm; Gonzàlez, Florenci V.; Engels, Bernd; Schirmeister, Tanja; Investigation of the Compatibility between Warheads and Peptidomimetic Sequences of Protease Inhibitors – A Comprehensive Reactivity and Selectivity Study. *Int. J. Mol. Sci.* **2023**, *24* (8), 7226. https://doi.org/10.3390/ijms24087226.

(7) Müller, Patrick; Zimmer, Collin; **Frey, Ariane F.**; Holzmann, Gideon; Weldert, Annabelle C.; Schirmeister, Tanja; Ligand-Based Design of Selective Peptidomimetic uPA and TMPRSS2 Inhibitors with Arg Bioisosteres. *Int. J. Mol. Sci.* **2024**, *25* (3), 1375. https://doi.org/10.3390/ijms25031375.

3 Project 1: Direct-to-Biology Strategies

3.1 Nanomole Scale Screening of Fluorescent RNA-Methyltransferase Probes Enables the Discovery of METTL1 Inhibitors.

3.1.1 Context and Project Summary

The development of Mtase inhibitors is limited by the lack of robust, HTS-compatible assays for ligand discovery and characterization. Previously, Zimmermann *et al*. introduced the SAH-like tracer 5-FAM-triazolyl-adenosyl-diaminobutyric acid (FTAD).[211] This enables a displacement assay compatible with MST and FP, providing a suitable setup for HTS.[211] However, despite its affinity to DNMT2, FTAD shows limited applicability to other RNA Mtases.

To address this limitation, this project aimed to identify novel, broadly applicable fluorescent tracers for RNA Mtases by combining the SAH-like scaffold of FTAD with a series of chemically diverse fluorophores differing in charge, polarity, size, and structural features. Due to the limited availability and high cost of fluorescent dyes, a D2B approach was implemented using CuAAC on a nanomole scale. Crude reaction mixtures were directly assessed in FP and MST assays without prior purification. In this screening, Cy5-triazolyl-adenosyl-diaminobutyric acid (Cy5TAD) – comprising a Cy5 fluorophore linked to an SAH-like core – was identified as a potent tracer for multiple RNA Mtases with a Rossmann fold, including NSUN2, NSUN6, METTL1, and the METTL3/14 complex.

However, Cy5TAD exhibited low affinity for the bacterial SPOUT-fold Mtase TrmD, revealing the structural limitations of the existing scaffold. To overcome this, a Protein Data Bank (PDB) mining approach was employed to identify SAH-displacement motifs. Eleven candidate scaffolds were synthesized bearing terminal alkynes and subsequently coupled to FAM-N_3 and Cy5-N_3 dyes via CuAAC and tested without purification in MST and FP. Among these, Cy5-thienopyrimidone (Cy5TPD) – featuring a thienopyrimidone scaffold – emerged as a suitable tracer for *H. influenzae* TrmD. A systematic workflow was established to enable the selection or design of suitable fluorescent tracers for specific RNA Mtases for future HTS campaigns.

As a proof-of-concept, the newly developed Cy5TAD tracer was utilized in an HTS campaign with 2 230 FDA-approved compounds against METTL1, an RNA Mtase implicated in tumorigenesis (see Chapter 1.1.3).[128–132] To date, only a few METTL1 inhibitors have been reported, and some of them with poor binding affinities (Figure 11).[135] (*S*)-Crizotinib was identified as a selective METTL1 inhibitor with a K_D-value of 138 µM. This finding provides a promising starting point for future METTL1-targeted drug discovery initiatives.

This work has been published in: Angewandte Chemie (International Edition) – A Journal of the German Chemical Society (impact factor: 16.9).

Article reprinted with open access permission from *Angew. Chem. Int. Ed Engl.,* **2024**, *63* (48), e202403792. 'Nanomole Scale Screening of Fluorescent RNA-Methyltransferase Probes Enables the Discovery of METTL1 Inhibitors.' © The Authors. Angewandte Chemie International Edition published by Wiley-VCH GmbH.

The full version of the article, including the electronic Supplementary Information, can be accessed online at doi: 10.1002/anie.202403792.

3.1.2 Contributions

Own contribution: Synthesis of scaffold alkynes (70%), D2B synthesis of fluorescent tracers, and preparative synthesis of tracer Cy5TPD, ^{3}H-incorporation assay of hit compounds from METTL1 screening, manuscript editing, and SI writing.

Contributions from other authors: Protein expression, FP and MST assay, preparative synthesis of Cy5TAD and SAH-like alkyne, synthesis of scaffold alkynes (30%), METTL1 assays, manuscript writing, SI writing.

3.1.3 Publication

The following publication quoted within "" from page 50 to page 56 is the same as the manuscript cited on page 49.[252] "

GDCh Communication Angewandte International Edition Chemie www.angewandte.org
Check for updates
How to cite: *Angew. Chem. Int. Ed.* **2024**, *63*, e202403792
doi.org/10.1002/anie.202403792

Drug Discovery

Nanomole Scale Screening of Fluorescent RNA-Methyltransferase Probes Enables the Discovery of METTL1 Inhibitors

*J. Laurenz Meidner[+], Ariane F. Frey[+], Robert A. Zimmermann[+], Mark O. Sabin, Zarina Nidoieva, Annabelle C. Weldert, Sabrina N. Hoba, Mackenzie W. Krone, and Fabian Barthels**

Abstract: RNA methylation is a metabolic process validated for its association with various diseases, and thus, RNA methyltransferases (MTases) have become increasingly important in drug discovery. Yet, most frequently utilized RNA MTase assays are limited in their throughput and hamper this rapidly evolving field of medicinal chemistry. In this study, we describe a modular nanomole scale building block system that allowed the identification of tailored fluorescent MTase probes to unlock a broad selection of MTase drug targets for fluorescence-based binding assays. Probe candidates were initially prepared on a 4 nanomole scale and could be tested directly from crude reaction mixtures to allow rapid probe identification and optimization. Using an alkyne-azide click late-stage functionalization strategy and in silico protein databank mining, we established a selection of fluorescent probes suitable for relevant drug targets from the METTL and NSUN families, as well as bacterial and viral MTases. Using this concept, a high-throughput screening on the unexplored drug target METTL1 discovered three hit compounds with micromolar potency providing a (1*H*-pyrazol-4-yl)pyridine-based starting point for METTL1 drug discovery.

RNA has become increasingly important in modern drug discovery as a drug itself, a target for drugs, and not at last a key component in cellular pathways associated with malignancies and infections.[3,4] In this regard, methylation of RNA is a metabolic process in many organisms validated for their association with various diseases.[5] With STC-15, the first-in-class RNA methyltransferase (MTase) inhibitor targeting METTL3/14 was brought into clinical trials just in 2023 highlighting the recent shift of paradigm.[6] During the preparation of this manuscript, the discovery of a series of small-molecule inhibitors of METTL1 was reported by Nai et al.[7]

Currently, enzymatic scintillation assays using ^{3}H-labelled *S*-adenosylmethionine (SAM) and the LC/MS-based detection of the MTase reaction co-product *S*-adenosylhomocysteine (SAH) are the state-of-the-art for screening drug candidates on RNA MTases such as METTL3/14,[8] DNMT2,[1] NSUN2,[9] and anti-infective targets like *H. influenzae* TrmD or SARS-CoV2 nsp10/16.[10,11] Such enzyme activity-based assay formats are valuable for the determination of inhibitory constants (IC_{50}, K_I) of advanced drug- and lead-like candidates but have significant drawbacks compared to biophysical ligand binding assays such as increased susceptibility to assay interference and poor reproducibility at high ligand concentrations.[12] Despite these limitations, time consumption and reagent/instrument costs of current activity-based and biophysical MTase assays are inherently high, thus, limiting the application for medium- to high-throughput applications and hampering this steadily evolving field of medicinal chemistry.[13]

To tackle this methodological gap, we recently introduced a fluorescent probe for screening DNMT2 inhibitors using microscale thermophoresis (MST) and fluorescence polarisation (FP) assays.[14] The 5-FAM-triazolyl-adenosyl-diaminobutyric acid (**FTAD**) probe binds to DNMT2's active site where it is displaced by ligands such as drug candidates, offering a convenient primary assay for drug screening. Compared to label-free screening methods such as SPR (Surface plasmon resonance) or ITC (Isothermal titration calorimetry), this active site probe shows a major advantage over the previous methods for MTase drug screening applications. Allosteric non-inhibiting binders are not detected, as these do not influence the catalytic MTase function and are mostly false-positive hits in terms of inhibitor development. Yet, this concept shows its severe limitation for usage with numerous other RNA MTases e.g., from the NSUN-, and METTL-families, as well as non-Rossmann-fold MTases such as bacterial TrmD, because **FTAD** shows only weak protein binding affinity (K_D > 20 μM) to many of those disease-associated potential drug targets (Figure S1 A).

[*] J. L. Meidner,[+] A. F. Frey,[+] Dr. R. A. Zimmermann,[+] M. O. Sabin, Dr. Z. Nidoieva, A. C. Weldert, S. N. Hoba, Dr. F. Barthels
Institute of Pharmaceutical and Biomedical Sciences
Johannes Gutenberg-University, 55128 Mainz, Germany.
E-mail: barthels@uni-mainz.de
Dr. M. W. Krone, Dr. F. Barthels
Department of Molecular, Cellular, and Developmental Biology
Yale University, New Haven, CT 06511, USA.
[+] Authors have contributed equally.

© 2024 The Authors. Angewandte Chemie International Edition published by Wiley-VCH GmbH. This is an open access article under the terms of the Creative Commons Attribution License, which permits use, distribution and reproduction in any medium, provided the original work is properly cited.

© 2024 The Authors. Angewandte Chemie International Edition published by Wiley-VCH GmbH

GDCh Communication Angewandte International Edition Chemie

15213773, 2024, 48, Downloaded from https://onlinelibrary.wiley.com/doi/10.1002/anie.202403792 by Universitatsbibliothek Mainz, Wiley Online Library on [23/10/2025]. See the Terms and Conditions (https://onlinelibrary.wiley.com/terms-and-conditions) on Wiley Online Library for rules of use; OA articles are governed by the applicable Creative Commons License

In this current study, we describe a modular building block system using combinational nanomole-scale chemistry that allowed us to identify tailored fluorescent probes consisting of two recombined segments (a fluorophore & an MTase recruiter), to unlock a much broader selection of MTase targets for drug discovery including previously untargeted MTases from the NSUN- and METTL-families (Figure 1). Subsequently, we have shown the general usability of this system for a drug screening application of the untargeted MTase METTL1 (Figure 5).

In the first step of our probe development campaign, we considered SAH-triazole-derived chemotypes as probe candidates because a.) the SAH-triazole motif is well established among MTase inhibitors,[−15–17] and b.) we could rapidly employ a selection of diverse fluorophore azides to be attached to the existing SAH-alkyne building block by copper-catalyzed alkyne-azide click (CuAAC) late-stage functionalization reaction. To cover a broad spectrum of physicochemical fluorophore properties, we utilized fluorophore azides which can be categorized into three groups: globular dyes, like 5-FAM, Atto488, Atto590, and Atto647N; small organic fluorophores like NBD or BODIPY; and cyanine-type elongated fluorophores like Cy3/Cy5. From a physicochemical view, this set of fluorophores can also be characterized by molecular charge (from Atto488: X^{-1} to Atto590: X^{+1}) or hydrophobicity (NBD: most polar, Cy5: least polar). While all of our selected fluorophore azides are biocompatible and show similar suitability for MST- resp. FP-based assays, it is noteworthy that when selecting your fluorophores, those that do not have a flexible linker ("propeller effect") and whose fluorescence lifetime is short (<10 ns) are best suited to develop FP assays.[18] For initial probe screening, the probe synthesis was conducted on a 4 nanomole scale (416 μM in 12 μL) according to conventional CuAAC conditions with Cu(II), ascorbate, and tris((1-benzyl-4-triazolyl)methyl)amine in 1:1 DMSO/water (Figure 2A).[2]

Afterward, the success of the reaction was verified by LC/MS. The reaction was considered successful if a product conversion of >85 % was achieved (Figure S5), and hence, the probes could be tested directly from the crude reaction mixture by an MST displacement experiment with the natural ligand SAH (Figure 2B).[14] Importantly, we ensured that the CuAAC additives did not interfere with the MST assay by validating the MST binding characteristics of in situ synthesized **FTAD** vs. HPLC-purified **FTAD** as indistinguishable (Figure S1B,C). Subsequently, these probe candidates were screened on two selected model MTases, METTL1 and NSUN6, for which currently no selective inhibitors are available, while overexpression was found to drive oncogenesis, rendering these enzymes potential, yet unexplored, drug targets.[19,20] For primary probe screening, an MTase solution (2 μM) was treated with the respective probe candidate (100 nM), and the thermophoresis profile was acquired both with or without the addition of the active site ligand SAH (100 μM). The probe with the largest MST shift between the presence of SAH and without this competitor was considered a promising probe candidate. During this probe screening, for METTL1 (Figure 2C) and NSUN6 (Figure S2A), two BODIPY- resp. Cy5-containing probes were identified. Subsequently, these probes were resynthesized, purified, and validated on a preparative scale.

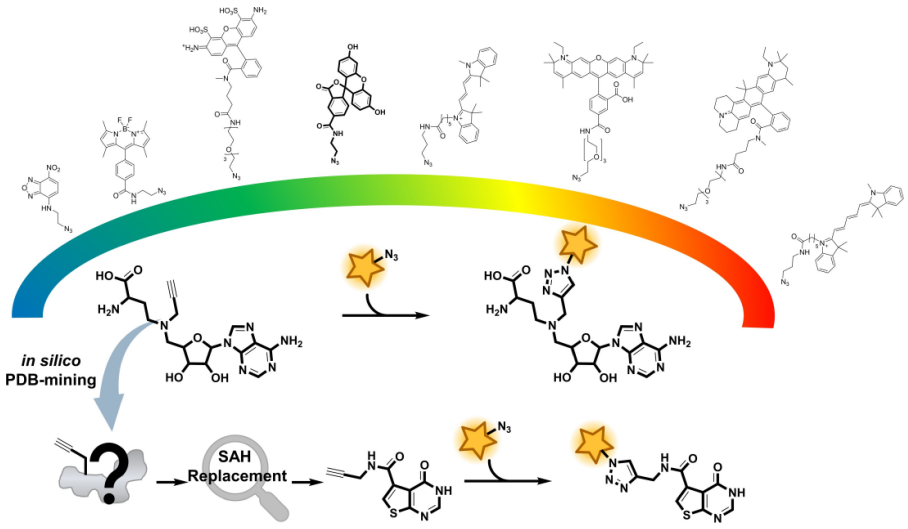


Figure 1. Overview of the nanomole-scale strategy for the development of MTase probes. Eight diverse fluorophore azides (represented as stars) were attached to a SAH-alkyne building block by CuAAC late-stage functionalization reactions.[1,2] By this, probe candidates were prepared on a 4 nanomole scale and tested directly from crude reaction mixtures for target affinity. Secondly, the variation of the SAH-core structure by a protein databank (PDB)-mining allowed the identification of eleven SAH-replacement scaffolds that were also introduced to fluorophore functionalization to expand the chemical space of MTase probes. This strategy led to the identification of a thienopyrimidine probe suitable for SPOUT-fold bacterial MTases which did not bind the SAH-alkyne building block.

© 2024 The Authors. Angewandte Chemie International Edition published by Wiley-VCH GmbH

GDCh Communication Angewandte International Edition Chemie

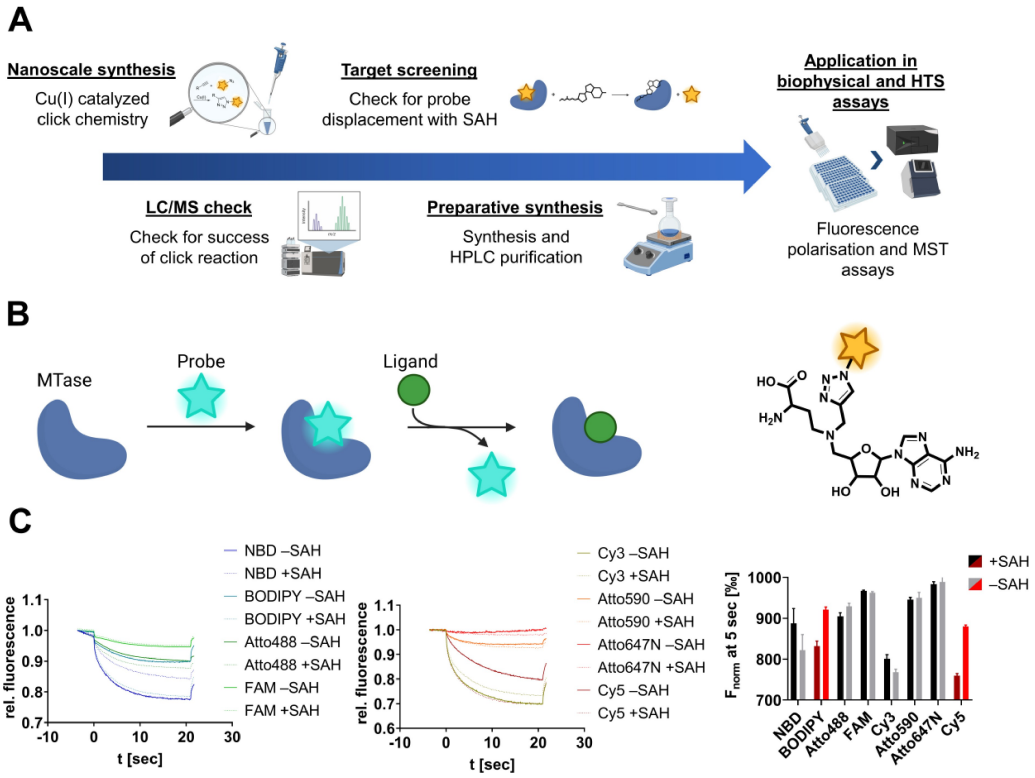


Figure 2. MTase probe development strategy. (**A**) Fluorescent probe development was achieved in five sequential steps. (**B**) Schematic depiction of the displacement assay: Functional probes form complexes with MTases, and thus, the thermophoresis (MST assay) or polarisation (FP assay) is altered compared to the unbound probe. Titration with a competitive ligand (such as SAH) leads to the displacement of the probe and restores the initial unbound fluorescence properties. (**C**) Screening results of TAD-probe candidates (100 nM) on METTL1 (2 μM) by displacement MST assays. The MST traces (**left**) in the presence of SAH (100 μM) or without the SAH competitor yielded MST shifts (**right**) revealing Cy5-TAD displays the largest SAH-induced shift (ΔF_{norm} at 5 sec), thus, rendering this probe a promising probe candidate for METTL1 (mean ± SD, $n = 3$).

By this, it turned out that **Cy5TAD** is well suitable for probing METTL1 (Figure 4A) and NSUN6 (Figure S3A), while BODIPY-TAD was found to be unstable in buffer due to spontaneous deborylation.

Also, we applied the newly discovered TAD probes to the homologous NSUN2 and METTL3/14: two cancer targets for which few inhibitors have been developed lately, but no probe or biophysical screening assay has been reported yet.[8,9,21] Here, **Cy5TAD** (NSUN2) and **FTAD** (METTL3/14) were found to be effective probes, respectively (Figure S3).

As a next step, we aimed to assay the newly discovered probes on MTases outside of the NSUN- and METTL families. Hence, to develop a suitable probe for a drug-relevant bacterial MTase, we performed analogous MST displacement screenings on the pathogen-associated MTase *H. inf.* TrmD, which is known for its unique SPOUT-fold binding mode of the SAM cofactor.[10] Initially, no TAD-probe candidate with a significant MST shift could be identified (Figure S2B). We hypothesized that the SAH-triazole (TAD) chemotype is not suitable for non-Rossmannfold MTases. To address this issue, we designed a strategy to vary the MTase recruiter part to obtain SAH replacements that are suitable for a more diverse set of MTases (Figure 1). To establish SAH-replacement scaffolds, we followed a protein databank (PDB) mining strategy (details and code in SI). Principally, we established a chemoinformatic pipeline that searches the PDB for SAH-binding pockets in which only chemically dissimilar non-SAH-like ligands are bound (Figure 3A).

Clustering of the results yielded eleven SAH replacement lead scaffolds **1**–**11**, which can be implemented for CuAAC functionalization and probe screening (Figure 3B). With this expanded set of alkynes, analogous nanomole-scale coupling to 5-FAM-N_3 resp. Cy5-N_3 and subsequent MST displacement assays were performed, yielding a thienopyrimidine probe (**Cy5TPD**) which was found to be suitable for probing TrmD in MST and FP assays (Figure 4C). Validation on a preparative scale was accomplished for all three probes (**FTAD**, **Cy5TAD**, and **Cy5TPD**) which were effective on this investigated set of MTase targets (Figure 4A–C). For biophysical characterization, we deter-

© 2024 The Authors. Angewandte Chemie International Edition published by Wiley-VCH GmbH

15213773, 2024, 48, Downloaded from https://onlinelibrary.wiley.com/doi/10.1002/anie.202403792 by Universitatsbibliothek Mainz, Wiley Online Library on [23/10/2025]. See the Terms and Conditions (https://onlinelibrary.wiley.com/terms-and-conditions) on Wiley Online Library for rules of use; OA articles are governed by the applicable Creative Commons License

GDCh Communication Angewandte International Edition Chemie

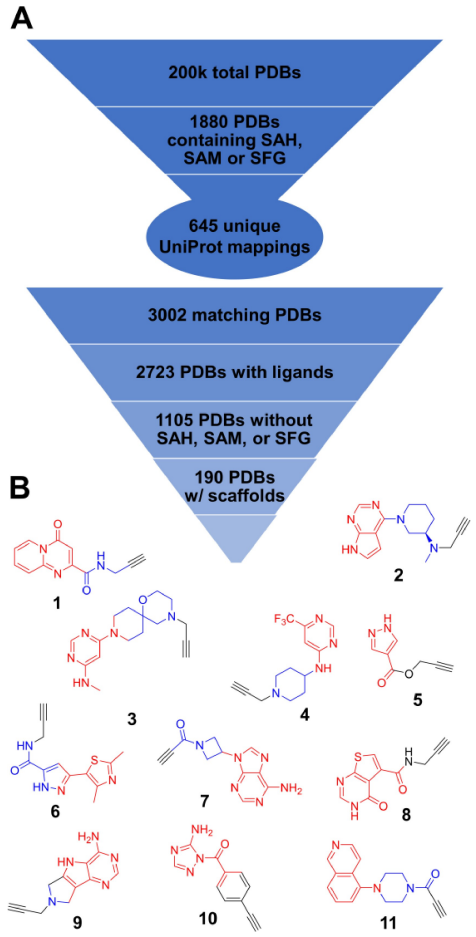


Figure 3. Description of the PDB-mining strategy. (**A**) Cheminformatic pipeline for the search of non-SAH scaffolds binding to SAH-pockets in crystallographic PDB structures. (**B**) Clustering of 190 ligands revealed eleven SAH-replacement alkyne **1–11** suitable for CuAAC functionalization. Red: adenine replacement; blue: ribose replacement; black: alkyne handle (see Figure S4 for crystallographic ligand poses).

Table 1: Characterization of fluorescent MTase probes by MST/FP-assays (mean ± SD, $n = 3$).

MTase	Probe	Probe K_D by FP [μM]	Probe K_D by MST [μM]	SAH K_D FP/MST [μM]	SAH K_D by ITC [μM]
DNMT2	FTAD	6.4 ± 0.7	2.1 ± 0.1	13.6 ± 2.3	13.6 ± 4.4[a]
NSUN2	Cy5TAD	2.4 ± 0.5	6.9 ± 0.3	7.9 ± 0.6	4.7 ± 0.8
NSUN6	Cy5TAD	6.4 ± 0.6	6.5 ± 1.0	4.5 ± 1.1	4.2 ± 0.2
METTL1	Cy5TAD	1.6 ± 0.3	3.2 ± 0.2	1.6 ± 0.1	3.1 ± 0.1
METTL3/14	FTAD	1.1 ± 0.1	1.1 ± 0.1	3.1 ± 0.7	3.7 ± 0.1[a]
***H. inf.* TrmD**	Cy5TPD	2.0 ± 0.7	1.3 ± 0.3	13.9 ± 1.7	9.2 ± 0.4
SARS-CoV2 nsp10/16	FTAD	n.d.	1.2 ± 0.1	4.2 ± 0.9	5.7 ± 1.9[a]

[a] Value determined in the literature.[1,25,26]

mined probe-target binding affinities by MST/FP assays, as well as SAH affinities by preparative displacement assays which were agreeing with the ITC-derived SAH binding affinities (Table 1, Figure S6).

Also, we could confirm that protein binding of all three probes leads only to a minimal change in the fluorescence quantum yield. By this, we assured that local changes in fluorescence levels are not distorting apparent fluorescence polarisation values (Figure S7). Furthermore, we have worked on a structural rationale to predict which probe is suitable for a particular MTase. Two factors were found decisive in the choice of a functional probe: The conformation of the SAH molecule in the crystal structure and the flexibility of the MTase binding pocket determined by crystallographic B'-factors (Table S1).[22] If a crystal structure is available, a suitable probe can be chosen using a decision tree (Figure 4E). First, MTases that have bound a kinked SAH ligand (< 100°) might not be suitable for the two TAD probes, so in this case, the Cy5-TPD probe should be used (Figure 4D). Secondly, MTases with greater flexibility (B' > 0) in the binding pocket enable the use of **FTAD**, whereas MTases with more rigid binding pocket elements prefer **Cy5TAD** (Table S1).

Finally, we utilized the newly identified **Cy5TAD** probe for a high-throughput drug screening on the largely unexplored cancer drug target METTL1, which introduces the m^7G modifications to various tRNAs.[20] Using an FP assay screening setup, we have tested an in-house library of 2230 drug-like candidates to identify initial binding scaffolds suitable for subsequent lead optimization (Figure 5).

The drug candidate library was added to a master mix of recombinantly expressed METTL1 protein (1 μM), the **Cy5TAD** probe (20 nM), and a final drug compound concentration of 200 μM (Figure 5A). Compounds that displaced the **Cy5TAD** probe by at least 50 % (< 20 mP) and did not interfere with the fluorescence properties of the probe were defined as screening hits (see details of screening setup and hit selection in the SI).

By this, we identified three hit compounds with micromolar potency which could be also validated by orthogonal biophysical (ITC, FP, SPR) and enzymatic METTL1 assays (Figure 5D–I). Among those hits, (*S*)-crizotinib was found to be the most promising starting point to kick-off drug discovery on METTL1 as it showed binding during FP ($K_D = 138$ μM), ITC ($K_D = 177$ μM), SPR ($K_D = 178$ μM), and enzyme inhibition ($IC_{50} = 158$ μM) in all biophysical and enzymatic ^{3}H-experiments. Of note, (*S*)-crizotinib did not bind or inhibit any of the other RNA MTases at ligand concentrations as high as 1 mM (Figure 5C), rendering this compound a METTL1 selective HTS hit. Interestingly, the corresponding kinase inhibiting eutomer (*R*)-crizotinib (marketed as Xalkori) did not bind to METTL1 providing beneficial intrinsic structural selectivity.

While tanespimycin and entacapone could be identified as METTL1 binders during FP- and ITC experiments, these two hit compounds showed only weak inhibition of the heterodimeric METTL1/WDR4 complex in the presence of ^{3}H-SAM and tRNA substrates (Figure 5F) limiting their use as potential drug discovery starting points. This is presum-

© 2024 The Authors. Angewandte Chemie International Edition published by Wiley-VCH GmbH

15213773, 2024, 48, Downloaded from https://onlinelibrary.wiley.com/doi/10.1002/anie.202403792 by Universitatsbibliothek Mainz, Wiley Online Library on [23/10/2025]. See the Terms and Conditions (https://onlinelibrary.wiley.com/terms-and-conditions) on Wiley Online Library for rules of use; OA articles are governed by the applicable Creative Commons License

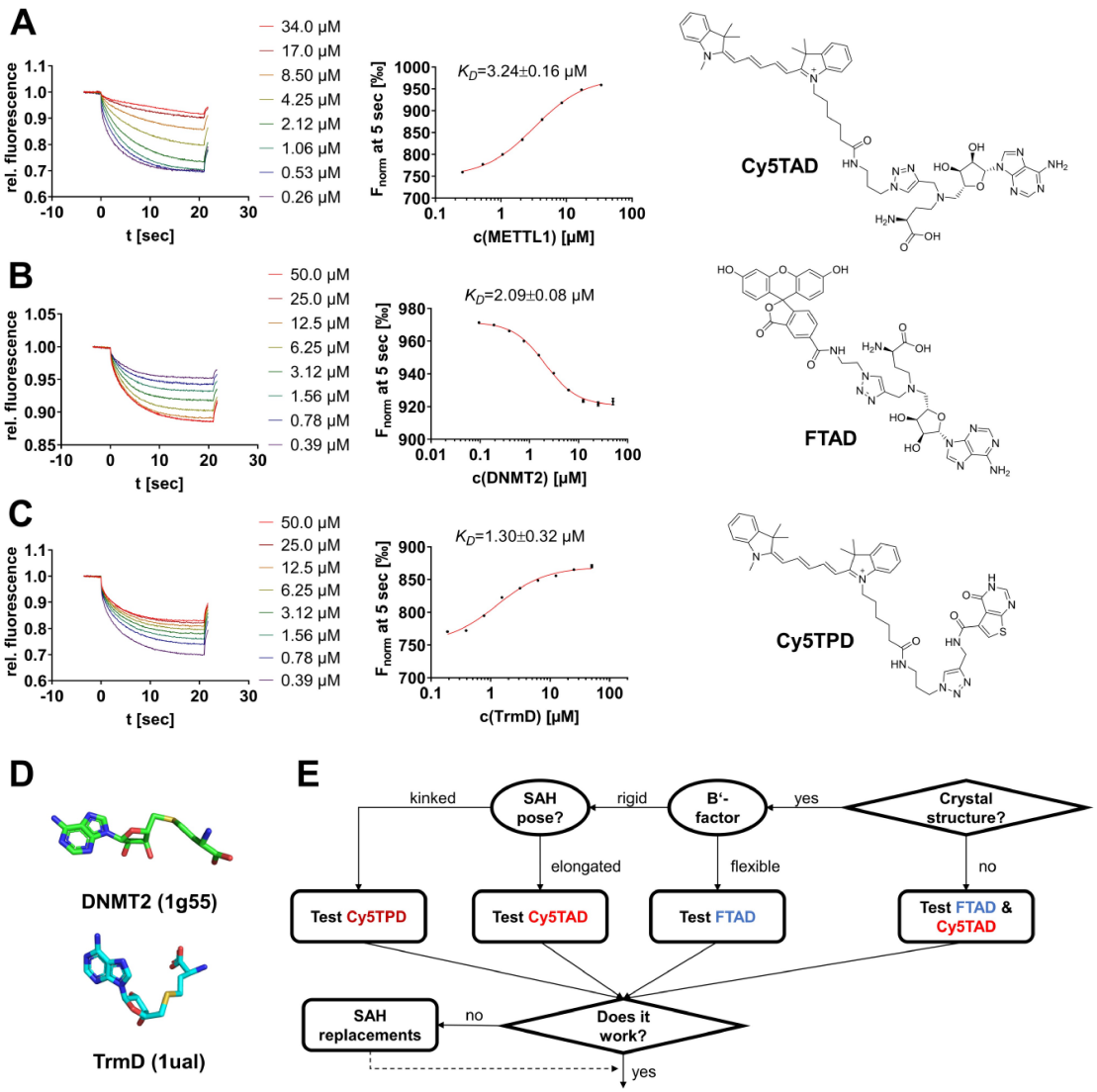


Figure 4. Validation of fluorescent MTase probes. (**A**) Validation of the HPLC-purified **Cy5TAD** probe (10 nM) with METTL1 by MST assays (mean ± SD, $n = 3$). (**B**) **FTAD** probe (100 nM) with DNMT2 (mean ± SD, $n = 3$). (**C**) **Cy5TPD** probe (10 nM) with TrmD (mean ± SD, $n = 3$). (**D**) Two distinct binding modes of SAH in MTases: DNMT2 binds SAH in an elongated mode, while TrmD shows a characteristically kinked SAH ligand. PDB-ID in brackets. (**E**) Decision tree for the choice of a probe based on the SAH conformation and MTase flexibility. The active site flexibility (B'-factors) was determined by the BANΔIT web toolkit.[21] See Table S1 for details.

ably due to the fact these hit compounds bind either to the protein-protein interaction interface or to the tRNA binding site, which is occupied in the presence of WDR4.[24] The complete METTL1 HTS assay data with the identification of additional hits can be found in the SI.

Lastly, we would like to outline the limitations of our approach described here. A general limitation of competition probe-based assays compared to label-free methods (e.g., SPR or ITC) is that inhibitors with K_D values more than one order of magnitude better than the probe affinity can only be extrapolated because of enzyme inhibitor tight-binding.[25] To illustrate this limitation and to guide a mitigation strategy, we characterized the high-affinity METTL3/14 inhibitor STM2457 ($IC_{50} = 5$ nM)[8] using the **FTAD** probe, which resulted in a tight-binding behavior ([E] = 1 µM), and thus, an apparent K_D at half-enzyme concentration of 500 nM (Figure S3G). Yet, we could overcome this limitation by synthesizing a novel high-affinity

© 2024 The Authors. Angewandte Chemie International Edition published by Wiley-VCH GmbH

15213773, 2024, 48, Downloaded from https://onlinelibrary.wiley.com/doi/10.1002/anie.202403792 by Universitatsbibliothek Mainz, Wiley Online Library on [23/10/2025]. See the Terms and Conditions (https://onlinelibrary.wiley.com/terms-and-conditions) on Wiley Online Library for rules of use; OA articles are governed by the applicable Creative Commons License

GDCh Communication Angewandte International Edition Chemie

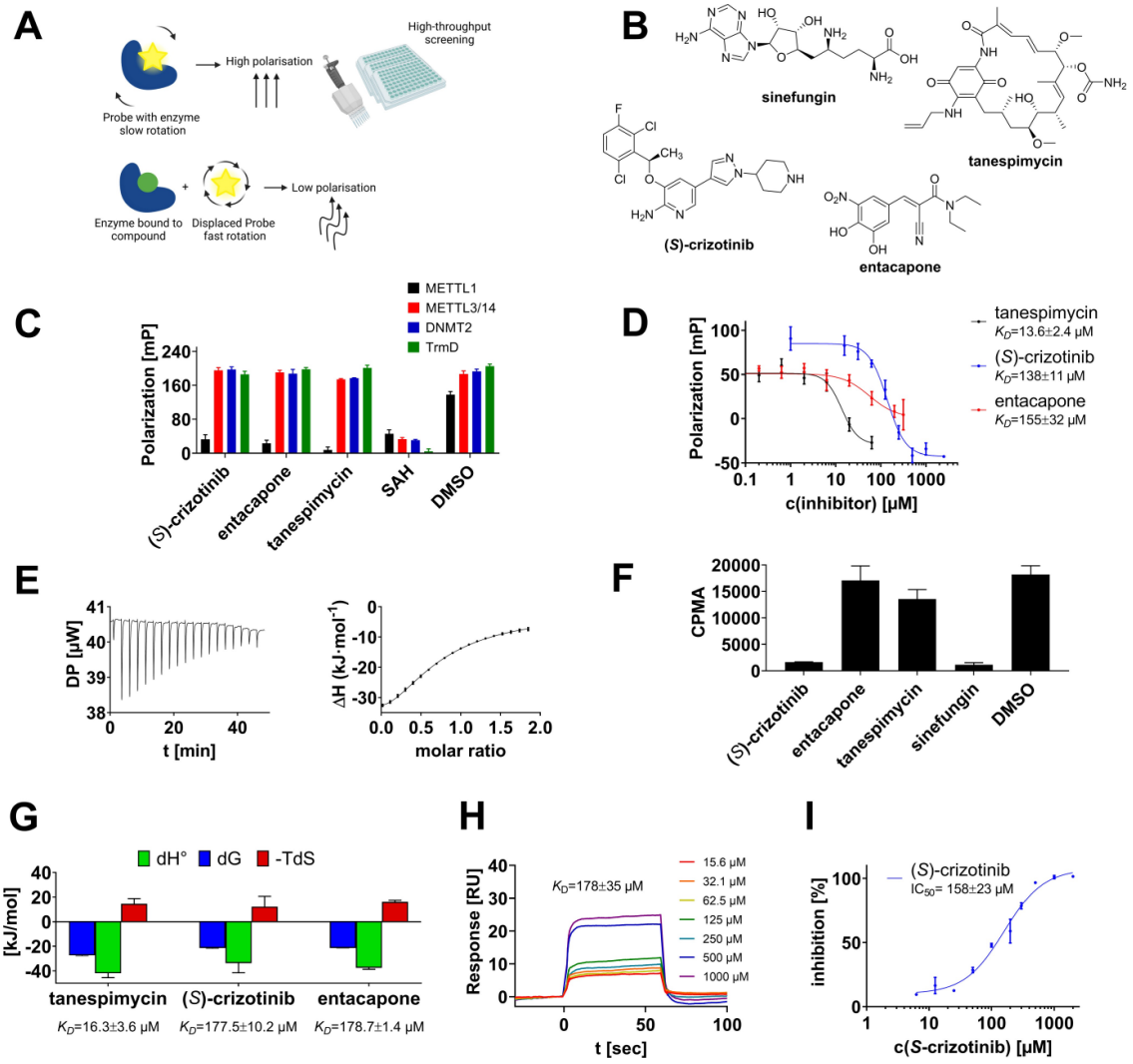


Figure 5. Using **Cy5TAD** for a high-throughput drug screening on METTL1. (**A**) Schematic depiction of the METTL1 FP screening assay. (**B**) Chemical structures of the identified METTL1 HTS-hits and positive control sinefungin. (**C**) Binding selectivity determined by FP assays against various recombinantly expressed MTases and 200 µM of the respective hit compound (mean ± SD, $n = 3$). (**D**) Dose-response curves and K_D determination by METTL1 FP assays (mean ± SD, $n = 3$). (**E**) ITC thermogram and stoichiometry plot of tanespimycin (250 µM) titrated to METTL1 (25 µM). (**F**) Screening of hit compounds (500 µM) by METTL1/WDR4 inhibition ^{3}H scintillation assays (mean ± SD, $n = 3$). Only (*S*)-crizotinib and the pan-MTase inhibitor sinefungin inhibited the METTL1/WDR4 MTase activity (CPMA). (**G**) Signature plots summarizing the ITC binding thermodynamics of all HTS hits (mean ± SD, $n = 3$). (*S*)-crizotinib and entacapone were determined by ITC displacement titrations (details in the SI).[22] Additional thermograms and stoichiometry plots can be found in Figure S6. (**H**) Determination of (*S*)-crizotinib vs. METTL1 binding affinity by SPR. Sensorgrams of triplicates and dose-response curves can be found in the Figure S9. (**I**) Dose-response curve for the ^{3}H-based IC_{50} determination of (*S*)-crizotinib inhibiting the METTL1/WDR4 complex (mean ± SD, $n = 3$).

FAM-labeled STM2457-probe (**STM-FL**, $K_D = 19$ nM) which allowed the determination of a literature-agreeing binding affinity for STM2457 with a K_D of 9.9 nM (Figure S8). This mitigation procedure might be used as a common guide for future MTase probe development: for de novo probe development the decision tree in Figure 4E is suitable for probe development, while well-known high-affinity MTase ligands offer the opportunity to decorate them directly with a fluorophore.

In addition to the identification of the highlighted probe candidates, the outlined development protocol is scalable for subsequent probe development campaigns and community researchers should expect 2–3 weeks from nanoscale synthesis to preparative validation of a probe candidate. To

© 2024 The Authors. Angewandte Chemie International Edition published by Wiley-VCH GmbH

15213773, 2024, 48, Downloaded from https://onlinelibrary.wiley.com/doi/10.1002/anie.202403792 by Universitatsbibliothek Mainz, Wiley Online Library on [23/10/2025]. See the Terms and Conditions (https://onlinelibrary.wiley.com/terms-and-conditions) on Wiley Online Library for rules of use; OA articles are governed by the applicable Creative Commons License

share the output of this study widely, the probes are available upon request: https://ak-barthels.pharmazie.uni-mainz.de/probes-request.

Acknowledgements

Financial support by the German Research Foundation (DFG) in the framework of the Transregio Collaborative Research Center RMAP (TRR319 RMaP) is gratefully acknowledged. We would like to thank Prof. Craig Crews who generously enabled us to perform SPR experiments with his device. The Figures were created with https://www.biorender.com/ assisted by Dr. Klein. Open Access funding enabled and organized by Projekt DEAL.

Conflict of Interest

The authors declare no conflict of interest.

Data Availability Statement

The data that support the findings of this study are available in the supplementary material of this article.

Keywords: Drug discovery · Fluorescent probes · RNA

[1] M. Schwickert, T. R. Fischer, R. A. Zimmermann, S. N. Hoba, J. L. Meidner, M. Weber, M. Weber, M. M. Stark, J. Koch, N. Jung, C. Kersten, M. Windbergs, F. Lyko, M. Helm, T. Schirmeister, *J. Med. Chem.* **2022**, *65*, 9750–9788.

[2] P. Gehrtz, S. Marom, M. Bührmann, J. Hardick, S. Kleinbölting, A. Shraga, C. Dubiella, R. Gabizon, J. N. Wiese, M. P. Müller, G. Cohen, I. Babaev, K. Shurrush, L. Avram, E. Resnick, H. Barr, D. Rauh, N. London, *J. Med. Chem.* **2022**, *65*, 10341–10356.

[3] P. A. Boriack-Sjodin, S. Ribich, R. A. Copeland, *Nat. Rev. Drug Discovery* **2018**, *17*, 435–453.

[4] N. Jonkhout, J. Tran, M. A. Smith, N. Schonrock, J. S. Mattick, E. M. Novoa, *RNA* **2017**, *23*, 1754–1769.

[5] A. Cayir, *WIREs RNA* **2022**, *13*, e1702.

[6] Y. Ofir-Rosenfeld, L. Vasiliauskaitė, C. Saunders, A. Sapetschnig, G. Tsagkogeorga, M. Albertella, M. Carkill, J. Self-Fordham, J. B. Holz, O. Rausch, *Eur. J. Cancer* **2022**, *174*, S123.

[7] F. Nai, M. P. Flores Espinoza, A. Invernizzi, P. A. Vargas-Rosales, O. Bobileva, M. Herok, and A. Caflisch, *ACS Bio & Med Chem Au* **2024**, *4*, 100–110.

[8] E. Yankova, W. Blackaby, M. Albertella, J. Rak, E. De Braekeleer, G. Tsagkogeorga, E. S. Pilka, D. Aspris, D. Leggate, A. G. Hendrick, N. A. Webster, B. Andrews, R. Fosbeary, P. Guest, N. Irigoyen, M. Eleftheriou, M. Gozdecka, J. M. L. Dias, A. J. Bannister, B. Vick, I. Jeremias, G. S. Vassiliou, O. Rausch, K. Tzelepis, T. Kouzarides, *Nature* **2021**, *593*, 597–601.

[9] Y. Tao, J. G. Felber, Z. Zou, E. Njomen, J. R. Remsberg, D. Ogasawara, C. Ye, B. Melillo, S. L. Schreiber, C. He, D. Remillard, B. F. Cravatt, *Angew. Chem. Int. Ed.* **2023**, *62*, e202311924.

[10] P. J. Hill, A. Abibi, R. Albert, B. Andrews, M. M. Gagnon, N. Gao, T. Grebe, L. I. Hajec, J. Huang, S. Livchak, S. D. Lahiri, D. C. McKinney, J. Thresher, H. Wang, N. Olivier, E. T. Buurman, *J. Med. Chem.* **2013**, *56*, 7278–7288.

[11] N. L. Inniss, J. Kozic, F. Li, M. Rosas-Lemus, G. Minasov, J. Rybáček, Y. Zhu, R. Pohl, L. Shuvalova, L. Rulíšek, J. S. Brunzelle, L. Bednárová, M. Štefek, J. M. Kormaník, E. Andris, J. Šebestík, A. S. M. Li, P. J. Brown, U. Schmitz, K. Saikatendu, E. Chang, R. Nencka, M. Vedadi, K. J. F. Satchell, *ACS Infect. Dis.* **2023**, *9*, 1918–1931.

[12] J.-P. Renaud, C. Chung, U. H. Danielson, U. Egner, M. Hennig, R. E. Hubbard, H. Nar, *Nat. Rev. Drug Discovery* **2016**, *15*, 679–698.

[13] T. R. Fischer, L. Meidner, M. Schwickert, M. Weber, R. A. Zimmermann, C. Kersten, T. Schirmeister, M. Helm, *Nucleic Acids Res.* **2022**, gkac224.

[14] R. A. Zimmermann, M. Schwickert, J. L. Meidner, Z. Nidoieva, M. Helm, T. Schirmeister, *ACS Pharmacol. Transl. Sci.* **2022**, *5*, 1079–1085.

[15] T.-R. Chern, L. Liu, E. Petrunak, J. A. Stuckey, M. Wang, D. Bernard, H. Zhou, S. Lee, Y. Dou, S. Wang, *ACS Med. Chem. Lett.* **2020**, *11*, 1348–1352.

[16] J. Dowden, W. Hong, R. V. Parry, R. A. Pike, S. G. Ward, *Bioorg. Med. Chem. Lett.* **2010**, *20*, 2103–2105.

[17] G. Zhang, S. L. Richardson, Y. Mao, R. Huang, *Org. Biomol. Chem.* **2015**, *13*, 4149–4154.

[18] A. M. Rossi, C. W. Taylor, *Nat. Protoc.* **2011**, *6*, 365–387.

[19] M. Li, Z. Tao, Y. Zhao, L. Li, J. Zheng, Z. Li, X. Chen, *J. Transl. Med.* **2022**, *20*, 214.

[20] W. Cheng, A. Gao, H. Lin, W. Zhang, *Mol. Ther. Oncolytics* **2022**, *26*, 27–34.

[21] A. Dolbois, R. K. Bedi, E. Bochenkova, A. Müller, E. V. Moroz-Omori, D. Huang, A. Caflisch, *J. Med. Chem.* **2021**, *64*, 12738–12760.

[22] F. Barthels, T. Schirmeister, C. Kersten, *Mol. Inf.* **2020**, *40*, 202000144.

[23] S. J. Hammerschmidt, F. Barthels, A. C. Weldert, C. Kersten, *J. Chem. Educ.* **2024**, DOI 10.1021/acs.jchemed.3c01133.

[24] V. M. Ruiz-Arroyo, R. Raj, K. Babu, O. Onolbaatar, P. H. Roberts, Y. Nam, *Nature* **2023**, *613*, 383–390.

[25] P. J. Tonge, *ACS Infect. Dis.* **2019**, *5*, 796–808.

[26] S. Perveen, A. Khalili Yazdi, K. Devkota, F. Li, P. Ghiabi, T. Hajian, P. Loppnau, A. Bolotokova, M. Vedadi, *SLAS Discovery* **2021**, *26*, 620–627.

[27] X. Wang, J. Huang, T. Zou, P. Yin, *RNA Biol.* **2017**, *14*, 300–304.

Manuscript received: February 23, 2024
Accepted manuscript online: August 15, 2024
Version of record online: October 24, 2024

© 2024 The Authors. Angewandte Chemie International Edition published by Wiley-VCH GmbH

15213773, 2024, 48, Downloaded from https://onlinelibrary.wiley.com/doi/10.1002/anie.202403792 by Universitatsbibliothek Mainz, Wiley Online Library on [23/10/2025]. See the Terms and Conditions (https://onlinelibrary.wiley.com/terms-and-conditions) on Wiley Online Library for rules of use; OA articles are governed by the applicable Creative Commons License

3.1.4 Supporting Information

The following supporting information quoted within "" from page 57 to page 91 is the same as the manuscript cited on page 49.[252] "

SUPPORTING INFORMATION WILEY-VCH

Supporting Information
©Wiley-VCH 2021
69451 Weinheim, Germany

Nanomole Scale Screening of Fluorescent RNA-Methyltransferase Probes Enables the Discovery of METTL1 Inhibitors

J. Laurenz Meidner,[†[a]] Ariane F. Frey,[†[a]] Robert A. Zimmermann,[†[a]] Mark O. Sabin,[[a]] Zarina Nidoieva,[[a]] Annabelle C. Weldert,[[a]] Sabrina N. Hoba,[[a]] Mackenzie W. Krone,[[b]] and Fabian Barthels*[[a,b]]

Abstract:

RNA methylation is a metabolic process validated for its association with various diseases, and thus, RNA methyltransferases (MTases) have become increasingly important in drug discovery. Yet, most frequently utilized RNA MTase assays are limited in their throughput and hamper this rapidly evolving field of medicinal chemistry. In this study, we describe a modular nanomole scale building block system that allowed the identification of tailored fluorescent MTase probes to unlock a broad selection of MTase drug targets for fluorescence-based binding assays. Probe candidates were initially prepared on a 4 nanomole scale and could be tested directly from crude reaction mixtures to allow rapid probe identification and optimization. Using an alkyne-azide click late-stage functionalization strategy and in silico protein databank mining, we established a selection of fluorescent probes suitable for relevant drug targets from the METTL and NSUN families, as well as bacterial and viral MTases. Using this concept, a high-throughput screening on the unexplored drug target METTL1 discovered three hit compounds with micromolar potency providing a first-in-class starting point for METTL1 drug discovery.

DOI: 10.1002/anie.2021XXXXX

Table of Contents

Table of Contents 1
Experimental Procedures 2
Reagents and general methods 2
Protocol for the nanomole-scale synthesis of MTase probes 2
Preparative synthesis of fluorescent MTase probes 2
Synthesis of alkyne and azide building blocks 4
Biophysical and enzymatic MTase assayss 16
Protein preparation and purification 17
In silico protein databank (PDB) mining 19
Supplementary results 21
High-throughput drug screening results on METTL1 (raw data) 27
Author contributions 35
NMR and LC/MS spectra 36

Experimental Procedures

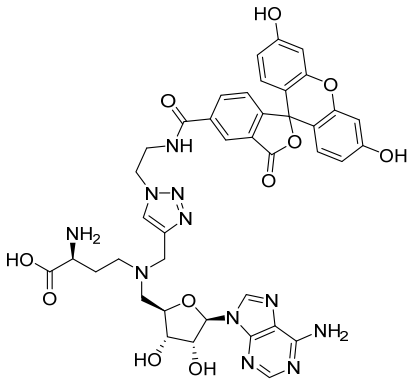
Reagents and general methods

All reagents and solvents were of analytical grade quality and purchased from standard commercial suppliers. Chemicals were used without further purification unless otherwise noted. ^{1}H and ^{13}C spectra were recorded on Bruker Fourier 300 MHz, Bruker Avance Neo 400 MHz, Bruker Avance III 600 MHz, and Bruker Avance III HD 850 MHz spectrometers. Chemical shifts δ are given in parts per million (ppm) using residual proton peaks of the solvent as the internal standard. HPLC and mass spectra were obtained by LC/MS consisting of an 1100 series HPLC system from Agilent with an Agilent Poroshell 120 EC-C18 150×2.10 mm, 4 µm column. The detection wavelengths were dependent on the specific compound absorbance characteristics: 210 nm, 254 nm, 280 nm, and 310 nm. The preparative MTase probes were additionally analyzed for their purity at 650 nm (Cy5) and 480 nm (FAM). The molecular mass was detected by an Agilent 1100 series LC/MSD trap with electron spray ionization (ESI) in positive mode. Column chromatography was performed with silica gel (0.06–0.02 mm) obtained from Macherey-Nagel or prepacked Biotage reverse phase silica columns for flash chromatography (Biotage Isolera One) eluting with ACN/H_2O. Preparative HPLC was performed on an Agilent 1290 system with an MZ-Aqua Perfect C18 7 µm column.

Protocol for the nanomole-scale synthesis of MTase probes

Nanomole-scale synthesis of the fluorescent probes was accomplished by combining 2.5 µL of the alkyne building block (2 mM, DMSO) and 2.5 µL of the fluorophore azide (2 mM, DMSO) in a 1.5 mL Eppendorf vial, followed by the addition of 1 µL of tris((1-benzyl-4-triazolyl)methyl)amine (TBTA, 12.5 mM in DMSO). Subsequently, 3 µL of a freshly prepared sodium ascorbate solution (33.3 mM in water) and 3 µL of $CuSO_4 \cdot 5H_2O$ (4.8 mM in degassed water) were added. The reaction was incubated for 12 hours at room temperature under an argon atmosphere. The conversion of the reaction was monitored via LC/MS (254 nm, 480 nm, and 650 nm, see Fig. S5). The final probe stock solution had a concentration of 416 µM in 12 µL DMSO/water (1:1). The following fluorophore azides were either commercially obtained or in-house synthesized: NBD-azide (synthesized; compound **20**), 5-FAM-azide (synthesized; compound **24**), BODIPY-azide (synthesized; compound **23**), Atto488-azide (ATTO-TEC), Cy3-azide (Lumiprobe), Atto590-azide (ATTO-TEC), Atto647N-azide (ATTO-TEC), Cy5-azide (Lumiprobe).

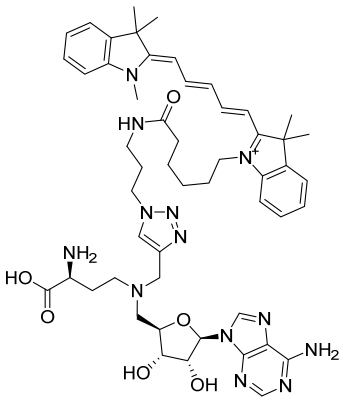
Preparative synthesis of fluorescent MTase probes



FTAD

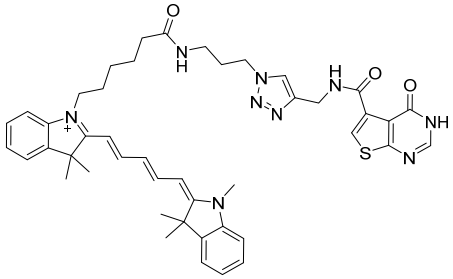
FTAD: Compound **29** (11 mg, 0.02 mmol, 1.0 eq.) was dissolved in a mixture of DMF (500 µL) and degassed water (100 µL). To this solution, intermediate **24** (8.1 mg, 0.02 mmol, 1.0 eq.), tris(3-hydroxypropyltriazolylmethyl)amine (THPTA) (2.4 mg, 0.005 mmol, 0.3 eq.), and $CuSO_4 \cdot 5H_2O$ (1.4 mg, 0.005 mmol) were successively added. After stirring for 10 min, sodium ascorbate (1.8 mg, 0.01 mmol, 0.5 eq.) was added and the solution was stirred at room temperature for 18 hours. Subsequent reversed-phase (RP) flash chromatography of the mixture led to the isolation of the protected triazole intermediate. This intermediate was then dissolved in 2,2,2-trifluoroethanol (2.0 mL) and water (10 µL) followed by HCl in dioxane (4 M, 100 µL). The mixture was stirred at 5 °C for 72 h. The solvent was removed under reduced pressure and the residue was purified by preparative HPLC yielding the desired product as an orange solid (9 mg, 59%). ^{1}H NMR (600 MHz, CD_3OD): δ = 8.31–8.19 (m, 3H), 8.16–8.11 (m, 1H), 8.08–8.03 (m, 1H), 7.23 (d, *J* = 8.0 Hz, 1H), 6.65–6.62 (m, 2H), 6.53–6.44 (m, 4H), 6.05–5.98 (m, 1H), 4.69–4.58 (m, 3H), 4.51–4.43 (m, 1H), 4.38–4.25 (m, 3H), 3.89–3.79 (m, 3H), 3.48–3.40 (m, 1H), 3.36–3.27 (m, 2H), 2.36–2.25 (m, 1H), 2.13–2.01 (m, 1H), 1.33–1.29 (m, 1H) ppm. ^{13}C NMR (150 MHz, CD_3OD): δ = 170.6, 168.7, 161.5, 156.7, 154.0, 150.0, 143.1, 137.5, 135.4, 130.2, 128.6, 127.7, 125.8, 125.0, 113.7,

110.7, 103.6, 91.4, 81.2, 74.7, 73.5, 57.5, 56.5, 55.8, 54.3, 53.0, 51.2, 47.9, 41.2, 26.7, 18.7, 17.3. ppm. LC/MS: m/z calculated for $C_{40}H_{39}N_{11}O_{11}$ $[M+2H]^{2+}$: 425.6, found: 425.6. Purity: 98%.



Cy5TAD

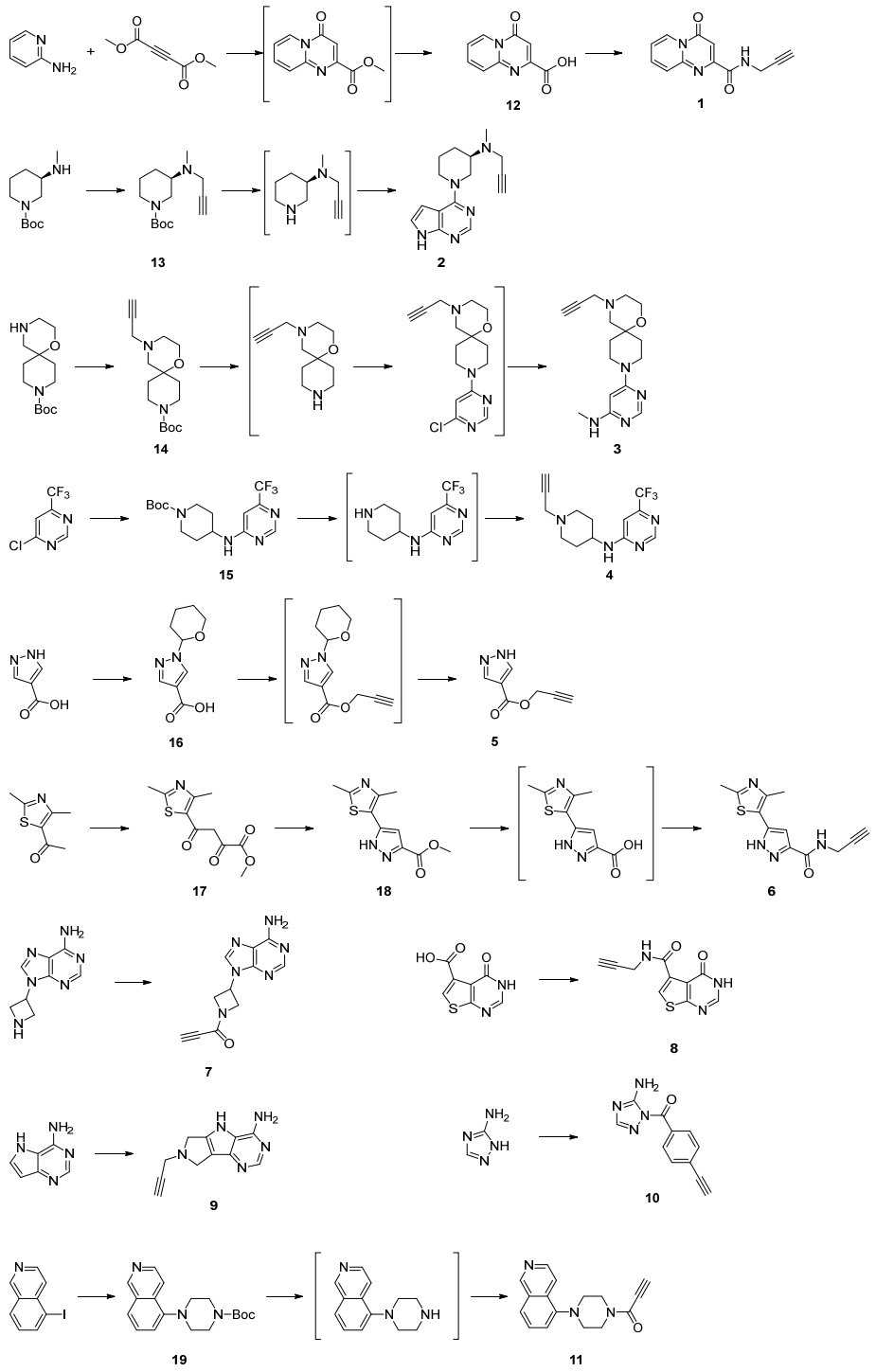
Cy5TAD: Compound **29** (1 mg, 0.002 mmol, 1.0 eq.) was dissolved in 2,2,2-trifluoroethanol (1.0 mL) and water (5 µL) followed by HCl in dioxane (4 M, 50 µL). The mixture was stirred at 5 °C for 72 h. The solvent was removed under reduced pressure and the residue was redissolved in a mixture of DMF (500 µL), and degassed water (100 µL). Cy5-azide (1 mg, 0.002 mmol, 1.0 eq.), TBTA (0.9 mg, 0.002 mmol, 1.0 eq.), and $CuSO_4 \cdot 5H_2O$ (0.4 mg, 0.002 mmol, 1.0 eq.) were successively added to the solution. After stirring for 10 min at room temperature, sodium ascorbate (0.3 mg, 0.002 mmol, 1.0 eq.) was added, and stirring was continued for 18 h at room temperature. Water (20 mL) was added to the reaction mixture and the solvents were removed by lyophilization. The resulting residue was purified by preparative HPLC to yield the desired product as a dark blue solid (0.38 mg, 15%). ^{1}H NMR (850 MHz, DMSO-d_6): δ = 8.30 (t, *J* = 13.1 Hz, 2H), 8.25 (s, 1H), 8.14 (d, *J* = 7.2 Hz, 1H), 7.96 (s, 1H), 7.59 (t, *J* = 6.8 Hz, 2H), 7.42–7.35 (m, 4H), 7.27 – 7.22 (m, 2H), 7.16 (s, 2H), 6.56 (t, *J* = 12.3 Hz, 1H), 6.29 (d, *J* = 13.7 Hz, 1H), 6.24 (d, *J* = 13.8 Hz, 1H), 5.86 (d, *J* = 5.3 Hz, 1H), 5.29 (s, 1H), 4.59 (d, *J* = 5.2 Hz, 1H), 4.29 (t, *J* = 1.3 Hz, 2H), 4.10–4.06 (m, 4H), 3.80 (d, *J* = 14.6 Hz, 1H), 3.72 (d, *J* = 14.6 Hz, 1H), 3.60 (s, 3H), 3.03–2.94 (m, 2H), 2.80–2.77 (m, 1H), 2.71–2.67 (m, 1H), 2.64–2.59 (m, 1H), 2.58 (p, *J* = 1.9 Hz, 1H), 2.53–2.51 (m, 1H), 2.42 (p, *J* = 1.8 Hz, 1H), 2.07 (t, *J* = 7.4 Hz, 2H), 2.04–1.97 (m, 1H), 1.95–1.87 (m, 1H), 1.82–1.78 (m, 1H), 1.72–1.66 (m, 14H), 1.55 (p, *J* = 7.4 Hz, 2H), 1.38–1.33 (m, 2H), 1.29–1.22 (m, 2H) ppm. LC/MS: m/z calculated for $C_{52}H_{68}N_{13}O_6$ $[M+2H]^{3+}$: 324.2, found: 324.2. Purity: 99%.



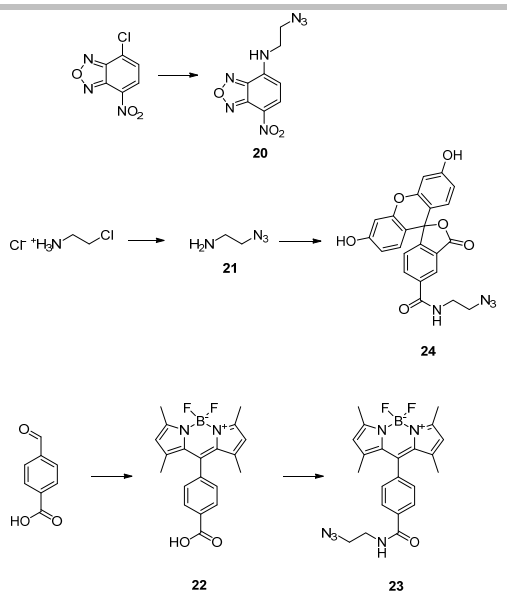
Cy5TPD

CyTPD: Compound **8** (0.629 mg, 2.7 µmol, 1.5 eq.), TBTA (0.287 mg, 0.54 µmol, 0.3 eq.), and Cy5-azide (1.06 mg, 1.8 µmol, 1.0 eq) were dissolved in DMSO (1.2 mL). Subsequently, $CuSO_4 \cdot 5H_2O$ (0.135 mg, 0.0054 mmol, 0.3 eq.) and sodium ascorbate (0.713 mg, 3.6 µmol, 2.0 eq.) dissolved in degassed water (1.2 mL) were added. The reaction was allowed to stir under an argon atmosphere for 12 hours at room temperature. Afterward, the solvents were removed in vacuo and the crude product was purified by RP-flash chromatography. Yield: 1.5 mg, 95%, purple solid. ^{1}H NMR (600 MHz, DMSO-d_6) δ = 9.96 (d, *J* = 2.8 Hz, 1H), 8.76 (s, 1H), 8.41 – 8.25 (m, 2H), 8.18 (s, 1H), 7.87 (t, *J* = 5.7 Hz, 1H), 7.72 (d, *J* = 2.9 Hz, 1H), 7.60 (dd, *J* = 14.3, 7.4 Hz, 2H), 7.46 – 7.33 (m, 3H), 7.28 – 7.15 (m, 2H), 6.51 (t, *J* = 12.3 Hz, 1H), 6.32 – 6.20 (m, 2H), 5.33 (s, 1H), 4.30 (t, *J* = 7.1 Hz, 2H), 4.07 (t, *J* = 7.4 Hz, 2H), 3.59 (s, 3H), 2.99 (q, *J* = 6.4 Hz, 2H), 2.64 – 2.58 (m, 1H), 2.55 – 2.51 (m, 2H), 2.42 – 2.34 (m, 1H), 2.03 (t, *J* = 7.3 Hz, 2H), 1.92 – 1.82 (m, 2H), 1.72 – 1.60 (m, 7H), 1.55 – 1.47 (m, 2H), 1.34 – 1.27 (m, 2H), 1.26 – 1.18 (m, 1H) ppm. ^{13}C NMR (151 MHz, DMSO-d_6) δ = 173.3, 172.5, 172.0, 166.1, 161.7, 158.3, 154.0, 148.5, 142.8, 142.1, 141.8, 141.1, 132.7, 132.3, 128.4, 125.3, 124.8, 124.0, 122.5, 122.4, 118.9, 111.1, 103.1, 48.9, 47.4, 43.3, 41.8, 40.1, 35.7, 35.1, 31.1, 29.9, 27.2, 27.0, 26.8, 25.7, 24.9 ppm. LC/MS: m/z calculated for $C_{45}H_{52}N_9O_3S$ $[M+H]^{2+}$: 399.7, found: 399.7. Purity: 99%.

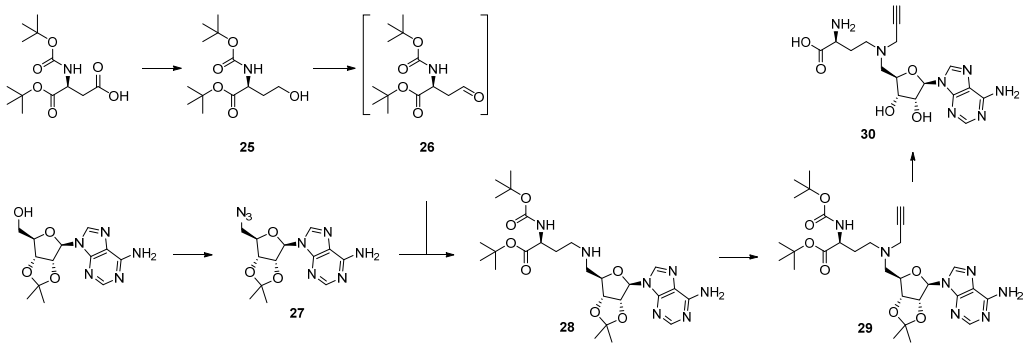
Synthesis of alkyne and azide building blocks



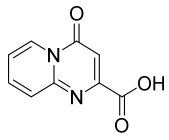
Scheme S1: Synthesis overview and compound numbering of the SAH replacement scaffold alkynes.



Scheme S2: Synthesis overview and compound numbering of fluorophore azides.

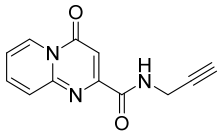


Scheme S3: Synthesis overview and compound numbering of SAH-based alkyne building blocks.



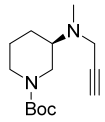
12

Compound **12 (4-oxo-4*H*-pyrido[1,2-*a*]pyrimidine-2-carboxylic acid)**: 2-aminopyridine (1.00 g, 10.62 mmol, 1.0 eq.) was dissolved in water (900 mL) and dimethyl acetylene dicarboxylate (2.72 g, 19.12 mmol, 1.8 eq.) was added to the solution. The reaction was allowed to stir for 3 hours at room temperature and the crude product was extracted with DCM and dried with Na_2SO_4. The solution was filtered over silica gel and the intermediate was eluted with methanol. The solvent was removed in vacuo and the residue was dissolved in methanol (68 mL). Then, sodium hydroxide (3.59 g, 90.00 mmol) dissolved in water (30 mL) was added to the reaction mixture. The reaction was allowed to stir for one hour at room temperature before it was neutralized with HCl (25 mL, 2 M). Methanol was evaporated in vacuo and the product was extracted with ethyl acetate. The organic phase was removed in vacuo and the aqueous phase was lyophilized. Yield: 0.600 g, 65%, off-white solid.^{1}H NMR (300 MHz, DMSO-d_6) δ = 11.53 (s, 2H), 9.09 – 9.01 (m, 1H), 8.33 – 8.24 (m, 1H), 8.14 – 8.05 (m, 1H), 7.68 – 7.58 (m, 1H), 6.93 (s, 1H) ppm. ^{13}C NMR (75 MHz, DMSO-d_6) δ = 163.6, 157.1, 149.4, 148.2, 141.6, 128.4, 123.4, 119.0, 104.1 ppm. LC/MS: m/z calculated for $C_9H_6N_2O_3$ $[M+H]^+$: 191.0, found: 190.8.



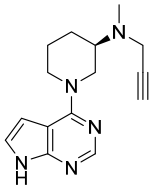
1

Compound **1** **(4-oxo-*N*-(prop-2-yn-1-yl)-4*H*-pyrido[1,2-*a*]pyrimidine-2-carboxamide)**: Intermediate **12** (150 mg, 0.789 mmol, 1.0 eq.) was suspended with propargylamine (60 µL, 0.947 mmol, 1.2 eq.) in pyridine (3 mL). $POCl_3$ (70 µL, 0.789 mmol, 1.0 eq.) was added dropwise at 0 °C. Subsequently, water (5 mL) was added, and the reaction mixture was extracted with DCM. The organic phase was removed in vacuo and the crude product was purified by column chromatography (CH/EA = 1:1). Yield: 7 mg, 4%, colorless solid. ^{1}H NMR (300 MHz, C*D*Cl$_3$) δ = 9.07 (d, *J* = 7.2 Hz, 1H), 8.15 (s, 1H), 7.92 – 7.63 (m, 2H), 7.21 (m, 1H), 4.26 (d, *J* = 5.4 Hz, 2H), 2.35 – 2.25 (m, 1H) ppm. ^{13}C NMR (75 MHz, *C*DCl$_3$) δ = 162.9, 158.6, 153.0, 150.8, 137.1, 127.8, 126.7, 116.4, 103.0, 79.2, 72.0, 29.5 ppm. LC/MS: m/z calculated for $C_{12}H_9N_3O_2$ [M+H]$^+$: 228.1, found: 227.9.



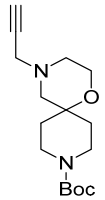
13

Compound **13** **(*tert*-butyl (*R*)-3-(methyl(prop-2-yn-1-yl)amino)piperidine-1-carboxylate)**: (*R*)-1-*N*-Boc-3-methylaminpiperidine (10 mg, 0.047 mmol, 1.0 eq.), propargyl bromide (80% w/w in toluene) (6 µL, 0.052 mmol, 1.1 eq.), and cesium carbonate (31 mg, 0.094 mmol, 2.0 eq.) were suspended in acetonitrile (1 mL). The reaction mixture was heated in a sealed tube for 3 hours to 90 °C before the solvent was removed in vacuo. The product was purified via column chromatography (CH/EA = 1:2). Yield: 11 mg, 93%, colorless solid. ^{1}H NMR (300 MHz, C*D*Cl$_3$) δ = 4.09 (s, 1H), 3.84 (d, *J* = 13.2 Hz, 1H), 3.53 – 3.38 (m, 2H), 2.83 – 2.70 (m, 2H), 2.45 – 2.40 (m, 1H), 2.38 (s, 3H), 2.21 (t, *J* = 2.4 Hz, 1H), 2.03 – 1.93 (m, 1H), 1.76 – 1.64 (m, 1H), 1.51 – 1.37 (m, 11H) ppm. ^{13}C NMR (75 MHz, *C*DCl$_3$) δ = 154.9, 79.6, 78.8, 73.4, 57.8, 44.1, 43.3, 39.1, 28.6, 24.1 ppm. LC/MS: m/z calculated for $C_{14}H_{24}N_2O_2$ [M+H]$^+$: 253.2, found: 253.1.



2

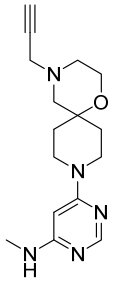
Compound **2** **((*R*)-N-methyl-*N*-(prop-2-yn-1-yl)-1-(7*H*-pyrrolo[2,3-*d*]pyrimidin-4-yl)piperidine-3-amine)**: Intermediate **13** (20 mg, 0.079 mmol, 1.1 eq.) was dissolved in TFA/DCM (0.5+0.5 mL). The reaction mixture was stirred for 30 min at room temperature. Afterward, all volatiles were removed in vacuo, and 4-chloro-7*H*-pyrrolo[2,3-d]pyrimidine (11 mg, 0.072 mmol, 1.0 eq.), DIPEA (19 µL, 0.108 mmol, 1.5 eq.), and *n*-butanol (1 mL) were added. The reaction was stirred in a sealed tube for 72 hours at 80 °C. Subsequently, the solvent was removed, and the crude product was purified via RP-flash chromatography. Yield: 2 mg, 7%, brown solid. ^{1}H NMR (300 MHz, C*D*Cl$_3$) δ = 8.32 (s, 1H), 7.10 (d, *J* = 3.6 Hz, 1H), 6.61 – 6.56 (m, 1H), 4.87 (d, *J* = 12.6 Hz, 1H), 4.59 (d, *J* = 12.8 Hz, 1H), 3.61 (d, *J* = 2.4 Hz, 2H), 3.35 – 3.17 (m, 2H), 2.98 (s, 1H), 2.81 – 2.71 (m, 1H), 2.56 (s, 3H), 2.32 – 2.28 (m, 1H), 2.17 (s, 1H), 1.99 – 1.90 (m, 1H), 1.77 – 1.58 (m, 2H) ppm. ^{13}C NMR (75 MHz, *C*DCl$_3$) δ = 150.5, 150.1, 149.6, 120.9, 102.8, 102.0, 77.4, 74.6, 58.3, 49.1, 46.7, 43.4, 39.1, 28.4, 24.3 ppm. LC/MS: m/z calculated for $C_{15}H_{19}N_5$ [M+H]$^+$: 270.2, found: 270.1.



14

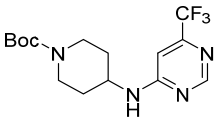
Compound **14** **(*tert*-butyl 4-(prop-2-yn-1-yl)-1-oxa-4,9-diazaspiro[5.5]undecane-9-carboxylate)**: *tert*-butyl 1-oxa-4,9-diazaspiro[5.5]undecane-9-carboxylate (80 mg, 0.311 mmol, 1.0 eq.), potassium carbonate (65 mg, 0.467 mmol, 1.5 eq.), and propargyl bromide (80% w/w in toluene) (37 µL, 0.342 mmol, 1.1 eq.) were suspended in acetonitrile (1 mL) and stirred for 12 hours at room temperature. The solvent was removed in vacuo and the crude product was purified via RP chromatography. Yield: 64 mg, 70%, colorless oil. ^{1}H NMR (300 MHz, C*D*Cl$_3$) δ = 3.77 – 3.61 (m, 4H), 3.23 (d, *J* = 2.4 Hz, 2H), 3.20 – 3.08 (m, 2H), 2.53 – 2.46 (m,

2H), 2.33 (s, 2H), 2.24 (t, *J* = 2.4 Hz, 1H), 1.91 (d, *J* = 13.8 Hz, 2H), 1.44 (m, 11H) ppm. ^{13}C NMR (75 MHz, *C*DCl$_3$) δ = 155.0, 79.4, 78.5, 73.6, 70.4, 61.0, 60.6, 52.2, 47.4, 39.4, 33.0, 28.6 ppm. LC/MS: m/z calculated for $C_{16}H_{26}N_2O_3$ [M+H]$^+$: 295.2, found: 295.1.



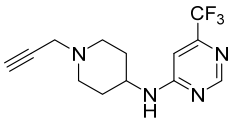
3

Compound **3** (***N*-methyl-6-(4-(prop-2-yn-1-yl)-1-oxa-4,9-diazaspiro[5.5]undecan-9-yl)pyrimidine-4-amine)**: Intermediate **14** (40 mg, 0.136 mmol, 1.0 eq.) was dissolved in TFA/DCM (1+1 mL) and stirred for 1 hour at room temperature. Subsequently, all volatiles were removed in vacuo and anhydrous acetonitrile (2 mL), DIPEA (95 µL, 0.544 mmol, 4.0 eq.), and 4,6-dichloropyrimidine (20 mg, 0.136 mmol, 1.0 eq.) were added. The reaction was stirred for 4 hours at room temperature. Afterward, the solvent was removed in vacuo, and methylamine (3 mL, 33% (w/w) in EtOH) and potassium carbonate (19 mg, 0.136 mmol, 1.0 eq.) were added. The reaction was stirred in a sealed tube for additional 12 hours at 80 °C. The solvent was removed in vacuo and the crude product was purified via RP-flash chromatography. Yield: 5 mg, 12%, yellowish oil. ^{1}H NMR (300 MHz, C*D*Cl$_3$) δ = 8.15 (s, 1H), 5.41 (s, 1H), 5.13 (s, 1H), 3.99 – 3.88 (m, 2H), 3.81 – 3.74 (m, 2H), 3.42 – 3.32 (m, 1H), 3.32 – 3.28 (m, 1H), 3.25 (d, *J* = 2.5 Hz, 2H), 2.87 (s, 3H), 2.56 – 2.49 (m, 2H), 2.37 (s, 2H), 2.27 – 2.24 (m, 1H), 2.04 (d, *J* = 13.8 Hz, 2H), 1.61 – 1.44 (m, 2H) ppm. ^{13}C NMR (75 MHz, *C*DCl$_3$) δ = 162.7, 88.5, 78.5, 77.4, 73.7, 70.6, 61.0, 60.7, 52.2, 47.4, 40.1, 32.7, 28.6 ppm. LC/MS: m/z calculated for $C_{16}H_{23}N_5O$ [M+H]$^+$: 302.2, found: 302.1.



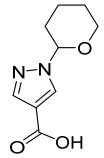
15

Compound **15** (***tert*-butyl 4-((6-(trifluoromethyl)pyrimidin-4-yl)amino)piperidine-1-carboxylate)**: 4-chloro-6-(trifluoromethyl)pyrimidine (91 mg, 0.500 mmol, 1.0 eq.), *tert*-butyl 4-aminopiperidine-1-carboxylate (100 mg, 0.500 mmol, 1.0 eq.), and potassium carbonate (104 mg, 0.750 mmol, 1.5 eq.) were suspended in THF (10 mL) and stirred in a sealed tube for 2 hours at 70 °C. The suspension was filtered through a plunge of silica and the solvent was removed in vacuo. Yield: 90 mg, 52%, colorless solid. ^{1}H NMR (300 MHz, C*D*Cl$_3$) δ = 8.60 (s, 1H), 6.65 (d, *J* = 1.2 Hz, 1H), 5.78 (d, *J* = 7.8 Hz, 1H), 4.06 (d, *J* = 13.8 Hz, 2H), 2.91 (t, *J* = 12.7 Hz, 2H), 2.06 – 1.95 (m, 2H), 1.46 – 1.37 (m, 12H) ppm. ^{13}C NMR (75 MHz, *C*DCl$_3$) δ = 162.0, 159.3, 154.8, 122.7, 119.1, 80.1, 48.4, 42.7, 31.8, 30.4, 28.5 ppm. LC/MS: m/z calculated for $C_{15}H_{21}F_3N_4O_2$ [M+H]$^+$: 347.2, found: 347.1.



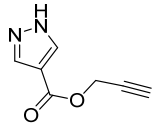
4

Compound **4** (***N*-(1-(prop-2-yn-1-yl)piperidin-4-yl)-6-(trifluoromethyl)pyrimidine-4-amine)**: Intermediate **15** (80 mg, 0.230 mmol, 1.0 eq.) was dissolved in TFA/DCM (1+1 mL). Subsequently, the reaction was allowed to stir for 1 hour at room temperature. The solution was concentrated in vacuo and resolved in acetonitrile (1 mL). Then, potassium carbonate (69 mg, 0.500 mmol, 2.2 eq.) and propargyl bromide (80% w/w in toluene) (27 µL, 0.240 mmol, 1.0 eq.) were added, and the reaction was heated in a sealed tube for 3 hours to 90 °C. The solvent was removed in vacuo and the crude product was purified via RP-flash chromatography. Yield: 37 mg, 57%, yellow solid. ^{1}H NMR (300 MHz, C*D*Cl$_3$) δ = 8.61 (s, 1H), 6.61 (s, 1H), 5.30 (s, 1H), 3.33 (d, *J* = 2.5 Hz, 2H), 2.88 (m, *J* = 3.9 Hz, 2H), 2.42 (m, 2.7 Hz, 2H), 2.26 (t, *J* = 2.4 Hz, 1H), 2.15 – 1.96 (m, 2H), 1.69 – 1.50 (m, 2H) ppm. ^{13}C NMR (75 MHz, *C*DCl$_3$) δ = 162.1, 159.5, 122.8, 119.1, 78.7, 73.5, 50.9, 48.0, 47.9, 47.0, 31.9 ppm. LC/MS: m/z calculated for $C_{13}H_{15}F_3N_4$ [M+H]$^+$: 285.1, found: 285.0.



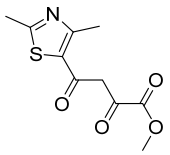
16

Compound **16 (1-(tetrahydro-2*H*-pyran-2-yl)-1*H*-pyrazole-4-carboxylic acid)**: Tetrahydropyranol (430 µL, 4.400 mmol, 2.0 eq.), 1*H*-pyrazole-4-carboxylic acid (246 mg, 2.200 mmol, 1.0 eq.), and *p*-toluenesulfonic acid (38 mg, 0.220 mmol, 0.1 eq.) were dissolved in ethyl acetate (10 mL) and DMF (2 mL). The reaction was stirred for 16 hours at room temperature, the solvents were removed in vacuo, and the crude product was purified via column chromatography (DCM/MeOH, 20:1). Yield: 0.308 g, 71%, colorless solid. ^{1}H NMR (300 MHz, CH_3OD) δ = 8.27 (s, 1H), 7.90 (s, 1H), 5.49 – 5.39 (m, 1H), 4.13 – 3.95 (m, 1H), 3.79 – 3.66 (m, 1H), 2.17 – 1.94 (m, 3H), 1.86 – 1.56 (m, 3H) ppm. ^{13}C NMR (75 MHz, CH_3OD) δ = 166.2, 142.0, 133.4, 116.7, 89.1, 68.9, 31.6, 26.0, 23.2 ppm. LC/MS: m/z calculated for $C_9H_{12}N_2O_3$ $[M+Na]^+$: 218.1, found: 217.9.



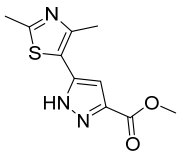
5

Compound **5 (prop-2-yn-1-yl 1*H*-pyrazole-4-carboxylate)**: Intermediate **16** (98 mg, 0.500 mmol, 1.0 eq.), propargyl bromide (80% w/w in toluene) (54 µL, 0.500 mmol, 1.0 eq.), and DIPEA (250 µL, 1.43 mmol, 2.9 eq.) were dissolved in DMF (3 mL) and stirred for 3 hours at room temperature. The solvent was removed in vacuo and the residue was resolved in TFA/DCM (1+1 mL). The reaction mixture was stirred for 1 hour at room temperature and the solvent was removed in vacuo. The crude product was purified via RP-flash chromatography. Yield: 18 mg, 24%, colorless solid. ^{1}H NMR (300 MHz, $CDCl_3$) δ = 10.32 (s, 1H), 8.13 (s, 2H), 4.87 (d, *J* = 2.5 Hz, 2H), 2.51 (t, *J* = 2.4 Hz, 1H) ppm.^{13}C NMR (75 MHz, $CDCl_3$) δ = 162.3, 136.9, 114.2, 77.8, 75.2, 52.0 ppm. LC/MS: m/z calculated for $C_7H_6N_2O_2$ $[M+H]^+$: 151.0, found: 150.9.



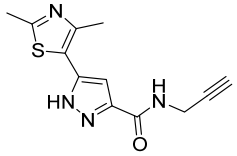
17

Compound **17 (methyl 4-(2,4-dimethylthiazol-5-yl)-2,4-dioxobutanoate):** 5-Acetyl-2,4-dimethylthiazole (135 µL, 1.000 mmol, 1.0 eq.) and diethyl oxalate (149 µL, 1.100 mmol, 1.1 eq.) were dissolved in methanol (1 mL), and sodium methanolate (50 mg, 1.000 mmol, 1.0 eq.) in methanol (1 mL) was added dropwise to this solution. The reaction was allowed to stir for 12 hours at room temperature. Subsequently, the precipitate was filtered off, washed with methanol, and dissolved in 2 M hydrochloric acid. The final product was extracted with DCM. The solution was dried over sodium sulfate and concentrated in vacuo. Yield: 79 mg, 33%, yellowish solid.^{1}H NMR (300 MHz, $CDCl_3$) δ = 6.67 (s, 1H), 3.92 (s, 3H), 2.75 (s, 3H), 2.72 (s, 3H) ppm. ^{13}C NMR (75 MHz, $CDCl_3$) δ = 185.9, 170.4, 165.8, 162.5, 160.3, 129.0, 102.0, 53.4, 19.7, 18.6 ppm. LC/MS: m/z calculated for $C_{10}H_{11}NO_4S$ $[M+H]^+$: 242.0, found: 241.9.



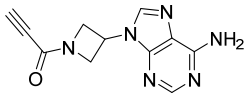
18

Compound **18 (methyl 5-(2,4-dimethylthiazol-5-yl)-1*H*-pyrazole-3-carboxylate)**: A solution of intermediate **17** (50 mg, 0.207 mmol, 1.0 eq.) and hydrazine hydrate (10 µL, 0.207 mmol, 1.0 eq.) in dioxane (2 mL) was refluxed for 1 hour. Subsequently, the reaction mixture was concentrated in vacuo and purified via column chromatography (CH/EA = 1:1). Yield: 23 mg, 47%, off-white solid. ^{1}H NMR (300 MHz, DMSO-d_6) δ = 6.96 (s, 1H), 3.85 (s, 3H), 2.60 (s, 3H), 2.45 (s, 3H) ppm. ^{13}C NMR (75 MHz, DMSO-d_6) δ = 106.8, 54.9, 52.0, 18.6, 16.3 ppm. LC/MS: m/z calculated for $C_{10}H_{11}N_3O_2S$ $[M+H]^+$: 238.1, found: 238.0.



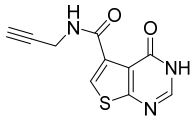
6

Compound **6 (5-(2,4-dimethylthiazol-5-yl)-*N*-(prop-2-yn-1-yl)-1*H*-pyrazole-3-carboxamide)**: A solution of intermediate **18** (23 mg, 0.097 mmol, 1.0 eq.) and lithium hydroxide hydrate (15 mg, 0.357 mmol, 3.7 eq.) in deionized water/THF (1+1 mL) was stirred for 12 hours at room temperature. THF was removed in vacuo and the reaction mixture was lyophilized. Subsequently, the carboxylate intermediate was dissolved in DMF (1 mL), after which TBTU (62 mg, 0.194 mmol, 2.0 eq.) and DIPEA (51 µL, 0.291 mmol, 3.0 eq.) were added. The reaction was stirred for 30 minutes at room temperature before the addition of propargylamine (14 µL, 0.213 mmol, 2.2 eq.). The reaction was stirred for 12 hours at room temperature, the solvent was removed in vacuo, and the crude product was purified via RP-flash chromatography. Yield: 12 mg, 48%, white solid. ^{1}H NMR (300 MHz, DMSO-d_6) δ = 8.97 (s, 1H), 7.12 (s, 1H), 4.09 – 4.03 (m, 2H), 3.18 (s, 1H), 2.60 (s, 3H), 2.47 (s, 3H) ppm. ^{13}C NMR (75 MHz, DMSO-d_6) δ = 80.9, 73.2, 27.9, 18.7, 16.3 ppm. LC/MS: m/z calculated for $C_{12}H_{12}N_4OS$ [M+H]$^+$: 261.1, found: 261.0.



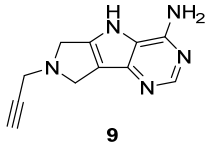
7

Compound **7 (1-(3-(6-amino-9*H*-purin-9-yl)azetidin-1-yl)prop-2-yn-1-one):** 9-(azetidine-3-yl)-9*H*-purin-6-amine (13 mg, 0.050 mmol, 1.0 eq.), propiolic acid (6 µL, 0.100 mmol, 2.0 eq.), HATU (19 mg, 0.05 mmol, 1.0 eq.), and DIPEA (50 µL, 0.300 mmol, 6.0 eq.) were suspended in DCM (3 mL) and stirred for 16 hours at room temperature. The solvent was removed in vacuo and the crude product was purified by RP-flash chromatography. Yield: 12 mg, 99%, colorless solid. ^{1}H NMR (400 MHz, C*D*$_3$CN) δ = 8.23 (s, 1H), 8.01 (s, 1H), 5.95 (s, 2H), 5.41 – 5.34 (m, 1H), 4.77 – 4.64 (m, 2H), 4.52 – 4.43 (m, 2H), 3.44 (s, 1H) ppm. ^{13}C NMR (101 MHz, *C*D$_3$*C*N) δ = 153.7, 141.3, 79.4, 57.9, 55.6, 44.9 ppm. LC/MS: m/z calculated for $C_{11}H_{10}N_6O$ [M+H]$^+$: 243.1, found: 243.0.



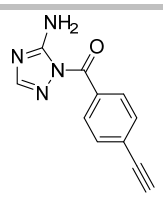
8

Compound **8 (4-oxo-*N*-(prop-2-yn-1-yl)-3,4-dihydrothieno[2,3-*d*]pyrimidine-5-carboxamide)**: 4-oxo-3,4-dihydrothieno[2,3-*d*]pyrimidine-5-carboxylic acid (12 mg, 0.061 mmol, 1.0 eq.) was suspended in anhydrous DCM (1 mL). Then, DIPEA (43 µL, 0.244 mmol, 4.0 eq.) and HATU (23 mg, 0.061 mmol, 1.0 eq.) were added, and the reaction was stirred for 15 minutes at room temperature. Subsequently, propargylamine (5 µL, 0.073 mmol, 1.2 eq.) was added, and the reaction was stirred for additional 12 hours at room temperature. Subsequently, the solution was washed with a saturated sodium bicarbonate solution, 1 M HCl, and brine. The solvent was removed in vacuo and the crude product was purified via RP-flash chromatography. Yield: 9 mg, 63%, off-white solid. ^{1}H NMR (300 MHz, DMSO-d_6) δ = 11.24 (t, *J* = 5.1 Hz, 1H), 8.39 (s, 1H), 8.29 (s, 1H), 4.19 – 4.06 (m, 2H), 3.19 – 3.15 (m, 1H) ppm. ^{13}C NMR (75 MHz, DMSO-d_6) δ = 167.1, 159.9, 159.6, 146.0, 131.8, 131.6, 119.2, 80.6, 73.5, 28.5 ppm. LC/MS: m/z calculated for $C_{10}H_7N_3O_2S$ [M+H]$^+$: 234.0, found: 233.9.



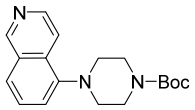
9

Compound **9 (7-(prop-2-yn-1-yl)-5,6,7,8-tetrahydropyrrolo[3',4':4,5]pyrrolo[3,2-*d*]pyrimidin-4-amine)**: 7-deazaadenine (34 mg, 0.250 mmol, 1.0 eq.), propargylamine (20 µL, 0.300 mmol, 1.2 eq.), and formaldehyde solution (37% w/w in water) (39 µL, 0.500 mmol, 2.0 eq.) were dissolved in water/dioxane (1+1 mL) and heated for 3 hours to 100 °C. The solvent was removed in vacuo, and the crude product was purified via RP-flash chromatography: Yield: 21 mg, 39%, colorless solid. ^{1}H NMR (300 MHz, C*D*Cl$_3$) δ = 8.39 (s, 1H), 7.27 – 7.23 (m, 1H), 6.60 (d, *J* = 3.1 Hz, 1H), 6.23 (s, 1H), 5.17 (s, 2H), 4.58 (s, 2H), 3.49 (d, *J* = 2.5 Hz, 2H), 2.31 (t, *J* = 2.5 Hz, 1H) ppm. ^{13}C NMR (75 MHz, *C*DCl$_3$) δ = 161.9, 150.8, 150.8, 130.2, 103.7, 78.6, 73.9, 68.9, 63.8, 37.1 ppm. LC/MS: m/z calculated for $C_{11}H_{11}N_5$ [M+H]$^+$: 214.1, found: 214.0.



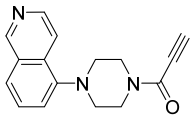
10

Compound **10 ((5-amino-1*H*-1,2,4-triazol-1-yl)(4-ethynylphenyl)methanone)**: 4-ethynylbenzoic acid (146 mg, 1.000 mmol, 1.0 eq.), TBTU (321 mg, 1.000 mmol, 1.0 eq.), and DIPEA (500 µL, 2.862 mmol, 2.9 eq.) were suspended in ethyl acetate (10 mL). After 30 minutes, 1*H*-1,2,4-triazol-5-amine (84 mg, 1.000 mmol, 1.0 eq.) was added and the reaction was stirred for 12 hours at room temperature. The precipitate was isolated by filtration and purified by RP-flash chromatography. Yield: 20 mg, 9%, yellowish solid. ^{1}H NMR (300 MHz, DMSO-d_6) δ = 8.07 – 8.02 (m, 2H), 7.74 (s, 2H), 7.68 – 7.59 (m, 3H), 4.49 (s, 1H), 3.35 (s, 1H) ppm. ^{13}C NMR (75 MHz, DMSO-d_6) δ = 167.0, 158.3, 151.6, 132.1, 131.2, 130.9, 126.0, 84.0, 82.7 ppm. LC/MS: m/z calculated for $C_{11}H_8N_4O$ $[M+H]^+$: 213.1, found: 212.9.



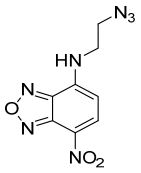
19

Compound **19 (*tert*-butyl 4-(isoquinolin-5-yl)piperazine-1-carboxylate)**: 5-iodoisoquinoline (54 mg, 0.212 mmol, 1.0 eq.), cesium carbonate (311 mg, 0.953 mmol, 4.5 eq.), palladium acetate (5 mg, 0.021 mmol, 0.1 eq.), *tert*-butyl piperazine-1-carboxylate (39 mg, 0.212 mmol, 1.0 eq.), and XPhos (20 mg, 0.042 mmol, 0.2 eq.) were suspended in degassed toluene (5 mL) and the reaction was heated in a sealed tube for 3 hours to 100 °C. The reaction mixture was filtered, and the solvent was removed in vacuo. The crude product was purified via column chromatography (CH/EA = 3:2). Yield: 30 mg, 45%, yellowish oil. ^{1}H NMR (300 MHz, C*D*Cl$_3$) δ = 9.21 (s, 1H), 8.52 (d, *J* = 5.9 Hz, 1H), 7.90 (d, *J* = 5.9 Hz, 1H), 7.65 (d, *J* = 8.2 Hz, 1H), 7.50 (t, *J* = 7.8 Hz, 1H), 7.24 – 7.20 (m, 1H), 3.69 (s, 4H), 3.03 (t, *J* = 5.0 Hz, 4H), 1.49 (s, 9H) ppm. ^{13}C NMR (75 MHz, *C*DCl$_3$) δ = 154.9, 153.0, 148.6, 142.8, 131.8, 130.0, 127.4, 123.1, 116.4, 80.1, 52.8, 44.2, 28.5 ppm. LC/MS: m/z calculated for $C_{18}H_{23}N_3O_2$ $[M+H]^+$: 314.2, found: 314.1.



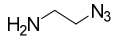
11

Compound **11 (1-(4-(isoquinolin-5-yl)piperazin-1-yl)prop-2-yn-1-one)**: Intermediate **19** (30 mg, 0.096 mmol, 1.0 eq.) was dissolved in TFA/DCM (1+1 mL) and stirred for 30 minutes at room temperature. Subsequently, all volatiles were removed in vacuo. The residue was resolved in DCM (1 mL) and TBTU (31 mg, 0.096 mmol, 1.0 eq.), propiolic acid (6 µL, 0.096 mmol, 1.0 eq.), and DIPEA (50 µL, 0.287 mmol, 3.0 eq.) were added. The reaction was stirred for 12 hours at room temperature before the solvent was removed in vacuo. The crude product was purified via RP-flash chromatography. Yield: 7 mg, 27%, brownish solid. ^{1}H NMR (300 MHz, C*D*Cl$_3$) δ = 9.35 (s, 1H), 8.57 (s, 1H), 8.18 – 8.05 (m, 2H), 7.85 – 7.79 (m, 1H), 7.76 – 7.60 (m, 2H), 7.41 – 7.36 (m, 1H), 4.13 – 3.91 (m, 4H), 3.20 – 3.08 (m, 5H) ppm. LC/MS: m/z calculated for $C_{16}H_{15}N_3O$ $[M+H]^+$: 266.1, found: 266.0.



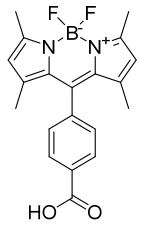
20

Compound **20 (*N*-(2-azidoethyl)-7-nitrobenzo[*c*][1,2,5]oxadiazol-4-amine)**: Intermediate **21** (18 mg, 0.200 mmol,1.0 eq.) was dissolved in a mixture of water (1 mL) and saturated sodium bicarbonate solution (2 mL). *N*-(2-chloroethyl)-7-nitrobenzo[*c*][1,2,5]oxadiazol-4-amine (40 mg, 0.200 mmol, 1.0 eq.) was added in acetonitrile (1 mL). The reaction mixture was stirred for 16 hours at room temperature and purified by RP-flash chromatography. Yield: 12 mg, 24%, green solid. ^{1}H NMR (300 MHz, C*D*Cl$_3$) δ = 8.53 – 8.48 (m, 1H), 8.20 – 8.14 (m, 1H), 7.64 – 7.58 (m, 1H), 3.75 (m, 4H) ppm. ^{13}C NMR (75 MHz, *C*DCl$_3$) δ = 143.4, 136.0, 131.9, 131.3, 49.8, 43.0 ppm. LC/MS: m/z calculated for $C_8H_7N_7O_3$ $[M+H]^+$: 250.1, found: 249.8.



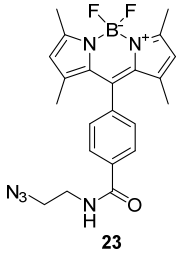
21

Compound **21 (2-azidoethan-1-amine):** 2-chloroethylamine hydrochloride (1.50 g, 12.90 mmol, 1.0 eq.) and sodium azide (2.52 g, 38.8 mmol, 3.0 eq.) were dissolved in water, and the mixture was stirred for 24 h at 80–90 °C. An aqueous KOH solution (4 mL, 15 wt-%) was added at room temperature and the reaction mixture was extracted with diethyl ether (4×10 mL). After drying the combined organic layers over anhydrous sodium sulfate, the solvent was removed under reduced pressure to yield the desired product as a colorless oil (1.06 g, 67%). ^{1}H NMR (300 MHz, C*D*Cl$_3$): δ = 3.37 (t, *J* = 5.7 Hz, 1H), 2.88 (t, *J* = 5.7 Hz 1H), 1.48 (s, 2H). ^{13}C NMR (75.5 MHz, *C*DCl$_3$): *δ* = 54.7, 41.5.



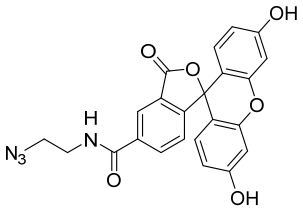
22

Compound **22 (4-(5,5-difluoro-1,3,7,9-tetramethyl-5*H*-4*λ*^{4},5*λ*^{4}-dipyrrolo[1,2-*c*:2',1'-*f*][1,3,2]diazaborinin-10-yl)benzoic acid):** 4-formylbenzoic acid (600 mg, 4.00 mmol, 1.0 eq.) and 2,4-dimethylpyrrole (601 mg, 8.96 mmol, 2.3 eq.) were dissolved in dry DCM (10 mL). One drop of trifluoroacetic acid was added and the mixture was stirred for 12 h at room temperature under an argon atmosphere. To DCM (100 mL) was added DDQ (907 mg, 4.00 mmol, 1.0 eq.), and this solution was slowly dropped into the reaction mixture. After 10 min of stirring at room temperature, triethylamine (8 mL) and boron trifluoride etherate (8 mL) were added, and stirring was continued for six hours. The reaction mixture was filtered through a plunge of celite, the filtrate was collected, and the solvent was removed under reduced pressure. The residue was purified by column chromatography (CH/EA = 3:1 + 0.1% formic acid) which yielded the desired product as an orange solid (245 mg, 17%). ^{1}H NMR (300 MHz, DMSO-*d*$_6$): δ = 8.15 – 8.05 (m, 2H), 7.58 – 7.48 (m, 2H), 6.20 (s, 2H), 2.46 (s, 6H), 1.33 (s, 6H) ppm. ^{13}C NMR (75 MHz, DMSO-d$_6$): δ = 167.3, 155.7, 143.1, 141.2, 138.9, 131.9, 130.7, 130.6, 128.8, 122.0, 14.5 ppm. LC/MS: m/z calculated for $C_{20}H_{19}BF_2N_2O_2$ $[M+H]^+$: 369.2, found: 369.1.



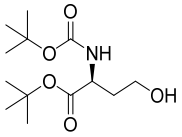
23

Compound **23 (*N*-(2-azidoethyl)-4-(5,5-difluoro-1,3,7,9-tetramethyl-5*H*-4*λ*^{4},5*λ*^{4}-dipyrrolo[1,2-*c*:2',1'-*f*][1,3,2]diazaborinin-10-yl)benzamide):** Intermediate **22** (400 mg, 1.09 mmol, 1.0 eq.) was dissolved in DMF (8 mL) and the solution was cooled to 0 °C. DIPEA (554 µL, 3.26 mmol, 3.0 eq.) and TPTU (484 mg, 1.63 mmol, 1.5 eq.) were successively added to the mixture at 0 °C and stirring was continued for 45 min at 0 °C. Intermediate **21** (94 mg, 1.09 mmol, 1.0 eq.) was added and the mixture was stirred at room temperature for 48 hours. After removing the solvent under reduced pressure, the residue was purified by RP-flash chromatography to yield the desired product as a green shimmering solid (340 mg, 72%). ^{1}H NMR (300 MHz, C*D*Cl$_3$): δ = 7.92 (d, *J* = 7.5 Hz, 2H), 7.36 (d, *J* = 7.3 Hz, 2H), 6.78 (s, 1H), 5.97 (s, 2H), 3.73 – 3.51 (m, 4H), 2.54 (s, 6H), 1.33 (s, 6H) ppm. ^{13}C NMR (75 MHz, *C*DCl$_3$): δ = 166.8, 156.0, 143.0, 140.2, 138.6, 134.6, 131.0, 128.5, 127.9, 121.5, 50.8, 39.6, 14.6 ppm. LC/MS: m/z calculated for $C_{22}H_{23}BF_2N_6O$ $[M+H]^+$: 437.2, found: 437.1.



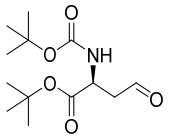
24

Compound **24 (*N*-(2-azidoethyl)-3',6'-dihydroxy-3-oxo-3*H*-spiro[isobenzofuran-1,9'-xanthene]-5-carboxamide):** 5-FAM (200 mg, 0.53 mmol, 1.0 eq.) was dissolved in DMF (6 mL) and the solution was cooled to 0 °C. DIPEA (316 µL, 1.86 mmol, 3.5 eq.) was added dropwise to the solution followed by the addition of TPTU (236 mg, 0.78 mmol, 1.5 eq.) while stirring. After stirring for 45 min at 0 °C, intermediate **21** (68.6 mg, 0.80 mmol, 1.5 eq.) was added. Stirring was continued for 1 h at 0 °C and subsequently for 48 h at room temperature. The solvent was removed under reduced pressure, and the residue was purified by column chromatography (DCM/MeOH = 9:1 + 0.1% TFA) which yielded the desired product as an orange solid (226 mg, 96%). ^{1}H NMR (300 MHz, CD_3O*D*): δ = 8.44 (d, *J* = 1.6 Hz, 1H), 8.20 (dd, *J* = 8.0, 1.6 Hz, 1H), 7.31 (d, *J* = 8.0 Hz, 1H), 6.71 (d, *J* = 2.3 Hz, 2H), 6.63 (d, *J* = 8.7 Hz, 2H), 6.56 (dd, *J* = 8.7, 2.3 Hz, 2H), 3.65–3.57 (m, 2H), 3.57–3.49 (m, 2H) ppm.^{13}C NMR (75 MHz, *C*D_3OD): δ = 169.7, 168.6, 164.2, 155.7, 137.7, 134.8, 131.1, 129.6, 127.2, 126.5, 115.6, 112.5, 103.6, 51.4, 40.8, 30.7, 24.2 ppm. LC/MS: m/z calculated for $C_{23}H_{16}N_4O_6$ $[M+H]^+$: 445.1, found: 445.0.



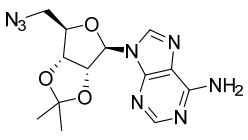
25

Compound **25 (*tert*-butyl (*tert*-butoxycarbonyl)-L-homoserinate):** Boc-Asp-O*t*Bu (3 g, 10.37 mmol, 1.0 eq.) was dissolved in dry THF (30 mL). *N*-methylmorpholine (1.27 mL, 11.41 mmol, 1.1 eq.) was added and the solution was cooled to 0 °C while stirring. Ethyl chloroformate (1.09 mL, 11.41 mmol, 1.1 eq.) was added dropwise to the solution at 0 °C, and stirring was continued for 30 minutes. Ice water (6 mL, 0 °C) was used to dissolve sodium borohydride (1.18 g, 31.11 mmol, 3.0 eq.) and the cold solution was added dropwise to the reaction mixture and stirring at 0 °C was continued for 30 min. Saturated sodium bicarbonate solution (30 mL) was added and the reaction mixture was extracted with chloroform (4×20 mL). The combined organic phases were dried with anhydrous sodium sulfate and the solvent was removed under reduced pressure to yield the desired product as a transparent oil (2.59 g, 91%). ^{1}H NMR (300 MHz, C*D*Cl_3): δ = 5.36 (d, *J* = 7.9 Hz, 1H), 4.35 – 4.22 (m, 1H), 3.73 – 3.52 (m, 2H), 2.19 – 1.98 (m, 1H), 1.61 – 1.48 (m, 1H), 1.48 (s, 9H), 1.41 (s, 9H) ppm. ^{13}C NMR (75 MHz, *C*DCl_3): δ = 172.1, 156.6, 82.3, 80.3, 58.4, 51.1, 36.5, 28.3, 28.0 ppm.



26

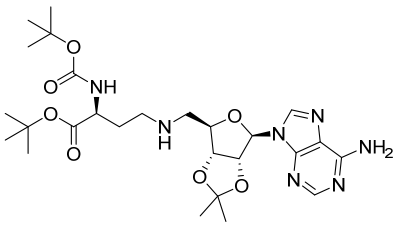
Compound **26 (*tert*-butyl (*S*)-2-((*tert*-butoxycarbonyl)amino)-4-oxobutanoate):** Intermediate **25** (887 mg, 3.22 mmol, 1.0 eq.) was dissolved in DCM (20 mL) and molecular sieve (3 Å, 5 g) was added while stirring at 0 °C. Pyridinium chlorochromate (1.04 g, 4.83 mmol, 1.5 eq.) was added to the suspension at 0 °C. After 30 minutes, the suspension was allowed to warm to room temperature and stirring was continued for one additional hour. Subsequently, the suspension was filtered through a plunge of silica gel and the silica was washed with additional DCM. The filtrates were combined, and the solvent was removed under reduced pressure to yield the raw aldehyde (370 mg, 42%), which was immediately used without further purification and characterization.



27

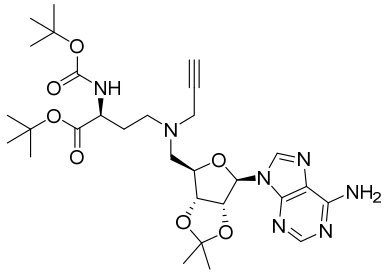
Compound **27 (9-((3a*R*,4*R*,6*R*,6a*R*)-6-(azidomethyl)-2,2-dimethyltetrahydrofuro[3,4-*d*][1,3]dioxol-4-yl)-9*H*-purin-6-amine):** 2′,3′-*O*-isopropylideneadenosine (1 g, 3.25 mmol, 1.0 eq.) was dissolved in dry 1,4-dioxane (10 mL) and diphenylphosphoryl azide (1.79 g, 6.51 mmol, 2.0 eq.) and DBU (1.49 g, 9.76 mmol, 3.0 eq.) were added successively to the solution. The mixture was stirred

at room temperature for four hours, and subsequently, sodium azide (1.06 g, 16.27 mmol, 5.0 eq.) and 15-crown-5 (71 mg, 0.33 mmol, 0.1 eq.) were added. Stirring was continued for 4 hours at 110 °C. The solvent was removed under reduced pressure and the residue was taken up in chloroform (50 mL). The organic phase was washed once with water (50 mL) and twice with brine (50 mL). The aqueous phase was then reextracted once with chloroform (30 mL) and the combined organic layers were dried over anhydrous sodium sulfate. After removing the solvent under reduced pressure, the residue was purified first by silica column chromatography (DCM + 0–5% MeOH) and afterward by RP-flash chromatography (water/ACN 65:35) to give the desired product as a colorless solid (984 mg, 91%). ^{1}H NMR (300 MHz, C*D*Cl$_3$): δ = 8.33 (s, 1H), 7.92 (s, 1H), 6.34 (s, 1H), 6.10 (d, *J* = 2.3 Hz, 1H), 5.45 (dd, *J* = 6.4, 2.3 Hz, 1H), 5.04 (dd, *J* = 6.3, 3.4 Hz, 1H), 4.37 (td, *J* = 5.8, 3.4 Hz, 1H), 3.56 (dd, *J* = 5.8, 2.7 Hz, 2H), 1.60 (s, 3H), 1.37 (s, 3H) ppm. ^{13}C NMR (75 MHz, *C*DCl$_3$): δ = 155.9, 153.1, 149.2, 140.0, 120.3, 114.8, 90.7, 85.7, 84.2, 82.1, 52.4, 27.2, 25.4 ppm.



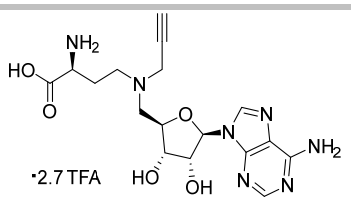
28

Compound **28 (*tert*-butyl (*S*)-4-((((3a*R*,4*R*,6*R*,6a*R*)-6-(6-amino-9*H*-purin-9-yl)-2,2-dimethyltetrahydrofuro[3,4-*d*][1,3]dioxol-4-yl)methyl)amino)-2-((*tert*-butoxycarbonyl)amino)butanoate)**: Intermediate **27** (400 mg, 1.20 mmol, 1.0 eq.) was solved in ethanol (10 mL) and Pd/C (20 mg, 10%) was added to the solution. Stirring under a hydrogen atmosphere (1 atm, room temperature) was conducted for 18 hours. The suspension was filtered over celite. After removing the solvent under reduced pressure, the residue was taken up in 1,2-dichloroethane (20 mL), and intermediate **26** (370 mg,1.32 mmol, 1.1 eq.) was added to the solution. The solution was stirred for 15 minutes at room temperature after which sodium triacetoxyborohydride (280 mg, 1.32 mmol, 1.1 eq.) was added, and stirring was continued for 18 hours at room temperature. Removal of the solvent under reduced pressure followed by purification of the residue via column chromatography (DCM/MeOH = 30:1 + 0.5% Et$_3$N) gave the desired product as a colorless solid (510 mg, 75%). ^{1}H NMR (300 MHz, C*D*Cl$_3$): δ = 8.31 (s, 1H), 7.90 (s, 1H) 6.04 – 5.93 (m, 4H), 5.47 (d, *J* = 6.2 Hz, 1H), 5.07 (dd, *J* = 6.2, 3.1 Hz, 1H), 4.40–4.32 (m, 1H), 4.31–4.22 (m, 1H), 2.94 (dd, *J* = 12.5, 3.9 Hz, 1H), 2.86–2.69 (m, 2H), 2.66–2.55 (m, 1H), 1.96–1.72 (m, 2H), 1.60 (s, 3H), 1.42 (d, *J* = 5.9 Hz, 9H), 1.37 (s, 12H) ppm. ^{13}C NMR (75 MHz, *C*DCl$_3$): δ = 171.9, 155.8, 153.2, 149.6, 140.1, 120.6, 114.7, 91.2, 85.1, 83.2, 82.3, 81.8, 79.5, 53.5, 53.1, 51.5, 46.4, 32.4, 28.4, 28.1, 27.5, 25.7 ppm.



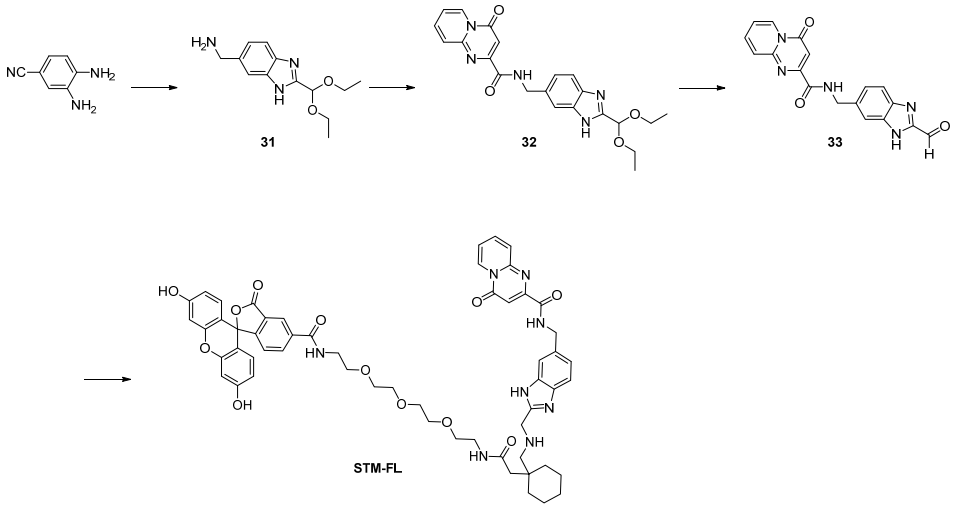
29

Compound **29 (*tert*-butyl (*S*)-4-((((3a*R*,4*R*,6*R*,6a*R*)-6-(6-amino-9*H*-purin-9-yl)-2,2-dimethyltetrahydrofuro[3,4-*d*][1,3]dioxol-4-yl)methyl)(prop-2-yn-1-yl)amino)-2-((*tert*-butoxycarbonyl)amino)butanoate):** Intermediate **28** (0.300 g, 0.530 mmol, 1.0 eq.) was dissolved in DMF (6 mL). DIPEA (100 µL, 0.59 mmol, 1.1 eq.) and propargyl bromide (40 µL, 0.53 mmol, 1.0 eq.) were added to the solution. After stirring for 18 hours at room temperature, the solvent was removed in vacuo and the residue was purified by silica chromatography (DCM + 0–3% MeOH) to yield the desired product as a colorless solid (272 mg, 85%). ^{1}H NMR (300 MHz, C*D*Cl$_3$): δ = 8.34 (s, 1H), 7.98 (s, 1H), 6.04 (d, *J* = 18.2 Hz, 3H), 5.59 – 5.39 (m, 2H), 4.98 (s, 1H), 4.36 (s, 1H), 4.27 – 4.13 (m, 1H), 3.42 (d, *J* = 2.8 Hz, 2H), 2.87 – 2.67 (m, 2H), 2.57 (t, *J* = 6.9 Hz, 2H), 2.10 (d, *J* = 2.3 Hz, 1H), 2.05 – 1.86 (m, 1H), 1.85 – 1.71 (m, 1H), 1.60 (s, 4H), 1.48 – 1.33 (m, 21H) ppm. ^{13}C NMR (75 MHz, *C*DCl$_3$): δ = 171.6, 171.6, 155.5, 155.4, 152.7, 149.2, 140.2, 120.4, 114.5, 90.9, 86.4, 85.5, 83.9, 83.1, 81.8, 79.6, 73.5, 55.3, 52.6, 50.2, 42.5, 29.8, 28.4, 28.0, 27.1, 25.4 ppm. LC/MS: m/z calculated for $C_{29}H_{43}N_7O_7$ $[M+H]^+$: 602.3, found: 602.0.

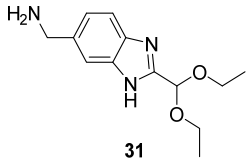


30

Compound **30 ((*S*)-2-amino-4-((((2*R*,3*S*,4*R*,5*R*)-5-(6-amino-9*H*-purin-9-yl)-3,4-dihydroxytetrahydrofuran-2-yl)methyl)(prop-2-yn-1-yl)amino)butanoic acid):** To a solution of intermediate **29** (134 mg, 0.22 mmol) in DCM (1.5 mL) were added TFA (1.5 mL) and H_2O (200 µL) at 5 °C. The solution was kept at 5 °C for 3 d. After dilution and co-distillation with DCM (3×20 mL), the residue was once more dissolved in DCM (1.5 mL) and TFA (1.5 mL). The solution was kept again at 5 °C until full conversion was detected by LC/MS. Then, the reaction was diluted and co-distilled with DCM (5×20 mL) again. The residue was dissolved in water (7 mL) and was dried by lyophilization to give (157 mg, 99% with 2.7 eq. TFA) as a colorless trifluoroacetate salt. ^{1}H NMR (300 MHz, C*D*$_3$O*D*): δ = 8.23 (s, 1H), 8.06 (s,1H), 5.83 (d, *J* = 4.9 Hz, 1H), 4.45 (t, *J* = 4.9 Hz, 1H), 4.20 (d, *J* = 7.0 Hz, 1H), 4.09 (t, *J* = 4.9 Hz, 1H), 3.88 (t, *J* = 2.8 Hz, 2H), 3.85 −3.76 (m, 1H), 3.51−3.28 (m, 2H), 3.24 (t, *J* = 7.1 Hz, 2H), 2.96 (s, 1H), 2.22−2.04 (m, 1H), 1.99−1.84 (m, 1H) ppm. ^{13}C NMR (75 MHz, *C*D$_3$OD): δ = 172.2, 152.3, 149.7, 145.8, 144.5, 120.6, 91.1, 81.1, 80.7, 74.9, 73.4, 72.9, 56.8, 52.8, 52.5, 42.9, 26.3 ppm. LC/MS: m/z calculated for $C_{17}H_{23}N_7O_5$ $[M+H]^+$: 406.2, found: 406.2.

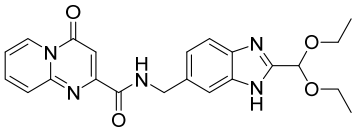


Scheme S4: Synthesis overview and compound numbering of the METTL3 probe **STM-FL** and its precursors.



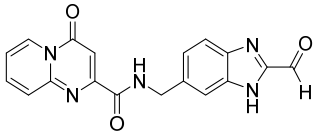
31

Compound **31 ((2-(diethoxymethyl)-1*H*-benzo[*d*]imidazol-6-yl)methanamine):** To a solution of sodium ethoxide (437 mg, 19 mmol of Na in 10 mL of dry ethanol) was added *o*-phenylenediamine derivate (1.3 g, 10 mmol, 1.0 eq.) and ethyl diethoxyacetate (2.1 mL, 12 mmol, 1.2 eq.). The mixture was heated in a sealed tube to 120 °C for 16 h, cooled to room temperature, and the solvent was removed under vacuum. The residue was dissolved in water, neutralized with acetic acid, and extracted with ethyl acetate. Then, the combined organic phases were purified over a short column (CH/EA 1:1 +1%TEA) and concentrated under reduced pressure. To a solution of this intermediate (1.6 g, 6.53 mmol) in methanol (10 mL) was added Raney Ni (200 mg) followed by 7 M ammonia in methanol (3 mL). The reaction solution was hydrogenated at 4 bar for 4 h at room temperature. The reaction mixture was filtered through a plug of silica. The raw product was purified by column chromatography (EA/MeOH 1:1 + 1% TEA) to give the title compound as yellowish oil (1.16 g, 47%). ^{1}H NMR (300 MHz, C*D*Cl$_3$): δ = 7.49 (d, *J* = 8.3 Hz, 1H), 7.45 (s, 1H), 5.68 (s, 1H), 7.09 (dd, *J* = 8.3, 1.5 Hz, 1H), 3.87 (s, 2H), 3.74 – 3.50 (m, 4H), 3.39 (s, 3H), 1.16 (t, *J* = 7.1 Hz, 6H) ppm. ^{13}C NMR (75 MHz, *C*DCl$_3$): δ = 151.8, 137.3, 122.3, 115.8, 113.7, 97.2, 62.3, 49.8, 46.4, 15.0 ppm. LC/MS: m/z calculated for $C_{13}H_{20}N_3O_2$ $[M+H]^+$: 250.2, found: 249.7.



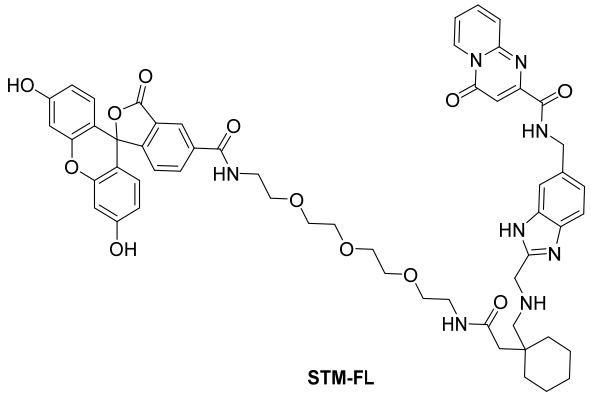
32

Compound **32** ***N*-((2-(diethoxymethyl)-1*H*-benzo[*d*]imidazol-6-yl)methyl)-4-oxo-4*H*-pyrido[1,2-*a*]pyrimidine-2-carboxamide:** A solution of intermediate **12** (452 mg, 2 mmol, 1.0 eq.), TBTU (642 mg, 2 mmol, 1.0 eq.) and intermediate **31** (500 mg, 2 mmol, 1.0 eq.) in dry DMF (10 mL) was treated with *N*-ethyl-*N*-isopropyl-propan-2-amine (1 mL, 6.00 mmol, 3.0 eq.) and the suspension was stirred at room temperature for 16 hours. The suspension was concentrated under vacuum and the residue was diluted with water and dichloromethane. Subsequently, the organic layer was extracted with $NaHCO_3$ sat. and purified over a short silica column (DCM/MeOH 10:1 + 1% TEA). Evaporation gave the title compound as an off-white solid (472 mg, 56%). ^{1}H NMR (300 MHz, C*D*Cl$_3$): δ = 10.02 (s, 1H), 9.05 (d, *J* = 7.1 Hz, 1H), 8.37 (s, 1H), 7.83 – 7.68 (m, 2H), 7.60 (dt, *J* = 9.0, 1.3 Hz, 1H), 7.54 – 7.38 (m, 1H), 7.30 (s, 1H), 7.26 – 7.12 (m, 1H), 5.74 (s, 1H), 4.75 (d, *J* = 6.0 Hz, 2H), 3.81 – 3.58 (m, 4H), 1.17 (t, *J* = 7.2 Hz, 6H) ppm. ^{13}C NMR (75 MHz, *C*DCl$_3$): δ = 163.0, 158.7, 153.6, 152.0, 150.6, 137.0, 132.5, 127.7, 126.6, 116.3, 110.9, 102.9, 97.0, 62.4, 46.1, 44.2, 15.2, 10.4 ppm. LC/MS: m/z calculated for $C_{22}H_{24}N_5O_4$ $[M+H]^+$: 422.2, found: 422.0.



33

Compound **33** ***N*-((2-formyl-1*H*-benzo[*d*]imidazol-6-yl)methyl)-4-oxo-4*H*-pyrido[1,2-*a*]pyrimidine-2-carboxamide:** A solution of intermediate **32** (230 mg, 0.55 mmol) in THF/H_2O/conc HCl (3+3+2 mL) was stirred for 3 h at 80 °C under argon flow atmosphere. Evaporation and lyophilization afforded the dihydrochloride which was suspended in DCM/MeOH/TEA (10:1:1). Filtration over silica and evaporation yielded the free base as an off-white solid (192 mg, 99%). ^{1}H NMR (300 MHz, DMSO-d_6): δ = 9.62 (t, *J* = 6.3 Hz, 1H), 9.01 (d, *J* = 6.6 Hz, 1H), 8.09 (ddd, *J* = 8.6, 6.7, 1.5 Hz, 1H), 7.79 (d, *J* = 8.8 Hz, 1H), 7.76 – 7.68 (m, 2H), 7.57 (d, *J* = 9.8 Hz, 1H), 7.47 (td, *J* = 7.0, 1.3 Hz, 1H), 6.94 – 6.87 (m, 1H), 6.25 (s, 1H), 4.65 (d, *J* = 6.3 Hz, 2H) ppm. ^{13}C NMR (75 MHz, DMSO-d_6): δ = 163.1, 157.9, 154.5, 153.5, 150.5, 138.8, 137.7, 130.9, 129.9, 127.5, 126.1, 126.0, 117.5, 114.1, 113.0, 101.0, 83.6, 43.1 ppm. LC/MS: m/z calculated for $C_{18}H_{16}N_5O_4$ $[M+H_2O+H]^+$: 366.1, found: 365.9.



STM-FL

STM-FL: Intermediate **33** (17 mg, 0.05 mmol, 1.8 eq.) and FAM-PEG3-gabapentyl-NH_2 (20 mg, 0.028 mmol, 1.0 eq.) were solved in DCE/HFIP/trimethyl orthoformate (500+100+50 µL) and incubated for incubated for 48 h at 30 °C. Afterward, MeOH (200 µL) and $NaBH_4$ (1 mg) were added at 0 °C, and the mixture was incubated for 30 min at room temperature. The reaction was quenched by the addition of 0.1% TFA in water (10 µL). and the residue was purified by RP-flash chromatography (6 mg, 20%). ^{1}H NMR (300 MHz, C*D*$_3$O*D*): δ = 9.13 – 8.96 (m, 1H), 8.48 – 8.36 (m, 1H), 8.27 – 8.13 (m, 1H), 8.13 – 8.01 (m, 1H), 8.01 – 7.89 (m, 1H), 7.87 – 7.70 (m, 1H), 7.68 – 7.52 (m, 2H), 7.47 – 7.32 (m, 3H), 7.28 (d, *J* = 8.0 Hz, 1H), 7.07 (s, 1H), 6.74 – 6.69 (m, 1H), 6.68 – 6.66 (m, 1H), 6.62 (d, *J* = 7.2 Hz, 1H), 6.60 – 6.48 (m, 4H), 4.70 (s, 2H), 4.57 – 4.50 (m, 2H), 3.73 – 3.42 (m, 20H), 3.24 – 3.17 (m, 2H), 1.58 – 1.34 (m, 12H) ppm. ^{13}C NMR (75 MHz, *C*D$_3$OD): δ = 174.6, 168.2, 161.8, 154.2, 139.1, 135.5, 130.4, 130.2, 128.5, 127.7, 125.9, 125.1, 118.4, 116.3, 114.0, 111.0, 103.6, 71.7, 71.6, 71.3, 71.2, 71.0, 70.4, 70.3, 62.8, 45.6, 44.5, 43.9, 41.2, 40.7, 37.0, 34.8, 30.8, 30.4, 28.1, 27.3, 26.7, 22.2 ppm. LC/MS: m/z calculated for $C_{56}H_{59}N_8O_{12}$ $[M+2H]^{2+}$: 518.2, found:518.2. Purity: 98%.

Biophysical and enzymatic MTase assays

Microscale thermophoresis (MST-assay)

Probe screening by MST displacement assays:

MST experiments were carried out using a Monolith NT.115 instrument (NanoTemper Technologies) using Monolith standard capillaries. The instrument was calibrated according to the manufacturer's instructions. The laser type was chosen dye-dependently (NanoBlue laser for NBD, BODIPY, 4-FAM, Atto488, and Cy3; resp. PicoRed laser for Atto590, Atto647N, and Cy5). General settings were applied for all MST experiments as follows: manual temperature control: 25 °C, fluorescence measurement before MST: 4 s, MST (IR laser) on: 20 s, fluorescence after MST: 2 s, delay: 25 s. The laser power was adjusted to optimize the signal-to-noise ratio and the fluorescence signal. LED and MST power settings were chosen individually for each sample set by adjusting the LED power to yield fluorescence signals of at least 300 units (blue laser) or 3000 units (red laser) and medium MST power to achieve an appropriate thermophoretic response. MST measurements were analyzed using the NT analysis software (version 1.5.41) and exported for statistical analysis of MST shifts and plotting in GraphPad Prism 7.01.

The reaction mixtures used for MST probe screening experiments contained 2 µM of the investigated MTase and the respective probe candidate (100 nM probe for NanoBlue laser and 10 nM probe for PicoRed laser) both dissolved in screening assay buffer (50 mM HEPES pH7.5, 150 mM NaCl, 1 mM DTT, 0.1% PEG-8000, 0.05% PS-20). In situ-prepared probe stocks (416 µM, 12 µL) were pre-diluted with the same assay buffer to a concentration of 1 µM. After 5 minutes of enzyme-probe mixture preincubation at room temperature, either SAH (dissolved in buffer) or pure buffer (mock treatment) was added resulting in the following final concentrations: 2 µM MTase, 10 nM or 100 nM respective probe candidate, and 100 µM SAH competitor. After 10 minutes of incubation at room temperature, reaction mixtures were loaded as triplicates at a total volume of 10 µL into capillaries and subjected to MST measurement as described above. F_{norm} values at 5 sec from the start of the thermophoresis laser were utilized for MST-shift determination and analysis

MST assays with preparative probes for affinity determination:

HPLC-purified probe preparations (Cy5TAD, FTAD, and Cy5TPD) were used for the determination of MTase-probe binding affinities and apparent SAH resp. inhibitor dissociation constants according to the general MST protocol as described above with minor adaptions. Probe stocks were prepared in DMSO at 1 mM and diluted with buffer to a final concentration of 10 nM for Cy5TAD/Cy5TPD and 100 nM for FTAD. Experiments were conducted in the following enzyme-specific buffers and supplemented with ligands or additives if needed:

METTL1: 50 mM Tris-HCl pH8.0, 250 mM NaCl, 0.1% PS-20
METTL3/14: 25 mM Tris HCl, pH7.5, 100 mM NaCl
DNMT2/NSUN2/NSUN6: 50 mM HEPES pH7.5, 150 mM NaCl, 1 mM DTT, 0.1% PEG-8000, 0.05% PS-20
TrmD: 50 mM HEPES pH7.5, 500mM NaCl, 5% glycerol
Nsp10/16: 20 mM HEPES pH7.4, 150 mM NaCl, 4 mM $MgCl_2$

SAH was commercially obtained from Sigma-Aldrich and STM2457 was bought from Cayman Chemicals. Stock solutions were prepared in DMSO. The MTase-probe binding affinities and ligand dissociation constants were evaluated from F_{norm} values at 5 sec vs. the respective concentration using a 4-parameter Hill equation to determine a K_D value: $y(F_{norm}) = bottom + ([ligand]^{slope}) \times (top - bottom)/([ligand]^{slope} + K_D^{slope})$.

Fluorescence polarization (FP-assay)

Fluorescence polarization assays were conducted with a similar sample composition as described for preparative MST assays. Triplicates were prepared in black 96-well half-area plates (Greiner) and measured using a Spark 10M plate reader (Tecan) equipped with polarization filters coupled to a monochromator setup (FTAD: λ_{ex}=480 nm, λ_{em}=530 nm; Cy5TAD/Cy5TPD: λ_{ex}=635 nm, λ_{em}=680 nm). For MTase-probe affinity and ligand dissociation constant determination, FTAD was used at a final concentration of 100 nM, and Cy5TAD resp. Cy5TPD was used at a concentration of 20 nM. Proteins were diluted in their enzyme-specific buffers at a volume of 50 µL per replicate and supplemented with ligands if needed. Device calibration of the FP-z-factor was conducted as stated in the device manual using 1 nM fluorescein (pH8.0). Despite slight dispersion of the FP-z-factor, the same configuration was used for the Cy5-containing probes. Polarization values (in mP) were calculated from polarization-specific parallel and orthogonal fluorescence intensities according to the Tecan in-built calculation routine. K_D values were calculated and plotted in GraphPad Prism 7.01 using the 4-parameter Hill equation as described above.

(*S*)-crizotinib, entacapone, and tanespimycin were commercially obtained from BLDpharmatech for preparative hit validation of METTL1 HTS hits.

High-throughput drug screening on METTL1

A high-throughput screening of the DiscoveryProbe™ FDA-approved Drug Library (Apexbio Technology) was conducted using the METTL1/Cy5TAD fluorescence polarization setup. This library contains 2320 FDA-approved drugs in 10 mM DMSO stocks. Screening conditions were established according to the results of initial FP assays on METTL1. First, the high-throughput screening setup was validated by the determination of the Z-factor as a statistical parameter of the capability of hit identification. For this, a master mix solution containing 1 µM METTL1 and 20 nM Cy5TAD in HTS buffer (50 mM Tris-HCl pH8.0, 250 mM NaCl, 0.1% (w/w) polysorbate-20) was prepared. 50 µL of this master mix was filled to each well of a black 96-well half-area plate (Greiner). Either 1 µL of sinefungin (10 mM in DMSO, final 200 µM) or pure DMSO as mock treatment were added and 48 replicates for such negative and

positive controls, respectively, were determined (Fig. S3F). The statistical Z-factor was determined from FP-values (Z=0.519), and thus, this assay setup is sufficient for the performance of a high-throughput screening campaign.
For high-throughput screening, 50 µL of this master mix was filled to each well of a black 96-well half-area plate and 1 µL of the respective drug compound stock (10 mM in DMSO) was added to achieve a final drug compound concentration of 200 µM. DMSO and sinefungin (100 µM) were measured in each experiment as negative and positive controls, respectively. Plates were incubated for 10 min on an orbital shaker, centrifuged at 500g for 30 sec, and submitted to FP measurement as described above (Cy5TAD λ_{ex}=635 nm, λ_{em}=680 nm). Hits were identified based on the raw polarization value (<20 mP) and in rare cases false-positive results were discarded due to the blue coloring of the drug compound solution (complementary color to the fluorescence of Cy5). For complete screening results see raw fluorescence polarization data below.

Surface plasmon resonance (SPR)
All SPR experiments were performed on a Biacore 8K (Cytiva) at 25 °C, and TBS-T (Cytiva) with 5% DMSO was used as the running buffer. His6-METTL1 was diluted in TBS and immobilized on a XanTec NiHC 200M high affinity poly-Ni-NTA sensor chip until a response unit (RU) of 3000 was achieved. For multi-cycle experiments, a contact time of 60 s and dissociation time of 200 s was performed (30 µL/min), and (*S*)-crizotinib was tested with a two-fold dilution series from 1000–15 µM. After blank subtraction, reference subtraction, and DMSO/solvent correction were applied, the steady-state affinity model of 1:1 binding in Biacore Insight Evaluation Software (Cytiva) was used to quantify binding.

Isothermal titration calorimetry (ITC)
Determination of MTase ligand affinities by direct titrations:
Prior to ITC experiments, the respective MTase was thawed on ice, and eventually, the buffer was exchanged to an ITC buffer using Amicon Ultra 15 mL centrifugal filters with a 10 kDa cut-off:
METTL1: 50 mM Tris-HCl pH8.0, 250 mM NaCl
DNMT2/NSUN2/NSUN6: 50 mM sodium phosphate pH8.0, 300 mM NaCl, 1 mM EDTA, 2 mM mercaptoethanol
TrmD: 50 mM HEPES pH7.5, 500mM NaCl, 5% glycerol
SAH and tanespimycin were dissolved in DMSO to a final concentration of 25 mM resp. 10 mM and were then diluted in ITC buffer to give ligand solutions at 500 µM. The final MTase solution was adjusted to a concentration of 50 µM and according to the ligand solution, 2% resp. 5% DMSO was added to match the buffers exactly. For the ITC measurements, a MicroCal PEAQ-ITC Automated workstation (Malvern Panalytical) with a 200 µL Hastelloy cell and an injection syringe volume of 40 µL was used. All experiments were performed in triplicates at 25 °C with a stirring speed of 750 rpm and a reference power of 42 µW. 19 injections at 2 µL were added to the reaction cell with an injection speed of 0.5 µL/s and a spacing time of 150 s. Data was analyzed and fitted using the MicroCal PEAQ-ITC Analysis Software 1.21 and plotted in GraphPad Prism 7.01.

Determination of apparent METTL1 hit binding thermodynamics by displacement titrations:
Displacement titrations were performed analogously to direct titrations with the following modifications. The METTL1 protein (50 µM) was preincubated with (*S*)-crizotinib or entacapone, respectively (500 µM, 5% DMSO). Afterward, SAH (500 µM) was titrated to the METTL1-ligand complex as described above. Displacement titrations were fitted using the MicroCal PEAQ-ITC Analysis Software 1.21. and apparent SAH binding affinities were utilized for the calculation of thermodynamic binding profiles of (*S*)-crizotinib or entacapone using the ITCcalc webserver (www.itccalc.uni-mainz.de).

METTL1 inhibition by ^{3}H scintillation assay
Radiometric METTL1 inhibition assays were carried out by mixing the synthetic hs-tRNA^{Phe} substrate (GenScript, GCCGAAAUAGCUCAGUUGGGAGAGCGUUAGACUGAAGAUCUAAAG**G**UCCCUGGUUCGAUCCCGGGUUUCGGCACCA, final: 2 µM), the METTL1/WDR4 enzyme (ActiveMotif, final: 162 nM), the cofactor ^{3}H-SAM (Hartmann Analytics 15 Ci mmol−1, final 2.3 µM) and variable concentrations of the identified METTL1 hits in 10 µL of assay buffer (20 mM Tris-HCl, pH8.0, 1 mM TCEP, 1 mM $MgCl_2$, 0.01% triton, 1% glycerol). The reactions were started by the addition of the cofactor ^{3}H-SAM and were carried out at 37 °C for 60 min. Aliquots of 8 µL were taken from the reaction mixture and spotted on Whatman glass microfiber filters (GF/C, 25 mm, Cytiva). The RNA was precipitated on the filters in 5% ice-cold trichloroacetic acid (TCA) for 15 min. The filters were washed twice with 5% TCA at room temperature for 20 and 10 min and once in EtOH for 10 min. After drying, the filters were transferred into scintillation vials and 3 mL of Gold MV liquid scintillation cocktail (PerkinElmer) was added. Scintillation was measured on a scintillation counter (TriCarb Liquid Scintillation Analyzer 4810TR) with a measurement time of 1 min. Statistical analysis and plotting were performed in GraphPad Prism 7.01 as described above.

Protein preparation and purification

Bacterial expression and purification of human full-length DNMT2
A plasmid coding for the full-length human DNMT2 was kindly provided by Albert Jeltsch (University of Stuttgart, Germany). Transformed *E. coli* Rosetta (DE3) pLysS cells were grown in TB medium at 37 °C till an optical density at 600 nm wavelength reached 0.7. Then cells were precooled to 20 °C for 30 min and overexpression was induced by IPTG at a final concentration of 500 µM. After 18–20 hours cells were collected, and cell pellets were flash-frozen in liquid nitrogen and stored at −80°C. For protein isolation, cell pellets were disrupted in lysis buffer (50 mM sodium phosphate pH8.0, 300 mM NaCl, 25 mM imidazole, 0.1% polysorbate-20), incubated with lysozyme (Carl Roth) and DNAse I (Roche CustomBiotech) for 60 min on ice with subsequent 10

rounds of 30 s sonication at 50% power with 30 s intervals on ice. The lysate was centrifuged at 20,000g for 30–60 min at 4 °C, then filtered and loaded onto HisTrap HP 5 mL (Cytiva) column with the ÄKTA start system (Cytiva). To remove unspecific bound impurities, the column was washed with several column volumes of lysis buffer and afterward with several column volumes of a mixture of 92% lysis buffer: 8% elution buffer (50 mM sodium phosphate pH8.0, 500 mM NaCl, 800 mM imidazole, 0.1% polysorbate-20). The protein was eluted in a mixture 30% lysis buffer: 70% elution buffer. Size exclusion chromatography (SEC) was performed on a Superdex 16/600 75 pg column equilibrated in SEC buffer (50 mM sodium phosphate pH8.0, 300 mM NaCl, 1 mM EDTA, 2 mM DTT, 0.1% polysorbate-20). The DNMT2 protein was concentrated with Amicon Ultra 15 mL centrifugal filters (10 kDa cut-off) aliquoted, flash frozen with liquid nitrogen, and kept at −80°C until further usage.

Bacterial expression and purification of human full-length NSUN2

Expression and purification were performed similarly to DNMT2, as described above. Plasmid used for overexpression is available at Addgene (Addgene ID: 188059). Overexpression was conducted at 16 °C. Cells were disrupted in lysis buffer (50 mM sodium phosphate pH8.0, 300 mM NaCl, 10 mM imidazole, 0.1% polysorbate-20). After lysate loading, the HisTrap HP 5 mL column was washed with several column volumes of lysis buffer and afterward with several column volumes of a mixture of 96% lysis buffer: 4% elution buffer (50 mM sodium phosphate pH8.0, 300 mM NaCl, 500 mM imidazole, 0.1% polysorbate-20) to remove unspecific bound impurities. Subsequently, the protein was eluted in elution buffer and was further purified using a Superdex 16/600 75 pg column equilibrated with SEC buffer (50 mM sodium phosphate pH8.0, 300 mM NaCl, 1 mM EDTA, 2 mM DTT, 0.1% polysorbate-20). NSUN2 protein was concentrated, aliquoted, flash-frozen with liquid nitrogen, and kept at −80°C until further usage.

Bacterial expression and purification of human full-length NSUN6

Expression and purification were performed similarly to DNMT2, as described above. Plasmid used for overexpression is available at Addgene (Addgene ID: 188060). Overexpression was conducted at 16 °C. Transformed *E. coli* Rosetta (DE3) pLysS cells were grown and overexpression was induced as described above. Cells were disrupted in lysis buffer (50 mM sodium phosphate pH7.5, 150 mM NaCl, 10 mM imidazole, 0.1% polysorbate-20). After lysate loading, the HisTrap HP 5 mL column was washed with several column volumes of lysis buffer and afterward with several column volumes of a mixture of 96% lysis buffer:4% elution buffer (50 mM sodium phosphate pH7.5, 150 mM NaCl, 500 mM imidazole, 0.1% polysorbate-20) to remove unspecific bound impurities. Subsequently, the protein was eluted in elution buffer and was further purified with a Superdex 16/600 75 pg column equilibrated with SEC buffer (25 mM HEPES pH7.5, 300 mM NaCl, 1 mM DTT, 0.1% polysorbate-20, 10% glycerol). Concentrated NSUN6 protein was aliquoted, flash-frozen with liquid nitrogen, and kept at −80°C until further usage. NSUN6 should be used within 2 weeks after preparation, to avoid substantial activity loss.

Recombinant expression of TrmD (*Haemophilus influenzae*)

Plasmid coding for the TrmD of *Haemophilus influenzae* was kindly provided by Se Won Suh (Addgene ID: 12665). The plasmid was used to transform competent BL21 *E. coli* cells. The cells were grown in LB medium at 37 °C until an OD_{600} of ~0.7 was reached. To overexpress TrmD, the temperature was reduced to 16 °C, and IPTG was added to a final concentration of 500 µM. The overexpression was maintained overnight at 16 °C. After harvesting the cells by centrifugation, the cells were suspended in lysis buffer (20 mM HEPES pH7.5, 300 mM NaCl, 0.5 mM TCEP, 5% glycerol, 0.1% polysorbate-20). Additionally, lysozyme and DNAse I were added before incubating the cells on ice for 30 min. The cells were disrupted by sonication and the cell debris was removed by centrifugation. The clear supernatant was filtrated and loaded on a HisTrap HP 5 mL column. The column was washed with several column volumes of wash buffer (20 mM HEPES pH7.5, 300 mM NaCl, 5 mM imidazole, 0.5 mM TCEP, 5% glycerol, 0.1% polysorbate-20). Finally, the TrmD was eluted in elution buffer (20 mM HEPES pH7.5, 300 mM NaCl, 500 mM imidazole, 0.5 mM TCEP, 5% glycerol, 0.1% polysorbate-20). In a second purification step, a Superdex 16/600 75 pg size-exclusion column equilibrated with SEC buffer (25 mM HEPES pH7.5, 300 mM NaCl, 1 mM TCEP, 10% glycerol, 0.1% polysorbate-20) was used to remove residual impurities. Until further use the TrmD was flash-frozen in liquid nitrogen and stored at –80°C.

Recombinant expression of human METTL1

The plasmid coding for the human METTL1 MTase domain was kindly provided by Cheryl Arrowsmith (Addgene ID: 25264). The plasmid was used to transform competent BL21 *E. coli* cells. The cells were grown in LB medium at 37 °C until an OD_{600} of ~0.8 was reached. To overexpress METTL1 the temperature was reduced to 19 °C and IPTG was added to a final concentration of 200 µM. The overexpression was maintained overnight at 19 °C. After harvesting the cells by centrifugation, the cells were suspended in lysis buffer (100 mM Tris HCl, pH8.0, 500 mM NaCl, 0,1% Tween). Additionally, lysozyme and DNAse I were added before incubating the cells on ice for 30 min. The cells were disrupted by sonication and the cell debris was removed by centrifugation. The clear supernatant was filtrated and loaded on a HisTrap HP 5 mL column. The column was washed with several column volumes of lysis buffer (100 mM Tris HCl, pH8.0, 500 mM NaCl, 0,1% Tween). Finally, METTL1 was eluted in a gradient with elution buffer (100 mM Tris HCl, pH8.0, 500 mM NaCl, 250 mM imidazole, 0,1% Tween). In a second purification step, a Superdex 16/600 75 pg size-exclusion column equilibrated with SEC buffer (10 mM Tris HCl, pH 8, 150 mM NaCl) was used to remove residual impurities. Until further use the METTL1 was flash-frozen in liquid nitrogen and stored at –80°C.

Recombinant expression of human METTL3/14

The plasmid was designed and manufactured by Genscript. The sequence coding for MTase domains of human METTL3 (UniProt: Q86U44 aa 252–580) harboring a Strep tag-II at the C-terminus and METTL14 (UniProt: Q9HCE5 aa 108–444) harboring a hexahistidine (His_6) at the N-terminus were cloned into a pETduet-1 vector (cloning sites: EcoRI/XhoI). The resulting plasmid was sequence-checked and used to transform calcium-competent *E. coli* BL21(DE3). The cells were grown in LB medium at 37 °C until

an OD_{600} of ~0.6 was reached. To overexpress METTL3/14 the temperature was reduced to 18 °C. IPTG and $ZnCl_2$ were added to a final concentration of 100 µM. The overexpression was maintained overnight at 18 °C. After harvesting the cells by centrifugation, the cells were suspended in cold lysis buffer (10 mM potassium phosphate, pH7.5, 300 mM KCl, 20 mM imidazole, 10% glycerol, 0.1 mM TCEP). Additionally, lysozyme, one tablet of protease inhibitor, and DNAse I were added before incubating the cells on ice for 30 min. The cells were disrupted by sonication and the cell debris was removed by centrifugation. The clear supernatant was kept on ice. The pellet was dissolved in lysis buffer and sonicated for a second time. Insoluble parts were removed by centrifugation. The supernatants of both centrifugation steps were pooled, filtrated, and loaded on a HisTrap HP 5 mL column, preequilibrated in binding buffer (10 mM potassium phosphate, pH7.5, 300 mM KCl, 20 mM imidazole). The column was washed with several column volumes of wash buffer (10 mM potassium phosphate, pH7.5, 500 mM KCl, 20 mM imidazole). Finally, METTL3/14 was eluted with the elution buffer (10 mM potassium phosphate, pH7.5, 300 mM KCl, 250 mM imidazole). In a second purification step, a Superdex 16/600 75 pg size-exclusion column equilibrated with SEC buffer (25 mM Tris HCl, pH7.5, 100 mM NaCl) was used to remove residual impurities. Until further use, the METTL3/14 protein was flash-frozen in liquid nitrogen and stored at –80°C.

The recombinant SARS-CoV2 nsp10/16 protein, co-expressed in a HEK293 cell system, was obtained commercially (BPSBioscience BPS-100747-1). The recombinant METTL1/WDR4 complex was obtained commercially from ActiveMotif (ACM-81206). The recombinant FLAG-METTL3, expressed by baculovirus in Sf9 insect cells, was obtained commercially (BPSBioscience BPS-100055).

In silico protein databank (PDB) mining

PDB mining of SAH-replacement scaffolds was conducted by REST calls related to the PDBe service. For documentation of the PDBe REST API see https://www.ebi.ac.uk/pdbe/api/doc/search.html. Individual steps of the PDB mining strategy are briefly explained in the Python code below:

Fetch all SAH, SAM, and sinefungin (SFG) containing PDB structure IDs:

```
import requests
import json
import urllib.request
# All SAH&SFG&SAM pdb entries:
ligands = ['SAH', 'SAM', 'SFG']
pdb_ids = set()
for ligand in ligands:
    url = f'https://www.ebi.ac.uk/pdbe/graph-api/compound/in_pdb/{ligand}'
    response = requests.get(url).json()
    for pdb_id, value in response.items():
        pdb_ids |= set(value)
```

Determine the Uniprot mappings of all SAH-containing PDB IDs:

```
# PDB2Uniprot mapping
def get_uniprot_ids(pdb_ids):
    uniprot_ids = set()
    for pdb_id in pdb_ids:
        response = requests.get(f'https://www.ebi.ac.uk/pdbe/graph-
api/pdbe_pages/uniprot_mapping/{pdb_id}/1')
        data = json.loads(response.text)
        try:
            uniprot_id = data[pdb_id]["data"][0]["accession"]
            uniprot_ids.add(uniprot_id)
        except KeyError:
            pass
    return list(uniprot_ids)

uniprot_ids = get_uniprot_ids(pdb_ids)
```

Find matching PDB entries to a non-duplicate list of Uniprot mappings:

```
# Matching pdb entries
def get_pdb_ids_from_uniprot_ids(uniprot_ids):
    all_pdb_ids = []
    for uniprot_id in uniprot_ids:
        try:
```

```
            response =
requests.get(f"https://www.ebi.ac.uk/pdbe/api/mappings/best_structures/{uniprot_id}").json()
            for i in range(len(response[uniprot_id])):
                all_pdb_ids.append(response[uniprot_id][i]["pdb_id"])
        except:
            pass
    return all_pdb_ids

all_pdb_ids = get_pdb_ids_from_uniprot_ids(uniprot_ids)
all_pdb_ids = list(set(all_pdb_ids))
```

Return a matrix of all ligands bound to the list of SAH-pocket containing PDB entries:

```
##All bound ligands
with open("Allpdb.csv", "r") as csv_file:
    csv_reader = csv.DictReader(csv_file, delimiter=';')
    for lines in csv_reader:
        accession = lines['1']
        try:
            with urllib.request.urlopen("https://www.ebi.ac.uk/pdbe/graph-
api/pdb/bound_molecules/"+accession) as url:
                temp_dict = json.loads(url.read().decode())
        except:
            pass
        try:
            print(accession+"; ")
            for i in range(20):
                print(str(temp_dict[accession][i]["composition"]["ligands"][0]["chem_comp_id"])+";
")
        except:
            print("")
            print("")
```

Return a SMILES string for extracted PDB ligand IDs:

```
import requests
from bs4 import BeautifulSoup

#Return SMILES for enriched ligand IDs
def get_Smiles(lig_id):
    response = requests.get("https://www.ebi.ac.uk/pdbe-
srv/pdbechem/chemicalCompound/show/"+lig_id)
    if response.status_code == 200:
        soup = BeautifulSoup(response.text, 'html.parser')
        table = soup.find('table', id="topDescTable")
        if table:
            rows = table.find_all('tr')
            if 4 < len(rows):
                cells = rows[4].find_all('td')
                if 3 < len(cells):
                    return cells[3].text.strip()
    return None

cell_content = get_Smiles(lig_id)
```

Tuples of “PDB IDs, Uniprot IDs, ligand IDs, and SMILES strings” were imported to Excel for inspection and clustering. After duplicate removal and exclusion of records that contain the “SAH or SAM or SFG” ligands, 1105 PDB entries with non-SAH-like ligands in SAH binding pockets were obtained. These results were clustered by the “SMILES string” attribute using JChem for Excel and the mcs (Maximum Common Substructure) algorithm. After manual inspection, 190 valid PDB IDs clustered in eleven distinct SAH replacement clusters were obtained which are presented in detail in Fig. S4.

Supplementary results

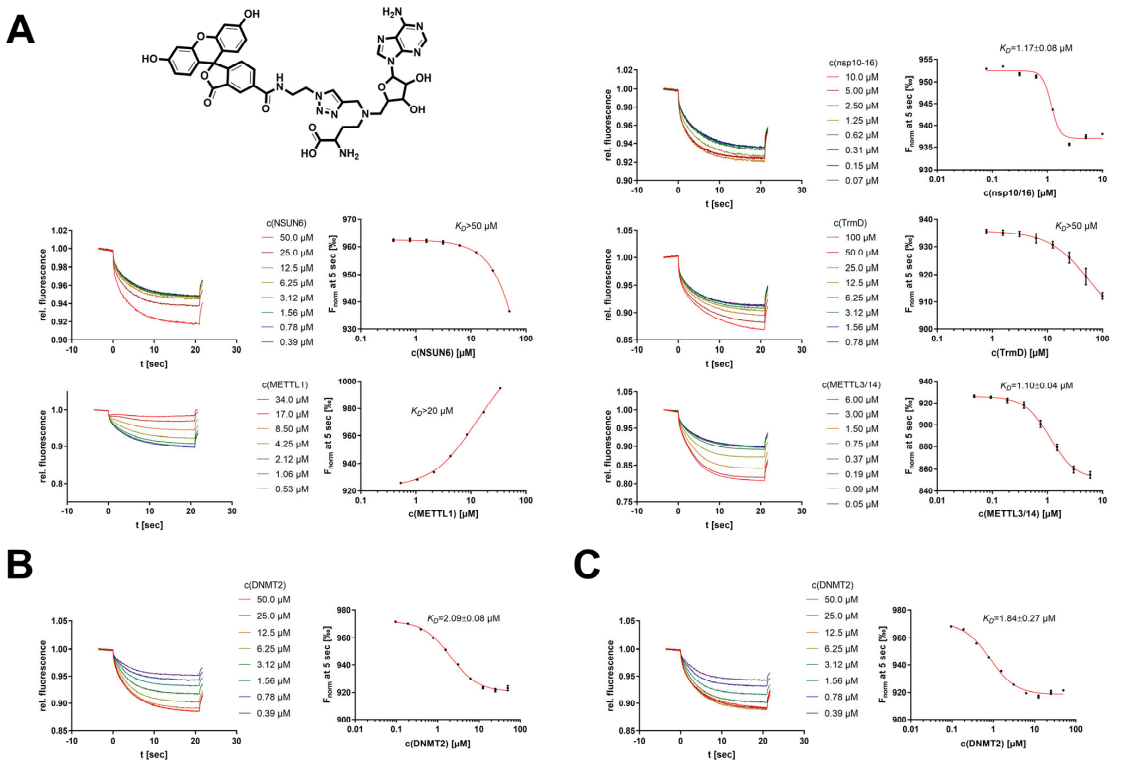


Figure S1. FTAD binding affinity to various RNA-MTases determined by MST assays (mean ± SD, n=3). (**A**) The respective MTases were titrated to 100 nM FTAD, and the thermodynamic binding profile was determined by MST shift analysis at F_{norm}=5 sec. (**B**) DNMT2 vs. HPLC-purified FTAD shows MST traces and binding characteristics that are statistically indistinguishable from (**C**) in situ-clicked FTAD during nanomole scale synthesis of the probe libraries, highlighting that the CuAAC components (1 mM TBTA, 8.3 mM sodium ascorbate, 1.2 mM copper(II)sulfate) do not interfere with the MST-based MTase assay.

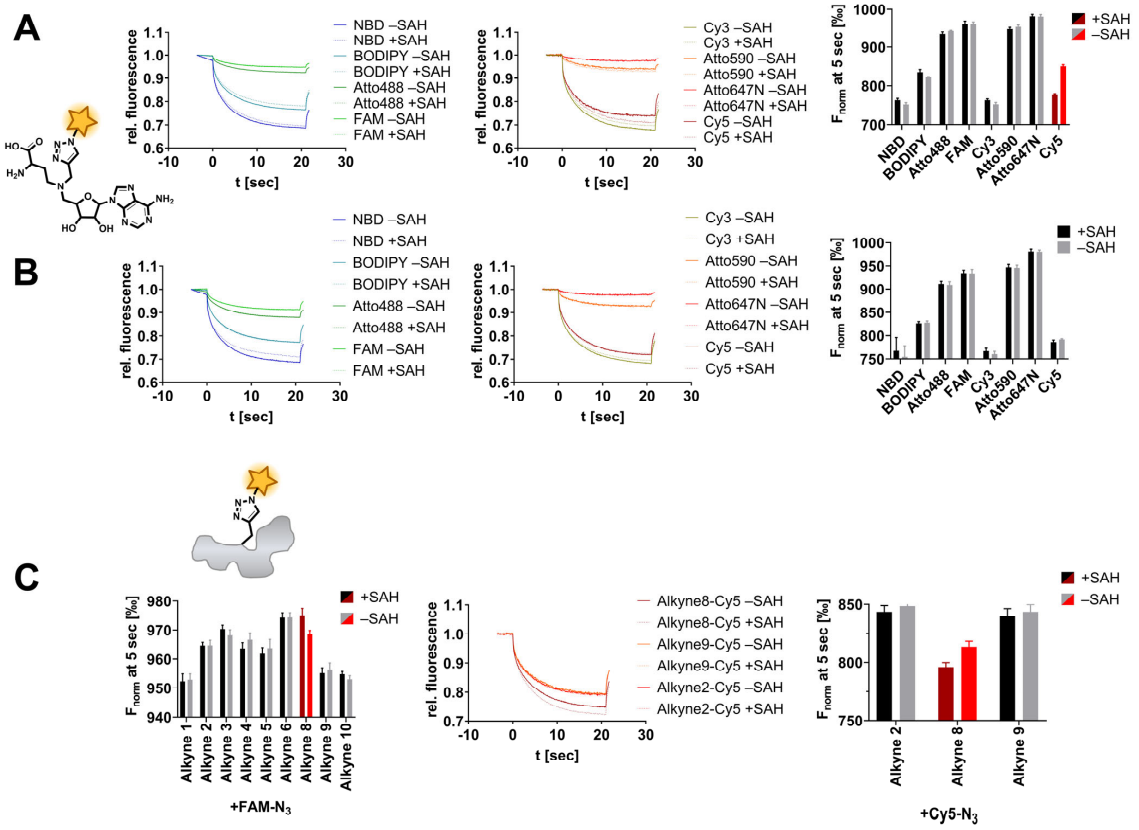


Figure S2. Fluorescent probe screening results on NSUN6 and TrmD (mean ± SD, n=3). (**A**) Screening results of TAD-probe candidates (100 nM) on NSUN6 (2 µM) by displacement MST assays. The MST traces (**left**) in the presence of the SAH competitor (100 µM) or without the SAH competitor yielded MST shifts (**right**) revealing Cy5-TAD displays the largest SAH-induced shift (ΔF_{norm} at 5 sec). (**B**) The screening of TAD-probe candidates on TrmD did not reveal any functional probe because of non-significant MST shifts. (**C**) Thus, SAH-replacement alkynes **1–11** were reacted with FAM-azide on a nanomole scale. Alkynes **7** & **11** did not result in successful product formation and thus were omitted from the analysis. The other successfully synthesized SAH-replacement triazoles were used for MST screening on TrmD (2 µM) and revealed Alkyne **8** coupled to FAM-azide resp. Cy5-azide displays the largest SAH-induced shift (ΔF_{norm} at 5 sec).

Table S1. Correlation between MTase active site flexibility, SAH conformation, and FTAD binding affinity determined by MST assays. The active site flexibility was determined by B'-factor normalization (www.bandit.uni-mainz.de) and a comparison of the maximum B-factor within a defined stretch of FTAD fluorophore interacting residues. Fluorophore-interacting residues were defined by manual inspection of the SAH binding pose in the crystal structure (PDB ID and residue numbers are given below). *The active site loop was not resolved in the crystal structures of DNMT2 and METTL3/14 due to very high intrinsic flexibility. The conformation of the SAH molecule bound in the crystal structure can be geometrically described as the angle between the SAH atom coordinates for "N6, O4', and N" (PDB naming). From these findings, we conclude that MTases that have bound a curved SAH ligand (<100°) are not suitable for the two TAD probes, in this case, the Cy5-TPD probe must be used. MTases with greater flexibility (B'>0) in the binding pocket enable the use of FTAD, whereas MTases with more rigid binding pocket elements prefer Cy5TAD (B'<0).

MTase	PDB ID	FTAD interacting residues	B'-factor maximum	SAH curvature [°]	K_D FTAD [µM]
DNMT2	1G55	P78–T83	>3.00*	152°	2.09 µM
NSUN6	5WWQ	A324–G328	–1.01	141°	>50 µM
METTL3/14	5L6D	M402–Y406	>5.00*	151°	1.10 µM
METTL1	8D5B	T155–F161	–0.65	142°	>20 µM
nsp10/16	7JHE	Surface exposed	–	146°	1.17 µM
***H. inf.* TrmD**	4YVH	V137–G140	–0.57	89°	>50 µM

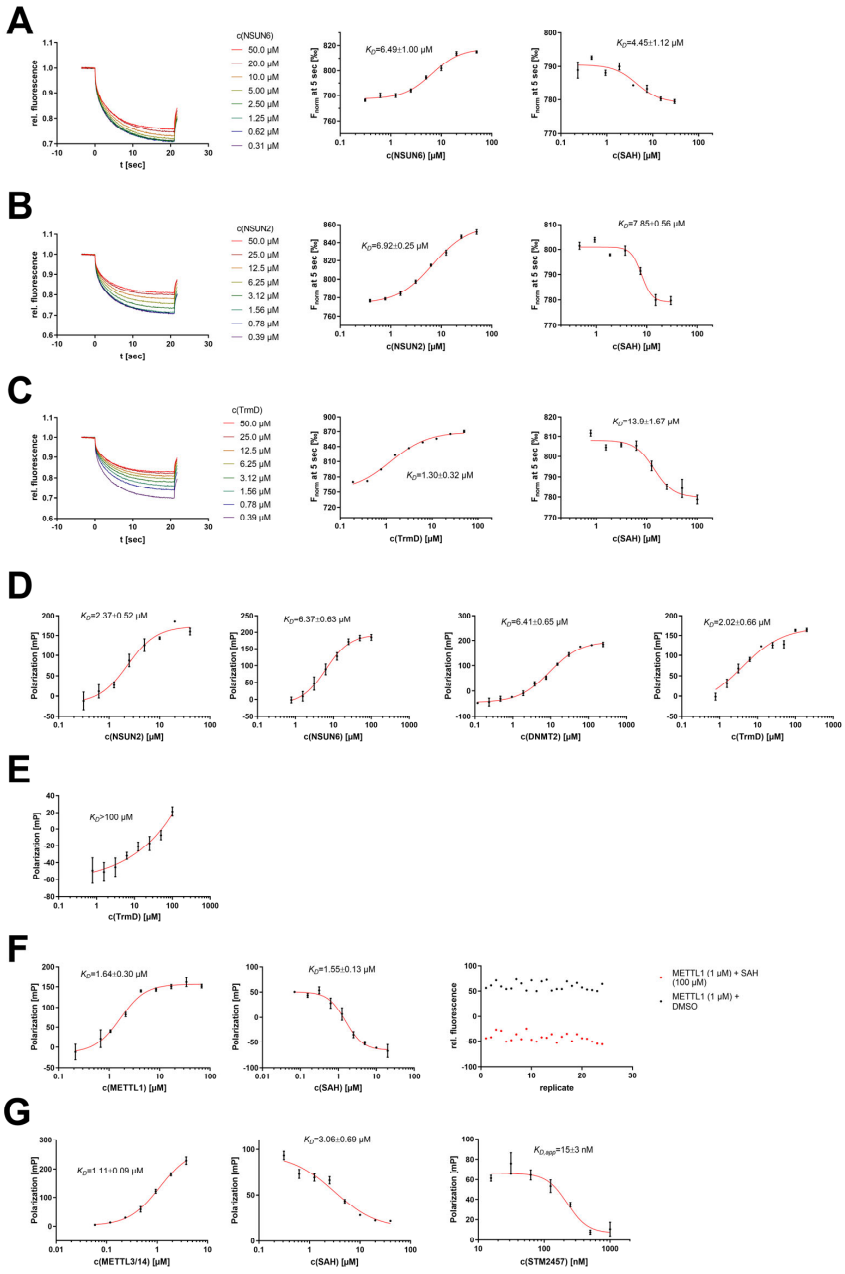


Figure S3. Supplementary MST- and FP-assay results using HPLC-purified Cy5TAD, Cy5TPD, and FTAD probes (mean ± SD, n=3). (**A**) NSUN6/Cy5TAD MST assays; left/middle: probe affinity determination; right: the natural ligand SAH was titrated to 5 µM NSUN6 and 10 nM Cy5TAD to determine the apparent SAH dissociation constant. (**B**) NSUN2/Cy5TAD MST assays; left/middle: probe affinity determination; right: SAH was titrated to 2 µM NSUN2 and 10 nM Cy5TAD. (**C**) TrmD/Cy5TPD MST assays; left/middle: probe affinity determination; right: SAH was titrated to 2 µM TrmD and 10 nM Cy5TPD. (**D**) FP-assay for probe affinity determination of NSUN2 (Cy5TAD, 20 nM), NSUN6 (Cy5TAD, 20 nM), TrmD (Cy5TPD, 20 nM), and DNMT2 (FTAD, 100 nM). (**E**) FP-assay for TrmD (Cy5TAD, 20 nM) to highlight probe selectivity. (**F**) FP-assays on METTL1; left: probe affinity determination (Cy5TAD, 20 nM); middle: SAH was titrated to 1 µM METTL1 and 20 nM Cy5TAD to determine the apparent SAH dissociation constant; right: Z-factor determination for high-throughput assay setup validation (Z=0.51). (**G**) FP-assays on METTL3/14; left: probe affinity determination (Cy5TAD, 20 nM); middle: SAH was titrated to 1 µM METTL3/14 and 20 nM Cy5TAD; right: Determination of the apparent STM2457 inhibitor dissociation constant by a Morisson quadratic fit due to inhibitor tight-binding [E]=1 µM. The binding affinity of STM2457 was determined by an LC/MS-based enzyme assay to be IC_{50}=5 nM.[7]

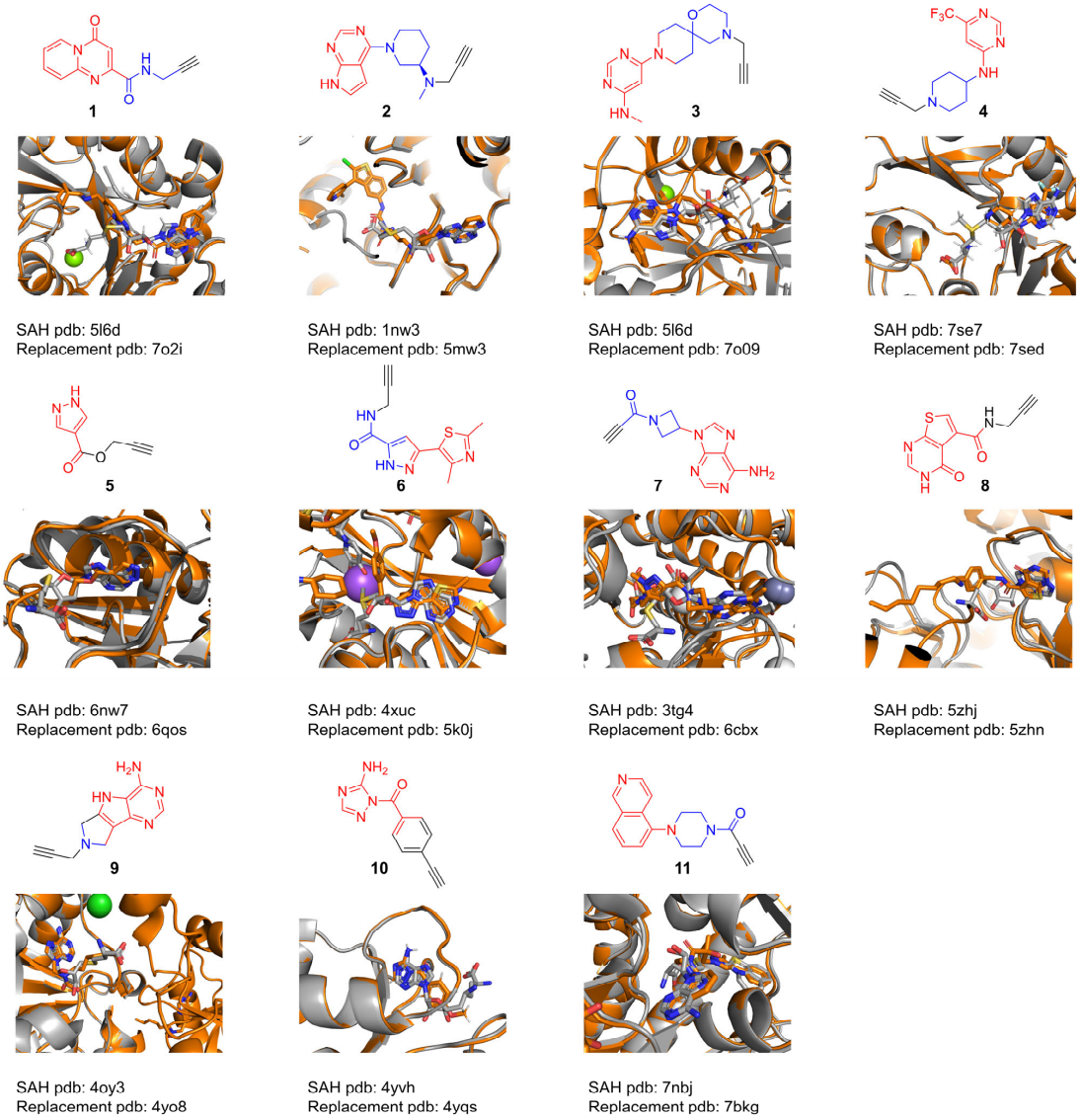


Figure S4. Clustered results of the PDB-mining strategy. Eleven SAH replacements are presented in orange cartoon representation (PDB ID below the ligand binding pose) as an overlay with the orthologous SAH-containing crystal structure in grey (=SAH PDB ID). On top of each ligand binding pose, the respective chemical structure of the resulting SAH replacement alkyne is shown. Coloring of the chemical structure was accomplished according to the superimposed element of the natural SAH ligand from the crystal structure: red: adenine replacement; blue: ribose replacement; black: alkyne handle.

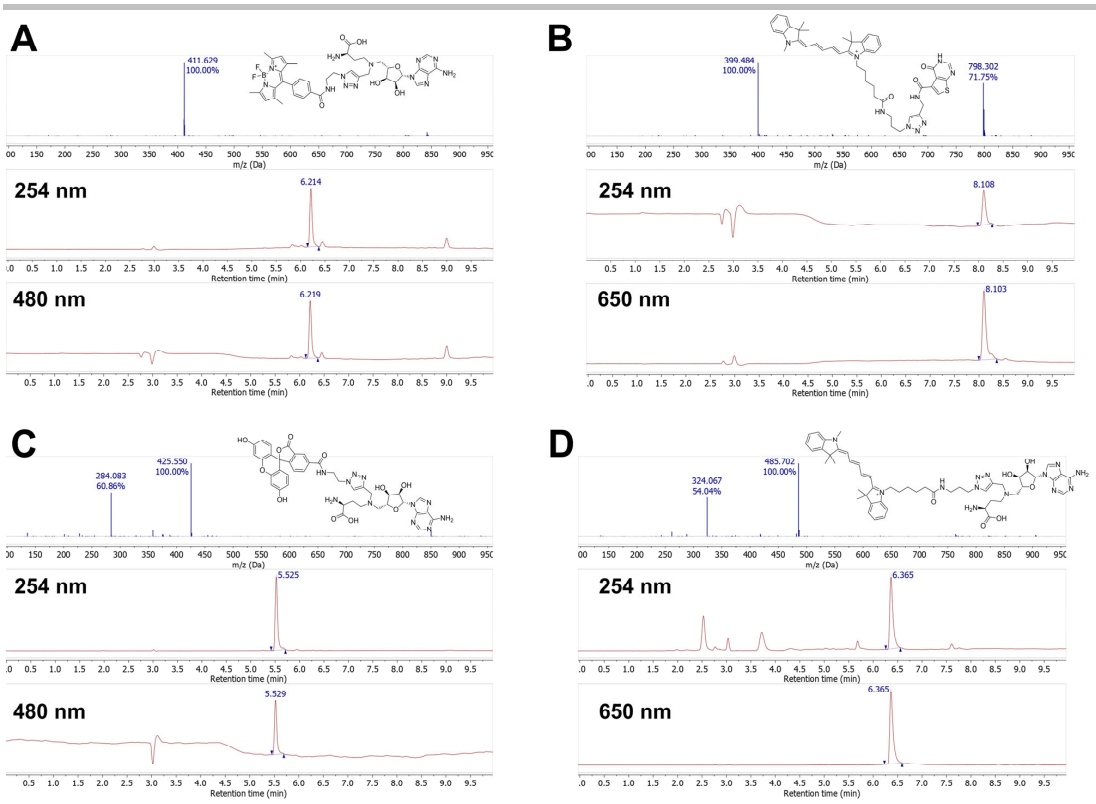


Figure S5. LC/MS spectra and UV chromatograms of in situ-clicked nanomole-scale MTase probe reaction mixture. (**A**) BODIPY-TAD (**B**) Cy5TPD (**C**) FTAD (**D**) Cy5TAD.

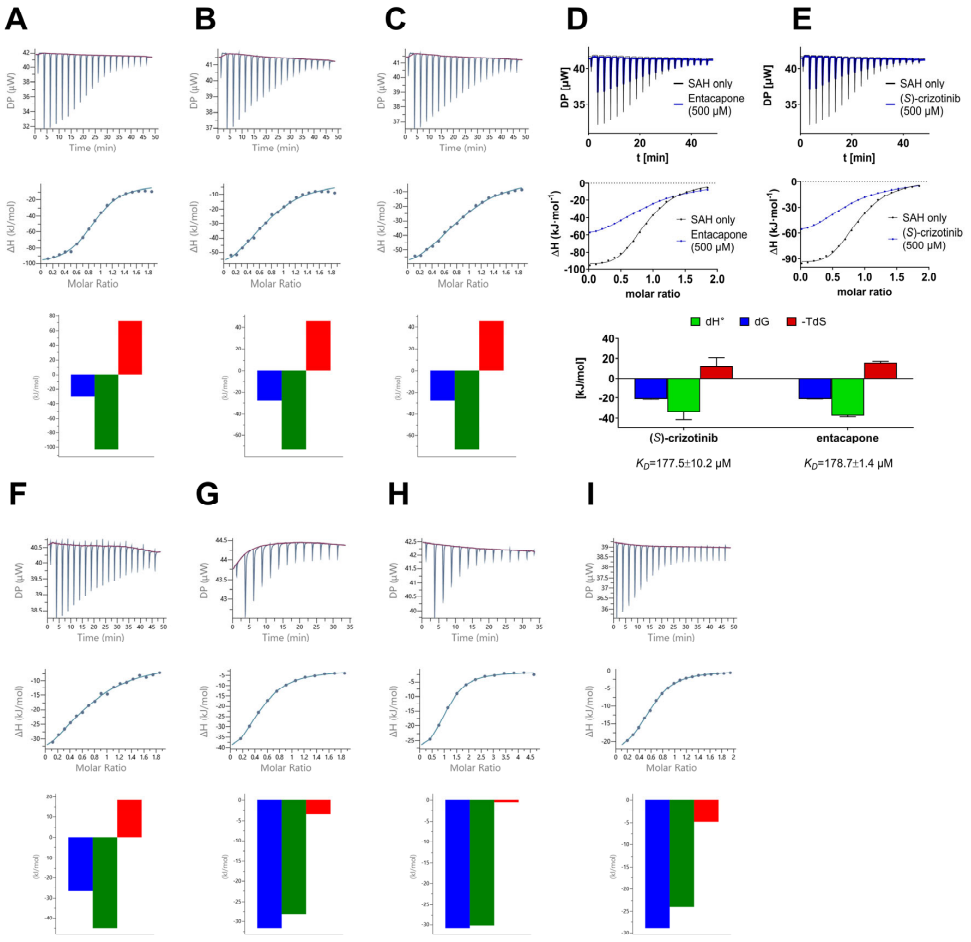


Figure S6. Isothermal titration calorimetry of MTase ligand interactions. A representative titration replicate is shown for each titrant MTase pair by thermograms, stoichiometry plots, and ITC signature plots. (**A**) Titration of SAH (500 µM) into METTL1 (50 µM). (**B**) Titration of SAH (500 µM) into METTL1 (50 µM) preincubated with (*S*)-crizotinib (500 µM). (**C**) Titration of SAH (500 µM) into METTL1 (50 µM) preincubated with entacapone (500 µM). (**D**) Displacement ITC analysis of entacapone binding to METTL1 with differential thermogram and signature plot (mean ± SD, n=3). (**E**) Displacement ITC analysis of (*S*)-crizotinib binding to METTL1 (mean ± SD, n=3). (**F**) Titration of tanespimycin (500 µM) into METTL1 (50 µM). (**G**) Titration of SAH (500 µM) into NSUN2 (50 µM). (**H**) Titration of SAH (500 µM) into NSUN6 (50 µM). (**I**) Titration of SAH (500 µM) into TrmD (50 µM).

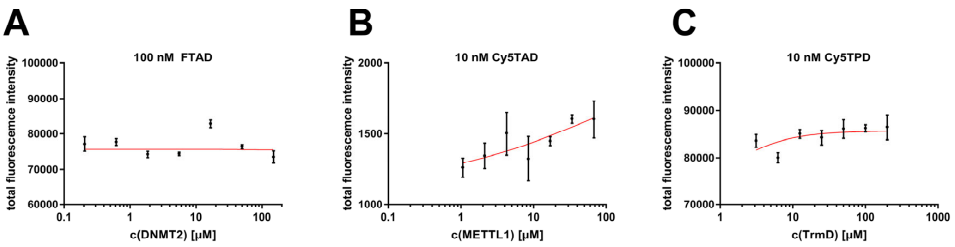


Figure S7. Total fluorescence intensity of the three privileged probes in the presence of variable concentrations of MTases shows only slight changes in probe quantum yield upon protein-ligand binding (mean ± SD, n=3). (**A**) 100 nM FTAD with DNMT2 (**B**) 10 nM Cy5TAD with METTL1 (**C**) 10 nM Cy5TPD with TrmD.

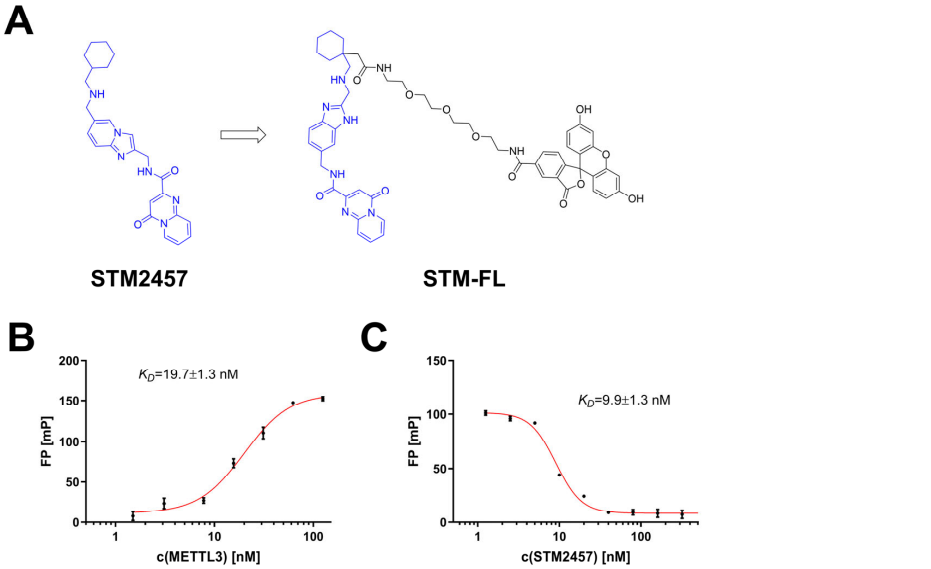


Figure S8. Development and characterization of the METTL3-specific probe STM-FL derived from the high-affinity inhibitor STM2457. This probe allows the characterization of high-affinity ligands (K_D>5 nM) which lead to tight-binding behavior using the FTAD probe (see Fig. S3G). (**A**) Chemical structure of STM2457 and the development of STM-FL by attachment of a fluoresceine-based fluorophore to the ligand. (**B**) FP-assays (mean ± SD, n=3) for METTL3 affinity determination (STM-FL, 5 nM); (**C**) Determination of the STM2457 inhibitor dissociation constant (FLAG-METTL3: 15 nM; STM-FL: 5 nM; mean ± SD, n=3).

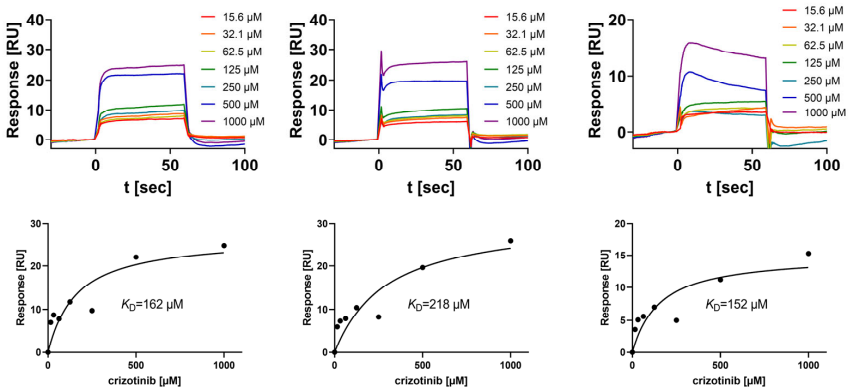


Figure S9. SPR characterization of the (*S*)-crizotinib METTL1 interaction. Triplicates of sensorgrams and the coresponding dose-response curves.

High-throughput drug screening results on METTL1 (raw data)

Presentation of the raw data from the 2320 drug compound screening on METTL1. 96-well plates are presented below with the respective compound name and raw fluorescence polarization (in mP) for each well. 18 compounds with a polarization value <20 mP were considered as initial hit candidates. By subsequent validation experiments, we found that 15 compounds resulted in false-positive results because of: a.) a deep blue color of the test compound which is complementary to the Cy5 excitation maximum, or b.) known promiscuous reactivity of the compounds (PAINs behavior). These false positives were highlighted with red resp. blue background in the raw data below (FPR=0.6%). The remaining four hit candidates (crizotinib, entacapone, and tanespimycin [aka 17-AAG]) could be confirmed by orthogonal assays and thus were validated as true METTL1 binders (hit rate=3/2320=0.13%).

Plate layout: L1021-01

	1	2	3	4	5	6	7	8	9	10	11	12
a	77	46	50	49	153	60	43	70	52	37	27	Empty
	Angiotensin II	Levetiracetan	Daptomycin	Lansoprazole	Adapalene	Granisetron H	Exemestane	Letrozole	Gatifloxacin	Mosapride Cit	Rocuronium Bromide	
b	90	60	82	78	39	47	78	66	81	57	42	Empty
	Biapenem	Nelarabine	Gemcitabine H	Rigosertib (ON	Clofarabine	Losartan Pota	Fulvestrant	CP-945598 HC	Cilnidipine	Lidocaine	Dexrazoxane	Empty
c	106	60	54	68	80	27	85	87	60	70	70	Empty
	Prasugrel	Epothilone B (	Dimesna	Dutasteride	Celecoxib	Enzastaurin (L	Aprepitant	Posaconazole	IPI-145 (INK1	Roscovitine (S	PA-824	Empty
d	82	36	50	83	58	56	41	64	47	46	97	Empty
	Galanthamine	Ramelteon	Tenofovir Dis	Vincristine	Entecavir Hyd	Vatalanib (PTI	LY2835219	Mianserin HCl	Imatinib Mes	Doxorubicin (A	Pelitinib (EKB-	Empty
e	52	23	67	79	47	61	83	67	57	74	41	Empty
	Bumetanide	Cediranib (AZI	E 64d	Decitabine (N	5-Azacytidine	Macitentan	(-)-Huperzine	Carfilzomib (P	Etomidate	Etoposide	Bendamustine	Empty
f	89	62	47	58	37	50	56	80	84	40	56	Empty
	Plerixafor (AM	Doripenem Hy	Ifosfamide	Saracatinib (A	Bosutinib (SKI	Dovitinib (TKI-	Carboplatin	Lenvatinib (E7	Cladribine	Dacarbazine	Genistein	Empty
g	63	23	39	70	34	50	82	82	46	51	22	Empty
	Tivozanib (AV	Ellagic acid	TAK-438	Dexamethaso	Cyclophospha	Mercaptopuri	Floxuridine	Acitretin	Acarbose	Fluoxetine HC	Epirubicin HCl	Empty
h	90	1	47	82	65	107	65	79	87	91	71	Empty
	Pamidronate I	Idarubicin HCl	Malotilate	Leucovorin Ca	Ampicillin	Carbenicillin, I	Chloramphen	Geneticin, G-4	Gentamycin S	Hygromycin B	Kanamycin Su	Empty

Plate layout: L1021-02

	1	2	3	4	5	6	7	8	9	10	11	12
a	73	50	78	102	64	59	66	91	96	61	74	Empty
	Tetracycline H	Vortioxetine (	Carmofur	Quercetin dih	Fluvoxamine r	Altretamine	Aprotinin	Bestatin	Batimastat (B	Nafamostat M	PMSF	
b	117	72	76	90	90	82	99	70	76	77	87	Empty
	(-)-Epigallocat	Fenbendazole	Bortezomib (P	VX-661	Amonafide	Ivermectin	Melatonin	Omeprazole	Leflunomide	Camptothecin	Doxazosin Me	Empty
c	49	66	74	75	78	81	68	74	89	87	89	Empty
	Nepafenac	Flumazenil	Masitinib (AB	Linifanib (ABT	Loratadine	Foretinib (GSK	Cabozantinib	PCI-32765 (Ib	ABT-888 (Veli	MDV3100 (En	Vemurafenib	Empty
d	45	68	108	67	104	82	51	77	70	80	104	Empty
	CAL-101 (Idel	ABT-263 (Nav	Sorafenib	Ruxolitinib (IN	Dasatinib (BM	Trametinib (G	(R)-Crizotinib	GDC-0449 (Vis	Pazopanib (GS	Abacavir	Acamprosate	Empty
e	66	80	84	88	78	74	85	80	96	77	71	Empty
	Afatinib dima	Alarelin Aceta	Aliskiren	Alogliptin Ben	Alosetron Hyc	Alvimopan	Ampalex	AN-2690	AN-2728	Anamorelin	Ascomycin(FK	Empty
f	79	91	64	73	55	83	81	70	80	67	65	Empty
	Asunaprevir (E	AXL1717	Bardoxolone	Baricitinib pho	Bazedoxifene	Bitopertin	Bivalirudin Tri	Boceprevir	Calcipotriol	Capsaicin	Cariprazine	Empty
g	51	71	62	69	66	74	83	65	75	68	67	Empty
	Cetirizine	Choline Fenof	Cinacalcet	Clemizole	Clemizole hyd	Clozapine N-c	CO-1686 (AVL	Cobimetinib	Colchicine	Costunolide	Curcumin	Empty
h	60	97	67	105	81	70	83	63	78	87	39	Empty
	Dabigatran et	Dabrafenib M	Daminozide	Dasatinib hyd	Desmopressin	Docetaxel Tril	Doramectin	Dronedarone	Edoxaban	Edoxaban tos	Elacridar	Empty

Plate layout: L1021-03

	1	2	3	4	5	6	7	8	9	10	11	12
a	74	57	88	85	69	87	80	114	74	79	87	Empty
	Eltrombopag	EMD-121406	Emodin	Erlotinib	Esomeprazole	Etofenamate	Etoricoxib	Fenretinide	Flecainide ace	Fluvastatin	Fosamprenavir Calcium Salt	
b	87	87	88	81	73	78	79	98	58	63	97	Empty
	Galanthamine	Gefitinib hydr	Guanfacine hy	Hydroxyfasud	Indacaterol	Ixabepilone	Kinetin	LDE225 Dipho	Ledipasvir	Lesinurad	Letermovir	Empty
c	64	101	80	97	62	77	123	71	104	78	109	Empty
	Leuprolide Ac	Luliconazole	LY2835219 fre	Matrine	Mefloquine hy	Metoclopram	Micafungin so	MK-4827	MK-5172	Monomethyl	Nelfinavir Me	Empty
d	105	88	98	86	92	72	105	79	102	86	91	Empty
	Nilotinib mon	Nordihydrogu	Olmesartan	Olprinone Hyc	Oseltamivir	Oseltamivir ac	Pemetrexed d	Pentostatin	Peramivir	Phenylpiracet	Pitolisant hyd	Empty
e	60	88	73	77	106	114	80	149	89	73	77	Empty
	Pramipexole d	PSI-7977	Puromycin an	Quetiapine	Regorafenib H	Regorafenib n	Retigabine dih	RG7388	Rilpivirine	Riociguat	Rivastigmine	Empty
f	72	125	40	73	76	106	100	61	70	87	83	Empty
	Ruxolitinib ph	Salirasib	Salmeterol xir	Saquinavir me	Sildenafil	Simeprevir	Tamibarotene	Tedizolid	Teneligliptin h	TH-302	Tianeptine	Empty
g	83	98	64	76	92	82	74	119	60	82	68	Empty
	Tiotropium Br	Tipiracil hydro	Tirofiban hydr	Trametinib DM	Trelagliptin	Triptolide	Triptonide	Troglitazone	Umeclidinium	Vilazodone Hy	Vinblastine su	Empty
h	48	40	64	49	67	85	77	80	90	75	66	Empty
	Vinorelbine di	Vortioxetine	Ziprasidone	Ziprasidone hy	Doxorubicin	Lapatinib Dito	MLN9708	MLN2238	CEP-18770	Gabexate mes	Aspirin (Acety	Empty

Plate layout: L1021-04

	1	2	3	4	5	6	7	8	9	10	11	12
a	49	54	85	57	73	95	69	77	77	71	75	Empty
	Artemether (S	Disulfiram	BMS-708163 (	Danoprevir (R	Telaprevir (VX	VX-222 (VCH-	Glimepiride	Linagliptin (BI	Sitagliptin pho	Vildagliptin (L	Alogliptin (SYR-322)	
b	69	69	71	60	-36	73	93	87	84	80	69	Empty
	Atazanavir sul	Marimastat	GM 6001	Doxycycline h	17-AAG (KOS9	AT13387	Elvitegravir (G	Fluorouracil (A	Raltegravir (M	S/GSK134957	Captopril	Empty
c	72	60	62	79	69	93	74	69	85	68	95	Empty
	Moxonidine	Olmesartan m	Rocilinostat (A	Vorinostat (SA	Mocetinostat	CUDC-101	Pracinostat (S	Belinostat (PX	PCI-24781 (CR	Valproic acid	Sodium Pheny	Empty
d	58	82	79	64	53	64	79	85	77	74	41	Empty
	MLN8237 (Ali	VX-680 (MK-0	Barasertib (AZ	Tofacitinib (CI	TG101348 (SA	Tofacitinib (CI	Baricitinib (LY	LY2784544	BMN 673	Olaparib (AZD	Rucaparib (AC	Empty
e	70	9	64	67	84	65	73	73	78	75	52	Empty
	Iniparib (BSI-2	Entacapone	Thioguanine	EX 527 (SENO	Resveratrol	FG-4592 (ASP	2-Methoxyest	Lenalidomide	Pomalidomide	Thalidomide	Birinapant (TL	Empty
f	75	58	81	72	64	74	65	72	77	76	78	Empty
	YM155	Tipifarnib (Zar	Cyclophospha	Methylpredni	Amuvatinib (M	Abiraterone	Rosiglitazone	Rosiglitazone	Ciprofibrate	Rosiglitazone	Cobicistat (GS	Empty
g	71	61	72	75	61	66	79	68	73	72	74	Empty
	Ketoconazole	Apremilast (C	Roflumilast	Voriconazole	Sildenafil Citra	Clarithromyci	Vardenafil HC	Pioglitazone H	Tadalafil	Rolipram	Cilomilast	Empty
h	48	67	70	56	81	51	65	76	79	73	81	Empty
	Isotretinoin	Avanafil	Mycophenola	Cilostazol	Rivaroxaban	Pimobendan	Apixaban	Gimeracil	Dyphylline	Ozagrel	Aminophylline	Empty

Plate layout: L1021-05

	1	2	3	4	5	6	7	8	9	10	11	12
a	53	75	70	61	85	88	79	87	92	69	71	Empty
	Methotrexate	Trilostane	S- (+)-Rolipran	Pralatrexate	Anagrelide HC	Pyrimethamin	Dorzolamide I	Brinzolamide	Topiramate	Tioxolone	Fluvastatin Sodium	
b	73	63	75	116	75	89	85	126	89	61	78	Empty
	Methazolamic	Lovastatin	Rasagiline Me	Atorvastatin C	Safinamide M	Pravastatin so	Moclobemide	Evacetrapib (L	Torcetrapib	Lonafarnib	Tolcapone	Empty
c	81	72	76	83	77	79	74	89	85	79	77	Empty
	Ganetespib (S	Pemetrexed	Paclitaxel (Ta	Docetaxel	10-DAB (10-D	Actinomycin D	Mitomycin C	Streptozocin	Cesium chlori	Melphalan	Empagliflozin	Empty
d	71	93	74	86	85	91	64	58	95	81	76	Empty
	Asenapine	Ivacaftor (VX-	Edaravone	Bicalutamide	Heparin sodiu	Meropenem	Irinotecan	Finasteride	Ondansetron	Alfuzosin HCl	Linezolid	Empty
e	78	73	27	82	92	85	74	63	75	74	82	Empty
	Clopidogrel	Vecuronium B	Tigecycline	Tenofovir	Risedronate S	Sumatriptan S	Ranolazine 2H	Repaglinide	Prazosin HCl	Tianeptine so	Moxifloxacin	Empty
f	49	47	75	51	78	84	55	81	85	85	67	Empty
	TSU-68 (SU66	Ispinesib (SB-	Marbofloxaci	Ziprasidone H	Zonisamide	Venlafaxine	Tranilast	Zileuton	Varenicline Ta	Iloperidone	HMN-214	Empty
g	75	70	84	66	83	86	75	67	153	75	54	Empty
	Fludarabine	Ponatinib (AP	Zibotentan (ZI	Ofloxacin	Cefaclor	LY2228820	Pimasertib (AS	Daclatasvir (B	SAR245409 (X	BIRB 796 (Do	Tazarotene	Empty
h	66	88	69	90	86	93	68	62	70	87	61	Empty
	Fasudil (HA-1(	Sulfasalazine	Natamycin	Cidofovir	Ibuprofen Lys	Quizartinib (A	Dapagliflozin	Febuxostat	Aztreonam	Candesartan	Irbesartan	Empty

Plate layout: L1021-06

	1	2	3	4	5	6	7	8	9	10	11	12
a	83	88	83	98	77	68	76	71	71	79	87	Empty
	H-D-Ser-OH	H-Cys-OH	H-Ser-OH	H-Cit-OH	Biotin	Perindopril Er	Cyclo (-RGDfK	Rapamycin (Si	Everolimus (R	Entinostat (M	Romidepsin (FK228, depsipep	
b	67	75	75	63	122	68	84	79	67	62	72	Empty
	Panobinostat	AICAR	Semagacestat	Staurosporine	ABT-199	DAPT (GSI-IX)	Amprenavir (a	Abiraterone a	Ritonavir	Lopinavir	Atazanavir	Empty
c	67	77	35	95	62	51	108	73	0	91	92	Empty
	Darunavir	AZD6244 (Sel	GDC-0941	Lapatinib	Gefitinib (ZD1	EPZ-6438	Nilotinib(AMN	Erlotinib Hydr	Embelin	Regorafenib	Sorafenib Tos	Empty
d	57	52	45	47	96	58	74	67	72	67	16	Empty
	Afatinib (BIBV	Nintedanib (B	Sunitinib mala	Crenolanib (C	Perifosine	Maraviroc	Temsirolimus	PD 0332991 (I	Fludarabine P	Dacomitinib (I	Cisplatin	Empty
e	57	87	-266	51	73	86	69	66	56	31	70	Empty
	Neratinib (HK	Tivantinib (AR	Verteporfin	LDK378	CX-4945 (Silm	Bleomycin Sul	R788 disodiun	Canagliflozin	Linsitinib	Palbociclib (PI	BYL-719	Empty
f	41	60	91	89	76	69	93	86	56	77	80	Empty
	Pazopanib Hy	LY2157299	VX-809	Arsonic acid	Acetylcysteine	Albendazole	Alendronate s	Allopurinol	Arbidol HCl	Argatroban	ARN-509	Empty
g	64	21	50	69	71	67	148	59	74	72	78	Empty
	Atropine sulfa	Axitinib (AG 0	Bephenium H	Betacarotene	Betamethaso	Betamethaso	Bexarotene	BIBR-1048	Blonanserin	Busulfan	Calcium Gluce	Empty
h	66	46	59	66	74	65	79	53	52	60	66	Empty
	Carbadox	Carbenoxolor	Casanthranol	Cefdinir	Cefoperazone	CH5424802	Chlorothiazid	Chlorprothixe	Clotrimazole	Conivaptan H	Cyproterone A	Empty

Plate layout: L1021-07

	1	2	3	4	5	6	7	8	9	10	11	12
a	68	71	71	64	65	84	80	71	70	72	73	Empty
	Cytarabine	Dextrose (D-g	Dibucaine (Cir	Dichlorphena	Dicyclomine H	Didanosine	Difloxacin HC	Dinaciclib (SC	Diperodon HC	Diphemanil M	Diphenylpyraline HCl	
b	96	83	63	78	67	65	80	81	83	68	68	Empty
	Docosanol (Al	Dofetilide	Dovitinib Dila	Doxapram HC	Doxycycline H	Duloxetine HC	Emtricitabine	Enoxacin (Per	Eplerenone	Estradiol	Estrone	Empty
c	56	78	83	81	61	80	81	70	71	95	76	Empty
	Ethambutol H	Ethinyl Estrad	Ethionamide	Ezetimibe	Famprofazone	Fenticonazole	Flucytosine	Flurbiprofen	Furosemide	Gabapentin	Gemcitabine	Empty
d	74	80	100	79	69	70	65	88	85	65	83	Empty
	Glipizide	Guaifenesin	Guanethidine	Ibuprofen	Imidapril HCl	Indomethacin	Ipratropium B	ODM-201	Isradipine (Dy	Istradefylline	Nilvadipine	Empty
e	67	69	99	96	82	205	73	60	86	85	78	Empty
	Lamivudine	Laquinimod (A	Levodopa	L-Glutamine	Lithium Citrat	Lithocholic Ac	Meloxicam (M	Mepenzolate	Mepiroxol	Mesna	Mestranol	Empty
f	72	72	80	79	89	69	89	72	82	72	77	Empty
	Meticrane	Methimazole	Methyocarba	Mirabegron (Y	Mitotane (Lsc	Monobenzon	Noscapine HC	Nevirapine	Nicotine Difar	Nifenazone	Nimodipine	Empty
g	66	78	129	73	73	55	70	57	74	62	81	Empty
	Nitazoxanide	Nitrofurazone	Olsalazine Soc	Orlistat	Oxeladin Citra	Oxethazaine	Oxybutynin	Paliperidone	Pasiniazid	Piromidic Acic	Piroxicam	Empty
h	57	76	77	64	65	83	57	55	78	77	69	Empty
	Pitavastatin C	Potassium Ca	Pridinol Meth	Prochlorpera	Progesterone	Ranolazine	Rifaximin (Xif	Riluzole	Risperidone	Rivastigmine T	Rizatriptan Be	Empty

Plate layout: L1021-08

	1	2	3	4	5	6	7	8	9	10	11	12
a	68	78	58	70	71	91	75	76	107	84	81	Empty
	Rosuvastatin (	Silodosin	Simvastatin (Z	Sodium 4-ami	Sotrastaurin (	Sulfadiazine	Tebipenempiv	Telbivudine	Telmisattan	Teniposide	Terbinafine	
b	55	66	46	89	87	87	71	86	91	36	44	Empty
	Terfenadine	Thiabendazol	Thioridazine H	Tiopronin (Thi	Tretinoin (Abe	Triamcinolone	Triciribine	Triflurdine (Vi	Vitamin D2 (E	Fingolimod (F	LY335979 (Zo	Empty
c	78	53	48	63	74	79	111	70	77	84	68	Empty
	PTC124 (Atalu	Vandetanib (Z	GSK2126458	BI6727 (Volas	TOK-001	Chloroquine c	Deferasirox	LEE011	Acyclovir	Capecitabine	Oxaliplatin	Empty
d	71	66	68	68	63	77	74	13	64	60	74	Empty
	Saxagliptin	LY2940680	Cilengitide	VX-745	Mesoridazine	Stiripentol	ETC-1002	(S)-Crizotinib	Vorapaxar	Rucaparib (fre	Vilanterol trif	Empty
e	63	83	71	63	75	70	78	80	76	81	71	Empty
	Bafetinib (INN	2-Deoxy-D-glu	Alvelestat	Sunitinib	Ulipristal acet	Delavirdine m	Resiquimod (R	Mosapride	Tizanidine	AHU-377(Sac	Losartan	Empty
f	75	74	84	65	59	95	84	90	89	87	83	Empty
	Doripenem	Salicylic acid	Cytarabine hy	Brexpiprazole	AZD-9291	VRT752271	T 705	Efavirenz	Nelfinavir	Rosuvastatin	Pitavastatin	Empty
g	89	69	73	86	101	63	70	72	51	54	78	Empty
	Pravastatin	GLPG0634	Oxybutynin cl	Orotic acid	sn-Glycero-3-	Topiroxostat	Cisapride	Tandospirone	Ondansetron	Pizotifen	Aniracetam	Empty
h	89	61	79	98	75	82	75	66	69	81	70	Empty
	Gatifloxacin h	Meropenem t	Vancomycin h	Anidulafungin	Fluconazole h	Parecoxib Sod	(+)-Ketoconaz	Haloperidol h	Etomidate hy	Beclomethas	Valproic acid	Empty

Plate layout: L1021-09

	1	2	3	4	5	6	7	8	9	10	11	12
a	84	77	206	98	92	111	87	100	87	91	81	Empty
	Glycopyrrolat	Reserpine hyc	Adapalene so	Benazepril	Prilocaine hyc	Prasugrel hydi	AZD7545	Minoxidil	Lansoprazole	Glibenclamide	Amsacrine	
b	88	104	85	81	85	94	84	96	81	75	89	Empty
	Amsacrine hy	Epinephrine H	Terbutaline Si	Tolazoline HC	Acebutolol HC	Adrenalone H	Carvedilol	Clonidine HCl	Dexmedetom	Guanabenz Ac	Isoprenaline H	Empty
c	86	71	79	84	71	87	77	87	92	82	86	Empty
	Empty	Maprotiline H	Metoprolol Ta	Naphazoline H	Nebivolol	Phenoxybenz	Phenylephrine	Propranolol H	Ritodrine HCl	Salbutamol Su	Tetrahydrozo	Empty
d	82	95	98	89	96	103	86	88	88	85	84	Empty
	Timolol Male	Xylazine HCl	Betaxolol	Betaxolol HCl	Bisoprolol fur	Cisatracurium	Detomidine H	Dexmedetom	Epinephrine B	Ivabradine HC	Medetomidin	Empty
e	65	86	88	79	82	80	61	108	69	66	98	Empty
	Naftopidil	Phentolamine	Scopine	Terazosin HCl	Sotalol	Tizanidine HC	Indacaterol M	Miltefosine	Phenformin H	Dehydroepiar	Flutamide	Empty
f	73	85	72	91	96	81	81	81	72	81	71	Empty
	Megestrol Ac	Spironolactor	Aminogluteth	Formestane	Anastrozole	Ciclopirox eth	Milrinone	Esomeprazole	Amiodarone H	Carbamazepir	Divalproex So	Empty
g	73	91	71	78	72	90	74	81	85	75	64	Empty
	Loperamide H	Nitrendipine	Tamoxifen Cit	Sulfacetamide	Trifluoperazin	Azithromycin	Temozolomid	Cabozantinib	Dabrafenib (G	Benidipine HC	Amlodipine	Empty
h	58	77	76	90	92	72	84	83	86	77	79	Empty
	Amlodipine Be	Flunarizine 2H	Tetracaine HC	Azelnidipine	Clevidipine Bu	Felodipine	Lacidipine	Manidipine	Manidipine 2H	Bupivacaine H	Tasisulam	Empty

Plate layout: L1021-10

	1	2	3	4	5	6	7	8	9	10	11	12
a	79	82	97	84	89	94	99	87	83	97	82	Empty
	Cinacalcet HC	Rimonabant	Acemetacin	Lornoxicam	Bufexamac	Etodolac	Flunixin Megl	Ketoprofen	Ketorolac tro	Licofelone	Mefenamic Acid	
b	58	79	80	81	94	91	97	97	84	82	100	Empty
	Nabumetone	Nimesulide	Phenacetin	Rofecoxib	Tolfenamic Ac	Diclofenac So	Lumiracoxib	Valdecoxib	Zaltoprofen	Triflusal	KPT-330	Empty
c	105	83	92	85	93	90	87	94	84	71	74	Empty
	Plerixafor 8H	Adenine	Adenine sulfa	Procarbazine	Adenine HCl	Mizoribine	Uridine	FT-207 (NSC 1	Flupirtine mal	Raltitrexed	Lurasidone H	Empty
d	84	58	75	72	87	102	83	85	93	92	78	Empty
	Amisulpride	Chlorpromazi	Domperidone	Dopamine HC	Fenoldopam	Levosulpiride	Pergolide mes	Amantadine H	Pramipexole 2	Pramipexole	Benserazide H	Empty
e	44	72	99	80	81	68	75	86	78	85	85	Empty
	Quetiapine Fu	Icotinib	Estradiol Cypi	Ethisterone	Altrenogest	Clomiphene c	Epiandrosterc	Estradiol vale	Estriol	Ethynodiol dia	Hexestrol	Empty
f	56	75	70	75	56	69	93	81	56	93	80	Empty
	Medroxyprog	Mifepristone	Pregnenolone	Toremifene C	Equol	Raloxifene HC	Dienogest	Gestodene	Drospirenone	Bosentan Hyd	Gabapentin H	Empty
g	70	96	68	-18	52	69	66	59	80	40	73	Empty
	Niflumic acid	(R)-baclofen	Nefiracetam	Tideglusib	Mubritinib (TA	Brompheniran	Cetirizine DiH	Hydroxyzine 2	Levodropropi	Mizolastine	Nizatidine	Empty
h	87	70	67	76	73	51	84	81	86	82	84	Empty
	Tripelennamir	Benztropine n	Betahistine 2H	Chlorpheniran	Cimetidine	Clemastine Fu	Famotidine	Histamine 2H	Ketotifen Fun	Pemirolast po	Ranitidine	Empty

Plate layout: L1021-11

	1	2	3	4	5	6	7	8	9	10	11	12
a	64	57	65	83	79	69	94	92	93	61	64	Empty
	Roxatidine Ac	Rupatadine Fu	Azelastine HC	Bepotastine B	Desloratadine	Latrepirdine	Fexofenadine	Lafutidine	Olopatadine H	Pacritinib (SB3	Hexamethonium Bromide	
b	67	75	96	97	77	81	89	92	94	75	73	Empty
	Irsogladine	Neostigmine I	Succinylcholir	Acetylcholine	Biperiden HCl	Bethanechol (	Darifenacin H	Decamethoni	Donepezil HCl	Homatropine	Homatropine	Empty
c	71	81	32	82	82	76	83	96	89	62	78	Empty
	Hyoscyamine	Orphenadrine	Otilonium Bro	Tropicamide	Aclidinium Bro	Gallamine Trie	Methscopolar	Pancuronium	Pyridostigmin	Solifenacin su	Trospium chlo	Empty
d	66	62	69	79	87	67	80	84	72	85	71	Empty
	Tiotropium Br	Tolterodine ta	Ifenprodil Tar	MPEP	Fosbretabulin	Ridaforolimus	Sodium 4-Ami	Naltrexone H	Racecadotril	Trimebutine	1-Hexadecan	Empty
e	70	82	97	85	76	88	78	71	81	85	90	Empty
	Alverine Citra	Amfenac Sodi	Amikacin disu	Aminothiazole	Amoxapine	Amoxicillin	Ampicillin Trih	Amprolium H	Antazoline HC	Apramycin Su	Atracurium Be	Empty
f	59	64	78	79	38	77	164	43	80	78	67	Empty
	Azaguanine-8	Azaperone	Azithromycin	Bacitracin	Bacitracin Zin	Bemegride	Benzbromaro	Benzethonium	Benzocaine	Benzoic Acid	Benzydamine	Empty
g	77	89	76	61	70	76	80	59	88	88	71	Empty
	Penicillin G So	Betamipron	Bezafibrate	Bosentan	Brimonidine T	Bromfenac Sc	Broxyquinolin	Buspirone HC	Capreomycin	Carprofen	Ceftriaxone S	Empty
h	93	31	20	16	64	75	74	67	67	71	76	Empty
	Cephalexin	Cetrimonium	Cetylpyridiniu	Chlorhexidine	Chlorocresol	Chlorpropami	Chlorquinaldo	Chlortetracyc	Chlorzoxazon	Choline Chlor	Chromocarb	Empty

Plate layout: L1021-12

	1	2	3	4	5	6	7	8	9	10	11	12
a	92	75	84	97	112	38	88	84	152	157	93	Empty
	Cinchophen	Climbazole	Clindamycin	Clindamycin P	Clodronate Di	Clofazimine	Clofibric Acid	Clorprenaline	Closantel	Closantel Sod	Colistin Sulfate	
b	97	87	90	100	102	84	89	75	93	94	91	Empty
	Creatinine	Cyclandelate	Cysteamine H	D-Cycloserine	Deferiprone	Deoxycortico	Dexlansoprazı	Diacerein	Dibenzothiopl	Difluprednate	Diminazene A	Empty
c	81	85	23	83	95	83	80	71	86	85	111	Empty
	Dinitolmide	Dirithromycin	Domiphen Bro	Doxofylline	Doxylamine S	Droperidol	Dropropizine	Ebastine	Efaproxiral So	Enrofloxacin	Epalrestat	Empty
d	84	92	74	84	87	62	67	84	85	146	92	Empty
	Epinastine HC	Eprazinone 2H	Eprosartan M	Erythritol	Esmolol HCl	Ethacridine la	Ethamsylate	Etidronate	Fenspiride HC	Fidaxomicin	Flopropione	Empty
e	81	89	93	81	103	80	92	82	88	92	101	Empty
	Florfenicol	Flubendazole	Flufenamic ac	Flumethasone	Fudosteine	Furaltadone H	Gadodiamide	Halcinonide	Halobetasol P	Histamine Phc	Ibandronate s	Empty
f	82	89	87	78	79	75	100	71	83	86	77	Empty
	Idoxuridine	Isosorbide	Isovaleramide	(-)-Tetramisol	Levobetaxolo	Liothyronine S	Lomefloxacin	Lomerizine H	Loxapine Succ	Levobupivaca	Mechlorethar	Empty
g	72	80	75	91	82	95	118	70	84	95	97	Empty
	Meclizine 2HC	Methyldopa	Mevastatin	Mexiletine HC	Mezlocillin So	Minocycline H	Montelukast S	NAD+	Nefopam HCl	Neomycin sul	Netilmicin Sul	Empty
h	57	70	92	72	77	79	88	95	93	83	70	Empty
	Nicaraven	Nicardipine H	Nifuroxazide	Nithiamide	Oseltamivir pl	Oxaprozin	Oxybuprocain	Pamidronate	Paromomycin	Penciclovir	Penfluridol	Empty

Plate layout: L1021-13

	1	2	3	4	5	6	7	8	9	10	11	12
a	68	65	79	81	73	89	76	90	78	72	76	Empty
	Pentoxyverine	Phenazopyrid	Phenindione	Pheniramine M	Pilocarpine HC	Pimecrolimus	Piperacillin So	Pramoxine HC	Primaquine Di	Proflavine He	Quinacrine 2HCl	
b	101	85	64	94	69	101	98	107	83	88	91	Empty
	Ribostamycin	Salicylanilide	Sasapyrine	Serotonin HCl	Sertaconazole	Sodium ascor	Sodium butyra	Sodium Monc	Sodium Nitrite	Spiramycin	Sucralose	Empty
c	84	87	67	115	133	89	87	101	83	73	140	Empty
	Sulfadoxin	Sulfaguanidin	Sulfapyridine	Taurine	Teicoplanin	Tenoxicam	Teriflunomide	Thiamine HCl	Thiamphenicc	Ticarcillin sod	Tiratricol	Empty
d	107	86	99	75	85	91	86	84	77	74	84	Empty
	Tobramycin	Tolperisone H	Tranexamic A	Triamcinolone	Triclabendazo	Trometamol	Troxipide	Uracil	Valganciclovir	Valnemulin HC	Verapamil HC	Empty
e	70	86	71	77	86	91	83	79	79	58	81	Empty
	Vitamin A Ace	Retinyl (Vitam	Voglibose	Zoxazolamine	2-Thiouracil	4-Aminohippu	Acesulfame P	Adenosine	Adiphenine HC	Albendazole C	Alibendol	Empty
f	58	79	78	76	94	92	89	88	74	84	81	Empty
	Allylthiourea	Amidopyrine	Amiloride HCl	Amphotericin	Antipyrine	Articaine HCl	Aspartame	Buflomedil HC	Azacyclonol	Azathioprine	Azlocillin sodi	Empty
g	96	75	61	83	97	72	85	74	68	72	66	Empty
	Besifloxacin H	Betamethaso	Bifonazole	Bisacodyl	Bromhexine H	Budesonide	Butenafine HC	Butoconazole	Carbazochron	Carbidopa	Carbimazole	Empty
h	70	52	38	79	86	84	77	66	82	80	71	Empty
	Cefoselis Sulf	Ceftiofur HCl	Chenodeoxyc	Chlormezanor	Chloroxine	Cinepazide ma	Clindamycin H	Clobetasol pr	Clorsulon	Cloxacillin So	Cortisone ace	Empty

Plate layout: L1021-14

	1	2	3	4	5	6	7	8	9	10	11	12
a	-60	86	73	82	84	90	95	122	83	91	83	Empty
	Crystal Violet	Cyclamic acid	Cyclosporin A	Cytidine	Deflazacort	Deoxyarbutin	Dexamethaso	Diclazuril	Diclofenac Di	Diclofenac Po	Dimethyl Fumarate	
b	86	85	96	73	72	78	83	88	71	73	90	Empty
	Diphenhydran	Dipyridamole	DL-Carnitine H	Dronedarone	Dycloninе HCl	Econazole nit	Erdosteine	Erythromycin	Erythromycin	Estradiol Ben	Famciclovir	Empty
c	85	61	59	96	81	100	91	85	86	99	77	Empty
	Fenofibrate	Fenoprofen C	Fenoprofen ca	Foscarnet Soc	Gemfibrozil	Guanidine HC	Hydrochlorotl	Hydrocortisor	Indapamide	Inulin	Isoconazole n	Empty
d	93	88	79	75	96	78	87	90	69	89	82	Empty
	Isoniazid	Levofloxacin	Levonorgestre	Levosimendar	Lincomycin H	Lomustine	Lonidamine	Meglumine	Menadione	Mepivacaine I	Mequinol	Empty
e	84	103	63	88	77	77	81	82	80	100	84	Empty
	Mesalamine	Metformin HC	Methacycline	Methenamine	Methylthioura	Metolazone	Metronidazol	Miconazole	Miconazole N	Mometasone	Moroxydine H	Empty
f	90	90	90	91	73	93	93	84	72	87	72	Empty
	Mycophenolic	Nadifloxacin	Nafcillin Sodi	Naftifine HCl	Nalidixic acid	Nedaplatin	Nicotinic Acid	Nifedipine	Nisoldipine	Noradrenaline	Norethindron	Empty
g	83	92	84	85	90	49	76	94	85	85	80	Empty
	Novobiocin Sc	Nystatin (Fung	(+,-)-Octopam	Ornidazole	Oxacillin sodi	Oxfendazole	Oxibendazole	Oxytetracyclir	Oxytetracyclir	Pefloxacin Me	Phenylbutazo	Empty
h	71	56	77	105	89	72	67	57	74	62	79	Empty
	Pidotimod	Pizotifen Mal	Potassium Ioc	Pranlukast	Pranoprofen	Praziquantel	Prednisolone	Prednisolone	Probenecid	Probucol	Protionamide	Empty

Plate layout: L1021-15

	1	2	3	4	5	6	7	8	9	10	11	12
a	64	81	86	74	86	104	77	290	62	97	87	Empty
	Pyridoxine HC	Rebamipide	Retapamulin	Rifampin	Ronidazole	Ropivacaine H	Roxithromycii	Sodium Nitrop	Sodium Picos	Sodium salicy	Sorbitol	
b	91	102	104	76	93	83	95	90	86	83	80	Empty
	Sparfloxacin	Streptomycin	Sulbactam sod	Sulconazole N	Sulfamerazine	Sulfameter	Sulfamethizol	Sulfamethoxa	Sulfanilamide	Sulfathiazole	Sulfisoxazole	Empty
c	77	85	83	82	76	71	75	101	83	83	80	Empty
	Sulindac	Terbinafine H	Tilmicosin	Tinidazole	Tioconazole	Tolnaftate	Toltrazuril	Torsemide	Trichlormethi	Trimethoprim	Tylosin tartra	Empty
d	76	92	73	69	99	78	84	195	82	92	76	Empty
	Valaciclovir H	Vidarabine	Vitamin B12	Vitamin C	Vitamin D3	Xylometazolir	Xylose	Zafirlukast	5-Aminolevuli	Acetanilide	Acipimox	Empty
e	102	90	99	87	64	80	87	28	87	90	79	Empty
	Alendronate	Ambrisentan	(6-)ε-Aminoca	Amorolfine H	Atovaquone	Avobenzone	Camostat Me	Caspofungin A	Cefditoren Piv	Ciclopirox	Diethylstilbes	Empty
f	65	75	86	76	84	91	64	81	69	77	102	Empty
	Diltiazem HCl	D-Mannitol	Doxercalcifer	Doxifluridine	Felbamate	Fluconazole	Fluocinolone A	Fluticasone pr	Ganciclovir	Haloperidol	Hydralazine H	Empty
g	78	58	61	72	62	65	60	74	78	88	80	Empty
	Hydroxyurea	Idebenone	Itraconazole	Loteprednol e	L-Thyroxine	Lubiprostone	Mecarbinate	Meptazinol HC	Miglitol	Milnacipran H	Mirtazapine	Empty
h	28	75	82	89	83	86	90	83	74	77	77	Empty
	Mitoxantrone	Moguisteine	Ozagrel HCl	Pioglitazone	Pramiracetam	Prilocaine	Primidone	Propylthioura	Pyrazinamide	Quinine HCl D	Reboxetine m	Empty

Plate layout: L1021-16

	1	2	3	4	5	6	7	8	9	10	11	12
a	86	89	85	99	94	90	89	82	77	96	81	Empty
	Ribavirin	Rifabutin	Rifapentine	Ropinirole HC	Sulbactam	Sulfamethazir	Suprofen	Ulipristal	Ursodiol	Zanamivir	Bimatoprost	
b	93	58	83	84	72	86	89	94	127	86	86	Empty
	Calcifediol	Calcitriol	Cefprozil hydr	Tacrolimus (FI	Fluocinonide	Fosaprepitant	Peramivir Trih	Prednisone	Pyrantel Pam	Sitafloxacin H	Alfacalcidol	Empty
c	77	85	72	79	55	93	108	89	89	75	98	Empty
	Alprostadil	Bindarit	Cabazitaxel	Desonide	Eltrombopag	Secnidazole	Ticlopidine HC	Ticagrelor	Imatinib (STI5	Mitiglinide Ca	Tolbutamide	Empty
d	88	85	91	75	82	-16	145	87	65	83	78	Empty
	Gliclazide	Gliquidone	Nicorandil	Nateglinide	Esomeprazole	Zinc Pyrithion	Candesartan (	Enalapril Mal	Quinapril HCl	Ramipril	Azilsartan	Empty
e	81	75	52	87	121	103	64	101	82	58	88	Empty
	Temocapril H	Valsartan	Aliskiren Hem	Benazepril HC	Azilsartan Me	Abacavir sulfa	Zidovudine	Adefovir Dipiv	Zalcitabine	Etravirine (TM	Stavudine (d4	Empty
f	99	78	66	68	72	91	83	69	74	84	65	Empty
	Palonosetron	Trazodone HC	Amitriptyline I	Aripiprazole	Clomipramine	Clozapine	Desvenlafaxir	Eletriptan HB	Escitalopram	Olanzapine	Ondansetron	Empty
g	85	60	70	77	58	81	69	66	83	51	78	Empty
	Urapidil HCl	Almotriptan M	Atomoxetine	Desvenlafaxir	Ketanserin	Lamotrigine	Naratriptan	Paroxetine HC	Prucalopride	Sertraline HCl	Tropisetron	Empty
h	86	88	69	78	74	82	88	73	91	79	66	Empty
	Zolmitriptan	Agomelatine	Dapoxetine H	LDE225 (NVP-	Ambroxol HCl	Amiloride HCl	Ouabain	Phenytoin	Phenytoin soc	Proparacaine	Triamterene	Empty

Plate layout: L1021-17

	1	2	3	4	5	6	7	8	9	10	11	12
a	75	82	62	95	44	143	82	77	97	89	94	Empty
	Vinpocetine	Ibutilide Fuma	Oxcarbazepin	Rufinamide	Propafenone	Niclosamide	Fostamatinib	Daunorubicin	Pirfenidone	Pefloxacin Me	Flumequine	
b	76	79	82	87	105	104	98	74	51	87	94	Empty
	Irinotecan HC	Pirarubicin	Topotecan HC	Tolvaptan	Empty	Triapine	BAF312 (Sipor	Betrixaban	Meisoindigo	Ipragliflozin	AHU-377 hem	Empty
c	66	102	90	97	98	95	74	106	92	102	95	Empty
	PF-04449913	Lisinopril dihy	Cromolyn sod	Sulfadimetho	ATP disodium	Memantine hy	Cyproheptadi	Bupropion hy	Sotalol hydro	Spectinomycii	Vardenafil	Empty
d	69	91	93	67	109	90	99	93	83	88	80	Empty
	Xylazine	Amoxicillin tri	Arecoline hyd	Dibucaine	Ropivacaine h	Verbascoside	Tirapazamine	Methylcobala	Dexrazoxane	Ketorolac	Latanoprost	Empty
e	94	97	94	87	88	63	69	81	95	90	89	Empty
	Amikacin	Flavoxate hyd	Procaine	Ouabain Octa	Udenafil	Nicergoline	Tiagabine hyd	Dapsone	Warfarin	Metaxalone	Balsalazide	Empty
f	71	81	63	92	69	83	111	69	82	89	91	Empty
	Eicosapentae	UK 14,304	Rabeprazole s	Rabeprazole	Etonogestrel	Medroxyprog	Amifostine	Ciclesonide	Mafenide Ace	Misoprostol	Eslicarbazepir	Empty
g	91	89	59	65	68	86	92	53	79	79	68	Empty
	Tiagabine	Carmustine	Eptifibatide	Bedaquiline fu	Bedaquiline	Sarpogrelate l	Diclofenac	Ademetionine	Alcaftadine	Cefepime Dih	Chlorhexidine	Empty
h	80	107	101	91	97	91	81	70	28	73	92	Empty
	Nitisinone	4-Aminopyrid	Acetaminoph	Iohexol	Ceftazidime	Trandolapril	Tetrabenazine	GS-9973	Crizotinib hyd	Clofibrate	Moxidectin	Empty

Plate layout: L1021-18

	1	2	3	4	5	6	7	8	9	10	11	12
a	98	99	91	90	88	106	79	90	93	77	87	Empty
	Artesunate	Cinchonidine	Sodium Mone	Hypoxanthine	Rotundine	Inosine	Vanillin	Griseofulvin	Cyromazine	Midostaurin (I	Chlorambucil	
b	86	78	101	89	87	106	106	97	78	95	94	Empty
	Thio-TEPA	Losmapimod	Vidofludimus	Pantoprazole	2'-Deoxyguan	Oxytocin	Pneumocandi	Oxybenzone	(S)-10-Hydrox	Oxiracetam	Diphenidol HC	Empty
c	78	87	89	88	116	94	93	67	95	97	81	Empty
	Promethazine	Labetalol HCl	Meclofenama	Procainamide	Defactinib	Brivaracetam	K-115	Afuresertib	LCZ696	Isavuconazole	Efinaconazole	Empty
d	91	96	92	110	45	92	83	84	94	80	88	Empty
	Cyclocytidine	Ospemifene	Mupirocin	Hydroxychlor	PF-06463922	Abscisic Acid (	Lomitapide	Obeticholic Ac	Darunavir Eth	Methylpredni	Sulfisoxazole	Empty
e	44	76	151	88	45	89	89	113	91	87	63	Empty
	Thonzonium B	(-)-epicatechi	(-)-epicatechi	Rilmenidine P	Caspofungin	Cefpodoxime	Cefprozil	Cetrorelix	Desogestrel	Octreotide ac	Pentamidine i	Empty
f	78	98	102	70	103	94	99	87	69	70	84	Empty
	Sumatriptan	Topotecan	Rotenone	Carbetocin	Poziotinib	Radotinib(IY-5	Pexidartinib (P	GSK1349572 s	Entrectinib	Molidustat (B	Fruquintinib(H	Empty
g	86	92	82	86	75	78	83	118	66	43	96	Empty
	MK3102	Retigabine	Regadenoson	Chlorotrianise	Carteolol HCl	Dovitinib (TKI	Dasatinib Mo	Oltipraz	Tamoxifen	Sanguinarine	Naproxen Soc	Empty
h	41	64	103	57	88	75	74	99	96	74	80	Empty
	Enoxolone	Troxerutin	Diosmetin	Cyclobenzapr	Calcium D-Pa	Motolimod (V	4-Methylumb	Pexmetinib (A	Cyclo(RGDyK)	Sodium Tauro	Metoprolol Su	Empty

Plate layout: L1021-19

	1	2	3	4	5	6	7	8	9	10	11	12
a	73	91	112	79	80	100	81	-231	97	77	83	Empty
	Napabucasin	CB-5083	INCB-024360	Ozanimod (RP	Tedizolid HCl	Deferoxamine	Sildenafil mes	Resazurin sod	Fomepizole	Acetazolamid	17-Hydroxyprogesterone	
b	89	81	81	102	96	74	204	83	92	87	91	Empty
	Fenofibric aci	Fluphenazine	Amodiaquine	Nitroxoline	Diflunisal	(+/-)-Sulfinpyr	Hexachloroph	Etretinate	Eugenol	Isatin	Benzenesulfo	Empty
c	94	71	60	76	87	86	77	73	80	81	82	Empty
	Lauric Acid	Cinnarizine	Perphenazine	LOXO-101	ACP-196	Sivelestat (ON	Bromocriptine	Dantrolene, s	Mepyramine r	Aminoguanidi	(S)-(-)-Propran	Empty
d	-144	96	96	88	79	105	85	82	127	76	85	Empty
	Evans Blue tet	(RS)-(±)-Sulpir	Spermine tetr	Diazoxide	Tacrine hydro	(-)-Lobeline hy	2-APB	Citalopram hy	Suramin hexa	Combretastat	Prostaglandin	Empty
e	83	91	78	80	85	85	85	78	74	104	111	Empty
	6-Hydroxydop	Pentylenetetr	DCA	Carbamoylcho	α-Estradiol	Mecamylamir	Atipamezole h	Desipramine h	Tetraethylam	Sodium phosp	DL-Dithiothre	Empty
f	94	90	78	85	73	73	109	77	83	88	85	Empty
	Citric acid	Thiostrepton	Canrenone	Metyrapone	Astemizole	Estropipate	Tramiprosate	Allopregnanol	Corticosteron	Tranylcyprom	Puromycin dih	Empty
g	83	108	103	71	-28	100	100	90	92	69	69	Empty
	Quinidine	Prostaglandin	Phosphocreat	Digoxin	Auranofin	Lithium carbo	L-Glutathione	Urea	AG-221 (Enasi	AG-120	Olmutinib (HN	Empty
h	87	92	86	74	72	91	76	81	76	95	100	Empty
	Imidazole	sodium fluori	Rimantadine h	o-Phenanthro	2-Deoxy-D-rib	2-Deoxyuridir	4-Aminobenz	4-Hydroxyber	5-Methoxytry	Adenosine 5-t	Cellobiose	Empty

Plate layout: L1021-20

	1	2	3	4	5	6	7	8	9	10	11	12
a	72	59	65	70	81	103	79	58	72	70	43	Empty
	L-Arabinose	Malonic acid	Melibiose	m-Hydroxybe	myo-Inositol	N-Acetylneura	N-Carbamyl-L	Pyridoxal 5 ph	Pyridoxal hyd	Pyridoxine	Vanillic acid	
b	113	67	52	81	68	90	76	70	115	45	36	Empty
	Flavin adenine	Vadadustat	Pimavanserin	GS-7340	Dihydrotestos	Avibactam so	Harmine	Urethane	α-L-Rhamnos	Indinavir sulfa	Erdafitinib	Empty
c	83	63	31	70	104	85	65	63	68	65	74	Empty
	Butamben	Remdesivir (G	Baloxavir mar	Roquinimex	Thiamine pyro	L-Arginine (hy	R-(−)-Mandeli	Irinotecan hy	Vitamin K1	L-Cycloserine	Vitamin A	Empty
d	76	83	83	106	97	108	65	56	70	95	90	Empty
	Isosorbide Dir	Cilastatin	Bambuterol (h	Ceftazidime p	Chlortalidone	Etidronate dis	Terconazole	Fenoldopam (	Nitrofurantoi	Guanethidine	Nilutamide	Empty
e	103	81	72	74	49	72	50	70	86	76	88	Empty
	Acetohydroxa	Penicillamine	Atropine	Crotamiton	Fluoromethol	Flunisolide	Rasagiline	Quinine	Dolasetron	Tolazamide	Dibutyryl-cAM	Empty
f	85	90	68	167	77	36	97	79	88	158	108	Empty
	3-acetyl-11-k	Polymyxin B (s	Pargyline (hyd	Linoleic Acid	Clenbuterol (h	Tauroursodec	Methicillin (so	α-Asarone	Proxyphylline	Sofalcone	DL-α-Difluoro	Empty
g	63	97	74	103	67	68	49	61	63	70	56	Empty
	(S)-Ketoprofe	Vincamine	Isoxsuprine (h	Oxiconazole (	D-(+)-Raffinos	Thymidine	Chlorprothixe	4-Methylbenz	SKF 525A (hyd	L-(−)-Fucose	Danazol	Empty
h	68	152	108	76	83	94	72	74	63	76	72	Empty
	DL-α-Lipoic A	Cefonicid (soc	Pentoxifylline	Pimozide	Tropine	Trehalose (hy	Glycocholic A	Stearic Acid m	Chlorcyclizine	Cefadroxil (hy	5-hydroxy-L-T	Empty

Plate layout: L1021-21

	1	2	3	4	5	6	7	8	9	10	11	12
a	77	121	101	114	75	100	100	107	104	84	89	Empty
	CP21R7	Triclosan	L-Selenometh	(±)-Baclofen	Nortriptyline (	Mebendazole	Maltotriose	Imipramine (hydrochloride)		Ethacrynic Ac	Sulfaphenazole	
b	79	95	95	96	115	86	98	86	91	82	92	Empty
	Clorgyline (hy	Edrophonium	Doxepin (hydr	Pyrogallol	Tyramine	Cefazolin (soc	Iopromide	Docosahexae	Menaquinone	Androsterone	Quinestrol	Empty
c	119	95	104	97	98	102	104	93	92	104	99	Empty
	Myristic Acid	Adenosine-5'-	Guaiacol	Isoprinosine	Scopoletin	Midodrine (hy	6-Aminonicot	Taurolidine	Cefotaxime (s	Stearic Acid	Cefoxitin (sod	Empty
d	45	121	88	111	116	93	54	89	87	98	114	Empty
	1,2-Dioleoyl-3	Pentadecanoi	Spermine	Oleic Acid	Clodronate (s	Palmitic Acid (	Amlexanox	Fusidic Acid (s	Ibudilast	Ingenol	Citicoline (soc	Empty
e	71	96	104	133	100	78	119	96	82	79	72	Empty
	(S)-Flurbiprofe	BHT	(R,S)-Atenolol	Morin	Cefixime	tetrahydro-L-	Palmitoleic Ac	Undecanoic A	Kasugamycin	γ-Linolenic Ac	Ciprofloxacin	Empty
f	115	138	94	91	97	73	96	75	98	86	69	Empty
	Anisodamine	Cefsulodin (sc	Phytol	Spectinomycii	Folinic Acid (c	Fendiline (hyd	N-acetyl-D-Gl	Trimipramine	(S)-Naproxen	Carazolol	Lutein	Empty
g	103	116	92	111	98	99	112	96	82	105	83	Empty
	Glycine	L-Proline	L-Valine	L-Leucine	L-Tryptophan	L-Alanine	L-Hydroxypro	L-Methionine	beta-Alanine	Sodium benzo	Benzophenon	Empty
h	82	107	96	93	118	17	91	120	58	90	96	Empty
	Benzyl alcoho	D-Alanine	L(+)-Ornithine	Methylparabe	L-Threonine	Hydroquinone	L-Pyroglutami	D-Tartaric aci	4-Aminophen	L-Lysine hydr	Isonicotinic a	Empty

Plate layout: L1021-22

	1	2	3	4	5	6	7	8	9	10	11	12
a	93	113	132	87	67	77	99	73	59	79	83	Empty
	Resorcinol	DL-Serine	Sodium dodec	Thymol	2-Naphthol	Propylparabe	L-Asparagine	Butylparaben	Benzyl benzo	Piperazine	4-Aminosalicylic acid	
b	94	90	76	78	80	67	93	93	68	-32	72	Empty
	Methyl salicyl	L-Menthol	Salicylamide	Malic acid	delta-Gluconc	o-Toluic acid	3-Hydroxy-2-r	Levulinic acid	4-Nitropheno	1,4-Benzoquin	Melamine	Empty
c	89	82	96	74	80	78	82	87	97	71	75	Empty
	Dexpantheno	Carvacrol	Sitagliptin	o-Cresol	Propofol	Acetamide	Pyrocatechol	Ethyl gallate	Glycylglycine	Geraniol	Tryptamine	Empty
d	90	89	90	77	72	73	81	79	112	179	79	Empty
	Bisphenol A	Furfural	Terephthalic a	Furazolidone	Phthalic acid	m-Cresol	Isosorbide 5-r	p-Cresol	D-Glutamine	(R)-(+)-1,2-Dit	DL-α-Tocophe	Empty
e	114	74	86	63	46	48	89	80	58	101	75	Empty
	Fluorescein	Dapagliflozin	Delamanid	Tucidinostat	Calcium dobe	Dantrolene (s	Adenosine 5'-	Vidarabine mo	Pikamilone	UTP, Trisodiu	Sultamicillin T	Empty
f	47	86	86	66	72	87	93	86	73	96	145	Empty
	Sultamicillin	Loxoprofen S	Clindamycin a	Disopyramide	Econazole	Atropine sulfa	Salbutamol	Betahistine m	Dehydroepian	Balofloxacin I	Indigo carmin	Empty
g	75	90	67	82	103	92	100	79	92	71	77	Empty
	Omeprazole S	Orphenadrine	Chloropyrami	Isoproterenol	Icatibant Acet	edetate calciu	Triiodothyron	Metronidazol	Scopolamine	Creatine mon	Terpinen-4-ol	Empty
h	82	70	67	-27	91	96	83	100	155	77	63	Empty
	Octanoic acid	Orcinol	Valbenazine t	Octenidine (di	Canagliflozin (	L-Arginine	Camphor	Cyclic somato	Calcitonin (sa	Eptifibatide A	Gonadorelin A	Empty

Plate layout: L1021-23

	1	2	3	4	5	6	7	8	9	10	11	12
a	81	74	100	105	98	91	42	101	86	101	66	Empty
	GHRP-2	Nafarelin Ace	Cinchonine(LA	Naringin Dihy	Diammonium	Promestriene	Levamlodipin	Vitamin E Ace	N-Ethylmaleir	Mafenide hyd	Testosterone	Enanthate
b	109	133	103	102	92	107	117	42	94	103	96	Empty
	Iron sucrose	Levothyroxine	Flavone	(-)-Borneol	Metoclopram	Fosfomycin Ti	Bendroflumet	Ademetionine	(+)-Camphor	8-Hydroxyquii	Eprodisate dis	Empty
c	91	109	105	100	99	94	84	91	87	90	58	Empty
	Sodium sulfac	Saxagliptin hy	Sulfacetamide	Cefuroxime a	L-Cysteine HC	Manganese cl	Acotiamide hy	Levocetirizine	Squalene	Cefetamet piv	Propacetamo	Empty
d	97	52	81	94	104	73	90	97	91	93	106	Empty
	Sulfamethoxa	Lynestrenol	Perospirone h	Indobufen	Mebeverine H	Melitracen hy	Actarit	Bevantolol hy	Rifamycin soc	Ganciclovir so	Geranyl aceta	Empty
e	99	74	102	82	105	94	93	100	66	100	47	Empty
	Methotrexate	Pralidoxime Ic	Ropivacaine M	Diaveridine	Ciprofloxacin	D-Pantethine	Minoxidil sulp	Maltitol	Sorbic acid	Laurocapram	Diatrizoate so	Empty
f	57	117	104	101	97	120	82	95	68	72	49	Empty
	Clioquinol	4-(Aminometh	Ethosuximide	Amitraz	(2S,3R,4S,5R)-	Dexamethaso	Caryophyllene	α-santonin	9-Aminoacrid	Ethidium bror	Dimenhydrina	Empty
g	50	98	74	91	110	72	112	96	72	-156	100	Empty
	Dithranol	Purine	Tetracycline	Propantheline	Emeramide	3-Phenoxyber	Cyclen	Bendazol	Idramantone	Methylene Blu	Amifampridin	Empty
h	85	62	100	51	89	92	85	88	45	59	63	Empty
	Sophoricoside	Benactyzine h	Methylbenact	Diiodohydrox	Succinylsulfat	Methacholine	Ceftiofur sodi	Dehydrocholi	Amlodipine m	Anethole trith	Hydroquinidin	Empty

Plate layout: L1021-24

	1	2	3	4	5	6	7	8	9	10	11	12
a	103	97	90	94	97	99	98	94	99	93	82	Empty
	Pazufloxacin r	Diethylcarban	Pyrantel tartr	Niketamide	Theophylline-	1H-pyrazole	Dehydroaceti	Terpin hydrat	DEET	Triacetonami	Chloroxylenol	
b	86	99	100	104	83	112	78	104	96	93	86	Empty
	Carbendazim	Batyl alcohol	4-Aminoantip	Ethylvanillin	Bronopol	Piperazine adi	Danthron	DL-Panthenol	Oxaceprol	Osalmid	Citiolone	Empty
c	110	91	95	83	87	98	106	83	95	88	106	Empty
	Methionine	Acetylcholine	4-Phenylbutyr	Oxytetracyclir	Maleimide	Veratric acid	Benzamidine I	Cloxiquine	Deoxycholic a	Acetylleucine	2-Phenylaceta	Empty
d	63	109	70	64	97	93	99	93	99	91	113	Empty
	4-Biphenylace	ATP	Carsalam	Robenidine hy	Carboxine	Perflubron	Sulfabenzamic	Menadiol Dia	Menbutone	Lawsone	Thiamine nitra	Empty
e	99	132	101	79	100	107	87	92	94	96	84	Empty
	Diatrizoic acic	10-Undeceno	Acetophenon	Trimethobenz	Sparteine	Citicoline	Sulfaquinoxal	Febantel	Enoxacin Sesc	Cetilistat	2'-Deoxyaden	Empty
f	74	86	93	188	89	98	95	85	87	77	97	Empty
	Triflupromazi	6-Methoxy-2-	Apronal	Oxyclozanide	Phenazine me	Pempidine	Hydroquinine	Olivetol	Clonixin	Hodostin	Hydroxylamm	Empty
g	94	87	98	77	102	88	86	110	106	99	78	Empty
	Bromisoval	Ensulizole	DL-Methionin	Choline bitart	Diazolidinyl ur	(1S)-(-)-α-Pine	Isoeugenol	Dichlorophen	L-Glutamic ac	Etofylline	Herniarin	Empty
h	31	84	91	89	103	97	83	84	84	87	91	Empty
	Chlorhexidine	2-Aminoethar	D-Pantothena	2-Hydroxyber	D-Phenylalani	2,4-Dichlorob	Penicillin V po	Benzylpenicill	D-Ribose	(S)-(+)-Carvon	Uridine triace	Empty

Plate layout: L1021-25

	1	2	3	4	5	6	7	8	9	10	11	12
a	100	75	71	93	94	80	77	87	70	79	77	Empty
	Gastrodenol	L-Xylose	Amodiaquine	DL-Arginine	(-)-Fenchone	Sodium ferulic	Cholic acid so	Kojic acid	Pralidoxime c	Propyphenazc	1,2-propanediol	
b	82	87	87	92	94	88	94	104	85	71	70	Empty
	xanthine	gentisate	hippurate	galactose	glucuronate	lactose	sucrose	mannose	cis-aconitate	adipate	fumarate	Empty
c	101	86	61	72	86	77	92	76	77	82	100	Empty
	maleate	oxalate	azelate (nona	caprate (10:0)	pelargonate (9	sebacate (dec	glycolate (hyd	lactate	pyruvate	histamine	thiamine	Empty
d	79	87	98	87	96	91	91	87	87	77	75	Empty
	alpha-tocoph	guanosine	cytosine	UMP	cortisone	D-(−)-Fructos	Puerarin	Neohesperidi	Geniposidic ac	Vindoline	5-Methoxypsc	Empty
e	70	80	68	80	71	90	0	78	80	99	86	Empty
	8-Methoxypsc	Parthenolide	Vitexicarpin	Loganin	Psoralen	5-hydroxymet	Sanguinarine	Asiatic acid	Asiaticoside	Isorhamnetin	Magnolol	Empty
f	88	89	81	90	85	88	90	97	89	85	84	Empty
	Geniposide	Berberine	Bergenin	Catharanthine	Dehydroandrc	Irisflorentin	Theophylline	Harpagoside	Crotaline	Cinnamaldehy	Lathyrol	Empty
g	78	77	95	77	96	78	74	84	79	80	83	Empty
	Brucine	vitexin-2"-o-r	Tyrosol	Germacrone	Fructose	Homoharringt	Nuciferine	Helicid	Evodiamine	Echinacoside	Ginsenoside R	Empty
h	75	66	59	119	69	82	76	82	70	97	56	Empty
	Ginsenoside R	Ginsenoside R	Formononetir	Indigo	Hyodeoxycho	Ligustrazine H	Nicotinamide	Madecassosic	Deoxycholic a	Honokiol	Piperine	Empty

Plate layout: L1021-26

	1	2	3	4	5	6	7	8	9	10	11	12
a	6	21	68	74	68	98	75	66	86	81	66	Empty
	Sennoside B	Sennoside A	Cholic acid	(+)-Catechin h	Berberine hyd	Betaine hydro	Yohimbine Hy	Coumarin	Stevioside	Betaine	Gastrodin	
b	98	69	74	75	78	72	91	101	66	85	60	Empty
	Silymarin	Dihydroartem	Arbutin	Kaempferol	Sinomenine	Dioscin	Xylitol	Sodium Aescir	Caffeic acid	Cytisine	Scutellarin	Empty
c	82	82	58	75	59	86	85	72	87	82	53	Empty
	6,7-Dihydroxy	Esculin	Rosmarinic ac	Chlorogenic a	Baicalin	Polydatin	Salidroside	Podophylloto	Glycyrrhizic ac	Coenzyme Q1	Tetrandrine	Empty
d	86	69	87	75	74	69	85	66	131	56	98	Empty
	Sodium Dansh	Salvianolic ac	Daidzin	Hesperidin	Ursolic acid	Osthole	Oleanolic acic	Artemisinine	Apigenin	Gallic acid	Luteolin	Empty
e	73	78	92	80	75	114	66	54	58	73	73	Empty
	Rutin	Oxymatrine	Amygdalin	Hyperoside	Quercitrin	Quercetin	Taxifolin	Tanshinone I	Tanshinone II	Paeonol	Andrographol	Empty
f	77	36	69	69	77	96	76	78	68	75	74	Empty
	Hesperitin	Baicalein	Daidzein	Reserpine	DL-Menthol	Phloridzin	Cinnamic acid	Fumalic acid	D-(-)-Salicin	Saikosaponin	Ginkgolide A	Empty
g	62	81	66	74	17	70	80	67	66	71	91	Empty
	Z-Ligustilide	Rhynchophylli	Ginkgolide C	L-Carnitine in	Tanshinone IIA	Butane diacid	Panaxtriol	Aristolochic A	Folic acid	Berberine Sul	L-Theanine	Empty
h	61	105	70	73	221	224	67	74	86	67	38	Empty
	(+)- Corydalin	cis-Anethol	3-n-Butylphat	Wedelolactor	Acetate gossy	Gossypol	Eupatilin	Harmine hydr	Sinomenine H	Fargesin	Vinorelbine	Empty

Plate layout: L1021-27

	1	2	3	4	5	6	7	8	9	10	11	12
a	85	68	77	61	96	Empty	Empty	Empty	Empty	Empty	Empty	Empty
	vinblastine	Dehydrocostu	Berbamine hy	10-Hydroxyca	Trigonelline							
b	76	80	86	92	96	Empty	Empty	Empty	Empty	Empty	Empty	Empty
	Lannaconitine	Gramine	Neosperidin d	Chitosamine h	4-Aminobutyric acid							Empty
c	72	72	82	78	81	Empty	Empty	Empty	Empty	Empty	Empty	Empty
	Protopine	Madecassic a	Aloin	Nicotine	Prulifloxacin (Pruvel)							Empty
d	74	86	89	79	Empty	Empty	Empty	Empty	Empty	Empty	Empty	Empty
	Umbelliferone	Naringin	Scopolamine	Synephrine								Empty
e	80	76	68	102	Empty	Empty	Empty	Empty	Empty	Empty	Empty	Empty
	Allantoin	Genipin	Diosimin	Chondroitin sulfate								Empty
f	88	68	71	72	Empty	Empty	Empty	Empty	Empty	Empty	Empty	Empty
	D-Pinitol	Linalool	Sclareol	Glucosamine sulfate								Empty
g	85	91	83	67	Empty	Empty	Empty	Empty	Empty	Empty	Empty	Empty
	Eriodictyol	Palmitic acid	Scopolamine	Aucubin								Empty
h	78	81	79	68	Empty	Empty	Empty	Empty	Empty	Empty	Empty	Empty
	Curculigoside	3,4-Dihydroxy	Trigonelline H	Cepharanthine								Empty

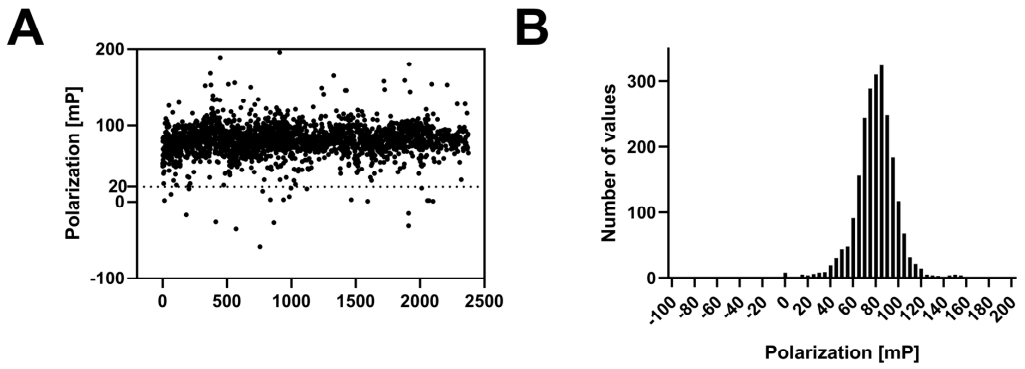


Figure S10. Statistical analysis of METTL1 high-throughput screening results. (**A**) Each point reflects the fluorescence polarization data from a single screening compound at 200 µM. 18 compounds with a polarization value <20 mP were considered as initial hit candidates. (**B**) Histogram of high-throughput screening results. Compounds were binned according to their fluorescence polarization (bin size 5 mP).

Author contributions

JLM synthesized and characterized Cy5TAD and FTAD; AFF synthesized and characterized Cy5TPD. FB performed the PDB mining. JLM and AFF synthesized scaffold alkynes and fluorophore azides. SNH synthesized compound **30**. AFF performed nanomole-scale click reactions for nanoSAR probe screening. FB performed MST and FP measurements for probe characterization. FB and MWK performed SPR measurements with METTL1. RAZ conducted ITC measurements for SAH affinity determination. RAZ and MOS performed the HTS on METTL1 and subsequent hit characterization by FP and ITC assays. AFF performed ^{3}H-based inhibition assays on METTL1. Proteins were prepared and purified by: DNMT2 (ZN), NSUN2 (ZN), NSUN6 (ZN), METTL1 (RAZ/MOS), METTL3/14 (ACW), TrmD (RAZ/ACW). FB, JLM, and AFF designed the experiments and analyzed the data; FB, JLM, and AFF wrote the manuscript.

3.2 Nanoscale Direct-to-Biology Optimization and Structural Insights into Selective *S. aureus* TrmD Inhibitors

3.2.1 Context and Project Summary

S. aureus is a clinically relevant pathogen responsible for numerous deaths each year due to its resistance to multiple antibiotics.[96–102] TrmD represents a promising target due to its essential role in bacterial survival and its critical function in protein biosynthesis. However, to date, only a limited number of TrmD inhibitors targeting *S. aureus* TrmD or various TrmD orthologs have been reported – specifically, 15 publications since 2011 according to a PubMed search using the term "TrmD inhibitor".[103–106,253] Among these, only one has demonstrated antibacterial activity against *S. aureus*.[253]

This project aimed to identify novel, selective inhibitors of *S. aureus* TrmD with antibacterial activity. The thienopyrimidone scaffold, originally identified by Hill *et al*. and applied for the fluorescent tracer Cy5TPD (see 3.1.1), was utilized as a starting point and optimized for *S. aureus* TrmD.[106] Here, a scaffold hopping strategy was implemented, leading to the design of a tracer with a pyrrolylpyrimidone core structure. The resulting tracer displayed nanomolar affinity for *S. aureus* TrmD and served as the foundation for a D2B campaign.

Following optimization of the D2B reaction conditions using a model triazole, a library of 320 azides was conjugated to the pyrrolopyrimidone alkyne via CuAAC. Preliminary screenings in an FP assay revealed strong binding interactions. Thus, a full screening of the triazole library at 1 µM was conducted. This effort yielded five top hits that caused nearly complete displacement of the tracer at the screening concentration. These hits were resynthesized on a preparative scale, validated for TrmD binding and inhibition, assessed for selectivity (Trm5 and different TrmD isozymes), and evaluated for antibacterial activity against *S. aureus* and *E. coli*. All five compounds were confirmed as selective and potent *S. aureus* TrmD inhibitors, with enzymatic IC_{50} values ranging from nanomolar to low micromolar efficacy. However, none of the compounds exhibited antibacterial activity, suggesting that poor cellular permeability may be a contributing factor. Simultaneously, two protected carbamate intermediates of a hit (Cbz- and *tert*-butyloxycarbonyl (Boc)-protected forms) were tested in antibacterial assays for *S. aureus* and *E. coli*. Notably, the Cbz-protected compound showed significant antibacterial activity with an IC_{50} of 10.8 µM on *S. aureus*. Subsequent lysate assays confirmed that both Cbz- and Boc-protecting groups are cleaved in *S. aureus* lysate, thereby releasing the active inhibitor. These findings confirmed the suggestion that initial hit compounds suffer from low permeability. Finally, crystallographic studies were performed to elucidate the binding mode of the lead compound, providing structural insights for future optimization.

This work has been published in: Journal of Medicinal Chemistry (impact factor: 6.8).

Article reprinted (unmodified) with open access permission from *J Med Chem.,* **2025,** *68* (24), 26246–26262. 'Nanoscale Direct-to-Biology Optimization and Structural Insights into Selective S. aureus TrmD Inhibitors' ©2025 The Authors. The work is licensed under CC BY 4.0. (https://creativecommons.org/licenses/by/4.0/).

The full version of the article, including the electronic Supplementary Information, can be accessed online at doi: 10.1021/acs.jmedchem.5c02323.

3.2.2 Contributions

Own contribution: Establishing CuAAC for alkyne scaffold and adaptation for D2B strategy, D2B synthesis of triazole library, establishing FP assay with new tracer, D2B library FP-screening, preparative synthesis (tracer, hit compounds, prodrugs and starting point compounds), validation of hit compounds and prodrugs in FP and ^{3}H-incorporation assay (selectivity and inhibitory efficiency), manuscript and SI writing and editing.

Contributions from other authors: Protein preparation and crystallization, FP selectivity assay, aptamer assay, bacterial growth inhibition assays, Cell Titer Glo cell viability assay, lysate assay, manuscript and SI writing and editing.

.

3.2.3 Publication

The following publication quoted within “” from page 94 to page 110 is the same as the manuscript cited on page 93.[254] “

Journal of Medicinal Chemistry

Open Access
This article is licensed under CC-BY 4.0

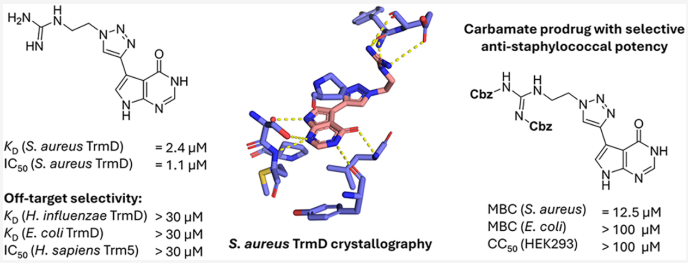
pubs.acs.org/jmc Article

Nanoscale Direct-to-Biology Optimization and Structural Insights into Selective *S. aureus* TrmD Inhibitors

Ariane F. Hübner,[‖] Annabelle C. Weldert,[‖] Tessa Marciniak, Florian Hof, Vivien S. Beck, Samuel Carien, Sophie N. Mulartschyk, Eva Wolf, Wilma Ziebuhr, and Fabian Barthels*

Cite This: *J. Med. Chem.* 2025, 68, 26246−26262 Read Online

ACCESS | Metrics & More | Article Recommendations | Supporting Information



ABSTRACT: The tRNA m^{1}G37 methyltransferase (TrmD) is considered essential in various bacteria, including *Staphylococcus aureus*, a pathogen responsible for a wide range of diseases. Here, we have performed a high-throughput nanomole-scale synthesis campaign (nanoSAR) by late-stage copper(I)-catalyzed alkyne−azide cycloaddition (CuAAC)-functionalizing a library of structurally diverse azides (N = 320) to a pyrrolopyrimidone alkyne. We have identified selective *S. aureus* TrmD inhibitors with inhibitory activity in the nanomolar to low micromolar range using a direct-to-biology assay read-out. A carbamate-masked guanidine intermediate of the lead structure selectively inhibited *S. aureus* growth at low micromolar concentrations in cell-based assays, while Gram-negative bacteria and an off-target panel of methyltransferases were not affected. Subsequent cocrystallization resulted in a crystal structure of *S. aureus* TrmD bound to an inhibitor, providing detailed insights into its binding mode and enabling future structure-guided optimization.

INTRODUCTION

Staphylococcus aureus is a prevalent bacterial pathogen, causing a broad spectrum of diseases ranging from skin infections to life-threatening conditions such as pneumonia and sepsis.[1] The treatment of *S. aureus* infections is increasingly difficult due to the antibiotic resistance of the pathogen, including the emergence of multidrug-resistant isolates.[2] Particularly, methicillin-resistant *S. aureus* (MRSA) currently represents the deadliest resistance-pathogen pairing globally, causing more than 100,000 deaths in 2019 alone.[3,4] Therefore, the identification of new antimicrobial drugs is strongly desired to overcome resistance issues in *S. aureus*.

One enzyme essential for *S. aureus* among many other bacteria is the tRNA m^{1}G37 methyltransferase (TrmD), which catalyzes the methyl group transfer from *S*-adenosylmethionine (SAM) to the N^1 position of guanosine 37 in a defined subset of tRNAs.[5−8] Since this modification is located in close proximity to the 3′-side of the anticodon, its absence can lead to tRNA misrecognition during translation and +1-frameshift errors during protein synthesis.[9,10] In eukaryotes and archaea, the m^{1}G37 modification is introduced by the structurally unrelated tRNA methyltransferase 5 (Trm5).[11,12] Trm5 belongs to class I of methyltransferases, while bacterial TrmD belongs to the unique class IV, also known as SPOUT class.[11] TrmD was identified as a potentially selective antimicrobial drug target, due to its essential role as well as the structural differences from Trm5.[13] Crystal structures of inhibitor-bound TrmD complexes from several organisms, including *Haemophilus influenzae* and *Escherichia coli*, have been solved in the past, offering starting points for drug discovery campaigns.[14−17]

To date, a limited number of TrmD inhibitors targeting diverse bacterial organisms have been reported (15 publications since 2011, according to a PubMed search using the keyword “TrmD Inhibitor”),[14,18−20] but so far, only very few TrmD inhibitors have been effective in targeting *S. aureus*.[16] Despite the urgent need for new antibiotics targeting *S. aureus*,

Received: August 18, 2025
Revised: November 2, 2025
Accepted: December 4, 2025
Published: December 10, 2025



Downloaded via UNIV MAINZ on January 5, 2026 at 12:40:01 (UTC).
See https://pubs.acs.org/sharingguidelines for options on how to legitimately share published articles.

ACS Publications
© 2025 The Authors. Published by American Chemical Society

https://doi.org/10.1021/acs.jmedchem.5c02323
J. Med. Chem. 2025, 68, 26246−26262

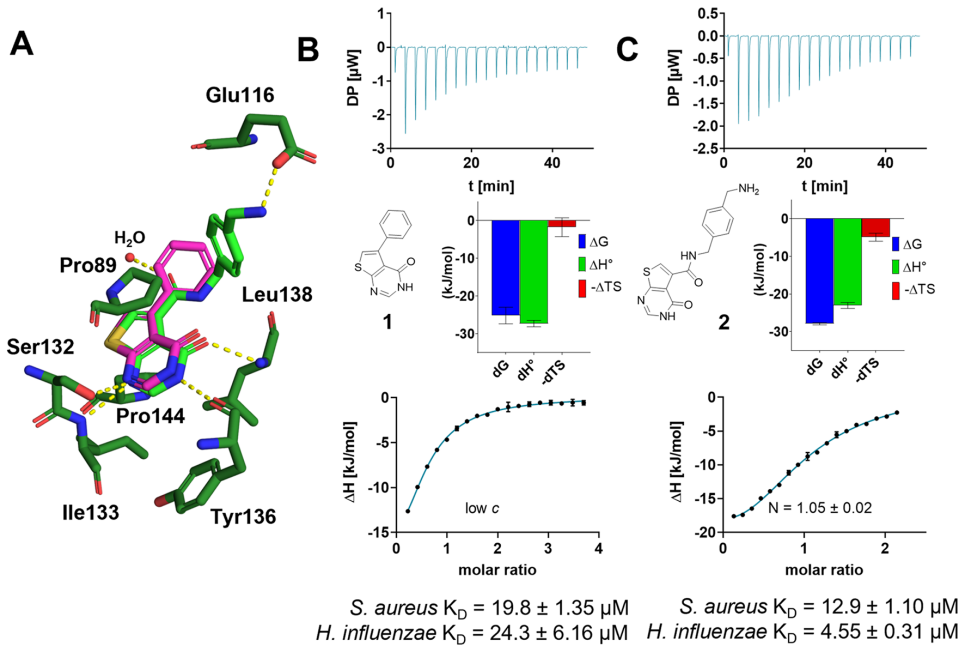


Figure 1. Definition of starting points for the development of *S. aureus* TrmD inhibitors. (A) Crystallographic overlay of literature-known inhibitors **1** (PDB: 4MCD) and **2** (PDB: 4MCC) in the *H. influenzae* SAM-binding pocket. Ligands and amino acids are shown in stick representation; polar interactions are shown as yellow lines, and water as red spheres. The carbon atoms of **1** are shown in pink and those of compound **2** in light green. Interacting residues are displayed in dark green. (B, C) Structures and affinities of inhibitors **1** (B) and **2** (C) binding to *S. aureus* TrmD determined by ITC, incl. thermograms, stoichiometry, and signature plots (data for *H. influenzae* TrmD in Figure S2). Due to low enthalpy signals, a low *c*-titration was performed for inhibitor **1**, resulting in $N < 1$.

previous studies focused mainly on developing TrmD inhibitors for *H. influenzae*, *E. coli*, *Mycobacterium abscessus*, and *Mycobacterium tuberculosis*.[14,18−20] In a development campaign conducted by AstraZeneca, Hill et al. screened a fragment collection to identify *H. influenzae* TrmD inhibitors.[14] They investigated thienopyrimidone-based inhibitors that showed inhibitory activity against a panel of TrmD orthologs (*E. coli*, *H. influenzae*, *Acinetobacter baumanni*, *Klebsiella pneumoniae*, and *Pseudomonas aeruginosa*), offering broadband starting points for drug discovery, but this also suggested only limited interspecies selectivity.[14]

To target this gap, in this present study, we employed the thienopyrimidone scaffold discovered by Hill et al. and optimized the inhibitory profile to develop selective inhibitors targeting *S. aureus* TrmD using a high-throughput nanomole-scale (final: 96 nmol) synthesis strategy. Reactions conducted with less than 300 nmol of starting material are commonly referred to as being performed on the nanomole scale.[21] This miniaturized format offers advantages compared to flask-oriented synthesis campaigns in throughput, development time, and in conserving valuable synthetic intermediates.[22] Notable contributions in this field feature the implementation of a range of standard medicinal chemistry transformations in plate-based formats, including the development of a copper-catalyzed alkyne−azide click reaction (CuAAC) pipeline as described by Gehrtz et al., suitable for our inhibitor development campaign.[21,23−25] If the resulting crude nanomole-scale reaction mixtures are directly analyzed using *in vitro* or *in cellulo* assays to derive structure−activity relationship (SAR) insights, this strategy was coined by several recent reports (2021−) as a *direct-to-biology* (D2B) approach.[26−30]

RESULTS AND DISCUSSION

Definition of an *S. aureus* Targeting Lead Structure.

To date, no dedicated *S. aureus* TrmD inhibitors have been reported. Hence, to define a suitable lead for nanoSAR-based optimization, we analyzed literature-known ligands of TrmD isoenzymes from diverse microorganisms. Hill et al. discovered the thienopyrimidone inhibitor **1** by screening a collection of fragments against *H. influenzae* TrmD, and their subsequent optimization resulted in inhibitor **2** with activities in the nanomolar to micromolar range.[14] X-ray cocrystal structures with *H. influenzae* TrmD were previously solved for inhibitor **1** (PDB: 4MCD) and the optimized *H. influenzae* inhibitor **2** (PDB: 4MCC). Both inhibitors were found to occupy the SAM binding pocket of TrmD (Figure 1A), while the thienopyrimidone moieties targeted the adenine binding pocket, and the phenyl ring of inhibitor **1** extended into the ribose pocket (Figure 1A, Figure S1A). The phenylmethyl-amine moiety of inhibitor **2** reaches further into the methionine part of the SAM pocket (Figure S1B), where an additional interaction with Glu116 can be formed (Figure 1A).[14] Due to the considerable sequence similarity (65%) between *H. influenzae* TrmD and *S. aureus* TrmD, we hypothesized that this thienopyrimidone chemotype might provide a reasonable lead for *S. aureus* drug development. To assess if the thienopyrimidone-based compounds, developed as dedicated *H. influenzae* TrmD inhibitors, are suitable starting points for targeting the *S. aureus* orthologous enzyme, we

https://doi.org/10.1021/acs.jmedchem.5c02323
J. Med. Chem. 2025, 68, 26246−26262

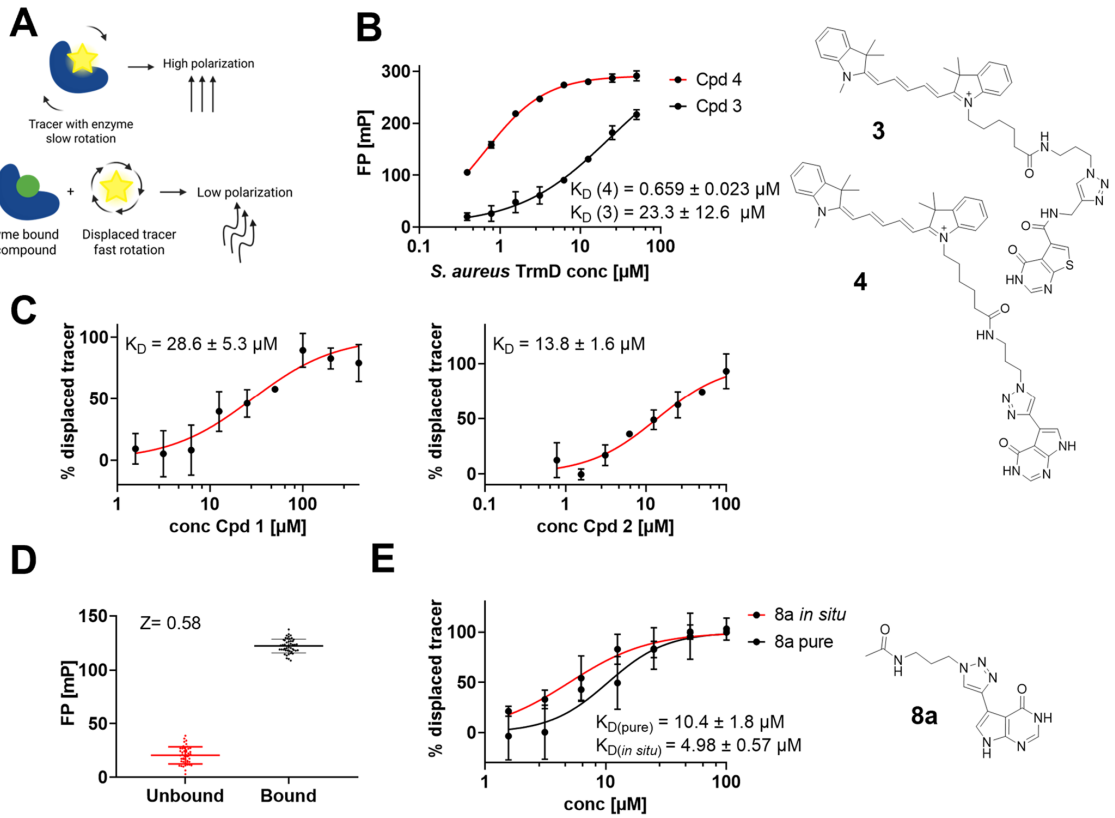


Figure 2. Fluorescence polarization (FP) assays for *S. aureus* TrmD ligand investigation. (A) Concept of the FP displacement assay. (B) Chemical structures and FP-derived affinity of tracers **3** and **4** binding to *S. aureus* TrmD. (C) FP displacement assays for the determination of apparent affinities of parent compounds **1** and **2**. (D) Evaluation of statistical *Z*-factors to assess the high-throughput capability of this FP assay setup. (E) FP displacement assays of nanoSAR test triazole **8a** *in situ* vs chromatographically purified compound.

evaluated the binding thermodynamics of **1** and **2** via isothermal titration calorimetry (ITC) on the recombinant *S. aureus* TrmD enzyme (Figure 1B,C, Figure S2). **1** and **2** showed enthalpy-dominated binding profiles in the micromolar range on both *H. influenzae* and *S. aureus* enzymes, with an unfavorable selectivity toward targeting *S. aureus* TrmD for **2**. The determined dissociation constants were 19.8 and 12.9 μM, respectively, and thus, were deemed suitable as starting points for *S. aureus* targeting ligand optimization.

Development of a Direct-to-Biology Assay Platform for Inhibitor Optimization. To enable the screening of hundreds of nanomole-scale synthesized compounds, the implementation of a high-throughput-capable RNA methyltransferase (MTase) assay is considered fundamental. In a previous publication, we demonstrated the suitability of fluorescence polarization (FP)-based assays as a screening method to identify and characterize MTase inhibitors.[31] In this assay format, a fluorescent, SAM-pocket binding tracer can be displaced by the compound under investigation, and the resulting change in fluorescence polarization defines the readout of the inhibitor compound's affinity (Figure 2A).

Previously, we developed an *H. influenzae* TrmD targeting fluorescent tracer **3**, which we originally intended to adapt for *S. aureus* TrmD.[31] Compared to *H. influenzae* TrmD (K_D = 2.0 μM, Figure S4A), however, this tracer showed only weak affinity for the *S. aureus* orthologous enzyme (K_D = 23.3 μM, Figure 2B). To address this issue, we employed scaffold hopping from a thieno- to a pyrrolopyrimidone, as demonstrated in the study by Hill et al., which resulted in improved binding affinities for *S. aureus* TrmD compared to *H. influenzae* TrmD. Thus, here, we report a new fluorescent tracer **4** dedicated to *S. aureus* TrmD with a pyrrolopyrimidone motif and without the amide linker (Figure 2B). Evaluation of tracer **4** in FP assays confirmed this hypothesis and revealed a K_D-value of 659 nM for *S. aureus* TrmD, suitable for the establishment of a high-throughput-capable assay format (Figure 2B). The structural reason for the preference of the thienopyrimidone motif and an amide-free linker for *S. aureus* TrmD could be rationalized by crystallographic analysis of our *S. aureus* TrmD inhibitor complexes (*vide infra*).

To validate that optimized *S. aureus* tracer **4** is suitable for a direct-to-biology screening of TrmD inhibitors, we investigated dose−response series of parent compounds **1** and **2** by FP displacement assays, yielding apparent binding affinities (K_D = 28.6 and 13.8 μM), and hence, agreeing with the magnitude and relative order determined via ITC (Figure 2C vs Figure 1B,C). Furthermore, we were able to confirm that the assay setup consisting of *S. aureus* TrmD (500 nM) and tracer **4** (10 nM) is suitable as a high-throughput-capable format by determining the assay-specific *Z*-factor (*Z* = 0.58, Figure

https://doi.org/10.1021/acs.jmedchem.5c02323
J. Med. Chem. 2025, 68, 26246−26262

Journal of Medicinal Chemistry pubs.acs.org/jmc Article

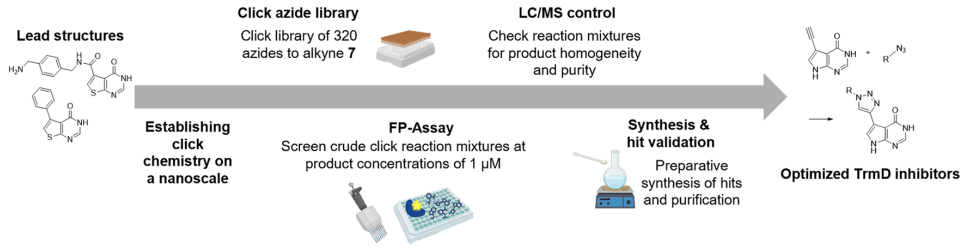
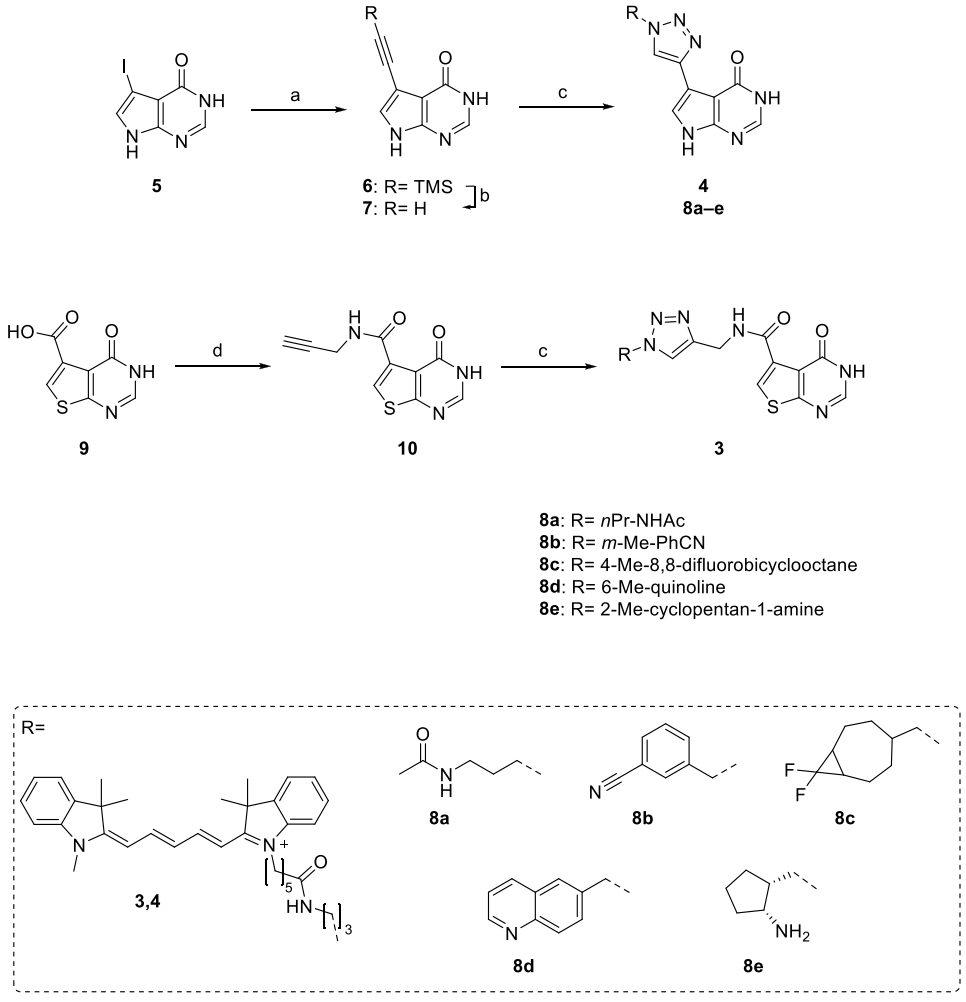


Figure 3. Workflow of the nanoSAR strategy for optimization of *S. aureus* TrmD inhibitors. Reaction of the alkyne precursors 7 with 320 chemically diverse azides resulted in a plate-based library of inhibitor triazoles, which were measured in a direct-to-biology FP displacement assay, followed by an LC/MS confirmation of hit compounds' crude reactions, and subsequently, the preparative synthesis and validation of the selected candidate compounds.

Scheme 1. Overview of Synthetic Procedures[a]

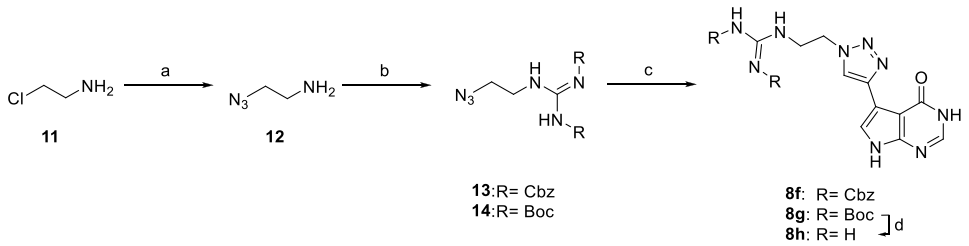


[a]Reagents and conditions: (a) CuI, TMS-acetylene, $Pd(PPh_3)_4$, triethylamine, DMF/THF, rt, 16 h, 29%; (b) 1 M tetra-*n*-butylammonium fluoride, THF/ACN, 0 °C−rt, 1.5 h, 68%; (c) $CuSO_4$×5 H_2O, TBTA, sodium ascorbate, DMSO, H_2O, rt, 16 h, 25−74%; (d) HATU, DIPEA, DCM/DMF, rt, 16 h, 77%−quant.

2D). The *Z*-factor is a statistical parameter that assesses the dynamic range of an assay to determine its suitability for HTS; a *Z*-factor >0.5 is generally considered indicative of an excellent assay.[32] Based on the assay results gleaned from the

https://doi.org/10.1021/acs.jmedchem.5c02323
J. Med. Chem. 2025, 68, 26246−26262

Scheme 2. Overview of the Synthetic Procedure for Compounds 8h−g[a]



[a](a) Sodium azide, water, 90 °C, 16 h, quant.; (b) *N*,*N*′-Bis-Boc- or *N*,*N*′-Bis-Cbz-guanylpyrazole, THF, triethylamine, rt, 72 h, 47−90%; (c) $CuSO_4$×5 H_2O, TBTA, sodium ascorbate, DMSO, H_2O, rt, 16 h, 25−74%; (d) TFA, DCM, 30 min, rt, quant.

tracer experiments, we decided to use the alkyne handle of the compound **4** precursor (cpd **7**) to build a CuAAC-derived nanoSAR triazole library for the development of new *S. aureus* selective TrmD inhibitors. The workflow is illustrated in Figure 3.

To confirm that alkyne **7** (Scheme 1) and the resulting crude nanomole-scale triazoles are compatible with the established direct-to-biology platform, we performed a pilot exploration including the *in situ* synthesis and screening of a representative triazole candidate **8a** (Figure 2E). LC/MS reaction control of pilot alkyne−azide coupling reactions showed consistently >90% conversion rates and no production of side-products; thus, we concluded that this D2B outline is suitable for the generation of a TrmD inhibitor library. The nanomole scale reaction mixture was subsequently tested by FP assay both in crude and after chromatographic purification of this test compound, revealing only slight variation in K_D-values of 4.98 and 10.4 μM, respectively, along with a minimal variation of the Hill slope (Figure 2E). This suggests that crude reactions from the azide library provide a reliable semi-quantitative indication of binding affinities, as the objective of D2B screenings is to rank the potency of substituents in relative order. Also, the FP assay setup using tracer **4** and *S. aureus* TrmD was found to be insensitive toward all components of the *in situ* click reaction, including unreacted alkyne **7** (K_D > 100 μM, Figure S4B).

Chemistry. In this present study, a new alkyne-decorated pyrrolo[2,3-*d*]pyrimidone with similar chemical properties to parent structures **1** and **2** was synthesized (Scheme 1) for the preparation of triazole-based *S. aureus* TrmD inhibitors **8a−e**.

For inhibitor generation, this precursor alkyne **7** was subsequently reacted with diverse aromatic and aliphatic azides via copper(I)-catalyzed azide−alkyne cycloaddition (CuAAC). The thieno-subunit from literature TrmD inhibitors (e.g., **1** and **2**) was substituted with a pyrrolo-unit to facilitate synthesis, without compromising binding affinity. According to Hill et al., replacing the sulfur atom in the thienopyrimidone moiety of the scaffold with a nitrogen was favorable for *S. aureus* selectivity, which allowed us to develop a high-affinity fluorescent tracer **4** (Figure 2).[14] The unoccupied TrmD methionine pocket (Figure S1) leaves space for modifications at the pyrrolo unit, and thus, we synthesized triazole derivatives for both tracer and inhibitor development. The synthetic routes of compounds **6−14**, including the fluorescent tracers and the compounds originating from nanoSAR screening, are described in Schemes 1 and 2.

Literature-known compound **2** was synthesized by a HATU-mediated coupling of *tert*-butyl (4-(aminomethyl)benzyl)-carbamate and 4-oxo-3,4-dihydrothieno[2,3-*d*]pyrimidine-5-carboxylic acid, followed by a Boc-deprotection with TFA in DCM. The synthesis route for alkyne **7** started with a Sonogashira reaction using commercially available 5-iodo-3,7-dihydro-4*H*-pyrrolo[2,3-*d*]pyrimidin-4-one (**5**) and TMS-acetylene, catalyzed by Tetrakis(triphenylphosphine)-palladium(0) and copper(I) iodide, yielding compound **6**. Finally, alkyne **7** was obtained by deprotection of the TMS-group by tetra-*n*-butylammonium fluoride (TBAF). Subsequent CuAAC with alkyne **7** and various azides was performed using $CuSO_4$×5 H_2O, which was reduced *in situ* to copper(I) by sodium ascorbate and stabilized by *tris*((1-benzyl-4-triazolyl)methyl)amine (TBTA) in DMSO and water (1:1).[21] Hit compounds of the nanoSAR study and fluorescent tracers were resynthesized by the same procedure on a preparative scale and purified by reverse-phase flash chromatography.

Preparative synthesis of **8h** started with 2-chloroethylamine (**11**), which was converted to the corresponding azide (**12**) with sodium azide. To introduce the guanidine group, *N*,*N*′-Bis-Boc-1-guanylpyrazole was reacted under basic conditions in THF to afford intermediate **14**. Subsequently, intermediate **14** was reacted with alkyne **7** via CuAAC to yield **8g**. Under similar conditions, compound **8f** was synthesized with *N*,*N*′-Bis-Cbz-1-guanylpyrazole. Final deprotection of the Boc-group of **8g** with TFA and DCM (1:1) yielded lead compound **8h**.

Preparation of a nanoSAR Triazole Library and FP-Based TrmD Screening. Next, we conducted an *S. aureus* TrmD-targeting nanoSAR study. For this, alkyne **7** was reacted on a 96 nmol scale with an in-house diversity-oriented azide library (N = 320, mean pairwise Tanimoto similarity = 0.11) designed to cover a large chemical fragment space, generating a panel of 320 crude triazoles ready for FP assay investigation. The composition of the azide library is designed to be chemically diverse in several categories, including physico-chemical properties such as polar surface area, lipophilicity, and the number of hydrogen bond donors and acceptors, as well as structural features like the number of aromatic rings (Figure S23). A complete list of chemical structures included in the azide library can be found in Table S4. *In situ* reaction conditions for CuAAC were adapted from Gehrtz et al., utilizing $CuSO_4$, which is reduced *in situ* to Cu(I) by sodium ascorbate and stabilized by TBTA.[21] Degassed water and DMSO (1:1) were used as solvents to prevent the oxidation from Cu(I) to Cu(II). For the synthesis of the triazole library, a master mix was prepared, containing all reaction components except the azides. All reactions were started by the addition of the respective azide in 24 μL at a final product concentration

https://doi.org/10.1021/acs.jmedchem.5c02323
J. Med. Chem. 2025, 68, 26246−26262

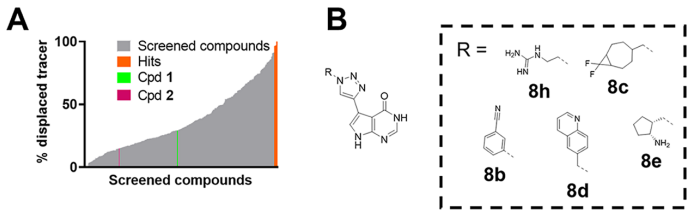


Figure 4. Results, analysis, and hit selection of the nanoSAR TrmD screening. (A) Waterfall plot summarizing the screening of 320 triazole inhibitor candidates at 1 μM. In orange, the five compounds ("hits") with the highest potency (>93% displaced tracer, **8b−e,h**) are shown. (B) Chemical structure representation of the five hits **8b−e,h** that were identified during screening.

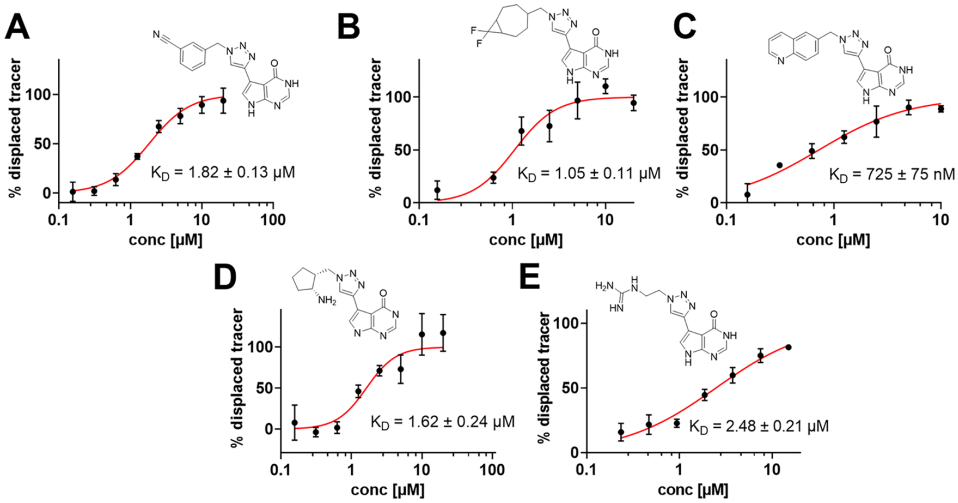


Figure 5. FP-assay of chromatographically purified (A) **8b** (B) **8c** (C) **8d** (D) **8e** (E) **8h** with the respective structures and K_D-values.

of 4 mM (96 nmol). Reaction mixtures were incubated for 16 h at room temperature and under an argon atmosphere in sealed 96-well plates.

Based on the pilot explorations of pyrrolopyrimidine triazoles **4** and **8a** (K_D = 0.66 and 4.98 μM), we adjusted the final concentration of the triazoles for FP screening to 1 μM, assuming full conversion of the click reaction. In this regard, conversion rates were tested for 24 random reaction mixtures by LC/MS and were found consistently to be >90%. For FP assay screening, we used 500 nM of *S. aureus* TrmD and 10 nM of tracer **4** in a total volume of 40 μL in 96-well plates. We performed control measurements and defined 10 nM of tracer **4** in buffer as 100% displacement and the DMSO control as 0% tracer displacement. As primary hits, we intended to select the top 5 compounds that exhibited tracer displacements >93%. The results of the FP screening were visualized in a waterfall plot and plate-based heatmaps (Figure 4, Figure S3).

Five compounds (**8b−e,h**) showed near complete displacement during FP screening at an inhibitor concentration of 1 μM, and consequently, these discovered structures ("hits") were verified for reaction conversion and identity via LC/MS (>90% crude purity). A comprehensive overview of the FP assay results for all compounds generated from the azide library can be found in Table S4. Structurally, hits **8b−e,h** appear to have limited similarity; yet **8b−d** contain hydrophobic, sterically demanding decorations, whereas **8b,e,h** share a basic amine or amidine moiety, and thus, these five hit compounds (**8b−e,h**) were selected for preparative resynthesis and validation. SAR of these enriched ligand features is discussed by crystallography and molecular modeling (*vide infra*).

Resynthesis and Characterization of *S. aureus* TrmD Inhibitors. The five hit compounds identified during the FP screening were subsequently resynthesized on a preparative scale, and binding profiles were validated using the FP assay with >95% chromatographically purified inhibitors. Synthesis procedures of the hits can be found in Schemes 1 and 2. K_D-values and the respective curves for all hit compounds **8b−e,h** were determined by dose−response experiments in the FP assay and can be found in Figure 5 and Table 1. To further investigate the inhibitory efficacy of **8b−e,h**, we utilized a literature-known aptamer-based *S. aureus* TrmD enzyme assay for IC_{50} determination (Table 1) and an orthogonal label-free ^{3}H-scintillation MTase assay (Figures S9, S10).[33] Both K_D and IC_{50} values ranged from 390 nM to 3.22 μM, and in summary, it can be concluded that the nanoSAR strategy has led to a successful optimization of parent compounds **1** and **2** (28.6 and 13.8 μM).

Next, we employed the FP-assay using tracers **3** and **4** to test the selectivity of **8b−e,h** against a panel of TrmD isoenzymes from *S. aureus*, *E. coli*, and *H. influenzae* (Figures S7, S8). Furthermore, we tested the inhibitory potency of **8b−e,h** for the human MTase homologue Trm5 (Figure S6). Since no

https://doi.org/10.1021/acs.jmedchem.5c02323
J. Med. Chem. 2025, 68, 26246−26262

Table 1. Overview of K_D-Values (Determined by FP Assays) and IC_{50}-Values (Determined by Aptamer-Based Enzyme Assays for *S. aureus* TrmD and ^{3}H-Based Enzyme Assay for Trm5) for 8b−e,h[a]

	S. aureus		*E. coli*	*H. influenzae*	Trm5
Cpd	K_D [μM]	IC_{50} [μM]	K_D [μM]	K_D [μM]	IC_{50} [μM]
8a	10.4 ± 1.8	n.d.	n.d.	n.d.	n.d.
8b	1.82 ± 0.13	3.22 ± 1.80	>30	>30	>30
8c	1.05 ± 0.11	0.71 ± 0.10	>30	>30	>30
8d	0.72 ± 0.07	0.39 ± 0.07	>30	>30	>30
8e	1.62 ± 0.24	0.48 ± 0.06	>30	>30	>30
8h	2.48 ± 0.21	1.16 ± 0.12	>30	>30	>30

[a]n.d.: not determined.

suitable fluorescent tracer was available, a functional ^{3}H-based enzyme assay was performed to assess Trm5 selectivity. All hit compounds exhibited at least >10× K_D- or IC_{50}-values for all off-targets compared to the *S. aureus* TrmD, and thus, we conclude that nanoSAR optimization provided not only affine but also selective *S. aureus* TrmD inhibitors (Table 1). In summary, the hit compounds **8b−e,h** demonstrated a significant improvement regarding selectivity and affinity toward the *S. aureus* TrmD compared to the parent compounds **1** and **2**. Also, we investigated mammalian cytotoxicity of the hits **8b−e,h** using CellTiterGlo assays following cell viability in HEK293 cells. In summary, the hit compounds showed no significant effects on cell viability at relevant concentrations up to 100 μM (Figure S11). Slight cytotoxic effects were only observed for compounds **8b** and **8c** at 100 μM, and for **8e** at >10 μM, whereas the identified lead *S. aureus* TrmD inhibitor compound **8h** showed no mammalian cytotoxicity up to 100 μM.

Antibacterial Assays and Potential Prodrug Identification. To assess the antibacterial activity of **8b−e,h**, the effect on *S. aureus* RN4220 was investigated using a dose−response bacterial growth inhibition assay. Also, two synthetic carbamate intermediates (**8f** and **8g**, Figure 6) obtained during the preparation of **8b−e,h** were included in this assay through their similarity with the hit compounds. Here, initial screenings of **8b−h** were conducted at 1, 10, and 100 μM but revealed that the growth of *S. aureus* was not affected by most compounds at concentrations up to 100 μM compared to the untreated controls in bacterial growth inhibition (Figure 6, details for hit compounds from the library **8b-e,h** are shown in Figure S12). Also, none of the compounds showed significant growth inhibition for *E. coli* (Figures S13, S14). As TrmD is an essential protein in *S. aureus*, successful inhibition is expected to lead to cell death and/or growth inhibition, which has been substantiated in numerous literature studies to date.[5,8,34] Yet, it has been observed in similar TrmD drug development campaigns that, despite nanomolar affinity, a majority of TrmD inhibitors fail in terms of antibacterial potency, presumably due to their large polar surface area and insufficient permeability through the bacterial cell wall.[14,18−20,35] Surprisingly, a significant reduction in *S. aureus* growth was observed during treatment of RN4220 with di-Cbz intermediate **8f** (Figure 6A, Figure S15B: MIC = 12.5 μM), while **8f** and **8g** showed no inhibition of Gram-negative *E. coli* (Figures S13, S14). In fact, a slight increase in *E. coli* growth rate at the highest concentration (100 μM) of **8f** could be observed, possibly due to a compensatory effect of this more permeable drug acting on an unknown Gram-negative off-target (Figure S14B).

We hypothesized that the activity of **8f** against *S. aureus* could be attributed to the di-Cbz carbamate moiety, masking the large polar surface area of the guanidine motif of hit **8h**, which itself did not influence bacterial growth, presumably due to the charged nature and limited permeability (Figures S12, S13). The strategy of conjugating a lipophilic tag has previously been shown to improve the permeability of antibacterials.[16,36,37] To determine the minimal bactericidal concentration (MBC) of the substances, bacterial cultures were prepared as in the bacterial growth inhibition assay. While cell growth is not negatively affected by treatment with Boc-carbamate **8g**, and more CFU/mL were observed after incubation, Cbz-carbamate **8f** affects growth starting at 12.5 μM treatment (Figure S16). On average, fewer CFU/mL were determined after 24 h of incubation, but bacteria were not killed completely. This indicates a rather bacteriostatic mode of action.

Subsequently, both synthetic intermediates **8f** (di-Cbz) and **8g** (di-Boc) were evaluated for their *in vitro* TrmD affinity using FP assays. **8g** displayed a K_D-value of 19.8 μM, while **8f** showed no *S. aureus* TrmD binding up to 100 μM (Figure S5A,B), and thus, we concluded that the antistaphylococcal activity of **8f** is not mediated by direct TrmD inhibition. Hence, we developed a mechanistic hypothesis evaluated below: Since carbamates are known to be susceptible to cleavage by esterases, we hypothesized that *in situ* deprotection

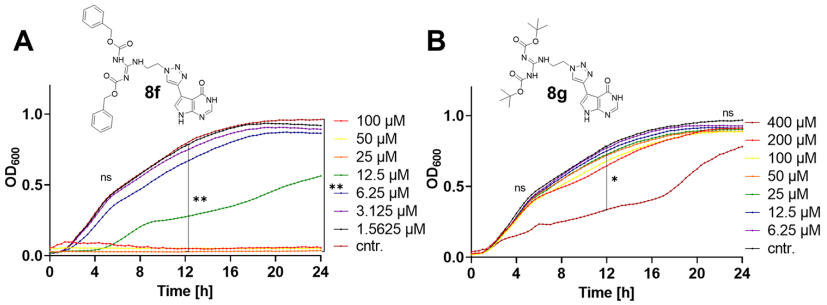


Figure 6. *S. aureus* growth inhibition by **8f** (di-Cbz) and **8g** (di-Boc). (A) *S. aureus* RN4220 treated with **8f** and (B) *S. aureus* RN4220 treated with **8g**. Only **8f** showed a significant effect on *S. aureus* bacteria in lower concentrations. Two-way ANOVA with Dunnett's multiple comparisons test was used for statistical analysis, using a confidence interval of 95% (Time points: 6, 12, and 24 h).

https://doi.org/10.1021/acs.jmedchem.5c02323
J. Med. Chem. 2025, 68, 26246−26262

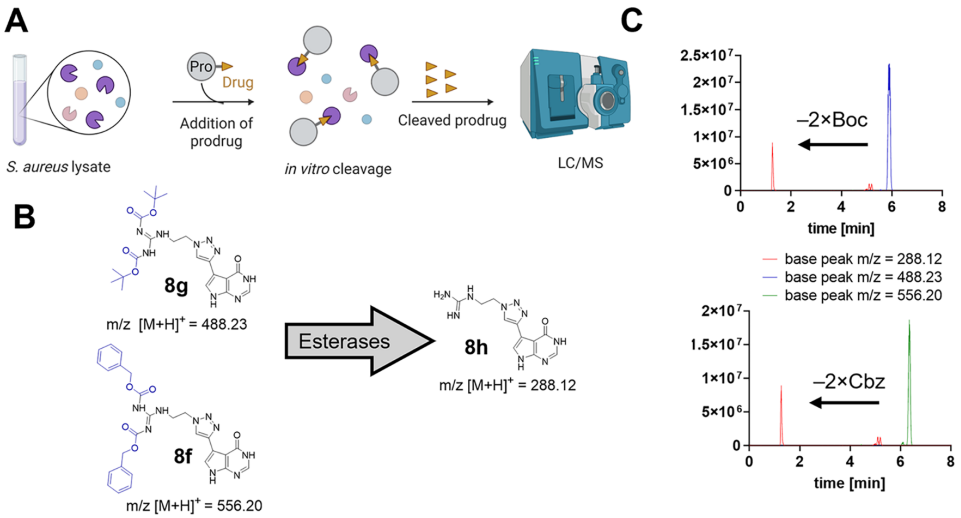


Figure 7. Carbamate-containing synthetic intermediates are readily cleaved by an *S. aureus* cell lysate. (A) Methodology of the conducted prodrug cleavage assay. (B) Structures and calculated masses of carbamates **8f**, **8g**, and for the deprotected hit compound **8h**. (C) LC/MS base-peak chromatograms of *S. aureus* lysates treated with **8f** or **8g** (400 μM) for 16 h. Detailed results of reference and base-peak chromatograms can be found in Figure S17.

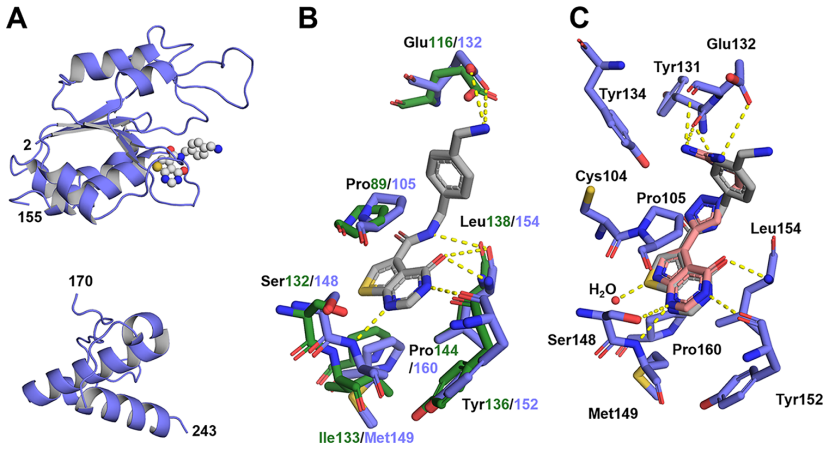


Figure 8. Crystal structures of compounds **2** and **8h** binding to *S. aureus* TrmD. (A) Structure of *S. aureus* TrmD bound to **2**. The protein is depicted as a violet-blue cartoon, and the ligand's carbon atoms as gray spheres. (B) Compound **2** bound to *S. aureus* TrmD (PDB: 9SDV) overlaid with *H. influenzae* TrmD (PDB: 4MCC) binding pocket amino acids. (C) Overlay of **2** (PDB: 9SDV) and **8h** (PDB: 9SDW) in the *S. aureus* binding pocket. Ligands and amino acids are shown in stick representation; polar interactions are shown as yellow lines, and water as red spheres. The carbon atoms of **2** are shown in gray and those of compound **8h** in salmon. Interacting residues are displayed in violet-blue (*S. aureus*) or dark green (*H. influenzae*).

by cytosolic esterases might catalyze the transformation of **8f** (di-Cbz) to **8h** (free guanidine), the potent TrmD inhibitor, suggesting that **8f** might function as a more permeable prodrug.[37−40]

To test this hypothesis, we investigated whether carbamates **8f** and **8g** can be cleaved by total *S. aureus* lysates. A native *S. aureus* RN4220 lysate was prepared and incubated for 16 h with carbamates **8f** and **8g** (c = 400 μM), followed by LC/MS base-peak analysis of the lysate (Figure 7A). Interestingly, both carbamates **8f** and **8g** were readily cleaved in the presence of the lysate, yielding the production of hit compound **8h**, which could be detected in both lysates (Figure 7C). Both di-Boc and di-Cbz prodrugs appeared to be cleaved to a similar degree (~30%) even at the very high concentration of 400 μM.

In this context, single Boc- or Cbz-conjugated guanidines as intermediary deprotection products were not found by LC/MS analysis. Detailed results of reference and base-peak chromatograms can be found in Figure S17. Since carbamate **8g** (di-Boc) was found to be cleaved in the bacterial lysate, too, its lower antistaphylococcal potency in *S. aureus* experiments might be due to lower permeability compared to **8f** (di-Cbz). In summary, we were able to effectively reduce the growth of *S. aureus* cells with **8f**, which was not the primary end point of the nanoSAR optimization, but potentially acts as a *S. aureus*

https://doi.org/10.1021/acs.jmedchem.5c02323
J. Med. Chem. 2025, 68, 26246−26262

carbamate prodrug, which is metabolized by *S. aureus* cells to yield the actual inhibitor **8h** through cleavage of the di-Cbz carbamate.

Previous studies on TrmD inhibitors have also demonstrated that the incorporation of lipophilic moieties enhances antibacterial efficacy compared to analogous compounds lacking such features, which were not effective in the Gram-positive bacterium *S. aureus*.[14,16] Thus, far, lipophilic tags of this Cbz-carbamate type have not been applied as prodrugs in contexts where the differences between IC_{50}-values and MICs were mechanistically explainable. Our findings suggest that, through prodrug strategies, *S. aureus* TrmD can be more effectively targeted, demonstrating that TrmD can, in principle, be targeted with more permeable inhibitors.

To further validate our prodrug hypothesis *in vivo*, we next investigated the intracellular formation of the active TrmD inhibitor **8h** in growing *S. aureus* cells by LC/MS-based quantification. Bacterial cultures were treated with sublethal concentrations (4 μM) of compounds **8f**, **8g**, and **8h**, respectively, followed by cell harvesting and metabolite extraction. Remarkably, only treatment with the di-Cbz carbamate **8f** resulted in detectable intracellular levels of **8h**, while no formation of **8h** could be observed upon treatment with equimolar concentrations of **8g** or **8h** (Figure S18). This finding is in line with our prodrug hypothesis, demonstrating that **8f** undergoes enzymatic cleavage in *S. aureus* cells *in vivo* to release the active TrmD inhibitor **8h**. The absence of measurable intracellular **8h** upon direct treatment with **8h** or **8g** suggests limited uptake of these more polar species, further supporting that the improved antibacterial efficacy of **8f** originates from its enhanced permeability combined with intracellular prodrug activation.

Crystal Structures of TrmD-Inhibitor Complexes. To date, no ligand-bound structure of *S. aureus* TrmD has been reported, with the PDB containing only one apo structure (PDB: 3KY7) of this enzyme.[41] To analyze the binding mode of the compounds identified in the nanoSAR study and to guide future inhibitor optimization, we cocrystallized *S. aureus* TrmD with inhibitor **2** and the new TrmD inhibitor **8h.**

The cocrystal structure of **2** (Figure 8A) was solved at a resolution of 2.5 Å in the space group $P4_32$, containing one protein molecule per asymmetric unit. The structure exhibited a fold similar to that of the apo *S. aureus* TrmD structure (PDB: 3KY7) and other members of the SPOUT-class TrmD enzymes, as reflected by an overall C_α RMSD of 0.50 Å (Figure S19A). The N- and C-terminal domains of the monomer were resolved, but the highly flexible linker connecting the domains could not be resolved, similar to many published TrmD structures.[17,42−44] For the cocrystallized complex, the N-terminal domain showed discrete electron density for inhibitor **2** (Figure 8A, Figure S19). Comparison with the cocrystal structure of inhibitor **2** bound to *H. influenzae* TrmD (PDB: 4MCC) highlights that the structures adopted a similar fold with an overall C_α RMSD of 1.44 Å (Figure S19B). Also, the conformation and ligand interactions of **2** were found to be similar for both *H. influenzae* and *S. aureus* enzymes (Figure 8B). An ionic interaction was formed between the primary amine of **2** and Glu132 in *S. aureus* (Glu116 in *H. influenzae*), a residue highly conserved among TrmD orthologues.[8] The thienopyrimidone ring system displayed interactions with *S. aureus* Met149 (*H. influenzae* Ile133), Tyr152 (Tyr136), Leu154 (Leu138), and Pro105 (Pro89), within the conserved SAM pocket (Figure 8B).

To analyze the differences in binding affinity of parent compound **2** between the *H. influenzae* and *S. aureus* enzymes, we used the HYDE scoring function in the SeeSAR toolkit to predict favorable and unfavorable contributions of individual ligand atoms to the overall binding energy (Figure S20). The computer-aided investigation revealed that the main difference stems from the amide group interactions, which contributed favorably to *H. influenzae* TrmD (HYDE: −3.8 kJ/mol), but unfavorably to the *S. aureus* enzyme (HYDE: +11.0 kJ/mol). This is in line with the observation that fluorescent tracer **3** (K_D = 23.3 μM), containing an amide moiety, showed lower *S. aureus* TrmD affinity to the target than tracer **4** (K_D = 659 nM), where the amide bond was omitted (Figure 2B). Additionally, the terminal amine of inhibitor **2** contributed favorably (HYDE: −3.0 kJ/mol) for the *H. influenzae* enzyme, whereas it resulted in a slightly unfavorable interaction for the *S. aureus* enzyme (HYDE: +0.3 kJ/mol). Also, these two crystallographic findings rationalize the results gleaned from the nanoSAR optimization: the transformation of amide to triazole and the transformation of benzylamine to guanidine were beneficial for *S. aureus* TrmD affinity due to their protein−ligand interactions.

To evaluate the binding interactions and conformation of hit compound **8h**, we cocrystallized this compound with the *S. aureus* TrmD (Figure 8C, Figure S21A). The structure was solved at a resolution of 2.6 Å in the space group $P4_32$. The fold compared to the apo structure (PDB: 3KY7) had an overall RMSD(C_α) of 0.51 Å (Figure S21B), indicating minimal changes in the conformation after ligand binding. For the cocrystallized complex, electron density for **8h** was visible in the SAM-binding N-terminal domain (Figure S21). A comprehensive schematic of ligand-protein interactions for compound **2** and hit compound **8h** was generated with LigPlot + (Figure S22).[45] In the ligand-binding pocket, the pyrrolopyrimidone ring of **8h** occupies a subpocket analogous to the thienopyrimidone ring system of compound **2** (Figure 8C). In both compounds, the pyrimidone N^1 nitrogen formed hydrogen bonds to the backbone of Met149; in **8h**, it additionally formed a hydrogen bond to the Ser148 side-chain hydroxyl. The pyrimidone N^3 nitrogen formed hydrogen bonds to the backbone of Tyr152 in both compounds. Likewise, the pyrimidone carbonyl oxygen interacts with the backbone of Leu154 in each compound. Unique to **8h**, the pyrrole nitrogen atom was found to interact with a water molecule inside the binding pocket, and the guanidine group of **8h** displayed ionic interactions with the side chain of Glu132, analogous to the primary amine of **2**. However, the orientation of the guanidine group differs from that of the amine, extending slightly deeper into the binding pocket and forming additional polar interactions with the backbone of Glu132 and Tyr131, rationalizing the improved affinity and selectivity for *S. aureus* TrmD.

To gain further insights into the selectivity and binding mode of parent compound **2** and compounds **8b−e,h** for the TrmD isoenzymes used in this study, molecular docking was conducted using the Glide algorithm.[46] This analysis compared TrmD structures from *H. influenzae* (PDB: 4MCC), *E. coli* (PDB: 1P9P), and the *S. aureus* structure containing compound **8h** (PDB: 9SDW). Analysis of the docking scores (Table S3) was highly consistent with the ITC and FP assay results: parent compound **2** is predicted with higher binding affinity than compounds **8b−e,h** for *H. influenzae* and *E. coli* isoenzymes, while for *S. aureus* TrmD the triazole-containing

https://doi.org/10.1021/acs.jmedchem.5c02323
J. Med. Chem. 2025, 68, 26246−26262

8b−e,h is preferred over compound **2.** Comparing the predicted poses, in general for compounds **8b−e,h**, we found either ionic interactions between Glu132 and the basic moieties (guanidine and amine) of the inhibitor or hydrophobic interactions between the nonpolar aliphatic and aromatic proportions of the ligand with the binding pocket (Figure S24). The relative affinity differences between TrmD isoenzymes, aside from the scaffold exchange from thienopyrimidone to pyrrolopyrimidone, likely arise from linker-dependent differences in positioning (azide vs amide), which modulate interactions of the azide/amide moiety and the placement of azide-connected substituents within the pocket. This is reflected in both docking scores (Table S3) and predicted poses (Figure S24).

Notably, Tyr134 in *S. aureus* is positioned close to the substituents of the compounds; for example, the side chain oxygen lies only 5.2 Å from the guanidine group carbon of compound **8h**. As this residue is replaced by isoleucine in the *H. influenzae* and *E. coli* isoenzymes, selectivity might be enhanced by targeting this position. In addition, Cys104, which is not conserved in TrmD isoenzymes, is located near the ligands, and addressing this residue with a covalent warhead could further increase selectivity.[8]

CONCLUSION

In this work, we employed a nanoSAR triazole synthesis strategy coupled with a direct-to-biology FP read-out assay to develop affine and selective *S. aureus* TrmD inhibitors. This screening pipeline identified five hit compounds, which exhibited IC_{50}-values and K_D-values in the nanomolar to low micromolar range. In line with previous TrmD drug development campaigns, the identified inhibitors engage the adenine binding subpocket, and the substituents identified by nanoSAR screening expand toward the conserved acidic residue containing TrmD loop.[14,16,18−20] Ionic interactions with Glu132 (or orthologous residues) are a frequently identified interaction fingerprint of previous TrmD inhibitors.[14,16,18−20] Yet, the D2B optimization presented here was able to identify not only potent but also selective *S. aureus* TrmD inhibitors. Yet, during cellular screening, none of these initial inhibitors showed antibacterial activity against *S. aureus*, a property several disclosed TrmD inhibitors with diverse chemotypes share.[14,16,18−20] Surprisingly, one of the synthetic intermediates (**8f**, di-Cbz-masked form of **8h**) showed antimicrobial effects at low micromolar concentrations. We hypothesized that ligand permeability was preventing active inhibitors from engaging cytosolic TrmD target localization, an assumption that has been made in previous TrmD drug discovery campaigns.[14,16,18−20] In a prodrug-lysate assay, we observed that compound **8f** is indeed readily cleaved to form the active inhibitor **8h**, thereby confirming our hypothesis that **8f** might function as a prodrug of **8h**. This concept of Cbz-based prodrug might have broader applicability beyond the presented TrmD inhibitor type, both for other TrmD inhibitors incorporating amine/amidine chemotype and for a broader range of antibiotics.

Subsequently, X-ray crystallography of hit **8h** revealed its binding mode within the SAM-binding pocket of *S. aureus* TrmD, providing structural insights into key interactions. These findings will enable structure-guided optimization of this scaffold to further enhance both the affinity and selectivity of future inhibitors. In this regard, molecular modeling revealed two key targets for selectively increasing the affinity to *S. aureus* TrmD compared to other isoenzymes: Cys104 and Tyr134, which are located in close proximity to the bound ligand **8h** (PDB: 8SDW). These two residues are a unique feature of *S. aureus* TrmD and do not exist in most other TrmD isoenzymes; thus, it is conceivable that future campaigns could address these residues, for example, by covalent warheads.[8]

EXPERIMENTAL PROCEDURES

Protein Preparation and Purification. *Recombinant Expression of H. influenzae TrmD.* TrmD of *H. influenzae* was expressed as described previously.[31] In short, the pET28b(+) plasmid encoding for TrmD of *H. influenzae*, kindly provided by Se Won Suh (Addgene ID: 12665), was used to transform competent BL21 *E. coli* cells. The cells were grown in LB medium containing 50 μg/mL kanamycin at 37 °C and 160 rpm until they reached an OD_{600} of ∼0.7. After reducing the temperature to 16 °C, 0.5 mM isopropyl-β-D-1-thiogalactopyranoside (IPTG) was added to induce overexpression, which was maintained overnight. The cells were harvested by centrifugation and suspended in lysis buffer (20 mM HEPES pH 7.5, 300 mM NaCl, 0.5 mM TCEP, 5% glycerol, 0.1% polysorbate-20). Lysozyme and DNase I were added, and after a 30 min incubation on ice, the cells were lysed by sonication. Cell debris was removed by centrifugation. The supernatant was applied to a HisTrap HP column for affinity purification, pre-equilibrated in binding buffer (20 mM HEPES pH 7.5, 300 mM NaCl, 5 mM imidazole, 0.5 mM TCEP, 5% glycerol, 0.1% polysorbate-20) and washed with several column volumes of binding buffer. Afterward, the protein was eluted in elution buffer (20 mM HEPES pH 7.5, 300 mM NaCl, 500 mM imidazole, 0.5 mM TCEP, 5% glycerol, 0.1% polysorbate-20). Finally, *H. influenzae* TrmD was purified via size-exclusion chromatography (SEC), on a Superdex 16/600 75 pg SEC column equilibrated with SEC buffer (25 mM HEPES pH 7.5, 300 mM NaCl, 1 mM TCEP, 10% glycerol, 0.1% polysorbate-20). The enzyme was flash-frozen in liquid nitrogen and stored at −80 °C until further use.

Recombinant Expression of S. aureus TrmD. Expression and purification were performed similarly to *H. influenzae* TrmD, as described above. The pET28b(+) plasmid encoding for TrmD of *S. aureus*, kindly provided by Angelika Gründling, was used to transform competent BL21 *E. coli* cells. The cells were grown in LB medium containing 50 μg/mL kanamycin at 37 °C and 160 rpm until they reached an OD_{600} of ∼0.7. After reducing the temperature to 16 °C, 0.5 mM IPTG was added to induce overexpression, which was maintained overnight. The cells were harvested by centrifugation and suspended in lysis buffer (20 mM HEPES pH 7.5, 300 mM NaCl, 0.5 mM TCEP, 5% glycerol, 0.1% polysorbate-20). Lysozyme and DNase I were added, and after a 30 min incubation on ice, the cells were lysed by sonication. Cell debris was removed by centrifugation. The supernatant was applied to a HisTrap HP column for affinity purification, pre-equilibrated in binding buffer (20 mM HEPES pH 7.5, 300 mM NaCl, 5 mM imidazole, 0.5 mM TCEP, 5% glycerol, 0.1% polysorbate-20) and washed with several column volumes of binding buffer. Afterward, the protein was eluted in elution buffer (20 mM HEPES pH 7.5, 300 mM NaCl, 500 mM imidazole, 0.5 mM TCEP, 5% glycerol, 0.1% polysorbate-20). Finally, *S. aureus* TrmD was purified on a Superdex 16/600 75 pg SEC column equilibrated with SEC buffer (40 mM Tris pH 7.5, 100 mM NaCl, 10 mM $MgCl_2$, 5% Glycerol). The enzyme was flash-frozen in liquid nitrogen and stored at −80 °C until further use.

Recombinant Expression of E. coli TrmD. Bacterial strains carrying the expression pCA24N plasmid of *E. coli* TrmD were received from the Microbial Physiology Laboratory of the National Institute of Genetics in Japan (National BioResource Project). Expression and purification were performed as described in the original publication with slight adaptations.[47] The cells were grown in LB medium containing 30 μg/mL chloramphenicol at 37 °C and 160 rpm. After the cells reached an OD_{600} of ∼0.7, 1 mM IPTG was added to induce overexpression. After a 2 h incubation, the cells were harvested by centrifugation and suspended in binding buffer (50 mM sodium

https://doi.org/10.1021/acs.jmedchem.5c02323
J. Med. Chem. 2025, 68, 26246−26262

phosphate pH 7.5, 150 mM NaCl, 10 mM imidazole, 0.1% Tween 20). Lysozyme was added, and after a 30 min incubation on ice, the cells were lysed by sonication. Cell debris was removed by centrifugation. The supernatant was applied to a HisTrap HP column for affinity purification, pre-equilibrated in binding buffer, and washed with several column volumes of binding buffer. Afterward, the protein was eluted in elution buffer (50 mM sodium phosphate pH 7.5, 150 mM NaCl, 500 mM imidazole, 0.1% Tween 20). Finally, *E. coli* TrmD was mixed 1:5 with storage buffer (50 mM sodium phosphate pH 8.0, 300 mM NaCl, 2 mM DTT, 1 mM EDTA, 0.1% Tween 20, 60% Glycerol). The enzyme was flash-frozen in liquid nitrogen and stored at −20 °C until further use.

Recombinant Expression of Human Trm5. A pET-28a(+) plasmid encoding a truncated construct of Trm5 (aa 66−475), with flexible termini omitted, carrying the putative RNA and SAH binding sites, was used to transform competent *E. coli* Rosetta2 (DE3) cells. The cells were grown at 37 °C and 160 rpm in LB medium containing 50 μg/mL kanamycin and 25 μg/mL chloramphenicol. After reaching an OD_{600} of ∼0.7. The temperature was reduced to 18 °C. 0.2 mM IPTG was added to induce overexpression, and the cells were incubated overnight. After harvesting the bacteria by centrifugation, these were suspended in lysis buffer (50 mM Tris HCl, 500 mM sodium chloride, 1 mM β-mercaptoethanol, 0.5 mM PMSF, 5% glycerol, pH 7.5). A protease inhibitor tablet (cOmplete) was added, and the cells were lysed by sonication. After removing the cell debris by centrifugation, the supernatant was applied to a HisTrap FF column for affinity purification, pre-equilibrated in binding buffer (20 mM Tris HCl, 500 mM sodium chloride, 1 mM β-mercaptoethanol, 0.5 mM PMSF, 25 mM imidazole, 5% glycerol, pH 7.5). After washing the column with several column volumes of binding buffer, the protein was eluted in elution buffer (20 mM Tris HCl, 500 mM sodium chloride, 1 mM β-mercaptoethanol, 0.5 mM PMSF, 250 mM imidazole, 5% glycerol, pH 7.5). As a final purification step, Trm5 was purified on a Superdex 16/600 75 pg SEC column equilibrated with SEC buffer (20 mM HEPES, 250 mM sodium chloride, 10 mM β-mercaptoethanol, 10% glycerol, pH 7.5). The enzyme was flash-frozen in liquid nitrogen and stored at −80 °C until further use.

Fluorescence Polarization (FP) Assays. Fluorescence polarization (FP) assays were performed as follows. The assays for *H. influenzae* TrmD have been described previously.[31] All assays were conducted in technical triplicate using black 96-well half area plates. For the FP assays, a tracer (20 nM CySTPD[31] for *E. coli* and *H. influenzae* TrmD, 10 nM tracer **4** for *S. aureus* TrmD) was mixed with the respective enzyme (2 μM *E. coli* TrmD, 2 μM *H. influenzae* TrmD, 500 nM *S. aureus* TrmD) in buffer (*E. coli* and *H. influenzae* TrmD: 50 mM HEPES, 500 mM NaCl, 5% Glycerol, pH 7.5, *S. aureus* TrmD: 40 mM Tris HCl, 100 mM NaCl, 10 mM $MgCl_2$, 5% Glycerol, pH 7.5). The compounds were added in varying concentrations for K_D-value determination. For K_D-value determination of tracers, the enzyme concentration was varied, and no inhibitory compounds were added (DMSO < 0.5% for TrmDs). The Z-factor for tracer **4** was determined by measuring 48 replicates of the free tracer (positive controls, PC) and 48 replicates of a mixture of enzyme and tracer (negative controls, NC). The *Z*-factor is defined in terms of the means (μ) and standard deviations (σ) of the positive and negative controls and calculated as $Z = 1-(3*(\sigma_{nc} + \sigma_{pc})/(\mu_{nc}-\mu_{pc}))$. Fluorescence polarization was measured using a Spark 10 M plate reader (Tecan) equipped with polarization filters and a monochromator setup (λ_{ex} = 635 nm, λ_{em} = 680 nm). Polarization values (mP) were determined from polarization-specific parallel and orthogonal fluorescence intensities. K_D-values were calculated in GraphPad Prism 8.0.1 using the four-parameter Hill equation: y(% tracer bound) = bottom + ([ligand]slope) × (top−bottom)/([ligand]slope + $K_D$slope).

Aptamer-Based MTase Enzyme Inhibition Assay. For the determination of *S. aureus* TrmD IC_{50}-values, a split aptamer assay according to Nidoieva et al. was employed.[33] The assay was performed in 40 mM Tris HCl, 100 mM NaCl, 10 mM $MgCl_2$, 5% Glycerol, pH 7.5. Enzyme reaction mixtures contained synthetic $tRNA^{LeuCAG}$ substrate (synthetic $tRNA^{Leu}$: 5′-GCGAAGGUGGCGGAAUUGGUAGACGCGCUAGCUUCAGGUGUUAGUGUCCUUACGGACGUGGGGGUUCAAGUCCCCCCCCUCGCACCA-3′, Genscript, final concentration: 2 μM), *S. aureus* TrmD (final concentration: 100 nM), SAM (New England Biolabs, final concentration: 2 μM), and the test compounds in varying concentrations (3% DMSO, final volume 10 μL). Pure DMSO was used as a mock treatment reaction control. The assay was carried out in triplicate in black 384-well plates (Greiner). Enzyme reactions were quenched by the addition of 1 μL SDS (3%) after an incubation time of 60 min at room temperature. Subsequently, the aptamer detection mix described in Nidoieva et al. was added to the reactions, and samples were measured using a Tecan Spark 10 M plate reader equipped with a monochromator setup (λ_{ex} = 485 nm; λ_{em} = 600 nm) exported for statistical analysis and plotting in GraphPad Prism 8.0.1.

^{3}H-based MTase Enzyme Inhibition Assay. ^{3}H-based inhibition assays for TrmD *S. aureus* were performed in 50 mM HEPES, 5 mM $MgCl_2$, 80 mM NaCl, 0.005% Tween-20, 1 mM DTT, pH 7.5 buffer; and for Trm5[48] in 100 mM Tris-HCl, 0.1 mM EDTA, 6 mM $MgCl_2$, 100 mM KCl, 2 mM DTT, pH 7.4. The reaction mixture contained for *S. aureus* TrmD: 1 μM synthetic $tRNA^{Leu}$ (Genscript, see above) and 100 nM *S. aureus* TrmD; For human Trm5:10 μM synthetic $tRNA^{Leu}$ and 1.5 μM Trm5. Compounds were screened for *S. aureus* TrmD at 1 μM and for Trm5 at 30 μM. The enzymatic reactions were started by the addition of SAM as a mixture of ^{3}H-SAM (Hartmann Analytics, *S. aureus* TrmD: 0.5 μM, Trm5: 2 μM) and cold SAM (New England Biolabs, *S. aureus* TrmD: 0.5 μM, Trm5: 98 μM) to a final activity of 0.04 μCi μL^{-1} (TrmD) or 0.16 μCi μL^{-1} (Trm5). The reaction mixtures were incubated in duplicate for 60 min (TrmD)/30 min (Trm5) at 37 °C. As a negative control, the reaction mixture without the enzyme was used, and as a positive control, the reaction mixture without the test compound was used. After the enzyme incubation time, aliquots of 8 μL were taken from the reaction mixture and spotted on Whatman glass microfiber filters (GF/C, 25 mm). The tRNA was precipitated on the filters with 5% ice-cold TCA for 15 min. The filters were washed twice with 5% TCA at room temperature for 20 and 10 min, and once in EtOH for 10 min. After drying, the filters were transferred into scintillation vials with 3 mL of PerkinElmer Gold MV liquid scintillation cocktail. Scintillation was measured with a scintillation counter (TriCarb Liquid Scintillation Analyzer 4810TR; measurement time of 1 min).

Isothermal Titration Calorimetry (ITC). Experiments were conducted in the *S. aureus* TrmD SEC buffer (40 mM Tris, pH 7.5, 100 mM NaCl, 10 mM $MgCl_2$, 5% glycerol) for the *S. aureus* enzyme. The *H. influenzae* enzyme was buffer exchanged into its ITC buffer (50 mM HEPES, pH 7.5; 500 mM NaCl; 5% glycerol) using Amicon Ultra-15 centrifugal filter units (Merck) prior to use. Compound **1** (BLD Pharmatech) and compound **2** were dissolved in DMSO to a final concentration of 20.0 and 11.6 mM, respectively, and diluted in ITC buffer to give ligand solutions at 1 and 0.58 mM, respectively. Due to a low enthalpy signal, a low c-value titration was performed for compound **1**. In this type of experiment, the ligand is typically added at high concentration and in large excess relative to its binding partner, driving more binding events per injection. This causes the equivalence point to be reached after only a few injections and leads to the loss of the characteristic sigmoidal binding curve. TrmD was diluted to a final concentration of 50 μM, and DMSO was added to a final concentration of 5% to match the buffers. ITC measurements were performed using a MicroCal PEAQ-ITC Automated workstation (Malvern Panalytical) equipped with a 200 μL Hastelloy cell and a 40 μL injection syringe. The experiments were conducted in duplicates at 25 °C with a stirring speed of 750 rpm and a reference power of 42 μW. Each titration consisted of 19 injections of 2 μL compound solution, delivered into the cell containing 50 μM TrmD at 0.5 μL/s, with 150 s between injections. Control experiments were performed by titrating ligands into the ITC buffer. Data were analyzed and fitted using the MicroCal PEAQ-ITC Analysis Software 1.21 and plotted in GraphPad Prism 8.0.1.

Bacterial Growth Inhibition Assays. Compounds were dissolved in DMSO to a final concentration of 20 mM. To determine the compound's activity against different bacteria, a bacterial culture

https://doi.org/10.1021/acs.jmedchem.5c02323
J. Med. Chem. 2025, 68, 26246−26262

(*E. coli* ATCC10536, *S. aureus* RN4220) was set up to an optical density at 600 nm (OD_{600}) of 0.05 from an overnight culture in Mueller-Hinton broth (Carl Roth). The compound was added in different concentrations ranging from 400 μM to 1 μM. DMSO concentration was constantly adjusted to be 1% in the final culture. Cultures of 200 μL were incubated for 24 h at 37 °C in flat-bottom 96-well polystyrene culture plates (Greiner) using a BioTek Synergy H1 plate reader. Plates were incubated under constant shaking, and absorbance at 600 nm was measured every 20 min. The experiment was performed in three biological replicates with three technical replicates each. For the statistics, two-way ANOVA with Dunnett's multiple comparisons test was used because results were affected by two factors (time and compound concentration). As all results were compared to an untreated sample, Dunnett's test was used to correct for multiple comparisons using a confidence interval of 95%. Time points 360 min (6 h), 720 min (12 h), and 1440 min (24 h) were chosen and analyzed using GraphPad PRISM (10.4.2).

To determine the minimal bactericidal concentration of the substances, bacterial cultures were prepared as in the bacterial growth inhibition assay but incubated statically at 37 °C. A serial dilution of the initial culture was made and plated on a TSB agar plate to determine the CFU/mL of the original culture. After 24 h, the cultures were diluted again and plated. Bacterial colonies were counted, and the CFU/mL was calculated. The experiment was performed in n = 3 biological replicates. Data evaluation was done using GraphPad Prism. One-way ANOVA with Dunnett's multiple comparisons test was used for statistical analysis, and all samples were compared to the starting CFU/mL.

Cell Titer Glo Cell Viability Assay. Cell viability assays were conducted with HEK293 cells (ATCC) to investigate the compounds' mammalian cytotoxicity. Cells were cultured according to standard protocols (DMEM, 10% FBS, 1× Penicillin/Streptomycin, 37 °C, 5% CO_2). Cell viability was assessed using the Promega CellTiterGlo assay kit. Briefly, 1000 cells were seeded in white half a rea 96-well plates (Greiner) and incubated for 48 h with inhibitors from DMSO stocks (final: 0.1% DMSO) under standard cultivation conditions. Then, the cell titer reagent was added to each well according to the manufacturer's protocols, and luminescence was measured using a Tecan Spark 10 M plate reader.

Bacterial Lysate Carbamate Cleavage Assays. An overnight culture of *S. aureus* RN4220 was set up in TSB medium (BD Bacto Tryptic Soy Broth). The next day, a 150 mL day culture was started at an initial OD_{600} of 0.1. The culture was incubated at 200 rpm shaking at 37 °C. The bacteria were harvested after 3 h and 40 min (OD_{600} = 3.30). A 1 mL aliquot was retained to determine cell number. 150 mL of the culture was centrifuged at 4000 rpm for 10 min at 4 °C. The resulting pellet was resuspended in 10 mL of JB Lysis Buffer (0.1% Triton X-100, 20 mM Tris-HCl, 150 mM KCl, 1 mM $MgCl_2$, 1 mM DTT, and protease inhibitors) and transferred to FastPrep tubes. Cells were mechanically lysed (2 × 30 s, 6.5 m/s) and cooled for 5 min on ice. The samples were centrifuged, and the supernatant was transferred to a new tube. Subsequently, it was centrifuged again at 5000 rpm for 30 min at 4 °C. The pellet was washed three times with 1× PBS, reducing the volume to 1 mL. Protein concentration was determined using the Pierce BCA Protein Assay Kit (Thermo Scientific). The final sample was frozen in liquid nitrogen and stored at −80 °C. 100 μL of this lysate was incubated with **8f−h** (final concentration 400 μM, 2% DMSO) for 16 h at 30 °C. Afterward, 100 μL acetonitrile was added, and the samples were passed through a syringe filter. Ten μL of the samples were injected during LC/MS (Agilent 1100 system, LC/MSD trap) using an Agilent Poroshell 120 EC-C18 150 × 2.10 mm 4 μm column; mobile phase (gradient: acetonitrile/H_2O, 0.1% formic acid). The LC/MS chromatograms and their corresponding mass spectra (base-peak) were analyzed using MestReNova (12.0.4) for prodrug deprotection products.

***S. aureus* Inhibitor Uptake Assay.** An overnight culture of *S. aureus* RN4220 was set up in Müller-Hinton medium. The next day, a 100 mL day culture with 4 μM of compound (**8f**, **8g**, **8h**, or DMSO) was started at an initial OD_{600} of 0.05. The culture was incubated at 200 rpm shaking at 37 °C. The total bacterial culture was harvested after reaching an OD_{600} of 0.3 by centrifugation at 4,000 rpm for 10 min at 4 °C. The resulting pellet was washed twice with 1× PBS, then resuspended in 1 mL of JB Lysis Buffer (0.1% Triton X-100, 20 mM Tris-HCl, 150 mM KCl, 1 mM $MgCl_2$, 1 mM DTT, and protease inhibitors) and transferred to Lysis matrix E tubes. Cells were mechanically lysed by Fast prep (2 × 30 s, 6.5 m/s) and cooled for 5 min on ice. The samples were centrifuged, and the supernatants were transferred to a new tube. Subsequently, they were centrifuged again at 5000 rpm for 30 min at 4 °C. The resulting pellet was washed twice with 1× PBS, reducing the volume to 100 μL, while the resulting supernatant was cleared once more by centrifugation. The samples were frozen in liquid nitrogen and stored at −80 °C. The prepared lysates were loaded on a solid-phase extraction cartridge (C18 Chromabond, Macherey-Nagel) and eluted with 30% ACN in water (1 mL). The collected eluate was lyophilized and resolved in 100 μL ACN/water. 10 μL of the samples were injected during LC/MS (Waters Alliance 2695 coupled to a Waters QDa mass-sensitive detector) using an Agilent Poroshell 120 EC-C18 150 × 2.10 mm 4 μm column; mobile phase (gradient: acetonitrile/H_2O, 0.1% formic acid). The LC/MS chromatograms and their corresponding mass spectra (base-peak) were analyzed using MestReNova (12.0.4) for prodrug deprotection products.

Crystallization, Data Collection, Model Building, and Refinement. Co-crystals of the *S. aureus* TrmD protein and compounds **2** or **8h** were obtained at 20 °C with a hanging drop setup. The protein (271 μM) was incubated with compounds in 7-fold molar excess (2 mM final concentration) for 30 min on ice before crystallization. The reservoir solution contained 1.4 M Na Malonate pH 7.4, 0.1 M Bis-Tris Propane.[42] Crystallization drops consisted of 1 μL reservoir solution and 1 μL of the preincubated protein and compound. Cubic crystals grew within 2 weeks. Crystals were frozen in liquid nitrogen using 25% glycerol as the cryo-protectant. Diffraction data were collected at the Diamond Light Source Beamline I03 (Oxfordshire, U.K.). All data sets were processed with XDS[49] and scaled with AIMLESS within the CCP4[50] cloud.[50−52] The resulting data sets had a maximum resolution of 2.50 Å (Structure with compound **2**) or 2.60 Å (Structure with compound **8h**). The crystals belong to space group $P4_32$ with one TrmD molecule per asymmetric unit. The structures were solved by molecular replacement with PHASER using Apo-TrmD (PDB: 3KY7) as the search model.[53,54] The compounds were parametrized from SMILES using phenix.elbow.[55] Model building and refinement were performed with Coot, Refmac, and phenix.refine.[50,56−58] The quality of the resulting structural models was assessed using MolProbity.[59,60] Due to the high flexibility of the loop between amino acids Val175 and Ser188, this region was not modeled. Additionally, some amino acids with flexible side chains and insufficient electron density to fit the side chain were truncated to alanine residues. In the structure with compound **2**, residues Leu35, Asn36, Lys41, Arg42, Gln44, Lys48, Gln50, Lys63, Glu90, Glu193, and Lys204 were truncated. In the structure with compound **8h**, residues Asn36, Lys41, Arg42, Lys48, and His64 were truncated. The crystallographic data are summarized in Tables S1 and S2. Coordinates and structure factors are deposited at the Protein Data Bank (PDB) under accession codes: 9SDV and 9SDW.

Molecular Modeling. For molecular docking of compounds **2** and **8b−e,h**, a Glide docking protocol was conducted within the Schrödinger Maestro 2020.04 worksuite.[46] The protein structures 4MCC (*H. influenzae* TrmD) and 1P9P (*E. coli* TrmD) were downloaded from the PDB, and 9SDW was used for docking into the *S. aureus* isoenzyme. Receptor preparation was performed with the automated binding site, protonation, and energy minimization routine within Maestro "Protein preparation" and "Receptor grid generation". Energy minimization of ligands was conducted using the "LigPrep" routine. The docking protocol was performed under default parameters with standard precision settings. Ligand binding poses were visualized using PyMol.

General Synthesis Procedures. All reagents and solvents were of analytical grade quality and purchased from standard commercial suppliers. Chemicals were used without further purification unless

https://doi.org/10.1021/acs.jmedchem.5c02323
J. Med. Chem. 2025, 68, 26246−26262

otherwise noted. ^{1}H and ^{13}C spectra were recorded on Bruker Fourier 300 MHz, Bruker Avance Neo 400 MHz, and Bruker Avance III 600 MHz spectrometers. Chemical shifts δ are given in parts per million (ppm) using residual proton peaks of the solvent as the internal standard. HPLC and mass spectra were obtained by LC/MS, consisting of an 1100 series HPLC system from Agilent with an Agilent Poroshell 120 EC-C18 150 × 2.10 mm, 4 μm column. The detection wavelengths were dependent on the specific compound absorbance characteristics: 210 and 254 nm. The MTase tracers (**3** and **4**) were analyzed for their purity at 650 nm (Cy5). The molecular mass of all compounds and intermediates was analyzed by an Agilent 1100 series LC/MSD trap with electron spray ionization (ESI) in positive mode. Preparative column chromatography was performed with silica gel (0.06−0.02 mm) obtained from Macherey-Nagel or prepacked Biotage reverse-phase silica columns for flash chromatography (Biotage Isolera One) eluting with ACN/H_2O. Preparative HPLC was performed on an Agilent 1290 system with an MZ-Aqua Perfect C18 7 μm column. All compounds are >95% pure by HPLC analysis.

Protocol for the Nanomole-Scale Synthesis. A commercial azide diversity library (Enamine) containing 320 azides at a concentration of 100 mM in DMSO in a 96-well tube rack was employed for this nanoSAR study. For the reaction of the azides with alkyne **7** via CuAAC, a master mix was prepared. The master mix contained for one 96-well plate: 600 μL of a 33.33 mM sodium ascorbate solution dissolved in Milli-Q water, 200 μL of a 12.52 mM TBTA solution dissolved in DMSO, 500 μL of a 20 mM alkyne **7** solution dissolved in DMSO, 600 μL of a 4.81 mM $CuSO_4$×5 H_2O solution dissolved in Milli-Q water and 400 μL of pure DMSO. The solvents were degassed with argon to avoid oxidation of the copper(I) during the reaction. To each well of a 96-well PCR plate (Applied Biosystems MicroAmp) were added 23 μL of the master mix and 1 μL of the 100 mM azide stock. The final concentrations in the Mastermix were: 8.7 mM sodium ascorbate (8.3 mM in reaction well), 1.1 mM TBTA (1.0 mM in reaction well), 4.3 mM **7** (4.1 mM in reaction well), 1.3 mM $CuSO_4$×5 H_2O (1.2 mM in reaction well). The 96-well PCR plate was purged with argon, and the implementation of the experiments was conducted under an argon atmosphere. The reactions were mixed, centrifuged, and sealed airtight. The plate was allowed to incubate at room temperature for 16 h before the formed triazoles were investigated via FP-assays.

General Procedure for Preparative CuAAC. Compound **7** (2−5 mg, 0.013−0.031 mmol, 1.0 equiv), the respective azide (0.015−0.037 mmol, 1.2 equiv), TBTA (2−5 mg, 0.004−0.009 mmol, 0.3 equiv), copper(II)sulfate pentahydrate (1−2 mg, 0.004−0.009 mmol, 0.3 equiv), and sodium ascorbate (5−12 mg, 0.026−0.062 mmol, 2.0 equiv) were dissolved in water (500 μL) and DMSO (1.0 mL). The reaction was stirred for 16 h at room temperature under an argon atmosphere before the solvents were removed *in vacuo*. Afterward, the crude product was purified via reverse-phase flash chromatography.

*Compound **2**: N-(4-(Aminomethyl)benzyl)-4-oxo-3,4-dihydrothieno[2,3-d]pyrimidine-5-carboxamide.* 4-Oxo-3,4-dihydrothieno[2,3-*d*]pyrimidine-5-carboxylic acid (22 mg, 0.110 mmol, 1.0 equiv) and *tert*-butyl (4-(aminomethyl)benzyl)carbamate (26 mg, 0.110 mmol, 1.0 equiv) were mixed with HATU (42 mg, 0.110 mmol, 1.0 equiv) and DIPEA (60 μL, 0.343 mol, 3.0 equiv) in 4 mL anhydrous DMF. The mixture was stirred for 16 h at room temperature before the organic solvent was removed *in vacuo*. The residue was dissolved in DCM (1 mL) and TFA (1 mL) and stirred for 30 min at room temperature. The crude product was purified via flash chromatography. Yield: 17 mg, quant. ^{1}H NMR (300 MHz, MeOD) δ [ppm] = 8.40 (s, 1H), 8.18 (s, 1H), 7.52−7.43 (m, 4H), 4.66 (d, J = 2.3 Hz, 2H), 4.13 (s, 2H). ^{13}C NMR (75 MHz, MeOD) δ [ppm] = 168.9, 163.1, 161.2, 146.7, 141.0, 133.4, 132.8, 130.2, 129.4, 121.0, 44.1. LC/MS: m/z calculated for $C_{15}H_{14}N_4O_2S$ $[M + H]^+$: 315.1, found: 315.0.

*Compound **3**: 3,3-Dimethyl-1-(6-oxo-6-((3-(5-((4-oxo-3,4-dihydrothieno[2,3-d]pyrimidine-5-carboxamido)methyl)-1H-1,2,3-triazol-1-yl)propyl)amino)hexyl)-2-((1E,3E)-5-((E)-1,3,3-trimethylindolin-2-ylidene)penta-1,3-dien-1-yl)-3H-indol-1-ium trifluoroacetate.* The compound was synthesized according to the general procedure for preparative click reactions with alkyne **10** (0.63 mg, 0.0027 mmol, 1.5 equiv) and Cy5-azide (1.1 mg, 0.0018 mmol, 1.0 equiv). Yield: 1.5 mg, quant. LC/MS: m/z calculated for $C_{45}H_{52}N_9O_3S^+$ $[M + H]^{2+}$: 399.7, found: 399.6. Purity (HPLC): 98%.

*Compound **4**: 3,3-Dimethyl-1-(6-oxo-6-((3-(4-(4-oxo-4,7-dihydro-3H-pyrrolo[2,3-d]pyrimidin-5-yl)-1H-1,2,3-triazol-1-yl)propyl)amino)hexyl)-2-((1E,3E)-5-((E)-1,3,3-trimethylindolin-2-ylidene)-penta-1,3-dien-1-yl)-3H-indol-1-ium trifluoroacetate.* The compound was synthesized according to the general procedure for preparative click reactions with alkyne **7** (0.19 mg, 0.0016 mmol, 1.3 equiv) and Cy5-azide (0.7 mg, 0.0012 mmol, 1.0 equiv). LC/MS: m/z calculated for $C_{43}H_{50}N_9O_2^+$ $[M + H]^{2+}$: 362.7, found: 362.7. Purity (HPLC): 97%.

*Compound **6**: 5-((Trimethylsilyl)ethynyl)-3,7-dihydro-4H-pyrrolo[2,3-d]pyrimidin-4-one.* To a minimum volume flask was added 5-iodo-3,7-dihydro-4*H*-pyrrolo[2,3-*d*]pyrimidin-4-one (232 mg, 0.890 mmol, 1.0 equiv), CuI (34 mg, 0.178 mmol, 0.2 equiv), TMS-acetylene (190 μL, 1.832 mmol, 2.0 equiv), $Pd(PPh_3)_4$ (54 mg, 0.046 mmol, 0.05 equiv), THF (5.0 mL), DMF (2.0 mL), and triethylamine (70 μL). The reaction was stirred for 16 h at room temperature. Subsequently, the solvent was removed *in vacuo*, and the residue was dissolved in DCM (10 mL). The solution was washed with water (3 × 10 mL), and the solvent was removed. The crude product was purified via reverse-phase flash chromatography. Yield: 60 mg, 29%. ^{1}H NMR (300 MHz, DMSO-d_6) δ [ppm] = 12.17 (s, 1H), 11.86 (s, 1H), 7.84 (s, 1H), 7.39 (d, J = 2.6 Hz, 1H), 0.20 (s, 9H). ^{13}C NMR (75 MHz, DMSO) δ [ppm] = 157.5, 147.8, 144.6, 126.4, 107.2, 99.9, 98.4, 93.6, 0.1. LC/MS: m/z calculated for $C_{11}H_{13}N_3OSi$ $[M + H]^+$: 232.1, found: 231.8.

*Compound **7**: 5-Ethynyl-3,7-dihydro-4H-pyrrolo[2,3-d]-pyrimidin-4-one.* Intermediate **6** (30 mg, 0.129 mmol, 1.0 equiv) was dissolved under an argon atmosphere in anhydrous acetonitrile (5.0 mL). Subsequently, TBAF (1 M in THF, 261 μL, 0.261 mmol, 2.0 equiv) was added dropwise at 0 °C. The reaction was stirred for 1.5 h at room temperature before it was terminated by the addition of 2.0 mL of saturated ammonium chloride solution. The solution was lyophilized, and the crude product was purified via reverse-phase flash chromatography. Yield: 14 mg, 68%. ^{1}H NMR (300 MHz, DMSO-d_6) δ [ppm] = 7.85 (s, 1H), 7.38 (s, 1H), 3.90 (s, 1H). ^{13}C NMR (75 MHz, DMSO) δ [ppm] = 157.7, 147.8, 144.6, 126.1, 107.4, 97.7, 80.6, 77.9. LC/MS: m/z calculated for $C_8H_5N_3O$ $[M + H]^+$: 160.0, found: 159.9.

*Compound **8a**: N-(3-(4-(4-Oxo-4,7-dihydro-3H-pyrrolo[2,3-d]-pyrimidin-5-yl)-1H-1,2,3-triazol-1-yl)propyl)acetamide.* The compound was synthesized according to the general procedure for *in situ* click reactions and to general procedure for preparative click reactions with alkyne **7** and azide **15**. Yield (preparative): 2.0 mg, 51%. LC/MS: m/z calculated for $C_{13}H_{15}N_7O_2$ $[M + H]^+$: 302.1, found: 302.0.

*Compound **8b**: 3-((4-(4-Oxo-4,7-dihydro-3H-pyrrolo[2,3-d]-pyrimidin-5-yl)-1H-1,2,3-triazol-1-yl)methyl)benzonitrile.* The compound was synthesized according to the general procedure for preparative click reactions with alkyne **7** and commercially available 3-(azidomethyl)benzonitrile. Yield: 2.5 mg, 25%. ^{1}H NMR (400 MHz, DMSO-d_6) δ [ppm] = 8.76 (s, 1H), 7.84 (d, J = 15.0 Hz, 3H), 7.67−7.53 (m, 3H), 5.75 (s, 2H). ^{13}C NMR (101 MHz, DMSO) δ [ppm] = 143.9, 138.0, 132.8, 131.9, 131.5, 130.1, 122.9, 118.5, 118.1, 117.3, 111.7, 109.5, 104.1, 51.7. LC/MS: m/z calculated for $C_{16}H_{11}N_7O$ $[M + H]^+$: 318.1, found: 317.9. Purity (HPLC): 96%.

*Compound **8c**: 5-(1-((8,8-Difluorobicyclo[5.1.0]octan-4-yl)-methyl)-1H-1,2,3-triazol-4-yl)-3,7-dihydro-4H-pyrrolo[2,3-d]-pyrimidin-4-one.* The compound was synthesized according to the general procedure for preparative click reactions with alkyne **7** and commercially available 4-(azidomethyl)-8,8-difluorobicyclo[5.1.0]-octane. Yield: 3 mg, 28%. ^{1}H NMR (400 MHz, DMSO-d_6) δ [ppm] = 8.64 (t, J = 4.1 Hz, 1H), 7.86 (s, 1H), 7.52 (d, J = 3.0 Hz, 1H), 4.39 (d, J = 8.0 Hz, 2H), 1.96−1.41 (m, 9H), 1.21 (q, J = 13.4, 12.1 Hz, 3H). ^{13}C NMR (101 MHz, DMSO) δ [ppm] = 158.8, 148.7, 143.9, 123.1, 117.1, 109.7, 104.1, 55.4, 50.8, 44.0, 37.1, 32.0, 29.3,

https://doi.org/10.1021/acs.jmedchem.5c02323
J. Med. Chem. 2025, 68, 26246−26262

25.1, 25.0, 24.9, 20.4, 16.7. LC/MS: m/z calculated for $C_{17}H_{18}F_2N_6O$ $[M + H]^+$: 361.2, found: 361.1. Purity (HPLC): 100%.

*Compound **8d**: 5-(1-(Quinolin-6-ylmethyl)-1H-1,2,3-triazol-4-yl)-3,7-dihydro-4H-pyrrolo[2,3-d]pyrimidin-4-one.* The compound was synthesized according to the general procedure for preparative click reactions with alkyne **7** and commercially available 6-(azidomethyl)-quinoline. Yield: 6 mg, 56%. ^{1}H NMR (400 MHz, DMSO-d_6) δ [ppm] = 8.93−8.81 (m, 1H), 8.58 (t, J = 7.2 Hz, 1H), 8.26−7.49 (m, 6H), 5.92 (s, 2H). ^{13}C NMR (101 MHz, DMSO) δ [ppm] = 148.5, 143.9, 137.7, 135.2, 130.0, 129.9, 127.1, 126.9, 117.2, 117.0, 109.6, 52.3, 52.2. LC/MS: m/z calculated for $C_{18}H_{13}N_7O$ $[M + H]^+$: 344.2, found:344.0. Purity (HPLC): 99%.

*Compound **8e**: 5-(1-(((1R,2R)-2-Aminocyclopentyl)methyl)-1H-1,2,3-triazol-4-yl)-3,7-dihydro-4H-pyrrolo[2,3-d]pyrimidin-4-one.* The compound was synthesized according to the general procedure for preparative click reactions with alkyne **7** and commercially available (1*R*,2*R*)-2-(azidomethyl)cyclopentan-1-amine. Yield: 6 mg, 64%. ^{1}H NMR (400 MHz, DMSO-d_6) δ [ppm] = 8.73 (s, 1H), 7.98 (s, 2H), 7.87 (d, J = 3.5 Hz, 1H), 7.56−7.52 (m, 1H), 4.57 (dd, J = 13.7, 5.7 Hz, 1H), 4.41 (dd, J = 13.7, 9.8 Hz, 1H), 3.70−3.66 (m, 1H), 2.61 (dq, J = 13.0, 6.7 Hz, 1H), 2.02 (dh, J = 13.1, 6.1 Hz, 1H), 1.86−1.67 (m, 2H), 1.64−1.46 (m, 3H). ^{13}C NMR (101 MHz, DMSO) δ [ppm] = 158.8, 148.8, 144.0, 122.8, 117.2, 109.6, 104.1, 52.9, 48.6, 42.7, 30.0, 26.6, 20.9. LC/MS: m/z calculated for $C_{14}H_{17}N_7O$ $[M + H]^+$: 300.2, found: 300.1. Purity (HPLC): 96%.

*Compound **8f**: Di-Cbz-1-(3-(4-(4-oxo-4,7-dihydro-3H-pyrrolo-[2,3-d]pyrimidin-5-yl)-1H-1,2,3-triazol-1-yl)propyl)guanidine.* The compound was synthesized according to the general procedure for preparative click reactions with alkyne **7** and azide **13**. Yield: 4 mg, 29%. ^{1}H NMR (400 MHz, DMSO-d_6) δ [ppm] = 8.68 (s, 1H), 8.62 (t, J = 5.7 Hz, 1H), 7.85 (s, 1H), 7.54−7.52 (m, 1H), 7.38 (dd, J = 8.4, 3.5 Hz, 6H), 7.31 (d, J = 3.1 Hz, 4H), 5.19 (s, 2H), 5.00 (s, 2H), 4.59 (t, J = 5.9 Hz, 2H), 3.81 (q, J = 5.8 Hz, 2H). ^{13}C NMR (101 MHz, DMSO) δ [ppm] = 162.9, 158.8, 155.4, 152.4, 148.7, 143.9, 141.3, 136.8, 135.1, 128.6, 128.5, 128.4, 128.3, 128.0, 127.8, 123.0, 117.1, 109.8, 104.2, 67.7, 66.5, 48.1, 40.8. LC/MS: m/z calculated for $C_{27}H_{25}N_9O_5$ $[M + H]^+$: 556.2, found: 556.0. Purity (HPLC): 98%.

*Compound **8g**: Di-Boc-1-(3-(4-(4-oxo-4,7-dihydro-3H-pyrrolo-[2,3-d]pyrimidin-5-yl)-1H-1,2,3-triazol-1-yl)propyl)guanidine.* The compound was synthesized according to the general procedure for preparative click reactions with alkyne **7** and azide **14**. Yield: 9 mg, 74%. ^{1}H NMR (400 MHz, DMSO-d_6) δ [ppm] = 8.68 (s, 1H), 8.49 (t, J = 5.7 Hz, 1H), 7.85 (d, J = 3.3 Hz, 1H), 7.52 (d, J = 2.4 Hz, 1H), 4.58 (t, J = 5.9 Hz, 2H), 3.76 (q, J = 5.9 Hz, 2H), 1.45 (s, 9H), 1.36 (s, 9H). ^{13}C NMR (101 MHz, DMSO) δ [ppm] = 163.0, 158.8, 155.5, 151.7, 148.7, 143.9, 141.2, 123.0, 117.0, 109.8, 104.2, 82.9, 78.3, 48.2, 27.9, 27.6. LC/MS: m/z calculated for $C_{21}H_{29}N_9O_5$ $[M + H]^+$: 488.2, found: 488.0. Purity (HPLC): 96%.

*Compound **8h**: 1-(3-(4-(4-Oxo-4,7-dihydro-3H-pyrrolo[2,3-d]-pyrimidin-5-yl)-1H-1,2,3-triazol-1-yl)propyl)guanidine.* The compound was synthesized according to the general procedure for preparative click reactions with azide **14**. Subsequently, DCM (0.5 mL) and TFA (0.5 mL) were added to the residues, and the mixture was stirred for 30 min at room temperature. Afterward, the solvents were removed *in vacuo*, and the crude product was purified via reverse-phase flash chromatography. Yield: 3 mg, 32%. ^{1}H NMR (400 MHz, DMSO-d_6) δ [ppm] = 12.14 (s, 1H), 11.93 (d, J = 3.8 Hz, 1H), 8.73 (s, 1H), 7.87 (d, J = 3.2 Hz, 1H), 7.54 (m, 1H), 4.54 (t, J = 6.0 Hz, 2H), 3.69−3.63 (m, 2H), 2.54 (s, 1H), 1.39−1.16 (m, 2H). ^{13}C NMR (101 MHz, DMSO) δ [ppm] = 158.8, 156.9, 156.8, 148.8, 143.9, 141.3, 123.0, 117.2, 109.6, 104.1, 48.3, 40.8. LC/MS: m/z calculated for $C_{11}H_{13}N_9O$ $[M + H]^+$: 288.1, found: 288.0. Purity (HPLC): 98%.

*Compound **10**: 4-Oxo-N-(prop-2-yn-1-yl)-3,4-dihydrothieno[2,3-d]pyrimidine-5-carboxamide.* 4-Oxo-3,4-dihydrothieno[2,3-*d*]-pyrimidine-5-carboxylic acid (12 mg, 0.061 mmol, 1.0 equiv), DIPEA (43 μL, 0.244 mmol, 4.0 equiv), and HATU (23 mg, 0.061 mmol, 1.0 equiv) were dissolved in 3 mL anhydrous DCM. The mixture was stirred for 15 min at room temperature before propargylamine (5 μL, 0.073 mmol, 1.2 equiv) was added in one portion. The reaction was stirred for 16 h at room temperature. The reaction mixture was washed with a saturated sodium bicarbonate solution and 1 M HCl. The crude reaction mixture was purified via reverse-phase flash chromatography. Yield: 11 mg, 77%. ^{1}H NMR (300 MHz, DMSO-d_6) δ [ppm] = 8.39 (s, 1H), 8.29 (s, 1H), 4.13 (dd, J = 5.1, 2.5 Hz, 2H), 3.17 (t, J = 2.5 Hz, 1H). ^{13}C NMR (75 MHz, DMSO) δ [ppm] = 167.1, 159.9, 159.6, 146.0, 131.8, 131.6, 119.2, 80.6, 73.5, 28.5. LC/MS: m/z calculated for $C_{10}H_7N_3O_2S$ $[M + H]^+$: 234.0, found: 233.9.

*Compound **12**: 2-Azidoethan-1-amine.* 2-Chloroethylamine hydrochloride (100 mg, 0.862 mmol, 1.0 equiv) was dissolved in water (5.0 mL). Sodium azide (168 mg, 2.586 mmol, 3.0 equiv) was added, and the reaction was allowed to stir for 12 h at 90 °C. Subsequently, a 15% potassium hydroxide solution (8.0 mL) was added, and the product was extracted with diethyl ether. The organic solvent was removed *in vacuo*. Yield: 85 mg, quant. ^{1}H NMR (300 MHz, C*D*Cl$_3$) δ [ppm] = 3.36 (t, J = 5.7 Hz, 2H), 2.87 (t, J = 5.7 Hz, 2H), 1.51 (s, 2H). ^{13}C NMR (75 MHz, CDCl$_3$) δ [ppm] = 77.5, 77.1, 76.6, 54.6, 53.5, 41.4.

*Compound **13**: Benzyl N-[(1Z)-[(2-azidoethyl)amino]-({[(benzyloxy)carbonyl]amino}) methylidene]carbamate.* *N,N′*-Di-Cbz-1*H*-pyrazol-1-carbamidine (380 mg, 1.005 mmol, 1.0 equiv) was dissolved in THF (2.0 mL), and **12** (185 mg, 2.150 mmol, 2.2 equiv) in THF (2.0 mL) was added dropwise. One drop of triethylamine was added, and the reaction was allowed to stir for 16 h at room temperature. The solvent was removed *in vacuo*, and the crude product was purified via reverse-phase flash chromatography. Yield: 357 mg, 90%. ^{1}H NMR (300 MHz, C*D*Cl$_3$) δ [ppm] = 8.54 (s, 1H), 7.34−7.14 (m, 10H), 5.06 (d, J = 11.0 Hz, SH), 3.43 (dt, J = 33.8, 5.2 Hz, 4H). ^{13}C NMR (75 MHz, CDCl$_3$) δ [ppm] = 163.0, 156.0, 153.6, 136.4, 134.4, 128.8, 128.6, 128.42, 128.35, 128.1, 128.0, 68.3, 67.3, 50.1, 40.3. LC/MS: m/z calculated for $C_{19}H_{20}N_6O_4$ $[M + H]^+$: 397.2, found: 397.1.

*Compound **14**: [N,N′-Bis(tert-butoxycarbonyl)-N″-2-azidoethyl]-guanidine.* *N,N′*-Di-Boc-1*H*-pyrazol-1-carbamidine (310 mg, 1.005 mmol, 1.0 equiv) was dissolved in THF (2.0 mL), and **12** (85 mg, 1.000 mmol, 1.0 equiv) in THF (1.0 mL) was added dropwise. One drop of triethylamine was added, and the reaction was allowed to stir for 72 h at room temperature. The solvent was removed *in vacuo*, and the crude product was purified via reverse-phase flash chromatography. Yield: 153 mg, 47%. ^{1}H NMR (300 MHz, DMSO-d_6) δ [ppm] = 3.49 (s, 4H), 3.37 (s, 2H), 1.48 (d, J = 3.9 Hz, 9H), 1.39 (s, 9H). ^{13}C NMR (75 MHz, DMSO) δ [ppm] = 83.1, 78.3, 49.4, 28.0, 27.6. LC/MS: m/z calculated for $C_{13}H_{24}N_6O_4$ $[M + H]^+$: 329.2, found: 329.0.

*Compound **15**: N-(3-Azidopropyl)acetamide.* 3-Azidopropan-1-amine (20 mg, 0.200 mmol, 1.0 equiv), acetic anhydride (30 mg, 0.249 mmol, 1.5 equiv), and acetic acid (40 μL) were mixed at room temperature. The reaction was left to stand for 3 min, then 1.0 mL acetonitrile was added, and the mixture was lyophilized. Yield: 22 mg, 77%. ^{1}H NMR (300 MHz, C*D*Cl$_3$) δ [ppm] = 3.32 (dt, J = 16.9, 6.6 Hz, 4H), 1.96 (s, 3H), 1.77 (p, J = 6.7 Hz, 2H). ^{13}C NMR (75 MHz, CDCl$_3$) δ [ppm] = 170.6, 49.4, 37.3, 28.8, 23.3. LC/MS: m/z calculated for $C_5H_{10}N_4O$ $[M + H]^+$: 143.1, found: 143.0.

■ ASSOCIATED CONTENT

Supporting Information

The Supporting Information is available free of charge at https://pubs.acs.org/doi/10.1021/acs.jmedchem.5c02323.

Supplementary results, NMR, and LC/MS spectra (PDF)

Supplementary Data set including azide library decoding and SMILES strings (XLSX)

Molecular formula strings and associated biochemical and biological data (CSV)

https://doi.org/10.1021/acs.jmedchem.5c02323
J. Med. Chem. 2025, 68, 26246−26262

Accession Codes

PDB ID Code: Coordinates and structure factors have been deposited at the PDB with PDB codes: 9SDV and 9SDW. The authors will release the atomic coordinates upon article publication.

AUTHOR INFORMATION

Corresponding Author

Fabian Barthels − *Institute of Pharmaceutical and Biomedical Sciences, Johannes Gutenberg-University, 55128 Mainz, Germany;* orcid.org/0000-0001-7950-2158; Email: barthels@uni-mainz.de

Authors

Ariane F. Hübner − *Institute of Pharmaceutical and Biomedical Sciences, Johannes Gutenberg-University, 55128 Mainz, Germany*

Annabelle C. Weldert − *Institute of Pharmaceutical and Biomedical Sciences, Johannes Gutenberg-University, 55128 Mainz, Germany;* orcid.org/0009-0001-5016-0286

Tessa Marciniak − *Institute of Molecular Infection Biology, University of Würzburg, 97080 Würzburg, Germany*

Florian Hof − *Institute of Molecular Physiology, Johannes Gutenberg-University, 55128 Mainz, Germany;* orcid.org/0000-0002-6438-1784

Vivien S. Beck − *Institute of Molecular Infection Biology, University of Würzburg, 97080 Würzburg, Germany*

Samuel Carien − *Institute of Molecular Infection Biology, University of Würzburg, 97080 Würzburg, Germany*

Sophie N. Mulartschyk − *Institute of Pharmaceutical and Biomedical Sciences, Johannes Gutenberg-University, 55128 Mainz, Germany*

Eva Wolf − *Institute of Molecular Physiology, Johannes Gutenberg-University, 55128 Mainz, Germany*

Wilma Ziebuhr − *Institute of Molecular Infection Biology, University of Würzburg, 97080 Würzburg, Germany*

Complete contact information is available at: https://pubs.acs.org/10.1021/acs.jmedchem.5c02323

Author Contributions

[‖]The authors A.F.H. and A.C.W. contributed equally. The manuscript was written through the contributions of all authors. All authors have approved the final version of the manuscript.

Notes

The authors declare no competing financial interest.

ACKNOWLEDGMENTS

We would like to thank Angelika Gründling (Imperial College London, United Kingdom) for the gift of the *S. aureus* TrmD expression plasmid. The authors would like to thank Diamond Light Source for beamtime and the staff of beamline I03 for assistance with crystal testing and data collection. Further, we thank Dr. Andreas Krämer and Dr. Adarsh Kumar for their support during the measurements at the Diamond Light Source. Also, we would like to thank Dr. Michael Klein for assisting while generating figures with BioRender.com. Wilma Ziebuhr acknowledges financial support by the German Research Foundation (DFG) grant DFG-ZI665-3-2. Fabian Barthels acknowledges financial support by the DFG in the framework of the Transregio Collaborative Research Center RMAP (TRR319 RMaP) seed funding.

ABBREVIATIONS USED

ACN,acetonitrile; ANOVA,analysis of variance; CuAAC,copper-catalyzed alkyne−azide click reaction; D2B,direct-to-biology; DCM,dichloromethane; DIPEA,*N*,*N*-diisopropylethylamine; DMF,dimethylformamide; DMSO,dimethyl sulfoxide; FP,fluorescence polarization; HATU,*O*-(7-azabenzotriazol-1-yl)-*N*,*N*,*N*′,*N*′-tetramethyluronium hexafluorphosphate; HEPES,2-[4-(2-hydroxyethyl)piperazin-1-yl]ethanesulfonic acid; IPTG,isopropyl-*β*-D-1-thiogalactopyranoside; ITC,isothermal titration calorimetry; LB,lysogeny broth; m^1G,N^1-methylguanosine; MBC,minimum bactericial concentration; MTase,methyltransferase; NC,negative control; n. d.,not determined; PC,positive control PMSF, phenylmethylsulfonyl fluoride; quant.,quantitative; rt,room temperature; SAH,*S*-adenosylhomocysteine; SAM,*S*-adenosylmethionine; SEC,size exclusion chromatography; SPOUT,trefoil knot protein fold; TBAF,tetra-*n*-butylammonium fluoride; TBTA,*tris*((1-benzyl-4-triazolyl)methyl)amine; TCEP,*tris*(2-carboxyethyl)-phosphine; TFA,trifluoroacetic acid; THF,tetrahydrofuran; TrmD,tRNA (guanine-N^1-)-methyltransferase

REFERENCES

(1) Cheung, G. Y. C.; Bae, J. S.; Otto, M. Pathogenicity and virulence of *Staphylococcus aureus*. *Virulence* **2021**, *12*, 547−569.

(2) Kourtis, A. P.; Hatfield, K.; Baggs, J.; Mu, Y.; See, I.; Epson, E.; Nadle, J.; Kainer, M. A.; Dumyati, G.; Petit, S.; et al. Vital Signs: Epidemiology and Recent Trends in Methicillin-Resistant and in Methicillin-Susceptible *Staphylococcus aureus* Bloodstream Infections — United States. *MMWR. Morb. Mortal. Wkly. Rep.* **2019**, *68*, 214−219.

(3) Naghavi, M.; Vollset, S. E.; Ikuta, K. S.; Swetschinski, L. R.; Gray, A. P.; Wool, E. E.; Robles Aguilar, G.; Mestrovic, T.; Smith, G.; Han, C.; et al. Global burden of bacterial antimicrobial resistance 1990−2021: a systematic analysis with forecasts to 2050. *Lancet* **2024**, *404*, 1199−1226.

(4) Murray, C. J. L.; Ikuta, K. S.; Sharara, F.; Swetschinski, L.; Robles Aguilar, G.; Gray, A.; Han, C.; Bisignano, C.; Rao, P.; Wool, E.; et al. Global burden of bacterial antimicrobial resistance in 2019: a systematic analysis. *Lancet* **2022**, *399*, 629−655.

(5) Forsyth, R. A.; Haselbeck, R. J.; Ohlsen, K. L.; Yamamoto, R. T.; Xu, H.; Trawick, J. D.; Wall, D.; Wang, L.; Brown-Driver, V.; Froelich, J. M.; et al. A genome-wide strategy for the identification of essential genes in *Staphylococcus aureus*. *Mol. Microbiol.* **2002**, *43*, 1387−1400.

(6) Byström, A. S.; Björk, G. R. Chromosomal location and cloning of the gene (trmD) responsible for the synthesis of tRNA (m1G) methyltransferase in *Escherichia coli* K-12. *Mol. Gen. Genet.* **1982**, *188*, 440−446.

(7) Byström, A. S.; Björk, G. R. The structural gene (trmD) for the tRNA(m1G)methyltransferase is part of a four polypeptide operon in *Escherichia coli* K-12. *Mol. Gen. Genet.* **1982**, *188*, 447−454.

(8) Zhang, Y.; Agrebi, R.; Bellows, L. E.; Collet, J.-F.; Kaever, V.; Gründling, A. Evolutionary Adaptation of the Essential tRNA Methyltransferase TrmD to the Signaling Molecule 3′,5′-cAMP in Bacteria. *J. Biol. Chem.* **2017**, *292*, 313−327.

(9) Gamper, H. B.; Masuda, I.; Frenkel-Morgenstern, M.; Hou, Y.-M. Maintenance of protein synthesis reading frame by EF-P and m1G37-tRNA. *Nat. Commun.* **2015**, *6*, No. 7226.

(10) Bjork, G. R. A primordial tRNA modification required for the evolution of life? *EMBO J.* **2001**, *20*, 231−239.

(11) Christian, T.; Evilia, C.; Williams, S.; Hou, Y.-M. Distinct Origins of tRNA(m1G37) Methyltransferase. *J. Mol. Biol.* **2004**, *339*, 707−719.

(12) Christian, T.; Hou, Y.-M. Distinct Determinants of tRNA Recognition by the TrmD and Trm5Methyl Transferases. *J. Mol. Biol.* **2007**, *373*, 623−632.

(13) White, T. A.; Kell, D. B. Comparative genomic assessment of novel broad-spectrum targets for antibacterial drugs. *Comp. Funct. Genomics* **2004**, *5*, 304−327.
(14) Hill, P. J.; Abibi, A.; Albert, R.; Andrews, B.; Gagnon, M. M.; Gao, N.; Grebe, T.; Hajec, L. I.; Huang, J.; Livchak, S.; et al. Selective Inhibitors of Bacterial t-RNA-(N ^{1} G37) Methyltransferase (TrmD) That Demonstrate Novel Ordering of the Lid Domain. *J. Med. Chem.* **2013**, *56*, 7278−7288.
(15) Ito, T.; Masuda, I.; Yoshida, K.; Goto-Ito, S.; Sekine, S.; Suh, S. W.; Hou, Y.-M.; Yokoyama, S. Structural basis for methyl-donor−dependent and sequence-specific binding to tRNA substrates by knotted methyltransferase TrmD. *Proc. Natl. Acad. Sci. U.S.A.* **2015**, *112*, E4197−E4205.
(16) Zhong, W.; Pasunooti, K. K.; Balamkundu, S.; Wong, Y. H.; Nah, Q.; Gadi, V.; Gnanakalai, S.; Chionh, Y. H.; McBee, M. E.; Gopal, P.; et al. Thienopyrimidinone Derivatives That Inhibit Bacterial tRNA (Guanine37- N 1)-Methyltransferase (TrmD) by Restructuring the Active Site with a Tyrosine-Flipping Mechanism. *J. Med. Chem.* **2019**, *62*, 7788−7805.
(17) Elkins, P. A.; Watts, J. M.; Zalacain, M.; van Thiel, A.; Vitazka, P. R.; Redlak, M.; Andraos-Selim, C.; Rastinejad, F.; Holmes, W. M. Insights into Catalysis by a Knotted TrmD tRNA Methyltransferase. *J. Mol. Biol.* **2003**, *333*, 931−949.
(18) Whitehouse, A. J.; Thomas, S. E.; Brown, K. P.; Fanourakis, A.; Chan, D.S.-H.; Libardo, M. D. J.; Mendes, V.; Boshoff, H. I. M.; Floto, R. A.; Abell, C.; et al. Development of Inhibitors against *Mycobacterium abscessus* tRNA (m 1 G37) Methyltransferase (TrmD) Using Fragment-Based Approaches. *J. Med. Chem.* **2019**, *62*, 7210−7232.
(19) Thomas, S. E.; Whitehouse, A. J.; Brown, K.; Burbaud, S.; Belardinelli, J. M.; Sangen, J.; Lahiri, R.; Libardo, M. D. J.; Gupta, P.; Malhotra, S.; et al. Fragment-based discovery of a new class of inhibitors targeting mycobacterial tRNA modification. *Nucleic Acids Res.* **2020**, *48*, 8099−8112.
(20) Wilkinson, A. J.; Ooi, N.; Finlayson, J.; Lee, V. E.; Lyth, D.; Maskew, K. S.; Newman, R.; Orr, D.; Ansell, K.; Birchall, K.; et al. Evaluating the druggability of TrmD, a potential antibacterial target, through design and microbiological profiling of a series of potent TrmD inhibitors. *Bioorg. Med. Chem. Lett.* **2023**, *90*, No. 129331.
(21) Gehrtz, P.; Marom, S.; Bührmann, M.; Hardick, J.; Kleinbölting, S.; Shraga, A.; Dubiella, C.; Gabizon, R.; Wiese, J. N.; Müller, M. P.; et al. Optimization of Covalent MKK7 Inhibitors via Crude Nanomole-Scale Libraries. *J. Med. Chem.* **2022**, *65*, 10341−10356.
(22) Mahjour, B.; Zhang, R.; Shen, Y.; McGrath, A.; Zhao, R.; Mohamed, O. G.; Lin, Y.; Zhang, Z.; Douthwaite, J. L.; Tripathi, A.; Cernak, T. Rapid planning and analysis of high-throughput experiment arrays for reaction discovery. *Nat. Commun.* **2023**, *14*, No. 3924.
(23) Nolan, M. D.; Schüttel, M.; Scanlan, E. M.; Nielsen, A. L. Nanomole-scale photochemical thiol-ene chemistry for high-throughput late-stage diversification of peptide macrocycles. *Pept. Sci.* **2024**, *116*, No. e24310.
(24) Plesniak, M. P.; Taylor, E. K.; Eisele, F.; Kourra, C. M. B. K.; Michaelides, I. N.; Oram, A.; Wernevik, J.; Valencia, Z. S.; Rowbottom, H.; Mann, N.; et al. Rapid PROTAC Discovery Platform: Nanomole-Scale Array Synthesis and Direct Screening of Reaction Mixtures. *ACS Med. Chem. Lett.* **2023**, *14*, 1882−1890.
(25) Buitrago Santanilla, A.; Regalado, E. L.; Pereira, T.; Shevlin, M.; Bateman, K.; Campeau, L.-C.; Schneeweis, J.; Berritt, S.; Shi, Z.-C.; Nantermet, P.; et al. Nanomole-scale high-throughput chemistry for the synthesis of complex molecules. *Science* **2015**, *347* (1979), 49−53.
(26) Gesmundo, N. J.; Sauvagnat, B.; Curran, P. J.; Richards, M. P.; Andrews, C. L.; Dandliker, P. J.; Cernak, T. Nanoscale synthesis and affinity ranking. *Nature* **2018**, *557*, 228−232.
(27) Chen, S.; Wang, Z.; Gao, J.; Wang, Y.; Liang, J.; Zhu, Y.; Xu, H.; Chen, K.; Jin, L.; Zhang, H.; et al. Rapid Discovery of Celastrol Derivatives as Potent and Selective PRDX1 Inhibitors via Microplate-Based Parallel Compound Library and In Situ Screening. *J. Med. Chem.* **2025**, *68*, 13609−13627.
(28) Wilders, H.; Biggs, G.; Rowe, S. M.; Cawood, E. E.; Riziotis, I. G.; Rendina, A. R.; Grant, E. K.; Pettinger, J.; Fallon, D. J.; Skehel, M.; et al. Expedited SARS-CoV-2 Main Protease Inhibitor Discovery through Modular 'Direct-to-Biology' Screening. *Angew. Chem., Int. Ed.* **2025**, *64* (6), No. e202418314, DOI: 10.1002/anie.202418314.
(29) Stevens, R.; Bendito-Moll, E.; Battersby, D. J.; Miah, A. H.; Wellaway, N.; Law, R. P.; Stacey, P.; Klimaszewska, D.; Macina, J. M.; Burley, G. A.; Harling, J. D. Integrated Direct-to-Biology Platform for the Nanoscale Synthesis and Biological Evaluation of PROTACs. *J. Med. Chem.* **2023**, *66*, 15437−15452.
(30) Thomas, R. P.; Heap, R. E.; Zappacosta, F.; Grant, E. K.; Pogány, P.; Besley, S.; Fallon, D. J.; Hann, M. M.; House, D.; Tomkinson, N. C. O.; Bush, J. T. A direct-to-biology high-throughput chemistry approach to reactive fragment screening. *Chem. Sci.* **2021**, *12*, 12098−12106.
(31) Meidner, J. L.; Frey, A. F.; Zimmermann, R. A.; Sabin, M. O.; Nidoieva, Z.; Weldert, A. C.; Hoba, S. N.; Krone, M. W.; Barthels, F. Nanomole Scale Screening of Fluorescent RNA-Methyltransferase Probes Enables the Discovery of METTL1 Inhibitors. *Angew. Chem., Int. Ed.* **2024**, *63*, No. e202403792.
(32) Zhang, J.-H.; Chung, T. D. Y.; Oldenburg, K. R. A Simple Statistical Parameter for Use in Evaluation and Validation of High Throughput Screening Assays. *SLAS Discovery* **1999**, *4*, 67−73.
(33) Nidoieva, Z.; Sabin, M. O.; Dewald, T.; Weldert, A. C.; Hoba, S. N.; Helm, M.; Barthels, F. A microscale thermophoresis-based enzymatic RNA methyltransferase assay enables the discovery of DNMT2 inhibitors. *Commun. Chem.* **2025**, *8*, No. 32.
(34) Hou, Y.-M.; Matsubara, R.; Takase, R.; Masuda, I.; Sulkowska, J. I. Chapter Three - TrmD: A Methyl Transferase for tRNA Methylation With m1G37. *Enzymes* **2017**, *41*, 89−115.
(35) Zhong, W.; Koay, A.; Ngo, A.; Li, Y.; Nah, Q.; Wong, Y. H.; Chionh, Y. H.; Ng, H. Q.; Koh-Stenta, X.; Poulsen, A.; et al. Targeting the Bacterial Epitranscriptome for Antibiotic Development: Discovery of Novel tRNA-(N 1 G37) Methyltransferase (TrmD) Inhibitors. *ACS Infect. Dis.* **2019**, *5*, 326−335.
(36) Storck, P.; Umstätter, F.; Wohlfart, S.; Domhan, C.; Kleist, C.; Werner, J.; Brandenburg, K.; Zimmermann, S.; Haberkorn, U.; Mier, W.; Uhl, P. Fatty Acid Conjugation Leads to Length-Dependent Antimicrobial Activity of a Synthetic Antibacterial Peptide (Pep19−4LF). *Antibiotics* **2020**, *9*, 844.
(37) Jubeh, B.; Breijyeh, Z.; Karaman, R. Antibacterial Prodrugs to Overcome Bacterial Resistance. *Molecules* **2020**, *25*, 1543.
(38) Larsen, E. M.; Johnson, R. J. Microbial esterases and ester prodrugs: An unlikely marriage for combating antibiotic resistance. *Drug Dev. Res.* **2019**, *80*, 33−47.
(39) Miller, J. J.; Shah, I. T.; Hatten, J.; Barekatain, Y.; Mueller, E. A.; Moustafa, A. M.; Edwards, R. L.; Dowd, C. S.; Hoops, G. C.; Johnson, R. J.; et al. Structure-guided microbial targeting of antistaphylococcal prodrugs. *eLife* **2021**, *10*, No. e66657.
(40) Masson, P.; Shaihutdinova, Z.; Lockridge, O. Drug and prodrug substrates and pseudo-substrates of human butyrylcholinesterase. *Biochem. Pharmacol.* **2023**, *218*, No. 115910.
(41) Berman, H. M. The Protein Data Bank. *Nucleic Acids Res.* **2000**, *28*, 235−242.
(42) Halavaty, A. S.; Minasov, G.; Winsor, J.; Dubrovska, I.; Shuvalova, L.; See, R.; Zoraghi, R.; Reiner, N.; Anderson, W. F. (2009). 2.35 Angstrom resolution crystal structure of a putative tRNA (guanine-7-)-methyltransferase (trmD) from *Staphylococcus aureus* subsp. aureus MRSA252. Preprint, DOI: 10.2210/pdb3ky7/pdb.
(43) Ahn, H. J. Crystal structure of tRNA(m1G37)-methyltransferase: insights into tRNA recognition. *EMBO J.* **2003**, *22*, 2593−2603.
(44) Carlson, H. A.; Smith, R. D.; Damm-Ganamet, K. L.; Stuckey, J. A.; Ahmed, A.; Convery, M. A.; Somers, D. O.; Kranz, M.; Elkins, P. A.; Cui, G.; et al. CSAR 2014: A Benchmark Exercise Using Unpublished Data from Pharma. *J. Chem. Inf. Model.* **2016**, *56*, 1063−1077.

https://doi.org/10.1021/acs.jmedchem.5c02323
J. Med. Chem. 2025, 68, 26246−26262

(45) Laskowski, R. A.; Swindells, M. B. LigPlot+: Multiple Ligand−Protein Interaction Diagrams for Drug Discovery. *J. Chem. Inf. Model.* **2011**, *51*, 2778−2786.
(46) Friesner, R. A.; Banks, J. L.; Murphy, R. B.; Halgren, T. A.; Klicic, J. J.; Mainz, D. T.; Repasky, M. P.; Knoll, E. H.; Shelley, M.; Perry, J. K.; et al. Glide: A New Approach for Rapid, Accurate Docking and Scoring. 1. Method and Assessment of Docking Accuracy. *J. Med. Chem.* **2004**, *47*, 1739−1749.
(47) Kitagawa, M.; Ara, T.; Arifuzzaman, M.; Ioka-Nakamichi, T.; Inamoto, E.; Toyonaga, H.; Mori, H. Complete set of ORF clones of *Escherichia coli* ASKA library (A Complete Set of *E. coli* K-12 ORF Archive): Unique Resources for Biological Research. *DNA Res.* **2006**, *12*, 291−299.
(48) Brulé, H.; Elliott, M.; Redlak, M.; Zehner, Z. E.; Holmes, W. M. Isolation and Characterization of the Human tRNA-(N ^{1} G37) Methyltransferase (TRM5) and Comparison to the *Escherichia coli* TrmD Protein. *Biochemistry* **2004**, *43*, 9243−9255.
(49) Kabsch, W. XDS. *Acta Crystallogr., Sect. D: Biol. Crystallogr.* **2010**, *66*, 125−132.
(50) Winn, M. D.; Ballard, C. C.; Cowtan, K. D.; Dodson, E. J.; Emsley, P.; Evans, P. R.; Keegan, R. M.; Krissinel, E. B.; Leslie, A. G. W.; McCoy, A.; et al. Overview of the *CCP* 4 suite and current developments. *Acta Crystallogr., Sect. D: Biol. Crystallogr.* **2011**, *67*, 235−242.
(51) Evans, P. Scaling and assessment of data quality. *Acta Crystallogr., Sect. D: Biol. Crystallogr.* **2006**, *62*, 72−82.
(52) Evans, P. R.; Murshudov, G. N. How good are my data and what is the resolution? *Acta Crystallogr., Sect. D: Biol. Crystallogr.* **2013**, *69*, 1204−1214.
(53) McCoy, A. J.; Grosse-Kunstleve, R. W.; Adams, P. D.; Winn, M. D.; Storoni, L. C.; Read, R. J. *Phaser* crystallographic software. *J. Appl. Crystallogr.* **2007**, *40*, 658−674.
(54) Vagin, A.; Teplyakov, A. *MOLREP*: an Automated Program for Molecular Replacement. *J. Appl. Crystallogr.* **1997**, *30*, 1022−1025.
(55) Moriarty, N. W.; Grosse-Kunstleve, R. W.; Adams, P. D. *electronic Ligand Builder and Optimization Workbench* (*eLBOW*): a tool for ligand coordinate and restraint generation. *Acta Crystallogr., Sect. D: Biol. Crystallogr.* **2009**, *65*, 1074−1080.
(56) Emsley, P.; Cowtan, K. *Coot*: model-building tools for molecular graphics. *Acta Crystallogr., Sect. D: Biol. Crystallogr.* **2004**, *60*, 2126−2132.
(57) Afonine, P. V.; Grosse-Kunstleve, R. W.; Echols, N.; Headd, J. J.; Moriarty, N. W.; Mustyakimov, M.; Terwilliger, T. C.; Urzhumtsev, A.; Zwart, P. H.; Adams, P. D. Towards automated crystallographic structure refinement with *phenix.refine*. *Acta Crystallogr., Sect. D: Biol. Crystallogr.* **2012**, *68*, 352−367.
(58) Murshudov, G. N.; Skubák, P.; Lebedev, A. A.; Pannu, N. S.; Steiner, R. A.; Nicholls, R. A.; Winn, M. D.; Long, F.; Vagin, A. A. *REFMAC* 5 for the refinement of macromolecular crystal structures. *Acta Crystallogr., Sect. D: Biol. Crystallogr.* **2011**, *67*, 355−367.
(59) Chen, V. B.; Arendall, W. B.; Headd, J. J.; Keedy, D. A.; Immormino, R. M.; Kapral, G. J.; Murray, L. W.; Richardson, J. S.; Richardson, D. C. *MolProbity*: all-atom structure validation for macromolecular crystallography. *Acta Crystallogr., Sect. D: Biol. Crystallogr.* **2010**, *66*, 12−21.
(60) Williams, C. J.; Headd, J. J.; Moriarty, N. W.; Prisant, M. G.; Videau, L. L.; Deis, L. N.; Verma, V.; Keedy, D. A.; Hintze, B. J.; Chen, V. B.; et al. MolProbity: More and better reference data for improved all-atom structure validation. *Protein Sci.* **2018**, *27*, 293−315.



https://doi.org/10.1021/acs.jmedchem.5c02323
J. Med. Chem. 2025, 68, 26246−26262

3.2.4 Supporting Information

The following supporting information quoted within “” from page 111 to page 128 is the same as the manuscript cited on page 93.[254] “

Supporting Information

Nanoscale Direct-to-Biology Optimization and Structural Insights into Selective *S. aureus* TrmD Inhibitors

Ariane F. Hübner[‡,a], Annabelle C. Weldert[‡,a], Tessa Marciniak[b], Florian Hof[c], Vivien S. Beck[b], Samuel Carien[b], Sophie N. Mulartschyk[a], Eva Wolf[c], Wilma Ziebuhr[b], Fabian Barthels*[,a]

[a]Institute of Pharmaceutical and Biomedical Sciences, Johannes Gutenberg-University, Staudingerweg 5, 55128 Mainz, Germany.

[b]Institute of Molecular Infection Biology, University of Würzburg, Josef-Schneider-Strasse 2, 97080 Würzburg, Germany.

[c]Institute of Molecular Physiology, Johannes Gutenberg-University, Hanns-Dieter-Hüsch-Weg 17, 55128 Mainz, Germany.

Corresponding Author's email address: barthels@uni-mainz.de

Table of contents

Crystallography of parent compounds S3
Isothermal titration calorimetry (ITC) S3
Supplementary results of the nanoSAR screening S4
Fluorescence polarization (FP) assays and selectivity S4
S. aureus TrmD inhibition (aptamer-based enzyme assay) S6
TrmD inhibition (^{3}H incorporation enzyme assay) S6
Cell viability assay (Cell Titer Glo) S7
Supplementary results of anti-bacterial experiments S7
Carbamate cleavage assays (LC/MS lysate assay) S9
Supplementary crystallographic figures S11
Physicochemical properties of the azide-library S17
Docking poses compounds 2 and 8b-e,h S18
NMR and LC/MS Spectra S19

Crystallography of parent compounds

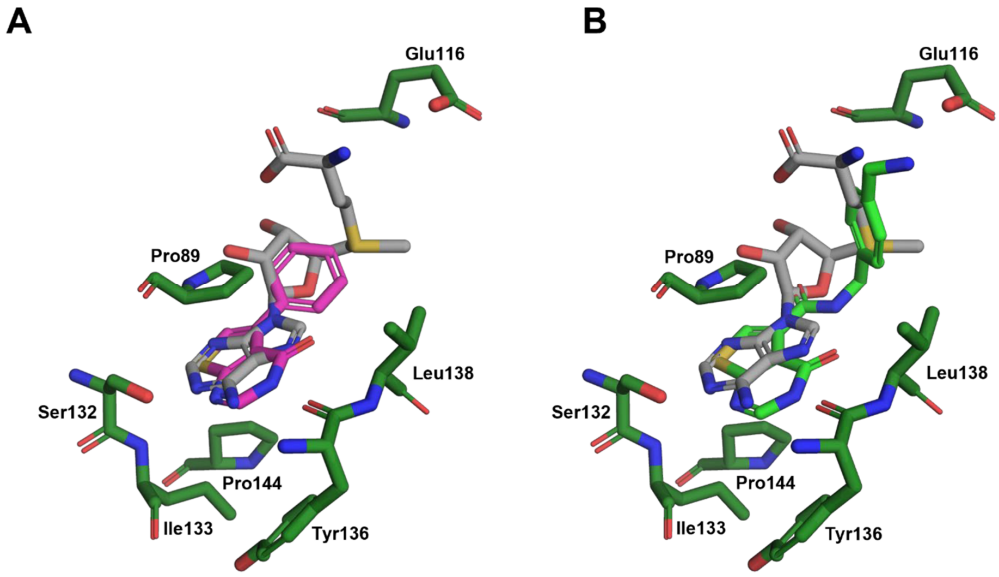


Figure S1: Parent structures for the development of *S. aureus* TrmD inhibitors. Crystallographic overlay with SAM (PDB:1UAK) of literature-known compounds **1** (**A**, PDB: 4MCD) and **2** (**B**, PDB 4MCC) in the *H. influenzae* SAM-binding pocket. Ligands and amino acids are shown in stick representation. The carbon atoms of SAM are shown in grey, those of **1** are shown in pink, and those of compound **2** are shown in lime. Interacting residues are displayed in dark green.

Isothermal titration calorimetry (ITC)

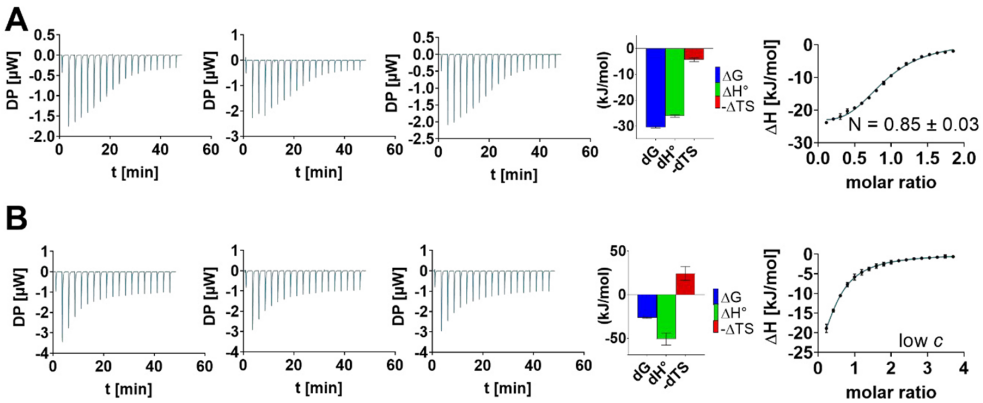


Figure S2. ITC data for the titration of compounds **1** and **2** against *Haemophilus influenzae* TrmD. (**A**) Compound **1** was titrated into *Haemophilus influenzae* TrmD. (**B**) Compound **2** was titrated into *Haemophilus influenzae* TrmD. Note: a low-c titration was performed for compound **2**.

Supplementary results of the nanoSAR screening

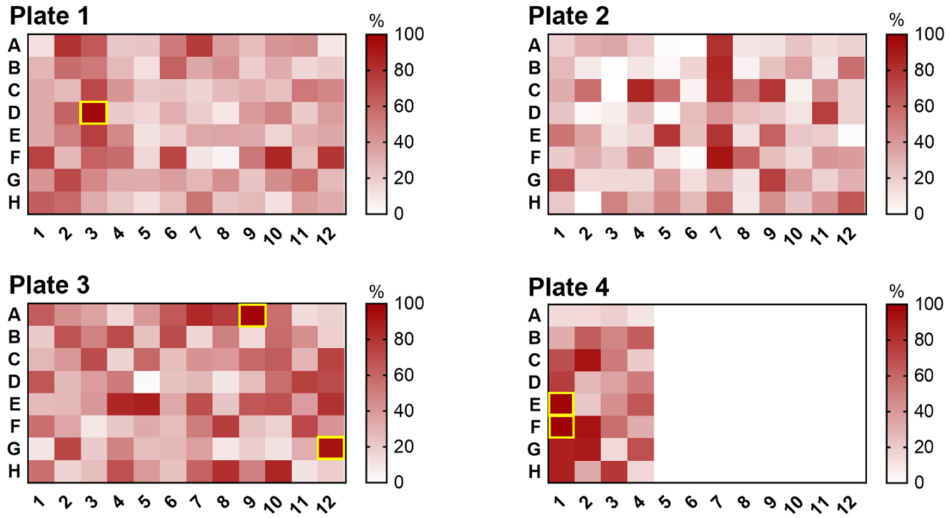


Figure S3. Results of the nanoSAR FP screening are presented in a heat-map format (displaced tracer [%]). The hit compounds **8b–e,h** are highlighted in yellow.

Fluorescence polarization (FP) assays and selectivity

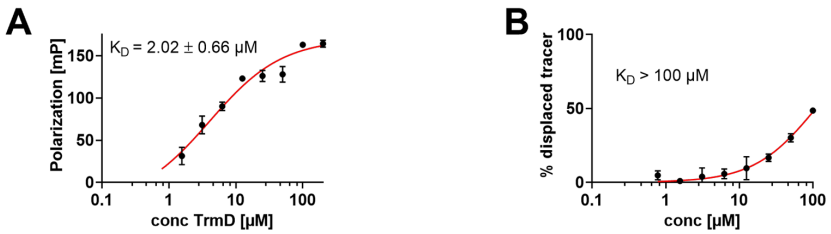


Figure S4. (**A**) Fluorescence polarization assay with tracer **3** titrated against *H. influenzae* TrmD. (**B**) K_D-value determination of alkyne **7** titrated against *S. aureus* TrmD.

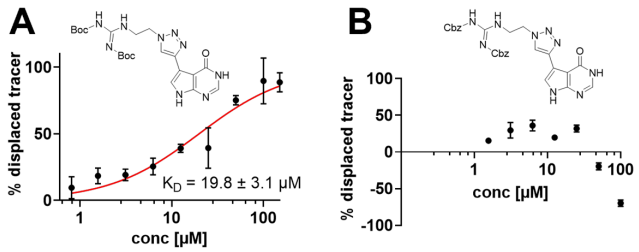


Figure S5. Supplementary FP-assay data on *S. aureus* TrmD. (**A**) **8f** (**B**) **8g.**

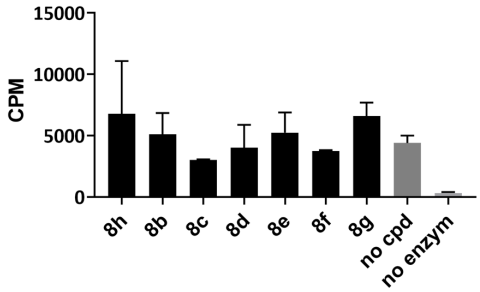


Figure S6. ^{3}H-based enzyme assay for Trm5 selectivity analysis of compound **8b**–**h**. Compounds were assayed at a final concentration of 30 µM, exhibiting no significant inhibition.

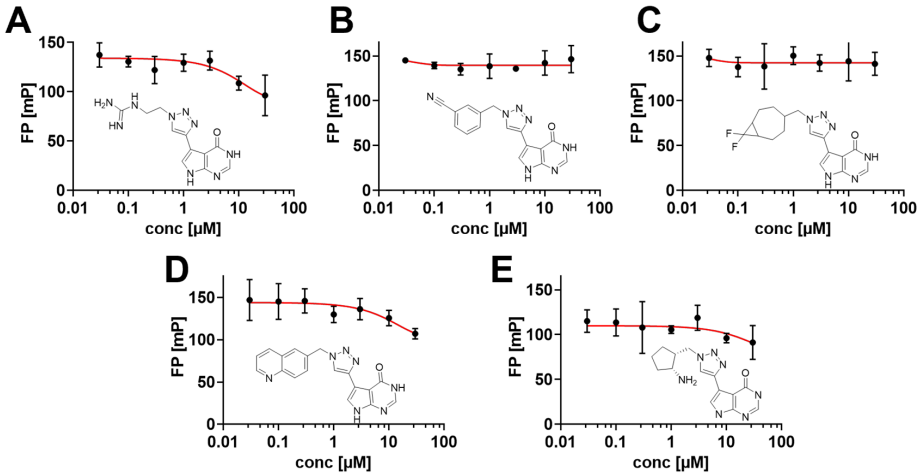


Figure S7. FP selectivity assays on *H. influenzae* TrmD for (**A**) **8h** (**B**) **8b** (**C**) **8c** (**D**) **8d** (**E**) **8e**.

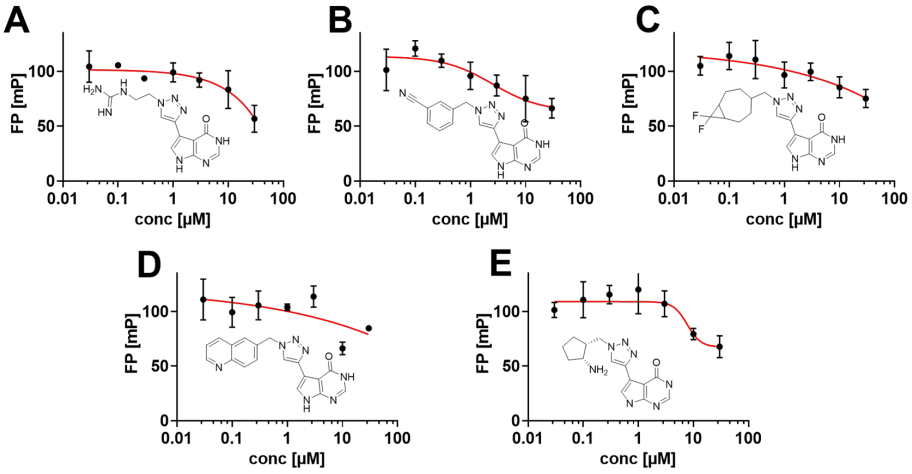


Figure S8. FP selectivity assays on *E. coli* TrmD for (**A**) **8h** (**B**) **8b** (**C**) **8c** (**D**) **8d** (**E**) **8e**.

***S. aureus* TrmD inhibition (aptamer-based enzyme assay)**

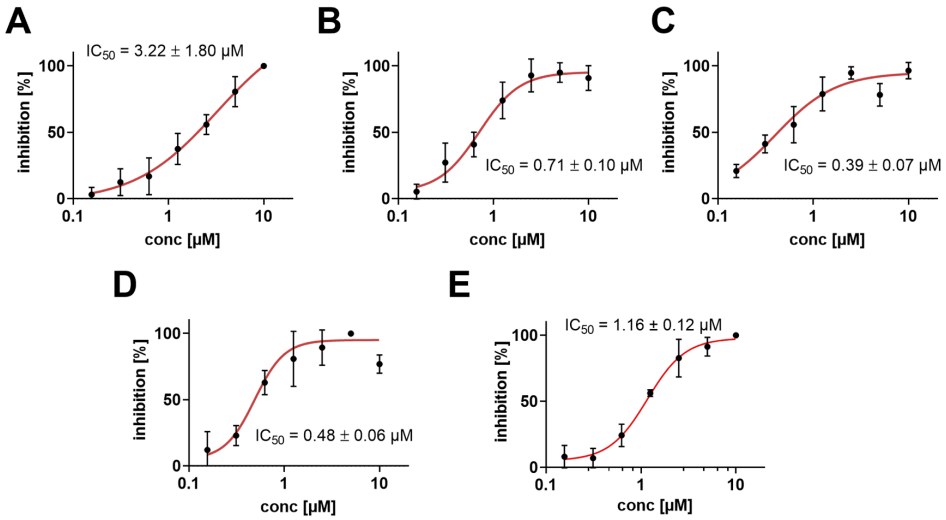


Figure S9. *S. aureus* TrmD inhibition measured by aptamer-based enzyme assay for the determination of IC_{50} values. (**A**) **8b** (**B**) **8c** (**C**) **8d** (**D**) **8e** (**E**) **8h**.

TrmD inhibition (^{3}H incorporation enzyme assay)

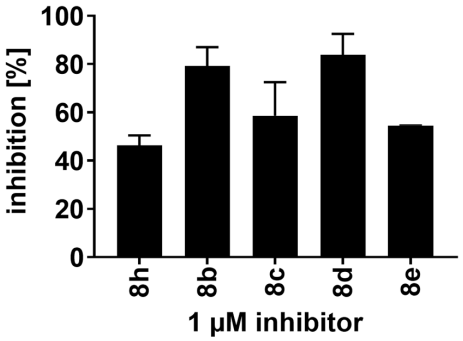


Figure S10. *S. aureus* TrmD inhibition measured by ^{3}H incorporation assay. Compounds were assayed at a final concentration of 1 µM, exhibiting inhibition values between 46% and 84%, confirming the inhibitory potency determined by aptamer-based assays (Figure S9).

Cell viability assay (Cell Titer Glo)

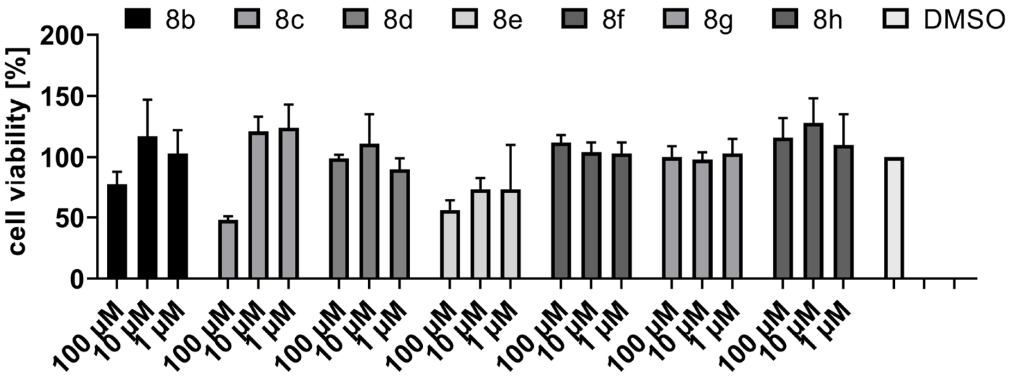


Figure S11. Screening results of the cell viability assay (HEK293). Pure DMSO was used as a control and set to 100% cell viability.

Supplementary results of anti-bacterial experiments

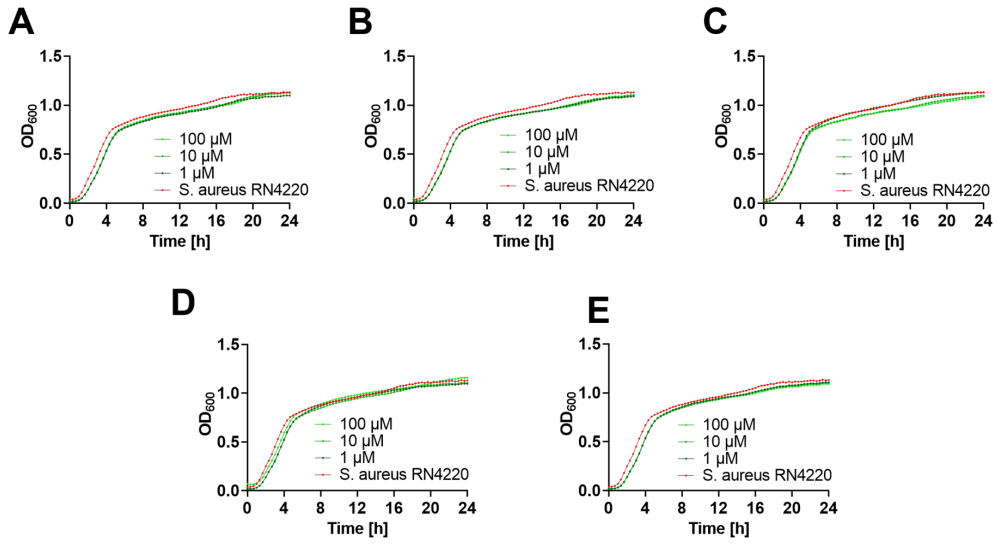


Figure S12. Growth curves of *S. aureus* RN4220 demonstrating the effect of compounds on bacterial growth. Compared to the negative control, no pronounced effect on growth was observed. (**A**) **8h** (**B**) **8b** (**C**) **8c** (**D**) **8d** (**E**) **8e**.

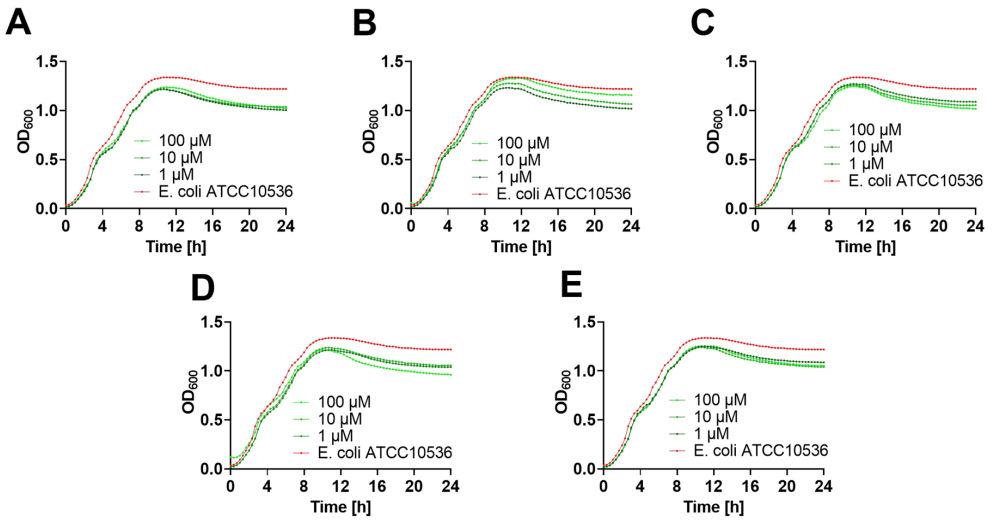


Figure S13. Growth curves of *E. coli* demonstrating the effect of compounds on bacterial growth. Compared to the negative control, no pronounced effect on growth was observed. (**A**) **8h** (**B**) **8b** (**C**) **8c** (**D**) **8d** (**E**) **8e**.

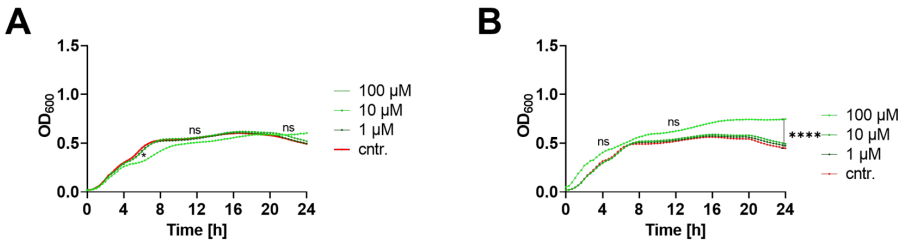


Figure S14. Growth curves of *E. coli* demonstrating the effect of **8g** (**A**) and **8f** (**B**) on bacterial growth. Compared to the negative control, no significant growth inhibition was observed. Two-way ANOVA with Dunnett's multiple comparisons test was used for statistical analysis, using a confidence interval of 95%.

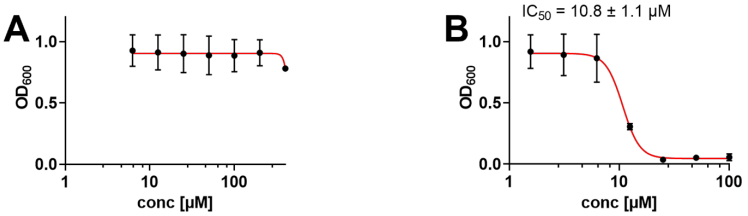


Figure S15. IC_{50} curves of **8g** (**A**) and **8f** (**B**) affecting *S. aureus* growth at 1440 min.

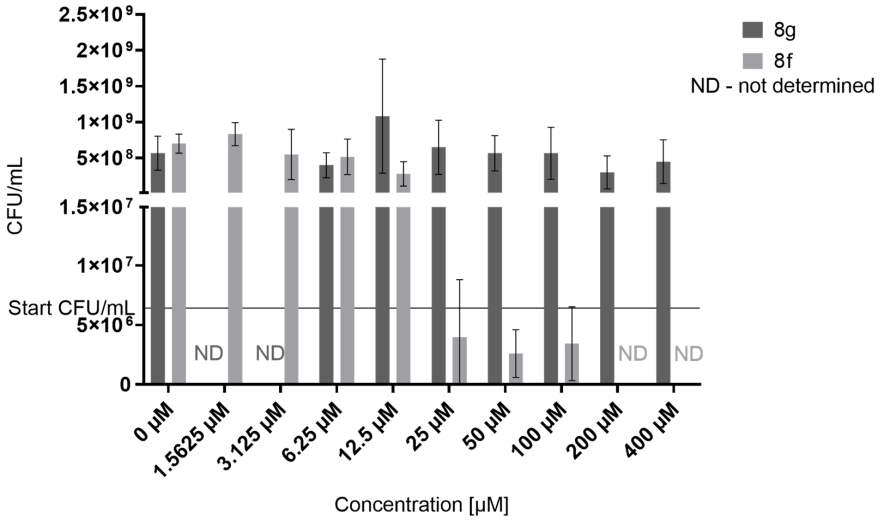


Figure S16. MBC determination of compounds **8f** and **8g**. Only **8f** affects growth starting at 12.5 µM.

Carbamate cleavage assays (LC/MS lysate assay)

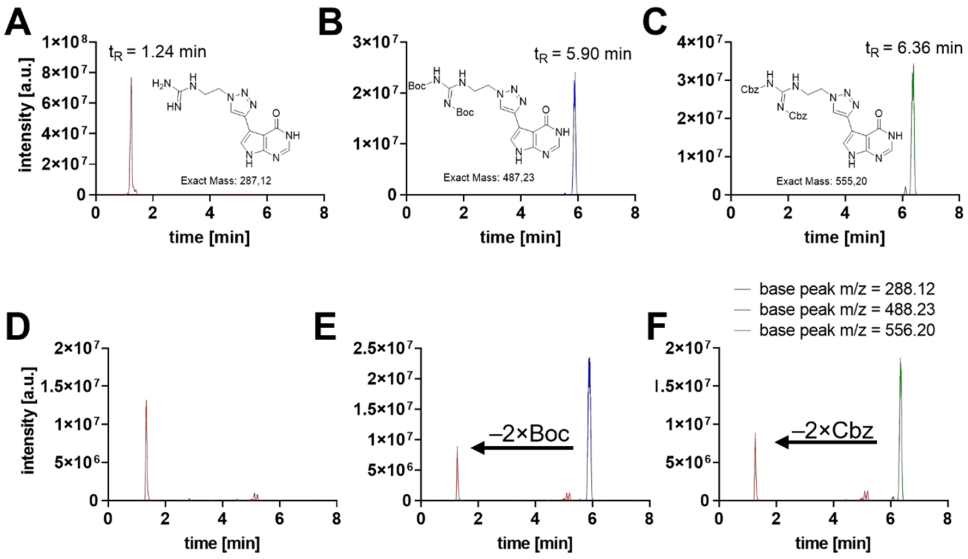


Figure S17. Supplementary results of the in vitro prodrug cleavage assay. (**A**) Basepeak chromatogram of pure reference compound **8h** m/z = 288±0.5. (**B**) Basepeak chromatogram of pure reference compound **8g** m/z = 488±0.5. (**C**) Basepeak chromatogram of pure reference compound **8f** m/z = 556±0.5. (**D**) Basepeak chromatogram of *S. aureus* lysate treated with **8h** m/z = 288±0.5. (**E**) Basepeak chromatogram of *S. aureus* lysate treated with **8g** m/z = 288±0.5; m/z = 488±0.5. (**F**) Basepeak chromatogram of *S. aureus* lysate treated with **8f** m/z = 288±0.5; m/z = 556±0.5.

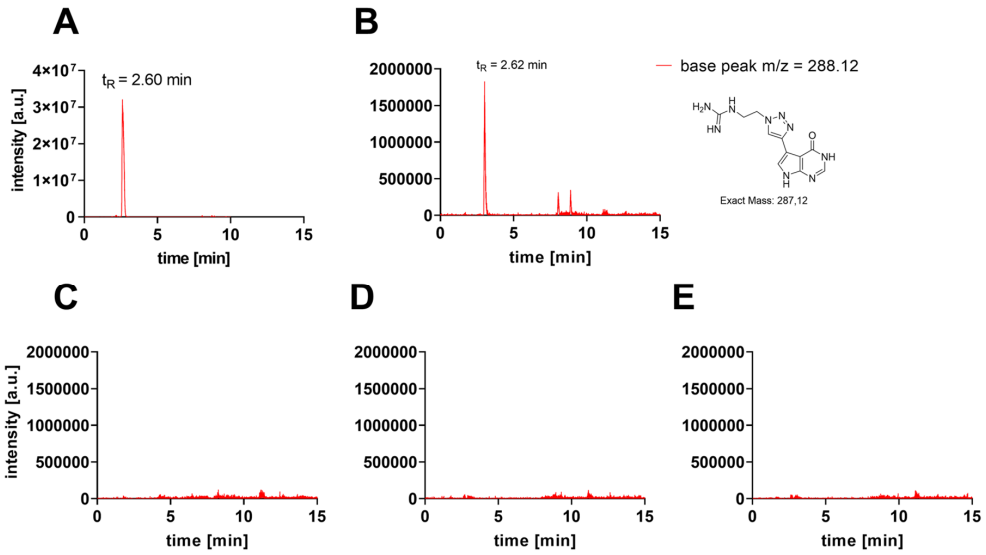


Figure S18. Supplementary results of the in vivo prodrug uptake and cleavage assay. (**A**) Basepeak chromatogram of pure reference compound **8h** m/z = 288±0.5. (**B**) Basepeak chromatogram of the sample derived from growing *S. aureus* culture incubated with compound **8f** and lysed after treatment. (**C**) Basepeak chromatogram of the sample derived from growing *S. aureus* culture incubated with compound **8g** and lysed after treatment. (**D**) Basepeak chromatogram of the sample derived from growing *S. aureus* culture incubated with compound **8h** and lysed after treatment. (**E**) Basepeak chromatogram of the sample derived from growing *S. aureus* culture mock-treated with DMSO and lysed after treatment.

Supplementary crystallographic figures

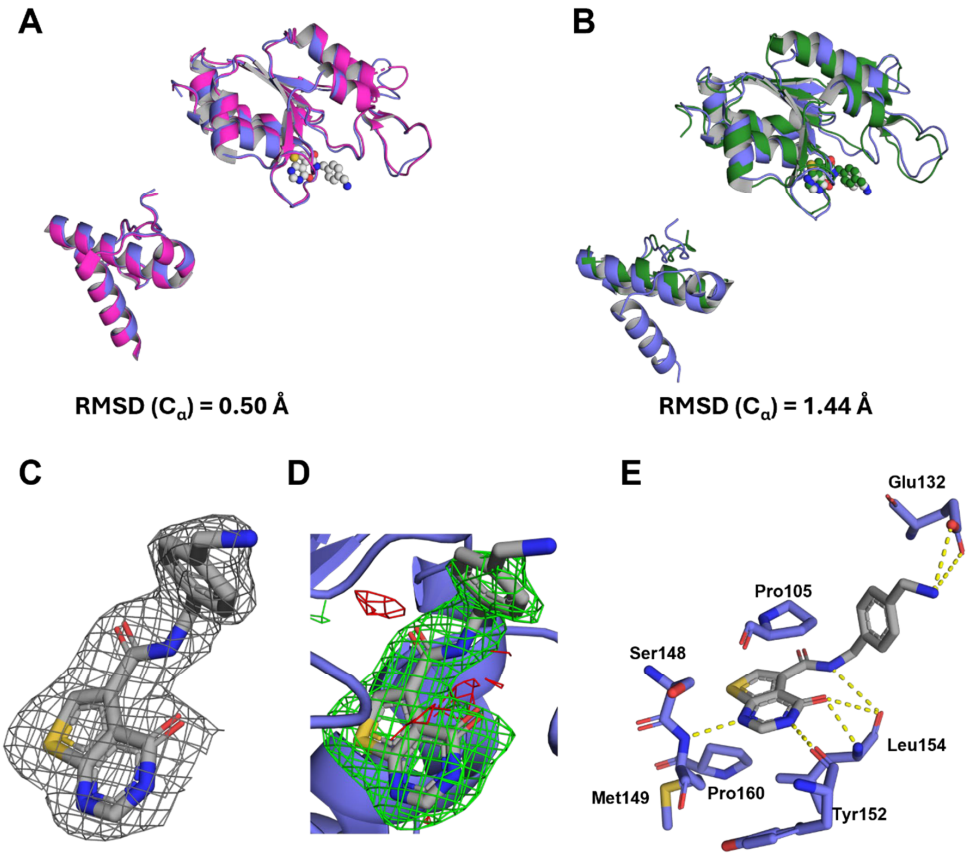


Figure S19. Supplementary crystallographic images for *S. aureus* TrmD co-crystallized with compound **2** (PDB: 9SDV). (**A**) Global superposition of the X-ray structures of *S. aureus* TrmD with compound **2** (violet-blue) and the apo structure (pink, 3KY7). (**B**) Global superposition of the X-ray structures of *S. aureus* TrmD with compound **2** (violet-blue) and *H. influenzae* TrmD with compound **2** (light blue, 4MCC). (**C**) Compound **2** bound *S. aureus* TrmD with $2mF_{obs}$-DF_{calc} electron density map at a contour level of +1σ. (**D**) Compound **2** bound *S. aureus* TrmD with mF_{obs}-DF_{calc} electron density map at a contour level of +3σ. (**E**) Compound **2** in the *S. aureus* SAH binding pocket. Protein structures are depicted as cartoons, interacting residues are shown as sticks, the ligand as spheres or in stick form, and polar interactions as yellow dashed lines.

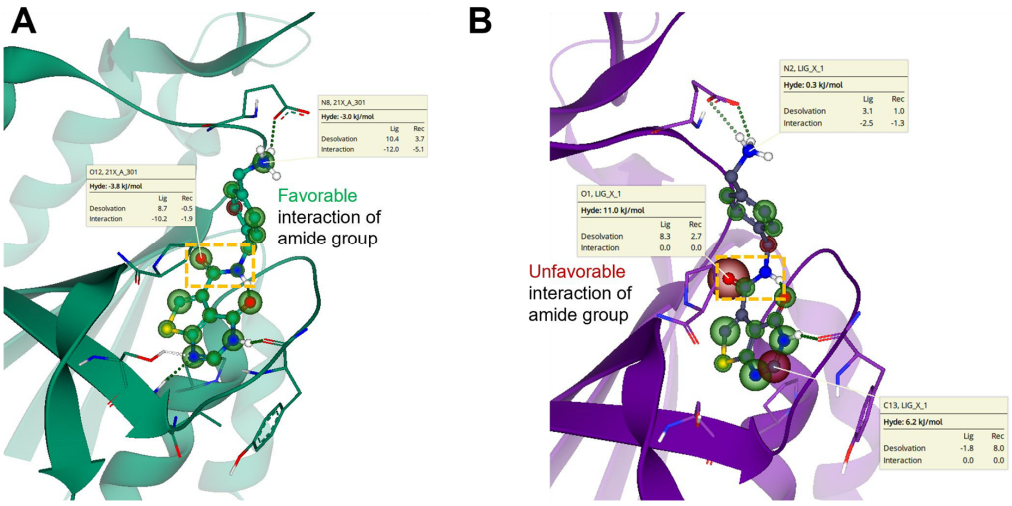


Figure S20. SeeSAR analysis by binding pose inspection of compound **2** bound to *H. influenzae* TrmD (**A**, green, PDB: 4MCC) and *S. aureus* TrmD (**B**, purple, PDB: 9SDV). Proteins are depicted as cartoons with representative binding site amino acids shown as lines. The compound is shown as stick. Hyde coloring enables the identification of favorable resp. unfavorable atom placements (colored spheres; green: favorable, red: unfavored).

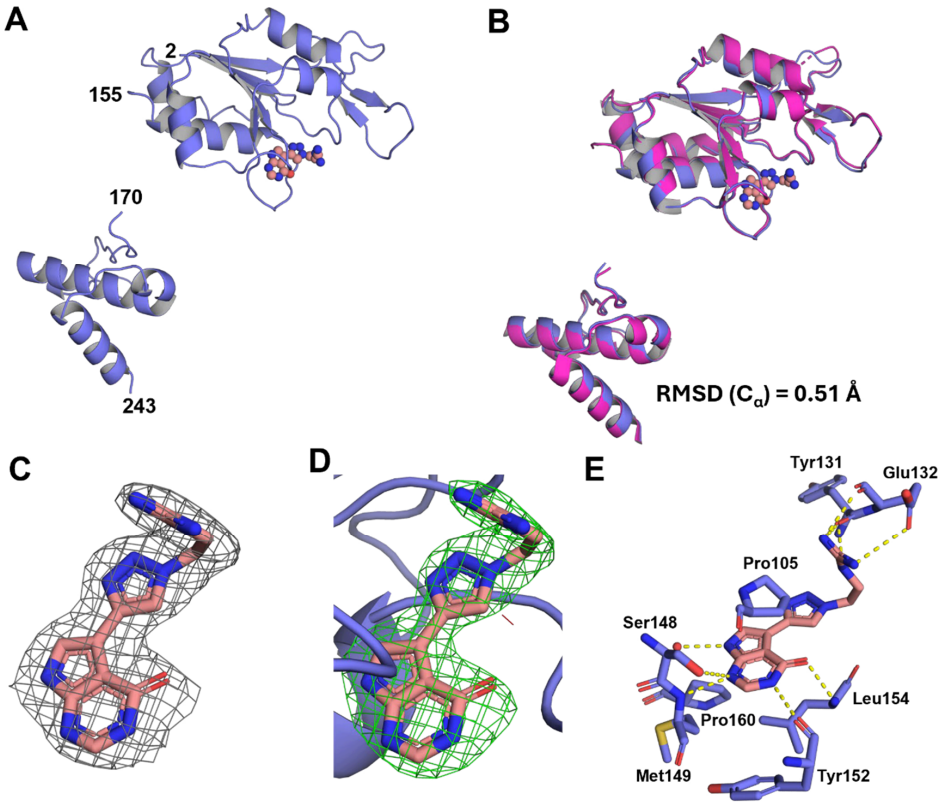


Figure S21. Supplementary crystallographic images for *S. aureus* TrmD co-crystallized with compound **8h** (PDB: 9SDW). (**A**) Structure of *S. aureus* TrmD bound to compound **8h.** (**B**) Global superposition of the X-ray structures of *S. aureus* TrmD with compound **8h** (violet-blue) and the apo structure (pink, 3KYZ). (**C**) Compound **8h** (salmon) bound *S. aureus* TrmD with $2mF_{obs}$-DF_{calc} electron density map at a contour level of +1σ. (**D**) Compound **8h** bound *S. aureus* TrmD with mF_{obs}-DF_{calc} electron density map at a contour level of +3σ. (**E**) Compound **8h** in the *S. aureus* SAH binding pocket. Protein structures are depicted as cartoons, interacting residues are shown as sticks, the ligand as spheres or in stick form, water molecules are shown as spheres, and polar interactions are shown as yellow dashed lines.

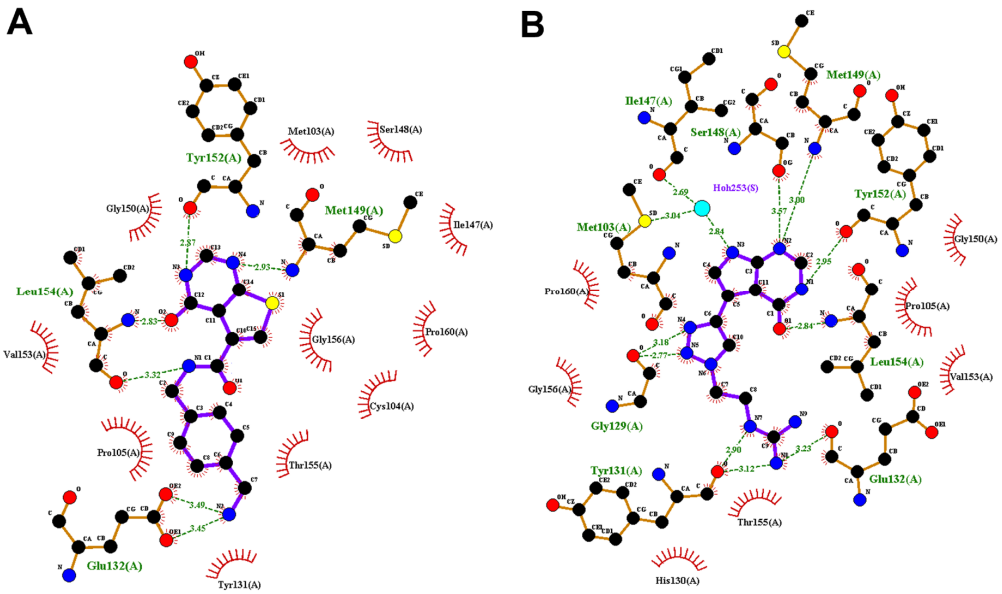


Figure S22. A schematic ligand-protein interaction diagram created with LigPlot+ for compound **2** (**A**) and compound **8h** (**B**). Intermolecular hydrogen bonds are given in green, hydrophobic interaction residues in red, and water as sky blue spheres.

Table S1: X-ray data collection refinement statistics of the structure co-crystalized with compound **2**.

PDB entry 9SDV	
Beamline	Diamond light source I03
Wavelength (Å)	0.976*
Resolution range(Å)	42.23 - 2.5 (2.75 - 2.5)
Space group	P 43 3 2
Unit cell	126.695 126.695 126.695 90 90 90
Total reflections	994338 (101554)*
Unique reflections	12564 (3062)
Multiplicity	78.90 (73.70)*
Completeness (%)	99.98 (99.93)
Mean I/sigma(I)	66.60 (13.10)*
Wilson B-factor (Å^2)	51.86
R-merge	0.06 (0.47)*
R-meas	0.06 (0.47)*
R-pim	0.01 (0.05)*
CC1/2	1.00 (0.99)*
Reflections used in refinement	12564 (3062)
Reflections used for R-free	608 (145)
R-work	0.2226 (0.2594)
R-free	0.2806 (0.3403)
Number of non-hydrogen atoms	1909
macromolecules	1825
Ligands	26
Solvent	58
Protein residues	231
RMS(bonds) (Å)	0.010
RMS(angles) (°)	1.13
Ramachandran favored (%)	95.15
Ramachandran allowed (%)	4.85
Ramachandran outliers (%)	0.00
Rotamer outliers (%)	0.52
Clashscore	8.08
Average B-factor (Å^2)	75.54
Macromolecules (Å^2)	76.10
Ligands (Å^2)	72.08
Solvent (Å^2)	59.51

Statistics for the highest resolution shell are shown in parentheses. * shows data from derived from ccp4.

Table S2: X-ray data collection refinement statistics of the structure co-crystalized with **8h**.

PDB entry 9SDW	
Beamline	Diamond light source I03
Wavelength (Å)	0.976*
Resolution range(Å)	44.86 - 2.6 (2.86 - 2.6)
Space group	P 43 3 2
Unit cell	126.875 126.875 126.875 90 90 90
Total reflections	899457 (112484)*
Unique reflections	11266 (2734)
Multiplicity	79.60 (83.90)*
Completeness (%)	99.97 (99.93)
Mean I/sigma(I)	44.70 (7.00)*
Wilson B-factor (Å^2)	59.97
R-merge	0.10 (0.97)*
R-meas	0.10 (0.98)*
R-pim	0.01 (0.11)*
CC1/2	1.00 (0.97)*
Reflections used in refinement	11266 (2734)
Reflections used for R-free	566 (140)
R-work	0.2275 (0.2534)
R-free	0.2912 (0.3343)
Number of non-hydrogen atoms	1883
macromolecules	1832
Ligands	21
Solvent	30
Protein residues	230
RMS(bonds) (Å)	0.007
RMS(angles) (°)	1.00
Ramachandran favored (%)	97.35
Ramachandran allowed (%)	2.65
Ramachandran outliers (%)	0.00
Rotamer outliers (%)	3.52
Clashscore	14.84
Average B-factor (Å^2)	79.94
Macromolecules (Å^2)	80.47
Ligands (Å^2)	66.73
Solvent (Å^2)	56.82

Statistics for the highest resolution shell are shown in parentheses. * shows data from derived from ccp4.

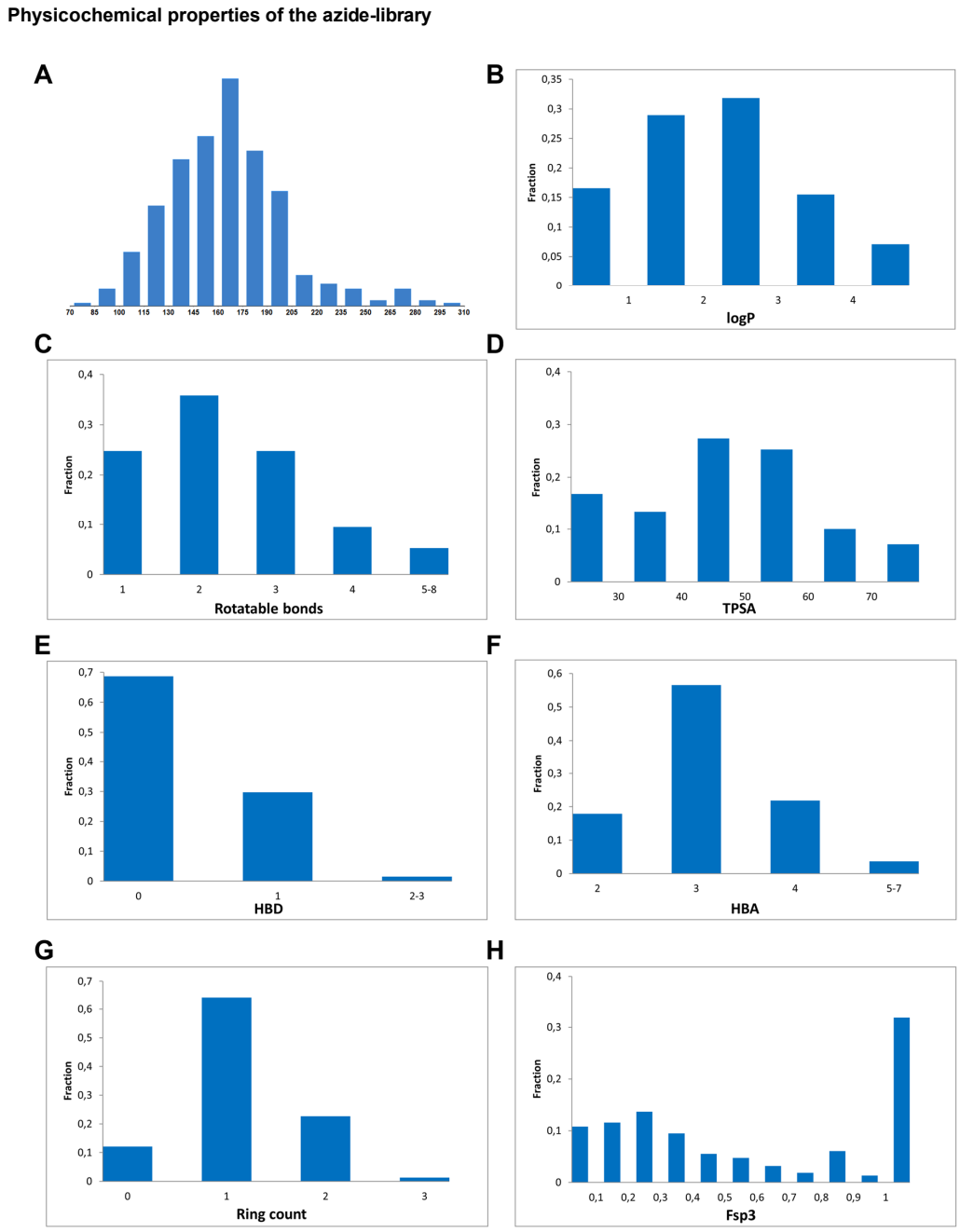


Figure S23. Overview of the physicochemical properties of the azide library purchase from Enamine.net. (**A**) Molecular weight [g/mol], (**B**) log P value, (**C**) Number of rotatable bonds, (**D**) Toplogical polar surface area [Å^2], (**E**) Number of H-bond donors, (**F**) Number of H-bond acceptors, (**G**) Number of rings, (**H**) Fraction of sp^3 atoms.

Docking poses compounds 2 and 8b–e,h

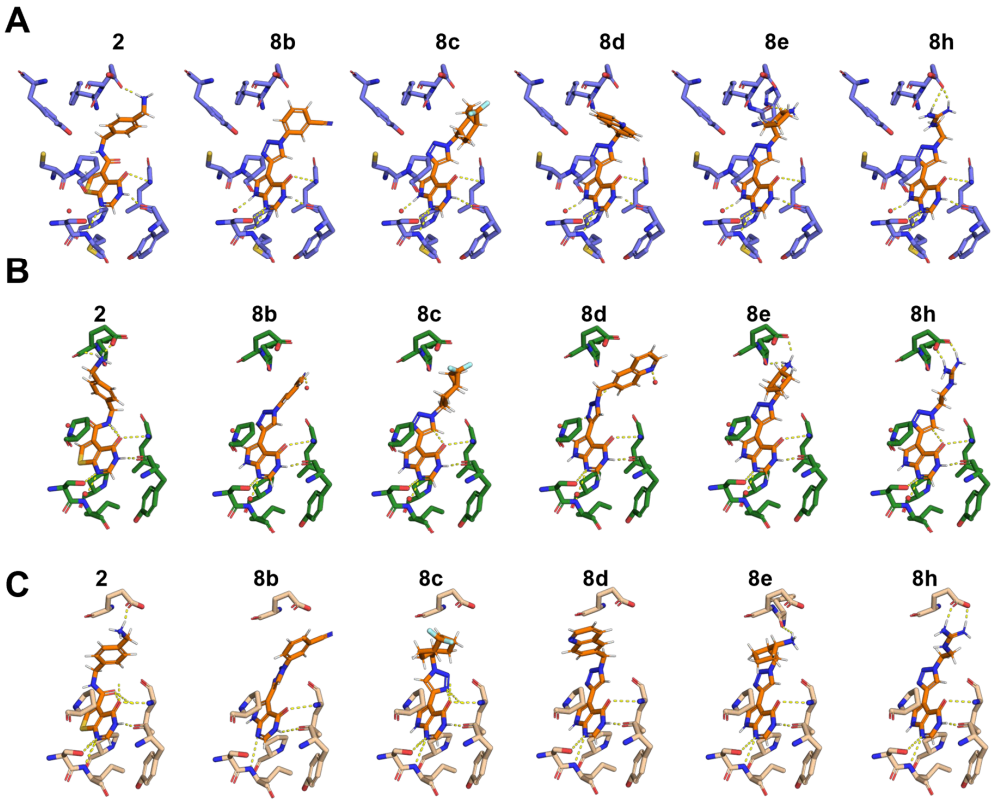


Figure S24: Glide docking poses for compounds **2** and **8b–e,h** after docking to (**A**) *Staphylococcus aureus* (PDB: 9SDW, purple carbons), (**B**) *Haemophilus influenzae* (PDB: 4MCC; green carbons), and (**C**) *Escherichia coli* (PDB: 1P9P, sand carbons). Ligand carbons are shown as sticks in orange, selected amino acids are shown as sticks, and water is shown as red spheres.

Table S3: Glide scores for compounds **2** and **8b–e,h** after docking to *Haemophilus influenzae* (PDB: 4MCC), *Escherichia coli* (PDB: 1P9P), and *Staphylococcus aureus* (PDB: 9SDW).

	2	**8b**	**8c**	**8d**	**8e**	**8h**
Haemophilus influenzae (PDB: 4MCC)	-13.44	-10.78	-11.03	-9.73	-10.74	-11.91
Escherichia coli (PDB: 1P9P)	-12.18	-8.28	-10.61	-11.32	-11.73	-11.38
Staphylococcus aureus (PDB: 9SDW)	-7.95	-11.623	-11.27	-11.80	-12.86	-12.74

“

4 Project 2: DNA-Encoded Library Screening

4.1 DNA-Encoded Library Screening Uncovers Potent DNMT2 Inhibitors Targeting a Cryptic Allosteric Binding Site

4.1.1 Context and Project Summary

RNA Mtase DNMT2 is implicated in various diseases, including cancer (chapter 1.1.1).[65–67] However, currently available DNMT2 inhibitors suffer from poor selectivity and limited cellular permeability.[3,74,75] To address this limitation, a DEL screening was conducted in collaboration with WuXi AppTec using the DELopen platform to discover novel DNMT2 inhibitors. DNMT2 was treated with the library under three distinct conditions – with SAH, with tRNA, and without any ligand – to investigate diverse binding sites.

Surprisingly, the most enriched compounds were recovered under all three conditions equally, suggesting a previously unknown binding mode in none of the known binding pockets (SAH/ tRNA). Among the five validated hits – three peptidomimetics and two triazine derivatives – only the peptidomimetics demonstrated inhibitory activity in functional enzymatic assays. To elucidate the inhibition mode, X-ray crystallographic investigations were conducted using the most potent peptidomimetic hit.

Structural analysis revealed a cryptic allosteric binding pocket that induces a conformational rearrangement in DNMT2 upon ligand binding. Specifically, the inhibitor causes the rearrangement of a flexible loop that in turn occludes the SAH/SAM cofactor binding site, effectively blocking enzymatic activity.

Guided by this structural insight, a SAR campaign was conducted using solid-phase peptide synthesis. This yielded a lead compound with a K_D-value of 3.04 µM. Notably, the compound represents the only molecule in the study (including DEL hits) to exhibit passive membrane permeability in a parallel artificial membrane permeability assay (PAMPA). In MOLM-13 cells, the compound significantly reduced m^5C modification levels in tRNA without exhibiting cytotoxicity in cancerous or non-cancerous cell lines. However, studies suggested a higher sensitivity of cancer cells to doxorubicin with a knockdown of DNMT2.[68] Indeed, cellular synergy assays with doxorubicin revealed a strong combinatorial effect, reducing the CC_{50} of doxorubicin from 45 nM to 10 nM.

To assess whether the newly discovered allosteric pocket may serve as a regulatory pocket for endogenous modulators of DNMT2 activity, displacement pull-down studies were performed with known DNMT2-interacting proteins, non-POU domain-containing octamer-binding protein (NonO),

and eukaryotic translation initiation factor 4E (eIF4E). None of the proteins were found to bind to the allosteric site, leaving room for future investigations.

Collectively, these findings uncover a novel, druggable allosteric site on DNMT2 and introduce the first selective, cell-permeable small-molecule inhibitor of DNMT2. This compound represents a promising starting point for future drug discovery efforts targeting DNMT2.

This work has been published in: iScience – a Cell Press journal (impact factor: 4.1).

Article reprinted with open access permission from *iScience,* **2025**, *28* (9), 113300. 'DNA-encoded library screening uncovers potent DNMT2 inhibitors targeting a cryptic allosteric binding site.' © The Authors. Published by Elsevier Inc.

The full version of the article, including the electronic Supplementary Information, can be accessed online at doi: 10.1016/j.isci.2025.113300.

4.1.2 Contributions

Own contribution: DEL panning, analysis of hit clustering data, hit selection, MST assay, ^{3}H-incorporation assay, synthesis of compounds and tracers (partly supervision of students Valerie Kadenbach and Hanna Bodenstaff), AS-MS and MST assay (supervision of Valerie Kadenbach and Hanna Bodenstaff), writing and editing manuscript and SI.

Contributions from other authors: Protein expression and purification, protein crystallization, ITC, pull-down assay, tRNA preparation, cell viability assays and tRNA LC/MS assay, PAMPA, and writing and manuscript and SI editing.

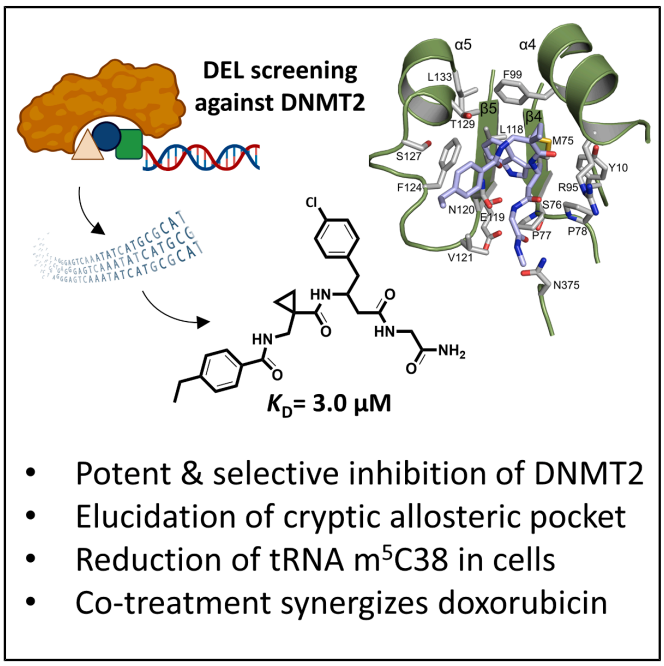
4.1.3 Publication

The following publication quoted within “” from page 131 to page 171 is the same as the manuscript cited on page 130.[255] “

iScience Article

DNA-encoded library screening uncovers potent DNMT2 inhibitors targeting a cryptic allosteric binding site

Graphical abstract



Authors

Ariane F. Frey, Merlin Schwan, Annabelle C. Weldert, ..., Mark Helm, Irmgard Sinning, Fabian Barthels

Correspondence

barthels@uni-mainz.de

In brief

Biochemistry; Molecular Structure; Properties of biomolecules; Structural biology

Highlights

- DEL screening identifies non-SAH-like, selective DNMT2 inhibitor chemotypes
- Lead compound binds allosterically to a cryptic pocket revealed by X-ray crystallography
- DNMT2 inhibitors reduce m^{5}C levels and enhance doxorubicin-induced cytotoxicity
- Structural insights enable selective targeting of DNMT2 over related methyltransferases

Frey et al., 2025, iScience 28, 113300
September 19, 2025 © 2025 The Author(s). Published by Elsevier Inc.
https://doi.org/10.1016/j.isci.2025.113300

CellPress

iScience

CellPress
OPEN ACCESS

Article

DNA-encoded library screening uncovers potent DNMT2 inhibitors targeting a cryptic allosteric binding site

Ariane F. Frey,[1,3] Merlin Schwan,[2,3] Annabelle C. Weldert,[1] Valerie Kadenbach,[1] Jürgen Kopp,[2] Zarina Nidoieva,[1] Robert A. Zimmermann,[1] Lukas Gleue,[1] Collin Zimmer,[1] Marko Jörg,[1] Kristina Friedland,[1] Mark Helm,[1] Irmgard Sinning,[2] and Fabian Barthels[1,4,*]

[1]Institute of Pharmaceutical and Biomedical Sciences (IPBS), 55128 Mainz, Germany
[2]Heidelberg University Biochemistry Center (BZH), 69120 Heidelberg, Germany
[3]These authors contributed equally
[4]Lead contact
*Correspondence: barthels@uni-mainz.de
https://doi.org/10.1016/j.isci.2025.113300

SUMMARY

DNMT2 (TRDMT1) is a human RNA methyltransferase implicated in various disease processes. However, small-molecule targeting of DNMT2 remains challenging due to poor selectivity and low cellular availability of known *S*-adenosylhomocysteine (SAH)-derived ligands. In this study, a DNA-encoded library (DEL) screen identified five non-SAH-like chemotypes that selectively bind DNMT2, including three peptidomimetics. Orthogonal assays confirmed target engagement, and X-ray crystallography revealed a previously unknown allosteric binding pocket formed via active site loop rearrangement. Guided by structural insights, the authors optimized a lead compound with a K_D of 3.04 μM that reduces m^5C levels in MOLM-13 tRNA and synergizes with doxorubicin to impair cell viability. These inhibitors exhibit unprecedented selectivity over other methyltransferases, offering a promising scaffold for future DNMT2-targeting therapeutics. Beyond pharmacological implications, the study provides conceptual advances in understanding allosteric modulation and structural plasticity of DNMT2.

INTRODUCTION

Targeting RNA methyltransferases (MTases) by active site-competitive small-molecule drugs proves challenging due to their universal dependence on *S*-adenosyl-L-methionine (SAM) as a methyl group donating substrate, which is transformed into *S*-adenosylhomocysteine (SAH) during this enzymatic reaction.[1,2] SAH itself presents a pan methyltransferases inhibitor used as a starting point for several RNA MTase drug discovery campaigns.[3–5] A unique representative of this enzyme family is the RNA MTase DNA methyltransferase 2 (DNMT2), also known as TRDMT1, which is structurally related to other DNMTs, but this paralogous enzyme deviates in function and cellular localization.[6–8] Instead of DNA, which is the main target of DNMT1 and DNMT3, DNMT2 introduces the m^5C38 modification in several tRNAs.[6,9] Furthermore, DNMT2 is controversially discussed to be found in both nuclear compartments and the cytoplasm, hinting at its diverse roles and influence in protein biosynthesis.[9–11] Its distinctive catalytic MTase domain, featuring the unique cysteine-phenylalanine-threonine (CFT) motif, underscores its evolutionary and functional uniqueness within the DNMT family.[11] Physiologically, DNMT2 targets various tRNAs, including $tRNA^{Gly}$, $tRNA^{Val}$, and $tRNA^{Asp}$.[9,12] tRNA methylation by DNMT2 plays a role in regulating RNA degradation by ribonucleases, thereby enhancing tRNA stability and overall protein expression.[9,13] Additionally, tRNA m^5C38 methylation improves codon recognition, particularly distinguishing between aspartate and glutamate, thus enhancing translational accuracy.[14] Given DNMT2's role in regulating protein expression and translational accuracy, it is not surprising that DNMT2 misregulation has been implicated in cancer pathogenesis.[15] DNMT2 seems to play a functional role in various cancer cell lines and tumorigenesis, such as cervical or bladder tissue, and leukemia.[15–17] Additionally, DNMT2 silencing was found to correlate with miRNA upregulation which is also related to proliferation and function as tumor suppressor.[18] Also, elevated m^5C levels in small non-coding RNA (sncRNA), introduced by DNMT2, have been linked to metabolic disorders, where these influence the disorders' inheritance induced by high-fat diets in mice.[19] During oxidative stress, a DNMT2 upregulation could be detected, leading to the assumption that DNMT2 also helps cells cope with exogenous stress factors, underscoring DNMT2's multifaceted involvement in disease mechanisms.[20]

Despite its association with various disease mechanisms, DNMT2 remains a challenging target for drug development.[21] This is primarily due to the abundance of SAH and SAM and their ubiquitous binding proteins in cells with which inhibitors must compete.[22–24] Moreover, the fact that over 200 human MTases

This is an open access article under the CC BY license (http://creativecommons.org/licenses/by/4.0/).

CellPress
OPEN ACCESS

iScience
Article

depend on SAM further complicates the discovery of selective inhibitors.[25] Efforts to develop inhibitors targeting DNMT2 have predominantly focused on SAH analogs, which have achieved on-target potency in the micromolar range, but all fail to demonstrate selectivity within the DNMT or NSUN family MTases.[1,3,4] Currently available inhibitors also failed to inhibit DNMT2 within cellular assays, probably due to the low permeability of zwitterionic SAH derivates.[3] The generation of first-in-class selective and cell-active DNMT2 inhibitors is a current requirement to further investigate the function and druggability of DNMT2.

To address the development of cellularly potent DNMT2 inhibitors, we have applied the DNA-encoded library (DEL) screening technology on DNMT2 to identify modulating small molecule chemotypes. The goal was to develop selective chemical tools for DNMT2 investigation, modulation, and inhibition. DEL have gained widespread popularity in both industry and academia as a powerful tool for drug-like hit generation.[26–28] Comprising unique molecular structures tagged with DNA barcodes, DEL enables efficient diverse compound library screening and groundbreaking identification of novel drug scaffolds.[29–32] Since 1992, the DEL technology has undergone continuous development, evolving from initial strategies based on amide bond formation to widely used reactions such as metal-catalyzed cross-couplings, heterocycle synthesis, Diels-Alder cycloaddition, nucleophilic aromatic substitution, and reductions.[32,33] More recently, the methodology has expanded to include advanced transformations like photo-promoted reactions, C–H activation, and functionalization, thereby enabling access to a broad and diverse chemical space.[33] Recently, Wuxi AppTec enabled academic users to open access DEL by providing a DELopen platform containing a library of 4.2 billion unique compounds.[34] Latest DELopen successes include the ligand discovery for diverse proteins such as thrombin, RNase L, E3 ligases, the transcription factor TEAD, and antibacterial drug targets, highlighting its broad utility across various target classes.[30,35–39]

RESULTS AND DISCUSSION

DELopen screening reveals DNMT2 ligand chemotypes

Recombinant human DNMT2 was screened against the fourth-generation DELopen (WuXi AppTec) library (4.2 billion compounds, 27 sub-libraries) to identify small molecule RNA methyltransferase ligands (Figure 1A). DEL pannings were carried out with His-tagged DNMT2 protein stably immobilized on nickel chelate (Tris-NTA) affinity resin (Figure S1B). Selection screens against Tris-NTA resin without protein loading served as a nonspecific binding control. Three successive panning rounds were conducted, while the second round was chosen for deep sequencing based on the total retained DNA conjugates (Figures S1A and S1E). Sequenced hits were decoded and filtered to remove commonly encountered false positives and nonspecific binders to the affinity resin.[40] After affinity enrichment, 1713 unique full-length molecules were identified across three positive selection conditions and their combinations: (**A**) native DNMT2 without additives (n = 28 compounds); (**B**) DNMT2 with SAH (competitor, 100 μM, n = 104 compounds); (**C**) DNMT2 with $tRNA^{Asp}$ (competitor, 10 μM, n = 207 compounds); (**AB**) n = 159 compounds, (**AC**) n = 217 compounds, (**BC**) n = 251 compounds, (**ABC**) n = 747 compounds (Figure 1B).

These post-DEL screening compounds had enrichment scores of at least 100 for DNMT2. The enrichment score was calculated by decoding the DNA tags from next-generation sequencing (NGS) results, considering the corrected copy number, library size, sequencing depth, and other normalization factors (see https://hits.wuxiapptec.com/delopen).[41] A molecule with an enrichment score of 100 is a hundred times more abundant in the sequencing data than the average molecule in the library. Interestingly, DEL sequencing analysis showed that most of the compounds enriched on DNMT2 were found within the condition **ABC**, which may reflect the inability of the low-affinity SAH competitor to completely occlude the active binding site during the panning. The five compounds with the highest confidence (enrichment scores >200 000 and copy number >10, Table S5) and structural diversity (from three sub-libraries in total, see Figure S1F) were selected for further investigation and downstream validation studies (Figures 1C and 1D).

Across the 747 **ABC**-enriched and the five highest-scoring representative molecules ("hits"), recurring patterns were apparent in each of the four building block positions (denoted BB1, BB2, BB3, and BB4), indicating structurally related families: two triazine-based DEL hits (**1**–**2**) and three peptide-based DEL hits (**3**–**5**). Hit molecules **3**–**5** can be described as β-homotripeptides with non-natural side chain groups in building block positions BB2 resp. BB3 and incorporating an N-terminal substituent in BB1. The BB4 C-terminus (corresponding to the DNA tag attachment position) was synthetically amidated with methylamine. These hit compounds were resynthesized without the encoding DNA tag and were studied for DNMT2 active site binding using an MST displacement assay as previously described by Zimmermann et al.[42] For the thermophoretic detection, 5-FAM-triazolyl-adenosyl-diaminobutyric acid (FTAD) was used as a fluorescent probe, which can bind to the DNMT2 SAH binding pocket.[42] When FTAD is bound to DNMT2 versus its unbound state, there is a measurable difference in the F_{norm} value represented by a distinct positive MST shift, and thus, a ligand that can displace the FTAD-DNMT2 interaction can be detected by competitive MST screening assays (Figures S2 and S3).

In this regard, two of the five tested DEL hit compounds, **3** and **5**, induced a quantitative FTAD displacement in the MST assay (Figure 1E). In subsequent dose-response experiments, **3** and **5** showed K_D-values of 48.2 μM and 241 μM, respectively (detailed information in Table 1). Interestingly, **3** and **5** are similar in structure, differing only by the first building block, 4-ethylbenzoic acid for **3** and 4-methylthiophene-2-carboxylic acid for **5** (Figure 1D), while compound **4** features a similar peptidomimetic structure but without β-homo amino acids. In contrast, **1** and **2** share a common triazine core structure due to their origin from the same sub-library (Figure 1C). Notably, compounds **1** and **4** did not lead to FTAD displacement but rather induced a negative MST shift toward a higher FTAD-bound degree thermophoresis resp. strengthened interaction. We speculated about an allosteric binding mode of these compounds, which agrees with the observation that these compounds were identified in the **ABC** panning cluster.

iScience
Article

CellPress
OPEN ACCESS

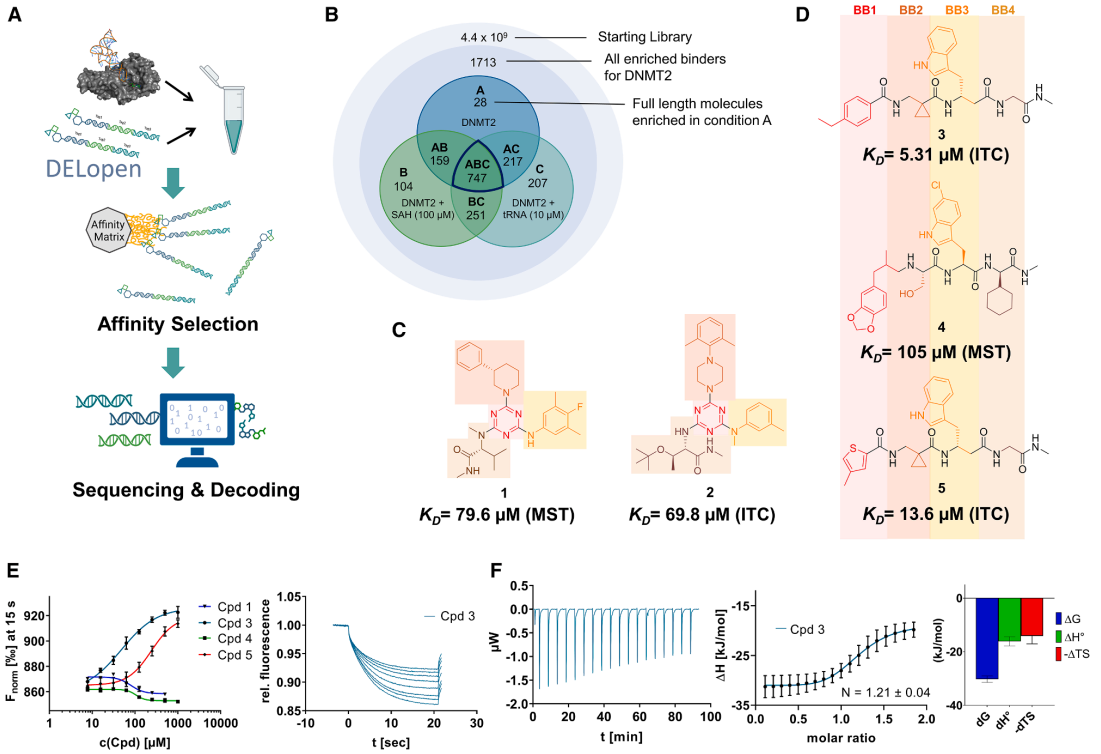


Figure 1. DEL screening reveals DNMT2 ligand chemotypes & biophysical characterization

(A) DELopen screening workflow. DELopen libraries consist of 4.2B compounds encoded by individual DNA barcodes. During affinity selection, small molecule-DNA conjugates are enriched, while non-binders are washed away.

(B) Conditions used during the DELopen screening: In condition A, native DNMT2 without additives was used; condition B: DNMT2 and SAH (100 µM) were mixed to block the SAH binding site; condition C: DNMT2 was incubated with $tRNA^{Asp}$ (10 µM). Most full-length molecules were enriched in condition ABC (unaffected by competitors), from which 5 selected compounds **1**–**5** were chosen for off-DNA synthesis and downstream characterization.

(C) Enriched triazine-based compounds selected from ABC.

(D) Peptidomimetic compounds enriched in ABC and chosen for further study. Building blocks BB1–BB4 are highlighted accordingly.

(E) MST dose-response curves for compounds **1**, **3**, **4**, and **5** with detailed MST traces for compound **3**.

(F) ITC data of compound **3** titrated to DNMT2. From left to right: Titration thermogram, stoichiometry plot, and signature plot. Data are represented as mean ± SEM. A comprehensive overview of the biophysical data for all compounds binding to DNMT2 can be found in the SI.

As an orthogonal biophysical binding experiment, we implemented isothermal titration calorimetry (ITC) ligand binding studies. In these experiments, **2**, **3**, and **5** showed significant binding enthalpy signals when titrated to DNMT2, with K_D-values of 69.8, 5.3, and 13.6 µM, respectively (Figure 1F; Figure S4). Of note, peptidomimetic hits **3** & **5** resulted in particularly long injection equilibration times in the minute magnitude, and thus, we speculated about a conformational change upon ligand binding, which could be confirmed by subsequent crystallography as described below. Interestingly, the thermodynamic profile showed that these hits had different enthalpy and entropy contributions despite their comparable affinity. During the ligand optimization from hit compound **3** to lead structure **16** (see below), this enthalpy contribution to the overall binding affinity increased continuously (Figure 5A). Additionally, an orthogonal and label-free affinity selection-mass spectrometry (AS-MS) assay for top-hit compound **3** was conducted (Figure S6), revealing a K_D-value of 8.40 ± 2.20 µM, which is in agreement with the ITC data.[43] Besides biophysical characterization utilizing DNMT2 binding assays, all five DEL hits were evaluated regarding their inhibitory effects using an enzymatic ^{3}H-incorporation assay, where the tritium-labeled methyl group incorporation from ^{3}H-SAM to the substrate $tRNA^{Asp}$ can be determined.[3,4] Compounds **3**, **4**, and **5** were able to inhibit DNMT2's MTase activity with IC_{50}-values of 38.9, 44.4, and 236 µM, respectively (Figure S7). Data and figures of additional ligand characterization experiments can be found in Figures S2–S7.

Taken together with the data gleaned from the DEL sequencing results, the combined ligand characterization data suggest that the DEL hits identified during this screening campaign are not binding to the DNMT2's active site nor tRNA pockets because hit compounds were enriched in condition

CellPress
OPEN ACCESS

iScience
Article

Table 1. Biophysical data of compounds 1–5 determined by various ligand binding and enzyme inhibition experiments

	^{3}H assay (IC_{50})	MST (K_D)	ITC (K_D)
1	n.i.	79.6 ± 10.0 μM	n.b.
2	n.i.	n.b.	69.8 ± 5.4 μM
3	38.9 ± 6.9 μM	48.2 ± 8.0 μM	5.31 ± 1.67 μM
4	44.4 ± 12.9 μM	105 ± 9 μM	n.b.
5	236 ± 63 μM	241 ± 36 μM	13.6 ± 1.6 μM

All results include the mean value and standard deviations from at least technical triplicate measurements. Raw data and analysis plots are depicted in Figure 1 and Figures S2–S7. n.i. = no inhibition/less than 50% inhibition at 500 μM//n.b. = no enthalpy signal observable (ITC)/no thermophoresis shift observable (MST).

ABC and show only partly competitive behavior during ligand binding experiments. The experimental findings from MST, ITC, and enzymatic ^{3}H-incorporation assay suggest that triazine compounds **1** and **2** act as non-competitive DNMT2 binders without inhibition potency, whereas β-homo-tripeptides **3–5** function as DNMT2 enzyme inhibitors. The mode of action resp. their binding site remained elusive from the biophysical investigations but could be finally solved by DNMT2 crystallography (vide infra). We speculated that the minor discrepancies between the enrichment scores' relative order and determined affinities may be due to the DNA tag sequence absence in the off-DNA synthesized hit compounds.

Development of fluorescent tracer molecules and binding site investigation

For further characterization of both triazine- and tripeptide-based DEL hits, fluorophore functionalized tracer compounds **6–8** were developed based on their parent compounds for target selectivity determination in fluorescence-based assays and as molecular probes for further investigations (Figure 2A; Figure S3). Three fluorescent probes were designed during this study for both identified DEL chemotypes: Alexa Fluor 488 (AF488) resp. tetramethylrhodamine (TAMRA) labeled β-homo-tripeptides (**6** and **8**), and a Cy5-labeled triazine-based probe (**7**). Apparent binding affinities of fluorescent probes were measured by MST experiments as described above with the modification that the respective probe was used instead of FTAD (Figure 2B; Figures S3E and S3F).[44] By this, probe binding affinities (**6**: 1.65 μM, **7**: 1.36 μM, and **8**: 0.70 μM) were determined which resemble the original DEL hit compounds' magnitude of potency, suggesting that the chosen fluorophores do not significantly interfere with their binding behavior and the probes are suitable for fluorometric MTase investigations.

Next, peptidomimetic probe **6** was utilized to determine MTase binding selectivity toward related DNMT resp. NSUN proteins and to investigate the competitivity of natural DNMT2 substrates (SAH and $tRNA^{Asp}$) by fluorescence polarization (FP) displacement experiments (Figure 2C). Fluorometric assays using DNMT2 revealed that the compound **6**-DNMT2 complex yields high fluorescence polarization (220 mP) compared to enzyme-free buffer conditions (5 mP). By examining whether this effect can be reversed by the addition of natural ligands, we found that SAH (100 μM) is able to displace probe **6**, while $tRNA^{Asp}$ (10 μM) does not show a significant effect, and high fluorescence polarization is retained during the tRNA substrate addition. These results were furthermore confirmed by an ITC displacement experiment, where **3** was able to displace SAH and vice versa (Figure 2D; Figure S5).[45] Interestingly, compound **3** appears to be partly competitive with SAH, although it behaves seemingly non-competitive in the DEL screening. We hypothesize that this discrepancy is due to the low affinity of SAH for DNMT2, and SAH is not retained in DNMT2-bound form during stringent washing steps to remove unspecific DEL-binders.

Probe **6** also enabled the determination of ligand binding selectivity toward other m^5C MTases using the FP assay setup. Since NSUN2, NSUN3, and NSUN6 introduce m^5C in other tRNA and DNMT1 resp. DNMT3A/3L in DNA, these enzymes were selected for the ligand selectivity profile determination. By incubating probe **6** with various related m^5C MTases, it was observed that this probe does not bind to related NSUN and DNMT families' MTase representatives at concentrations up to 20 μM, highlighting its unique DNMT2 binding selectivity (Figure 2C; Figure S3H). Due to the highest potency and excellent selectivity of hit compound **3**, we decided to conduct the following characterizations and further developments using this molecule as a starting point.

To investigate the competition of DEL hit compounds with the $tRNA^{Asp}$ substrate, we conducted an electrophoretic mobility shift assay (EMSA) to analyze the DNMT2-tRNA complex. Here, we found that none of the 5 hit compounds (100 μM) had an influence on the DNMT2-tRNA complex formation (Figure 2E).[46] Analogous MST displacement experiments with *in situ* fluorescently labeled $tRNA^{Asp}$ showed consistently no compound was able to dissociate the nucleic acid-protein complex formed by DNMT2 and $tRNA^{Asp}$ (K_D = 218 nM, Figures S8A and S8B). Furthermore, no compound (100 μM) had a significant influence on the thermophoresis of $tRNA^{Asp}$ in a protein-free solution (Figures S8C and S8D).[47] This finding is supported by our crystal structure of compound **3** with DNMT2 (vide infra). The previously elucidated RNA-binding residues (K122, R160, R162, R275, R289, K295, K367, and R371; mutagenesis study of Jurkowski et al., 2012) are in significant distance to the compound **3** binding pocket, and thus, allow the simultaneous binding of compound **3** and tRNA.[48] The exact binding mode of $tRNA^{Asp}$ to DNMT2 could not be elucidated by crystallography until now, therefore, we have created an Alphafold model illustrating the ternary complex of the SAH resp. compound **3**, and $tRNA^{Asp}$ (Figure S20).

Crystallography unravels an allosteric binding pocket of hit compound 3

For our crystallographic studies, we used a deletion construct of human DNMT2, dubbed DNMT2Δ47, in which residues 191 to 237 were deleted since this region is predicted as intrinsically disordered. A similar construct was successfully used for the only available X-ray structure of human DNMT2 bound to SAH (PDB 1G55[49]). We found that the deletion mutant's catalytical activity is indistinguishable from the full-length wild-type enzyme (Figure S7C), and that hit compound **3** displays medium-range micromolar affinity (48 vs. 102 μM) against both wild-type and DNMT2Δ47 enzymes (Figure 1E vs; Figure S3G).

iScience
Article

CellPress
OPEN ACCESS

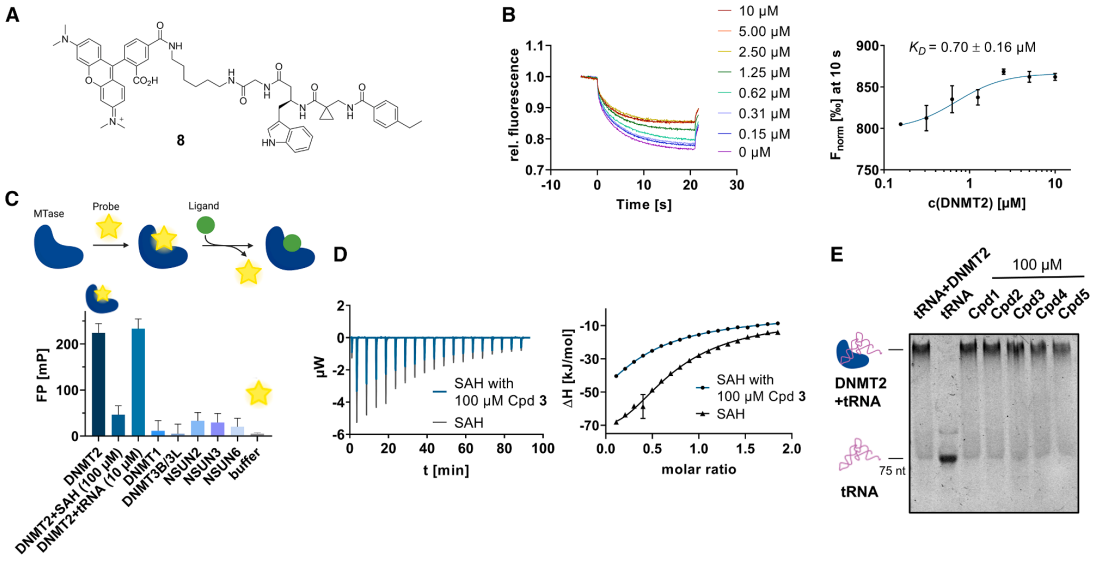


Figure 2. Investigating the ligand binding mode and selectivity with biophysical methods

(A) Chemical structures of probe **8**: TAMRA-labeled β-homo-tripeptide.

(B) MST dose-response curves for probe **8** binding to DNMT2.

(C) Fluorescence polarization assay for probe **6** binding to native DNMT2 (2 µM), DNMT2 (2 µM) preincubated with SAH (100 µM), DNMT2 (2 µM) with $tRNA^{Asp}$ (10 µM), and various related MTase off-targets (all 2 µM).

(D) DNMT2-SAH ITC displacement experiment for compound **3**. SAH was titrated to DNMT2 in the absence resp. presence of compound **3** (100 µM), yielding a significant enthalpy reduction.

(E) EMSA assay investigates the competition of hit compounds **1**–**5** with the tRNA substrate. Positive control: tRNA+DNMT2 (band at high molecular weights); negative control: only tRNA (band at low molecular weights). Hit compounds **1**–**5** (100 µM) were added to the DNMT2-tRNA complex (10 + 5 µM) and analyzed by native PAGE. No compound was able to dissociate the DNMT2-tRNA complex. Data are represented as mean ± SEM. Uncropped PAGE images can be found in Figure S22.

We could obtain an X-ray structure of human DNMT2Δ47 with bound compound **3** at 2.6 Å resolution, which shows an overall fold similar to DNMT2Δ47-SAH (PDB 1G55) as indicated by an overall rmsd (C_α) of 0.69 Å (Figure S17A). The asymmetric unit contains two very similar DNMT2Δ47-compound **3** complexes with an overall rmsd(C_α) of 0.354 Å and the largest differences in the loop region comprising residues 82 to 95 (Figure 3A). A large common surface area of 1685 $Å^2$ is present between these two protein complexes. Interface and packing analysis with PISA[50] supports a stable dimer formed by the two complexes in the asymmetric unit. Therefore, we used analytical size exclusion chromatography to investigate the oligomeric state of DNMT2Δ47-compound **3** in solution. We could show that DNMT2Δ47 with bound compound **3** is indeed dimeric in solution at a high protein concentration of 10 mg/mL (Figure S18), which was also used for crystallization. In contrast, DNMT2Δ47 without ligand is monomeric in solution under the same conditions.

Both complexes in the asymmetric unit show clear electron density for compound **3** (Figure S17C). Most interestingly, compound **3** is bound in a largely hydrophobic pocket adjacent to the active site (Figure 3B). For comparison, the structure with SAH bound in the active site is depicted in Figure 3C, and superpositions of the two different complexes without and with ligands are given in Figures S17A and S17B. Compound **3** is bound by residues mainly from the two regions β4-α4 and β5-α5, which is depicted in Figure 4A for chain A (interacting residues of chain B have been omitted for clarity).

A comprehensive schematic ligand-protein interaction diagram was created with LigPlot+[51] for both DNMT2Δ47-compound **3** complexes in the asymmetric unit (Figure S19). In the following, a detailed description of compound **3** binding to chain A and the differences between both complexes in the asymmetric unit are given. The indole ring of compound **3** is located in a hydrophobic cave formed by Y10, M75, backbone of S76, P77, F99, L118, F124, and L133. Additionally, the amine group of the indole ring forms a hydrogen bond with the backbone carbonyl of E119. The ethylbenzene moiety of compound **3** is bound between V121, F124, S127, T129 and $L279_B$. The ethyl group is also in contact with a glycerol molecule (used for cryo-protection) bound in the dimer interface. The amide group, which connects the ethylbenzene and cyclopropane moieties, is in van der Waals contact with P78 and R95 and forms three hydrogen bonds, namely with the main chain carbonyl of $L278_B$, with the side chain of N120, and an intramolecular H-bond to the amino group connecting the cyclopropane and indole moieties. The cyclopropane moiety is surrounded by the hydrophobic side chains of F99, $L278_B$, and $L279_B$. Finally, the two terminal amide groups of compound

CellPress
OPEN ACCESS

iScience
Article

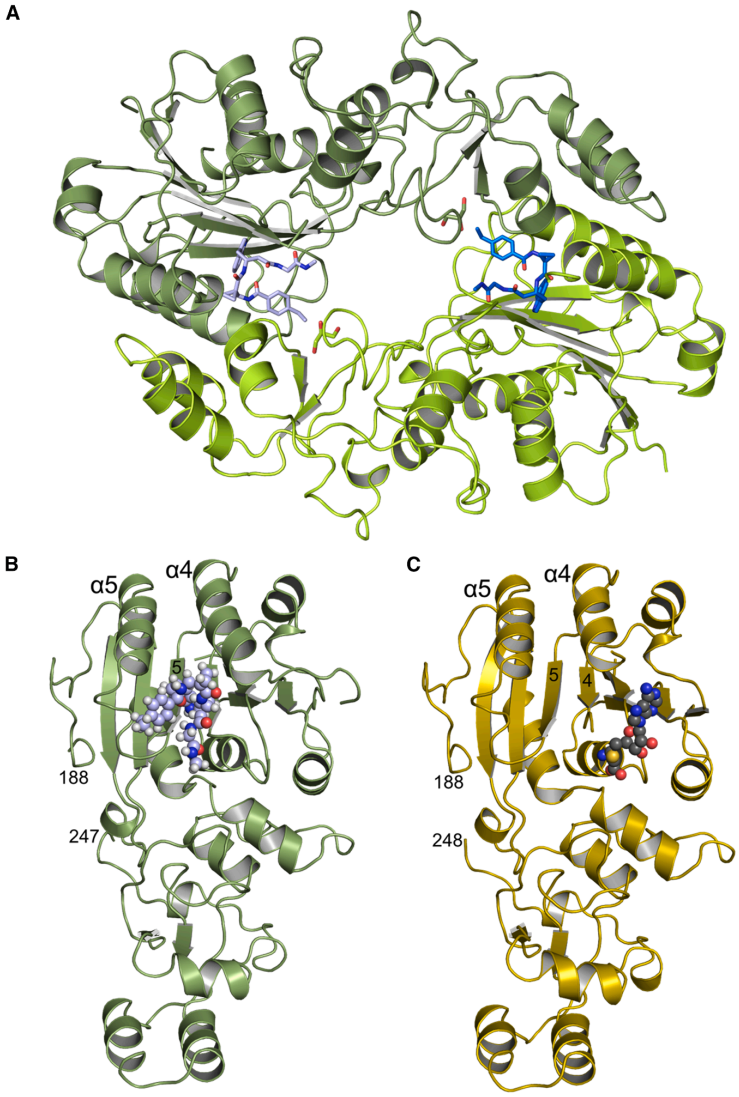


Figure 3. Crystallography unravels an allosteric binding pocket of hit compound 3

(A) X-ray structure of DNMT2Δ47 showing both molecules of the asymmetric unit. Bound compound **3** molecules are represented as sticks. Chain A is shown in green/light blue and chain B in light green/blue.

(B) X-ray structure of DNMT2Δ47-compound **3** chain A depicted as cartoon (green) with compound **3** as spheres (carbon atoms in light blue).

(C) The crystal structure of human DNMT2Δ47 (PDB 1G55) as cartoon (yellow) with bound SAH as spheres (carbon atoms in gray) is given for comparison.

3 form hydrogen bonds with the side chains of N120 and N375. Due to different side chain conformations in chain B, $R95_B$ forms an additional hydrogen bond to this part of compound $\mathbf{3}_B$, and $N281_A$ and $E302_A$ are in non-polar contact with compound $\mathbf{3}_B$. The molecular surface representations of the ligand binding site colored by hydrophobicity (Figure 4B) and electrostatic potential (Figure 4C) show a clear correlation with the properties of the individual moieties of the bound ligand, e.g., the binding of the ethylbenzene moiety to a hydrophobic patch and the interaction of the carbonyl groups with a highly positive patch.

In order to analyze the structural rearrangements induced by compound **3** upon binding to DNMT2Δ47, we created a local superposition with DNMT2Δ47-SAH onto the central β-sheet of the large domain, namely onto β3 to β7. As depicted in Figure 4D, the largest local movement upon binding of compound **3** is observed in the loop following β4 (M75 to P78), where P77 and P78 are rotated and shifted toward the SAH binding site. Additionally, subsequent residues could be built in both complexes with compound **3** (A: C79–F82; B: C79–I87), whereas in DNMT2Δ47-SAH, residues 79 to 96 are not resolved. Binding of compound **3** shifts residues into the SAH binding pocket. Moreover, the active site residue C79 is now resolved and moved into the SAH binding region. The superposition depicted in Figure 4D shows that binding of compound **3** narrows the active site, which prohibits SAH binding due to steric hindrance by P77, P78, and C79. As a consequence, compound **3** acts as an allosteric inhibitor by reshaping the active site.

Structure-activity study leads to structural optimization of hit compound 3

As the next step, we aimed to increase the affinity of the DEL hits to generate a cellularly effective DNMT2 modulator. Compound **3** was chosen for structure-activity-relationship studies (SAR) due to its favorable binding characteristics observed in ITC, MST, and ^{3}H-based enzyme assays. Its suitability for SAR investigation was enhanced by the feasibility of conducting solid-phase peptide synthesis (SPPS) to generate a diverse ligand analog set. A major advantage for compound **3** optimization is given by the elucidated crystal structure, which allows rational considerations for improving ligand interactions in the DNMT2 inhibitors design. First, a computational SeeSAR analysis of the ligand binding pose was performed, which provided information on putative approaches for ligand optimization (Figure S21).[52]

iScience
Article

CellPress
OPEN ACCESS

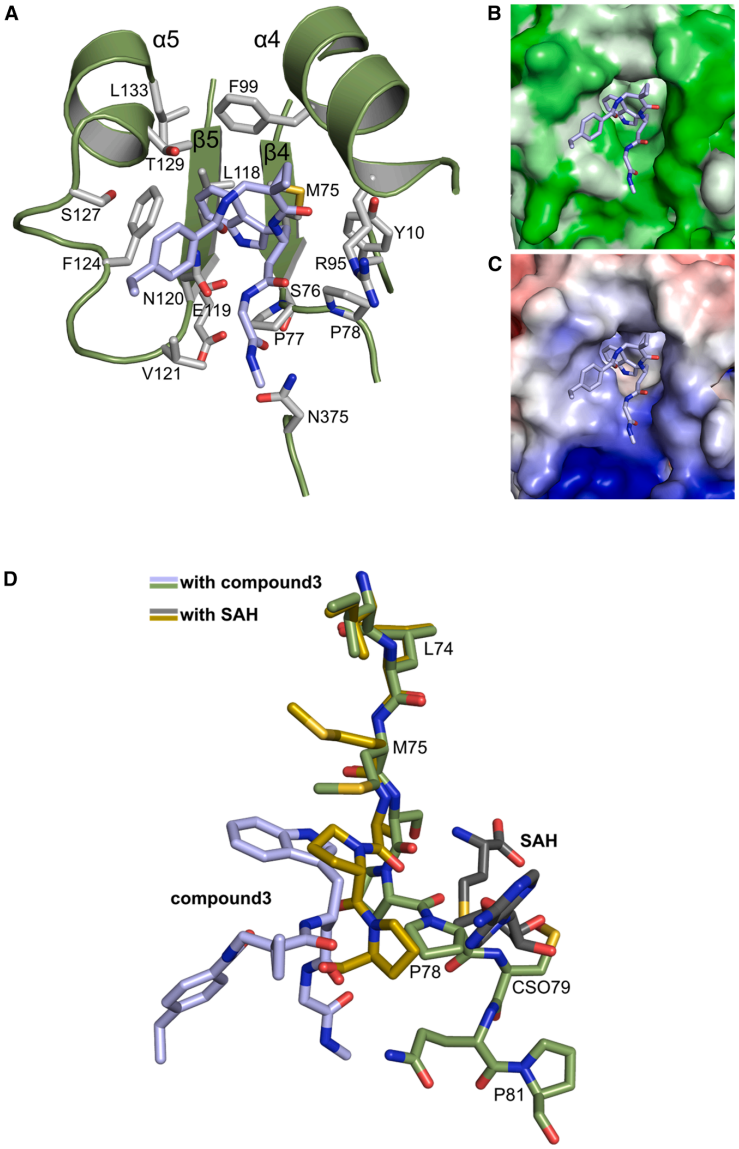


Figure 4. Ligand-protein interactions of compound 3

(A–C) (A) A detailed view of compound **3** (carbon atoms in light blue) bound to DNMT2Δ47 chain A (green cartoon) with interacting protein side chains in light gray. Side chains of chain B are omitted for clarity. Molecular surface representation of the binding site with compound **3** colored by (B) hydrophobicity (white -> green = high -> low) and (C) electrostatic potential from −5 kT/e (red) to +5 kT/e (blue).

(D) Superposition of compound **3**- & SAH-binding protein segments. Local superposition onto the central β-sheet in the large domain of DNMT2Δ47-compound **3** (green/light blue) with DNMT2Δ47-SAH (yellow/gray) showing the end of β4 and following residues with respective ligands. Residues P77, P78, and C79 are shifted toward the SAH binding site upon compound **3** binding.

The following hypotheses on the ligand binding characteristics were derived from this computer-assisted analysis: Most atoms of ligand **3** are already optimally positioned for interaction with the DNMT2 protein (green spheres). A few atoms that are assumed to have an unfavorable effect on the DNMT2 interaction (red spheres of the BB2 and BB3 carbonyl oxygens) cannot be exchanged without the loss of the characteristic U-shaped ligand. In conclusion, we hypothesized that modification to the peptide backbone would lead to a significant loss of binding affinity. The peptide backbone's dihedral angles are mostly in optimal shape for BB3 and BB4 but show minor potential for improvement in BB1 and BB2. Interestingly, there are three regions in the ligand binding pose that allow ligand expansion (gray shading) and thus enable additional potentially beneficial interactions. These regions are localized (1) between BB1 and the C-terminus, which may allow ligand macrocyclization, (2) in the homo-tryptophan residue 5-position, and (3) near the BB2 cyclopropyl motif. These regions were to be investigated by substitutions and scaffold-hopping strategies in the SAR study. Subsequently, a total of 40 derivatives derived from hit compound **3** were synthesized and screened for DNMT2 binding using the MST assay at a final ligand concentration of 100 μM. If significant binding to DNMT2 was measured (>25% FTAD displacement), the binding affinity was determined by following ITC experiments. A comprehensive overview of compound and assay data can be found in Table S1.

During this SAR study all building block positions (BB1–BB4) were systematically varied: For the BB1 variation (4-ethylbenzoyl), it was observed that the alkyl chain at the phenyl ring's *para* position was replaceable, still resulting in significant binding affinities. Notably, the presence of a (rigidized) alkyne group in this position resulted in the complete DNMT2 binding abolition. Furthermore, substitutions other than the *para* position, as well as the aromatic moiety's absence, failed to sustain ligand affinity. Next, we observed that any BB2 substitution, shortening, or decyclization of cyclopropyl-β-alanine was also not tolerated, highlighting the critical necessity of this special β-amino acid. For the BB3 substitution (β-homo-tryptophan), all attempts to

CellPress
OPEN ACCESS

iScience
Article

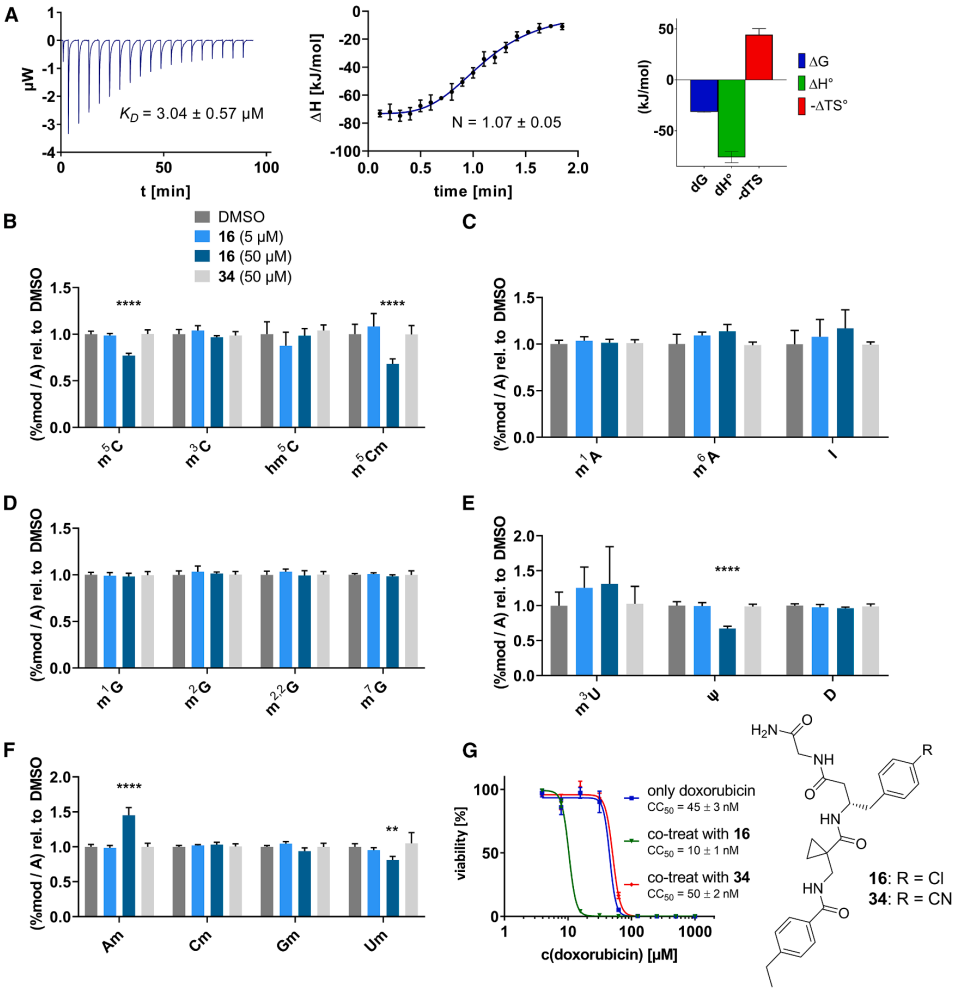


Figure 5. Biophysical and cellular evaluation of SAR study's most potent compound 16

(A) Compound **16** showed a K_D = 3.04 ± 0.57 µM in ITC experiments.

(B) MOLM-13 cells were treated for 72 h with compound **16** (5 and 50 µM) or **34** (50 µM). $tRNA^{Asp-GTC}$, $tRNA^{Val-AAC}$, and $tRNA^{Gly-GCC}$ were enriched by an antisense pull-down strategy. LC-MS/MS-based assay results for cellular tRNA modification changes analysis. Changes in cytosine modifications relative to the DMSO control.

(C) Changes in adenine modifications relative to the DMSO control.

(D) Changes in guanine modifications relative to DMSO control.

(E) Changes in uridine modifications relative to DMSO control.

(F) Changes in 2′*O*-methylations relative to the DMSO control. *$p < 0.05$, **$p < 0.01$, ***$p < 0.001$, ****$p < 0.0001$.

(G) Dose-response curves from cell viability assays of doxorubicin/compound **16** resp. **34** co-treated MOLM-13 cells. Cells were cultured for two passages of each three days in the presence of compound **16** or **34** (50 µM) and subsequently treated with varying concentrations of doxorubicin for 48 h. Data are represented as mean ± SEM. Supplementary cell viability assays can be found in Figure S9.

shorten the peptide backbone, altering the stereochemistry, and most tryptophan ring system replacements yielded no binding to DNMT2. However, replacement with the phenyl-containing analog (β-homo-(*R*)-phenylalanine, (**14**)) resulted in significant binding. Subsequent synthesis of diverse *para*-substituted derivatives showed improved binding affinity compared to parent compound **3**, which could be confirmed by subsequent dose-response MST and ITC experiments (K_D(**16**) = 3.04 ± 0.57 µM, Figure 5A). When substituting BB4 (glycine), extending the peptide backbone, or exchanging with either (*R*)- and (*S*)-alanine,

iScience
Article

CellPress
OPEN ACCESS

BB4 derivates showed significantly lower DNMT2 affinities. Interestingly, amide group methylation between BB1 to BB4, yielded no significant ligand affinity to DNMT2. As an exception, the peptide C-terminus methylation among other modifications (see also probes **6** and **8**) did not disturb the ligand affinity, and thus, represented a potential exit vector from the DNMT2 pocket suitable for ligand conjugation.

In summary, our experimental SAR is a major confirmation of the SeeSAR hypotheses and agrees well with the crystal structure's ligand pose. The BB3 replacement from β-homo-(*R*)-tryptophane (**3**) to β-homo-(*R*)-(4-chloro)phenylalanine (**16**) led to an improvement in ligand affinity, while most other modifications resulted in similar or lower ligand affinities. Since peptidomimetic drugs might be prone to cellular permeability issues, hit compound **3** and the most potent ligands **10**, **14**, **16**, **47**, and **54** were tested for passive membrane transport using a parallel artificial membrane permeation assay (PAMPA). While compounds **3**, **10**, **14**, **47**, and **54** failed to pass through the artificial membrane, compound **16** showed moderate passive permeability (P_{app} = 0.3 10^{-6} cm/s), rendering this compound as the most promising lead structure of this SAR optimization. Detailed PAMPA results can be found in the supporting information (Table S2). Overall, compound **16** showed the best ligand binding properties, and it also demonstrated the ability for passive membrane transport in the PAMPA, making it a promising candidate for cellular studies of DNMT2 inhibition.

Cellular potency of allosteric inhibitors targeting DNMT2

Next, we aimed to investigate whether compound **16** can affect enzymatic DNMT2 activity in a cellular context and is thus able to reduce RNA modification contents in living systems. Previously, DNMT2$^{-/-}$ mice were found to have reduced m^{5}C levels in corresponding tRNAs (tRNA$^{Asp-GTC}$, tRNA$^{Val-AAC}$, and tRNA$^{Gly-GCC}$), while only the double-knockout (DNMT2$^{-/-}$ & NSUN2$^{-/-}$) mutant resulted in a complete m^{5}C elimination in tRNA substrates of DNMT2.[13] Further experiments utilizing siRNA-mediated DNMT2 knockdown and chemical inhibition with the pan-DNMT/NSUN inhibitor azacitidine in leukemia cells demonstrated a total C38 methylation loss.[53,54] Following these observations, we aimed to investigate whether **16** can reduce m^{5}C modification levels in cells through isoacceptor-specific enrichment of DNMT2 tRNA substrates and modification analysis by means of an LC-MS/MS-based assay. In this regard, following previous studies investigating DNMT2's role in leukemia cells,[54,55] we treated MOLM-13 cells with **16** (5 and 50 μM) for 72 h, followed by the isolation of isoacceptor-specific tRNAs using biotinylated antisense DNA oligomers on magnetic beads. LC-MS/MS-based analysis of digested total tRNA isolates was used to determine relative changes in modification levels of 18 abundant tRNA modifications.[56]

As shown in Figure 5, levels of targeted tRNA modifications (m^{5}C and m^{5}Cm) were significantly reduced when MOLM-13 cells were treated with 50 μM of compound **16**. In this regard, the m^{5}C reduction (∼25%) is in agreement with previous knock-down experiments, highlighting that 75% of tRNA m^{5}C are mediated by NSUNs.[13] Notably, treatment with 5 μM of compound **16** was found to be too low to stimulate any significant change in RNA modifications, probably due to its moderate cell permeability and proportionally lower cellular concentration. In addition, only minor other modification changes were observed, including mildly reduced pseudouridine and Um levels resp. slightly increased Am levels, highlighting our inhibitor chemotype's DNMT2-selectivity. The origin of those off-target RNA modification alterations remains not entirely solved, but we speculate that RNA-modifying enzymes introducing those modifications are likely to be regulated by DNMT2-mediated m^{5}C modification, rendering them as hierarchical-type modifications.[57] In contrast, treatment of MOLM-13 cells with a tailor-made chemical negative control compound **34**, which does not bind DNMT2, showed, as expected, no reduction of m^{5}C in tRNA (Figures 5B–5F).

To confirm that our lead compound **16** successfully engages DNMT2 in the MOLM-13 cellular environment, we performed cellular thermal shift assays (CETSA) with compounds **16** (cell-active) and **3** (non-permeable control). As expected, we found thermal stabilization of DNMT2 in the CETSA assay after incubation with 50 μM of **16**, whereas no thermal stabilization occurred in a comparable experiment with compound **3** (Figures 6A and 6B). We conclude that our lead structure **16** engaged DNMT2 in MOLM-13 cells and that m^{5}C inhibition is likely mediated by DNMT2 inhibition.

Compound **3**, on the other hand, did not lead to effective DNMT2 engagement due to its lack of passive permeability (Table S2). Based on predictions from Molinspiration and SuperCypPred toolkits, cell-evaluated compounds **3**, **16**, and **34** display highly similar physicochemical profiles, suggesting no significant differences in their expected pharmacokinetic profile (Table S4). The values for molecular weight, topological polar surface area (TPSA), logP, hydrogen bond donors and acceptors, as well as the number of rotatable bonds are all similar. The compounds comply with Lipinski's Rule of Five, except for compound **3**, which violates one parameter (molecular weight >500 Da). According to SuperCypPred predictions, compounds **3** and **16** are inactive against all tested CYP isoforms except CYP3A4, while compound **34** shows no predicted CYP activity (Figure S23). In principle, these findings are in line with our expectations based on research in the literature: The DNMT2 inhibitors presented in this study belong to the class of ''peptidomimetics with non-natural amino acids'', which are known to be limited in their passive permeability, but have good proteolytic and metabolic stability.[58] From the combined results, including the CETSA assay results and the *in vitro* permeability studies (PAMPA), we conclude that only compound **16** but not compound **3** is permeable and that this permeability difference is the reason for the different cellular activities.

Since the genetic DNMT2 knockdown leads only to minor morphological changes in healthy and cancer cells, but the use of the FDA-approved pan-DNMT/NSUN inhibitor azacitidine is an effective cytostatic drug in leukemic cells, the question of whether DNMT2 is a cell viability-affecting drug target for cancer has been discussed for years.[59] We therefore investigated the effect of the DEL hit compounds **1**–**5** and **16** on the cell viability of a diverse panel of cancer cell lines (MOLM-13, HCT, Huh-7, and MDA-MB-231) and one non-cancerous cell line (HEK293)

CellPress
OPEN ACCESS

iScience
Article

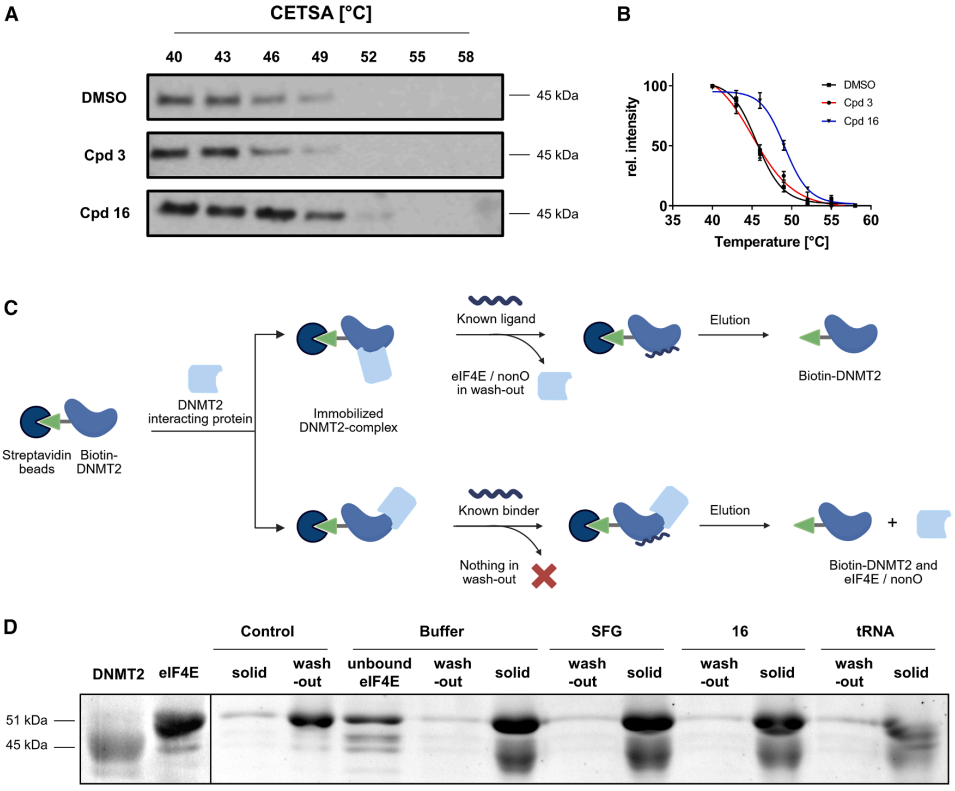


Figure 6. Investigation of allosteric DNMT2 interaction profiles and target engagement

(A) Cellular thermal shift assay (CETSA) to evaluate the DNMT2 target engagement of compounds **3** and **16** in MOLM-13 cells. Uncropped Western blots can be found in Figure S22.

(B) Densitometric analysis of CETSA Western blots highlights the stabilization of DNMT2 in the presence of compound **16** (50 μM) but not compound **3**.

(C) Pull-down competition assay workflow. Biotinylated DNMT2 was immobilized on magnetic streptavidin beads and incubated with recombinant eIF4E protein. Subsequent treatment with the known ligands sinefungin (SFG), compound **16**, or $tRNA^{Asp}$ was used to examine if such ligands can dissociate the DNMT2-eIF4E interaction.

(D) Results of the SDS-PAGE-based analysis. Lane description from left to right: DNMT2/eIF4E: recombinant proteins for size comparison. References were applied at another gel position and merged in this figure; Control: beads without immobilized DNMT2 served as the negative control, i.e., on these beads no binding of eIF4E was observed. Treatment (buffer, SFG, **16**, tRNA): The lane "unbound eIF4E" contains the supernatant after the immobilization of eIF4E, which showed low protein levels, thus, most eIF4E is effectively immobilized on DNMT2 beads. Lanes labeled with (wash-out) contain the supernatant of the respective treatment conditions (buffer, 100 μM SFG, 100 μM **16**, 10 μM $tRNA^{Asp}$), while bands labeled with (solid) contain the solid fraction obtained by boiling the residual beads in Laemmli buffer. Data are represented as mean ± SEM. Uncropped PAGE images can be found in Figure S22.

and compared it with the effect of azacitidine (Figure S9).[54,55] Using an ATP-quantifying cell viability assay, after treatment with varying concentrations of test compounds for 48 h, triazines (**1** and **2**) exhibited cellular toxicity only at concentrations >100 μM, while the peptidomimetic hit compounds (**3**–**5** and **16**) showed only slight reduction in cell viability even at high micromolar concentrations. This suggests that viability is not affected due to DNMT2 inhibition since 50 μM of **16** leads to an efficient m^5C level reduction in MOLM-13 cells. This is further supported by cell viability experiments in HCT mutant cells, including the investigation of HCT DNMT2 knock-down and HCT NSUN2 knock-down cell lines, highlighting low toxicity of all peptidomimetic compounds at 100 μM. From these cell-based investigations, we conclude that the cytotoxic effect of azacitidine (CC_{50} < 10 μM in all cell lines) is not a cause of DNMT2 inhibition but is mediated by DNMT1/3 and NSUNs inhibition. In summary, our DNMT2 inhibitor **16** is well capable of reducing tRNA m^5C levels in a cellular context, but at the same time not reducing the cell viability of cancer cells.

However, it is known from previous publications that a genetic DNMT2 knockdown makes cancer cells more vulnerable to chemotherapeutic treatment with doxorubicin on cancer cell lines.[60] Hence, we exposed selected cell lines to a co-treatment with compound **16** (50 μM) and a variable dose of doxorubicin to

iScience
Article

CellPress
OPEN ACCESS

analyze cell viability using the viability assay described above. Cultivation of MOLM-13, Huh-7 and MDA-MB-231 cells in the presence of 50 μM compound **16** for two passages of three days each led to no observable reduction in cellular viability but made the cells more susceptible to the subsequent treatment with doxorubicin (Figure 5G; Figures S9H and S9I). As expected, co-treatment with the tailor-made negative control **34** (50 μM) did not lead to a synergistic reduction in viability.

Known DNMT2-interacting proteins do not bind to the allosteric pocket

The discovery of allosteric DNMT2 modulators mediating cellular m^5C reduction implicates the question of whether this allosteric pocket may play a role in the cellular regulation of DNMT2 activity. The peptidomimetic structure of the identified hit compounds **3**–**5** might hint at a putative protein-based endogenous ligand, but so far, no allosteric DNMT2 interaction partners have been reported to regulate the enzymatic function. Yet, it was previously found by immunoprecipitation and peptide fingerprinting experiments that human DNMT2 shows interaction with a handful of cellular proteins, which are involved in RNA processing and stress response, including eIF4E, splicing factors NonO resp. SfpQ, and proteins involved in RNA transport.[20] However, it is unknown in which conformation these proteins bind to DNMT2 and whether these can influence DNMT2 activity.

To study a potential connection to our elucidated allosteric pocket, we probed the interaction between recombinant eIF4E resp. NonO proteins and DNMT2 by means of a pull-down competition assay. In this regard, we immobilized biotinylated DNMT2 on streptavidin-coated magnetic beads and incubated with recombinant eIF4E or NonO, which are able to bind to DNMT2. Subsequent treatment with the established DNMT2 ligands sinefungin (100 μM), compound **16** (100 μM), or $tRNA^{Asp}$ (10 μM) was used to analyze if those ligands are able to dissociate the complex between eIF4E/NonO and DNMT2. SDS-PAGE analysis of the pulled-down fractions, including the separated beads (solid) and supernatants (wash-out) revealed that NonO and eIF4E show efficient binding to DNMT2 on magnetic beads but do not bind to the unfunctionalized beads (Figures 6C and 6D; Figure S16), confirming the reports these proteins are in fact DNMT2 interacting proteins. Yet, neither NonO nor eIF4E could be displaced from binding to immobilized DNMT2 by competitive treatment with compound **16**, sinefungin (SFG), or $tRNA^{Asp}$, indicating that both NonO and eIF4E do not bind to the cryptic allosteric binding pocket identified. We hypothesize that both proteins might bind to a distinctive epitope outside of the MTase active site and reject the hypothesis that the identified allosteric pocket is an endogenous binding site at least for these known DNMT2 interacting proteins.

To summarize this study, our DEL screening successfully identified compounds that target a cryptic allosteric pocket of DNMT2, inducing a conformational change that blocks the SAH-binding active site and leads to subsequent DNMT2 inhibition. In-depth characterization of biomolecular interactions and the development of fluorescent DNMT2 probes revealed that this ligand chemotype showed strong selectivity for DNMT2 within the DNMT/NSUN family. The DNMT2-compound **3** crystal structure revealed the unique inhibitor binding mode causing an active site loop displacement. Synthetic structure-activity relationship studies were performed to improve the affinity of the allosteric ligand, which led to the discovery of a lead compound (K_D∼3 μM) with improved passive cell permeability and the ability to inhibit DNMT2 in a cellular context, as demonstrated by reduced tRNA m^5C content. By this, we could also confirm that selective chemical DNMT2 inhibition is not affecting cell viability in different DNMT2-insensitive cells, but co-treatment with doxorubicin can inhibit MOLM-13 proliferation synergistically. In summary, allosteric inhibition of DNMT2 could be a potential target for a synergistic cancer treatment strategy.

Limitations of the study

The physiological role of the ligand-induced conformational change remains partly unelucidated and will need further experimentation (e.g., the question of whether this allosteric pocket may play a role in the cellular regulation of DNMT2 activity) and the comprehensive assessment of potential non-m^5C MTase off-targets. Furthermore, the elucidation of ternary DNMT2-tRNA-SAH resp. compound **3** complexes would strengthen the understanding of the catalytic regulation of this conformational change. Whether this type of DNMT2 inhibitor is effective in more advanced cancer assays including *in vivo* treatment should be investigated once the binding affinity to DNMT2 has been further increased and a cellular high-potent tool compound with low nanomolar potency has been achieved. The double-digit micromolar concentrations needed for cellular m^5C reduction will leave room for improvement in future inhibitor designs. This could be attempted in the future by developing a compound **3**-based PROTAC, macrocyclization, or the development of covalent inhibitor conjugates, etc.

RESOURCE AVAILABILITY

Lead contact

Further information and requests for resources and reagents should be directed to and will be fulfilled by the lead contact, Fabian Barthels (barthels@uni-mainz.de).

Materials availability

Molecules generated in this study are available from the lead contact upon request and completion of an MTA. DNMT2Δ47 containing plasmid for recombinant protein expression has been deposited to Addgene: #198382.

Data and code availability

- Coordinates and structure factors of the DNMT2Δ47-compound **3** complex are deposited at the Protein DataBank PDB under accession code 9HGM.
- This paper does not report original code. All software and algorithms are listed in the key resources table.
- Any additional information required to analyze the data reported in this paper is available from the lead contact upon request.

ACKNOWLEDGMENTS

We thank Francesca Tuorto (Heidelberg) for providing NSUN2 knock-down cell lines, Ganna Podoprygorina (Mainz) for support during LC/MS measurements, WuXi AppTec for support during sequencing and data analysis of the

CellPress
OPEN ACCESS

iScience
Article

DEL screenings, Hanna Bodenstaff (Mainz) for support during the synthesis of the inhibitors, Karin Pauly (Mainz) for support during cell viability assays, and Michael Klein (Mainz) for support during the preparation of Biorender illustrations. We acknowledge access to ESRF Grenoble beamline ID30B and thank the ESRF staff for their support. We thank Claudia Siegmann from the CCTP/BZH crystallization platform for excellent technical support. F.B. acknowledges the support from TRR319 (Project-ID 439669440) TP A01. I.S., M.S., and J.K. acknowledge the service SDS@hd supported by the Ministry of Science, Research and Arts Baden-Württemberg and the DFG through grants INST 35/1314-1 FUGG, INST 35/1503-1 FUGG. Financial support by the Deutsche Forschungsgemeinschaft via TRR319 (Project-ID 439669440) B03 to I.S. and TP C01 to M.H. is gratefully acknowledged.

AUTHOR CONTRIBUTIONS

A.F.F. performed DEL panning, analysis of hit clustering data, hit selection, microscale thermophoresis, ^{3}H-assays, FP assays, synthesis of compounds, SeeSAR analysis, and writing of the manuscript; M.S. performed cloning, expression, purification, and characterization of DNMT2Δ47, protein crystallization, data collection, model building, and writing of the manuscript; A.C.W. performed ITC measurements, and cell cultivation; V. K. performed synthesis, MST measurements, AS-MS assay, and pull-down assays; J.K. performed protein crystallization, data collection, model building, and writing of the manuscript; Z.N. performed protein expression and tRNA preparation; R.A.Z. performed protein expression and developed the idea for DNMT2Δ47 mutant; L.G. performed cell viability assays and tRNA LC/MS sample preparation; C.Z. performed PAMPA; M.J. performed cell viability assays; K.F. performed concept of study, supervision, and writing of the manuscript; M.H. performed concept of study, supervision, and writing of the manuscript; I.S. performed concept of study, supervision, data analysis, and writing of the manuscript; F.B. performed concept of study, supervision, and writing of the manuscript. All authors commented on the manuscript.

DECLARATION OF INTERESTS

Mark Helm is a consultant for Moderna Inc.

STAR★METHODS

Detailed methods are provided in the online version of this paper and include the following:

- KEY RESOURCES TABLE
- METHOD DETAILS
  - DEL screening
  - Microscale thermophoresis (MST)
  - Isothermal titration calorimetry (ITC)
  - Fluorescence polarization (FP)
  - ^{3}H-based methyltransferase enzyme activity assays
  - Affinity selection-mass spectrometry (AS-MS)
  - Electrophoretic mobility shift assay (EMSA)
  - *In vitro* permeability assay (PAMPA)
  - Protein and tRNA production
  - DNMT2 cloning, expression, and purification for co-crystallization
  - Analytical size-exclusion chromatography of DNMT2Δ47 with compound **3**
  - Crystallization, data collection, model building, and refinement
  - SeeSAR analysis
  - Pull-down DNMT2 interaction assay
  - tRNA modification analysis by LC/MS
  - Cell viability assays
  - Cellular thermal shift assay (CETSA)
  - Synthesis and characterization of inhibitors and probes
- QUANTIFICATION AND STATISTICAL ANALYSIS

SUPPLEMENTAL INFORMATION

Supplemental information can be found online at https://doi.org/10.1016/j.isci.2025.113300.

Received: April 23, 2025
Revised: June 19, 2025
Accepted: August 1, 2025
Published: August 5, 2025

REFERENCES

1. Fischer, T.R., Meidner, L., Schwickert, M., Weber, M., Zimmermann, R.A., Kersten, C., Schirmeister, T., and Helm, M. (2022). Chemical biology and medicinal chemistry of RNA methyltransferases. Nucleic Acids Res. *50*, 4216–4245. https://doi.org/10.1093/nar/gkac224.
2. Schubert, H.L., Blumenthal, R.M., and Cheng, X. (2003). Many paths to methyltransfer: a chronicle of convergence. Trends Biochem. Sci. *28*, 329–335. https://doi.org/10.1016/S0968-0004(03)00090-2.
3. Schwickert, M., Fischer, T.R., Zimmermann, R.A., Hoba, S.N., Meidner, J. L., Weber, M., Weber, M., Stark, M.M., Koch, J., Jung, N., et al. (2022). Discovery of Inhibitors of DNA Methyltransferase 2, an Epitranscriptomic Modulator and Potential Target for Cancer Treatment. J. Med. Chem. *65*, 9750–9788. https://doi.org/10.1021/acs.jmedchem.2c00388.
4. Schwickert, M., Zimmermann, R.A., Habeck, T., Hoba, S.N., Nidoieva, Z., Fischer, T.R., Stark, M.M., Kersten, C., Lermyte, F., Helm, M., and Schirmeister, T. (2023). Covalent S -Adenosylhomocysteine-Based DNA Methyltransferase 2 Inhibitors with a New Type of Aryl Warhead. ACS Med. Chem. Lett. *14*, 777–787. https://doi.org/10.1021/acsmedchemlett.3c00062.
5. Ahmed-Belkacem, R., Troussier, J., Delpal, A., Canard, B., Vasseur, J.-J., Decroly, E., and Debart, F. (2024). N -Arylsulfonamide-based adenosine analogues to target RNA cap N 7-methyltransferase nsp14 of SARS-CoV-2. RSC Med. Chem. *15*, 839–847. https://doi.org/10.1039/D3MD00737E.
6. Goll, M.G., Kirpekar, F., Maggert, K.A., Yoder, J.A., Hsieh, C.L., Zhang, X., Golic, K.G., Jacobsen, S.E., and Bestor, T.H. (2006). Methylation of tRNAAsp by the DNA methyltransferase homolog Dnmt2. Science *311*, 395–398. https://doi.org/10.1126/science.1120976.
7. Rai, K., Chidester, S., Zavala, C.V., Manos, E.J., James, S.R., Karpf, A.R., Jones, D.A., and Cairns, B.R. (2007). Dnmt2 functions in the cytoplasm to promote liver, brain, and retina development in zebrafish. Genes Dev. *21*, 261–266. https://doi.org/10.1101/gad.1472907.
8. Bohnsack, K.E., Höbartner, C., and Bohnsack, M.T. (2019). Eukaryotic 5-methylcytosine (m5C) RNA Methyltransferases: Mechanisms, Cellular Functions, and Links to Disease. Genes *10*, 102. https://doi.org/10.3390/genes10020102.
9. Schaefer, M., Pollex, T., Hanna, K., Tuorto, F., Meusburger, M., Helm, M., and Lyko, F. (2010). RNA methylation by Dnmt2 protects transfer RNAs against stress-induced cleavage. Genes Dev. *24*, 1590–1595. https://doi.org/10.1101/gad.586710.
10. Muller, S., Windhof, I.M., Maximov, V., Jurkowski, T., Jeltsch, A., Forstner, K.U., Sharma, C.M., Graf, R., and Nellen, W. (2013). Target recognition, RNA methylation activity and transcriptional regulation of the Dictyostelium discoideum Dnmt2-homologue (DnmA). Nucleic Acids Res. *41*, 8615–8627. https://doi.org/10.1093/nar/gkt634.
11. Lyko, F. (2018). The DNA methyltransferase family: a versatile toolkit for epigenetic regulation. Nat. Rev. Genet. *19*, 81–92. https://doi.org/10.1038/nrg.2017.80.
12. Jeltsch, A., Ehrenhofer-Murray, A., Jurkowski, T.P., Lyko, F., Reuter, G., Ankri, S., Nellen, W., Schaefer, M., and Helm, M. (2017). Mechanism and biological role of Dnmt2 in Nucleic Acid Methylation. RNA Biol. *14*, 1108–1123. https://doi.org/10.1080/15476286.2016.1191737.

13. Tuorto, F., Liebers, R., Musch, T., Schaefer, M., Hofmann, S., Kellner, S., Frye, M., Helm, M., Stoecklin, G., and Lyko, F. (2012). RNA cytosine methylation by Dnmt2 and NSun2 promotes tRNA stability and protein synthesis. Nat. Struct. Mol. Biol. *19*, 900–905. https://doi.org/10.1038/nsmb.2357.

14. Tuorto, F., Herbst, F., Alerasool, N., Bender, S., Popp, O., Federico, G., Reitter, S., Liebers, R., Stoecklin, G., Gröne, H.J., et al. (2015). The tRNA methyltransferase Dnmt2 is required for accurate polypeptide synthesis during haematopoiesis. EMBO J. *34*, 2350–2362. https://doi.org/10.15252/embj.201591382.

15. Lewinska, A., Adamczyk-Grochala, J., and Wnuk, M. (2023). TRDMT1-mediated RNA C-5 methylation as a novel target in anticancer therapy. Biochim. Biophys. Acta. Rev. Cancer *1878*, 188964. https://doi.org/10.1016/j.bbcan.2023.188964.

16. Towns, W.L., and Begley, T.J. (2012). Transfer RNA Methytransferases and Their Corresponding Modifications in Budding Yeast and Humans: Activities, Predications, and Potential Roles in Human Health. DNA Cell Biol. *31*, 434–454. https://doi.org/10.1089/dna.2011.1437.

17. Li, L., and Wang, S. (2017). DNA methyltransferase (DNMTs) expression in cervical cancer tissues and its relationship with HPV infection and tumor malignancy. J. Hainan Med. Univ. *23*, 136–139.

18. Lewinska, A., Adamczyk-Grochala, J., Kwasniewicz, E., Deregowska, A., Semik, E., Zabek, T., and Wnuk, M. (2018). Reduced levels of methyltransferase DNMT2 sensitize human fibroblasts to oxidative stress and DNA damage that is accompanied by changes in proliferation-related miRNA expression. Redox Biol. *14*, 20–34. https://doi.org/10.1016/j.redox.2017.08.012.

19. Zhang, Y., Zhang, X., Shi, J., Tuorto, F., Li, X., Liu, Y., Liebers, R., Zhang, L., Qu, Y., Qian, J., et al. (2018). Dnmt2 mediates intergenerational transmission of paternally acquired metabolic disorders through sperm small non-coding RNAs. Nat. Cell Biol. *20*, 535–540. https://doi.org/10.1038/s41556-018-0087-2.

20. Thiagarajan, D., Dev, R.R., and Khosla, S. (2011). The DNA methyltranferase Dnmt2 participates in RNA processing during cellular stress. Epigenetics *6*, 103–113. https://doi.org/10.4161/epi.6.1.13418.

21. Zimmermann, R.A., Fischer, T.R., Schwickert, M., Nidoieva, Z., Schirmeister, T., and Kersten, C. (2023). Chemical Space Virtual Screening against Hard-to-Drug RNA Methyltransferases DNMT2 and NSUN6. Int. J. Mol. Sci. *24*, 6109. https://doi.org/10.3390/ijms24076109.

22. Loenen, W.A.M. (2006). S -Adenosylmethionine: jack of all trades and master of everything? Biochem. Soc. Trans. *34*, 330–333. https://doi.org/10.1042/BST0340330.

23. Fontecave, M., Atta, M., and Mulliez, E. (2004). S-adenosylmethionine: nothing goes to waste. Trends Biochem. Sci. *29*, 243–249. https://doi.org/10.1016/j.tibs.2004.03.007.

24. Grillo, M.A., and Colombatto, S. (2008). S-adenosylmethionine and its products. Amino Acids *34*, 187–193. https://doi.org/10.1007/s00726-007-0500-9.

25. Petrossian, T.C., and Clarke, S.G. (2011). Uncovering the Human Methyltransferasome. Mol. Cell. Proteomics *10*, M110.000976.000976. https://doi.org/10.1074/mcp.M110.000976.

26. Yuen, L.H., and Franzini, R.M. (2017). Achievements, Challenges, and Opportunities in DNA-Encoded Library Research: An Academic Point of View. Chembiochem *18*, 829–836. https://doi.org/10.1002/cbic.201600567.

27. Goodnow, R.A., Dumelin, C.E., and Keefe, A.D. (2017). DNA-encoded chemistry: enabling the deeper sampling of chemical space. Nat. Rev. Drug Discov. *16*, 131–147. https://doi.org/10.1038/nrd.2016.213.

28. Satz, A.L., Brunschweiger, A., Flanagan, M.E., Gloger, A., Hansen, N.J.V., Kuai, L., Kunig, V.B.K., Lu, X., Madsen, D., Marcaurelle, L.A., et al. (2022). DNA-encoded chemical libraries. Nat. Rev. Methods Primers *2*, 3. https://doi.org/10.1038/s43586-021-00084-5.

29. Franzini, R.M., and Randolph, C. (2016). Chemical Space of DNA-Encoded Libraries. J. Med. Chem. *59*, 6629–6644. https://doi.org/10.1021/acs.jmedchem.5b01874.

30. Collie, G.W., Clark, M.A., Keefe, A.D., Madin, A., Read, J.A., Rivers, E.L., and Zhang, Y. (2024). Screening Ultra-Large Encoded Compound Libraries Leads to Novel Protein–Ligand Interactions and High Selectivity. J. Med. Chem. *67*, 864–884. https://doi.org/10.1021/acs.jmedchem.3c01861.

31. Brenner, S., and Lerner, R.A. (1992). Encoded combinatorial chemistry. Proc. Natl. Acad. Sci. USA *89*, 5381–5383. https://doi.org/10.1073/pnas.89.12.5381.

32. Peterson, A.A., and Liu, D.R. (2023). Small-molecule discovery through DNA-encoded libraries. Nat. Rev. Drug Discov. *22*, 699–722. https://doi.org/10.1038/s41573-023-00713-6.

33. Ma, P., Zhang, S., Huang, Q., Gu, Y., Zhou, Z., Hou, W., Yi, W., and Xu, H. (2024). Evolution of chemistry and selection technology for DNA-encoded library. Acta Pharm. Sin. B *14*, 492–516. https://doi.org/10.1016/j.apsb.2023.10.001.

34. Gong, Z., Hu, G., Li, Q., Liu, Z., Wang, F., Zhang, X., Xiong, J., Li, P., Xu, Y., Ma, R., et al. (2017). Compound Libraries: Recent Advances and Their Applications in Drug Discovery. Curr. Drug Discov. Technol. *14*, 216–228. https://doi.org/10.2174/1570163814666170425155154.

35. Proj, M., Bozovičar, K., Hrast, M., Frlan, R., and Gobec, S. (2022). DNA-encoded library screening on two validated enzymes of the peptidoglycan biosynthetic pathway. Bioorg. Med. Chem. Lett. *73*, 128915. https://doi.org/10.1016/j.bmcl.2022.128915.

36. Dawadi, S., Simmons, N., Miklossy, G., Bohren, K.M., Faver, J.C., Ucisik, M.N., Nyshadham, P., Yu, Z., and Matzuk, M.M. (2020). Discovery of potent thrombin inhibitors from a protease-focused DNA-encoded chemical library. Proc. Natl. Acad. Sci. USA *117*, 16782–16789. https://doi.org/10.1073/pnas.2005447117.

37. Meyer, S.M., Tanaka, T., Zanon, P.R.A., Baisden, J.T., Abegg, D., Yang, X., Akahori, Y., Alshakarchi, Z., Cameron, M.D., Adibekian, A., and Disney, M.D. (2022). DNA-Encoded Library Screening To Inform Design of a Ribonuclease Targeting Chimera (RiboTAC). J. Am. Chem. Soc. *144*, 21096–21102. https://doi.org/10.1021/jacs.2c07217.

38. Chana, C.K., Maisonneuve, P., Posternak, G., Grinberg, N.G.A., Poirson, J., Ona, S.M., Ceccarelli, D.F., Mader, P., St-Cyr, D.J., Pau, V., et al. (2022). Discovery and Structural Characterization of Small Molecule Binders of the Human CTLH E3 Ligase Subunit GID4. J. Med. Chem. *65*, 12725–12746. https://doi.org/10.1021/acs.jmedchem.2c00509.

39. Ibrahim, M.T., Verkhivker, G.M., Misra, J., and Tao, P. (2023). Novel Allosteric Effectors Targeting Human Transcription Factor TEAD. Int. J. Mol. Sci. *24*, 9009. https://doi.org/10.3390/ijms24109009.

40. Su, W., Ge, R., Ding, D., Chen, W., Wang, W., Yan, H., Wang, W., Yuan, Y., Liu, H., Zhang, M., et al. (2021). Triaging of DNA-Encoded Library Selection Results by High-Throughput Resynthesis of DNA–Conjugate and Affinity Selection Mass Spectrometry. Bioconjug. Chem. *32*, 1001–1007. https://doi.org/10.1021/acs.bioconjchem.1c00170.

41. Kuai, L., O'Keeffe, T., and Arico-Muendel, C. (2018). Randomness in DNA Encoded Library Selection Data Can Be Modeled for More Reliable Enrichment Calculation. SLAS Discov. *23*, 405–416. https://doi.org/10.1177/2472555218757718.

42. Zimmermann, R.A., Schwickert, M., Meidner, J.L., Nidoieva, Z., Helm, M., and Schirmeister, T. (2022). An Optimized Microscale Thermophoresis Method for High-Throughput Screening of DNA Methyltransferase 2 Ligands. ACS Pharmacol. Transl. Sci. *5*, 1079–1085. https://doi.org/10.1021/acsptsci.2c00175.

43. Prudent, R., Annis, D.A., Dandliker, P.J., Ortholand, J.-Y., and Roche, D. (2021). Exploring new targets and chemical space with affinity selection-mass spectrometry. Nat. Rev. Chem. *5*, 62–71. https://doi.org/10.1038/s41570-020-00229-2.

44. Meidner, J.L., Frey, A.F., Zimmermann, R.A., Sabin, M.O., Nidoieva, Z., Weldert, A.C., Hoba, S.N., Krone, M.W., and Barthels, F. (2024). Nanomole Scale Screening of Fluorescent RNA-Methyltransferase Probes Enables the Discovery of METTL1 Inhibitors. Angew. Chem., Int. Ed. Engl. *63*, e202403792. https://doi.org/10.1002/anie.202403792.

45. Hammerschmidt, S.J., Barthels, F., Weldert, A.C., and Kersten, C. (2024). Advanced Isothermal Titration Calorimetry for Medicinal Chemists with ITCcalc. J. Chem. Educ. *101*, 1086–1095. https://doi.org/10.1021/acs.jchemed.3c01133.

46. Nidoieva, Z., Sabin, M.O., Dewald, T., Weldert, A.C., Hoba, S.N., Helm, M., and Barthels, F. (2025). A microscale thermophoresis-based enzymatic RNA methyltransferase assay enables the discovery of DNMT2 inhibitors. Commun. Chem. *8*, 32. https://doi.org/10.1038/s42004-025-01439-9.

47. Kallert, E., Behrendt, M., Frey, A., Kersten, C., and Barthels, F. (2023). Non-covalent dyes in microscale thermophoresis for studying RNA ligand interactions and modifications. Chem. Sci. *14*, 9827–9837. https://doi.org/10.1039/D3SC02993J.

48. Jurkowski, T.P., Shanmugam, R., Helm, M., and Jeltsch, A. (2012). Mapping the tRNA Binding Site on the Surface of Human DNMT2 Methyltransferase. Biochemistry *51*, 4438–4444. https://doi.org/10.1021/bi3002659.

49. Dong, A., Yoder, J.A., Zhang, X., Zhou, L., Bestor, T.H., and Cheng, X. (2001). Structure of human DNMT2, an enigmatic DNA methyltransferase homolog that displays denaturant-resistant binding to DNA. Nucleic Acids Res. *29*, 439–448. https://doi.org/10.1093/nar/29.2.439.

50. Krissinel, E., and Henrick, K. (2007). Inference of Macromolecular Assemblies from Crystalline State. J. Mol. Biol. *372*, 774–797. https://doi.org/10.1016/j.jmb.2007.05.022.

51. Laskowski, R.A., and Swindells, M.B. (2011). LigPlot+: Multiple Ligand–Protein Interaction Diagrams for Drug Discovery. J. Chem. Inf. Model. *51*, 2778–2786. https://doi.org/10.1021/ci200227u.

52. BioSolveIT GmbH (2024). SeeSAR Version 13.1.1 (BioSolveIT GmbH).

53. Schaefer, M., Hagemann, S., Hanna, K., and Lyko, F. (2009). Azacytidine Inhibits RNA Methylation at DNMT2 Target Sites in Human Cancer Cell Lines. Cancer Res. *69*, 8127–8132. https://doi.org/10.1158/0008-5472.CAN-09-0458.

54. Aumer, T., Gremmelmaier, C.B., Runtsch, L.S., Pforr, J.C., Yeşiltaç, G.N., Kaiser, S., and Traube, F.R. (2022). Comprehensive comparison between azacytidine and decitabine treatment in an acute myeloid leukemia cell line. Clin. Epigenet. *14*, 113. https://doi.org/10.1186/s13148-022-01329-0.

55. Noronha, N., Durette, C., Cahuzac, M., E Silva, B., Courtois, J., Humeau, J., Sauvat, A., Hardy, M.-P., Vincent, K., Laverdure, J.-P., et al. (2024). Autophagy degrades immunogenic endogenous retroelements induced by 5-azacytidine in acute myeloid leukemia. Leukemia *38*, 1019–1031. https://doi.org/10.1038/s41375-024-02250-6.

56. Thüring, K., Schmid, K., Keller, P., and Helm, M. (2016). Analysis of RNA modifications by liquid chromatography–tandem mass spectrometry. Methods *107*, 48–56. https://doi.org/10.1016/j.ymeth.2016.03.019.

57. Huang, S., Wylder, A.C., and Pan, T. (2024). Simultaneous nanopore profiling of mRNA m6A and pseudouridine reveals translation coordination. Nat. Biotechnol. *42*, 1831–1835. https://doi.org/10.1038/s41587-024-02135-0.

58. Lenci, E., and Trabocchi, A. (2020). Peptidomimetic toolbox for drug discovery. Chem. Soc. Rev. *49*, 3262–3277. https://doi.org/10.1039/D0CS00102C.

59. Li, H., Liu, H., Zhu, D., Dou, C., Gang, B., Zhang, M., and Wan, Z. (2024). Biological function molecular pathways and druggability of DNMT2/TRDMT1. Pharmacol. Res. *205*, 107222. https://doi.org/10.1016/j.phrs.2024.107222.

60. Adamczyk-Grochala, J., Bloniarz, D., Zielinska, K., Lewinska, A., and Wnuk, M. (2023). DNMT2/TRDMT1 gene knockout compromises doxorubicin-induced unfolded protein response and sensitizes cancer cells to ER stress-induced apoptosis. Apoptosis *28*, 166–185. https://doi.org/10.1007/s10495-022-01779-0.

61. Winn, M.D., Ballard, C.C., Cowtan, K.D., Dodson, E.J., Emsley, P., Evans, P.R., Keegan, R.M., Krissinel, E.B., Leslie, A.G.W., McCoy, A., et al. (2011). Overview of the CCP 4 suite and current developments. Acta Crystallogr. D Biol. Crystallogr. *67*, 235–242. https://doi.org/10.1107/S0907444910045749.

62. Liebschner, D., Afonine, P.V., Baker, M.L., Bunkóczi, G., Chen, V.B., Croll, T.I., Hintze, B., Hung, L.-W., Jain, S., McCoy, A.J., et al. (2019). Macromolecular structure determination using X-rays, neutrons and electrons: recent developments in Phenix. Acta Crystallogr. D Struct. Biol. *75*, 861–877. https://doi.org/10.1107/S2059798319011471.

63. Emsley, P., Lohkamp, B., Scott, W.G., and Cowtan, K. (2010). Features and development of Coot. Acta Crystallogr. D Biol. Crystallogr. *66*, 486–501. https://doi.org/10.1107/S0907444910007493.

64. Chen, V.B., Arendall, W.B., Headd, J.J., Keedy, D.A., Immormino, R.M., Kapral, G.J., Murray, L.W., Richardson, J.S., and Richardson, D.C. (2010). MolProbity : all-atom structure validation for macromolecular crystallography. Acta Crystallogr. D Biol. Crystallogr. *66*, 12–21. https://doi.org/10.1107/S0907444909042073.

65. Jumper, J., Evans, R., Pritzel, A., Green, T., Figurnov, M., Ronneberger, O., Tunyasuvunakool, K., Bates, R., Žídek, A., Potapenko, A., et al. (2021). Highly accurate protein structure prediction with AlphaFold. Nature *596*, 583–589. https://doi.org/10.1038/s41586-021-03819-2.

66. Banerjee, P., Dunkel, M., Kemmler, E., and Preissner, R. (2020). SuperCYPsPred—a web server for the prediction of cytochrome activity. Nucleic Acids Res. *48*, W580–W585. https://doi.org/10.1093/nar/gkaa166.

67. Simon, R.P., Winter, M., Kleiner, C., Wehrle, L., Karnath, M., Ries, R., Zeeb, M., Schnapp, G., Fiegen, D., Häbe, T.T., et al. (2021). MALDI-TOF-Based Affinity Selection Mass Spectrometry for Automated Screening of Protein–Ligand Interactions at High Throughput. SLAS Discov. *26*, 44–57. https://doi.org/10.1177/2472555220959266.

68. Zimmer, C., Brauer, J., Ferenc, D., Meyr, J., Müller, P., Räder, H.-J., Engels, B., Opatz, T., and Schirmeister, T. (2024). Substitution-Induced Mechanistic Switching in SNAr-Warheads for Cysteine Proteases. Molecules *29*, 2660. https://doi.org/10.3390/molecules29112660.

69. Bogomolovas, J., Simon, B., Sattler, M., and Stier, G. (2009). Screening of fusion partners for high yield expression and purification of bioactive viscotoxins. Protein Expr. Purif. *64*, 16–23. https://doi.org/10.1016/j.pep.2008.10.003.

70. Kabsch, W. (2010). XDS. Acta Crystallogr. D Biol. Crystallogr. *66*, 125–132. https://doi.org/10.1107/S0907444909047337.

71. Evans, P.R., and Murshudov, G.N. (2013). How good are my data and what is the resolution? Acta Crystallogr. D Biol. Crystallogr. *69*, 1204–1214. https://doi.org/10.1107/S0907444913000061.

72. McCoy, A.J., Grosse-Kunstleve, R.W., Adams, P.D., Winn, M.D., Storoni, L.C., and Read, R.J. (2007). Phaser crystallographic software. J. Appl. Crystallogr. *40*, 658–674. https://doi.org/10.1107/S0021889807021206.

73. Moriarty, N.W., Grosse-Kunstleve, R.W., and Adams, P.D. (2009). electronic Ligand Builder and Optimization Workbench (eLBOW): a tool for ligand coordinate and restraint generation. Acta Crystallogr. D Biol. Crystallogr. *65*, 1074–1080. https://doi.org/10.1107/S0907444909029436.

74. Afonine, P.V., Grosse-Kunstleve, R.W., Echols, N., Headd, J.J., Moriarty, N.W., Mustyakimov, M., Terwilliger, T.C., Urzhumtsev, A., Zwart, P.H., and Adams, P.D. (2012). Towards automated crystallographic structure refinement with phenix.refine. Acta Crystallogr. D Biol. Crystallogr. *68*, 352–367. https://doi.org/10.1107/S0907444912001308.

75. Eisenberg, D., Schwarz, E., Komaromy, M., and Wall, R. (1984). Analysis of membrane and surface protein sequences with the hydrophobic moment plot. J. Mol. Biol. *179*, 125–142. https://doi.org/10.1016/0022-2836(84)90309-7.

76. Jurrus, E., Engel, D., Star, K., Monson, K., Brandi, J., Felberg, L.E., Brookes, D.H., Wilson, L., Chen, J., Liles, K., et al. (2018). Improvements to the APBS biomolecular solvation software suite. Protein Sci. *27*, 112–128. https://doi.org/10.1002/pro.3280.

77. Yokogawa, T., Kitamura, Y., Nakamura, D., Ohno, S., and Nishikawa, K. (2010). Optimization of the hybridization-based method for purification of thermostable tRNAs in the presence of tetraalkylammonium salts. Nucleic Acids Res. *38*, e89. https://doi.org/10.1093/nar/gkp1182.

78. Kellner, S., Ochel, A., Thüring, K., Spenkuch, F., Neumann, J., Sharma, S., Entian, K.-D., Schneider, D., and Helm, M. (2014). Absolute and relative quantification of RNA modifications via biosynthetic isotopomers. Nucleic Acids Res. *42*, e142. https://doi.org/10.1093/nar/gku733.

CellPress
OPEN ACCESS

iScience
Article

STAR★METHODS

KEY RESOURCES TABLE

REAGENT or RESOURCE	SOURCE	IDENTIFIER
Bacterial and virus strains		
E. coli Rosetta 2 (DE3) pLysS cells	Merck KGaA	71403
Chemicals, peptides, and recombinant proteins		
Recombinant human DNMT2 (full-length)	Schwickert et al.[3]	N/A
Recombinant human DNMT2Δ47	Schwickert et al.[4]	N/A
Recombinant human DNMT1	ActiveMotif	31404
Recombinant human DNMT3A/3L	Schwickert et al.[3]	N/A
Recombinant human NSUN2	Schwickert et al.[3]	N/A
Recombinant human NSUN3	Schwickert et al.[3]	N/A
Recombinant human NSUN6	Schwickert et al.[3]	N/A
Recombinant human NonO	ActiveMotif	31539
Recombinant human eIF4E	Cayman Chemicals	15137
Anti-DNMT2 (rabbit)	Abcam	ab308120
IRDye 680RD Goat anti-Rabbit	LI-COR	926–68071
TEV protease	New England Biolabs	P8112S
S-adenosylhomocysteine (SAH)	Sigma-Aldrich	A9384
Sinefungin	Sigma-Aldrich	S8559
^{3}H-*S*-adenosylmethionine (SAM)	Hartmann Analytics	ART0288
S-adenosylmethionine (cold)	New England Biolabs	B9003S
L-α-phosphatidylcholine	Sigma-Aldrich	P3556
5-FAM-triazolyl-adenosyl-Dab (fluorescent DNMT2 tracer)	Zimmermann et al.[42]	FTAD
ProteOrange staining	Lumiprobe	10210
Sybr Gold nucleic acid stain	ThermoFisher	S11494
RPMI-1640 medium	ThermoFisher	11875093
McCoys's 5A medium	ThermoFisher	16600082
DMEM medium	ThermoFisher	10564011
Fetal bovine serum	ThermoFisher	12662029
Penicillin/Streptomycin	ThermoFisher	15070063
Doxorubicin	BLDpharm	BD32885
L-Glutamine	ThermoFisher	A2916801
TRIzol reagent	ThermoFisher	15596026
Nuclease P1 from Penicillium citrinum	Sigma-Aldrich	N8630
Snake venom phosphodiesterase from Crotalus adamanteus	Sigma-Aldrich	P3243
Bovine intestine phosphatase	Sigma-Aldrich	A2356
Benzonase	Sigma-Aldrich	70746
Pentostatin	Sigma-Aldrich	SML0508
Milk powder (blotting grade)	Carl-Roth	T145.3
Critical commercial assays		
DELopen screening library	WuXiAppTec	k00000664
Gold MV liquid scintillation cocktail	PerkinElmer	6013151
Cell Titer Glo assay kit	Promega	G7570

(*Continued on next page*)

CellPress
OPEN ACCESS

Continued

REAGENT or RESOURCE	SOURCE	IDENTIFIER
ViaLight Plus Cell Proliferation and Cytotoxicity BioAssay Kit	Lonza	LT07-221
Deposited data		
Crystal structure DNMT2Δ47-compound 3 complex	This paper	PDB 9HGM
Experimental models: Cell lines		
Human MOLM-13 cells	DSMZ	ACC 554; CVCL_2119
Human HCT 116 cells	ATCC	CCL-247; CVCL_0291
Human MDA-MB-231 cells	DSMZ	ACC 732; CVCL_0062
Human Huh-7 cells	DSMZ	PTA-7435; CVCL_0336
Human HEK-293 cells	ATCC	CRL-1573; CVCL_0045
Oligonucleotides		
Human IVT $tRNA^{Asp}$-GUC	Schwickert et al.[3]	N/A
5′-GTGACAGGCGGGGATACTCACCACT-Biotin-3′	GenScript	Custom synthesis
5′-CGTGGCAGGCGAGAATTCTACCACT-Biotin-3′	GenScript	Custom synthesis
5′-CGTGTTAGGCGAACGTGATAACCACT-Biotin-3′	GenScript	Custom synthesis
Recombinant DNA		
pET-Dnmt3A3L-sc27	Addgene	Addgene_71827
pET-28a(+)-DNMT2Δ47	Addgene	Addgene_198382
pET-28a(+)-NSUN2	Addgene	Addgene_188059
pET-28a(+)-NSUN6	Addgene	Addgene_188060
Software and algorithms		
MO.Affinity Analysis 2.3	Nanotemper Technologies	https://nanotempertech.com/
PEAQ-ITC Analysis Software 1.21	MicroCal	https://www.malvernpanalytical.com/
Prism 8.0.1	GraphPad	https://www.graphpad.com/
Unicorn7	Cytiva	https://cytivalifesciences.com
CCP4 software package	Winn et al.[61]	https://ccp4.ac.uk
Phenix software package	Liebschner et al.[62]	https://phenix-online.org
Coot 0.9.8.5	Emsley et al.[63]	https://www2.mrc-lmb.cam.ac.uk/personal/pemsley/coot
MolProbity	Chen et al.[64]	http://molprobity.biochem.duke.edu
PyMol 2.5.7	Schrödinger LLC	https://pymol.org
BioLuminate 5.8	Schrödinger LLC	https://schrodinger.com
SeeSAR 13.0.1	BiosolveIT	https://biosolveit.de
Agilent MassHunter B.05.00	Agilent	https://agilent.com
MestReNova 14.0.1	Mestrelab	https://mestrelab.com
Alphafold 3	Jumper et al.[65]	https://alphafoldserver.com/
Molinspiration property calculation service	Molinspiration Cheminformatics	https://molinspiration.com
SuperCYPsPrep	Banerjee et al.[66]	https://insilico-cyp.charite.de/SuperCYPsPred
ImageLab 6.1	Bio-Rad	https://bio-rad.com
Other		
HisPur Ni-NTA magnetic beads	ThermoFisher	88831
Monolith standard capillaries	Nanotemper Technologies	MO-K022
96-well half-area plates	Greiner Bio-One	675076
Zeba Spin Desalting columns 7K MWCO	ThermoFisher	89882
MAIPNTR10 donor plates	Sigma-Aldrich	MAIPNTR10
Superdex 200 Increase 3.2/300	Cytiva	28990946
EZ-Link Sulfo-NHS-LC-Biotinylation kit	ThermoFisher	21435

(*Continued on next page*)

CellPress
OPEN ACCESS

iScience
Article

Continued

REAGENT or RESOURCE	SOURCE	IDENTIFIER
Streptavidin MagBeads	GenScript	L00936
Monarch RNA cleanup (500 μg)	New England Biolabs	T2050S
Whatman glass microfiber filters (GF/C, 25 mm)	Sigma-Aldrich	WHA1822025
Protran nitrocellulose membrane (0.45 μm)	Cytiva	10600003
Criterion TGX Precast Protein Gels (4–20%)	Bio-Rad	5671095

METHOD DETAILS

DEL screening

DEL screening against human DNMT2 protein was performed with the fourth-generation DELopen library (4.2 billion compounds, 27 sub-libraries) by WuXi AppTec. Screening was carried out according to the manufacturer's protocol (available online: https://hits.wuxiapptec.com/assets/pdf/DELopen_Protocol.pdf). Briefly, the DEL panning was performed with recombinant human full-length DNMT2 protein immobilized via the His-tag on ThermoScientific HisPur Ni-NTA magnetic beads. The beads were first washed in a magnetic separation rack with washing buffer (50 mM HEPES, 150 mM NaCl, 5 mM $MgCl_2$, 0.05% polysorbate-20, pH 7.5), and 250 μg beads were transferred for each selection condition to a separate tube. DNMT2 was diluted according to the manufacturer's protocol in selection buffer (50 mM HEPES, 150 mM NaCl, 5 mM $MgCl_2$, 0.05% Polysorbate-20, pH 7.5, 0.1 mg/mL sheared salmon sperm DNA, 1 mM TCEP, and 10 mM imidazole) and successful immobilization on the beads was confirmed by the SDS-PAGE protein capture assay described in manufacturer's protocol. A differential panning procedure was employed with four different selection conditions (A–D): (**A**) Native DNMT2 without additives; (**B**) DNMT2 with SAH (100 μM); (**C**) DNMT2 with $tRNA^{Asp}$ (10 μM); (**D**) No target control with no DNMT2 immobilized.

After three iterative selection rounds, the enriched DNA samples were transferred to WuXi AppTec for further processing, including PCR amplification, quantitation by qPCR, and deep sequencing. All samples passed the DELopen quality control (Figures S1A and S1E) and were forwarded to Illumina NovaSeq deep sequencing. Subsequently, DEL hits selection (Figure S1C) was decided based on enrichment scores, which were calculated by the DELopen unique algorithm described by Kuai et al.[41]

Microscale thermophoresis (MST)

Screening for ligand binding and evaluation of dose-response affinity profiles was performed via microscale thermophoresis (MST) as described previously.[42] The measurements were conducted with a Nanotemper Technologies Monolith NT.115 device. All samples were measured in Monolith standard capillaries at 25 °C. The acquisition mode was set to "Nano-Blue" with an excitation power of 30% and a medium MST power, while the system was controlled using the software MO.Control (version 1.6.1) and for evaluation MO.Affinity Analysis (version 2.3) was used. The samples contained 2 μM DNMT2, 100 nM FTAD (5-FAM-triazolyl-adenosyl-Dab) probe, and 1.3% DMSO in MST buffer (50 mM HEPES, 150 mM NaCl, 1 mM dithiothreitol (DTT), 0.1% PEG-8000, 0.05% polysorbate-20, pH 7.4).[42] All compounds were employed at a final concentration of 100 μM for the initial ligand screening.

For K_D-value determination of the DEL hit-derived fluorescent tracers **6**–**8**, the respective probe was used at a concentration of 100 nM (instead of FTAD), and the DNMT2 concentration was varied (50 μM–0 μM). All measurements were performed as triplicates. The K_D-value was calculated and plotted in GraphPad Prism 8.0.1. MST experiments with fluorescently labeled tRNA (non-covalent labeling with SybrGold) were used to investigate if hit compounds **1**–**5** can dissociate the nucleic acid-protein complex formed by DNMT2 and were conducted as described previously.[47] To assess the DEL ligands' effect on the RNA binding, the $tRNA^{Asp}$ substrate (100 nM) was mixed with the DNMT2 enzyme (2 μM) supplemented with 1x SybrGold and 100 μM of the respective ligand.

Isothermal titration calorimetry (ITC)

The DNMT2 protein was purified via size exclusion chromatography eluting in isothermal titration calorimetry (ITC) buffer (50 mM sodium phosphate pH 8.0, 300 mM NaCl, 1 mM EDTA, 2 mM β-mercaptoethanol, 0.1% polysorbate-20) and directly used for measurements.[3] All compounds were dissolved in DMSO to a concentration of 5 mM and were then diluted in ITC buffer to a final concentration of 500 μM. DNMT2 was diluted to a final concentration of 50 μM with 10% DMSO to match the ligand stocks' DMSO concentration. For the ITC measurements, a MicroCal PEAQ-ITC Automated workstation (Malvern Panalytical) with a 200 μL Hastelloy cell and an injection syringe volume of 40 μL was used. All experiments were performed in triplicates at 25 °C unless otherwise noted. For each measurement, 19 compound injections (2 μL each) with an injection speed of 0.5 μL/s were added to the reaction cell containing DNMT2. The spacing time between sequential injections was 300 s, and the stirring speed was set to 750 rpm with a reference power of 42 μW. As control experiments, ligands were titrated into ITC buffer. Data analysis and fitting were carried out using the MicroCal PEAQ-ITC Analysis Software 1.21 and plotted in GraphPad Prism 8.0.1.

Furthermore, displacement ITC experiments were performed as described for the direct titrations above with the following modifications: DNMT2 (50 μM) was preincubated with compound **10** (500 μM, 10% DMSO) or compound **3** (100 μM, 10% DMSO).

iScience
Article

CellPress
OPEN ACCESS

Subsequently, SAH (500 μM, 10% DMSO) was titrated to preincubated protein. During the same sample set, SAH (500 μM) was titrated directly into DNMT2 (50 μM) as a reference titration. Data analysis and displacement curve fitting were accomplished via the MicroCal PEAQ-ITC Analysis Software.

Fluorescence polarization (FP)

Fluorescence polarization (FP) measurements with RNA MTases and small-molecule fluorescent tracers were conducted in black Greiner 96-well half-area plates using a Tecan Spark 10M plate reader as described previously.[44] The reader was equipped with polarization filters coupled to a monochromator setup (λ_{ex} = 480 nm, λ_{em} = 530 nm). For selectivity screening, reaction mixtures contained varying concentrations of recombinant enzyme (DNMT1, DNMT2, DNMT3A/3L, NSUN2, NSUN3, or NSUN6; preparation see below) and 10 nM DEL hit-derived probe **6** in MST buffer. For displacement experiments, 100 μM SAH or 10 μM $tRNA^{Asp}$ were added from buffered stock solutions to the DNMT2-containing mixtures. All measurements were performed as triplicates. Polarization values (in mP) were calculated from polarization-specific parallel and orthogonal fluorescence intensities according to the Tecan in-built calculation routine. K_D-values were calculated and plotted in GraphPad Prism 8.0.1.

^{3}H-based methyltransferase enzyme activity assays

Enzymatic DNMT2 inhibition assays were carried out in 100 mM Tris-HCl, pH 8.0, 100 mM NH_4OAc, 0.1 mM EDTA, 10 mM $MgCl_2$, and 10 mM DTT as described previously.[3,4] First, the $tRNA^{Asp}$ substrate was heated to 75 °C for 5 min and cooled down to room temperature (RT) before it was added to the reaction mixture to a final concentration of 5 μM. The reaction mixture contained 250 nM DNMT2 and the ligand compounds at variable concentrations (5% DMSO). Enzymatic reactions were started by the addition of 0.9 μM SAM as a mixture of ^{3}H-SAM (Hartmann Analytics) resp. cold SAM (NEB) to a final activity of 0.025 μCi μL^{-1}. Enzyme assays were carried out for 30 min at 37 °C. As a negative control served the reaction mixture without DNMT2 and as a positive control the reaction mixture without test compound. After 30 min, aliquots of 8 μL were taken from the reaction mixture and spotted on Whatman glass microfiber filters (GF/C, 25 mm). The RNA was precipitated on the filters with 5% ice-cold TCA for 15 min. The filters were washed twice with 5% TCA at RT for 20 min and 10 min and once in EtOH for 10 min. After drying, the filters were transferred into scintillation vials, and 3 mL of PerkinElmer Gold MV liquid scintillation cocktail was added. Scintillation was measured with a scintillation counter (TriCarb Liquid Scintillation Analyzer 4810 TR; measurement time of 1 min). For IC_{50}-value determination, compounds were analyzed at a minimum of six different concentrations in triplicates. IC_{50}-values were calculated, evaluated, and plotted in GraphPad Prism 8.0.1.

Affinity selection-mass spectrometry (AS-MS)

Orthogonal K_D-value determination for compound **3** was conducted by an affinity selection-mass spectrometry (AS-MS) assay according to Prudent et al.[43] and Simon et al.[67] Compound **3** was dissolved in DMSO (20 mM) and a dilution series in Tris buffer (25 mM Tris, 100 mM NaCl, pH 7.5) was prepared to give final ligand concentrations of 100 μM, 50 μM, 25 μM, 12.5 μM, 6.25 μM, 3.12 μM, 1.56 μM, and 0 μM. DNMT2 was diluted in Tris buffer (130 μM) and added to the dilution series to give a final concentration of 5 μM DNMT2. Zeba Spin Desalting columns 7K MWCO were used for the affinity-based separation. These columns were centrifuged at 2000*g* for 1 min to remove the storage buffer. 20 μL of the prepared samples were loaded to the columns, and the protein-ligand complex was eluted by centrifugation at 2000*g* for 2 min. The centrifuged solutions were diluted with 10 μL ACN and analyzed by LC/MS with an Agilent 1100 Series HPLC system. The data evaluation and subsequent binding affinity determination were performed with MestReNova (version 14.0.1) and GraphPad Prism 8.0.1.

Electrophoretic mobility shift assay (EMSA)

EMSA assays were performed as described previously.[46] DNMT2 (10 μM) was mixed with $tRNA^{Asp}$ (5 μM) and treated with 100 μM of the respective hit compound in DNMT2 assay buffer (100 mM Tris-HCl, pH 8, 100 mM NH_4OAc, 0.1 mM EDTA, 10 mM $MgCl_2$, 10 mM DTT). Subsequently, reaction samples (each 5 μL) were loaded to a native 10% polyacrylamide gel and separated electrophoretically (1 h, 180 V) in 1x TBE. RNA was stained *in situ* with 1x GelRed, and PAGE analysis was conducted by fluorescence scanning at an excitation wavelength of 532 nm (Amersham Typhoon 9400).

In vitro permeability assay (PAMPA)

To determine the passive permeability of selected DNMT2 ligands, a parallel artificial membrane permeation assay (PAMPA) was performed as described previously.[68] The experiment was performed in duplicates with Sigma-Aldrich MAIPNTR10 donor plates with 5 μL of an artificial membrane (1% w/v L-α-phosphatidylcholine in *n*-dodecane) per well. After incubation for 7 h, the acceptor solutions were evaluated by LC/MS (HP Agilent 1100 Series). The peak areas in the UV chromatogram (λ = 210 nm) were used to calculate the areas under the curve (AUCs). The apparent permeability P_{app} was calculated using the following equation with V_D and V_A as volumes of donor and acceptor solutions (0.15 cm^3 and 0.4 cm^3), AUC_{acc} and AUC_{ref} as the area of the analyte signal in the respective chromatogram of sample and reference solutions, A as the porosity-corrected filter area (0.2113 cm^2) and t as the incubation time given in seconds: $P_{app} = -V_D \cdot V_A \cdot \ln(1 - AUC_{acc}/AUC_{ref})/[(V_D + V_A) \cdot A \cdot t]$.

CellPress
OPEN ACCESS

iScience
Article

Protein and tRNA production

DNMT2, NSUN2, NSUN6, and DNMT3A/3L were expressed from *E. coli* as described previously, while $tRNA^{Asp}$ was synthesized by *in vitro* transcription as described previously.[3]

DNMT2 cloning, expression, and purification for co-crystallization

For the co-crystallization of DNMT2Δ47 with compound **3**, the coding DNA sequence of human DNMT2 lacking residues 191–237 was amplified by PCR and cloned into a pETHis_1a vector.[69] For this purpose, overhangs for the restriction enzymes NcoI/BamHI were used. The plasmid was transformed in Rosetta II (DE3) *E. coli* (Merck-Novagen) and expressed in ZY autoinduction medium supplemented with trace elements, kanamycin, and chloramphenicol. The cells were grown to OD_{600} = 0.8 at 37 °C (220 rpm shaking) and further cultivated overnight at 20 °C. Harvesting was performed by centrifugation and washing with 1xPBS buffer (0.137 M NaCl, 2.7 mM KCl, 10 mM Na_2HPO_4, 1.8 mM KH_2PO_4). The resulting cell pellet was then resuspended in lysis buffer (20 mM HEPES, pH 7.5, 500 mM NaCl, 20 mM imidazole, 1 M urea, 4 mM β-mercaptoethanol), supplemented with a protease inhibitor mix (Roche) and 1:10000 benzonase. Lysis was performed with a microfluidizer (M1-10L, Microfluidics) followed by clearing the lysate applying centrifugation (40 min at 50,000*g*) and filtering through a 0.45 μm membrane. The supernatant was loaded twice on 4 mL Ni-NTA Agarose (Qiagen) for Ni-IMAC using gravity flow columns (Biorad). The beads were washed with ten column volumes (10 CV) wash buffer (20 mM HEPES, pH 7.5, 150 mM NaCl, 4 mM β-mercaptoethanol), followed by 10 CV high salt buffer (20 mM HEPES, pH 7.5, 2 M NaCl, 4 mM β-mercaptoethanol) and again 10 CV wash buffer. Elution of the His-tagged DNMT2Δ47 was performed with 5 CV elution buffer (20 mM HEPES, pH 7.5, 150 mM NaCl, 300 mM imidazole, 4 mM β-mercaptoethanol). Protein concentration was measured with a NanoPhotometer NP80 (Implen), and TEV protease was added in a 1:75 ratio. Cleavage of the protein by TEV results in two additional residues, namely Gly-Ala, at the N-terminus. The DNMT2Δ47-protease mix was dialyzed overnight against wash buffer using a 6–8 kDa dialysis tube (Spectra/Por). The sample was applied to a reverse Ni-IMAC using 2 mL Ni-NTA Agarose, which was washed with 5 CV wash buffer. The flow-through and wash fractions were pooled, concentrated with an Amicon Ultra concentrator (10 kDa cutoff, Merck KGaA) to 2 mL and loaded for further purification by SEC (size-exclusion chromatography) on a Superdex 75 16/600 gel filtration column (Cytiva) in wash buffer. The peak fractions were pooled, incubated with compound **3** in a 2-fold molar excess, and concentrated with an Amicon Ultra concentrator (10 kDa cutoff, Merck KGaA) to 10 mg/mL for subsequent crystallization.

Analytical size-exclusion chromatography of DNMT2Δ47 with compound 3

To assess the oligomeric state of DNMT2Δ47 upon compound **3** binding, *in vitro* analytical SEC runs were performed on a Superdex 200 Increase 3.2/300 (Cytiva). For the first run, the apo-protein was injected at a concentration of 10 mg/mL; for the second run, it was pre-incubated with a 2-fold molar excess of compound **3**. The resulting chromatograms were analyzed by superposing their 280 nm signals using the Unicorn7 evaluation software (Cytiva).

Crystallization, data collection, model building, and refinement

Crystals were grown at 291 K using sitting drop vapor diffusion. The crystallization reservoir was composed of 0.2 M $MgCl_2$, 0.1 M Tris, pH 8.5, and 12% PEG-8000. Crystallization drops contained 300 nL reservoir solution and 300 nL concentrated protein. Needle-shaped crystals grew within three days. Crystals were frozen in liquid nitrogen using glycerol as the cryo-protectant. Data were collected at ESRF beamline ID30B at cryogenic conditions, integrated using XDS,[70] and scaled using AIMLESS[71] as part of the CCP4 software package.[61] Phases were obtained by molecular replacement with PHASER[72] implemented in the Phenix package[62] using the structure of human DNMT2 (Dong et al.[49]; PDB 1G55) as the search model. The resulting dataset has space group $P2_12_12_1$, a maximum resolution of 2.60 Å, and contains two DNMT2 molecules per asymmetric unit. Compound **3** was parameterized from SMILES description using phenix.elbow.[73] Iterative model building and refinement were performed with Coot[63] and phenix.refine.[74] C24, C79, and C287 side chains show additional electron density in both chains and, therefore, were built as *S*-hydroxycysteine residues (CSO). The quality of the resulting structural models was analyzed with MolProbity.[64] Structure figures were prepared with PyMol 2.5.7 (The PyMol Molecular Graphics System, Schrödinger LLC.). Hydrophobicity of the binding site was visualized by a molecular surface representation colored from high (white) to low (green) hydrophobicity according to the Eisenberg hydrophobicity scale.[75] The electrostatic potential was calculated and visualized using the PyMol APBS plugin.[76] Crystallographic data are summarized in Table S3. Coordinates and structure factors are deposited at the Protein DataBank PDB under accession code 9HGM.

SeeSAR analysis

BiosolveIT SeeSAR (v13.0.1) was used to visualize the estimated binding affinity contributions of the co-crystallized DNMT2 ligand. SeeSAR concedes a semi-quantitative calculation of the thermodynamics using the HYDE algorithm and was used to evaluate torsions, desolvation, and interaction contributions for each ligand's heavy atom.[52] For this, the DNMT2Δ47-binding compound **3** complex (PDB 9HGM) was imported to SeeSAR and evaluated using the "Analyzer" functionalities.

Pull-down DNMT2 interaction assay

For immobilization on streptavidin beads, DNMT2 was biotinylated using the EZ-Link Sulfo-NHS-LC-Biotinylation kit. A 20-fold excess of Sulfo-NHS-LC-Biotin (10 mM in water) was added to DNMT2 and incubated for 2 h on ice. To remove the excess biotin

iScience
Article

CellPress
OPEN ACCESS

reagent, Zeba Spin desalting columns were equilibrated with 1 × PBS buffer, and the reaction mixture was loaded and centrifuged for 2 min at 1000*g*. The biotinylation level was estimated using a HABA assay included in the kit according to the manufacturer's protocols. By this, 4.7 biotin molecules were found to be attached per DNMT2 molecule. To confirm that the biotinylation did not affect the binding competence of the SAH and drug binding pockets, MST measurements with FTAD as a fluorescent tracer were performed as described above.

For *in vitro* pull-down assays, biotinylated DNMT2 was immobilized on streptavidin-coated paramagnetic beads (GenScript Streptavidin MagBeads). For this, beads were washed with PBS buffer containing 0.05% Triton X-100, and subsequently, DNMT2 (30 μg per 50 μL beads) was immobilized for 45 min at RT. As a negative control, beads were treated with a protein-free buffered solution. Beads were washed with PBS buffer, and for each sample, 5 μL beads were added to either 1.5 μg of recombinant NonO protein (Active Motif) or 3.0 μg of recombinant eIF4E protein (Cayman). Beads were incubated for 1 h at RT, and subsequently, the supernatant was removed. Afterward, 10 μL PBS-buffered elution solution (containing either 100 μM sinefungin or 100 μM compound **16** or 10 μM tRNA) was added. The samples were incubated for 45 min at RT, and the supernatant was treated with 2 μL 5× Laemmli buffer. For analysis of the proteins still bound to the beads after elution treatment, 10 μL Laemmli buffer supplemented with 10 mM biotin was added to the residual beads. All samples were heated to 95 °C for 10 min and analyzed via SDS-PAGE. Fluorometric protein detection was conducted using ProteOrange staining (Lumiprobe) according to the manufacturer's protocols. Protein bands were visualized using a GE Healthcare Typhoon Trio biomolecular scanner, with laser excitation at 488 nm and fluorescence detection at 580 nm.

tRNA modification analysis by LC/MS

MOLM-13 cells were seeded at a density of 5 × 10^6 cells in 15 mL RPMI-1640 medium (supplemented with 10% FBS) containing DNMT2 inhibitor **16** (5 μM and 50 μM), negative control compound **34** (50 μM), or DMSO as mock treatment. Cells were incubated for 72 h at 37 °C. Post-incubation, cells were harvested and washed with PBS. Cell pellets were lysed in 1.5 mL TRIzol, mixed thoroughly by pipetting, and incubated for 5 min at RT. Subsequently, 150 μL chloroform was added, vortexed, and incubated for 10 min at RT. Samples were centrifuged at 12,000*g* for 15 min at 4 °C. The upper aqueous layer was transferred to new tubes and mixed with 750 μL isopropanol, vortexed, and incubated for 10 min at RT. Following another centrifugation at 12,000*g* for 15 min at 4 °C, the supernatant was discarded. Pellets were washed with 750 μL of 75% ethanol, vortexed, and centrifuged again at 12,000*g* for 15 min at 4 °C. After discarding the supernatant, the pellets were air-dried at 37 °C and dissolved in 50 μL nuclease-free water. Total RNA samples were further purified by New England Biolabs Monarch RNA Cleanup (500 μg) kits according to the manufacturer's instructions (protocol for RNA size fractionation). Small RNA molecules (<100 nt) containing total tRNA were eluted in 50 μL nuclease-free water, and concentrations were determined using a Nanodrop spectrophotometer.

To enrich the DNMT2 tRNA substrates, a literature-known hybridization-based protocol for the purification of thermostable tRNA was adopted.[77] Therefore, three biotin-labeled anti-sense DNA oligonucleotides suitable for tRNA pull-down were designed and purchased from GenScript. Sequences complementary to $tRNA^{Asp-GUC}$: 5′-GTGACAGGCGGGGATACTCACCACT-Biotin-3′, $tRNA^{Gly-GCC}$: 5′-CGTGGCAGGCGAGAATTCTACCACT-Biotin-3′, $tRNA^{Val-AAC}$: 5′-CGTGTTAGGCGAACGTGATAACCACT-Biotin-3'. Next, GenScript streptavidin MagBeads (200 μL) were washed thrice with 1 mL TBST. Biotin-labeled DNA-oligonucleotide solutions were prepared at 7.5 μM in 3 × 400 μL TBST. MagBeads were incubated with 400 μL of each Biotin-oligo for 10 min at RT, then washed with TBST. Unbound oligos were measured by Nanodrop to confirm loading, assuming a theoretical capacity of 3 nmol per 200 μL beads. MagBeads were pooled in 1200 μL TBST and distributed into 12 PCR tubes with 100 μL TBST each. Total tRNA samples (100 μL) were mixed with 100 μL hybridization buffer (20 mM Tris, pH 7.6, 1.8 M NaCl, 0.2 mM EDTA) and added to the prepared MagBeads. The mixture was heated RT to 75 °C over 40 min using a PCR cycler and then cooled to 4 °C. Following centrifugation, supernatants were collected and saved. The beads were washed repeatedly with TBST at 4 °C until the absorbance at 260 nm was less than 0.01. tRNA was eluted by heating the beads in 30 μL Tris buffer (10 mM Tris, pH 7.6) at 75 °C, with the supernatant collected after each elution step, repeated three times. tRNA concentration and purity were determined using a Nanodrop spectrophotometer and 10% denaturing PAGE, respectively.

100 ng of enriched tRNA per sample was enzymatically digested into nucleosides using a mixture of 0.6 U nuclease P1 from *Penicillium citrinum* (Sigma-Aldrich), 0.2 U snake venom phosphodiesterase from *Crotalus adamanteus* (Worthington), 0.2 U bovine intestine phosphatase (Sigma-Aldrich), 10 U benzonase (Sigma-Aldrich), along with 200 ng of Pentostatin (Sigma-Aldrich). This reaction was conducted for 2 h at 37 °C in a buffer containing 5 mM Tris (pH 8) and 1 mM magnesium chloride. Following digestion, the nucleosides were spiked with an internal standard of ^{13}C stable isotope-labeled nucleosides derived from *Saccharomyces cerevisiae* and analyzed. 100 ng of the digested tRNA and 25 ng of the internal standard were analyzed using LC/MS (Agilent 1260 series coupled with an Agilent 6460 Triple Quadrupole mass spectrometer featuring an electrospray ion source). The mobile phase consisted of a 5 mM ammonium acetate buffer (pH 5.3) and LC/MS grade acetonitrile (VWR). The elution process began with 100% ammonium acetate buffer at a flow rate of 0.35 mL/min, transitioning to a linear gradient that reached 8% acetonitrile at 10 min and 40% at 20 min. The initial conditions were restored to 100% ammonium acetate buffer for an additional 10 min. A Synergi Fusion column (4 μm particle size, 80 Å pore size, 250 × 2.0 mm; Phenomenex) was utilized for the separation. The UV signal at 254 nm was monitored using a multiple wavelength detector (MWD) to track the primary nucleosides. The ESI parameters were set as follows: gas temperature at 350 °C, gas flow at 8 L/min, nebulizer pressure at 50 psi, sheath gas temperature at 350 °C, sheath gas flow at 12 L/min, and capillary voltage at 3000 V. The mass spectrometer operated in positive ion mode, employing Agilent MassHunter

CellPress
OPEN ACCESS

iScience
Article

B.05.00 software in dynamic MRM (multiple reaction monitoring) mode for analysis. Quantification was achieved through a combination of external and internal calibration methods, as outlined in Kellner et al.[78]

Cell viability assays

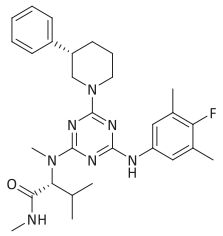
Cell viability assays were conducted with MOLM-13 cells, Huh-7, MDA-MB-231, HEK293, and HCT MTase mutant cell lines (WT, knock-down DNMT2, and knock-down NSUN2) to investigate the DNMT2 inhibiting compounds' cellular effect. Cells were cultured according to standard protocols: MOLM-13 (RPMI, 10% FBS, 1x Penicillin/Streptomycin, 37 °C, 5% CO_2), Huh-7/MDA-MB-231/HEK293 (DMEM, 10% FBS, 1x Penicillin/Streptomycin, 37 °C, 5% CO_2) and HCT (McCoys's 5A Medium, 10% FBS, L-Glutamine, 1x Penicillin/Streptomycin, 37 °C, 5% CO_2). Cell viability was assessed using Promega Cell Titer Glo assay kit (MOLM-13, Huh-7, MDA-MB-231, HEK293) or Lonza ViaLight Plus Cell Proliferation and Cytotoxicity BioAssay Kit (HCT cell lines). Briefly, 1000 cells were seeded in white Greiner half-area 96-well plates and incubated for 48 h with inhibitors/ligands from DMSO stocks (final: 0.1% DMSO) under standard cultivation conditions. Then, the cell titer reagent was added to each well according to the manufacturer's protocols, and luminescence was measured using a Tecan Spark 10M plate reader (MOLM-13, Huh-7, MDA-MB-231, HEK293) or Molecular Devices FlexStation (HCT cell lines). For the co-treatment with doxorubicin/compound **16** or **34**, cells were cultured for two passages of each three days in the presence of compound **16** or **34** (50 μM) and subsequently 1000 cells each in 96-well plates were treated with varying concentrations of doxorubicin for 48 h.

Cellular thermal shift assay (CETSA)

MOLM-13 cells were seeded at a density of 5×10^6 cells in 3 mL RPMI-1640 medium. Subsequently, compound **3** or **16** was added to the MOLM-13 cells to achieve a final concentration of 50 μM, with the same volume of DMSO (final: 0.2%) added as a control. After incubation for 16 h (37 °C, 5% CO_2), the cell suspensions were collected. The cells were washed twice and then counted, followed by the addition of 1 mL PBS. The cell suspension was divided into eight parts, and then heated for 4 min at various temperatures (40, 43, 46, 49, 52, 55, 58 °C) in a PCR thermocycler. The cells were lysed through a freeze-thaw process using liquid nitrogen. The supernatant solutions were used for immunoblotting analysis. Insoluble cellular parts were separated by centrifugation (12,000*g* for 10 min), subsequently, the supernatant was boiled with 1× Laemmli sample buffer for 5 min at 95 °C. Proteins were separated by SDS−PAGE on 4–20% Criterion TGX Precast Protein Gels (Bio-Rad) and transferred to Amersham Protean 0.45 μm nitrocellulose membrane (Cytiva) using semi-dry transfer (25 V, 1 A, Towbin buffer). The membrane was blocked with 5% milk (Carl Roth) in TBST buffer and incubated with anti-DNMT2 antibody (1:1000, Abcam, ab308120) overnight at 4 °C. Subsequently, the membrane was incubated for 3 h at RT with IRDye 680RD Goat anti-Rabbit (1:1000, LICOR, 926–68071). Protein bands were visualized using a GE Healthcare Typhoon Trio biomolecular scanner, with laser excitation at 637 nm and fluorescence detection at 670 nm. The ImageLab software (Bio-Rad) was used for band quantification.

Synthesis and characterization of inhibitors and probes

Rink amide AM resin (loading capacity: 0.6–0.8 mmol/g) or Wang Gly resin (loading capacity: 0.135 mmol/g) was swelled twice for 5 min in DMF. Fmoc-deprotection was performed by treating with 40% piperidine in DMF (2 × 10 min shaking). The resin was rinsed with DCM (3x) and DMF (3x). In the next step, the corresponding building block was coupled to the resin by dissolving the amino acid (3.0 eq. or 1.2 eq.), TBTU (3.0 eq. or 1.2 eq.), and NMM (9.0 eq.) in DMF and shaking for 1.5 h (or 16 h for 1.2 eq.). Subsequently, the resin was rinsed with DCM (3x) and DMF (3x). To couple the next amino acids, the procedure of deprotection and coupling was repeated. When the last amino acid was coupled, the resin was rinsed with DMF (3x) and DCM (3x). To cleave the peptide from the resin, the resin was treated with a mixture of TFA:TIPS:DCM (50:10:40) for 1.5 h. The resin was washed with DCM (3x) and treated again with TFA:TIPS:DCM (50:10:40) for 16 h. All cleavage and wash solutions combined were evaporated under reduced pressure. The crude product was purified by reversed-phase flash column chromatography (Biotage Isolera, ACN/H_2O + TFA), and the product containing fractions were lyophilized. Detailed characterization of the compounds synthesized can be found below:

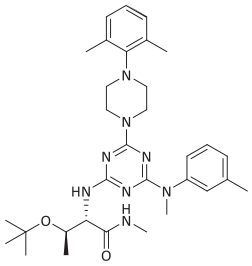


1

Compound **1**: ^{1}H-NMR (400 MHz, DMSO-d_6): δ [ppm] = 8.94 (s, 1H), 7.74–7.16 (m, 6H), 4.76 (s, 2H), 3.32 (d, *J* = 2.8 Hz, 2H), 3.05–2.83 (m, 3H), 2.58 (s, 13H), 2.34–1.90 (m, 6H), 1.79 (d, *J* = 13.0 Hz, 1H), 0.93 (d, *J* = 4.3 Hz, 2H), 0.79 (d, *J* = 6.6 Hz, 2H).

^{13}C-NMR (101 MHz, DMSO): δ [ppm] = 170.7, 170.1, 165.9, 165.8, 143.9, 143.9, 136.0, 128.4, 127.0, 126.4, 123.1, 119.8, 62.6, 49.7, 43.4, 42.2, 31.8, 26.4, 25.7, 25.5, 25.1, 20.0, 19.1, 18.8, 14.5.

LC/MS: m/z calculated for $C_{29}H_{38}FN_7O$ $[M + H]^+$: 520.3, found: 520.3.

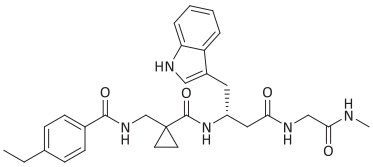


2

Compound **2**: ^{1}H-NMR (400 MHz, DMSO-d_6): δ [ppm] = 7.77–7.68 (m, 1H), 7.27–7.07 (m, 3H), 6.95 (h, *J* = 7.7, 7.1 Hz, 4H), 4.02 (t, *J* = 5.3 Hz, 1H), 3.78–3.68 (m, 3H), 3.38 (s, 3H), 3.32 (s, 3H), 2.97 (d, *J* = 6.0 Hz, 4H), 2.57 (d, *J* = 4.4 Hz, 3H), 2.32–2.23 (m, 9H), 1.06 (dd, *J* = 15.2, 8.3 Hz, 12H).

^{13}C-NMR (101 MHz, DMSO): δ [ppm] = 171.0, 165.6, 165.2, 164.4, 148.0, 144.7, 144.5, 137.6, 137.3, 136.1, 128.9, 128.1, 127.9, 127.0, 126.7, 125.7, 125.4, 124.9, 123.7, 123.0, 73.3, 67.2, 59.2, 49.3, 44.1, 37.3, 28.0, 25.7, 21.0, 20.7, 20.5, 19.4.

LC/MS: m/z calculated for $C_{32}H_{46}N_8O_2$ $[M + H]^+$: 575.3, found: 575.2.

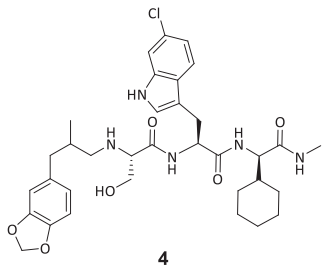


3

Compound **3**: ^{1}H-NMR (600 MHz, DMSO-d_6): δ [ppm] = 10.80–10.76 (m, 1H), 8.58 (t, *J* = 6.1 Hz, 1H), 8.13 (t, *J* = 5.9 Hz, 1H), 8.05 (d, *J* = 7.9 Hz, 1H), 7.76 (d, *J* = 8.2 Hz, 2H), 7.66 (d, *J* = 4.6 Hz, 1H), 7.59 (d, *J* = 7.9 Hz, 1H), 7.29 (t, *J* = 8.2 Hz, 3H), 7.09 (d, *J* = 2.2 Hz, 1H), 7.07–7.01 (m, 1H), 6.98–6.92 (m, 1H), 4.38–4.31 (m, 1H), 3.60 (ddd, *J* = 25.4, 15.6, 6.2 Hz, 2H), 3.48 (dd, *J* = 16.5, 5.7 Hz, 1H), 3.41 (dd, *J* = 14.8, 6.2 Hz, 1H), 2.83 (d, *J* = 6.5 Hz, 2H), 2.64 (q, *J* = 7.6 Hz, 2H), 2.54 (d, *J* = 4.6 Hz, 3H), 2.40–2.30 (m, 2H), 1.18 (t, *J* = 7.6 Hz, 3H), 0.91 (t, *J* = 3.6 Hz, 2H), 0.79 (dd, *J* = 9.4, 3.6 Hz, 2H).

^{13}C-NMR (151 MHz, DMSO): δ [ppm] = 171.6, 170.8, 169.3, 167.2, 147.5, 136.1, 131.4, 127.7, 127.6, 127.5, 123.3, 120.9, 118.6, 118.2, 111.3, 111.2, 47.8, 42.2, 42.1, 29.9, 28.1, 25.5, 25.3, 15.4, 13.2, 12.9.

LC/MS: m/z calculated for $C_{29}H_{35}N_5O_4$ $[M + H]^+$: 518.3, found: 518.2.



4

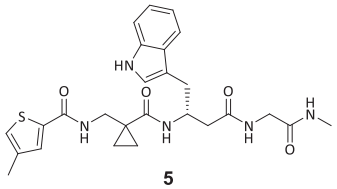
Compound **4**: ^{1}H-NMR (400 MHz, DMSO-d_6): δ [ppm] = 10.97 (s, 1H), 8.03 (d, *J* = 8.2 Hz, 1H), 7.90 (d, *J* = 10.1 Hz, 2H), 7.51 (d, *J* = 8.5 Hz, 1H), 7.31 (d, *J* = 6.4 Hz, 1H), 7.09 (s, 1H), 6.92 (d, *J* = 8.5 Hz, 1H), 6.76 (d, *J* = 7.8 Hz, 1H), 6.66 (s, 1H), 6.52 (d, *J* = 7.9 Hz, 1H), 5.94 (s, 2H), 4.92 (s, 1H), 4.62 (q, *J* = 6.9 Hz, 1H), 4.08 (t, *J* = 8.2 Hz, 1H), 3.47 (d, *J* = 11.1 Hz, 1H), 3.03 (ddt, *J* = 37.3, 22.9, 5.8 Hz, 3H), 2.62–2.54 (m, 4H), 2.37–1.94 (m, 4H), 1.58 (dt, *J* = 18.1, 11.0 Hz, 6H), 1.45 (d, *J* = 12.6 Hz, 1H), 1.21–0.77 (m, 6H), 0.63 (d, *J* = 6.4 Hz, 3H).

CellPress
OPEN ACCESS

iScience
Article

^{13}C-NMR (101 MHz, DMSO): δ [ppm] = 171.8, 171.0, 170.5, 147.0, 145.1, 136.3, 134.7, 126.4, 125.5, 124.9, 121.7, 120.0, 118.4, 110.7, 109.9, 109.2, 107.8, 100.5, 64.8, 62.1, 57.1, 53.9, 52.6, 35.1, 29.1, 28.3, 27.5, 25.8, 25.5, 25.4, 17.3.

LC/MS: m/z calculated for $C_{34}H_{44}ClN_5O_6$ $[M + H]^+$: 654.3, found: 654.3.

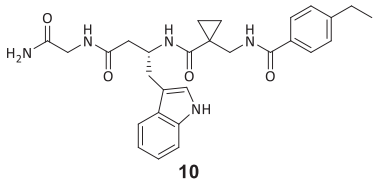


5

Compound **5**: ^{1}H-NMR (400 MHz, DMSO-d_6): δ [ppm] = 10.76 (s, 1H), 8.49 (t, *J* = 7.0 Hz, 1H), 8.10 (d, *J* = 6.6 Hz, 1H), 7.86–7.80 (m, 1H), 7.60 (q, *J* = 8.9, 7.7 Hz, 3H), 7.35 (s, 1H), 7.30 (d, *J* = 8.2 Hz, 1H), 7.09 (s, 1H), 7.07–7.00 (m, 1H), 6.99–6.92 (m, 1H), 4.41–4.30 (m, 1H), 2.82 (t, *J* = 4.7 Hz, 2H), 2.54 (d, *J* = 4.3 Hz, 4H), 2.34 (d, *J* = 7.0 Hz, 2H), 2.21 (d, *J* = 3.2 Hz, 3H), 1.24 (s, 1H), 1.03–0.85 (m, 3H), 0.76 (s, 2H).

^{13}C-NMR (101 MHz, DMSO): δ [ppm] = 172.0, 171.3, 169.7, 162.4, 139.2, 138.3, 136.6, 130.9, 128.0, 126.9, 123.8, 121.3, 119.0, 118.6, 111.7, 111.6, 48.3, 42.6, 30.4, 25.9, 25.6, 23.8, 15.9, 13.4, 13.1.

LC/MS: m/z calculated for $C_{26}H_{31}N_5O_4S$ $[M + H]^+$: 510.2, found: 510.1.



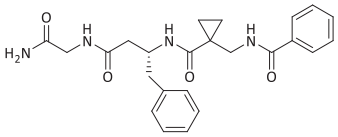
10

Compound **10**: Yield: 2.9 mg (5.80 μmol ≙ 13% of th.), colorless solid.

^{1}H-NMR (600 MHz, DMSO-d_6): δ [ppm] = 10.77 (s, 1H), 8.59 (t, *J* = 6.2 Hz, 1H), 8.07 (t, *J* = 5.9 Hz, 1H), 8.04 (d, *J* = 7.9 Hz, 1H), 7.81–7.71 (m, 2H), 7.59 (d, *J* = 7.9 Hz, 1H), 7.33–7.26 (m, 3H), 7.24 (s, 1H), 7.09 (d, *J* = 2.2 Hz, 1H), 7.04 (t, *J* = 7.3 Hz, 2H), 6.95 (t, *J* = 7.4 Hz, 1H), 4.34 (h, *J* = 6.9 Hz, 1H), 3.61 (dd, *J* = 16.8, 6.0 Hz, 1H), 3.56 (dd, *J* = 14.8, 6.1 Hz, 1H), 3.48 (dd, *J* = 16.8, 5.5 Hz, 1H), 3.41 (dd, *J* = 14.8, 6.1 Hz, 1H), 2.82 (d, *J* = 6.7 Hz, 2H), 2.64 (q, *J* = 7.6 Hz, 2H), 2.33 (d, *J* = 6.8 Hz, 1H), 1.18 (t, *J* = 7.6 Hz, 3H), 0.98–0.72 (m, 4H).

^{13}C-NMR (151 MHz, DMSO): δ [ppm] = 171.6, 171.1, 170.6, 167.2, 147.5, 136.1, 131.4, 127.7, 127.6, 127.5, 123.3, 120.8, 118.6, 118.2, 111.3, 111.2, 47.7, 42.3, 41.9, 40.1, 29.8, 28.1, 25.3, 15.4, 13.3, 12.9.

LC/MS: m/z calculated for $C_{28}H_{33}N_5O_4$ $[M + H]^+$: 504.3, found: 504.1.



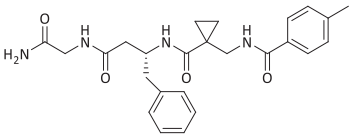
18

Compound **18**: Yield: 15.0 mg (0.034 mmol ≙ 75% of th.), colorless solid.

^{1}H-NMR (300 MHz, DMSO-d_6): δ [ppm] = 8.62 (t, *J* = 6.1 Hz, 1H), 8.10 (t, *J* = 5.9 Hz, 1H), 7.96 (d, *J* = 8.1 Hz, 1H), 7.91–7.75 (m, 2H), 7.67–7.36 (m, 3H), 7.24 (s, 1H), 7.20–7.03 (m, 5H), 7.03 (s, 1H), 4.30 (q, *J* = 7.5 Hz, 1H), 3.74–3.39 (m, 4H), 2.93–2.59 (m, 2H), 2.32 (d, *J* = 6.8 Hz, 2H), 1.04–0.56 (m, 4H).

^{13}C-NMR (75 MHz, DMSO): δ [ppm] = 171.5, 171.1, 170.4, 167.2, 138.8, 134.0, 131.5, 129.2, 128.3, 128.0, 127.4, 126.0, 48.4, 42.3, 41.9, 40.3, 25.2, 13.0.

LC/MS: m/z calculated for $C_{24}H_{28}N_4O_4$ $[M + H]^+$: 437.2, found: 437.2.



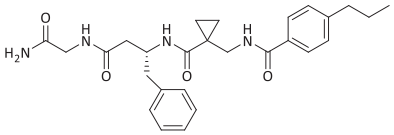
11

Compound **11**: Yield: 15.0 mg (0.033 mmol ≙ 75% of th.), colorless solid.

^{1}H-NMR (300 MHz, DMSO-d_6): δ [ppm] = 8.55 (t, J = 6.1 Hz, 1H), 8.09 (t, J = 5.9 Hz, 1H), 8.00 (d, J = 8.1 Hz, 1H), 7.82–7.69 (m, 2H), 7.32–7.26 (m, 2H), 7.24 (s, 1H), 7.17–7.07 (m, 5H), 7.03 (s, 1H), 4.30 (q, J = 7.0 Hz, 1H), 3.72–3.38 (m, 4H), 2.90–2.59 (m, 2H), 2.36 (s, 3H), 2.31 (d, J = 6.9 Hz, 2H), 0.96–0.68 (m, 4H).

^{13}C-NMR (75 MHz, DMSO): δ [ppm] = 171.5, 171.1, 170.3, 167.1, 141.4, 138.8, 131.1, 129.2, 128.9, 128.0, 127.4, 126.0, 48.4, 42.3, 41.9, 25.3, 21.0, 13.0.

LC/MS: m/z calculated for $C_{25}H_{30}N_4O_4$ $[M + H]^+$: 451.2, found: 451.1.



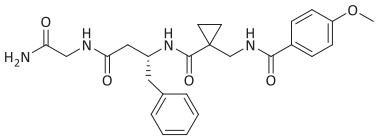
12

Compound **12**: Yield: 5.0 mg (0.010 mmol ≙ 23% of th.), colorless solid.

^{1}H-NMR (400 MHz, DMSO-d_6): δ [ppm] = 8.54 (t, J = 6.3 Hz, 1H), 8.08 (t, J = 6.0 Hz, 1H), 7.98 (d, J = 8.1 Hz, 1H), 7.81–7.73 (m, 2H), 7.33–7.26 (m, 2H), 7.23 (s, 1H), 7.17–7.05 (m, 5H), 7.01 (s, 1H), 4.29 (p, J = 7.2 Hz, 1H), 3.70–3.43 (m, 4H), 2.87–2.64 (m, 2H), 2.61 (t, J = 7.7 Hz, 2H), 2.31 (d, J = 6.9 Hz, 2H), 1.61 (h, J = 7.1 Hz, 2H), 0.93–0.72 (m, 7H).

^{13}C-NMR (101 MHz, DMSO): δ [ppm] = 171.5, 171.1, 170.3, 167.2, 145.9, 138.8, 131.4, 129.1, 128.3, 127.9, 127.4, 125.9, 48.4, 42.3, 41.9, 40.3, 37.0, 25.2, 23.9, 13.6, 13.0, 13.0.

LC/MS: m/z calculated for $C_{27}H_{34}N_4O_4$ $[M + H]^+$: 479.3, found: 479.2.



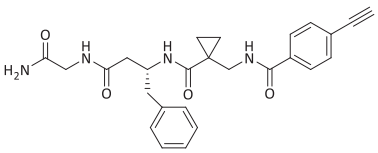
13

Compound **13**: Yield: 18.0 mg (0.040 mmol ≙ 86% of th.), colorless solid.

^{1}H-NMR (300 MHz, DMSO-d_6): δ [ppm] = 8.50 (t, J = 6.1 Hz, 1H), 8.16–7.98 (m, 2H), 7.91–7.76 (m, 2H), 7.24 (s, 1H), 7.20–7.07 (m, 4H), 7.06–6.91 (m, 3H), 4.29 (q, J = 8.5 Hz, 1H), 3.82 (s, 3H), 3.72–3.40 (m, 4H), 2.90–2.58 (m, 2H), 2.31 (d, J = 6.8 Hz, 2H), 0.98–0.61 (m, 4H).

^{13}C-NMR (75 MHz, DMSO): δ [ppm] = 171.5, 171.1, 170.4, 166.8, 161.8, 138.8, 129.3, 129.2, 128.0, 126.1, 126.0, 113.5, 55.4, 48.4, 42.3, 41.9, 25.3, 13.1.

LC/MS: m/z calculated for $C_{25}H_{30}N_4O_5$ $[M + H]^+$: 467.2, found: 467.1.



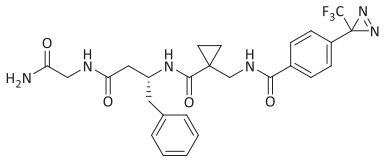
19

Compound **19**: Yield: 15.0 mg (0.033 mmol ≙ 71% of th.), pale brown solid.

^{1}H-NMR (300 MHz, DMSO-d_6): δ [ppm] = 8.69 (t, J = 6.1 Hz, 1H), 8.10 (t, J = 5.8 Hz, 1H), 7.96–7.76 (m, 3H), 7.59 (d, J = 8.2 Hz, 2H), 7.24 (s, 1H), 7.20–7.06 (m, 5H), 7.03 (s, 1H), 4.39 (s, 1H), 4.30 (q, J = 8.2 Hz, 1H), 3.70–3.38 (m, 4H), 2.86–2.57 (m, 2H), 2.32 (d, J = 6.8 Hz, 2H), 0.96–0.61 (m, 4H).

^{13}C-NMR (75 MHz, DMSO): δ [ppm] = 171.4, 171.1, 170.4, 166.4, 138.8, 134.0, 131.7, 129.1, 128.0, 127.7, 126.0, 124.7, 83.0, 82.9, 48.4, 42.5, 41.9, 40.2, 25.1, 12.9.

LC/MS: m/z calculated for $C_{26}H_{28}N_4O_4$ $[M + H]^+$: 461.2, found: 461.1.



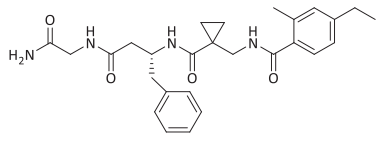
20

Compound **20**: Yield: 17.0 mg (0.031 mmol ≙ 69% of th.), colorless solid.

^{1}H-NMR (300 MHz, DMSO-d_6): δ [ppm] = 8.74 (t, J = 6.0 Hz, 1H), 8.09 (t, J = 5.9 Hz, 1H), 8.01–7.89 (m, 2H), 7.82 (d, J = 8.2 Hz, 1H), 7.39 (d, J = 8.1 Hz, 2H), 7.23 (s, 1H), 7.18–7.03 (m, 4H), 7.03 (s, 1H), 4.29 (p, J = 7.1 Hz, 1H), 3.80–3.39 (m, 4H), 2.94–2.57 (m, 2H), 2.31 (d, J = 6.8 Hz, 2H), 0.99–0.69 (m, 4H).

^{13}C-NMR (75 MHz, DMSO): δ [ppm] = 171.4, 171.1, 170.4, 166.1, 138.8, 135.6, 130.4, 129.1, 128.3, 127.9, 126.4, 125.9, 123.1, 120.4, 48.3, 42.5, 41.9, 40.2, 39.4, 28.3, 27.9, 25.1, 12.8.

LC/MS: m/z calculated for $C_{26}H_{27}F_3N_6O_4$ $[M + H]^+$: 545.2, found: 545.1.



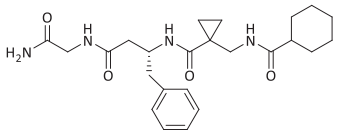
21

Compound **21**: Yield: 10.1 mg (0.021 mmol ≙ 46% of th.), colorless solid.

^{1}H-NMR (300 MHz, DMSO-d_6): δ [ppm] = 8.36 (t, J = 6.2 Hz, 1H), 8.09 (t, J = 5.8 Hz, 1H), 7.93 (d, J = 8.1 Hz, 1H), 7.30–7.11 (m, 7H), 7.11–6.92 (m, 3H), 4.40–4.20 (m, 1H), 3.69–3.45 (m, 3H), 3.43–3.25 (m, 1H), 2.74 (qd, J = 13.5, 6.8 Hz, 2H), 2.58 (q, J = 7.6 Hz, 2H), 2.39–2.16 (m, 5H), 1.17 (t, J = 7.6 Hz, 3H), 0.99–0.62 (m, 4H).

^{13}C-NMR (75 MHz, DMSO): δ [ppm] = 171.6, 171.1, 170.3, 170.0, 145.4, 138.9, 135.3, 134.0, 130.0, 129.2, 128.1, 127.4, 126.0, 124.9, 48.6, 41.9, 40.4, 28.0, 25.2, 19.6, 15.6, 12.9, 12.8.

LC/MS: m/z calculated for $C_{27}H_{34}N_4O_4$ $[M + H]^+$: 479.3, found: 479.2.



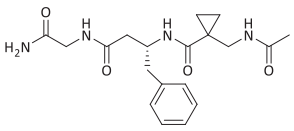
22

Compound **22**: Yield: 16.0 mg (0.036 mmol ≙ 79% of th.), colorless solid.

^{1}H-NMR (300 MHz, DMSO-d_6): δ [ppm] = 8.09 (t, J = 5.8 Hz, 1H), 7.96 (t, J = 6.2 Hz, 1H), 7.86 (d, J = 8.1 Hz, 1H), 7.34–7.09 (m, 6H), 7.02 (s, 1H), 4.38–4.10 (m, 1H), 3.60 (qd, J = 16.8, 5.8 Hz, 2H), 3.45–3.21 (m, 1H), 3.12 (dd, J = 14.7, 6.1 Hz, 1H), 2.89–2.56 (m, 2H), 2.27 (d, J = 6.9 Hz, 2H), 2.19–1.98 (m, 1H), 1.80–1.47 (m, 5H), 1.47–1.02 (m, 5H), 0.91–0.70 (m, 2H), 0.69–0.55 (m, 2H).

^{13}C-NMR (75 MHz, DMSO): δ [ppm] = 176.3, 171.5, 171.1, 170.3, 138.9, 129.2, 128.1, 126.0, 48.4, 43.9, 41.9, 41.3, 40.3, 29.2, 29.1, 25.4, 25.3, 25.1, 12.9, 12.8.

LC/MS: m/z calculated for $C_{24}H_{34}N_4O_4$ $[M + H]^+$: 443.3, found: 443.2.



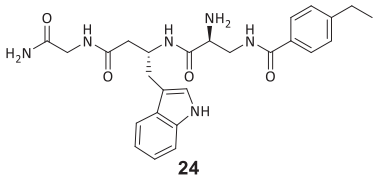
23

Compound **23**: Yield: 7.2 mg (0.018 mmol ≙ 41% of th.), colorless solid.

^{1}H-NMR (300 MHz, DMSO-d_6): δ [ppm] = 8.08 (q, J = 5.9 Hz, 2H), 7.78 (d, J = 8.0 Hz, 1H), 7.42–7.10 (m, 6H), 7.03 (s, 1H), 4.25 (p, J = 6.9 Hz, 1H), 3.80–3.46 (m, 2H), 3.22 (qd, J = 14.8, 6.2 Hz, 2H), 2.93–2.56 (m, 2H), 2.29 (d, J = 6.9 Hz, 2H), 1.80 (s, 3H), 1.01–0.72 (m, 2H), 0.71–0.56 (m, 2H).

^{13}C-NMR (75 MHz, DMSO): δ [ppm] = 171.4, 171.1, 170.3, 170.3, 138.8, 129.2, 128.1, 126.0, 48.3, 41.9, 41.7, 40.0, 39.4, 25.1, 22.5, 12.9.

LC/MS: m/z calculated for $C_{19}H_{26}N_4O_4$ $[M + H]^+$: 375.2, found: 375.2.



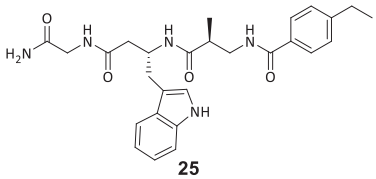
24

Compound **24**: Yield: 5.0 mg (0.010 mmol ≙ 23% of th.), colorless solid.

^{1}H-NMR (400 MHz, DMSO-d_6): δ [ppm] = 10.82 (s, 1H), 8.49 (d, J = 8.0 Hz, 1H), 8.41 (t, J = 5.7 Hz, 1H), 8.21 (s, 3H), 8.02 (t, J = 5.8 Hz, 1H), 7.76 (d, J = 7.9 Hz, 2H), 7.59 (d, J = 7.9 Hz, 1H), 7.43–7.21 (m, 4H), 7.13 (s, 1H), 7.10–7.00 (m, 2H), 6.95 (t, J = 7.4 Hz, 1H), 4.35 (q, J = 7.0 Hz, 1H), 3.94 (t, J = 6.1 Hz, 1H), 3.63 (d, J = 5.7 Hz, 2H), 3.59 (t, J = 5.9 Hz, 2H), 2.83 (m, 2H), 2.65 (q, J = 7.5 Hz, 2H), 2.44–2.29 (m, 2H), 1.18 (t, J = 7.6 Hz, 3H).

^{13}C-NMR (101 MHz, DMSO): δ [ppm] = 171.1, 170.3, 167.1, 166.0, 147.6, 136.2, 131.3, 127.6, 127.5, 127.4, 123.5, 120.9, 118.5, 118.2, 111.3, 110.7, 52.3, 47.8, 41.7, 40.2, 39.0, 29.9, 28.0, 15.4.

LC/MS: m/z calculated for $C_{26}H_{32}N_6O_4$ $[M + H]^+$: 493.3, found: 493.2.



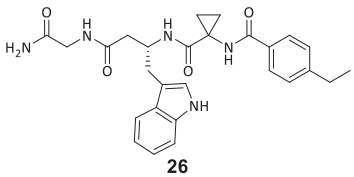
25

Compound **25**: Yield: 1.2 mg (2.520 μmol ≙ 1% of th.), colorless solid.

^{1}H-NMR (400 MHz, DMSO-d_6): δ [ppm] = 10.75 (s, 1H), 8.33 (t, J = 5.8 Hz, 1H), 7.96 (t, J = 5.8 Hz, 1H), 7.78 (d, J = 8.2 Hz, 1H), 7.73 (d, J = 7.9 Hz, 2H), 7.58 (d, J = 7.9 Hz, 1H), 7.31 (d, J = 8.1 Hz, 1H), 7.25 (d, J = 7.5 Hz, 3H), 7.09 (s, 1H), 7.07–6.99 (m, 2H), 6.94 (t, J = 7.4 Hz, 1H), 4.32 (q, J = 7.0 Hz, 1H), 3.69–3.48 (m, 2H), 3.28–3.12 (m, 2H), 2.81 (m, 2H), 2.69–2.53 (m, 3H), 2.38–2.16 (m, 2H), 1.21–1.09 (m, 3H), 0.98 (d, J = 6.8 Hz, 3H).

^{13}C-NMR (101 MHz, DMSO): δ [ppm] = 173.7, 171.1, 170.6, 166.3, 147.0, 136.1, 132.1, 127.6, 127.6, 127.2, 123.3, 120.8, 118.6, 118.2, 111.3, 111.1, 47.1, 42.5, 41.9, 30.2, 28.0, 15.6, 15.4.

LC/MS: m/z calculated for $C_{27}H_{33}N_5O_4$ $[M + H]^+$: 492.3, found: 492.1.



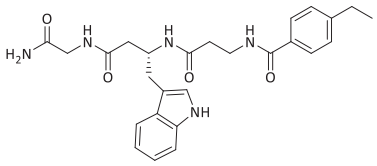
26

Compound **26**: Yield: 5.0 mg (0.010 mmol ≙ 23% of th.), colorless solid.

^{1}H-NMR (400 MHz, DMSO-d_6): δ [ppm] = 10.81 (s, 1H), 8.85 (s, 1H), 7.94 (t, J = 5.9 Hz, 1H), 7.87–7.73 (m, 3H), 7.60 (d, J = 7.9 Hz, 1H), 7.42–7.27 (m, 3H), 7.25 (s, 1H), 7.16 (s, 1H), 7.09–6.97 (m, 2H), 6.94 (t, J = 7.4 Hz, 1H), 4.30 (h, J = 6.6 Hz, 1H), 3.61 (t, J = 5.2 Hz, 2H), 2.99–2.71 (m, 2H), 2.66 (q, J = 7.6 Hz, 2H), 2.29 (ddd, J = 48.3, 14.5, 6.2 Hz, 2H), 1.44–1.28 (m, 2H), 1.26–1.10 (m, 3H), 1.06–0.86 (m, 2H).

^{13}C-NMR (101 MHz, DMSO): δ [ppm] = 171.1, 170.8, 170.8, 167.4, 147.4, 136.1, 131.8, 127.8, 127.5, 127.5, 123.6, 120.8, 118.5, 118.2, 111.2, 110.9, 41.8, 38.8, 34.7, 29.7, 28.1, 16.2, 15.5.

LC/MS: m/z calculated for $C_{27}H_{31}N_5O_4$ [M + H]$^+$: 490.2, found: 490.1.



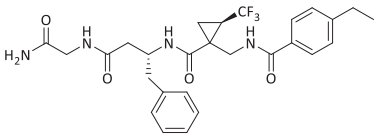
27

Compound **27**: Yield: 11.0 mg (0.023 mmol ≙ 50% of th.), colorless solid.

^{1}H-NMR (300 MHz, DMSO-d_6): δ [ppm] = 10.79 (d, J = 2.4 Hz, 1H), 8.38 (t, J = 5.6 Hz, 1H), 8.03 (t, J = 5.8 Hz, 1H), 7.87 (d, J = 8.2 Hz, 1H), 7.79–7.66 (m, 2H), 7.58 (d, J = 7.8 Hz, 1H), 7.37–7.19 (m, 4H), 7.11 (d, J = 2.2 Hz, 1H), 7.09–7.00 (m, 2H), 7.00–6.90 (m, 1H), 4.33 (q, J = 7.2 Hz, 1H), 3.69–3.50 (m, 3H), 3.49–3.29 (m, 2H), 2.83 (d, J = 6.5 Hz, 2H), 2.64 (q, J = 7.6 Hz, 2H), 2.42–2.18 (m, 3H), 1.18 (t, J = 7.6 Hz, 3H).

^{13}C-NMR (75 MHz, DMSO): δ [ppm] = 171.1, 170.6, 169.9, 166.1, 147.1, 136.1, 132.0, 127.6, 127.2, 123.4, 120.8, 118.6, 118.2, 111.3, 111.1, 47.2, 41.9, 40.0, 36.1, 35.7, 29.8, 28.0, 15.4.

LC/MS: m/z calculated for $C_{26}H_{31}N_5O_4$ [M + H]$^+$: 478.2, found: 478.1.



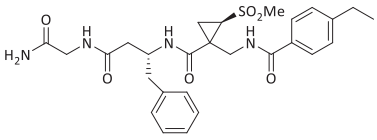
28

Compound **28**: Yield: 23.2 mg (0.040 mmol ≙ 87% of th.), colorless solid.

^{1}H-NMR (300 MHz, DMSO-d_6): δ [ppm] = 8.51 (s, 1H), 8.15 (d, J = 7.5 Hz, 1H), 7.81–7.74 (m, 2H), 7.37–7.13 (m, 6H), 7.07 (s, 4H), 3.70 (s, 4H), 3.63–3.56 (m, 2H), 2.72–2.58 (m, 3H), 2.41–2.29 (m, 2H), 2.05–1.83 (m, 1H), 1.48–1.28 (m, 2H), 1.19 (ddd, J = 7.5, 5.1, 2.7 Hz, 3H).

^{13}C-NMR (75 MHz, DMSO): δ [ppm] = 244.5, 237.0, 214.3, 204.3, 166.2, 148.9, 147.6, 138.2, 131.3, 129.3, 129.1, 128.0, 127.9, 127.7, 127.5, 127.5, 40.3, 40.0, 39.1, 38.8, 38.5, 28.1, 15.4.

LC/MS: m/z calculated for $C_{27}H_{31}F_3N_4O_4$ [M + H]$^+$: 533.2, found: 533.2.



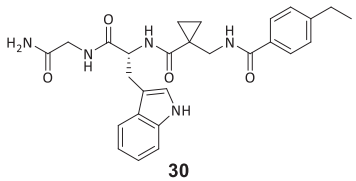
29

Compound **29**: Yield: 19.5 mg (0.036 mmol ≙ 72% of th.), colorless solid.

^{1}H-NMR (300 MHz, DMSO-d_6): δ [ppm] = 8.58–8.41 (m, 1H), 8.26 (t, J = 8.8 Hz, 1H), 8.12 (q, J = 5.8 Hz, 1H), 7.79 (d, J = 7.3 Hz, 2H), 7.36–7.09 (m, 6H), 7.04 (s, 3H), 4.33–4.16 (m, 5H), 3.83 (ddd, J = 30.8, 14.8, 5.2 Hz, 1H), 3.64–3.48 (m, 2H), 3.14 (s, 1H), 3.00–2.80 (m, 1H), 2.66 (qd, J = 7.4, 3.3 Hz, 3H), 2.41–2.26 (m, 2H), 1.73–1.62 (m, 2H), 1.19 (td, J = 7.6, 2.7 Hz, 3H).

^{13}C-NMR (75 MHz, DMSO): δ [ppm] = 171.1, 171.1, 170.3, 170.2, 167.8, 167.6, 167.3, 167.2, 147.8, 147.7, 138.6, 138.5, 131.2, 131.2, 129.3, 129.1, 128.1, 127.9, 127.7, 127.6, 127.5, 42.8, 42.8, 32.9, 32.8, 28.1, 15.4.

LC/MS: m/z calculated for $C_{27}H_{34}N_4O_6S$ [M + H]$^+$: 543.2, found: 543.2.



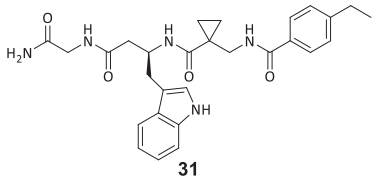
30

Compound **30**: Yield: 24.0 mg (0.049 mmol ≙ quant.), colorless solid.

^{1}H-NMR (300 MHz, DMSO-d_6): δ [ppm] = 10.77 (d, J = 2.4 Hz, 1H), 8.63 (t, J = 6.1 Hz, 1H), 8.44 (d, J = 6.7 Hz, 1H), 8.32 (t, J = 5.9 Hz, 1H), 7.80–7.67 (m, 2H), 7.60 (d, J = 7.7 Hz, 1H), 7.35–7.23 (m, 3H), 7.20 (d, J = 2.3 Hz, 1H), 7.14–7.01 (m, 3H), 6.97 (ddd, J = 8.0, 6.9, 1.1 Hz, 1H), 4.41 (dt, J = 9.4, 6.3 Hz, 1H), 3.74–3.56 (m, 2H), 3.56–3.44 (m, 2H), 3.17 (dd, J = 14.7, 4.8 Hz, 1H), 3.01 (dd, J = 14.7, 9.3 Hz, 1H), 2.65 (q, J = 7.6 Hz, 2H), 1.19 (t, J = 7.6 Hz, 3H), 0.98–0.71 (m, 4H).

^{13}C-NMR (75 MHz, DMSO): δ [ppm] = 172.9, 172.1, 171.1, 167.4, 147.5, 136.1, 131.4, 127.7, 127.5, 127.3, 123.6, 120.9, 118.4, 118.3, 111.4, 110.3, 54.8, 42.3, 42.2, 28.1, 27.1, 25.2, 15.4, 13.6.

LC/MS: m/z calculated for $C_{27}H_{31}N_5O_4$ $[M + H]^+$: 490.2, found: 490.1.



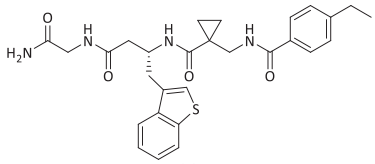
31

Compound **31**: Yield: 8.0 mg (0.016 mmol ≙ 35% of th.), colorless solid.

^{1}H-NMR (300 MHz, DMSO-d_6): δ [ppm] = 10.76 (d, J = 2.4 Hz, 1H), 8.57 (t, J = 6.1 Hz, 1H), 8.16–7.90 (m, 2H), 7.84–7.68 (m, 2H), 7.60 (d, J = 7.8 Hz, 1H), 7.35–7.25 (m, 3H), 7.23 (s, 1H), 7.09 (d, J = 2.2 Hz, 1H), 7.07–6.98 (m, 2H), 6.98–6.88 (m, 1H), 4.34 (q, J = 6.9 Hz, 1H), 3.72–3.36 (m, 4H), 2.83 (d, J = 6.5 Hz, 2H), 2.65 (q, J = 7.6 Hz, 2H), 2.34 (d, J = 6.8 Hz, 2H), 1.19 (t, J = 7.6 Hz, 3H), 1.06–0.59 (m, 4H).

^{13}C-NMR (75 MHz, DMSO): δ [ppm] = 171.5, 171.1, 170.6, 167.2, 147.5, 136.1, 131.5, 127.7, 127.6, 127.4, 123.3, 120.8, 118.6, 118.2, 111.3, 111.2, 47.7, 42.3, 41.9, 39.9, 29.8, 28.1, 25.3, 15.4, 13.2, 12.9.

LC/MS: m/z calculated for $C_{28}H_{33}N_5O_4$ $[M + H]^+$: 504.3, found: 504.1.



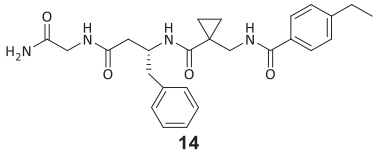
32

Compound **32**: Yield: 10.0 mg (0.019 mmol ≙ 43% of th.), colorless solid.

^{1}H-NMR (300 MHz, DMSO-d_6): δ [ppm] = 8.58 (t, J = 6.1 Hz, 1H), 8.22–8.05 (m, 2H), 8.02–7.93 (m, 1H), 7.93–7.85 (m, 1H), 7.81–7.68 (m, 2H), 7.47–7.18 (m, 6H), 7.03 (s, 1H), 4.42 (q, J = 7.0 Hz, 1H), 3.75–3.43 (m, 4H), 3.00 (qd, J = 14.2, 6.6 Hz, 2H), 2.65 (q, J = 7.5 Hz, 2H), 2.41 (d, J = 6.9 Hz, 2H), 1.19 (t, J = 7.6 Hz, 3H), 0.98–0.68 (m, 4H).

^{13}C-NMR (75 MHz, DMSO): δ [ppm] = 171.7, 171.0, 170.4, 167.2, 147.5, 139.6, 139.0, 133.2, 131.4, 127.7, 127.4, 124.2, 124.0, 123.3, 122.8, 122.1, 46.7, 42.3, 41.9, 40.2, 32.8, 28.1, 25.3, 15.4, 13.1.

LC/MS: m/z calculated for $C_{28}H_{32}N_4O_4S$ $[M + H]^+$: 521.2, found: 521.1.



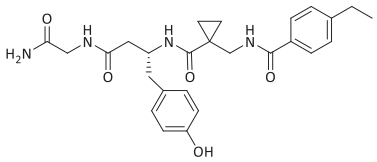
14

Compound **14**: Yield: 16.0 mg (0.034 mmol ≙ 77% of th.), colorless solid.

^{1}H-NMR (600 MHz, DMSO-d_6): δ [ppm] = 8.58 (t, J = 6.2 Hz, 1H), 8.11 (t, J = 5.9 Hz, 1H), 8.01 (d, J = 8.2 Hz, 1H), 7.82–7.74 (m, 2H), 7.32 (d, J = 8.2 Hz, 2H), 7.25 (s, 1H), 7.15–7.12 (m, 4H), 7.12–7.07 (m, 1H), 7.04 (s, 1H), 4.33–4.22 (m, 1H), 3.61 (dd, J = 16.8, 6.0 Hz, 1H), 3.54–3.45 (m, 3H), 2.78 (dd, J = 13.6, 5.1 Hz, 1H), 2.68–2.63 (m, 3H), 2.30 (d, J = 6.9 Hz, 2H), 1.19 (t, J = 7.6 Hz, 3H), 0.92–0.80 (m, 2H), 0.80–0.71 (m, 2H).

^{13}C-NMR (151 MHz, DMSO): δ [ppm] = 171.5, 171.1, 170.4, 167.2, 147.6, 138.9, 131.4, 129.2, 128.0, 127.7, 127.5, 126.0, 48.5, 42.3, 41.9, 40.3, 40.1, 28.1, 25.3, 15.5, 13.1.

LC/MS: m/z calculated for $C_{26}H_{32}N_4O_4$ $[M + H]^+$: 465.3, found: 465.1.



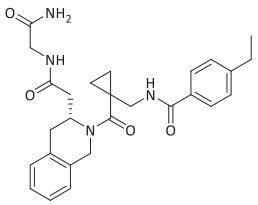
15

Compound **15**: Yield: 15.0 mg (0.031 mmol ≙ 69% of th.), colorless solid.

^{1}H-NMR (600 MHz, DMSO-d_6): δ [ppm] = 9.11 (s, 1H), 8.57 (t, J = 6.1 Hz, 1H), 8.05 (t, J = 5.8 Hz, 1H), 7.95 (d, J = 8.1 Hz, 1H), 7.85–7.71 (m, 2H), 7.41–7.27 (m, 2H), 7.22 (s, 1H), 7.02 (s, 1H), 6.97–6.86 (m, 2H), 6.64–6.49 (m, 2H), 4.21 (h, J = 7.3 Hz, 1H), 3.69–3.44 (m, 4H), 2.74–2.53 (m, 4H), 2.27 (d, J = 6.8 Hz, 2H), 1.19 (t, J = 7.6 Hz, 3H), 0.96–0.60 (m, 4H).

^{13}C-NMR (151 MHz, DMSO): δ [ppm] = 171.5, 171.1, 170.4, 167.2, 155.5, 147.6, 131.4, 130.0, 128.9, 127.7, 127.5, 114.8, 48.7, 42.3, 41.9, 40.2, 38.8, 28.1, 25.2, 15.4, 13.0.

LC/MS: m/z calculated for $C_{26}H_{32}N_4O_5$ $[M + H]^+$: 481.2, found: 481.1.



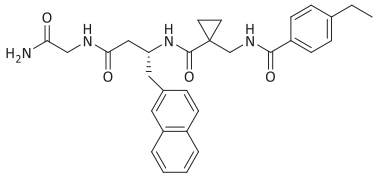
35

Compound **35**: Yield: 11.0 mg (0.023 mmol ≙ 50% of th.), colorless solid.

^{1}H-NMR (400 MHz, DMSO-d_6): δ [ppm] = 8.42 (t, J = 6.1 Hz, 1H), 8.08 (t, J = 6.0 Hz, 1H), 7.70 (d, J = 7.8 Hz, 2H), 7.26 (d, J = 7.9 Hz, 2H), 7.24–7.18 (m, 1H), 7.18–7.08 (m, 4H), 7.00 (s, 1H), 5.39–4.83 (m, 2H), 4.58 (s, 1H), 3.78–3.50 (m, 3H), 2.82–2.67 (m, 1H), 2.63 (q, J = 7.6 Hz, 3H), 2.45–2.23 (m, 2H), 1.18 (t, J = 7.6 Hz, 3H), 0.93–0.49 (m, 4H).

^{13}C-NMR (101 MHz, DMSO): δ [ppm] = 170.9, 170.2, 170.1, 166.5, 147.2, 131.8, 127.6, 127.3, 126.6, 126.0, 41.9, 37.0, 32.0, 28.0, 26.0, 15.4, 9.8, 9.5.

LC/MS: m/z calculated for $C_{27}H_{32}N_4O_4$ $[M + H]^+$: 477.3, found: 477.1.



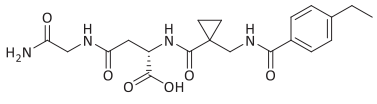
36

Compound **36**: Yield: 19.0 mg (0.037 mmol ≙ 80% of th.), colorless solid.

^{1}H-NMR (300 MHz, DMSO-d_6): δ [ppm] = 8.59 (t, J = 6.1 Hz, 1H), 8.23–8.03 (m, 2H), 7.88–7.72 (m, 3H), 7.69 (d, J = 8.4 Hz, 1H), 7.64–7.49 (m, 2H), 7.50–7.36 (m, 2H), 7.36–7.27 (m, 3H), 7.25 (s, 1H), 7.04 (s, 1H), 4.41 (p, J = 6.9 Hz, 1H), 3.77–3.46 (m, 3H), 3.46–3.26 (m, 1H), 2.98 (dd, J = 13.6, 4.9 Hz, 1H), 2.91–2.75 (m, 1H), 2.67 (q, J = 7.6 Hz, 2H), 2.43–2.28 (m, 2H), 1.21 (t, J = 7.6 Hz, 3H), 0.98–0.66 (m, 4H).

^{13}C-NMR (75 MHz, DMSO): δ [ppm] = 171.5, 171.1, 170.3, 167.2, 147.6, 136.6, 132.9, 131.6, 131.3, 127.9, 127.7, 127.5, 127.4, 127.4, 127.3, 127.2, 125.8, 125.2, 48.4, 42.3, 41.9, 40.5, 39.7, 28.1, 25.3, 15.4, 13.3, 13.0.

LC/MS: m/z calculated for $C_{30}H_{34}N_4O_4$ $[M + H]^+$: 515.3, found: 515.2.



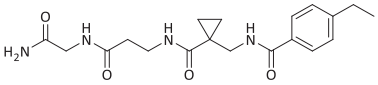
37

Compound **37**: Yield: 5.0 mg (0.012 mmol ≙ 26% of th.), colorless solid.

^{1}H-NMR (600 MHz, DMSO-d_6): δ [ppm] = 8.60 (t, *J* = 6.1 Hz, 1H), 8.26–8.20 (m, 2H), 7.81–7.74 (m, 2H), 7.35 (s, 1H), 7.30 (d, *J* = 8.1 Hz, 2H), 7.08 (s, 1H), 4.49 (q, *J* = 7.0 Hz, 1H), 3.62 (dd, *J* = 16.9, 6.1 Hz, 1H), 3.58–3.50 (m, 2H), 3.47 (dd, *J* = 16.9, 5.6 Hz, 1H), 2.71–2.60 (m, 3H), 1.19 (t, *J* = 7.6 Hz, 4H), 0.99–0.91 (m, 2H), 0.87–0.78 (m, 2H).

^{13}C-NMR (151 MHz, DMSO): δ [ppm] = 173.1, 172.2, 172.1, 171.2, 169.6, 167.3, 147.5, 131.5, 127.7, 127.6, 49.8, 42.1, 42.1, 40.1, 37.1, 28.1, 24.9, 15.5, 13.3, 13.0.

LC/MS: m/z calculated for $C_{20}H_{26}N_4O_6$ $[M + H]^+$: 419.2, found: 419.1.



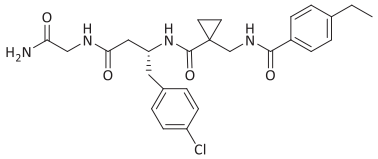
38

Compound **38**: Yield: 5.0 mg (0.013 mmol ≙ 29% of th.), colorless solid.

^{1}H-NMR (600 MHz, DMSO-d_6): δ [ppm] = 8.60 (t, *J* = 6.1 Hz, 1H), 8.10 (dt, *J* = 15.2, 5.6 Hz, 2H), 7.82–7.75 (m, 2H), 7.36–7.26 (m, 3H), 7.05 (s, 1H), 3.58 (d, *J* = 5.8 Hz, 2H), 3.51 (d, *J* = 6.0 Hz, 2H), 3.28 (td, *J* = 7.2, 5.3 Hz, 2H), 2.65 (q, *J* = 7.6 Hz, 2H), 2.30 (t, *J* = 7.3 Hz, 2H), 1.18 (t, *J* = 7.6 Hz, 3H), 0.95 (q, *J* = 3.7 Hz, 2H), 0.81 (q, *J* = 3.7 Hz, 2H).

^{13}C-NMR (151 MHz, DMSO): δ [ppm] = 172.2, 171.2, 170.8, 167.2, 147.6, 131.5, 127.8, 127.5, 42.2, 41.9, 40.1, 36.0, 35.2, 28.1, 25.1, 15.5, 13.1.

LC/MS: m/z calculated for $C_{19}H_{26}N_4O_4$ $[M + H]^+$: 375.2, found: 375.1.



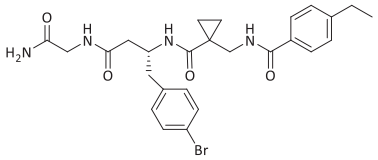
16

Compound **16**: Yield: 21.0 mg (0.042 mmol ≙ 26% of th.), colorless solid.

^{1}H-NMR (300 MHz, DMSO-d_6): δ [ppm] = 8.58 (t, *J* = 6.1 Hz, 1H), 8.11 (t, *J* = 5.8 Hz, 1H), 8.01 (d, *J* = 8.1 Hz, 1H), 7.77 (d, *J* = 8.2 Hz, 2H), 7.31 (d, *J* = 8.2 Hz, 2H), 7.25 (s, 1H), 7.13 (s, 4H), 7.03 (s, 1H), 4.28 (q, *J* = 7.8 Hz, 1H), 3.68–3.40 (m, 4H), 2.82 (dd, *J* = 13.6, 4.8 Hz, 1H), 2.74–2.60 (m, 3H), 2.32 (d, *J* = 6.9 Hz, 2H), 1.20 (t, *J* = 7.6 Hz, 3H), 0.93–0.72 (m, 4H).

^{13}C-NMR (75 MHz, DMSO): δ [ppm] = 171.6, 171.1, 170.3, 167.2, 147.6, 137.8, 131.4, 131.0, 130.6, 127.8, 127.7, 127.5, 54.9, 48.2, 42.3, 41.9, 40.2, 38.6, 28.1, 25.3, 15.4, 13.2, 13.1.

LC/MS: m/z calculated for $C_{26}H_{31}ClN_4O_4$ $[M + H]^+$: 499.2, found: 498.9.



17

Compound **17**: Yield: 29.1 mg (0.053 mmol ≙ 34% of th.), colorless solid.

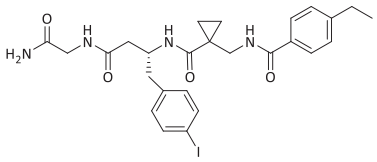
^{1}H-NMR (300 MHz, DMSO-d_6): δ [ppm] = 8.59 (t, *J* = 6.1 Hz, 1H), 8.12 (t, *J* = 5.9 Hz, 1H), 8.01 (d, *J* = 8.1 Hz, 1H), 7.77 (d, *J* = 8.3 Hz, 2H), 7.35–7.29 (m, 2H), 7.28–7.20 (m, 3H), 7.11–6.99 (m, 3H), 4.28 (td, *J* = 7.8, 4.8 Hz, 1H), 3.69–3.47 (m, 3H), 3.42 (d, *J* = 5.9 Hz, 1H), 2.80 (dd, *J* = 13.6, 4.8 Hz, 1H), 2.65 (p, *J* = 7.6 Hz, 3H), 2.32 (d, *J* = 6.9 Hz, 2H), 1.20 (t, *J* = 7.6 Hz, 3H), 0.95–0.71 (m, 4H).

^{13}C-NMR (75 MHz, DMSO): δ [ppm] = 172.0, 171.5, 170.7, 167.6, 148.0, 138.7, 131.8, 131.2, 128.2, 127.9, 119.6, 48.6, 42.8, 42.4, 28.5, 25.7, 15.9, 13.7, 13.5.

CellPress OPEN ACCESS

iScience
Article

LC/MS: m/z calculated for $C_{26}H_{31}BrN_4O_4$ $[M + H]^+$: 543.1, found: 543.1.



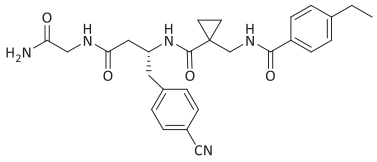
33

Compound **33**: Yield: 32.1 mg (0.054 mmol ≙ 34% of th.), colorless solid.

^{1}H-NMR (300 MHz, DMSO-d_6): δ [ppm] = 8.59 (t, J = 6.1 Hz, 1H), 8.11 (t, J = 5.9 Hz, 1H), 8.00 (d, J = 8.1 Hz, 1H), 7.77 (d, J = 8.3 Hz, 2H), 7.46–7.37 (m, 2H), 7.36–7.28 (m, 2H), 7.25 (s, 1H), 7.03 (s, 1H), 6.93 (d, J = 8.3 Hz, 2H), 4.27 (q, J = 7.2 Hz, 1H), 3.74–3.47 (m, 4H), 2.78 (dd, J = 13.7, 4.8 Hz, 1H), 2.72–2.56 (m, 3H), 2.31 (d, J = 6.9 Hz, 2H), 1.21 (t, J = 7.6 Hz, 3H), 0.95–0.71 (m, 4H).

^{13}C-NMR (75 MHz, DMSO): δ [ppm] = 172.0, 171.5, 170.7, 167.6, 148.0, 139.0, 137.1, 132.0, 131.8, 128.2, 127.9, 92.2, 48.6, 42.8, 42.4, 40.7, 28.6, 25.7, 15.9, 13.7, 13.5.

LC/MS: m/z calculated for $C_{26}H_{31}ClN_4O_4$ $[M + H]^+$: 591.1, found: 591.1.



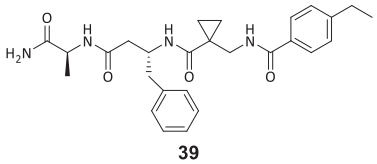
34

Compound **34**: Yield: 26.0 mg (0.044 mmol ≙ 28% of th.), colorless solid.

^{1}H-NMR (300 MHz, DMSO-d_6): δ [ppm] = 8.59 (t, J = 6.1 Hz, 1H), 8.15 (t, J = 5.9 Hz, 1H), 8.06 (d, J = 8.1 Hz, 1H), 7.74 (d, J = 8.3 Hz, 2H), 7.50 (d, J = 8.3 Hz, 2H), 7.30 (t, J = 7.9 Hz, 5H), 7.03 (s, 1H), 4.33 (dq, J = 11.7, 6.7 Hz, 1H), 3.68–3.49 (m, 3H), 3.33 (d, J = 5.9 Hz, 1H), 2.95 (dd, J = 13.6, 4.6 Hz, 1H), 2.81–2.60 (m, 3H), 2.35 (d, J = 7.0 Hz, 2H), 1.21 (t, J = 7.6 Hz, 3H), 0.94–0.70 (m, 4H).

^{13}C-NMR (75 MHz, DMSO): δ [ppm] = 172.1, 171.5, 170.6, 167.6, 148.1, 145.3, 132.2, 131.7, 130.6, 128.1, 127.9, 119.4, 109.2, 48.3, 42.8, 42.3, 40.7, 28.5, 25.7, 15.8, 13.7, 13.5.

LC/MS: m/z calculated for $C_{27}H_{31}N_5O_4$ $[M + H]^+$: 490.2, found: 490.2.



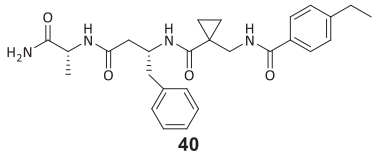
39

Compound **39**: Yield: 14 mg (0.029 mmol ≙ 64% of th.), colorless solid.

^{1}H-NMR (300 MHz, DMSO-d_6): δ [ppm] = 8.53 (t, J = 6.1 Hz, 1H), 8.03–7.90 (m, 2H), 7.85–7.69 (m, 2H), 7.39–7.28 (m, 2H), 7.26 (s, 1H), 7.20–7.01 (m, 5H), 6.96 (s, 1H), 4.29 (h, J = 7.4 Hz, 1H), 4.16 (p, J = 7.1 Hz, 1H), 3.48 (p, J = 8.5 Hz, 2H), 2.78 (dd, J = 13.5, 5.2 Hz, 1H), 2.72–2.58 (m, 3H), 2.28 (d, J = 6.9 Hz, 2H), 1.24–1.11 (m, 6H), 0.92–0.71 (m, 4H).

^{13}C-NMR (75 MHz, DMSO): δ [ppm] = 174.4, 171.5, 169.7, 167.2, 147.6, 138.8, 131.5, 129.1, 128.0, 127.7, 127.5, 126.0, 48.5, 48.0, 42.2, 28.1, 25.2, 18.2, 15.4, 13.0, 12.9.

LC/MS: m/z calculated for $C_{27}H_{34}N_4O_4$ $[M + H]^+$: 479.3, found: 479.2.



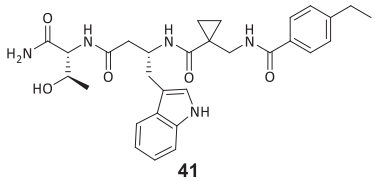
40

Compound **40**: Yield: 3.0 mg (6.263 μmol ≙ 14% of th.), colorless solid.

^{1}H-NMR (400 MHz, DMSO-d_6): δ [ppm] = 8.54 (t, J = 6.0 Hz, 1H), 8.01–7.90 (m, 2H), 7.77 (d, J = 7.8 Hz, 2H), 7.31 (d, J = 7.8 Hz, 2H), 7.25 (s, 1H), 7.18–7.02 (m, 5H), 6.95 (s, 1H), 4.28 (q, J = 7.0 Hz, 1H), 4.16 (p, J = 7.2 Hz, 1H), 3.62–3.51 (m, 1H), 3.44–3.34 (m, 1H), 2.83–2.60 (m, 4H), 2.30 (d, J = 6.9 Hz, 2H), 1.28–1.09 (m, 6H), 0.95–0.67 (m, 4H).

^{13}C-NMR (101 MHz, DMSO): δ [ppm] = 174.3, 171.4, 169.7, 167.2, 147.6, 138.8, 131.4, 129.1, 127.9, 127.7, 127.5, 125.9, 48.4, 48.0, 42.3, 40.2, 28.1, 25.2, 18.2, 15.4, 13.0, 12.9.

LC/MS: m/z calculated for $C_{27}H_{34}N_4O_4$ $[M + H]^+$: 479.3, found: 479.1.



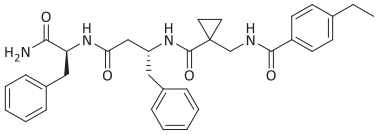
41

Compound **41**: Yield: 7.0 mg (0.013 mmol ≙ 28% of th.), colorless solid.

^{1}H-NMR (300 MHz, DMSO-d_6): δ [ppm] = 10.75 (d, J = 2.4 Hz, 1H), 8.56 (t, J = 6.1 Hz, 1H), 8.00 (d, J = 7.9 Hz, 1H), 7.86 (d, J = 8.6 Hz, 1H), 7.82–7.68 (m, 3H), 7.58 (d, J = 7.8 Hz, 1H), 7.37–7.19 (m, 5H), 7.12–6.98 (m, 3H), 6.98–6.88 (m, 1H), 4.35 (q, J = 6.9 Hz, 1H), 4.21 (dd, J = 8.6, 6.1 Hz, 1H), 3.84 (p, J = 6.3 Hz, 1H), 2.82 (d, J = 6.5 Hz, 2H), 2.65 (q, J = 7.6 Hz, 2H), 2.38 (d, J = 6.9 Hz, 2H), 1.19 (t, J = 7.6 Hz, 4H), 1.03 (d, J = 6.3 Hz, 3H), 0.93–0.86 (m, 2H), 0.81–0.73 (m, 2H).

^{13}C-NMR (75 MHz, DMSO): δ [ppm] = 172.3, 171.6, 170.5, 167.2, 147.5, 136.1, 131.5, 127.7, 127.7, 127.6, 127.4, 127.4, 123.2, 120.8, 118.6, 118.2, 111.3, 111.2, 66.8, 58.1, 47.9, 42.2, 40.2, 29.7, 28.1, 25.3, 19.5, 15.4, 13.3, 13.0.

LC/MS: m/z calculated for $C_{30}H_{37}N_5O_5$ $[M + H]^+$: 548.3, found: 547.8.



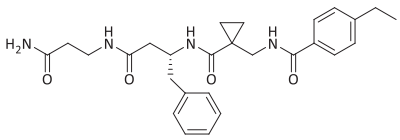
42

Compound **42**: Yield: 15.0 mg (0.027 mmol ≙ 59% of th.), colorless solid.

^{1}H-NMR (300 MHz, DMSO-d_6): δ [ppm] = 8.54 (t, J = 6.1 Hz, 1H), 8.14 (d, J = 8.4 Hz, 1H), 7.98 (d, J = 8.2 Hz, 1H), 7.87–7.71 (m, 2H), 7.39 (s, 1H), 7.31 (d, J = 8.2 Hz, 2H), 7.27–7.22 (m, 3H), 7.22–6.95 (m, 8H), 4.55–4.35 (m, 1H), 4.24 (q, J = 7.3 Hz, 1H), 3.59–3.42 (m, 2H), 3.02 (dd, J = 13.8, 4.7 Hz, 1H), 2.84–2.42 (m, 5H), 2.23 (qd, J = 14.2, 6.9 Hz, 2H), 1.19 (t, J = 7.6 Hz, 3H), 0.97–0.51 (m, 4H).

^{13}C-NMR (75 MHz, DMSO): δ [ppm] = 173.3, 171.5, 170.0, 167.2, 147.6, 138.8, 138.3, 131.5, 129.1, 128.1, 127.9, 127.7, 127.5, 126.2, 125.9, 53.9, 48.4, 42.3, 37.5, 28.1, 25.2, 15.4, 13.0, 13.0.

LC/MS: m/z calculated for $C_{33}H_{38}N_4O_4$ $[M + H]^+$: 555.3, found: 555.2.



43

Compound **43**: Yield: 18.0 mg (0.038 mmol ≙ 82% of th.), colorless solid.

^{1}H-NMR (300 MHz, DMSO-d_6): δ [ppm] = 8.57 (t, J = 6.1 Hz, 1H), 8.05–7.84 (m, 2H), 7.85–7.70 (m, 2H), 7.40–7.24 (m, 3H), 7.22–7.01 (m, 5H), 6.82 (s, 1H), 4.26 (h, J = 7.1 Hz, 1H), 3.61–3.39 (m, 2H), 3.29–3.06 (m, 2H), 2.81–2.57 (m, 4H), 2.32–2.04 (m, 4H), 1.19 (t, J = 7.6 Hz, 3H), 0.98–0.69 (m, 4H).

^{13}C-NMR (75 MHz, DMSO): δ [ppm] = 172.6, 171.4, 169.9, 167.2, 147.6, 138.8, 131.4, 129.2, 128.0, 127.7, 127.5, 125.9, 48.4, 42.2, 40.2, 35.2, 35.0, 28.1, 25.2, 15.4, 13.0.

CellPress
OPEN ACCESS

iScience
Article

LC/MS: m/z calculated for $C_{27}H_{34}N_4O_4$ $[M + H]^+$: 479.3, found: 479.2.



49

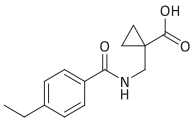
Compound **49**: 1-Cyanocyclopropane-1-carboxylic acid (500 mg, 4.500 mmol, 1.0 eq.) was dissolved in methanol (10 mL), ammonia in methanol (7 M, 1.0 mL), and Raney-nickel (50 mg, 5%) were added. The mixture was stirred under a hydrogen atmosphere (4 bar) for 16 h at RT. The reaction mixture was adjusted to alkaline pH (pH = 8) by adding ammonia in methanol (7 M, 0.5 mL), filtered over Celite S, and the solvent was removed under reduced pressure.

Yield: 574.0 mg (4.986 mmol ≙ quant.), colorless solid.

^{1}H-NMR (300 MHz, MeO*D*): δ [ppm] = 3.06 (s, 2H), 1.36–1.29 (m, 2H), 1.02–0.94 (m, 2H).

^{13}C-NMR (75 MHz, MeOD): δ [ppm] = 177.8, 101.2, 45.2, 15.0.

LC/MS: m/z calculated for $C_5H_9NO_2$ $[M + H]^+$: 116.1, found: 116.0.



50

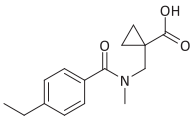
Compound **50**: The crude product **49** (518 mg, 4.500 mmol, 1.0 eq.) was suspended in DCM (10 mL), DMF (0.5 mL), and TEA (620 µL, 4.473 mmol, 1.0 eq.). The mixture was cooled to 0 °C, and a solution of acid 4-ethylbenzoyl chloride (662 µL, 4.500 mmol, 1.0 eq.) in DCM (0.3 mL) was added. The mixture was warmed to RT and stirred for 16 h. The reaction mixture was washed with 1 M hydrochloric acid thrice (5 mL each). The organic phase was separated, dried over sodium sulfate, and the solvents were removed under reduced pressure. The crude product was purified by column chromatography (mobile phase: CH:EtOAc 2:1 with 0.1% TFA)

Yield: 413.0 mg (1.670 mmol ≙ 37% of th.), colorless solid.

^{1}H-NMR (300 MHz, DMSO-d_6): δ [ppm] = 9.99 (s, 1H), 7.80–7.62 (m, 2H), 7.29–7.20 (m, 2H), 7.00 (t, *J* = 6.2 Hz, 1H), 3.62 (d, *J* = 6.1 Hz, 2H), 2.68 (q, *J* = 7.6 Hz, 2H), 1.35 (q, *J* = 4.2 Hz, 2H), 1.24 (t, *J* = 7.6 Hz, 3H), 1.15 (q, *J* = 4.3 Hz, 2H).

^{13}C-NMR (75 MHz, DMSO): δ [ppm] = 181.1, 167.9, 148.5, 131.6, 128.2, 127.3, 42.9, 28.9, 24.8, 16.0, 15.5.

LC/MS: m/z calculated for $C_{14}H_{17}NO_3$ $[M + H]^+$: 248.1, found: 248.0.



51

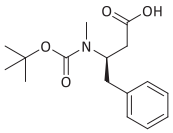
Compound **51**: Compound **50** (50 mg, 0.202 mmol, 1.0 eq.) was dissolved in anhydrous THF (5 mL) and cooled to 0 °C. Sodium hydride (60% suspension, 21 mg, 0.525 mmol, 2.6 eq.) was added and the mixture was stirred for 5 min. Then, methyl iodide (38 µL, 0.610 mmol, 3.0 eq.) was added dropwise. The mixture was warmed to RT and stirred for 16 h. A solution of sodium hydroxide (18 mg, 0.450 mmol, 2.2 eq.) in water (5 mL) was added and the mixture was stirred for 1 h. The mixture was adjusted to acidic pH (pH = 1) with 1 M hydrochloric acid and the solvents were removed under reduced pressure. The crude product was dissolved in sodium hydroxide solution (pH = 12) and was extracted three times with DCM (3 mL each). Then, the aqueous phase was brought to an acidic pH (pH = 1) with 1 M hydrochloric acid and extracted thrice with DCM (3 mL each). The organic phases from the acidic extraction were combined, and dried over sodium sulfate, and the solvent was removed under reduced pressure.

Yield: 44.0 mg (0.168 mmol ≙ 83% of th.), colorless solid.

^{1}H-NMR (300 MHz, C*D*Cl$_3$, 60 °C): δ [ppm] = 9.87 (s, 1H), 7.30 (d, *J* = 8.2 Hz, 2H), 7.19 (d, *J* = 7.9 Hz, 2H), 3.82 (s, 2H), 3.05 (s, 3H), 2.66 (q, *J* = 7.6 Hz, 2H), 1.39 (q, *J* = 4.1 Hz, 2H), 1.24 (t, *J* = 7.6 Hz, 3H), 1.15–0.94 (m, 2H).

^{13}C-NMR (75 MHz, *C*DCl$_3$, 60 °C): δ [ppm] = 179.1, 173.0, 146.2, 133.7, 128.1, 127.9, 127.4, 127.3, 28.8, 23.2, 16.2, 15.3.

LC/MS: m/z calculated for $C_{15}H_{19}NO_3[M + H]^+$: 262.2, found: 262.0.



52

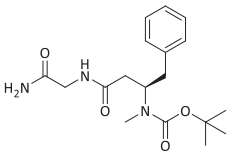
Compound **52**: (*R*)-3-*tert*-butoxycarbonylamino-4-phenylbutyric acid (100 mg, 0.358 mmol, 1.0 eq.) was dissolved in anhydrous THF (7 mL) and cooled to 0 °C. Sodium hydride (60% suspension, 39 mg, 0.975 mmol, 2.7 eq.) was added and the mixture was stirred for 5 min. Then, methyl iodide (67 µL, 1.074 mmol, 3.0 eq.) was added dropwise. The mixture was warmed to RT and stirred for 16 h. Because the reaction was not complete, methyl iodide (46 µL, 0.739 mmol, 2.1 eq.) and sodium hydride (34 mg, 0.850 mmol, 2.4 eq.) were added and the mixture was stirred for an additional 16 h. Water (2 mL) was added, and the pH was confirmed to be > 12. The mixture was stirred for 1 h and all solvents were removed under reduced pressure and the crude product was purified by reversed-phase flash column chromatography (Biotage Isolera, ACN/H_2O + TFA).

Yield: 39.0 mg (0.133 mmol ≙ 37% of th.), colorless solid.

^{1}H-NMR (300 MHz, *C*DCl_3, 60 °C): δ [ppm] = 8.92 (s, 1H), 7.28–6.94 (m, 5H), 4.45 (tt, *J* = 8.9, 6.1 Hz, 1H), 2.93–2.52 (m, 5H), 2.45 (dd, *J* = 15.5 Hz, 5.8 Hz, 1H), 1.27 (s, 9H).

^{13}C-NMR (75 MHz, *C*DCl_3, 60 °C): δ [ppm] = 176.1, 155.9, 138.2, 129.2, 128.7, 126.8, 80.3, 55.7, 38.9, 37.6, 30.8, 28.5.

LC/MS: m/z calculated for $C_{16}H_{23}NO_4$ [M-Boc+H]$^+$: 194.1, found: 194.0.



53

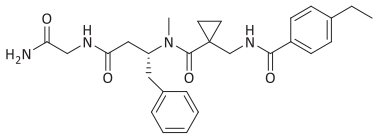
Compound **53**: Compound **52** (35 mg, 0.119 mmol, 1.0 eq.), glycine amide hydrochloride (14 mg, 0.127 mmol, 1.1 eq.), and TBTU (38 mg, 0.119 mmol, 1.0 eq.) were dissolved in anhydrous DMF (1.5 mL), and DIPEA (63 µL, 0.357 mmol, 3.0 eq.) was added. The mixture was stirred for 16 h at RT. All solvents were removed under reduced pressure, and the crude product was purified by reversed-phase flash column chromatography (Biotage Isolera, ACN/H_2O + TFA).

Yield: 33.0 mg (0.094 mmol ≙ 79% of th.), colorless solid.

^{1}H-NMR (300 MHz, *C*DCl_3): δ [ppm] = 7.37–6.99 (m, 6H), 6.85 (s, 1H), 5.92 (s, 1H), 4.62 (s, 1H), 4.17–3.65 (m, 2H), 3.11 (s, 1H), 2.97–2.54 (m, 5H), 2.55–2.34 (m, 1H), 1.33 (s, 9H).

^{13}C-NMR (75 MHz, $CDCl_3$): δ [ppm] = 138.0, 129.1, 128.6, 126.7, 80.2, 55.6, 43.0, 38.9, 30.6, 28.4.

LC/MS: m/z calculated for $C_{18}H_{27}N_3O_4$ [M-Boc+H]$^+$: 250.2, found: 250.1.



45

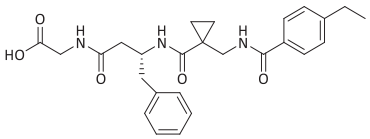
Compound **45**: Compound **53** (26 mg, 0.074 mmol, 1.0 eq.) was dissolved in DCM (1 mL) and TFA (1 mL) was added. The mixture was stirred at RT for 1.5 h. The solvents were removed under reduced pressure. The deprotected crude product (14 mg, 0.127 mmol, 1.1 eq.), **51** (18 mg, 0.074 mmol, 1.0 eq.), and TBTU (25 mg, 0.078 mmol, 1.1 eq.) were dissolved in anhydrous DMF (1.5 mL), and DIPEA (39 µL, 0.224 mmol, 3.0 eq.) was added. The mixture was stirred for 16 h at RT. The solvents were removed under reduced pressure and the crude product was purified by reversed-phase flash column chromatography (Biotage Isolera, ACN/H_2O + TFA).

Yield: 32.0 mg (0.669 mmol ≙ 90% of th.), colorless solid.

^{1}H-NMR (300 MHz, DMSO-d_6): δ [ppm] = 8.34–8.08 (m, 2H), 7.71 (d, *J* = 7.9 Hz, 2H), 7.31–7.08 (m, 8H), 7.03 (s, 1H), 4.82 (s, 1H), 3.60 (s, 2H), 3.35 (s, 2H), 3.08–2.70 (m, 5H), 2.63 (q, *J* = 7.6 Hz, 2H), 2.57–2.33 (m, 2H), 1.18 (t, *J* = 7.6 Hz, 3H), 0.70–0.28 (m, 4H).

^{13}C-NMR (75 MHz, DMSO): δ [ppm] = 171.2, 171.0, 170.5, 166.4, 147.3, 138.6, 131.8, 128.9, 128.1, 127.6, 127.3, 126.1, 41.9, 41.5, 37.4, 37.1, 30.7, 28.0, 26.0, 15.4, 9.5.

LC/MS: m/z calculated for $C_{27}H_{34}N_4O_4$ $[M + H]^+$: 479.3, found: 479.1.



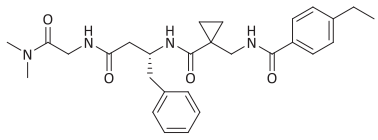
54

Compound **54**: Yield: 48.0 mg (0.103 mmol ≙ 76% of th.): colorless solid.

^{1}H-NMR (300 MHz, DMSO-d_6): δ [ppm] = 12.51 (s, 1H), 8.57 (t, J = 6.0 Hz, 1H), 8.24 (t, J = 5.9 Hz, 1H), 7.99 (d, J = 8.0 Hz, 1H), 7.78 (d, J = 7.9 Hz, 2H), 7.32 (d, J = 7.9 Hz, 2H), 7.23–6.96 (m, 5H), 4.41–4.10 (m, 1H), 3.88–3.56 (m, 2H), 3.58–3.16 (m, 2H), 2.82 (dd, J = 13.5, 5.0 Hz, 1H), 2.66 (q, J = 7.6 Hz, 3H), 2.40–2.14 (m, 2H), 1.20 (t, J = 7.5 Hz, 3H), 0.97–0.59 (m, 4H).

^{13}C-NMR (75 MHz, DMSO): δ [ppm] = 171.3, 170.4, 167.2, 147.6, 131.4, 138.9, 129.1, 128.0, 125.9, 127.7, 127.5, 48.5, 42.3, 39.8, 39.1, 28.1, 25.2, 15.4, 13.1.

LC/MS: m/z calculated for $C_{26}H_{31}N_3O_5$ $[M + H]^+$: 466.2, found: 466.1.



47

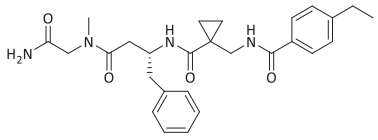
Compound **47**: Compound **54** (10 mg, 0.022 mmol, 1.0 eq.), dimethylamine hydrochloride (2.9 mg, 0.036 mmol, 1.7 eq.), DCC (5.6 mg, 0.027 mmol, 1.3 eq.) and HOBt (3.6 mg, 0.027 mmol, 1.3 eq.) were dissolved in DCM (1 mL). DIPEA (16 µL, 0.092 µmol, 4.3 eq.) was added dropwise and the mixture was stirred for 16 h at RT. More solvent (DCM, 1 mL), dimethylamine hydrochloride (2.6 mg, 0.032 mmol, 1.5 eq.), DCC (5 mg, 0.024 mmol, 1.1 eq.), and DIPEA (11.7 µL, 0.067 mmol, 2.5 eq.) were added and the mixture was stirred for additional 16 h at RT because the reaction was not completed. The solvents were removed under reduced pressure and the crude product was purified by reversed-phase column chromatography (Biotage Isolera, ACN/H_2O + TFA).

Yield: 8.0 mg (0.016 mmol ≙ 76% of th.), colorless solid.

^{1}H-NMR (300 MHz, DMSO-d_6): δ [ppm] = 8.54 (t, J = 6.0 Hz, 1H), 8.00–7.89 (m, 2H), 7.81–7.73 (m, 2H), 7.35–7.25 (m, 2H), 7.17–7.06 (m, 5H), 4.25 (p, J = 7.1 Hz, 1H), 3.96–3.66 (m, 2H), 3.47 (qd, J = 14.8, 6.1 Hz, 2H), 2.89 (s, 3H), 2.80 (s, 3H), 2.74–2.59 (m, 2H), 2.41–2.22 (m, 2H), 1.19 (t, J = 7.6 Hz, 3H), 0.95–0.67 (m, 4H).

^{13}C-NMR (75 MHz, DMSO): δ [ppm] = 171.4, 170.1, 168.1, 167.1, 147.5, 138.9, 131.4, 129.2, 128.0, 127.6, 127.5, 125.9, 48.5, 42.3, 40.5, 39.1, 35.6, 35.1, 28.1, 25.2, 15.4, 13.1, 13.0.

LC/MS: m/z calculated for $C_{28}H_{36}N_4O_4$ $[M + H]^+$: 493.3, found: 493.2.



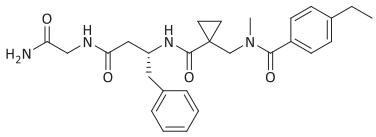
46

Compound **46**: Yield: 16.0 mg (0.033 mmol ≙ 74% of th.), colorless solid.

^{1}H-NMR (300 MHz, DMSO-d_6, 60 °C): δ [ppm] = 8.41–8.23 (m, 1H), 7.93–7.79 (m, 1H), 7.79–7.68 (m, 2H), 7.36–7.25 (m, 2H), 7.24–7.00 (m, 6H), 4.33 (q, J = 7.3 Hz, 1H), 4.04–3.69 (m, 2H), 3.62–3.34 (m, 2H), 2.99–2.72 (m, 4H), 2.72–2.60 (m, 2H), 2.60–2.27 (m, 2H), 1.21 (t, J = 7.6 Hz, 3H), 1.02–0.63 (m, 4H).

^{13}C-NMR (75 MHz, DMSO, 60 °C): δ [ppm] = 171.3, 170.3, 170.0, 166.9, 147.2, 138.8, 131.4, 128.8, 127.7, 127.3, 127.1, 125.6, 50.0, 48.2, 48.0, 42.2, 37.2, 35.9, 27.7, 25.0, 14.9, 12.6.

LC/MS: m/z calculated for $C_{27}H_{34}N_4O_4$ $[M + H]^+$: 479.3, found: 479.2.



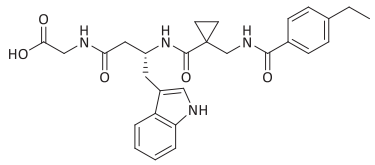
44

Compound **44**: Yield: 17.0 mg (0.036 mmol ≙ 79% of th.), colorless solid.

^{1}H-NMR (300 MHz, DMSO-d_6, 60 °C): δ [ppm] = 7.85 (t, *J* = 5.7 Hz, 1H), 7.53 (s, 1H), 7.28–7.10 (m, 10H), 4.34 (h, *J* = 7.1 Hz, 1H), 3.80–3.45 (m, 4H), 2.88–2.70 (m, 5H), 2.65 (q, *J* = 7.6 Hz, 2H), 2.38–2.28 (m, 2H), 1.21 (t, *J* = 7.6 Hz, 3H), 1.03–0 0.81 (m, 2H), 0.80–0.58 (m, 2H).

^{13}C-NMR (75 MHz, DMSO, 60 °C): δ [ppm] = 170.9, 170.9, 170.7, 170.0, 144.9, 138.5, 133.5, 128.8, 127.7, 127.2, 126.7, 125.7, 47.9, 41.8, 40.0, 39.4, 27.7, 23.7, 14.8, 12.0.

LC/MS: m/z calculated for $C_{27}H_{34}N_4O_4$ $[M + H]^+$: 479.3, found: 479.2.



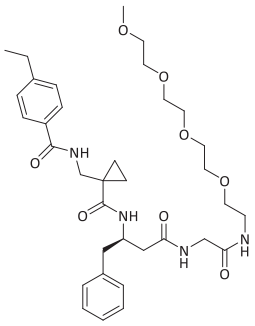
9

Compound **9**: Yield: 1.4 mg (0.028 mmol ≙ 43% of th.), colorless solid.

^{1}H-NMR (400 MHz, MeO*D*): δ [ppm] = 8.24 (d, *J* = 7.6 Hz, 1H), 7.66 (d, *J* = 7.8 Hz, 2H), 7.60 (d, *J* = 7.7 Hz, 1H), 7.25 (d, *J* = 6.5 Hz, 3H), 7.09–6.94 (m, 4H), 6.65 (d, *J* = 7.7 Hz, 1H), 4.56 (d, *J* = 6.4 Hz, 1H), 3.74 (q, *J* = 17.8 Hz, 2H), 3.55 (s, 2H), 3.01 (p, *J* = 7.9 Hz, 2H), 2.69 (q, *J* = 7.5 Hz, 2H), 2.51 (d, *J* = 6.5 Hz, 2H), 2.22 (s, 1H), 1.45 (s, 1H), 1.25 (t, *J* = 7.5 Hz, 3H), 1.10 (q, *J* = 9.8 Hz, 2H), 0.86 (s, 2H).

^{13}C-NMR (101 MHz, MeOD): δ [ppm] = 174.9, 173.8, 170.8, 156.0, 149.9, 138.0, 132.5, 130.8, 129.6, 129.2, 129.0, 128.6, 124.3, 122.2, 119.7, 119.6, 116.0, 112.2, 44.6, 40.9, 30.8, 29.7, 28.0, 26.8, 20.5, 15.8, 14.6, 14.4.

LC/MS: m/z calculated for $C_{28}H_{32}N_4O_5$ $[M + H]^+$: 505.2, found: 504.7.



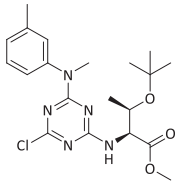
48

Compound **48**: Yield: 5.0 mg (7.641 μmol ≙ 44% of th.), colorless solid.

^{1}H-NMR (400 MHz, DMSO-d_6): δ [ppm] = 8.55 (t, *J* = 6.1 Hz, 1H), 8.13 (t, *J* = 5.9 Hz, 1H), 7.99 (d, *J* = 8.1 Hz, 1H), 7.83 (t, *J* = 5.7 Hz, 1H), 7.80–7.73 (m, 2H), 7.31 (d, *J* = 8.1 Hz, 2H), 7.21–7.02 (m, 5H), 4.29 (q, *J* = 7.1 Hz, 1H), 3.79–3.44 (m, 14H), 3.44–3.27 (m, 4H), 3.26–3.12 (m, 5H), 2.79 (dd, *J* = 13.5, 5.2 Hz, 1H), 2.72–2.58 (m, 3H), 2.31 (d, *J* = 6.8 Hz, 2H), 1.20 (t, *J* = 7.6 Hz, 3H), 0.96–0.66 (m, 4H).

^{13}C-NMR (101 MHz, DMSO): δ [ppm] = 171.5, 170.4, 169.0, 167.2, 147.6, 138.8, 131.4, 129.1, 128.0, 127.7, 127.5, 126.0, 71.3, 69.8, 69.7, 69.6, 69.0, 58.1, 48.4, 42.3, 42.0, 38.6, 30.7, 28.1, 25.2, 15.4, 13.0.

LC/MS: m/z calculated for $C_{35}H_{50}N_4O_8$ $[M + H]^+$: 655.4, found: 655.3.



55

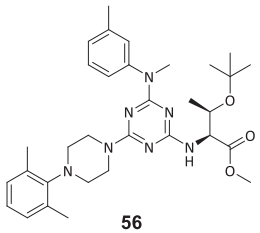
Compound **55**: Cyanuric chloride (195 mg, 1.057 mmol, 1.0 eq.) and methyl *O*-(*tert*-butyl)-L-threoninate (200 mg, 1.057 mmol, 1.0 eq.) were suspended in 2 mL of DCM. The solution was cooled to 0 °C and DIPEA (370 μL, 2.114 mmol, 2.0 eq.) was added. The reaction was allowed to stir for 10 min at 0 °C. Subsequently, *N*,3-dimethylaniline (128 mg, 1.057 mmol, 1.0 eq.), and DIPEA (370 μL, 2.114 mmol, 2.0 eq.) were added at 0 °C and the mixture was stirred for 12 h at 40 °C in a sealed tube. The crude product was purified by column chromatography (mobile phase: CH:EtOAc 20:1–10:1).

Yield: 331.0 mg (0.786 mmol ≙ 74% of th.), colorless oil.

^{1}H-NMR (300 MHz, C*D*Cl$_3$): δ [ppm] = 7.26 (s, 1H), 7.14–6.91 (m, 3H), 6.20–5.73 (m, 1H), 4.41–3.97 (m, 1H), 3.68 (d, *J* = 13.7 Hz, 3H), 3.44 (d, *J* = 7.4 Hz, 3H), 2.36 (d, *J* = 8.2 Hz, 3H), 1.38–0.97 (m, 12H).

^{13}C-NMR (75 MHz, C*D*Cl$_3$): δ [ppm] = 171.6, 165.3, 143.5, 138.8, 129.0, 127.4, 127.0, 124.0, 123.6, 77.4, 74.2, 67.3, 59.6, 52.2, 38.8, 28.4, 21.5.

LC/MS: m/z calculated for $C_{20}H_{28}ClN_5O_3$ $[M + H]^+$: 422.2, found: 422.1.



56

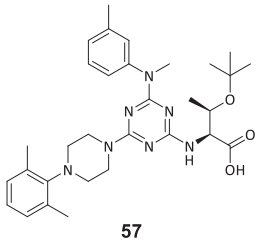
Compound **56**: Compound **55** (80 mg, 0.190 mmol, 1.0 eq.) was dissolved in DMF, 1-(2,6-dimethylphenyl)piperazine (43 mg, 0.228 mmol, 1.2 eq.) and potassium carbonate (65 mg, 0.475 mmol, 2.5 eq.) were added, and the mixture was allowed to stir for 45 min at 100 °C. The solvent was removed in vacuo and the residue was dissolved in DCM, which was washed three times with water. The organic phase was filtered over silica and the product was obtained as an orange oil.

Yield: 103.0 mg (0.179 mmol ≙ 94% of th.), orange oil.

^{1}H-NMR (300 MHz, C*D*Cl$_3$): δ [ppm] = 7.28–7.09 (m, 3H), 6.99 (h, *J* = 4.6, 4.1 Hz, 4H), 4.27–4.11 (m, 1H), 3.81 (d, *J* = 22.4 Hz, 3H), 3.69 (s, 3H), 3.47 (d, *J* = 11.3 Hz, 3H), 3.15–3.00 (m, 4H), 2.95 (s, 1H), 2.88 (s, 1H), 2.34 (dd, *J* = 8.9, 2.4 Hz, 9H), 1.24 (dd, *J* = 9.4, 6.3 Hz, 3H), 1.13 (d, *J* = 4.8 Hz, 9H).

^{13}C-NMR (75 MHz, C*D*Cl$_3$): δ [ppm] = 172.8, 162.6, 161.1, 148.3, 137.9, 136.9, 129.0, 128.0, 127.1, 125.7, 125.2, 123.5, 77.4, 73.9, 67.6, 59.6, 59.4, 51.9, 50.7, 49.8, 47.3, 44.6, 41.6, 36.5, 31.5, 28.4, 21.2, 19.8.

LC/MS: m/z calculated for $C_{32}H_{45}N_7O_3$ $[M + H]^+$: 576.4, found: 576.3.



57

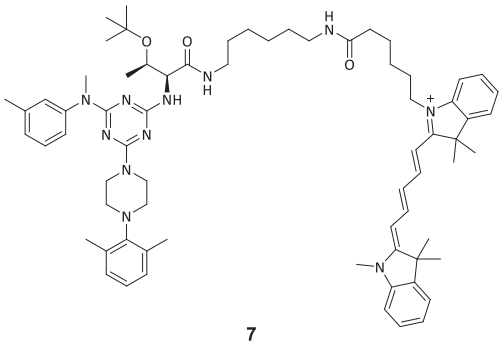
Compound **57**: Compound **56** (88 mg, 0.152 mmol, 1.0 eq.) was dissolved in 1 mL water and 1 mL THF, and sodium hydroxide (30 mg, 0.750 mmol, 5.0 eq.) was added. The mixture was stirred at RT for 48 h. The solvents were removed under reduced pressure and the crude product was purified by reversed-phase column chromatography (Biotage Isolera, ACN/H_2O + TFA).

Yield: 15.0 mg (0.027 mmol ≙ 18% of th.), colorless solid.

^{1}H-NMR (300 MHz, *C*DCl3): δ [ppm] = 7.39 (t, *J* = 7.5 Hz, 1H), 7.06–6.95 (m, 7H), 4.55 (d, *J* = 7.9 Hz, 1H), 4.21 (dd, *J* = 6.4, 2.3 Hz, 1H), 3.92 (s, 3H), 3.47 (s, 3H), 3.12 (t, *J* = 5.4 Hz, 4H), 2.37 (d, *J* = 8.3 Hz, 3H), 2.33 (s, 7H), 1.16 (d, *J* = 20.0 Hz, 12H).

^{13}C-NMR (75 MHz, $CDCl_3$): δ [ppm] = 184.5, 161.2, 147.6, 137.0, 136.8, 129.3, 129.3, 127.5, 125.9, 123.9, 77.4, 76.9, 75.3, 68.8, 67.0, 49.6, 46.0, 45.9, 39.4, 28.1, 21.4, 20.4, 19.8.

LC/MS: m/z calculated for $C_{31}H_{43}N_7O_3$ $[M + H]^+$: 562.3, found: 562.3.

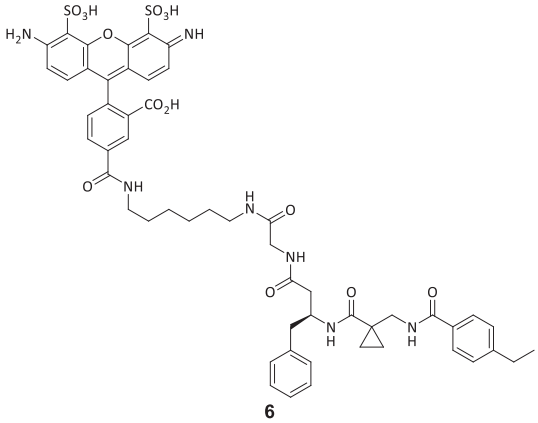


7

Compound **7**: Compound **57** (1.0 mg, 1.700 μmol, 1.0 eq.), Cy5 amine (1.0 mg, 1.700 μmol, 1.0 eq.), HATU (1 mg, 2.000 μmol, 1.2 eq.), and DIPEA (3 μL, 16.000 μmol, 9.5 eq.) were dissolved in 20 μL anhydrous DMF. The reaction was allowed to incubate for 16 h. The crude product was purified by reversed-phase column chromatography (Biotage Isolera, ACN/H_2O + TFA).

Yield: 1.0 mg (0.817 μmol ≙ 48% of th.), blue solid.

LC/MS: m/z calculated for $C_{69}H_{94}N_{11}O_3^+$ $[M + H]^{2+}$: 562.8, found: 562.9.



6

Compound **6**: Compound **54** (0.8 mg, 1.640 μmol, 1.2 eq.), AF 488 amine (1.0 mg, 1.390 μmol, 1.0 eq.), TBTU (0.5 mg, 1.680 μmol, 1.2 eq.), and DIPEA (2.3 μL, 13.200 μmol, 9.5 eq.) were dissolved in anhydrous DMF (0.6 mL) and stirred at RT for 48 h. The crude product was purified by reversed-phase column chromatography (Biotage Isolera, ACN/H_2O + TFA).

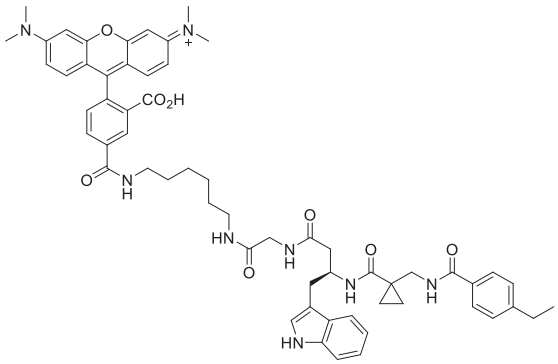
Yield: 0.4 mg (0.37 mmol ≙ 27% of th.), orange solid.

^{1}H-NMR (600 MHz, DMSO-d_6): δ [ppm] = 9.00 (s, 2H), 8.86 (s, 1H), 8.69 (s, 1H), 8.58 (t, *J* = 6.2 Hz, 1H), 8.50 (s, 2H), 8.26 (dd, *J* = 8.0, 1.8 Hz, 1H), 8.16 (t, *J* = 6.0 Hz, 1H), 8.03 (d, *J* = 8.1 Hz, 1H), 7.81–7.73 (m, 2H), 7.50 (d, *J* = 7.8 Hz, 1H), 7.31 (d, *J* = 8.0 Hz, 1H), 7.15–7.11 (m, 2H), 7.11–7.06 (m, 1H), 7.02–6.88 (m, 3H), 4.28 (dt, *J* = 14.2, 6.9 Hz, 1H), 3.69–3.60 (m, 1H), 3.58–3.50 (m, 1H), 3.50–3.45 (m, 2H), 3.33–3.22 (m, 1H), 3.07–2.99 (m, 2H), 2.78 (dd, *J* = 13.6, 5.2 Hz, 1H), 2.70–2.59 (m, 3H), 2.38 (p, *J* = 1.8 Hz, 1H), 2.31 (d, *J* = 6.9 Hz, 2H), 2.11 (s, 1H), 2.08 (s, 1H), 2.04–1.91 (m, 2H), 1.58–1.48 (m, 2H), 1.38 (q, *J* = 9.4 Hz, 2H), 1.35–1.20 (m, 5H), 1.19 (t, *J* = 7.6 Hz, 2H), 1.13 (s, 1H), 0.91–0.69 (m, 4H).

CellPress
OPEN ACCESS

iScience
Article

LC/MS: m/z calculated for $C_{53}H_{57}N_7O_{14}S_2$ $[M+2H]^{2+}$: 540.7 found: 540.6.



8

Compound **8**: Compound **9** (1.1 mg, 2.112 μmol, 1.2 eq.), TBTU (0.7 mg, 2.112 μmol, 1.2 eq.), and TAMRA-amine (1.0 mg, 1.760 μmol, 1.0 eq.) were dissolved in DMF (3 mL), and DIPEA (0.4 μL, 2.112 μmol, 1.2 eq.) was added. The reaction mixture was shaken for 16 h at RT. Afterward, the solvent was removed under reduced pressure and the crude product was purified by reversed-phase flash column chromatography (Biotage Isolera, ACN/H_2O + TFA).

Yield: 1.9 mg (1.871 μmol ≙ 89% of th.), red solid.

^{1}H-NMR (600 MHz, MeO*D*): δ [ppm] = 8.51 (s, 1H), 8.02 (d, *J* = 7.8 Hz, 1H), 7.88 (d, *J* = 8.2 Hz, 1H), 7.68 (dd, *J* = 8.2, 5.1 Hz, 1H), 7.61 (dd, *J* = 15.0, 8.3 Hz, 2H), 7.50 (d, *J* = 7.9 Hz, 1H), 7.33–7.23 (m, 3H), 7.20–7.12 (m, 3H), 6.98–6.85 (m, 5H), 4.60 (s, 2H), 4.52 (dd, *J* = 14.4, 5.9 Hz, 1H), 3.73 (d, *J* = 16.7 Hz, 1H), 3.66 (s, 1H), 3.63–3.52 (m, 3H), 3.45–3.35 (m, 3H), 3.32 (t, 1H), 3.21 (d, *J* = 2.8 Hz, 6H), 3.17–3.06 (m, 2H), 2.98–2.88 (m, 2H), 2.70–2.60 (m, 4H), 2.52 (dd, *J* = 14.3, 4.9 Hz, 1H), 2.43 (dd, *J* = 14.4, 8.7 Hz, 1H), 1.62–1.54 (m, 2H), 1.49–1.41 (m, 2H), 1.39–1.28 (m, 4H), 1.27–1.16 (m, 6H), 1.06–0.97 (m, 2H), 0.93 (t, *J* = 7.4 Hz, 1H), 0.89–0.76 (m, 3H).

^{13}C-NMR (151 MHz, MeOD): δ [ppm] = 175.0, 174.1, 171.6, 170.7, 169.0, 162.1, 159.0, 158.7, 149.8, 137.9, 132.5, 132.3, 131.0, 129.8, 129.1, 129.0, 128.9, 128.6, 128.5, 128.4, 124.2, 122.2, 119.6, 119.6, 115.1, 114.8, 112.2, 112.1, 97.3, 57.6, 57.5, 57.3, 52.6, 49.9, 49.6, 44.6, 43.7, 41.7, 40.9, 40.7, 40.2, 32.7, 31.1, 30.3, 29.9, 29.8, 27.5, 27.4, 26.9, 21.2, 17.4, 17.3, 17.2, 15.9, 15.9, 14.9, 14.6, 14.6, 14.2.

LC/MS: m/z calculated for $C_{59}H_{67}N_8O_8^+$ $[M + H]^{2+}$: 508.3, found: 508.4.

QUANTIFICATION AND STATISTICAL ANALYSIS

For all experiments, details of quantification, statistical methods, and the software used are described in the corresponding figure legends and methods. All data are expressed as mean ± SEM. *N* values indicate the number of technical or biological replicates per experiment. Each experiment was performed at least in triplicate. The statistical significance of differences of tRNA modification levels was determined by Student's t test with *p* values (**p* < 0.05, ***p* < 0.01, ****p* < 0.001, *****p* < 0.0001). All statistical test methods and analyses were performed using GraphPad Prism 8.05 and are shown in the figure legends. The dose-response curves were fit to four-parameter logistic (4-PL) curve using GraphPad Prism 8 (log[agonist] vs. response – variable slope; Equation: Y = Bottom + (Top–Bottom)/(1 + 10((LogEC$_{50}$-X)*HillSlope)).

“

4.1.4 Supporting Information

The following supporting information quoted within “” from page 172 to page 198 is the same as the manuscript cited on page 130.[255] “

iScience, Volume *28*

Supplemental information

DNA-encoded library screening uncovers potent DNMT2 inhibitors targeting a cryptic allosteric binding site

Ariane F. Frey, Merlin Schwan, Annabelle C. Weldert, Valerie Kadenbach, Jürgen Kopp, Zarina Nidoieva, Robert A. Zimmermann, Lukas Gleue, Collin Zimmer, Marko Jörg, Kristina Friedland, Mark Helm, Irmgard Sinning, and Fabian Barthels

Supplementary data of DNA encoded library screening

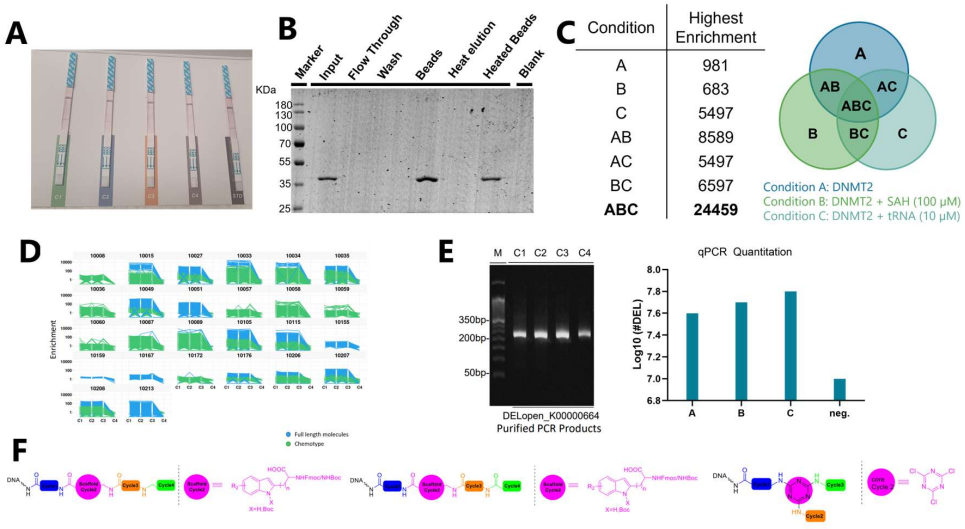
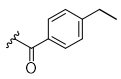
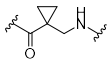
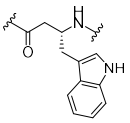
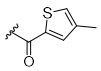
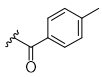
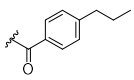
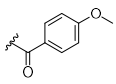
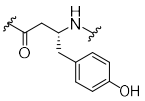
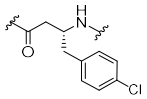
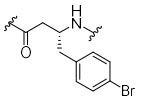
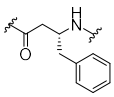
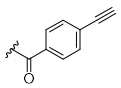
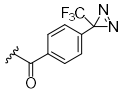
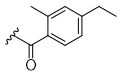


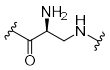
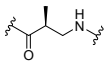
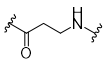
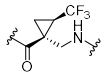
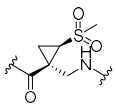
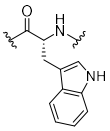
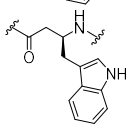
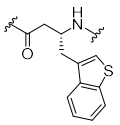
Figure S1: Supplementary data for the DNA encoded library screening on DNMT2. (**A**) Quality control test as provided by Wuxi AppTec. The four tested conditions mentioned in the manuscript are labeled here as C1–C4 (in the manuscript A–D). STD represents the internal standard according to the WuXi protocol (https://hits.wuxiapptec.com/assets/pdf/DELopen_Protocol.pdf). (**B**) DNMT2 capture assay was performed according to the protocol instructions to verify that DNMT2 can be stably immobilized on magnetic beads. The labeling is according to the original protocol. (**C**) Total count of highest enrichment scores for different panning conditions. The conditions are explained in the Venn diagram. (**D**) Overall performance and enrichment scores of the different libraries after the removal of NTC (no target control) binders. Most hits were enriched across C1–C3 equally, meaning neither SAH nor tRNA led to DEL hit displacement. (**E**) Quality control (gel electrophoresis and qPCR) was performed by Wuxi AppTec for all selection conditions after the second panning round. (**F**) Structures of the libraries featuring hit compounds chosen for off-DNA synthesis and further investigations.

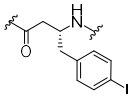
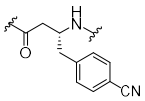
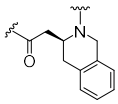
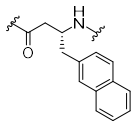
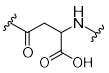
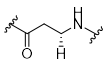
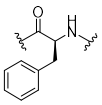
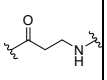
Summary of all synthesized compound 3 analogs

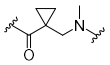
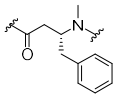
Table S1: Overview of all synthesized compounds during the SAR study around compound 3 and their characterization by MST (F_{norm}) and ITC (K_D). All results include the mean value and standard deviations from at least technical triplicate measurements. Raw data and analysis plots are depicted in Figures S2–S5.

Cpd	BB1	BB2	BB3	BB4	C-Term.	F_{norm} (% displ.)	K_D (ITC) [µM]
3	 (4-ethylbenzoyl)	 (cyclopropyl-β-alanine)	 (β-homo-(*R*)-tryptophane)	 (glycine)	NH-Me	912.1 (53%)	5.31 ± 1.67
5		cyclopropyl-β-alanine	β-homo-(*R*)-tryptophane	glycine	NH-Me	879.3 (13%)	13.6 ± 1.6
9	4-ethylbenzoyl	cyclopropyl-β-alanine	β-homo-(*R*)-tryptophane	glycine	OH	907.7 (46%)	n.d.
10	4-ethylbenzoyl	cyclopropyl-β-alanine	β-homo-(*R*)-tryptophane	glycine	NH_2	903.3 (40%)	n.d.
11		cyclopropyl-β-alanine	β-homo-(*R*)-phenylalanine	glycine	NH_2	891.2 (24%)	n.d.
12		cyclopropyl-β-alanine	β-homo-(*R*)-phenylalanine	glycine	NH_2	890.4 (23%)	n.d.
13		cyclopropyl-β-alanine	β-homo-(*R*)-phenylalanine	glycine	NH_2	897.7 (32%)	n.d.

14	4-ethylbenzoyl	cyclopropyl-β-alanine	β-homo-(*R*)-phenylalanine	glycine	NH_2	896.0 (29%)	3.27 ± 0.97
15	4-ethylbenzoyl	cyclopropyl-β-alanine		glycine	NH_2	862.9 (5%)	n.d.
16	4-ethylbenzoyl	cyclopropyl-β-alanine		glycine	NH_2	928.7 (76%)	3.04 ± 0.57
17	4-ethylbenzoyl	cyclopropyl-β-alanine		glycine	NH_2	924.6 (71%)	n.d.
18		cyclopropyl-β-alanine	 (β-homo-(*R*)-phenylalanine)	glycine	NH_2	868.2 (7%)	n.d.
19		cyclopropyl-β-alanine	β-homo-(*R*)-phenylalanine	glycine	NH_2	871.4 (8%)	n.d.
20		cyclopropyl-β-alanine	β-homo-(*R*)-phenylalanine	glycine	NH_2	876.5 (11%)	n.d.
21		cyclopropyl-β-alanine	β-homo-(*R*)-phenylalanine	glycine	NH_2	862.4 (5%)	n.d.
22		cyclopropyl-β-alanine	β-homo-(*R*)-phenylalanine	glycine	NH_2	864.4 (5%)	n.d.

23		cyclopropyl-β-alanine	β-homo-(*R*)-phenylalanine	glycine	NH_2	864.4 (5%)	n.d.
24	4-ethylbenzoyl		β-homo-(*R*)-tryptophane	glycine	NH_2	860.8 (4%)	n.d.
25	4-ethylbenzoyl		β-homo-(*R*)-tryptophane	glycine	NH_2	855.5 (3%)	n.d.
26	4-ethylbenzoyl		β-homo-(*R*)-tryptophane	glycine	NH_2	861.9 (5%)	n.d.
27	4-ethylbenzoyl		β-homo-(*R*)-tryptophane	glycine	NH_2	863.8 (5%)	n.d.
28	4-ethylbenzoyl		β-homo-(*R*)-phenylalanine	glycine	NH_2	871.9 (8%)	n.d.
29	4-ethylbenzoyl		β-homo-(*R*)-phenylalanine	glycine	NH_2	872.3 (9%)	n.d.
30	4-ethylbenzoyl	cyclopropyl-β-alanine		glycine	NH_2	861.5 (5%)	n.b.
31	4-ethylbenzoyl	cyclopropyl-β-alanine		glycine	NH_2	857.0 (4%)	n.d.
32	4-ethylbenzoyl	cyclopropyl-β-alanine		glycine	NH_2	856.7 (3%)	n.d.

33	4-ethylbenzoyl	cyclopropyl-β-alanine		glycine	NH_2	885.6 (18%)	n.d.
34	4-ethylbenzoyl	cyclopropyl-β-alanine		glycine	NH_2	879.4 (13%)	n.d.
35	4-ethylbenzoyl	cyclopropyl-β-alanine		glycine	NH_2	861.5 (5%)	n.d.
36	4-ethylbenzoyl	cyclopropyl-β-alanine		glycine	NH_2	861.7 (5%)	n.d.
37	4-ethylbenzoyl	cyclopropyl-β-alanine		glycine	NH_2	858.6 (4%)	n.d.
38	4-ethylbenzoyl	cyclopropyl-β-alanine		glycine	NH_2	859.4 (4%)	n.d.
39	4-ethylbenzoyl	cyclopropyl-β-alanine	β-homo-(*R*)-phenylalanine		NH_2	871.4 (8%)	n.d.
40	4-ethylbenzoyl	cyclopropyl-β-alanine	β-homo-(*R*)-phenylalanine		NH_2	870.1 (8%)	n.d.
41	4-ethylbenzoyl	cyclopropyl-β-alanine	β-homo-(*R*)-phenylalanine		NH_2	865.3 (6%)	n.d.
42	4-ethylbenzoyl	cyclopropyl-β-alanine	β-homo-(*R*)-phenylalanine		NH_2	858.8 (4%)	n.d.
43	4-ethylbenzoyl	cyclopropyl-β-alanine	β-homo-(*R*)-phenylalanine		NH_2	874.7 (10%)	n.d.

44	4-ethylbenzoyl		β-homo-(*R*)-phenylalanine	glycine	NH_2	869.7 (7%)	n.d.
45	4-ethylbenzoyl	cyclopropyl-β-alanine		glycine	NH_2	862.6 (5%)	n.d.
46	4-ethylbenzoyl	cyclopropyl-β-alanine	β-homo-(*R*)-phenylalanine		NH_2	868.4 (7%)	n.d.
47	4-ethylbenzoyl	cyclopropyl-β-alanine	β-homo-(*R*)-phenylalanine	glycine	NMe_2	901.0 (36%)	n.d.
48	4-ethylbenzoyl	cyclopropyl-β-alanine	β-homo-(*R*)-phenylalanine	glycine	NH-PEG4	894.1 (27%)	n.d.

MST supplementary data

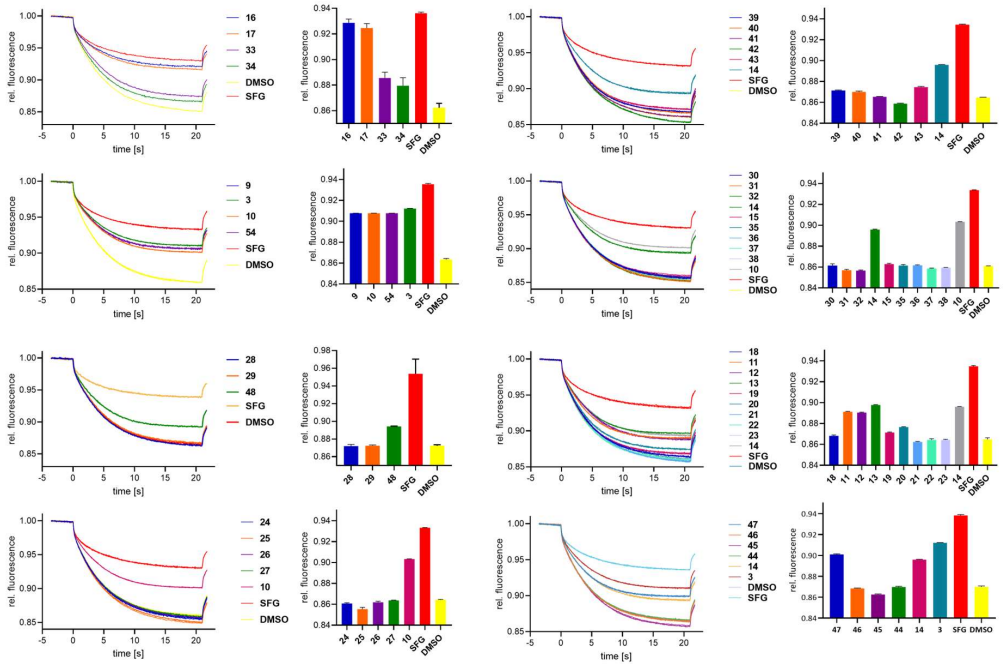


Figure S2: MST screening results of all compounds synthesized during the SAR study. Compounds were measured at a concentration of 100 µM. MST experiments were performed as described in the methods section using the fluorescent FTAD probe.

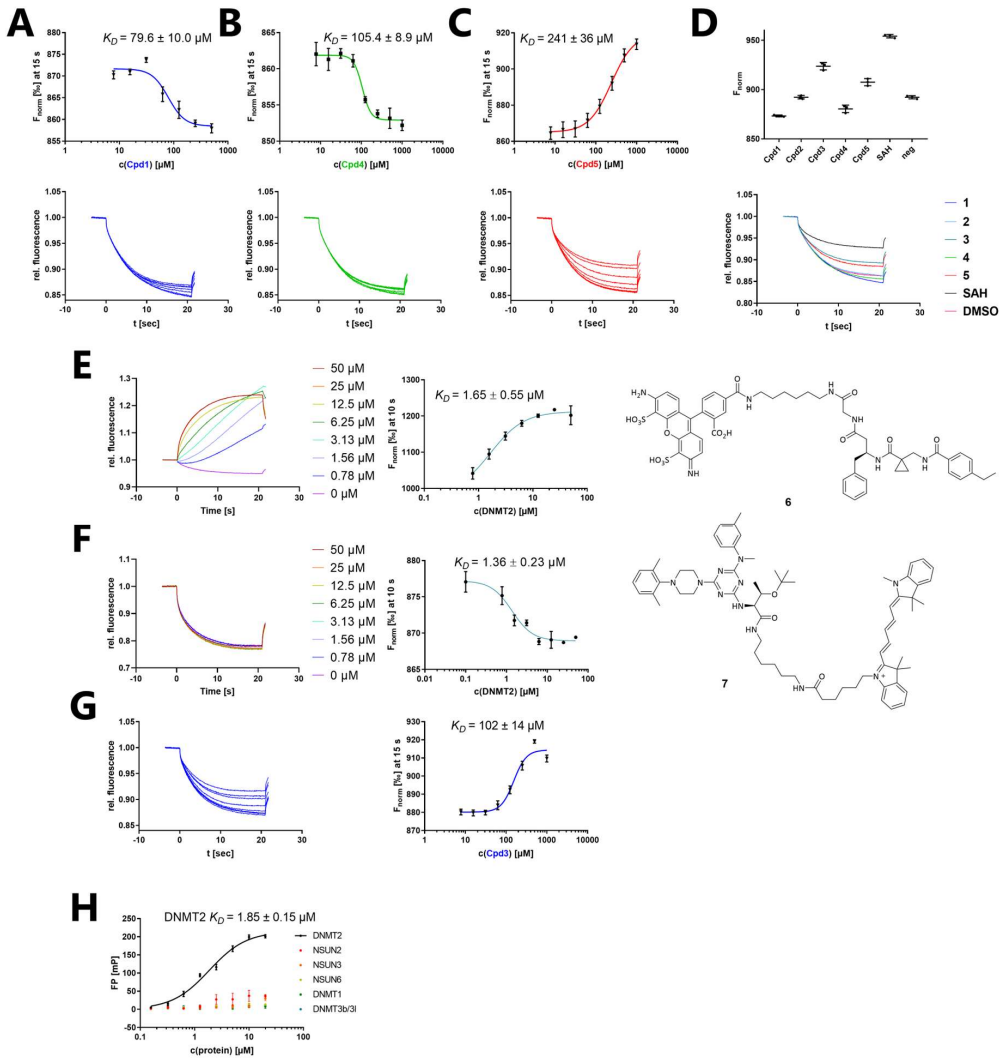


Figure S3: Supplementary MST and FP results for the hit compounds selected from the DEL screening. MST experiments were performed as described in the methods section using the fluorescent FTAD probe. (**A**) K_D-value determination of compound **1**. (**B**) K_D-value determination of compound **4**. (**C**) K_D-value determination of compound **5**. (**D**) Screening of all hit compounds **1–5** from the DEL Screening at 100 µM. (**E**) K_D-value determination of probe **6** by dose-response experiments using variable concentrations of DNMT2. (**F**) K_D-value determination of probe **7** by dose-response experiments using variable concentrations of DNMT2. (**G**) K_D-value determination of compound **3** using the DNMT2 deletion mutant DNMT2Δ47 (2 µM). (**H**) FP assay for probe **6** binding to native DNMT2 and various related MTase off-targets as determined by dose-response experiments.

ITC supplementary data

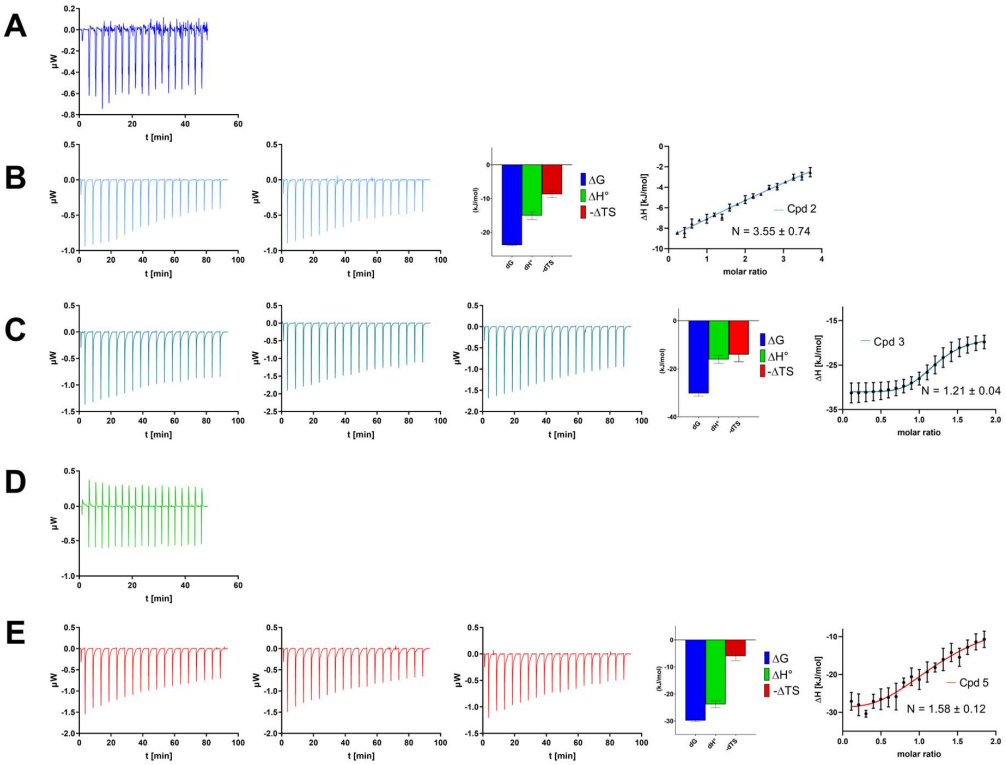


Figure S4: Supplementary ITC data for compounds 1–5. (**A**) Compound **1** was titrated into DNMT2. No enthalpy signal change was observed. (**B**) Compound **2** was titrated into DNMT2. Note: due to low solubility, the upper resp. lower limits of the stoichiometry plot are not reached, and thus, ΔH/ΔS determination might not be accurate. (**C**) Compound **3** was titrated into DNMT2. (**D**) Compound **4** was titrated into DNMT2. No enthalpy signal change was observed. (**E**) Compound **5** was titrated into DNMT2.

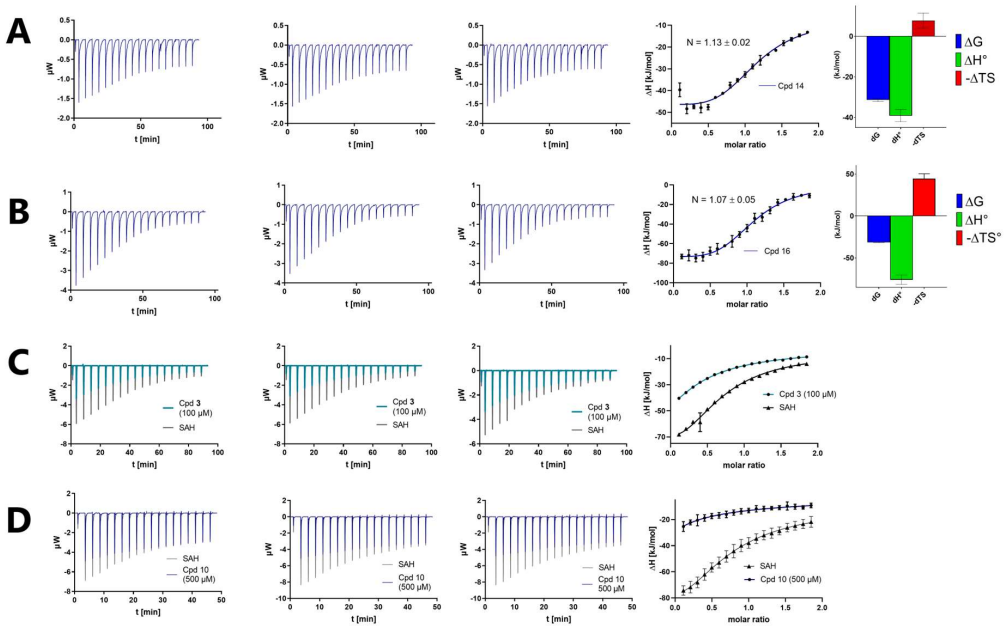


Figure S5: Supplementary ITC data for synthesized compound 3 analogs. (**A**) Compound **14** was determined by direct titration. (**B**) Compound **16** was determined by direct titration. (**C**) Compound **3** measured by SAH displacement. (**D**) Compound **10** measured by SAH displacement.

Affinity selection-mass spectrometry (AS-MS)

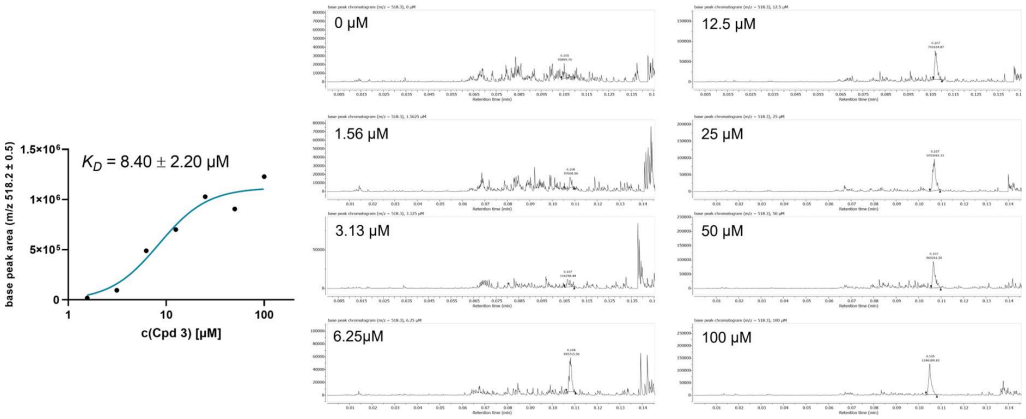


Figure S6: AS-MS-based determination of compound 3 binding affinity to DNMT2. (**left**) Dose-response curve for K_D determination. (**right**) Base peak chromatograms for compound **3** content analysis in the analyzed fractions.

Supplementary data of ^{3}H-based methyltransferase DNMT2 activity assays

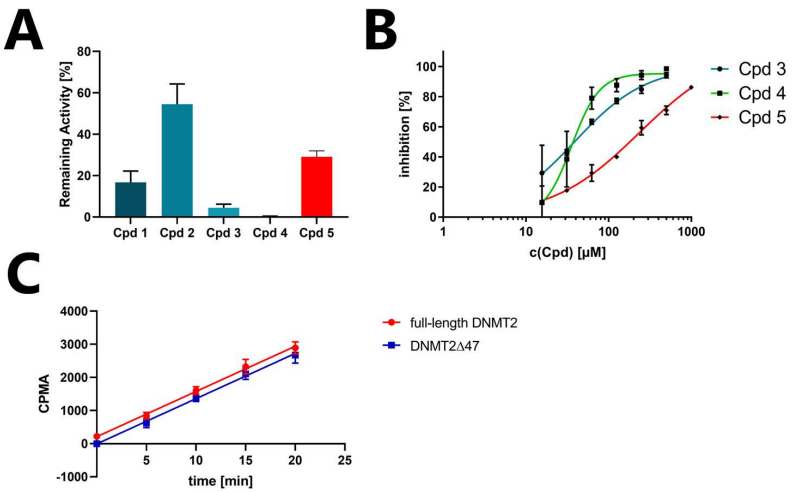


Figure S7: Data from ^{3}H-based methyltransferase enzyme activity assay. (**A**) Screening of compounds **1**–**5**, the remaining DNMT2 activity was determined at 500 µM of the respective compound. (**B**) IC_{50} determination for compounds **3**, **4**, and **5**. (**C**) ^{3}H-based methyltransferase enzyme activity assays with full-length and deletion mutant enzymes (250 nM DNMT2, 5 µM $tRNA^{Asp}$, 0.9 µM SAM), highlighting virtually identical substrate conversion plots (counts per minute [CPMA]) vs. time.

DNMT2-tRNA MST displacement experiments

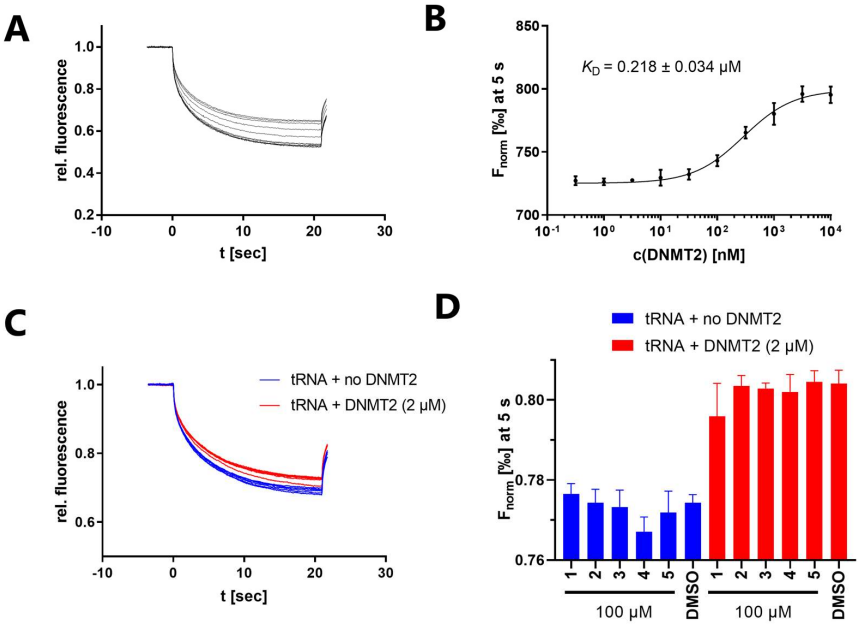


Figure S8: Analysis of DNMT2-RNA interaction by in situ labeling with SybrGold (1×). (**A**, **B**) Dissociation constant (K_D) of $tRNA^{Asp}$ (100 nM, labeled with SybrGold) towards DNMT2 (varying concentrations) was determined by dose-response experiments. (**C**, **D**). Neither the native $tRNA^{Asp}$ samples (blue) nor the DNMT2-tRNA complex (red) showed significant thermophoresis alterations when treated with the hit compounds **1**–**5**.

Cell viability assays

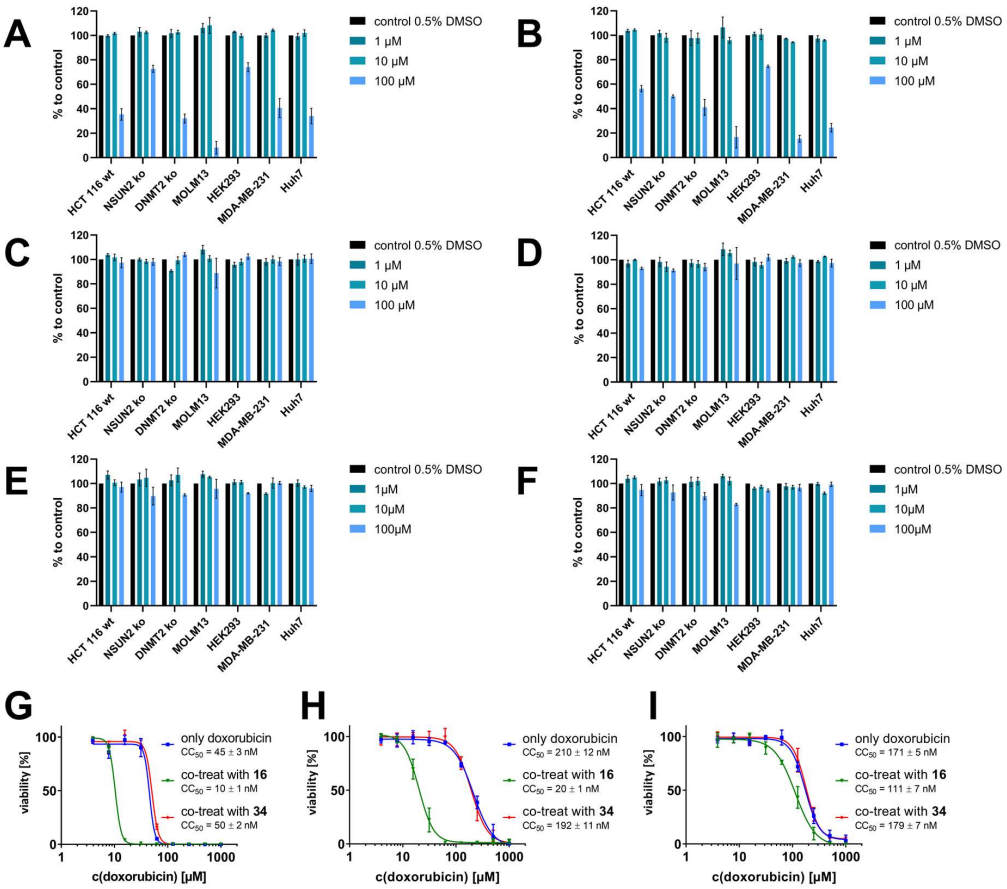
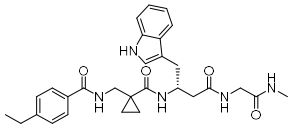
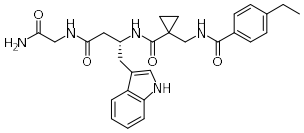
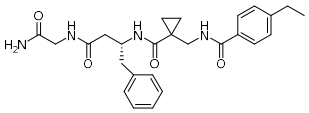
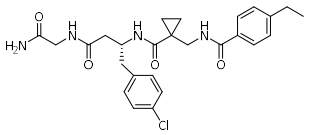
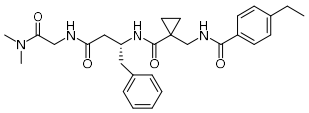
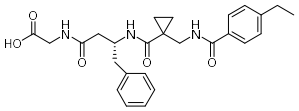


Figure S9: Cell viability assay data for compounds 1–5 and 16 used for the treatment of various cell lines. (**A**) Data for compound **1**. (**B**) Data for compound **2**. (**C**) Data for compound **3**. (**D**) Data for compound **4**. (**E**) Data for compound **5**. (**F**) Data for compound **16**. (**G**) Dose-response curves from cell viability assays of doxorubicin/compound **16** resp. **34** co-treated MOLM-13 cells, (**H**) cotreated MDA-MB-231 cells, and (**I**) cotreated Huh-7 cells.

Parallel Artificial Membrane Permeation Assay (PAMPA)

Table S2: PAMPA results of the investigated compounds determined in duplicates.

Compound	Compound structure	P_{app} [*10^{-6} cm/s]
3		below detection limit
10		below detection limit
14		below detection limit
16		~0.30
47		below detection limit
54		below detection limit

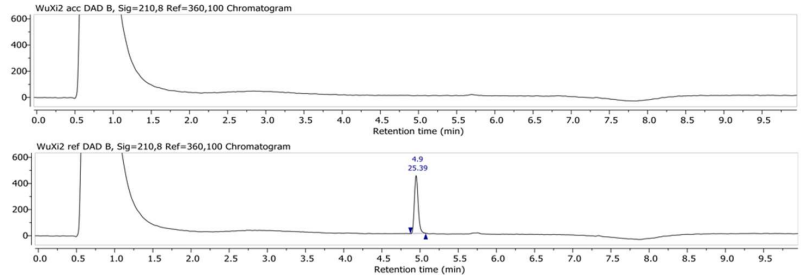


Figure S10: Base peak chromatogram at m/z = 518.3 ± 0.5 of acceptor and reference solution after incubating for compound 3. The peak of compound **3** is marked, and the area under the peak is stated above the peak.

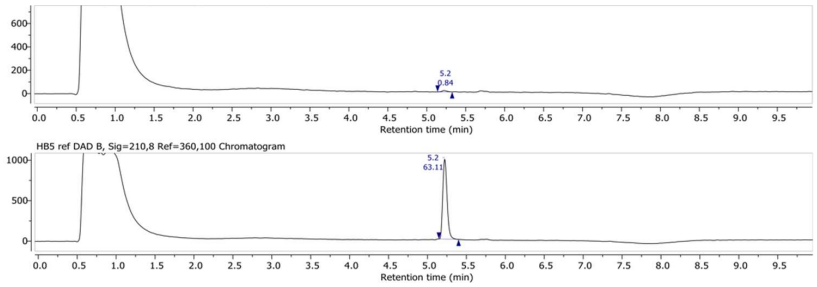


Figure S11: Base peak chromatogram at m/z = 499.2 ± 0.5 of acceptor and reference solution after incubating for compound 16. The peak of compound **16** is marked, and the area under the peak is stated above the peak.

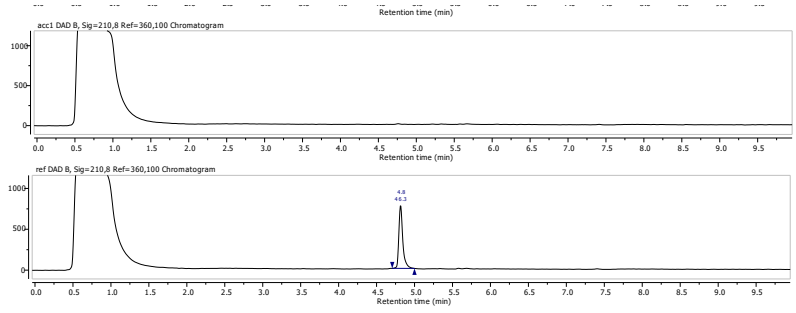


Figure S12: Base peak chromatogram at m/z = 504.3 ± 0.5 of acceptor and reference solution after incubating for compound 10. The peak of compound **10** is marked, and the area under the peak is stated above the peak.

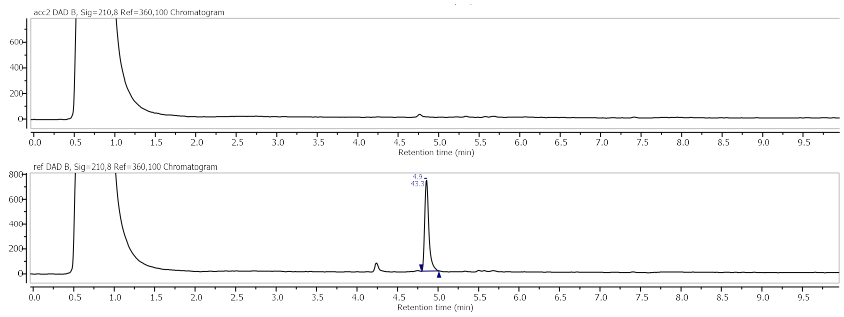


Figure S13: Base peak chromatogram at m/z = 465.3 ± 0.5 of acceptor and reference solution after incubating for compound 14. The peak of compound **14** is marked, and the area under the peak is stated above the peak.

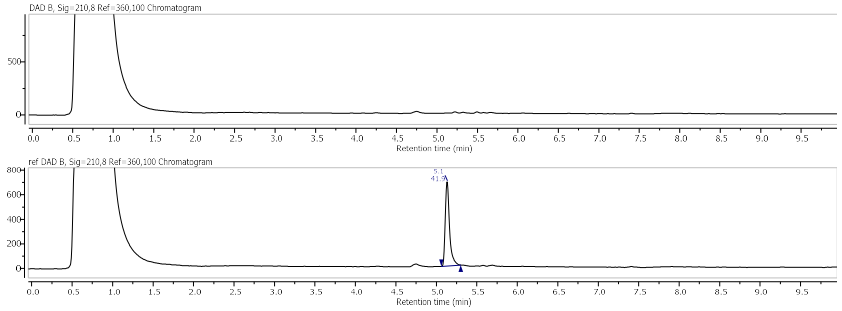


Figure S14: Base peak chromatogram at m/z = 493.3 ± 0.5 of acceptor and reference solution after incubating for compound 47. The peak of compound **47** is marked, and the area under the peak is stated above the peak.

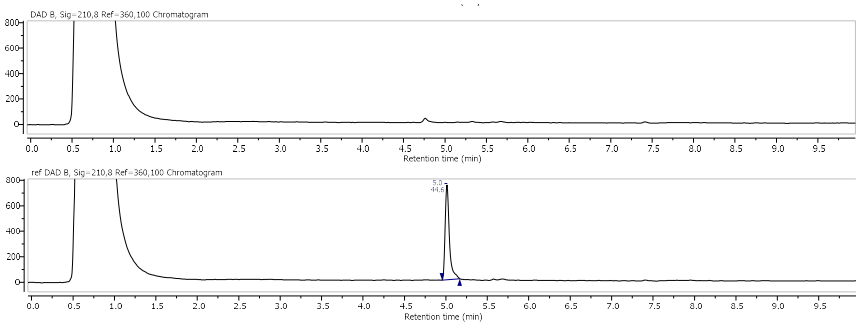


Figure S15: Base peak chromatogram at m/z = 466.2 ± 0.5 of acceptor and reference solution after incubating for compound 54. The peak of compound **54** is marked, and the area under the peak is stated above the peak.

Pull-down interaction assay

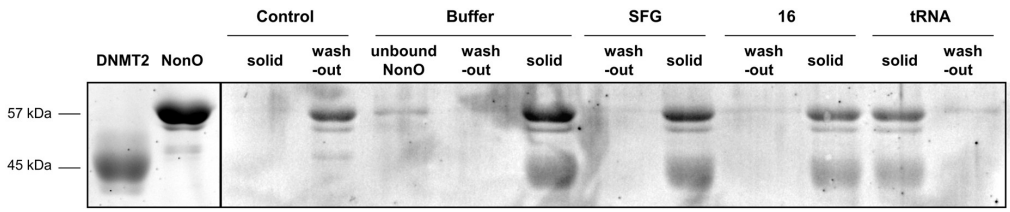


Figure S16: NonO does not bind to the allosteric pocket. Results of the SDS-PAGE-based analysis. Lane description from left to right: DNMT2/NonO: recombinant proteins for size comparison. References were applied at another gel position and merged in this figure; Control: beads without immobilized DNMT2 served as the negative control, i.e. on these beads no binding of NonO was observed. Treatments (buffer, SFG, **16**, tRNA): The lane "unbound NonO" contains the supernatant after immobilization of NonO, which showed low protein levels, thus most NonO is effectively immobilized on DNMT2 beads. Lanes labeled with (wash-out) contain the supernatant of the respective treatment conditions (buffer, 100 µM SFG, 100 µM **16**, 10 µM $tRNA^{Asp}$), while bands labeled with (solid) contain the solid fraction obtained by boiling the residual beads in Laemmli buffer. NonO could not be displaced from binding DNMT2 by competitive treatment with compound **16**, SFG, nor $tRNA^{Asp}$, indicating that NonO does not bind to the allosteric binding pocket identified. Uncropped PAGE images can be found in Figure S22.

Supplementary data for crystallographic investigations

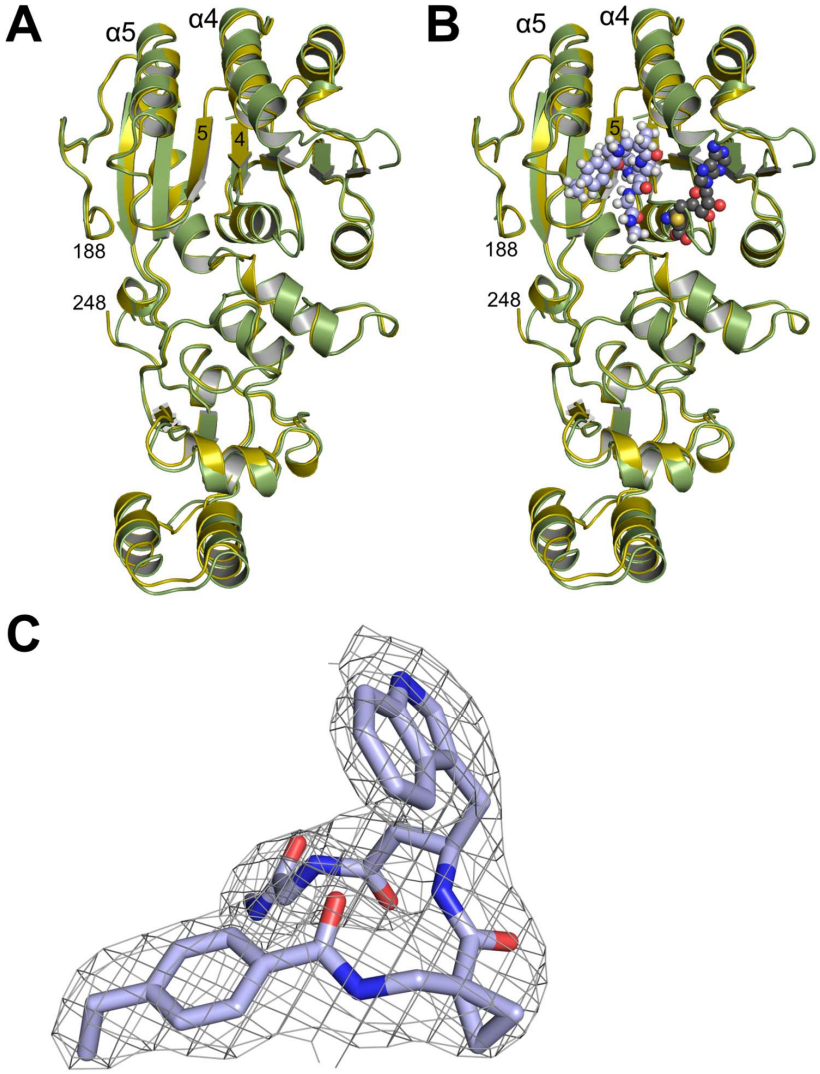


Figure S17: Global superposition of the X-ray structures of human DNMT2Δ47-compound 3 (green / light blue). Human DNMT2Δ47-SAH (yellow / grey) without (**A**) and with (**B**) ligands. (**C**) Compound **3** bound to DNMT2Δ47 (chain A) with $2mF_{obs}$-DF_{calc} electron density map at a contour level of +1σ.

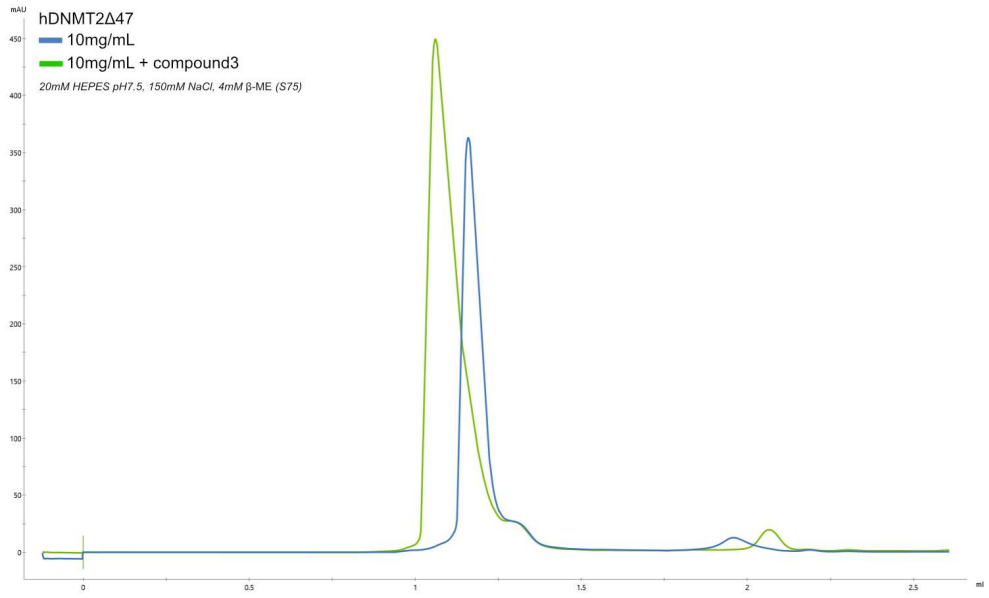


Figure S18: Analytical SEC elution profile of DNMT2Δ47 with and without compound 3. Superposition of two chromatograms showing the 280 nm signal of analytical SEC runs for hDNMT2Δ47 without ligand (blue) and pre-incubated with a 2-fold molar excess of compound **3** (green). For both runs the protein concentration was at 10 mg/mL as used for crystallization. A Superdex S75 3.2/300 column was used with a buffer consisting of 20 mM HEPES pH 7.5, 150 mM NaCl and 4 mM β-mercaptoethanol. The peak shift indicates the dimerization of DNMT2Δ47 upon compound **3** binding.

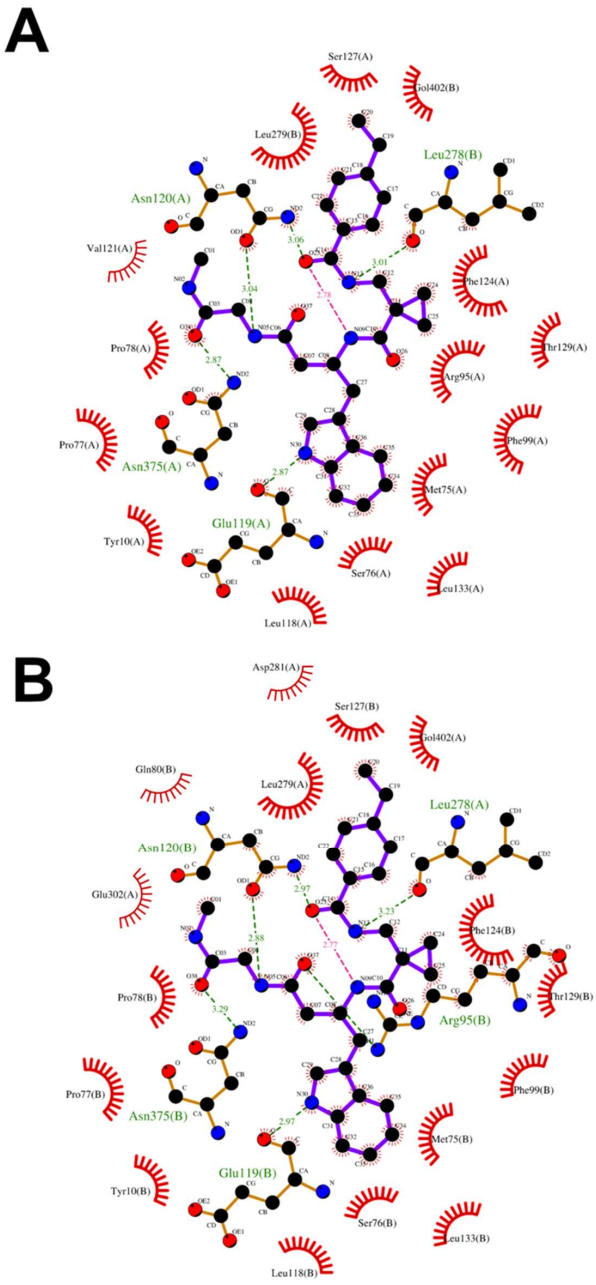


Figure S19: A schematic ligand-protein interaction diagram created with LigPlot+. For compound **3** bound to chain A (**A**) and chain B (**B**). Intermolecular hydrogen bonds are given in green, and the intramolecular hydrogen bond in compound **3** was added to the diagram in magenta.

Table S3: X-ray data collection refinement statistics.

PDB entry 9HGM	
Data Collection	
Beamline	ESRF Grenoble ID30B
Wavelength (Å)	0.8731
Resolution range (Å)	48.67-2.60 (2.72-2.60)
Space group	$P2_12_12_1$
a,b,c (Å)	71.20, 97.35, 125.02
α,β,γ (°)	90, 90, 90
Total reflections	263886 (33598)
Unique reflections	27445 (3300)
Multiplicity	9.6 (10.2)
Completeness (%)	100 (100)
Mean I/sigma(I)	10.6 (1.2)
R-merge	0.117 (1.966)
R-pim	0.042 (0.688)
CC1/2	0.999 (0.626)
Refinement	
Resolution range (Å)	48.67-2.60 (2.69-2.60)
Reflections used in refinement	27366 (2667)
Reflections used for R-free	1396 (132)
R-work	0.1995 (0.3377)
R-free	0.2454 (0.3798)
Number of non-hydrogen atoms	5410
Macromolecules	5276
Ligands	88
Solvent	46
Protein residues	656
RMS (bonds) (Å)	0.005
RMS (angles) (°)	0.580

Ramachandran favored (%)	97.4
Ramachandran allowed (%)	2.6
Ramachandran outliers (%)	0
Rotamer outliers (%)	0.84
Clashscore	2.02
Average B-factor (Å^2)	83.3
Macromolecules (Å^2)	83.6
Ligands (Å^2)	68.1
Solvent (Å^2)	74.1

Statistics for the highest-resolution shell are shown in parentheses.

Modeling of a ternary complex consisting of DNMT2-tRNA^{Asp} and small molecules

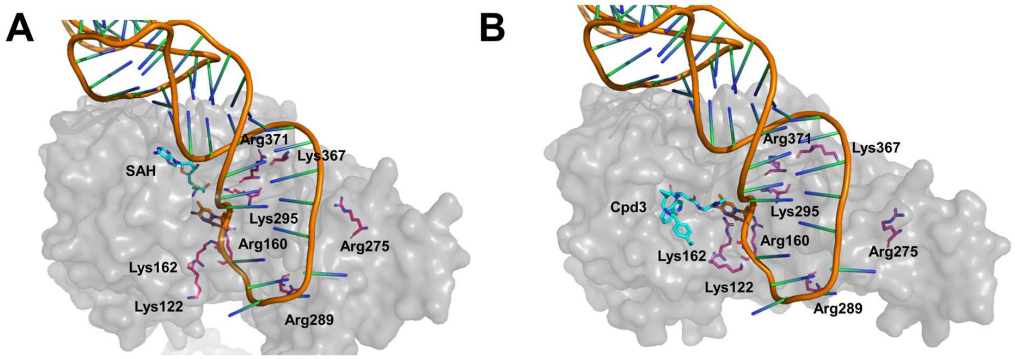


Figure S20: Modelling of ternary DNMT2-tRNA^{Asp} complexes. (**A**) Ternary complex (DNMT2-tRNA-SAH) modeled by AlphaFold, consisting of full-length DNMT2 (sequence from UniProt: O14717), tRNA^{Asp} (sequence: GGGUCGUUAGUAUAGUGGUGAGUAUCCCCGCCUGUCA{m5C}GCGGGAGACCGGGGUUCGAU UCCCCGACGGCCCGCCA), and SAH (relative coordinates from structural alignment with PDB 1G55). (**B**) Ternary complex (DNMT2-tRNA-cpd **3**) modelled by Schrödinger BioLuminate 5.8 consisting of compound **3**-bound DNMT2 (PDB 9HGM) and tRNA^{Asp}. The previously elucidated RNA-binding residues (K122, R160, R162, R275, R289, K295, K367, and R371) are at a significant distance from the allosteric binding pocket, and thus, allow the simultaneous binding of compound **3** and tRNA.

SeeSAR analysis by binding pose inspection of hit compound 3

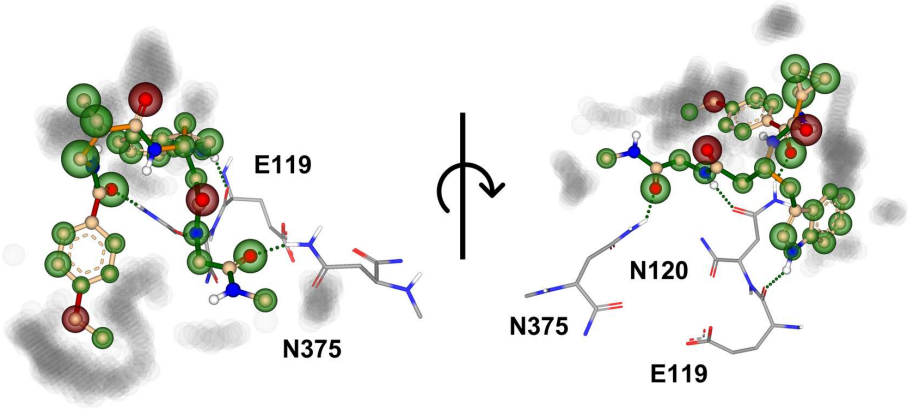


Figure S21: SeeSAR analysis by binding pose inspection of hit compound 3. Hyde coloring enabled the identification of contributing resp. unfavorable atom placements (colored spheres; green: contributing, red: unfavored); the peptide backbone's dihedral angles were evaluated for their torsional free energy (colored sticks). Characteristic hydrogen bonds are formed with the protein residues Glu119, Asn120, and Asn375. Potentially druggable yet unoccupied space in the protein binding pocket is highlighted by grey shadings.

Uncropped gel images

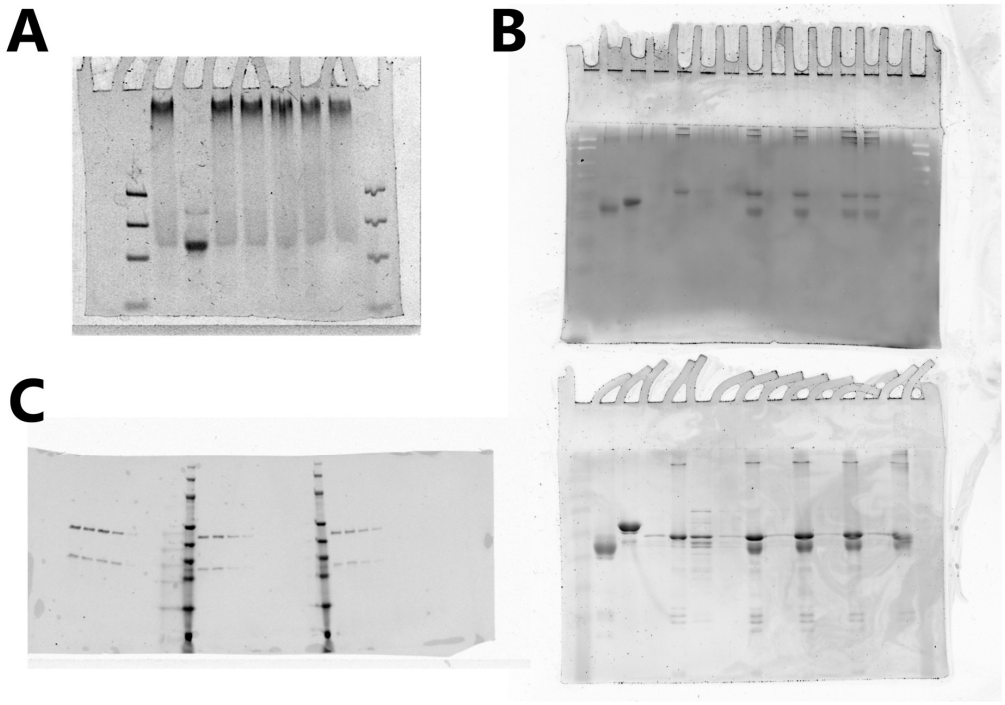


Figure S22: Uncropped PAGE and Western blot images. (**A**) EMSA. (**B**) DNMT2 interaction assays. (**C**) CETSA.

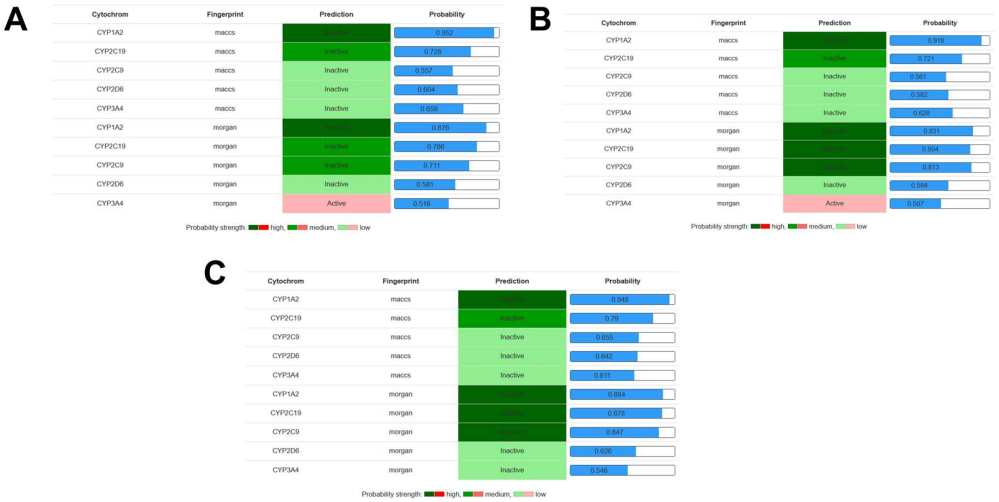
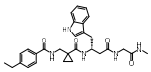
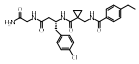
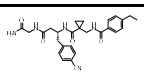


Figure S23: Cyp-enzyme reactivity profiles of compounds. 3 (**A**), **16** (**B**), and **34** (**C**) as determined by SuperCYPsPred.

Table S4: Overview of predicted physicochemical properties of cell evaluated compounds 3 (non-permeable control), 16 (cell-active), and 34 (taylor-made negative control). The values were obtained using the web tools molinspiration.com and SuperCYPsPred. Properties that violate Lipinski's Rule of Five are highlighted in red.

Cpd.	structure	MW [g/mol]	logP	TPSA	#H-acceptors	#H-donors	rotatable bonds
3		517.3	3.75	128.43	9	5	12
16		498.2	3.40	130.39	8	5	12
34		489.2	2.48	154.18	9	5	12

"

5 Project 3: Novel Modalities for Medicinal Chemistry of RNA and RNA Methyltransferases

5.1 Structure-Guided Design of a Methyltransferase-like 3 (METTL3) Proteolysis Targeting Chimera (PROTAC) Incorporating an Indole–Nicotinamide Chemotype

5.1.1 Context and Project Summary

PROTACs represent a new modality in medicinal chemistry, enabling targeted protein degradation through the recruitment of E3 ubiquitin ligases utilizing the intracellular ubiquitin-proteasome system.[256] PROTACs are heterobifunctional molecules comprising a POI ligand and an E3 ligase recruiter connected through a linker.[256] Unlike small-molecule inhibitors, PROTACs require only catalytic cellular concentrations to induce depletion of target proteins.[256] This results in reduced off-target effects and minimizes the need for high dosing. Moreover, PROTACs can function as chemical knockdown agents in cellular systems, making them valuable analytical tools for investigating cellular processes.

In this study, the focus was on the RNA Mtase METTL3, an enzyme implicated in oncogenic processes across various cancer types (chapter 1.1.3).[154–156,161] As a POI ligand, the selective and affine METTL3 inhibitor STM2457 served as a scaffold for the rational design and synthesis of four successive PROTAC generations.[166] The first-generation degraders explored a broad range of linker lengths and incorporated either CRBN or VHL E3 ligase recruiters. Subsequent generations refined these parameters by systematically varying linker rigidity and modifying the POI-binding moiety, with a remaining VHL recruiter, which showed favorable properties compared to CRBN recruiters. At each stage, the PROTACs were evaluated for their binding affinity to METTL3 and the respective E3 ligase.

This iterative optimization led to the discovery of compound AF 151 in the fourth generation, exhibiting potent degradation activity against METTL3 (DC_{50} = 430 nM). Biophysical characterization of AF 151 via FP assays showed a positive cooperativity, while Western blot analyses demonstrated selective target degradation of METTL3. AF 151 demonstrated a fourfold enhancement in its ability to reduce cell viability in MOLM-13 cells relative to STM2457 and a higher reduction of cellular m^6A levels, underscoring the enhanced therapeutic potential of targeted degradation over enzymatic inhibition.

Computational docking studies and molecular dynamics (MD) simulations provided structural insights into the binding mode and dynamic behavior of PROTAC-induced ternary complexes.

This work has been published in: RSC Medicinal Chemistry (impact factor: 3.6).

Article reprinted (unmodified) with open access permission from *RSC Med. Chem.,* **2025**, *16* (9), 4194–4207. 'Structure-guided design of methyltransferase-like 3 (METTL3) proteolysis targeting chimera (PROTAC) incorporating an indole-nicotinamide chemotype.' © The Royal Society of Chemistry. The work is licensed under CC BY 3.0 (https://creativecommons.org/licenses/by/3.0/).

The full version of the article, including the electronic Supplementary Information, can be accessed online at doi: 10.1039/D5MD00359H.

5.1.2 Contributions

Own contribution: Synthesis of compounds (45%, partly supervision of student Franziska Krähe), SI writing (synthesis and NMR) and editing, and manuscript editing.

Contributions from other authors: Synthesis of compounds (55%), protein preparation, FP-assay, Western Blot analysis, HTRF-assay, cultivation of cells, docking and MD simulations, cell assays, manuscript writing and editing, SI writing and editing.

5.1.3 Publication

The following publication quoted within "" from page 201 to page 214 is the same as the manuscript cited on page 200.[257]

"

RSC Medicinal Chemistry

ROYAL SOCIETY OF CHEMISTRY

RESEARCH ARTICLE



Cite this: *RSC Med. Chem.*, 2025, **16**, 4194

Structure-guided design of a methyltransferase-like 3 (METTL3) proteolysis targeting chimera (PROTAC) incorporating an indole–nicotinamide chemotype†

Annabelle C. Weldert, [a] Ariane F. Frey, [a] Mackenzie W. Krone, [b] Franziska Krähe,[a] Hannah Kuhn, [a] Christian Kersten [ac] and Fabian Barthels *[ab]

Methyltransferase-like 3 (METTL3) is the main catalytic subunit of the m^{6}A methyltransferase complex (MTC) and plays an essential role in various disease indications, including acute myeloid leukemia (AML). Here, we describe the structure-guided design and evaluation of METTL3 proteolysis-targeting chimeras (PROTACs), starting from the potent small-molecule inhibitor STM2457. Across four design generations, we highlight key considerations, particularly regarding the exit vector, linker mechanics, and METTL3-binding chemotype composition. Our most effective PROTAC, AF151, forms a stable complex between the E3 ligase von Hippel–Lindau (VHL) and the target-of-interest METTL3, demonstrating efficient METTL3 degradation (DC_{50} = 430 nM) in the AML cell line MOLM-13. This molecule candidate exhibits more pronounced effects on viability inhibition (IC_{50} = 0.45 μM) and more significant m^{6}A level reduction in cancer cells than its non-PRTOAC parent compounds. By incorporating the indole-nicotinamide chemotype as the METTL3-binding recruiter, this PROTAC is structurally distinct from recently published METTL3 PROTACs, expanding the design options for future METTL3 degrader development.

Received 25th April 2025,
Accepted 18th June 2025

DOI: 10.1039/d5md00359h

rsc.li/medchem

This article is licensed under a Creative Commons Attribution 3.0 Unported Licence.



Introduction

RNA modifications are critical for cellular activities, both at the transcriptional and post-transcriptional levels. Among the various RNA modifications, N^6-methyladenosine (m^{6}A) is the most prevalent in mammalian cells,[1] influencing gene expression and cellular processes such as differentiation and stress adaptation.[2–4] m^{6}A is regulated by three key protein groups: writers (methyltransferases), erasers (demethylases), and readers (m^{6}A-binding proteins).[5] The primary writer of m^{6}A in mRNA is the m^{6}A methyltransferase complex (MTC), consisting of methyltransferase-like 3 and 14 (METTL3 and METTL14) and their cofactors, like the Wilms' tumor 1-associating protein (WTAP).[6] As the enzymatic core of the MTC, METTL3 transfers methyl groups from its co-substrate *S*-adenosylmethionine (SAM) to target mRNA, while METTL14 facilitates RNA substrate recognition.[7]

The MTC plays a critical role in numerous diseases, including cardiovascular diseases,[8] viral infections,[9,10] and neurological disorders.[11] Additionally, METTL3 is overexpressed in various cancers, including hematological,[12] lung,[13] and liver cancer.[14] In acute myeloid leukemia (AML), METTL3 enhances the translation of oncogenes like Bcl2, promoting cell survival.[12] Moreover, its depletion leads to cell cycle arrest, differentiation, and apoptosis, delaying leukemia progression.[12,15] Similarly, small-molecule inhibition of METTL3 has been shown to reduce AML growth and increase differentiation and apoptosis, highlighting the pharmacological potential to target METTL3.[16] Several small-molecule METTL3 targeting SAM-competitive inhibitors have been reported, including the selective and highly potent UZH2,[17] EP652,[18] STM2457,[16] and STM3006.[19] The latter two compounds were developed by STORM Therapeutics, whose lead candidate, STC-15, recently entered clinical trials, being the first RNA methyltransferase inhibitor in this class.[20,21]

Despite their low nanomolar potency in biochemical assays, most METTL3 inhibitors require micromolar concentrations to reduce m^{6}A mRNA modification levels in cells,[16,17,19] likely due to competition with the high intracellular concentration of SAM and other

[a] *Institute of Pharmaceutical and Biomedical Sciences, Johannes Gutenberg-University, Staudingerweg 5, 55128 Mainz, Germany. E-mail: barthels@uni-mainz.de*
[b] *Department of Molecular, Cellular, and Developmental Biology, Yale University, 260 Whitney Ave, CT 06520-8103 New Haven, USA*
[c] *Institute for Quantitative and Computational Biosciences, Johannes Gutenberg-University, BioZentrum I, Hanns-Dieter-Hüsch Weg 15, 55128 Mainz, Germany*
† Electronic supplementary information (ESI) available. See DOI: https://doi.org/10.1039/d5md00359h

This journal is © The Royal Society of Chemistry 2025

pharmacokinetic effects.[22] Furthermore, m^6A-independent mechanisms for METTL3, which cannot be captured by competitive SAM inhibition, have been demonstrated to promote tumorigenesis and translation as well.[13,23] Hence, an alternative approach to target catalytic and non-catalytic functions of METTL3 at the same time is selective degradation using proteolysis-targeting chimeras (PROTACs). PROTACs are an emerging class of new modalities in drug discovery, with recent candidates entering late-stage clinical trials.[24,25] These heterobifunctional small molecules contain a protein of interest (POI) ligand, an E3 ligase ligand, and a linker connecting both. PROTACs form ternary complexes with the E3 ligase and POI, leading to ubiquitination and subsequent degradation of the POI *via* the ubiquitin–proteasome system (UPS). This targeted protein degradation impairs both enzymatic and structural functions, thereby expanding therapeutic applications.[26–29]

During the preparation of this manuscript (2024–2025), the first reports of heterobifunctional degraders targeting METTL3 have been published, highlighting the current interest in this specific target class.[30–33] Yet, all reported METTL3 PROTACs are based on the METTL3 recruiting chemotype of UZH2, limiting their structural diversity. Errani *et al.* developed degrader molecules that achieved approximately 50% degradation of METTL3 in multiple AML cell lines.[30] Almost simultaneously, Du *et al.* published the potent (D_{max} ~ 91%) METTL3 degrader WD6305.[31] Soon after, Hwang *et al.* further highlighted the therapeutic potential of METTL3 degradation in gastric cancer cells by targeting its non-catalytic function.[32] Meanwhile, Nar *et al.* demonstrated the synergistic effects of their METTL3 degraders with other anti-cancer agents.[33] While all these studies confirm the therapeutic potential of METTL3 degraders, particularly against AML, the METTL3 PROTACs developed so far lack structural diversity, as all of them use UZH2 (ref. 17) as the METTL3-recruiting chemotype.

In this study, we report the development of **AF151** (compound **41**), a potent METTL3 degrader with an indole-nicotinamide METTL3 binding chemotype based on a series of METTL3 ligands developed by STORM Therapeutics[16] and EPICS Therapeutics.[18] **AF151** exhibits efficient METTL3 degradation and reduces viability in AML cells, offering a structurally distinct alternative to previously reported UZH2-based PROTACs. Here, our synthesis and testing of over 40 PROTAC candidates will support the continued development of METTL3 PROTACs.

Experimental section

Synthesis

The synthetic procedures of all compounds, including NMR and LC-MS data, are detailed in the ESI.†

Reference compounds

WD6305, MLN4924, and elvitegravir were purchased from MedChemExpress. Venetoclax, STM3006, and bortezomib were purchased from BLDpharm. STM2457 was purchased from Cayman Chemicals. VH032 (ref. 34) was synthesized according to reported procedures. Crystal structures of ligand complexes were taken from the Protein Data Bank (PDB).[35]

Recombinant protein expression and purification

METTL3/14. A METTL3/14 expression plasmid was used as described previously.[36] In brief, a pETDuet-1 vector containing the MTase domains of human METTL3 (UniProt: Q86U44, aa 252–580) and METTL14 (UniProt: Q9HCE5, aa 108–444) was introduced into *E. coli* BL21 (DE3) cells. The METTL3 construct carried a C-terminal Strep-tag II, while METTL14 was fused to an N-terminal hexahistidine (His_6) tag. The cells were grown in LB medium containing 100 μg mL^{-1} ampicillin at 37 °C and 160 rpm until they reached an optical density (OD_{600}) of ~0.6. Protein overexpression was induced by adding 0.1 mM isopropyl-β-D-1-thiogalactopyranoside (IPTG) and 0.1 mM $ZnCl_2$, followed by incubation for ~16 h at 18 °C. Cells were harvested by centrifugation and suspended in cold lysis buffer (10 mM potassium phosphate, pH 7.5, 300 mM KCl, 20 mM imidazole, 10% glycerol, 0.1 mM TCEP). Lysozyme, one tablet of protease inhibitor (cOMPLETE), and DNAse I were added. After a 30 minute incubation on ice, the cells were lysed by sonication, and the cell debris was removed by centrifugation. The resulting clear supernatant was kept on ice. The pellet was resuspended in lysis buffer, subjected to a second round of sonication, and centrifuged again to remove insoluble components. The clarified lysates were applied to a HisTrap HP column for affinity purification, pre-equilibrated in binding buffer (10 mM potassium phosphate, pH 7.5, 300 mM KCl, 20 mM imidazole). After washing with several column volumes of wash buffer (10 mM potassium phosphate, pH 7.5, 500 mM KCl, 20 mM imidazole), the protein was eluted with elution buffer (10 mM potassium phosphate, pH 7.5, 300 mM KCl, 250 mM imidazole). Finally, METTL3/14 was purified *via* size-exclusion (SEC), on a Superdex 16/60075 pg SEC column equilibrated with SEC buffer (25 mM Tris HCl, pH 7.5, 100 mM NaCl). METTL3/14 was flash-frozen in liquid nitrogen and stored at −80 °C.

VHL, elongin B, and elongin C (VCB)

VHL (UniProt: P40337, aa 1–213), elongin B (UniProt: Q15370, aa 1–118), and elongin C (UniProt: Q15369, aa 17–112) were expressed as a complex (VCB) as described previously with slight modifications.[37] Briefly, a pCDFDuet-1 vector containing elongin B and C and a pET28a vector containing VHL, harboring a hexahistidine (His_6) tag at the N-terminus, were co-transformed in *E. coli* BL21 (DE3) cells. The cells were grown in LB medium containing 50 μg mL^{-1} kanamycin and 50 μg mL^{-1} streptomycin sulfate at 37 °C and 160 rpm until they reached an OD_{600} of ~0.7. Overexpression was induced by adding 0.3 mM IPTG for ~16 h at 24 °C. After harvesting the cells by centrifugation, the pellet was resuspended in cold lysis buffer (50 mM HEPES, pH 8.0,

500 mM NaCl, 20 mM imidazole, 5 mM mercaptoethanol). One tablet of protease inhibitor and DNAse I were added, and the cells were lysed by sonication. After removing the cell debris with centrifugation, the supernatant was filtered and applied to a HisTrap HP column for affinity purification, pre-equilibrated in lysis buffer. Unbound sample was washed with 10 CV lysis buffer, and the VCB complex was eluted in a linear gradient of elution buffer (50 mM HEPES, pH 8.0, 500 mM NaCl, 500 mM imidazole, 5 mM mercaptoethanol) from 0 to 100% over 20 CV. The pooled fractions were combined and dialyzed against 20 mM HEPES, pH 8.0, 20 mM NaCl, and 1 mM DTT at 4 °C overnight. Afterwards, the VCB complex was subjected to anion exchange chromatography (AEX) on a HiTrap HP column, preequilibrated in dialysis buffer. The protein complex was eluted in a linear gradient of elution buffer 2 (20 mM HEPES, pH 8.0, 500 mM NaCl, 1 mM DTT) from 0 to 100% over 20 CV. Lastly, the VCB complex was purified by SEC on a Superdex 16/600 75 pg SEC column equilibrated with SEC buffer (20 mM HEPES, pH 7.5, 100 mM NaCl, 1 mM TCEP). The VCB complex was flash-frozen in liquid nitrogen and stored at −80 °C.

Fluorescence polarization (FP) assays

Fluorescence polarization (FP) displacement assays with METTL3/14 (ref. 36) and VCB[38–40] were performed following previous protocols with slight adaptations. All experiments were conducted in black Greiner 96-well half-area plates using a Tecan Spark 10 M plate reader, equipped with polarization filters coupled to a monochromator setup (λ_{ex} = 480 nm, λ_{em} = 530 nm). Reaction mixtures for METTL3/14 contained 300 nM recombinant enzyme, 20 nM FAM-labelled displacement tracer (STM-FL[36]), and the test compounds at varying concentrations in 25 mM Tris HCl, pH 7.5, 100 mM NaCl, and 10% DMSO. For VCB, the mixtures contained 40 nM recombinant enzyme, 10 nM FAM-labelled probe (FAM-DEALAHypYIPMDDDFQLRSF, Tocris Bioscience), and the tested compounds, at varying concentrations, in 50 mM Tris, pH 7.5, 200 mM NaCl, 2 mM DTT, and 10% DMSO. For the ternary K_D determinations, METTL3/14 was added at 12 μM, corresponding to approximately a 30- to 100-fold excess of binary K_D. All measurements were performed at least as technical triplicates. Polarization values (mP) were determined from polarization-specific parallel and orthogonal fluorescence intensities using the Tecan in-built calculation routine. Using GraphPad Prism 8.0.1, the FP values were normalized, and K_D values were calculated using a 4-parameter Hill equation: y(% probe bound) = bottom + ([ligand]slope) × (top–bottom)/([ligand]slope + K_D slope).

Homogeneous time-resolved fluorescence (HTRF) assays

PROTACs binding to VHL or CRBN were measured using a homogeneous time-resolved fluorescence (HTRF) human VHL or CRBN binding kit (Revvity). Samples were prepared according to the manufacturer's protocol, with compounds diluted in the provided diluent while maintaining a constant DMSO concentration with a final concentration of 1.25%. For the ternary K_D determinations, METTL3/14 was added at 4 μM, corresponding to approximately a 20- to 40-fold excess of binary K_D, while all other component concentrations were kept as specified in the protocol. Measurements were performed in triplicate using a Tecan Spark 10 M plate reader, recording donor and acceptor emissions at λ_{em_donor} = 620 nm and $\lambda_{em_acceptor}$ = 665 nm, respectively, following excitation of the HTRF donor at λ_{ex} = 320 nm. The acceptor-to-donor emission ratio was calculated as ratio = signal 665 nm/signal 620 nm. Using GraphPad Prism 8.0.1, the fluorescence values were normalized, and K_D values were calculated as specified above.

Computational analysis

Docking. Ternary PROTAC docking was performed using method 4B of the degrader modeling tool in the Molecular Operating Environment (MOE) 2022.02.[41–43] Briefly, in this method, two protein–ligand complexes were provided, one for the E3 ligase and one for the target. Additionally, the structure of the entire degrader was provided. Protein–protein docking was conducted between the E3 ligase and target complex, and subsequently, different conformations for the PROTAC compound were generated. Lastly, the protein–protein docked ensemble and the PROTAC conformational ensemble were combined. A cluster number was generated for the protein and PROTAC conformations found across all poses, and a double cluster number was assigned by concatenating the two individual cluster numbers. This double cluster population can then be used to prioritize hit selection.[42] The following specifications were applied: PROTAC structures were protonated using Protonate3D[44] and energy-minimized using the MMFF94x[45] force field, while all other calculations employed the Amber10:EHT force field. For WD6305 (ref. 31) and KH12,[32] METTL3/14 (PDB: 7O2F[17]) and VCB (PDB: 4W9H[34]), crystallographic binding modes of the MTase and VHL ligands were directly used as templates in the docking protocol. For **AF151**, VCB (PDB: 4W9H[34]) was also used directly, whereas for METTL3/14 (PDB: 8BN8 (ref. 19)) a template docking with the METTL3/14-binding moiety of **AF151** was performed before ternary complex docking. Missing residues and loops were reconstructed before docking using MOE's *de novo* loop modeler. For MD simulations, for each ternary complex (VCB–**AF151**–METTL3/14, VCB–KH12–METTL3/14, and VCB–WD6305–METTL3/14), the best-scoring representative structures of the three largest double clusters were selected. All structures were protonated using Protonate3D within MOE to account for changes from the ternary complex formation.

Molecular dynamics (MD) simulations

PROTACS were parameterized using antechamber[46] and parmchk2 from the AmberTools24 (ref. 47) with the generalized amber force field (GAFF2 (ref. 48)) and AM1-BCC

 This journal is © The Royal Society of Chemistry 2025

charges.[49] Ternary complex structures were built with tleap and minimized using sander over 200 time steps. Complexes were then neutralized using sodium ions (Na^+) and solvated using a TIP3P[50] water box exceeding the complexes by 10.0 Å in every dimension. Equilibration and production were performed with NAMD2.14 (ref. 51) and the AMBER (ff19SB[52]) force field. Equilibration was performed over 1 ns with gradually releasing harmonic constraints on the PROTAC and protein atoms and heating from 100 to 300 K. Production MD simulations were performed over 20 ns (all) and prolonged to 100 ns for selected structures (see below) using time steps of 2 fs with rigid bond lengths and a van-der-Waals cut-off of 14.0 Å using periodic boundary conditions in an NPT ensemble. Simulations were visually inspected and analyzed using VMD-1.9.3.[53] Molecular mechanic-generalized born surface area (MM-GBSA) analysis was performed using the 1-trajectory (1A) method with the ante-MMPBSA.py and MMPBSA.py[54] implementation of AmberTools24 with GB model igb5.[55] Simulations of 20 ns or 100 ns, respectively, were analyzed using an interval of 0.1 ns and a salt concentration of 0.1 M. As described previously,[56] the energetic contributions were dissected into their respective parts from the individual binary and ternary complexes from target (T, here METTL3/14), E3 ligase (E, here VCB), and PROTAC (P) (Tables S2 and S3†).

Cell culture

Human acute myeloid leukemia MOLM-13 cells were cultured in Roswell Park Memorial Institute (RPMI 1640) medium with 10% fetal bovine serum (FBS) and 100 μg mL^{-1} penicillin–streptomycin mix at 5% CO_2 and 37 °C. Cell densities were maintained at 0.3–2 × 10^6 cells per mL. MOLM-13 cells were obtained from DSMZ-German Collection of Microorganisms and Cell Cultures GmbH. All reagents and tissue culture plastics were purchased from Thermo Fisher Scientific.

Immunoblotting

MOLM-13 were seeded in 12-well cell culture plates at a density of 1 × 10^6 cells per mL and treated with DMSO (final: 0.1%) or different concentrations of PROTAC degraders in DMSO at the indicated times. Treatments were conducted in biological triplicate with varying passages of MOLM-13 cells. The cells were harvested by centrifugation at 500*g* for 5 min and washed with PBS. The cells were lysed with RIPA lysis buffer with the addition of protease inhibitor (1× cOMPLETE), and insoluble cellular parts were separated by centrifugation (12 000*g* for 10 min), subsequently, the supernatant was boiled with 1× Laemmli sample buffer (Carl Roth) for 5 min at 95 °C. Proteins were separated by SDS–PAGE on 4–20% Criterion™ TGX™ Precast Protein Gels (Bio-Rad) and transferred to Amersham™ Protean® 0.45 μm nitrocellulose membrane (Cytiva) using semi-dry transfer (25 V, 1 A, Towbin buffer). The membrane was blocked with 5% milk (Carl Roth) in TBST buffer and incubated with the following primary antibodies: Anti-METTL3 (1 : 1000, Abcam, ab195352), anti-METTL14 (1 : 1000, Abcam, ab220030), anti-Bcl2 (1 : 1000, Cell Signaling Technology [CST], EPR16891), anti-Mcl-1 (1 : 1000, CST, 5453 T), anti-Bcl-XL (1 : 1000, CST, 2764 T), anti-vinculin (1 : 1000, CST, 13901) or anti-GAPDH (1 : 5000, CST, D17C4) overnight at 4 °C. Subsequently, the membrane was incubated for 1 h at RT with secondary antibodies: anti-rabbit (1 : 2000, VWR, NA934) or anti-mouse (1 : 2000, VWR, 102646-160). The protein bands were detected *via* chemiluminescence using Pierce™ ECL western blotting substrate and a Fusion FX imaging system (Vilber). The ImageLab software (Bio-Rad) was used for band quantification.

Reverse transcription polymerase chain reaction (RT-qPCR)

To determine mRNA expression levels of METTL3 and METTL14, MOLM-13 cells were treated in triplicate with compound **41** (**AF151**, 2 μM), STM2457 (10 μM), and DMSO for 24 resp. 48 h. Afterward, total RNA was extracted using the TRIzol™ reagent (Thermo Fisher Scientific) and purified with the Monarch® Spin RNA Cleanup Kit (New England Biolabs). RT-qPCR was conducted using the two-step GoTaq® RT-qPCR system (Promega) following the manufacturer's protocol. The data were normalized to the DMSO control and GAPDH housekeeping gene (ΔΔCt) using GraphPad Prism 8.0.1. The primer sequences used for RT-qPCR are listed in Table S4.†

Cell viability assays

To determine cell viability, MOLM-13 cells were treated with the indicated compounds in a 1 : 1 serial dilution, with pure DMSO (final: 0.1%) as the negative control. Briefly, 1000 cells were seeded in black Greiner half-area 96-well plates and incubated for 72 h with inhibitors from DMSO stocks under standard cultivation conditions. Then, Promega CellTiter Glo 2.0 reagent was added to each well according to the manufacturer's protocols, and luminescence was measured using a Tecan Spark 10 M. Experiments were conducted in technical triplicate. Data was normalized to the DMSO control and analyzed with GraphPad Prism 8.0.1 to determine EC_{50} values. Synergistic effects of venetoclax and **AF151** on cell MOLM-13 viability were conducted accordingly, with dilution series of both compounds analyzed using the SynergyFinder+ webtoolkit.[57]

RNA m^6A quantification

Quantification of m^6A levels upon compound treatment was conducted in analogy to the study introducing the WD6305 PROTAC.[31] MOLM-13 cells were treated with **AF151** (2 μM), STM2457 (10 μM), and DMSO in triplicate for 24 and 48 h. Total RNA was isolated as specified above. PolyA mRNA was then isolated using the PolyATtract® mRNA Isolation System (Promega). m^6A levels were quantified using a colorimetric m^6A RNA methylation Assay Kit (Abcam) as specified in the manufacturer's protocol. The data was normalized to the DMSO control and displayed using GraphPad Prism 8.0.1.

Real-time apoptosis assay

MOLM-13 cells were treated with **AF151** at the indicated concentrations for 48 h, with DMSO (final: 0.1%) as the negative control. Apoptosis of technical triplicate samples was detected in real-time using the RealTime-Glo™ annexin V apoptosis assay kit (Promega), following the manufacturer's protocol. Data were plotted using GraphPad Prism 8.0.1.

Results and discussion

Development and initial evaluation of PROTAC candidates

The development pipeline of our METTL3 PROTACs, spanning four molecular generations, is shown in Fig. 1. In our heterobifunctional designs, we aimed to recruit the E3 ligases von Hippel–Lindau (VHL) or cereblon (CRBN) in a ternary complex with METTL3, since well-established ligands are available for all proteins.[58] For VHL, we chose VH032 (ref. 34) and VL285 (ref. 59) (hereinafter referred to as VHL-LH and VHL-RH, respectively), and for CRBN, 4-hydroxy and 5-hydroxy thalidomide[60] as E3 ligase ligands. For METTL3, we chose the small molecule inhibitor STM2457, developed by STORM Therapeutics, due to its high selectivity and potency.[16] Compounds from the STM series show high *in vitro* potency, favourable ADME properties, and efficient m^{6}A level reduction in cancer cells. Compared to the UZH2-based degraders, the STM-based parent compound has been characterized more extensively in clinically relevant AML models. In this regard, STC-15 has shown a robust average reduction of 63% in m^{6}A levels in peripheral blood in humans in a phase 1 clinical trial.[20]

To identify a suitable attachment point for linker conjugation, we analyzed the X-ray structure of STM2457 bound to METTL3 (PDB: 7O2I[16]). Since the cyclohexyl moiety of STM2457 allows the attachment of a solvent-exposed exit vector (Fig. 1A), we selected this molecular segment for linker attachment. Based on the results of a SAR study reported by STORM Therapeutics,[61] we attached a linker segment directly to the secondary amine instead of the cyclohexyl moiety. Further, the original imidazopyridine scaffold was replaced with a benzimidazole for synthetic reasons, yielding **POI-1** (Fig. 1B). To connect **POI-1** to the E3 ligase ligands, we opted for polyethylene glycol (PEG$_n$, n = 1–5) linkers, yielding our first generation of METTL3 PROTACs (Fig. 1C). Synthesis and detailed structure of all generations are shown in the ESI.†

Next, we evaluate the affinity of the PROTAC candidates for METTL3 binding using a competitive fluorescence polarization (FP) assay (Table S1†). This revealed that VHL-based PROTACs exhibited an overall higher affinity for METTL3 compared to CRBN-based PROTACs. However, in general, the METTL3 affinities of our first-generation PROTACs were relatively low compared to the parent compound STM2457 (K_D = 1.4 nM[16]), with our best compounds showing affinities around K_D ~ 4 μM (Table S1†). We concluded that the cyclohexyl moiety of STM2457 is

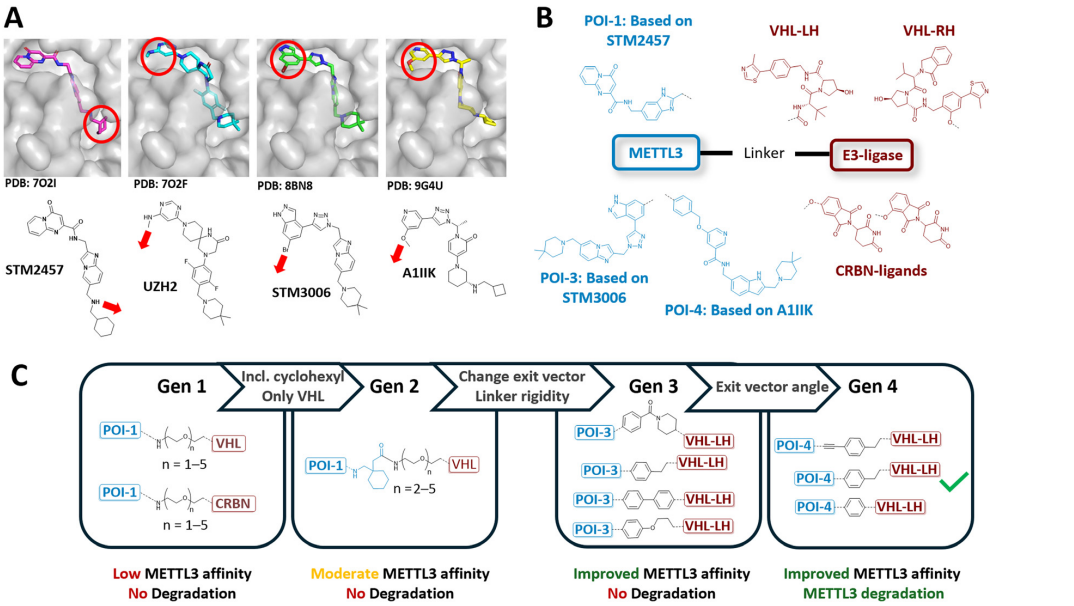


Fig. 1 Development pipeline of PROTACs targeting METTL3. (A) Crystal structures of various METTL3-targeting small-molecule inhibitor complexes: STM2457 (PDB: 7O2I), UZH2 (PDB: 7O2F), STM3006 (PDB: 8BN8), and A1IIK (PDB: 9G4U), showing solvent-exposed regions and thereby possible exit vectors for linker attachment sides. (B) General design and selected structures of our METTL3 PROTAC strategy, including METTL3 and E3 ligase binding moieties used in this study. (C) Structural representation of METTL3 PROTAC development across four generations, specifying changes made between each generation.

 This journal is © The Royal Society of Chemistry 2025

necessary for high-affinity METTL3 binding. Furthermore, Hwang *et al.* and Errani *et al.* have reported that CRBN-based METTL3 PROTACs exhibit lower degradation activity compared to their VHL-based counterparts.[30,32] Hence, we decided to focus only on the VHL-based PROTACs in the following generations of PROTACs.

Subsequently, we synthesized our second generation of VHL-based PROTACs, including a cyclohexyl motif (Fig. 1C), which demonstrated improved METTL3 affinity (K_D ~ 300 nM, Table S1†). Next, we screened the METTL3 degradation activities of our most promising 2nd-generation PROTACs in MOLM-13 cells. However, none of these molecule candidates showed significant METTL3 degradation activity after treatment (final: 0.1–10 μM) for 16 h (Fig. S4†). Apart from possessing nanomolar affinity to METTL3 and the E3 ligase (Table S1†), PROTACs, in general, need to facilitate the right spatial orientation and alignment of both proteins to achieve efficient target degradation. Linker geometry, length, and rigidity play a crucial role in this process.[28,62,63] Errani *et al.* showed that moving from flexible PEG linkers to more rigid benzyl, piperidine, and piperazine linkers can improve METTL3 degradation; additionally, the increase in lipophilicity enhanced cellular permeability.[30] Furthermore, WD6305 (Fig. 2A), the highly potent PROTAC developed by Du *et al.*, features a relatively rigid and short linker compared to the less potent ones in this study.[31] Based on these findings, we selected a series of shorter and more rigid linkers for our third-generation design (Fig. 1C). Additionally, we theorized that the previously used exit vector of STM2457 (pointing to the RNA binding site) might not be optimal for METTL3–VCB complex formation in cellulo.[6,64,65] All currently published METTL3 degraders base their METTL3-binding functionality on UZH2, with a distinct exit vector away from the RNA binding site (Fig. 1A).

Hence, we changed our METTL3 recruiting ligand from STM2457 to STM3006, which allows us to exit METTL3 at a

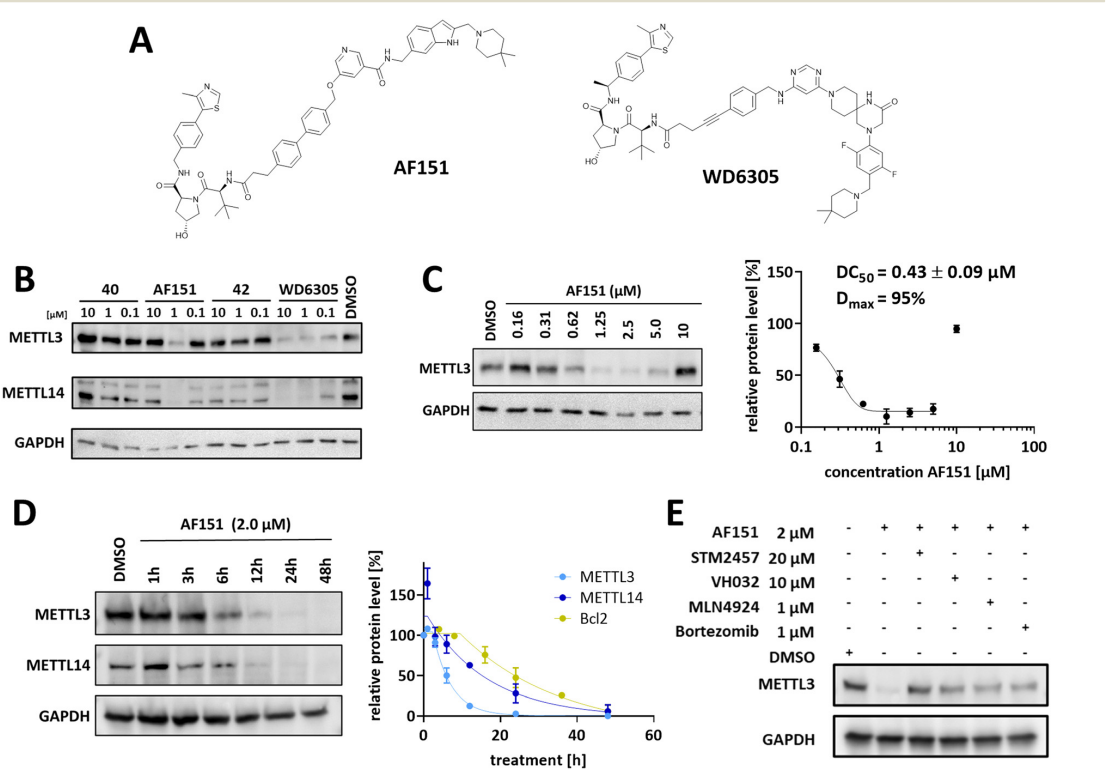


Fig. 2 Cellular characterization of METTL3 PROTAC **AF151**. (A) Structures of **AF151** and reference degrader WD6305, developed by Du *et al.*[31] (B) Western blots of PROTAC screening results analyzing the fourth generation of our PROTAC design. MOLM-13 cells were treated with the indicated compounds at different concentrations (10 μM, 1 μM, and 0.1 μM) for 16 h. WD6305 and DMSO were used as positive and negative controls. (C) Dose–response experiments and DC_{50} determination for **AF151** in MOLM-13 cells. Left: Western blot image after treatment at the indicated concentrations for 16 h. Right: Dose–response curve with different **AF151** concentrations plotted against METTL3 protein levels relative to the DMSO control. (D) Time course treatment experiments. Left: Western blot image after treatment with **AF151** at 2 μM at the indicated time points. Right: Time-response curve with different time points plotted against METTL3, METTL14, and Bcl-2 protein levels relative to the DMSO control. (E) Cellular PROTAC competition assay. MOLM-13 cells were treated with **AF151** in combination with the METTL3 inhibitor STM2457, VH032, MLN4924, or bortezomib at the indicated concentrations. Uncropped Western blot images can be found in Fig. S8–S11.†

similar position to UZH2 by linker attachment to the indazole ring of **POI-3** (Fig. 1B).[19] Yet, despite these optimizations, cellular degradation analysis still showed little effect on METTL3 protein levels (Fig. S4†). Compared to the potent literature-known WD6305 METTL3 degrader, our **POI-3** geometry differs only slightly by the angle and the rigidity of the exit vector, while linker lengths and position of the linkage are very similar to UZH2-based PROTACs (Fig. 1A). Hence, to further refine the flexibility and the angle of the exit vector, we continued optimizing **POI-3**: the co-crystal structure of EPICS Therapeutics' A1IIK (PDB: 9G4U[18]) showed that replacing STM3006's indazole moiety with a pyridine scaffold will allow an STM-based METTL3 recruiting chemotype but with a UZH2-like exit vector (Fig. 1A),[18] and thus, yielding our 4th generation METTL3 recruiter **POI-4** (Fig. 1B).

Cell-based METTL3 degradation analysis showed that compound **41** (**AF151**, Fig. 2A), a **POI-4**-based PROTAC, led to significant degradation of METTL3 and its heterodimerized partner METTL14 after treatment for 16 h with 1 μM (Fig. 2B). To summarize, while our initial designs showed no METTL3 degradation, optimization efforts, including replacing flexible PEG linkers with more rigid linkers and refining the METTL3 exit vector, led to a functional METTL3 degrader in MOLM-13 cells.

Analysis of AF151's degradation efficiency and mechanism

Encouraged by the initial screening results, we further analyzed compound **41**'s (**AF151**) efficiency in degrading METTL3 in MOLM-13 cells and investigated the underlying molecular mechanisms. The half-degrading concentration (DC_{50}) after 16 h of treatment was determined to be 430 nM (Fig. 2C). Maximal degradation ($D_{max} \sim 95\%$) occurred at 2.5 μM, while we noticed a characteristic "hook effect" >5 μM, where METTL3 degradation decreased. The high concentration of PROTAC leads to saturation of binding sites on both METTL3 and VHL, forming predominantly binary complexes and preventing the formation of ternary complexes and thereby degradation. However, at compound concentrations >5 μM, AF151 still acts as an inhibitor of METTL3, since the catalytic activity of the enzyme is still blocked by the binary complexes.

Time-course analysis revealed that **AF151** induces rapid METTL3 degradation, achieving over 50% METTL3 reduction within the first 6 h of treatment, reaching maximal effect at 24 h, and maintaining it for at least 48 h (Fig. 2D). METTL14 was reduced alongside METTL3, in agreement with prior METTL3 PROTAC studies.[30–33] Of note, treatment with **AF151** led to an initial but transient increase of METTL14 (~150%) after 1 h before inducing METTL14 degradation. Similarly, Errani *et al.* reported elevated levels of METTL3/14 after treatment with the small-molecule inhibitor UZH2. They proposed an unknown cellular compensatory mechanism, which might have led to an increase of METTL14.[30,66] Half-lives for the degradation kinetics of METTL3 and METTL14 were determined at $t_{1/2}$ = 4 h and 11 h, respectively. Thus, the degradation of METTL14 is significantly slower than that of METTL3, which can be explained by the fact that METTL3 occurs not only in complexes with METTL14 but also in a monomeric state and other protein complexes in cells.[67]

Next, we investigated the functional mechanism of **AF151** by confirming the involvement of the UPS. Co-treatment of the degrader with the proteasome inhibitor bortezomib (1 μM),[68] neddylation inhibitor MLN4924 (1 μM),[69] and VH032 (10 μM)[34] suppressed METTL3 degradation, indicating that the process is both proteasome and VHL-dependent. Furthermore, adding a competitive METTL3 ligand STM2457 (20 μM) also inhibited degradation, confirming that **AF151** binds to the SAM-binding site of METTL3 (Fig. 2E).

Interestingly, the dose–response evaluation revealed that **AF151** and WD6305 share DC_{50} values (430 nM for **AF151** *vs.* 140 nM for WD6305 (ref. 31)) in the same order of magnitude, but only **AF151** displays a characteristic hook effect at concentrations up to 10 μM. The relative ternary complex population, and thereby the hook effect, is known to be mainly influenced by the cooperativity of ternary complex formation.[70,71] PROTACs can introduce *de novo* stabilizing or destabilizing protein–protein interactions during ternary complex formation. Hence, the binary binding affinity to METTL3 or the E3 ligase may differ from the ternary affinity in the presence of the second binding partner. This effect is quantified by the cooperativity factor ($\alpha = K_D^{binary}/K_D^{ternary}$). Positive cooperativity ($\alpha > 1$) indicates stabilizing *de novo* effects during ternary complex formation, while negative cooperativity ($\alpha < 1$) signifies destabilizing *de novo* interactions.[70,72]

To assess the cooperativity of **AF151** and WD6305, we employed a displacement FP assay, previously described to assess PROTAC cooperativity.[38,39] In this assay, the VHL dissociation constants of both METTL3 PROTACs **AF151** and WD6305, with and without near-saturating METTL3 concentrations, were compared (Fig. 3A and B). Here, both PROTACs exhibited overall positive cooperativity (Fig. 3C), facilitating the interaction between METTL3 and VHL. Interestingly, the cooperativity factor of WD6305 (α = 23) is approximately five times higher than that of **AF151** (α = 4.5), which could possibly explain the observed differences in their hook effect characteristics (*i.e.*, lower binary affinity of WD6305 disfavors VHL-PROTAC complex formation in the absence of METTL3).

To validate these findings, we used a homogeneous time-resolved fluorescence (HTRF) assay to assess VHL affinity in the presence and absence of METTL3, confirming positive cooperativity for both PROTACs, with WD6305 displaying a higher α than **AF151** (Fig. S5†). Interestingly, the strong positive cooperativity for WD6305 is not due to an increased ternary affinity. The ternary K_D for **AF151** and WD6305 is very similar at 77 nM and 79 nM, respectively. Instead, the binary affinity of WD6305 for VHL (1.7 μM) is significantly reduced compared to **AF151** (363 nM) or parent compound VH032 (210 nM).

 This journal is © The Royal Society of Chemistry 2025

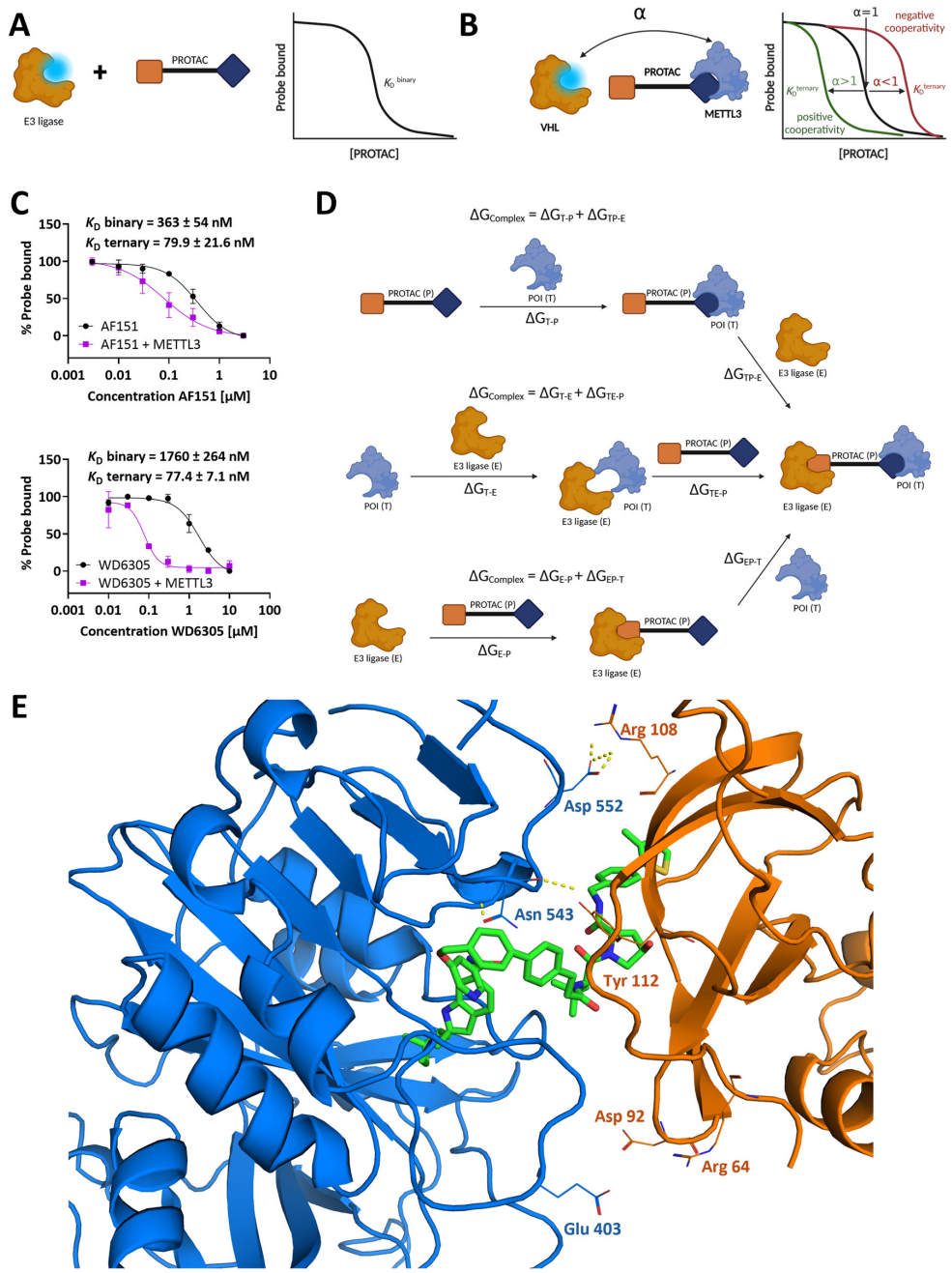


Fig. 3 Investigation of ternary complex formation and cooperativity for **AF151** and WD6305. (A and B) A fluorescent displacement probe binds to the E3 ligase and is displaced upon PROTAC molecule binding. The FP level of the displaced probe was used to determine the dissociation constant of PROTAC binding. Cooperativity is evaluated by comparing the PROTAC's affinity for the E3 ligase in the presence and the absence of METTL3. (C) Cooperativity factor (α) determination for **AF151** and WD6305 binding in the presence (purple) and absence (black) of METTL3 (12 μM). Each data point represents the mean ± SEM from triplicates repeated in two independent experiments. (D) Possible binary and ternary interactions between PROTAC (P), E3-ligase (E), and the protein of interest (target, T) can be described using Gibbs free energy (ΔG) for each interaction. The overall Gibbs free energy change for the formation of the ternary complex can be determined in three equivalent ways: $\Delta G_{complex} = \Delta G_{T-P} + \Delta G_{TP-E} = \Delta G_{E-P} + \Delta G_{EP-T} = \Delta G_{T-E} + \Delta G_{TE-P}$. (E) Most stable predicted binding mode for **AF151** in a ternary METTL3-VCB complex. The proteins are portrayed as cartoons, with the amino acids commonly found in protein–protein interactions across all simulations labeled as lines. Polar protein–protein interactions are shown as dashed yellow lines, and **AF151** is shown as green sticks. METTL3: blue, VHL: orange.

Computational analysis of METTL3 PROTAC complexes

For further investigation of the ternary complex formed by **AF151** and WD6305, the small molecule-induced protein–protein interface was evaluated using *in silico* PROTAC-docking with subsequent molecular dynamics (MD) simulations. Additionally, KH12, the METTL3 PROTAC from Hwang *et al.*, was included in this analysis, since this PROTAC has a comparable structure to WD6305 but exhibits a hook effect similar to **AF151**.[32] While PROTAC-docking provides possible geometries of ternary complexes, this coarse-grained method is not capable of discriminating the correct complex structure from incorrect ones, since the scoring function has insufficient accuracy.

Therefore, for each of the three PROTACs, three ternary complex structures were selected based on clustering and score for subsequent MD simulations. After short MD simulations of 20 ns, complex structures were evaluated based on their overall stability by root-mean-square-deviation (RMSD) analysis and complex stability using MM-GBSA calculations (Fig. S6, Table S2†). MM-GBSA was previously shown to be a good predictor for characterizing cooperativity, including stabilization and hook effects.[56] MD simulations of the most stable complexes per PROTAC, presumably representing the correct complex orientation, were prolonged to 100 ns each prior to MM-GBSA analysis of these effects (Fig. S7, Table S3†). As described previously, simulation times of 50–100 ns were found to be suitable for this analysis.[56] In these ternary complexes, there were only minor differences in MM-GBSA results between 50 ns and 100 ns, indicating sufficient sampling (Table S3†). Only the complex structure of WD6305 diverged from the starting structure after around 53 ns (Fig. S7C†). As the modeling of ternary PROTAC complexes is still in its infancy, some caveats must be raised. While MM-GBSA provides absolute binding free energy values, it should still be considered a coarse-grained method with limited accuracy. Therefore, instead of interpreting absolute ΔG-values, we performed only a qualitative, relative comparison between the ternary complexes. For higher accuracy, computationally more expensive absolute or relative binding free energy calculations (ABFE/RBFE) like free energy perturbations (FEP) or thermodynamic integration (TI) must be performed.[73–76] Likewise, the 1-trajectory (1A) MM-GBSA approach is a simplification assuming the different affinity contributions can be obtained from a single simulation of the ternary complex instead of seven simulations covering ternary and binary complexes and target, ligase, and PROTAC alone (Fig. 3D). Despite these limitations, some observations from MD simulations reveal trends for the molecules under discussion.

Within the 20 ns of simulation, the structurally most stable complexes (Fig. S6†) also showed stronger favorable binding free energies for the ternary complex ($\Delta G_{\text{complex}}$, Table S2†). METTL3/14 and VCB were internally very stable, while structural changes mostly occurred in the whole complex, hence the orientation between target and ligase.

The similar geometry of the complexes with the highest stability used for prolonged MD simulations of 100 ns hints towards the identification of the putatively correct geometry of the complexes (Fig. S7†). MM-GBSA analysis (Table S3†) showed a higher affinity of the PROTAC towards METTL3/14 ($\Delta G_{\text{T–P}}$) than to VCB ($\Delta G_{\text{E–P}}$) in line with FP binding assays. Further, all compounds show a stabilizing effect (positive cooperativity) caused by favorable METTL3/14-VCB (target–E3 ligase, $\Delta G_{\text{T–E}}$) interactions. Without PROTAC, $\Delta G_{\text{T–E}} \sim 0$ kcal mol^{-1}, strong protein–protein interactions should have stabilizing effects for ternary complex formation.

This is reflected in the predicted cooperativity ($\Delta G_{\text{TP–E}} - \Delta G_{\text{E–P}}$, Table S3†). Based on the predicted METTL3/14–**AF151**–VCB complex (Fig. 3E) and $\Delta G_{\text{T–E}}$ contribution from MM-GBSA, mainly hydrophobic contacts contribute to these direct target–ligase interactions. Additionally, some polar interactions are commonly found in the simulations, *e.g.*, Asp552 (METTL3) + Arg108 (VHL), Asn543 (METTL3) + Tyr112 (VHL), and Glu403 (METTL3) + Arg64 (VHL) (Fig. 3E). Hook effects can occur for PROTACs with high affinity to the target or ligase while having low or negative cooperativity. For KH12, the predicted affinity to both METTL3/14 ($\Delta G_{\text{T–P}}$) and VCB ($\Delta G_{\text{E–P}}$) is higher than for **AF151** and WD6305, which might explain the observed hook effect for this compound.[32]

However, this cannot explain the difference between **AF151** (hook effect) and WD6305 (no hook effect at given concentrations), as predicted affinities for METTL3/14 and VCB ($\Delta G_{\text{T–P}}$ and $\Delta G_{\text{E–P}}$, respectively) are similar, while the predicted stabilizing effect for **AF151** ($\Delta G_{\text{T–E}}$) is even higher. Notably, the simulations were performed considering only one possible geometry of the ternary complex, whereas *in vivo* and *in vitro*, different conformations of the complex might form, some of which could lead to less stable interactions.[77] Yet, ternary complex formation is crucial but insufficient by itself for protein degradation since ubiquitination and other cellular mechanisms also play an important role. Some of these alternative conformations possibly result in unproductive complexes.[78,79] Ultimately, the MD simulations reason that the differing degradation profile of **AF151** and WD6305 is not due to overall cooperativity differences and binding mode variation, but raises the hypothesis that one of the other effects influencing cellular degradation might be the reason for **AF151**'s hook effect.

Investigation of cellular response after AF151 treatment

Overall, **AF151** is able to form a stable ternary complex between VHL and METTL3, exhibiting positive cooperativity and effectively reducing METTL3 levels in MOLM-13 cells in a concentration-, time-, and UPS-dependent manner. To assess the cell biological effects of **AF151**, we investigated the cellular downstream responses of MOLM-13 cells following treatment with **AF151**. First, we evaluated METTL3 and METTL14 mRNA levels *via* RT-qPCR and found no significant changes in gene expression following **AF151** or STM2457

 This journal is © The Royal Society of Chemistry 2025

treatment after 24 h and 48 h (Fig. 4A), thereby verifying that the alteration of METTL3 and METTL14 protein levels by **AF151** is due to degradation rather than inhibited protein expression or feedback stimulation of RNA synthesis. This is in agreement with literature experiments conducted for the WD6305 degrader.[31]

Parent compound STM2457 has been shown to suppress the methyltransferase activity of METTL3, leading to reduced m^{6}A levels and antiproliferative effects on AML cells.[16] Thus, we examined whether the compound-induced degradation of METTL3 similarly resulted in reduced cell viability. For comparison, we determined the reduction in MOLM-13 cell viability caused by **AF151**, WD6305, and STM2457. **AF151** (IC_{50} = 0.45 μM) exhibited a similar reduction in cell viability as WD6305 (IC_{50} = 0.78 μM) and fourfold more efficient cellular inhibition than parent compound STM2457 (IC_{50} = 1.82 μM) (Fig. 4B). This agrees with previous reports that the degradation of METTL3 provides a greater benefit in suppressing cell viability, and METTL3 degraders effectively promote apoptosis in cancer cell lines.[31–33] Next, we compared the effect of **AF151** and STM2457 on global m^{6}A levels in MOLM-13 cell total mRNA, finding that **AF151** caused a more pronounced m^{6}A reduction than the competitive inhibitor STM2457 alone (Fig. 4C).

METTL3 has been shown to regulate the translation of the anti-apoptotic protein Bcl-2 in cancer cells, and METTL3 inhibition using STM2457 leads to a reduction in Bcl-2 protein levels in AML.[16,80] Thus, we evaluated whether the degradation of METTL3 by **AF151** would lead to a decrease in Bcl-2 protein levels. Analysis of the MOLM-13 treatment time course showed that Bcl-2 protein levels decreased alongside METTL3 (Fig. 2D), albeit with slower kinetics ($t_{1/2}$ = 18 h), likely due to a delay in the reduction of METTL3-mediated RNA modifications on Bcl-2 mRNA (Fig. 4E). Recently, Jiao *et al.* demonstrated that inhibition of METTL3 by STM2457 leads to a decrease in Mcl-1 levels in AML cells, another antiapoptotic protein and member of the Bcl-2 family.[81] Thus, we evaluated the impact of METTL3 degradation by **AF151** on Mcl-1 levels. Additionally, we tested the effect on Bcl-XL, another Bcl-2 family member, whose protein levels, however, were not affected by METTL3 inhibition in the study by Jiao *et al.* In summary, we were able to reproduce these results: **AF151** leads to a time-dependent reduction of Bcl-2 and Mcl-1 but not Bcl-XL (Fig. 4E).

Next, we used a homogeneous luminogenic annexin V binding assay to follow MOLM-13 apoptosis levels and progressions in real time, revealing that **AF151** induces apoptosis after approximately 10 h in a dose-dependent manner (Fig. 4D), which is consistent with both the reduction

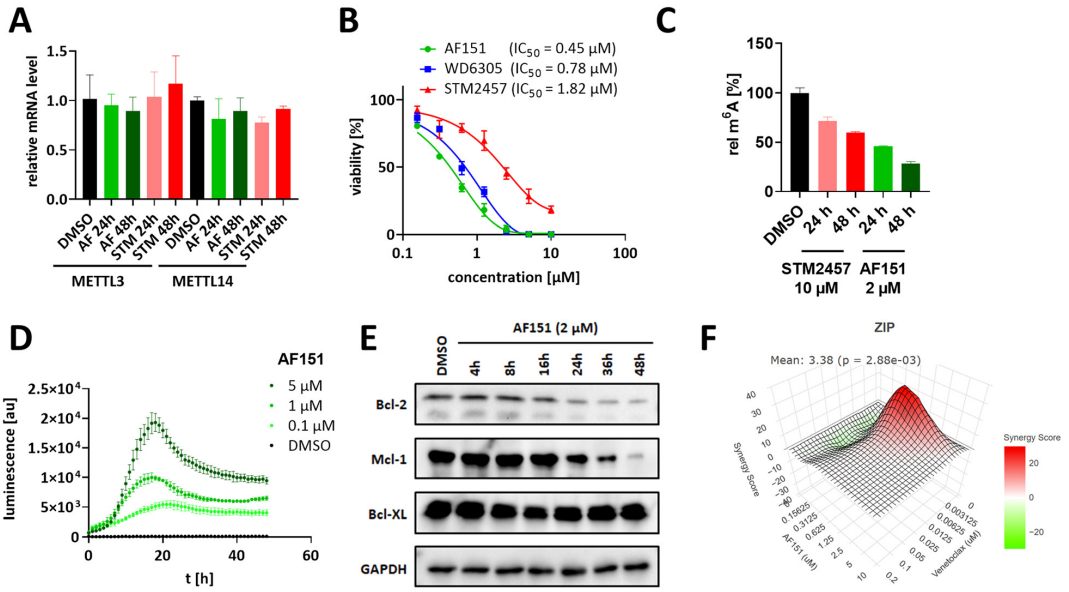


Fig. 4 Evaluation of **AF151** in MOLM-13 cells. (A) Relative METTL3 and METTL14 mRNA levels (ΔΔCt) after treatment with **AF151** (2 μM) or STM2457 (10 μM) for 24 h resp. 48 h. (B) Cell viability inhibition after treatment with varying concentrations of **AF151**, WD6305, and STM2457. (C) m^{6}A quantification of total mRNA isolated from MOLM-13 cells after treatment with **AF151** (2 μM) or STM2457 (10 μM) for the indicated durations. (D) Real-time apoptosis assay (homogeneous luminogenic annexin V binding assay). MOLM-13 cells were treated with **AF151** at the indicated concentrations, and apoptosis was monitored *via* luminescence over 48 h. (E) Time course treatment experiment of Bcl-like proteins performed analogously to Fig. 2D. Western blot image after treatment with **AF151** at 2 μM at the indicated time points. The corresponding time-response plot can be found in Fig. 2D. (F) Zero interaction potency (ZIP) analysis of co-treatment (72 h) with **AF151** and venetoclax in MOLM-13 cells. Quantification and illustration were generated with the SynergyFinder+ webserver.

in cell viability and the kinetics of Bcl-2 level reduction. Jiao *et al.* showed that STM2457 synergistically enhances the antileukemic efficacy of the Bcl-2 inhibitor venetoclax and can overcome venetoclax resistance in *in vivo* experiments and resistance models. Hence, we hypothesized that co-treatment with a METTL3 degrader and venetoclax could equally lead to synergistic effects on cell viability reduction.

To test this hypothesis, we treated MOLM-13 cells with varying concentrations of **AF151** and venetoclax (Fig. 4F). The matrix of cell viability reduction was analyzed using the zero interaction potency (ZIP) model and quantified with the SynergyFinder method.[57,82] Co-treatment with **AF151** and venetoclax exhibited a slight synergistic reduction in cell viability, predominantly at lower concentrations of venetoclax (mean ZIP = 3.38, maximum ZIP = 28.87; Fig. 4F), *i.e.*, **AF151** is sensitizing MOLM-13 cells for treatment with venetoclax as the apoptosis-inducing effector, possibly by downregulation of Bcl-2 family proteins. Altogether, targeted degradation of METTL3 seems to be an effective strategy against AML and exhibits enhanced efficacy when combined with other agents.

Conclusions

In this work, we developed and characterized **AF151**, a functional METTL3 degrader, in MOLM-13 cells. In-depth characterization proved that **AF151** is an effective and rapid degrader of METTL3, utilizing the UPS. Our PROTAC candidates were developed across four design generations, including the evaluation of target affinities (*via* FP assays) and degradation potency (*via* immunoblotting). In this regard, we explored new chemotypes for METTL3 PROTAC development, offering a structurally distinct alternative to current UZH2-based PROTACs.[30–33] During our development process, we demonstrated that targeting the E3 ligase VHL is preferable to CRBN. Moreover, strategic improvements in METTL3 affinity, exit vector orientation, and linker flexibility were found to be essential. These insights and design guidelines will be a useful resource for following METTL3 PROTAC discovery campaigns.

In the course of this study, we have established an FP-based assay to assess binary METTL3 PROTAC affinities and utilized a literature-reported FP assay for binary and ternary VHL PROTAC interactions. Additionally, we performed MD simulations to analyze the ternary complex formation and cooperativity between METTL3 PROTACs and VHL. In this regard, we noticed the interesting finding that the potent published METTL3 PROTAC WD6305 has a reduced VHL affinity compared to the parent compound VH032, and this generates its strong positive cooperativity and efficient degradation profile.

Overall, we highlighted key design considerations when developing PROTACs targeting METTL3 and proved that an alternative METTL3-binding chemotype, distinct from previously published structures, can lead to the efficient degradation of METTL3. These degradation results, in conjunction with biophysical characterization of the PROTAC-mediated complexes, expand the toolbox for the development of future targeted METTL3 degraders.

Data availability

The data supporting this article have been included as part of the ESI.†

Author contributions

A. C. W.: data curation, formal analysis, investigation, validation, visualization, writing – original draft, A. F. F.: formal analysis, investigation, writing – original draft, M. W. K.: methodology, resources. FK: investigation. HK: investigation. CK: formal analysis, investigation, writing – original draft. FB: conceptualization, methodology, project administration, writing – review & editing.

Conflicts of interest

There are no conflicts of interest to declare.

Acknowledgements

Financial support by the Deutsche Forschungsgemeinschaft (DFG, German Research Foundation) project number 439669440 TRR319 RMaP A01 is gratefully acknowledged. We thank Prof. Craig M. Crews for the helpful discussions and his generosity in allowing us to conduct parts of the study in his laboratory. We thank Dr. Marco Jörg for his support during the Western blot experiments. We thank Axel Guthart for his support in preliminary docking experiments. Some Figures were created with **https://www.biorender.com/** and assisted by Dr. Michael Klein.

References

1 P. Boccaletto, F. Stefaniak, A. Ray, A. Cappannini, S. Mukherjee, E. Purta, M. Kurkowska, N. Shirvanizadeh, E. Destefanis, P. Groza, G. Avşar, A. Romitelli, P. Pir, E. Dassi, S. G. Conticello, F. Aguilo and J. M. Bujnicki, *Nucleic Acids Res.*, 2022, **50**, D231–D235.
2 J. Zhou, J. Wan, X. Gao, X. Zhang, S. R. Jaffrey and S.-B. Qian, *Nature*, 2015, **526**, 591–594.
3 J. Chen, C. Wang, W. Fei, X. Fang and X. Hu, *Am. J. Cancer Res.*, 2019, **9**, 752–764.
4 Y. Wang, Y. Li, J. I. Toth, M. D. Petroski, Z. Zhang and J. C. Zhao, *Nat. Cell Biol.*, 2014, **16**, 191–198.
5 Y. Yang, P. J. Hsu, Y.-S. Chen and Y.-G. Yang, *Cell Res.*, 2018, **28**, 616–624.
6 J. Liu, Y. Yue, D. Han, X. Wang, Y. Fu, L. Zhang, G. Jia, M. Yu, Z. Lu, X. Deng, Q. Dai, W. Chen and C. He, *Nat. Chem. Biol.*, 2014, **10**, 93–95.
7 P. Śledź and M. Jinek, *eLife*, 2016, **5**, e18434.
8 X.-Q. Gao, Y.-H. Zhang, F. Liu, M. Ponnusamy, X.-M. Zhao, L.-Y. Zhou, M. Zhai, C.-Y. Liu, X.-M. Li, M. Wang, C. Shan, P.-P. Shan, Y. Wang, Y.-H. Dong, L.-L. Qian, T. Yu, J. Ju, T.

 This journal is © The Royal Society of Chemistry 2025

Wang, K. Wang, X.-Z. Chen, Y.-H. Wang, J. Zhang, P.-F. Li and K. Wang, *Nat. Cell Biol.*, 2020, **22**, 1319–1331.
9 N. S. Gokhale, A. B. R. McIntyre, M. J. McFadden, A. E. Roder, E. M. Kennedy, J. A. Gandara, S. E. Hopcraft, K. M. Quicke, C. Vazquez, J. Willer, O. R. Ilkayeva, B. A. Law, C. L. Holley, M. A. Garcia-Blanco, M. J. Evans, M. S. Suthar, S. S. Bradrick, C. E. Mason and S. M. Horner, *Cell Host Microbe*, 2016, **20**, 654–665.
10 N. Li, H. Hui, B. Bray, G. M. Gonzalez, M. Zeller, K. G. Anderson, R. Knight, D. Smith, Y. Wang, A. F. Carlin and T. M. Rana, *Cell Rep.*, 2021, **35**, 109091.
11 A. M. Shafik, F. Zhang, Z. Guo, Q. Dai, K. Pajdzik, Y. Li, Y. Kang, B. Yao, H. Wu, C. He, E. G. Allen, R. Duan and P. Jin, *Genome Biol.*, 2021, **22**, 17.
12 L. P. Vu, B. F. Pickering, Y. Cheng, S. Zaccara, D. Nguyen, G. Minuesa, T. Chou, A. Chow, Y. Saletore, M. MacKay, J. Schulman, C. Famulare, M. Patel, V. M. Klimek, F. E. Garrett-Bakelman, A. Melnick, M. Carroll, C. E. Mason, S. R. Jaffrey and M. G. Kharas, *Nat. Med.*, 2017, **23**, 1369–1376.
13 S. Lin, J. Choe, P. Du, R. Triboulet and R. I. Gregory, *Mol. Cell*, 2016, **62**, 335–345.
14 M. Chen, L. Wei, C.-T. Law, F. H.-C. Tsang, J. Shen, C. L.-H. Cheng, L.-H. Tsang, D. W.-H. Ho, D. K.-C. Chiu, J. M.-F. Lee, C. C.-L. Wong, I. O.-L. Ng and C.-M. Wong, *Hepatology*, 2018, **67**, 2254–2270.
15 I. Barbieri, K. Tzelepis, L. Pandolfini, J. Shi, G. Millán-Zambrano, S. C. Robson, D. Aspris, V. Migliori, A. J. Bannister, N. Han, E. de Braekeleer, H. Ponstingl, A. Hendrick, C. R. Vakoc, G. S. Vassiliou and T. Kouzarides, *Nature*, 2017, **552**, 126–131.
16 E. Yankova, W. Blackaby, M. Albertella, J. Rak, E. de Braekeleer, G. Tsagkogeorga, E. S. Pilka, D. Aspris, D. Leggate, A. G. Hendrick, N. A. Webster, B. Andrews, R. Fosbeary, P. Guest, N. Irigoyen, M. Eleftheriou, M. Gozdecka, J. M. L. Dias, A. J. Bannister, B. Vick, I. Jeremias, G. S. Vassiliou, O. Rausch, K. Tzelepis and T. Kouzarides, *Nature*, 2021, **593**, 597–601.
17 A. Dolbois, R. K. Bedi, E. Bochenkova, A. Müller, E. V. Moroz-Omori, D. Huang and A. Caflisch, *J. Med. Chem.*, 2021, **64**, 12738–12760.
18 G. Dutheuil, K. Oukoloff, J. Korac, F. Lenoir, M. El Bousmaqui, N. Probst, A. Lapin, G. Nakhabina, C. Sorlet, N. Parmentier, D. Karila, N. Ghavtadze, P. Casault, S. Claridge, S. Sapmaz, M. J. Slater and G. L. Fraser, *J. Med. Chem.*, 2025, **68**(3), 2981–3003.
19 A. A. Guirguis, Y. Ofir-Rosenfeld, K. Knezevic, W. Blackaby, D. Hardick, Y.-C. Chan, A. Motazedian, A. Gillespie, D. Vassiliadis, E. Y. N. Lam, K. Tran, B. Andrews, M. E. Harbour, L. Vasiliauskaite, C. J. Saunders, G. Tsagkogeorga, A. Azevedo, J. Obacz, E. S. Pilka, M. Carkill, L. MacPherson, E. N. Wainwright, B. Liddicoat, B. J. Blyth, M. R. Albertella, O. Rausch and M. A. Dawson, *Cancer Discovery*, 2023, **13**, 2228–2247.
20 J. C. Moser, K. P. Papadopoulos, J. Rodon Ahnert, Y. Ofir-Rosenfeld and J.-B. Holz, *J. Clin. Oncol.*, 2024, **42**, 2586.
21 Y. Ofir-Rosenfeld, L. Vasiliauskaitė, C. Saunders, A. Sapetschnig, G. Tsagkogeorga, M. Albertella, M. Carkill, J. Self-Fordham, J. B. Holz and O. Rausch, *Eur. J. Cancer*, 2022, **174**, S123.
22 S. Melnyk, M. Pogribna, I. P. Pogribny, P. Yi and S. J. James, *Clin. Chem.*, 2000, **46**, 265–272.
23 X. Wei, Y. Huo, J. Pi, Y. Gao, S. Rao, M. He, Q. Wei, P. Song, Y. Chen, D. Lu, W. Song, J. Liang, L. Xu, H. Wang, G. Hong, Y. Guo, Y. Si, J. Xu, X. Wang, Y. Ma, S. Yu, D. Zou, J. Jin, F. Wang and J. Yu, *Nat. Cell Biol.*, 2022, **24**, 1278–1290.
24 E. P. Hamilton, C. Ma, M. de Laurentiis, H. Iwata, S. A. Hurvitz, S. A. Wander, M. Danso, D. R. Lu, J. Perkins Smith, Y. Liu, L. Tran, S. Anderson and M. Campone, *Future Oncol.*, 2024, **20**, 2447–2455.
25 D. P. Petrylak, M. McKean, J. M. Lang, X. Gao, R. Dreicer, D. M. Geynisman, T. F. Stewart, M. Gandhi, L. J. Appleman, T. B. Dorff, G. S. Chatta, R. Tutrone, J. de La Cerda, E. Berghorn, J. Gong, T. Yu, E. Dominy, E. Chan and N. D. Shore, *J. Clin. Oncol.*, 2024, **42**, 5011.
26 M. Békés, D. R. Langley and C. M. Crews, *Nat. Rev. Drug Discovery*, 2022, **21**, 181–200.
27 A. C. Lai and C. M. Crews, *Nat. Rev. Drug Discovery*, 2017, **16**, 101–114.
28 D. P. Bondeson, A. Mares, I. E. D. Smith, E. Ko, S. Campos, A. H. Miah, K. E. Mulholland, N. Routly, D. L. Buckley, J. L. Gustafson, N. Zinn, P. Grandi, S. Shimamura, G. Bergamini, M. Faelth-Savitski, M. Bantscheff, C. Cox, D. A. Gordon, R. R. Willard, J. J. Flanagan, L. N. Casillas, B. J. Votta, W. den Besten, K. Famm, L. Kruidenier, P. S. Carter, J. D. Harling, I. Churcher and C. M. Crews, *Nat. Chem. Biol.*, 2015, **11**, 611–617.
29 C. Kim, X.-D. Wang, Z. Liu, S. Zha and Y. Yu, *Biochemistry*, 2023, **62**, 561–563.
30 F. Errani, A. Invernizzi, M. Herok, E. Bochenkova, F. Stamm, I. Corbeski, V. Romanucci, G. Di Fabio, F. Zálešák and A. Caflisch, *JACS Au*, 2024, **4**, 713–729.
31 W. Du, Y. Huang, X. Chen, Y. Deng, Y. Sun, H. Yang, Q. Shi, F. Wu, G. Liu, H. Huang, J. Ding, X. Huang and S. Xu, *Cell Chem. Biol.*, 2024, **31**, 177–183.e17.
32 K. Hwang, J. Bae, Y.-L. Jhe, J. Kim, J.-H. Cheong, H.-S. Choi and T. Sim, *Eur. J. Med. Chem.*, 2024, **279**, 116843.
33 R. Nar, Z. Wu, Y. Li, A. Smith, Y. Zhang, J. Wang, F. Yu, S. Gao, C. Yu, Z. Huo, G. Zheng and Z. Qian, *Genes Dis.*, 2025, **12**, 101452.
34 C. Galdeano, M. S. Gadd, P. Soares, S. Scaffidi, I. van Molle, I. Birced, S. Hewitt, D. M. Dias and A. Ciulli, *J. Med. Chem.*, 2014, **57**, 8657–8663.
35 H. M. Berman, J. Westbrook, Z. Feng, G. Gilliland, T. N. Bhat, H. Weissig, I. N. Shindyalov and P. E. Bourne, *Nucleic Acids Res.*, 2000, **28**, 235–242.
36 J. L. Meidner, A. F. Frey, R. A. Zimmermann, M. O. Sabin, Z. Nidoieva, A. C. Weldert, S. N. Hoba, M. W. Krone and F. Barthels, *Angew. Chem., Int. Ed.*, 2024, **63**, e202403792.
37 A. J. Wijaya, W. Farnaby and A. Ciulli, *Methods Enzymol.*, 2023, **681**, 241–263.

38 V. Zoppi, S. J. Hughes, C. Maniaci, A. Testa, T. Gmaschitz, C. Wieshofer, M. Koegl, K. M. Riching, D. L. Daniels, A. Spallarossa and A. Ciulli, *J. Med. Chem.*, 2019, **62**, 699–726.
39 I. van Molle, A. Thomann, D. L. Buckley, E. C. So, S. Lang, C. M. Crews and A. Ciulli, *Chem. Biol.*, 2012, **19**, 1300–1312.
40 P. Soares, M. S. Gadd, J. Frost, C. Galdeano, L. Ellis, O. Epemolu, S. Rocha, K. D. Read and A. Ciulli, *J. Med. Chem.*, 2018, **61**, 599–618.
41 M. L. Drummond and C. I. Williams, *J. Chem. Inf. Model.*, 2019, **59**, 1634–1644.
42 M. L. Drummond, A. Henry, H. Li and C. I. Williams, *J. Chem. Inf. Model.*, 2020, **60**, 5234–5254.
43 *Molecular Operating Environment (MOE)*, Chemical Computing Group ULC, 910–1010 Sherbrooke St. W., Montreal, QC H3A 2R7, 2025.
44 P. Labute, *J. Comput. Chem.*, 2008, **29**, 1693–1698.
45 T. A. Halgren, *J. Comput. Chem.*, 1996, **17**, 490–519.
46 J. Wang, W. Wang, P. A. Kollman and D. A. Case, *J. Mol. Graphics Modell.*, 2006, **25**, 247–260.
47 D. A. Case, H. M. Aktulga, K. Belfon, D. S. Cerutti, G. A. Cisneros, V. W. D. Cruzeiro, N. Forouzesh, T. J. Giese, A. W. Götz, H. Gohlke, S. Izadi, K. Kasavajhala, M. C. Kaymak, E. King, T. Kurtzman, T.-S. Lee, P. Li, J. Liu, T. Luchko, R. Luo, M. Manathunga, M. R. Machado, H. M. Nguyen, K. A. O'Hearn, A. V. Onufriev, F. Pan, S. Pantano, R. Qi, A. Rahnamoun, A. Risheh, S. Schott-Verdugo, A. Shajan, J. Swails, J. Wang, H. Wei, X. Wu, Y. Wu, S. Zhang, S. Zhao, Q. Zhu, T. E. Cheatham, D. R. Roe, A. Roitberg, C. Simmerling, D. M. York, M. C. Nagan and K. M. Merz, *J. Chem. Inf. Model.*, 2023, **63**, 6183–6191.
48 D. Vassetti, M. Pagliai and P. Procacci, *J. Chem. Theory Comput.*, 2019, **15**, 1983–1995.
49 A. Jakalian, D. B. Jack and C. I. Bayly, *J. Comput. Chem.*, 2002, **23**, 1623–1641.
50 W. L. Jorgensen, J. Chandrasekhar, J. D. Madura, R. W. Impey and M. L. Klein, *J. Chem. Phys.*, 1983, **79**, 926–935.
51 J. C. Phillips, R. Braun, W. Wang, J. Gumbart, E. Tajkhorshid, E. Villa, C. Chipot, R. D. Skeel, L. Kalé and K. Schulten, *J. Comput. Chem.*, 2005, **26**, 1781–1802.
52 C. Tian, K. Kasavajhala, K. A. A. Belfon, L. Raguette, H. Huang, A. N. Migues, J. Bickel, Y. Wang, J. Pincay, Q. Wu and C. Simmerling, *J. Chem. Theory Comput.*, 2020, **16**, 528–552.
53 W. Humphrey, A. Dalke and K. Schulten, *J. Mol. Graphics*, 1996, **14**, 33–38.
54 B. R. Miller, T. D. McGee, J. M. Swails, N. Homeyer, H. Gohlke and A. E. Roitberg, *J. Chem. Theory Comput.*, 2012, **8**, 3314–3321.
55 R. Anandakrishnan, A. Drozdetski, R. C. Walker and A. V. Onufriev, *Biophys. J.*, 2015, **108**, 1153–1164.
56 K. Xu, Z. Wang, S. Xiang, R. Tang, Q. Deng, J. Ge, Z. Jiang, K. Yang, T. Hou and H. Sun, *J. Chem. Inf. Model.*, 2024, **64**, 7666–7678.
57 S. Zheng, W. Wang, J. Aldahdooh, A. Malyutina, T. Shadbahr, Z. Tanoli, A. Pessia and J. Tang, *Genomics, Proteomics Bioinf.*, 2022, **20**, 587–596.
58 T. Ishida and A. Ciulli, *SLAS Discovery*, 2021, **26**, 484–502.
59 D. L. Buckley, K. Raina, N. Darricarrere, J. Hines, J. L. Gustafson, I. E. Smith, A. H. Miah, J. D. Harling and C. M. Crews, *ACS Chem. Biol.*, 2015, **10**, 1831–1837.
60 J. C. Swartzel, M. J. Bond, A. P. Pintado-Urbanc, M. Daftary, M. W. Krone, T. Douglas, E. J. Carder, J. T. Zimmer, T. Maeda, M. D. Simon and C. M. Crews, *ACS Chem. Biol.*, 2022, **17**, 1789–1798.
61 W. P. Blackaby, D. J. Hardick, E. J. Thomas, F. A. Brookfield, J. Shepherd, C. Bubert and M. P. Ridgill, Storm Therapeutics Ltd (GB) and WIPO (PCT), WO-2021111124-A1, 2021.
62 D. P. Bondeson, B. E. Smith, G. M. Burslem, A. D. Buhimschi, J. Hines, S. Jaime-Figueroa, J. Wang, B. D. Hamman, A. Ishchenko and C. M. Crews, *Cell Chem. Biol.*, 2018, **25**, 78–87.e5.
63 S. Alabi, S. Jaime-Figueroa, Z. Yao, Y. Gao, J. Hines, K. T. G. Samarasinghe, L. Vogt, N. Rosen and C. M. Crews, *Nat. Commun.*, 2021, **12**, 920.
64 R. P. Nowak, S. L. DeAngelo, D. Buckley, Z. He, K. A. Donovan, J. An, N. Safaee, M. P. Jedrychowski, C. M. Ponthier, M. Ishoey, T. Zhang, J. D. Mancias, N. S. Gray, J. E. Bradner and E. S. Fischer, *Nat. Chem. Biol.*, 2018, **14**, 706–714.
65 K.-H. Chan, M. Zengerle, A. Testa and A. Ciulli, *J. Med. Chem.*, 2018, **61**, 504–513.
66 H. Xiao, R. Zhao, W. Meng and Y. Liao, *J. Pharm. Anal.*, 2023, **13**, 625–639.
67 M. Esteva-Socias and F. Aguilo, *NAR Cancer*, 2024, **6**, zcae009.
68 J. Adams, V. J. Palombella, E. A. Sausville, J. Johnson, A. Destree, D. D. Lazarus, J. Maas, C. S. Pien, S. Prakash and P. J. Elliott, *Cancer Res.*, 1999, **59**, 2615–2622.
69 M. L. Hyer, M. A. Milhollen, J. Ciavarri, P. Fleming, T. Traore, D. Sappal, J. Huck, J. Shi, J. Gavin, J. Brownell, Y. Yang, B. Stringer, R. Griffin, F. Bruzzese, T. Soucy, J. Duffy, C. Rabino, J. Riceberg, K. Hoar, A. Lublinsky, S. Menon, M. Sintchak, N. Bump, S. M. Pulukuri, S. Langston, S. Tirrell, M. Kuranda, P. Veiby, J. Newcomb, P. Li, J. T. Wu, J. Powe, L. R. Dick, P. Greenspan, K. Galvin, M. Manfredi, C. Claiborne, B. S. Amidon and N. F. Bence, *Nat. Med.*, 2018, **24**, 186–193.
70 M. S. Gadd, A. Testa, X. Lucas, K.-H. Chan, W. Chen, D. J. Lamont, M. Zengerle and A. Ciulli, *Nat. Chem. Biol.*, 2017, **13**, 514–521.
71 C. Cecchini, S. Pannilunghi, S. Tardy and L. Scapozza, *Front. Chem.*, 2021, **9**, 672267.
72 M. J. Roy, S. Winkler, S. J. Hughes, C. Whitworth, M. Galant, W. Farnaby, K. Rumpel and A. Ciulli, *ACS Chem. Biol.*, 2019, **14**, 361–368.
73 Z. Cournia, B. Allen and W. Sherman, *J. Chem. Inf. Model.*, 2017, **57**, 2911–2937.
74 H. Fu, H. Chen, M. Blazhynska, E. Goulard Coderc de Lacam, F. Szczepaniak, A. Pavlova, X. Shao, J. C. Gumbart, F. Dehez, B. Roux, W. Cai and C. Chipot, *Nat. Protoc.*, 2022, **17**, 1114–1141.
75 C. E. M. Schindler, H. Baumann, A. Blum, D. Böse, H.-P. Buchstaller, L. Burgdorf, D. Cappel, E. Chekler, P. Czodrowski, D. Dorsch, M. K. I. Eguida, B. Follows, T.

 This journal is © The Royal Society of Chemistry 2025

Fuchß, U. Grädler, J. Gunera, T. Johnson, C. Jorand Lebrun, S. Karra, M. Klein, T. Knehans, L. Koetzner, M. Krier, M. Leiendecker, B. Leuthner, L. Li, I. Mochalkin, D. Musil, C. Neagu, F. Rippmann, K. Schiemann, R. Schulz, T. Steinbrecher, E.-M. Tanzer, A. Unzue Lopez, A. Viacava Follis, A. Wegener and D. Kuhn, *J. Chem. Inf. Model.*, 2020, **60**, 5457–5474.

76 T.-S. Lee, B. K. Allen, T. J. Giese, Z. Guo, P. Li, C. Lin, T. D. McGee, D. A. Pearlman, B. K. Radak, Y. Tao, H.-C. Tsai, H. Xu, W. Sherman and D. M. York, *J. Chem. Inf. Model.*, 2020, **60**, 5595–5623.

77 H. Zhao, *ChemMedChem*, 2024, **19**, e202400171.

78 K. M. Riching, E. A. Caine, M. Urh and D. L. Daniels, *Chem. Soc. Rev.*, 2022, **51**, 6210–6221.

79 B. E. Smith, S. L. Wang, S. Jaime-Figueroa, A. Harbin, J. Wang, B. D. Hamman and C. M. Crews, *Nat. Commun.*, 2019, **10**, 131.

80 Y. Zhang, S. Liu, T. Zhao and C. Dang, *Oncol. Rep.*, 2021, **46**(2), 163.

81 C.-Q. Jiao, C. Hu, M.-H. Sun, Y. Li, C. Wu, F. Xu, L. Zhang, F.-R. Huang, J.-J. Zhou, J.-F. Dai, M. Ruan, W.-C. Wang, Q.-S. Liu and J. Ge, *Cell Death Dis.*, 2025, **16**, 233.

82 B. Yadav, K. Wennerberg, T. Aittokallio and J. Tang, *Comput. Struct. Biotechnol. J.*, 2015, **13**, 504–513.

“

5.1.4 Supporting Information

The following supporting information quoted within "" from page 215 to page 275 is the same as the manuscript cited on page 200.[257] "

Structure-guided Design of a Methyltransferase-like 3 (METTL3) Proteolysis Targeting Chimera (PROTAC) Incorporating an Indole-Nicotinamide Chemotype

Annabelle C. Weldert[a], Ariane F. Frey[a], Mackenzie W. Krone[b], Franziska Krähe[a], Hannah Kuhn[a], Christian Kersten[a,c], Fabian Barthels[a,b]*

[a]Institute of Pharmaceutical and Biomedical Sciences, Johannes Gutenberg-University, Staudingerweg 5, 55128 Mainz, Germany.

[b]Department of Molecular, Cellular, and Developmental Biology, Yale University, 260 Whitney Ave, CT 06520-8103 New Haven, USA.

[c]Institute for Quantitative and Computational Biosciences, Johannes Gutenberg-University, BioZentrum I, Hanns-Dieter-Hüsch Weg 15, 55128 Mainz, Germany.

* E-Mail: barthels@uni-mainz.de

Table of contents

Biophysical investigation of PROTAC candidates ... 2

Supplementary FP and HTRF assay dose-response curves ... 7

Supplementary Western blots (screening results) ... 9

Supplementary data on biophysical investigation of ternary complexes ... 10

Molecular dynamics simulations ... 11

Primer sequences used for RT-qPCR ... 13

Uncropped Western blot images ... 14

References ... 15

Synthesis of E3 ligase recruiters with linker ... 16

- VHL-RH-based recruiters ... 16
- VHL-LH-based recruiters ... 18
- 4-Thalidomide-based recruiters ... 21
- 5-Thalidomid-based recruiters ... 23
- VHL-LH building blocks for Suzuki and Sonogashira reactions ... 26

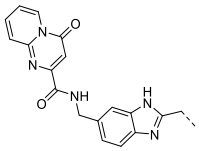
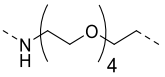
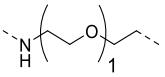
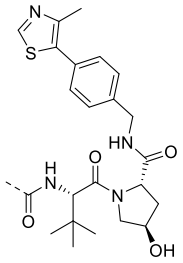
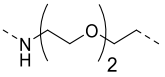
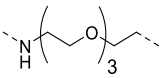
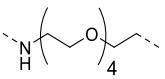
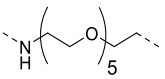
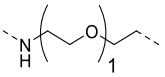
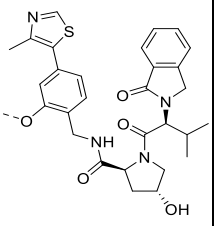
1st and 2nd generation METTL3 recruiter synthesis ... 28

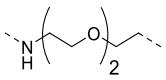
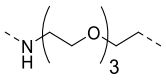
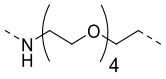
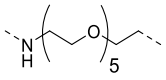
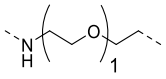
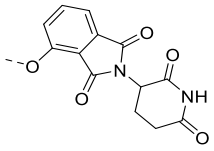
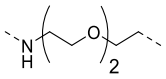
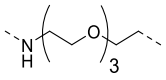
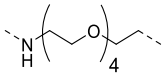
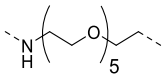
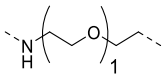
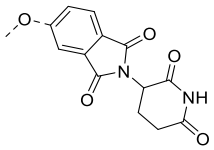
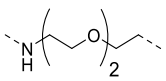
- Synthesis of 1st generation PROTACs ... 31
- Synthesis of 2nd generation PROTACs ... 38
- Synthesis of CRBN-based PROTACs ... 47
- Synthesis of 3rd generation PROTACs ... 54
- Synthesis of 4th generation PROTACs ... 57
- Spectral appendix ... 62

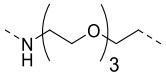
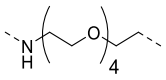
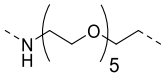
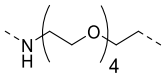
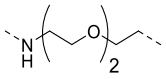
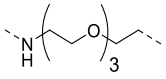
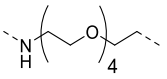
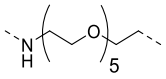
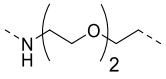
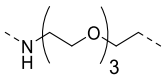
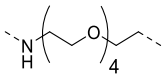
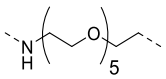
Supporting results & discussion

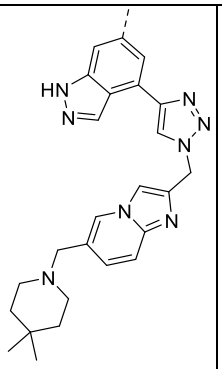
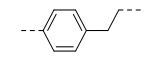
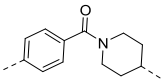
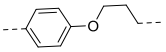
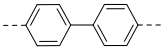
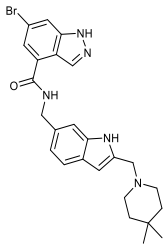
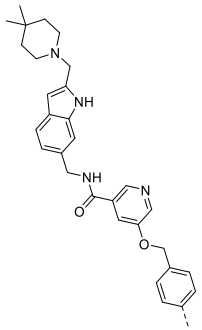
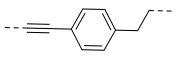
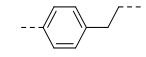
Biophysical investigation of PROTAC candidates

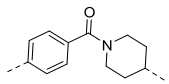
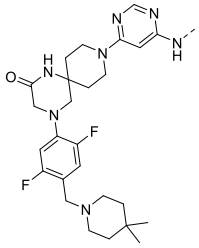
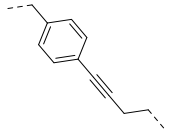
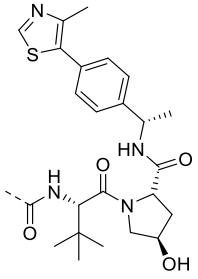
Table S1: Binary affinities to METTL3 were determined for all PROTACs synthesized in this work via FP assays. Selected affinities to the respective E3 ligase were determined via HTRF and FP assays. All K_D values include the mean value and standard deviations from at least technical triplicate measurements. Dose-response curves are depicted in Figures S1–S3 and S5.

Cpd No.	METTL3 recruiter	Linker	E3 ligase recruiter	K_D METTL3 [µM]	K_D E3-ligases [µM]
5	 **POI-1**		none	10.38 ± 0.98	n.d.
6	**POI-1**		 VHL-LH	>100	n.d.
7	**POI-1**		VHL-LH	12.47 ± 1.34	n.d.
8	**POI-1**		VHL-LH	16.07 ± 1.55	n.d.
9	**POI-1**		VHL-LH	37.59 ± 8.73	n.d.
10	**POI-1**		VHL-LH	16.33 ± 1.44	n.d.
11	**POI-1**		 VHL-RH	>100	n.d.

12	**POI-1**		VHL-RH	4.41 ± 1.25	n.d.
13	**POI-1**		VHL-RH	3.94 ± 0.53	n.d.
14	**POI-1**		VHL-RH	7.50 ± 1.07	n.d.
15	**POI-1**		VHL-RH	5.15 ± 0.59	n.d.
16	**POI-1**		 4-Thalidomide	8.06 ± 1.72	n.d.
17	**POI-1**		4-Thalidomide	10.58 ± 1.17	n.d.
18	**POI-1**		4-Thalidomide	26.51 ± 2.05	n.d.
19	**POI-1**		4-Thalidomide	10.58 ± 3.00	n.d.
20	**POI-1**		4-Thalidomide	6.13 ± 1.36	2.98 ± 0.23
21	**POI-1**		 5-Thalidomide	>100	n.d.
22	**POI-1**		5-Thalidomide	6.44 ± 0.54	2.20 ± 0.14

23	**POI-1**		5-Thalidomide	7.27 ± 0.89	n.d.
24	**POI-1**		5-Thalidomide	19.55 ± 2.85	n.d.
25	**POI-1**		5-Thalidomide	31.87 ± 9.06	n.d.
26	**POI-2**		none	0.433 ± 0.056	n.d.
27	**POI-2**		VHL-LH	0.429 ± 0.046	n.d.
28	**POI-2**		VHL-LH	0.309 ± 0.022	0.145 ± 0.04
29	**POI-2**		VHL-LH	1.53 ± 0.10	n.d.
30	**POI-2**		VHL-LH	0.725 ± 0.079	n.d.
31	**POI-2**		VHL-RH	1.15 ± 0.10	n.d.
32	**POI-2**		VHL-RH	2.05 ± 0.32	0.222 ± 0.05
33	**POI-2**		VHL-RH	2.04 ± 0.46	n.d.
34	**POI-2**		VHL-RH	2.49 ± 0.55	n.d.

35	 **POI-3**		VHL-LH	0.263 ± 0.015	n.d.
36	**POI-3**		VHL-LH	0.223 ± 0.045	n.d.
37	**POI-3**		VHL-LH	2.48 ± 0.392	n.d.
38	**POI-3**		VHL-LH	n.d.*	n.d.
39		none	none	0.0542 ± 0.0066	n.d.
40	 **POI-4**		VHL-LH	0.158 ± 0.019	n.d.
41 (AF151)	**POI-4**		VHL-LH	0.159 ± 0.026	0.363 ± 0.054 (FP) 0.740 ± 0.113 (HTRF)

42	**POI-4**		VHL-LH	0.295 ± 0.050	n.d.
WD6305[1]				0.096 ± 0.001	1.76 ± 0.26 (FP) 2.17 ± 0.28 (HTRF)

*The affinity could not be determined due to fluorescence interference of the biphenyl moiety with FP setup.

Supplementary FP and HTRF assay dose-response curves

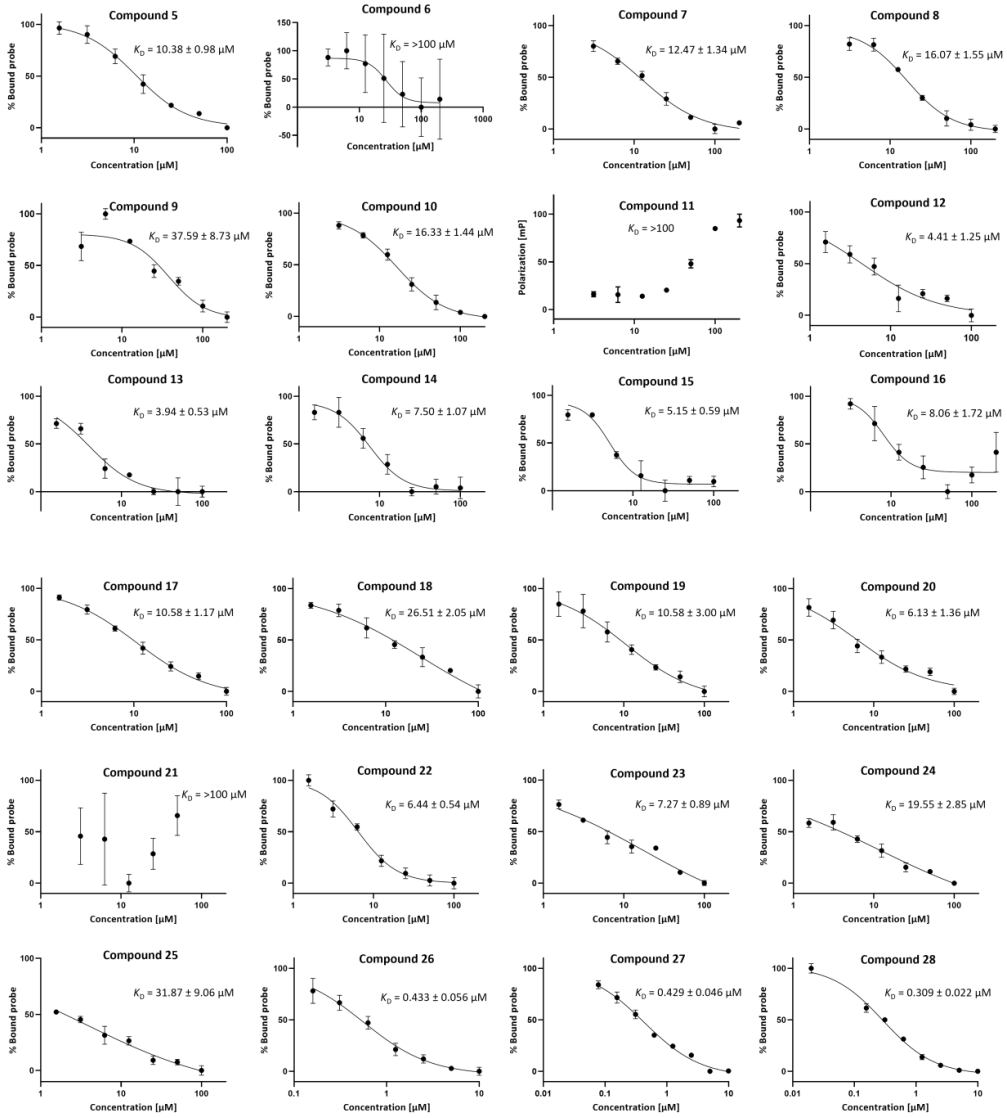


Figure S1: Supplementary FP assay dose-response curves of compounds **5**–**28**. Each experiment was carried out in triplicate. The ligand was titrated to 300 nM METTL3/14 and 20 nM of the displacement probe (STM-FL[2]) to determine the apparent dissociation constant, as specified in the experimental section. Compound **11** led to the visible formation of aggregates; thus, the distorted dose-response curve was not evaluated by non-linear regression.

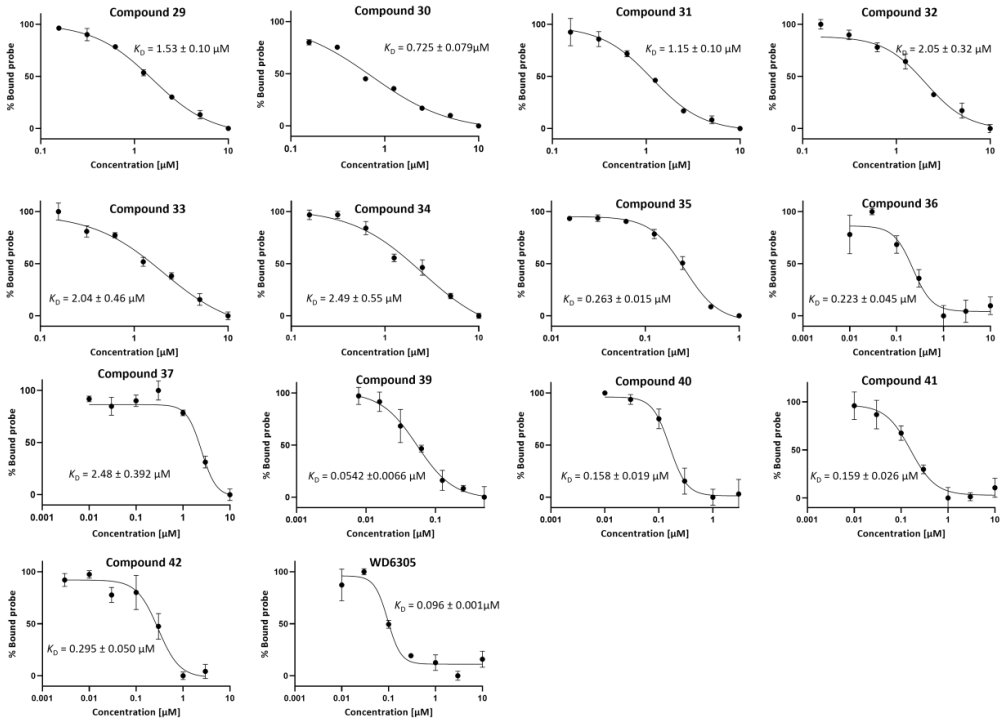


Figure S2: Supplementary FP assay dose-response curves of compounds **29**–**42** and WD6305[1]. Each experiment was carried out in triplicate. The ligand was titrated to 300 nM METTL3/14 and 20 nM of the displacement probe (STM-FL[2]) to determine the apparent dissociation constant, as specified in the experimental section.

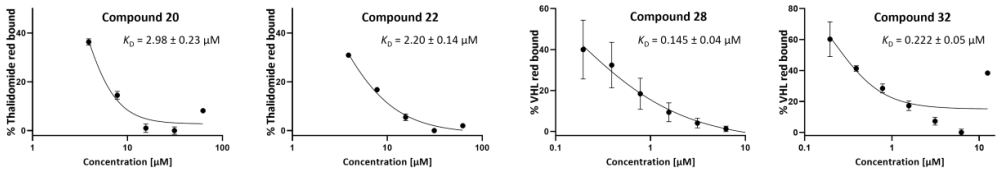


Figure S3: Supplementary Time-Resolved Fluorescence (HTRF) assay results for compounds **20**, **22**, **28**, and **32.** Each experiment was carried out in triplicate. The ligand PROTACs were titrated using an HTRF Human VHL Binding Kit (Revvity) or an HTRF Human Cereblon Binding Kit (Revvity) to determine the apparent dissociation constant, as specified in the experimental section.

Supplementary Western blots (screening results)

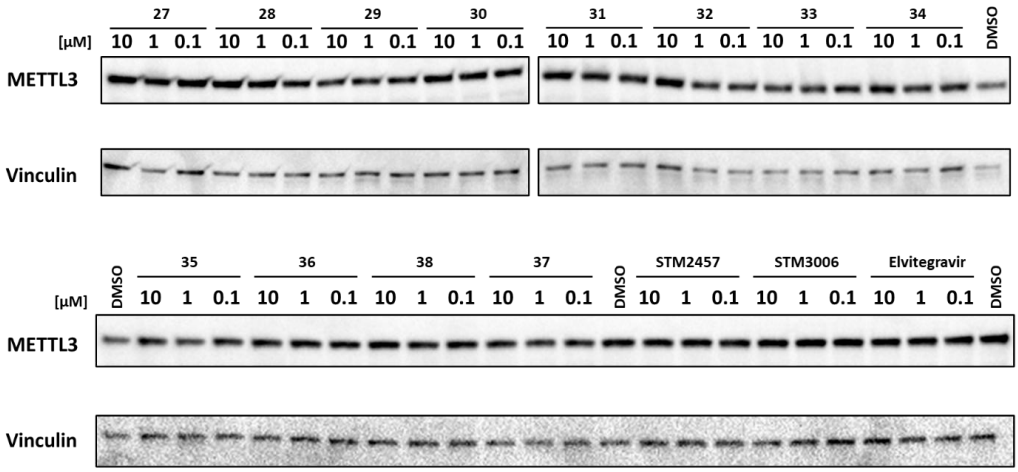


Figure S4: Western blot screening results of PROTAC candidates from the 2nd and the 3rd generation designs. MOLM-13 cells were treated with the indicated compounds at varying concentrations (10 µM, 1 µM, and 0.1 µM) for 16 h. DMSO was used as a negative control. None of the compounds showed significant degradation of METTL3. The METTL3 inhibitors STM2457[3] (Cayman Chemicals), STM3006[4] (BLDpharm), and Elvitegravir[5] (MedChemExpress), were used as conditional controls to prove that competitive METTL3 inhibitors do not function as METTL3 degraders. Shown is a representative Western blot image of two independent experiments.

Supplementary data on biophysical investigation of ternary complexes

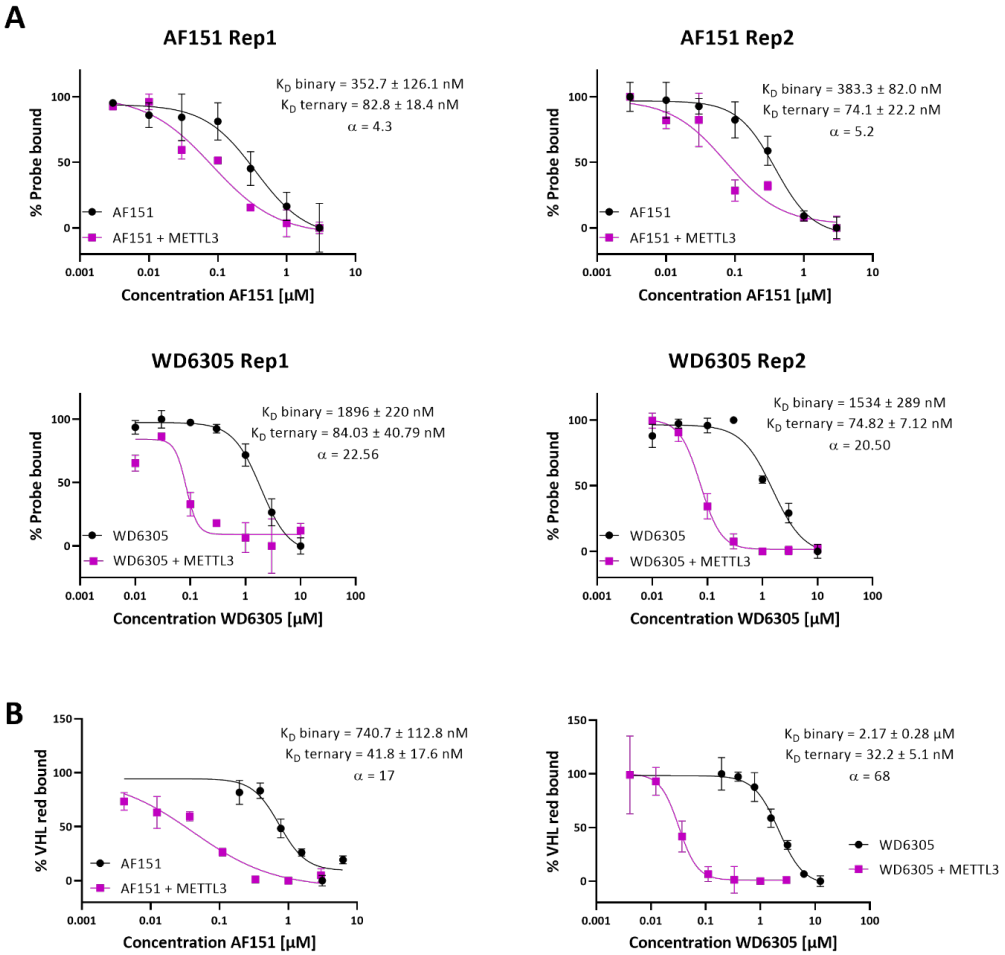


Figure S5. Supplementary data for ternary complex investigation. (**A**) FP dose-response curves for ternary affinity determination of **AF151** and WD6305. Each experiment was carried out in triplicate on two non-consecutive days (Rep1 & Rep2). PROTACs were titrated to 40 nM VCB complex and 10 nM displacement probe to determine the apparent dissociation constant, as specified in the experimental section. For ternary K_D determinations, METTL3/14 was added in near-saturating concentrations relative to the highest PROTAC concentration. (**B**) Homogeneous Time-Resolved Fluorescence (HTRF) assay results for **AF151** and WD6305. Each experiment was carried out in triplicate. The ligand PROTACs were titrated using an HTRF Human VHL Binding Kit (Revvity) to determine the apparent dissociation constant, as specified in the experimental section. For ternary K_D determinations, METTL3/14 was added in near-saturating concentrations relative to the highest PROTAC concentration.

Molecular dynamics simulations

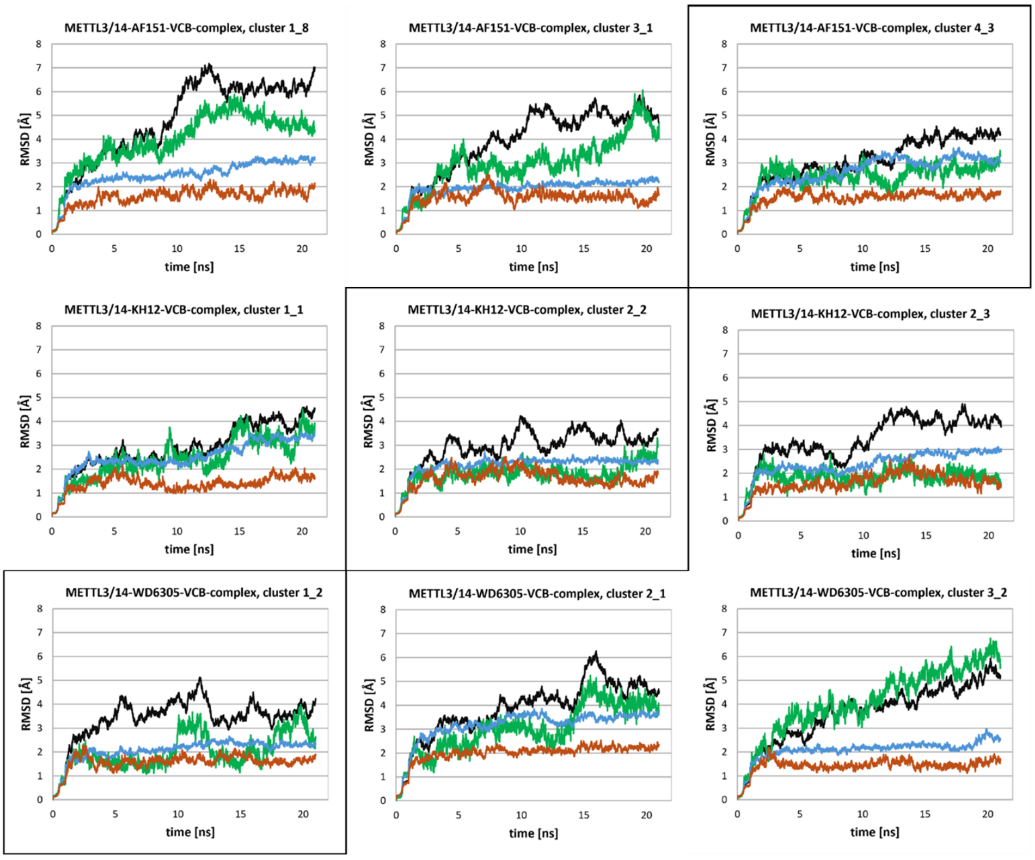


Figure S6: MD simulation RMSD-analysis of ternary METTL3/14-PROTAC-VCB complexes over 1 ns equilibration and 20 ns production. PROTACs **41** (**AF151**), KH12[6] and WD6305[1] were investigated. Complex protein backbone RMSD in Å is depicted in black, METTL3/14 in blue, VCB in orange, and ligand heavy atoms (non-hydrogen) in green. For complex and ligand RMSD, aligned complexes were evaluated, while for internal stability of METTL3/14 and VCB, alignment was performed on the respective target or VCB part. The best-scoring cluster representatives of ternary structures from PROTAC-docking were used as starting structures for MD simulations. In WD6305-complex cluster 1_2, the increased ligand RMSD values are caused by a flip of the phenyl linker. Structures for which MD simulations were prolonged to 100 ns production (Figure S7) are highlighted by a black border.

Table S2: 1A-MM-GBSA analysis of PROTAC-docking generated ternary complexes from 20 ns MD simulations. T: target (METTL3/14), P: PROTAC, E: E3 ligase (VCB). Binding free energy of ternary complex ΔGcomplex = $\Delta G_{T-P} + \Delta G_{TP-E} = \Delta G_{E-P} + \Delta G_{EP-T} = \Delta G_{T-E} + \Delta G_{TE-P}$ according to main manuscript Figure 3D. MM-GBSA scores are in kcal/mol.

	AF151 1_8	**AF151 3_1**	**AF151 4_3**	**KH12 1_1**	**KH12 2_2**	**KH12 2_3**	**WD6305 1_2**	**WD6305 2_1**	**WD6305 3_2**
ΔG_{TE-P}	-129.2	-136.2	-143.1	-150.5	-170.1	-154.7	-152.5	-161.1	-167.1
ΔG_{TP-E}	-68.3	-62.9	-72.3	-66.6	-67.5	-71.9	-70.3	-47.9	-61.6
ΔG_{EP-T}	-89.7	-92.0	-120.0	-123.2	-121.4	-111.6	-116.1	-100.9	-124.9
ΔG_{T-E}	-9.6	-5.5	-18.8	-13.6	-3.6	-9.2	-12.5	+9.7	-6.1
ΔG_{T-P}	-70.5	-62.9	-89.6	-97.5	-106.1	-91.9	-94.7	-103.6	-111.6
ΔG_{E-P}	-49.1	-49.6	-41.9	-41.0	-52.2	-52.2	-48.9	-50.5	-48.3
$\Delta G_{complex}$	-138.8	-141.7	-161.9	-164.1	-173.6	-163.9	-165.0	-151.4	-173.2

Table S3: 1A-MM-GBSA analysis of ternary complexes from 50 ns and 100 ns MD simulations, respectively. T: target (METTL3/14), P: PROTAC, E: E3 ligase (VCB). Binding free energy of ternary complex ΔGcomplex = $\Delta G_{T-P} + \Delta G_{TP-E} = \Delta G_{E-P} + \Delta G_{EP-T} = \Delta G_{T-E} + \Delta G_{TE-P}$ according to main manuscript Figure 3D. MM-GBSA scores are in kcal/mol.

	50 ns			**100 ns**		
	AF151 4_3	**KH12 2_2**	**WD6305 1_2**	**AF151 4_3**	**KH12 2_2**	**WD6305 1_2**
ΔG_{TE-P}	-146.4	-167.1	-146.1	-147.1	-166.6	-147.9
ΔG_{TP-E}	-77.8	-67.9	-64.4	-77.3	-67.5	-70.3
ΔG_{EP-T}	-123.4	-119.7	-105.7	-122.2	-118.1	-111.3
ΔG_{T-E}	-21.5	-4.7	-8.2	-20.3	-4.3	-13.1
ΔG_{T-P}	-90.1	-103.9	-90.0	-90.1	-103.3	-90.7
ΔG_{E-P}	-44.5	-52.1	-48.7	-45.3	-52.7	-49.7
$\Delta G_{TP-E} - \Delta G_{E-P}$	-33.3	-15.8	-15.7	-32.1	-14.8	-20.6
$\Delta G_{complex}$	-167.9	-171.8	-154.4	-167.4	-170.8	-161.0

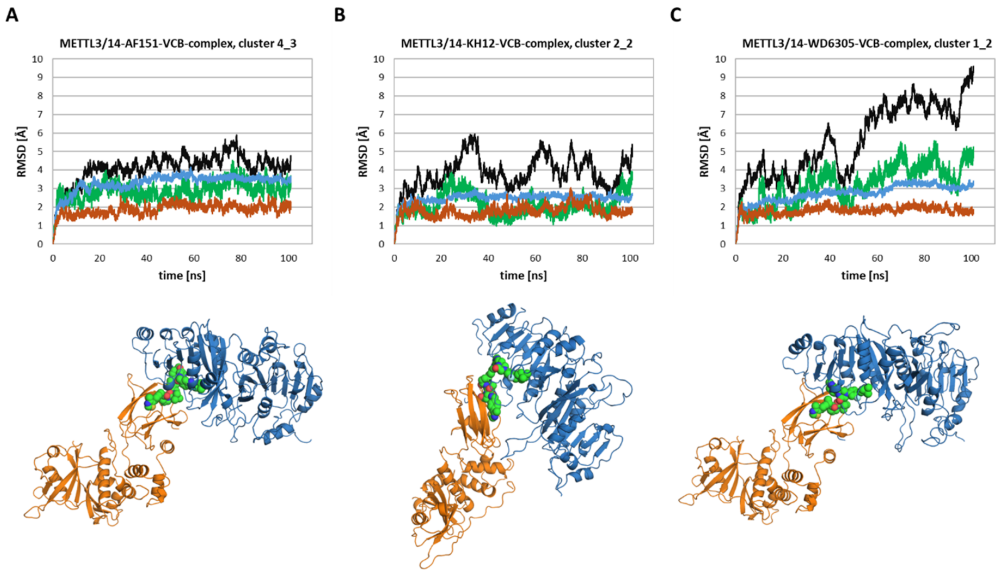


Figure S7: MD-based RMSD-analysis of ternary METTL3/14-PROTAC-VCB complexes over 1 ns equilibration and 100 ns production. Complex protein backbone RMSD in Å is depicted in black, METTL3/14 in blue, VCB in orange, and ligand heavy atoms (non-hydrogen) in green. For complex and ligand RMSD in Å, aligned complexes were evaluated, while for internal stability of METTL3/14 and VCB, alignment was performed on the respective target or VCB part. (**A**) prolonged simulation of **AF151-**complex, cluster 4_3, (**B**) prolonged simulation of KH12-complex, cluster 2_2, (**C**) prolonged simulation of WD6305-complex, cluster 1_2. The starting structures are depicted below the RMSD traces. METTL3/14 blue, VCB orange, and PROTAC carbon atoms green.

Primer sequences used for RT-qPCR

Table S4. Primers used for quantitative reverse transcription polymerase chain reaction.

Gene	Forward Primer	Reverse Primer
METTL3	TTGTCTCCAACCTTCCGTAGT	CCAGATCAGAGAGGTGGTGTAG
METTL14	GAACACAGAGCTTAAATCCCCA	TGTCAGCTAAACCTACATCCCTG
GAPDH	GGAGCGAGATCCCTCCAAAAT	GGCTGTTGTCATACTTCTCATGG

Uncropped Western blot images

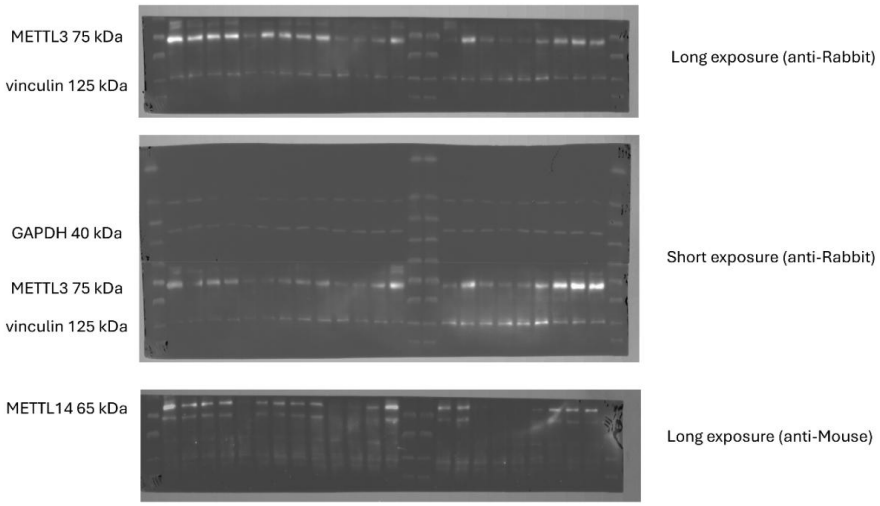


Figure S8: Uncropped images of Figure 2B,C: All data originates from a single blot cut between GAPDH (40 kDa) and METTL3 (75 kDa). For METTL14 ECL detection, the METTL3-detected slice was incubated with mouse anti-METTL14 antibody and anti-Mouse-HRP after the inactivation of anti-Rabbit-HRP with 0.05% sodium azide.

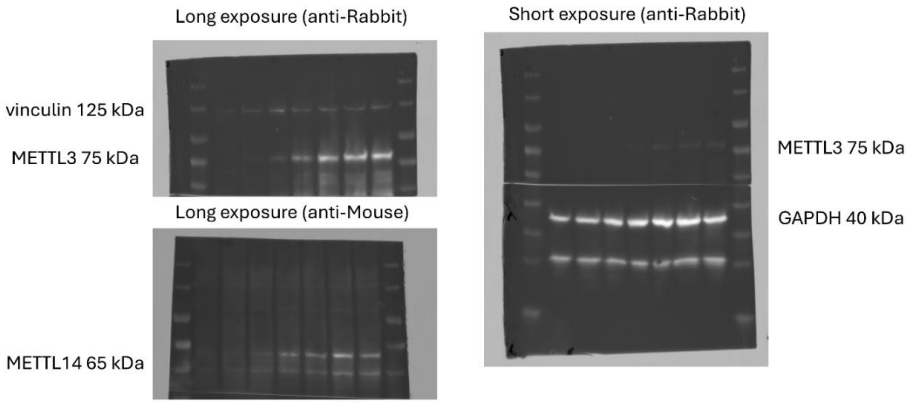


Figure S9: Uncropped images of Figure 2D: All data originates from a single blot cut between GAPDH (40 kDa) and METTL3 (75 kDa). For METTL14 ECL detection, the METTL3-detected slice was incubated with mouse anti-METTL14 antibody and anti-Mouse-HRP after the inactivation of anti-Rabbit-HRP with 0.05% sodium azide.

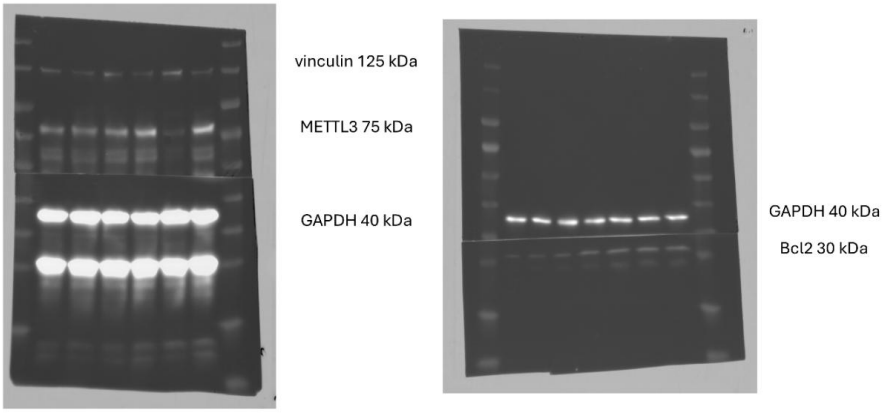


Figure S10: Uncropped images of Figures 2E&4E: Data originates from single blots cut between GAPDH (40 kDa) and METTL3 (75 kDa) for Figure 2E and GAPDH (40 kDa) and Bcl2 (30 kDa) for Figure 4E.

References

1 W. Du, Y. Huang, X. Chen, Y. Deng, Y. Sun, H. Yang, Q. Shi, F. Wu, G. Liu, H. Huang, J. Ding, X. Huang and S. Xu, *Cell chemical biology*, 2024, **31**, 177-183.

2 J. L. Meidner, A. F. Frey, R. A. Zimmermann, M. O. Sabin, Z. Nidoieva, A. C. Weldert, S. N. Hoba, M. W. Krone and F. Barthels, *Angewandte Chemie (International ed. in English)*, 2024, **63**, e202403792.

3 E. Yankova, W. Blackaby, M. Albertella, J. Rak, E. de Braekeleer, G. Tsagkogeorga, E. S. Pilka, D. Aspris, D. Leggate, A. G. Hendrick, N. A. Webster, B. Andrews, R. Fosbeary, P. Guest, N. Irigoyen, M. Eleftheriou, M. Gozdecka, J. M. L. Dias, A. J. Bannister, B. Vick, I. Jeremias, G. S. Vassiliou, O. Rausch, K. Tzelepis and T. Kouzarides, *Nature*, 2021, **593**, 597–601.

4 A. A. Guirguis, Y. Ofir-Rosenfeld, K. Knezevic, W. Blackaby, D. Hardick, Y.-C. Chan, A. Motazedian, A. Gillespie, D. Vassiliadis, E. Y. N. Lam, K. Tran, B. Andrews, M. E. Harbour, L. Vasiliauskaite, C. J. Saunders, G. Tsagkogeorga, A. Azevedo, J. Obacz, E. S. Pilka, M. Carkill, L. MacPherson, E. N. Wainwright, B. Liddicoat, B. J. Blyth, M. R. Albertella, O. Rausch and M. A. Dawson, *Cancer discovery*, 2023, **13**, 2228–2247.

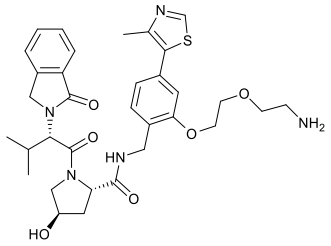
5 L. Liao, Y. He, S.-J. Li, G.-G. Zhang, W. Yu, J. Yang, Z.-J. Huang, C.-C. Zheng, Q.-Y. He, Y. Li and B. Li, *Cancer research*, 2022, **82**, 2444–2457.

6 K. Hwang, J. Bae, Y.-L. Jhe, J. Kim, J.-H. Cheong, H.-S. Choi and T. Sim, *European journal of medicinal chemistry*, 2024, **279**, 116843.

Synthesis of E3 ligase recruiters with linker

VHL-RH-based recruiters

General procedure: A mixture of VL-285 phenol (0.1 mmol, 1.0 eq.), Boc-NH-PEG$_n$-OTs (0.1 mmol, 1.0 eq.), and K_2CO_3 (1.0 mmol, 10.0 eq.) in DMF (3 mL) was stirred at 80 °C for 16 h. The solvent was evaporated, and the mixture was purified by RP flash chromatography to afford the desired intermediate. The residue was then resolved in DCM/TFA (2:1) and stirred at RT for 1 h. Evaporation and lyophilization gave the product.

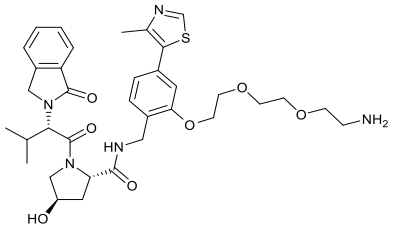


Compound **43**: Yield: 70 mg (94% of th.).

^{1}H NMR: (300 MHz, MeO*D*) δ [ppm] = 9.07 (s, 1H), 7.65 (d, *J* = 7.5 Hz, 1H), 7.51 – 7.31 (m, 5H), 6.98 – 6.92 (m, 2H), 4.72 (d, *J* = 10.9 Hz, 1H), 4.51 – 4.27 (m, 7H), 4.16 – 4.12 (m, 2H), 3.87 – 3.66 (m, 7H), 3.05 (t, *J* = 5.1 Hz, 2H), 2.42 – 2.26 (m, 5H), 2.15 – 2.06 (m, 1H), 1.95 (ddd, *J* = 19.2, 9.7, 5.2 Hz, 1H), 0.91 (d, *J* = 6.4 Hz, 3H), 0.70 (d, *J* = 6.7 Hz, 3H).

^{13}C NMR: (75 MHz, MeOD) δ [ppm] = 174.2, 170.9, 170.7, 157.9, 143.7, 133.2, 132.4, 132.1, 130.0, 129.2, 128.6, 124.4, 123.0, 113.4, 70.8, 70.8, 69.3, 68.1, 60.7, 60.1, 57.1, 40.7, 39.3, 39.1, 30.1, 19.7, 19.0, 15.2.

LC/MS: m/z calculated for $C_{33}H_{41}N_5O_6S$ $[M+H]^+$: 636.3, found: 635.9.

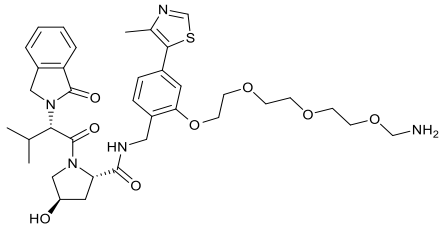


Compound **44**: Yield: 62 mg (78% of th.).

^{1}H NMR: (300 MHz, MeO*D*) δ [ppm] = 9.06 (s, 1H), 7.60 (dt, *J* = 7.6, 1.0 Hz, 1H), 7.46 – 7.36 (m, 2H), 7.35 – 7.25 (m, 2H), 6.90 (dq, *J* = 3.4, 1.6 Hz, 2H), 4.67 (d, *J* = 10.9 Hz, 1H), 4.49 – 4.21 (m, 6H), 4.13 – 3.92 (m, 2H), 3.83 (d, *J* = 11.1 Hz, 1H), 3.79 – 3.67 (m, 3H), 3.63 – 3.57 (m, 2H), 3.56 – 3.48 (m, 4H), 2.93 (t, *J* = 5.1 Hz, 2H), 2.35 (s, 3H), 2.26 (dt, *J* = 10.8, 6.5 Hz, 1H), 2.05 (dd, *J* = 12.9, 8.0 Hz, 1H), 1.88 (ddd, *J* = 13.3, 9.1, 4.4 Hz, 1H), 0.87 (d, *J* = 6.5 Hz, 3H), 0.65 (d, *J* = 6.6 Hz, 3H).

^{13}C NMR: (75 MHz, MeOD) δ [ppm] = 174.2, 171.0, 170.7, 161.1, 160.6, 158.1, 154.1, 147.0, 143.8, 134.8, 133.3, 132.4, 131.8, 130.0, 129.2, 128.9, 124.4, 123.0, 113.6, 71.7, 71.3, 69.3, 67.9, 60.7, 60.1, 57.2, 40.7, 39.4, 39.1, 30.1, 19.7, 19.0, 15.0.

LC/MS: m/z calculated for $C_{35}H_{45}N_5O_7S$ $[M+H]^+$: 680.3, found: 680.1.

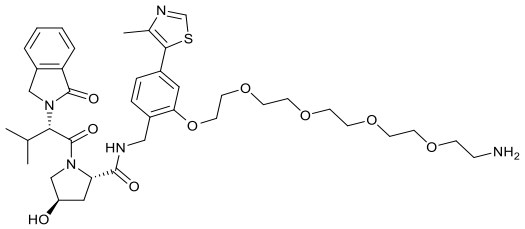


Compound **45**: Yield: 66 mg (79% of th.).

^{1}H NMR: (300 MHz, MeO*D*) δ [ppm] = 9.09 (s, 1H), 7.53 (d, *J* = 7.6 Hz, 1H), 7.40 – 7.29 (m, 2H), 7.24 (dd, *J* = 8.5, 6.3 Hz, 2H), 6.88 – 6.74 (m, 2H), 4.60 (d, *J* = 10.9 Hz, 1H), 4.42 – 4.15 (m, 6H), 4.00 (dd, *J* = 5.8, 3.3 Hz, 2H), 3.79 – 3.60 (m, 4H), 3.51 (dd, *J* = 6.2, 3.1 Hz, 2H), 3.47 – 3.31 (m, 9H), 2.85 (t, *J* = 4.9 Hz, 2H), 2.30 (s, 4H), 1.99 (dd, *J* = 13.4, 7.9 Hz, 1H), 1.82 (ddd, *J* = 13.3, 9.0, 4.5 Hz, 1H), 0.80 (d, *J* = 6.5 Hz, 3H), 0.58 (d, *J* = 6.5 Hz, 3H).

^{13}C NMR: (75 MHz, MeOD) δ [ppm] = 174.3, 171.0, 170.6, 158.1, 154.4, 146.4, 143.8, 135.1, 133.3, 132.4, 131.4, 130.1, 129.2, 129.1, 124.4, 122.9, 118.9, 117.9, 113.6, 71.7, 71.5, 71.2, 70.8, 70.8, 69.4, 67.8, 60.7, 60.1, 57.2, 40.6, 39.4, 39.1, 31.1, 30.1, 19.7, 19.0, 14.7.

LC/MS: m/z calculated for $C_{37}H_{49}N_5O_8S$ $[M+H]^+$: 724.3, found: 724.0.

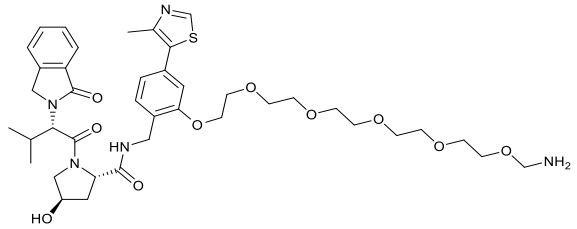


Compound **46**: Yield: 67 mg (76% of th.).

^{1}H NMR: (300 MHz, MeO*D*) δ [ppm] = 9.07 (s, 1H), 7.58 – 7.48 (m, 1H), 7.40 – 7.28 (m, 2H), 7.24 (ddd, *J* = 7.1, 4.7, 2.0 Hz, 2H), 6.87 – 6.75 (m, 2H), 4.60 (d, *J* = 10.9 Hz, 1H), 4.43 – 4.16 (m, 6H), 4.04 – 3.93 (m, 2H), 3.76 (d, *J* = 11.3 Hz, 1H), 3.71 – 3.59 (m, 3H), 3.51 (dt, *J* = 3.8, 2.3 Hz, 2H), 3.46 – 3.31 (m, 13H), 2.85 (t, *J* = 5.1 Hz, 2H), 2.30 (s, 3H), 2.19 (dt, *J* = 10.9, 6.5 Hz, 1H), 2.03 – 1.92 (m, 1H), 1.82 (ddd, *J* = 13.3, 9.0, 4.5 Hz, 1H), 0.80 (d, *J* = 6.5 Hz, 3H), 0.58 (d, *J* = 6.6 Hz, 3H).

^{13}C NMR: (75 MHz, MeOD) δ [ppm] = 174.2, 170.9, 170.6, 161.1, 160.6, 158.1, 154.4, 146.5, 143.7, 135.0, 133.3, 132.4, 131.5, 130.1, 129.2, 129.1, 124.4, 123.0, 118.9, 115.1, 113.7, 71.7, 71.4, 71.3, 71.1, 70.8, 70.8, 69.4, 67.8, 60.7, 60.1, 57.1, 40.6, 39.4, 39.1, 30.1, 19.7, 19.0, 14.8.

LC/MS: m/z calculated for $C_{39}H_{53}N_5O_9S$ $[M+H]^+$: 768.4, found: 768.0.



Compound **47**: Yield: 62 mg (67% of th.).

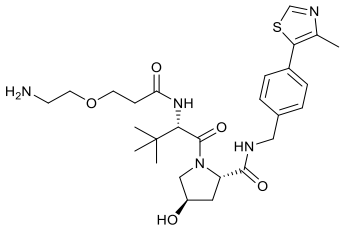
^{1}H NMR: (300 MHz, MeO*D*) δ [ppm] = 9.06 (s, 1H), 7.57 (d, *J* = 7.7 Hz, 1H), 7.44 – 7.33 (m, 2H), 7.28 (dt, *J* = 7.3, 3.7 Hz, 2H), 6.92 – 6.79 (m, 2H), 4.64 (d, *J* = 10.9 Hz, 1H), 4.47 – 4.20 (m, 6H), 4.05 (t, *J* = 4.3 Hz, 2H), 3.87 – 3.64 (m, 4H), 3.59 – 3.52 (m, 2H), 3.50 – 3.35 (m, 17H), 2.90 (t, *J* = 5.1 Hz, 2H), 2.33 (s, 3H), 2.28 – 2.17 (m, 1H), 2.06 – 1.81 (m, 2H), 0.84 (d, *J* = 6.5 Hz, 3H), 0.62 (d, *J* = 6.7 Hz, 3H).

^{13}C NMR: (75 MHz, MeOD) δ [ppm] = 174.2, 170.9, 170.6, 161.1, 160.6, 158.1, 154.2, 146.9, 143.8, 134.8, 133.3, 132.4, 131.7, 130.1, 129.2, 129.0, 124.4, 124.4, 123.0, 113.7, 71.6, 71.4, 71.3, 71.3, 71.2, 71.1, 70.8, 70.7, 69.4, 67.8, 60.7, 60.1, 57.1, 40.5, 39.4, 39.1, 30.1, 19.7, 19.0, 14.9.

LC/MS: m/z calculated for $C_{41}H_{57}N_5O_{10}S$ $[M+H]^+$: 812.4, found: 812.2.

VHL-LH-based recruiters

General procedure: VH032-amine (0.05 mmol, 1.0 eq.), TBTU (0.05 mmol, 1.0 eq.), and Boc-NH-PEG$_n$-COOH (0.05 mmol, 1.0 eq.) were solved in DMF (1 mL), and DIPEA (0.15 mmol, 3.0 eq.) was added. The suspension was stirred at RT for 16 h. The suspension was then concentrated under reduced pressure, purified by RP flash chromatography, and lyophilized. The resulting solid was resolved in dichloromethane (1 ml) and TFA (1 ml) and stirred at RT for 1 h. Evaporation and lyophilization gave the product.

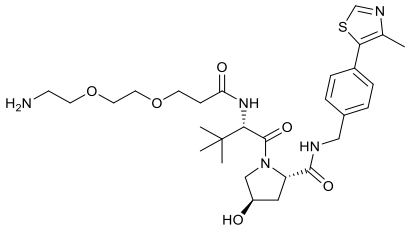


Compound **48**: Yield: 47 mg (quant.).

^{1}H NMR: (300 MHz, MeO*D*) δ [ppm] = 9.08 (s, 1H), 7.56 – 7.41 (m, 1H), 7.34 – 7.22 (m, 5H), 4.44 – 4.29 (m, 4H), 4.21 (d, *J* = 15.6 Hz, 1H), 3.65 – 3.43 (m, 6H), 2.94 (t, *J* = 5.1 Hz, 2H), 2.33 (s, 3H), 2.06 (ddt, *J* = 11.3, 7.6, 1.9 Hz, 1H), 1.91 (ddd, *J* = 13.3, 9.2, 4.3 Hz, 1H), 1.29 – 1.12 (m, 3H), 0.86 (s, 9H), 0.79 – 0.70 (m, 2H).

^{13}C NMR: (75 MHz, MeOD) δ [ppm] = 174.4, 173.9, 172.4, 154.2, 141.0, 132.4, 130.4, 130.3, 129.1, 71.1, 69.1, 67.9, 67.4, 60.9, 59.4, 58.0, 49.9, 49.6, 49.3, 49.0, 48.7, 48.4, 48.2, 43.7, 40.4, 40.2, 39.0, 36.7, 36.5, 31.6, 30.1, 27.0, 24.9, 24.0, 14.8, 14.4, 11.4.

LC/MS: m/z calculated for $C_{27}H_{39}N_5O_5S$ $[M+H]^+$: 546.3, found: 546.4.

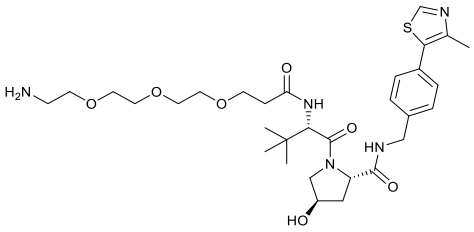


Compound **49**: Yield: 36 mg (quant.).

^{1}H NMR: (300 MHz, MeO*D*) δ [ppm] = 9.12 (s, 1H), 7.55 – 7.40 (m, 1H), 7.34 – 7.23 (m, 4H), 4.48 – 4.28 (m, 4H), 4.21 (d, *J* = 15.5 Hz, 1H), 3.65 – 3.42 (m, 9H), 2.92 (t, *J* = 5.0 Hz, 2H), 2.33 (s, 3H), 2.11 – 1.84 (m, 2H), 1.26 – 1.08 (m, 4H), 0.85 (s, 9H), 0.78 – 0.69 (m, 3H).

^{13}C NMR: (75 MHz, MeOD) δ [ppm] = 173.1, 172.3, 170.9, 152.9, 139.7, 132.2, 131.0, 129.0, 128.8, 127.8, 69.9, 69.9, 69.7, 67.7, 66.7, 66.4, 59.5, 57.7, 56.6, 48.5, 48.2, 47.9, 47.6, 47.3, 47.0, 46.8, 42.3, 39.2, 38.8, 37.7, 35.6, 35.3, 30.2, 28.7, 25.6, 23.5, 22.6, 13.3, 13.0, 10.0.

LC/MS: m/z calculated for $C_{29}H_{43}N_5O_6S$ $[M+H]^+$: 590.3, found: 589.9.

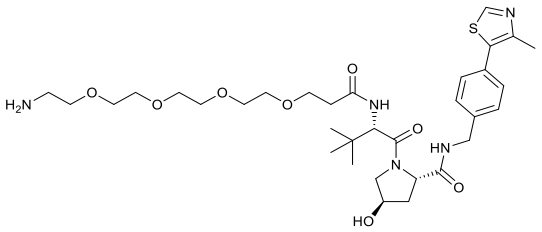


Compound **50**: Yield: 48 mg (quant.).

^{1}H NMR: (300 MHz, MeO*D*) δ [ppm] = 9.03 (s, 1H), 7.67 – 7.51 (m, 1H), 7.38 (q, *J* = 8.5 Hz, 4H), 4.56 (s, 1H), 4.52 – 4.48 (m, 1H), 4.43 (d, *J* = 4.2 Hz, 1H), 4.14 (dd, *J* = 5.7, 1.3 Hz, 1H), 3.83 (d, *J* = 11.1 Hz, 1H), 3.68 – 3.51 (m, 12H), 3.05 (t, *J* = 5.0 Hz, 2H), 2.42 (s, 3H), 2.21 – 2.10 (m, 1H), 2.01 (ddd, *J* = 13.3, 9.2, 4.4 Hz, 1H), 1.31 – 1.22 (m, 4H), 0.97 (s, 9H), 0.90 – 0.81 (m, 4H).

^{13}C NMR: (75 MHz, MeOD) δ [ppm] = 174.4, 173.8, 172.2, 169.3, 153.6, 140.7, 133.6, 132.4, 130.9, 130.4, 129.9, 129.1, 117.9, 114.1, 71.5, 71.4, 71.2, 71.1, 69.1, 68.3, 67.8, 60.9, 59.1, 58.0, 43.7, 40.6, 40.2, 39.0, 37.1, 36.7, 31.6, 30.1, 27.0, 24.9, 24.0, 15.3, 14.4, 11.4.

LC/MS: m/z calculated for $C_{31}H_{47}N_5O_7S$ $[M+H]^+$: 634.3, found: 634.0.

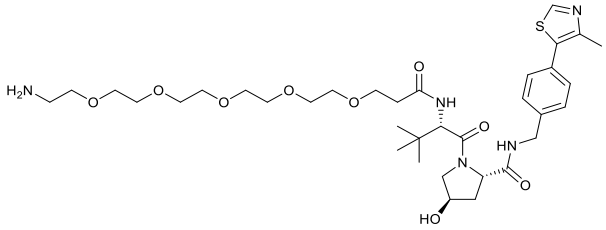


Compound **51**: Yield: 36 mg (91% of th.).

^{1}H NMR: (300 MHz, MeO*D*) δ [ppm] = 9.78 (s, 1H), 8.50 – 8.42 (m, 1H), 8.21 – 8.13 (m, 4H), 4.45 – 4.24 (m, 19H), 3.94 (s, 2H), 3.75 (h, *J* = 4.9, 4.3 Hz, 2H), 3.22 (s, 3H), 2.88 – 2.78 (m, 1H), 2.68 (ddd, *J* = 12.9, 8.6, 4.5 Hz, 1H), 2.17 – 1.97 (m, 3H), 1.71 (s, 9H), 1.63 (td, *J* = 7.2, 4.3 Hz, 3H).

^{13}C NMR: (75 MHz, MeOD) δ [ppm] = 181.7, 179.9, 179.2, 176.7, 161.3, 149.2, 141.4, 141.3, 139.2, 138.3, 137.1, 79.4, 79.3, 79.1, 78.6, 77.1, 76.6, 76.3, 68.4, 66.1, 58.3, 51.3, 47.8, 47.6, 45.3, 45.1, 39.5, 38.0, 32.9, 32.1, 25.5, 23.5, 20.4.

LC/MS: m/z calculated for $C_{33}H_{51}N_5O_8S$ $[M+H]^+$: 678.4, found: 678.2.



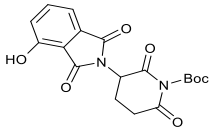
Compound **52**: Yield: 40 mg (96% of th.).

^{1}H NMR (300 MHz, MeO*D*) δ [ppm] = 9.09 (s, 1H), 7.67 – 7.59 (m, 1H), 7.57 – 7.49 (m, 1H), 7.37 (q, *J* = 8.4 Hz, 4H), 4.56 – 4.39 (m, 4H), 4.28 (d, *J* = 15.6 Hz, 1H), 3.71 – 3.47 (m, 22H), 2.41 (s, 3H), 2.15 (dd, *J* = 13.4, 7.6 Hz, 1H), 1.99 (ddd, *J* = 13.3, 9.3, 4.3 Hz, 1H), 1.24 (tt, *J* = 9.0, 3.9 Hz, 3H), 0.95 (s, 9H), 0.82 (dd, *J* = 8.1, 6.6 Hz, 3H).

^{13}C NMR (75 MHz, MeOD) δ [ppm] = 174.4, 173.8, 172.2, 169.3, 140.8, 133.5, 132.4, 130.6, 130.4, 129.8, 129.1, 71.4, 71.4, 71.3, 71.2, 71.2, 71.1, 71.1, 70.9, 69.1, 68.2, 67.9, 60.8, 43.7, 40.1, 39.0, 36.9, 36.6, 31.6, 30.1, 27.0, 24.9, 24.0, 15.1, 14.4, 11.4.

LC/MS: m/z calculated for $C_{35}H_{55}N_5O_9S$ $[M+H]^+$: 722.4, found: 722.2.

4-Thalidomide-based recruiters



Compound **53**: 4-Hydroxythalidomide (600 mg, 2.19 mmol, 1.0 eq.) was combined with DMAP (268 mg, 2.19 mmol, 1.0 eq.) in 1,4-Dioxane (10 mL), followed by the addition of Boc-anhydride (960 mg, 4.4 mmol, 2.0 eq.). The reaction mixture was stirred at RT for 1 h. Piperidine (0.22 mL, 2.19 mmol, 1.0 eq.) was added, and the mixture was stirred for 1 h. Afterward, the reaction mixture was partitioned between 1 M HCl and EtOAc. The organic phase was filtered over silica, followed by column chromatography (CH/EA 1:1) purification to give the product as a colorless solid.

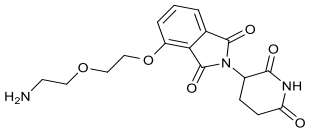
Yield: 510 mg (62% of th.).

^{1}H NMR: (300 MHz, Me*O*D) δ [ppm] = 7.90 (s, 1H), 7.65 (td, *J* = 7.8, 7.2, 1.3 Hz, 1H), 7.37 (d, *J* = 7.1 Hz, 1H), 7.20 (d, *J* = 8.4 Hz, 1H), 5.22 (dd, *J* = 12.7, 5.4 Hz, 1H), 3.07 – 2.68 (m, 3H), 2.20 – 2.08 (m, 1H), 1.55 (s, 9H).

^{13}C NMR: (75 MHz, MeOD) δ [ppm] = 171.3, 168.8, 168.6, 156.9, 137.6, 134.5, 124.6, 116.0, 87.5, 79.5, 50.3, 32.2, 27.7, 22.9.

LC/MS: m/z calculated for $C_{18}H_{18}N_2O_7$ $[M - Boc+H]^+$: 275.1, found: 274.9.

General Procedure: A mixture of **53** (0.1 mmol, 1.0 eq.), Boc-NH-PEG_n-OTs (0.1 mmol, 1.0 eq.), and K_2CO_3 (0.3 mmol, 3.0 eq.) in DMF (1 mL) was agitated at 80 °C for 3 h. The solvent was evaporated, and the mixture was purified by RP flash chromatography to afford the desired intermediate. The intermediate was then resolved in DCM/TFA (2:1) and stirred at RT for 1 h. Evaporation and lyophilization gave the product.

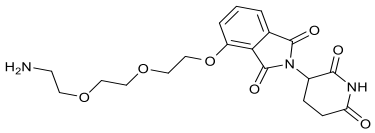


Compound **54**: Yield: 3 mg (6% of th.).

^{1}H NMR: (300 MHz, Me*O*D) δ [ppm] = 7.73 (dd, *J* = 8.5, 7.4 Hz, 1H), 7.44 – 7.37 (m, 2H), 5.05 (dd, *J* = 12.4, 5.4 Hz, 1H), 4.36 – 4.30 (m, 2H), 3.94 – 3.86 (m, 2H), 3.84 – 3.78 (m, 2H), 3.12 (t, *J* = 5.0 Hz, 2H), 2.89 – 2.57 (m, 3H), 2.11 – 2.02 (m, 1H), 1.32 – 0.73 (m, 2H).

^{13}C NMR: (75 MHz, MeOD) δ [ppm] = 174.6, 171.5, 168.5, 167.9, 157.5, 138.2, 135.0, 120.6, 118.2, 116.9, 70.2, 68.2, 50.5, 40.6, 32.2, 23.6.

LC/MS: m/z calculated for $C_{17}H_{19}N_3O_6$ $[M+H]^+$: 362.1, found: 362.0.

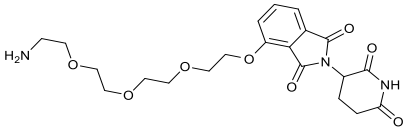


Compound **55**: Yield: 17 mg (33% of th.).

^{1}H NMR: (300 MHz, MeO*D*) δ [ppm] = 7.81 – 7.71 (m, 1H), 7.49 – 7.40 (m, 2H), 5.08 (dd, *J* = 12.4, 5.4 Hz, 1H), 4.43 – 4.32 (m, 2H), 3.95 – 3.87 (m, 2H), 3.77 (dt, *J* = 4.6, 3.1 Hz, 2H), 3.73 – 3.63 (m, 4H), 3.08 (t, *J* = 5.0 Hz, 2H), 2.92 – 2.59 (m, 3H), 2.15 – 2.04 (m, 1H), 1.44 – 0.77 (m, 1H).

^{13}C NMR: (75 MHz, MeOD) δ [ppm] = 174.5, 171.6, 168.5, 167.6, 157.6, 138.1, 135.1, 120.7, 118.3, 116.8, 72.0, 71.2, 70.3, 70.2, 67.9, 50.4, 40.7, 32.2, 23.7.

LC/MS: m/z calculated for $C_{19}H_{23}N_3O_7$ $[M+H]^+$: 406.2, found: 406.0.

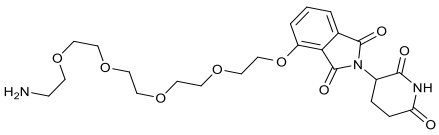


Compound **56**: Yield: 31 mg (55% of th.).

^{1}H NMR: (300 MHz, MeO*D*) δ [ppm] = 7.79 – 7.69 (m, 1H), 7.47 – 7.38 (m, 2H), 5.13 – 5.00 (m, 1H), 4.43 – 4.29 (m, 2H), 3.89 (p, *J* = 2.7 Hz, 2H), 3.76 – 3.70 (m, 2H), 3.69 – 3.57 (m, 8H), 3.07 (t, *J* = 5.1 Hz, 2H), 2.92 – 2.56 (m, 3H), 2.09 (dtd, *J* = 13.3, 5.4, 2.5 Hz, 1H), 1.37 – 0.79 (m, 1H).

^{13}C NMR: (75 MHz, MeOD) δ [ppm] = 174.6, 171.6, 168.4, 168.1, 157.6, 138.2, 135.0, 120.7, 118.2, 116.9, 71.6, 71.4, 71.3, 70.7, 70.3, 67.7, 50.5, 40.5, 32.1, 23.7.

LC/MS: m/z calculated for $C_{21}H_{27}N_3O_8$ $[M+H]^+$: 450.2, found: 450.1.

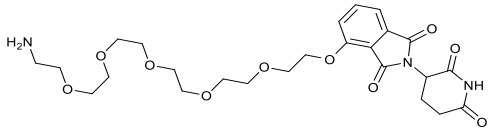


Compound **57**: Yield: 29 mg (48% of th.).

^{1}H NMR: (300 MHz, MeO*D*) δ [ppm] = 7.72 (dd, *J* = 8.6, 7.2 Hz, 1H), 7.45 – 7.38 (m, 2H), 5.04 (dd, *J* = 12.4, 5.5 Hz, 1H), 4.34 (t, *J* = 4.3 Hz, 2H), 4.19 – 4.09 (m, 2H), 3.91 – 3.83 (m, 2H), 3.74 – 3.69 (m, 2H), 3.67 – 3.53 (m, 12H), 3.07 (t, *J* = 5.0 Hz, 2H), 2.87 – 2.54 (m, 3H), 2.14 – 2.00 (m, 1H), 1.60 (q, *J* = 6.0 Hz, 1H).

^{13}C NMR: (75 MHz, MeOD) δ [ppm] = 173.2, 170.1, 167.9, 167.0, 156.2, 136.8, 133.7, 132.2, 131.0, 128.5, 119.5, 116.9, 115.6, 70.4, 70.0, 69.8, 69.5, 69.0, 67.7, 66.5, 49.1, 39.2, 38.8.

LC/MS: m/z calculated for $C_{23}H_{31}N_3O_9$ $[M+H]^+$: 494.2, found: 494.1.



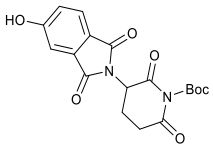
Compound **58**: Yield: 31 mg (48% of th.).

^{1}H NMR: (300 MHz, MeO*D*) δ [ppm] = 7.73 (dd, *J* = 8.6, 7.2 Hz, 1H), 7.41 (d, *J* = 7.7 Hz, 2H), 5.04 (dd, *J* = 12.3, 5.5 Hz, 1H), 4.34 (t, *J* = 4.3 Hz, 2H), 3.91 – 3.85 (m, 2H), 3.76 – 3.70 (m, 2H), 3.66 – 3.51 (m, 16H), 3.10 (t, *J* = 5.2 Hz, 2H), 2.89 – 2.58 (m, 3H), 2.11 – 2.01 (m, 1H).

^{13}C NMR: (75 MHz, MeOD) δ [ppm] = 174.6, 171.4, 168.4, 167.8, 157.5, 138.2, 135.1, 120.8, 118.3, 117.0, 71.5, 71.3, 71.3, 71.2, 71.2, 71.1, 71.0, 70.6, 70.3, 70.1, 67.8, 50.5, 40.7, 32.2, 23.6.

LC/MS: m/z calculated for $C_{25}H_{35}N_3O_{10}$ $[M+H]^+$: 538.2, found: 538.0.

5-Thalidomid-based recruiters



Compound **59**: 5-Hydroxythalidomide (600 mg, 2.19 mmol, 1.0 eq.) was combined with DMAP (268 mg, 2.19 mmol, 1.0 eq.) in 1,4-Dioxane (10 mL), followed by the addition of Boc-anhydride (960 mg, 4.4 mmol, 2.0 eq.). The reaction mixture was then stirred at RT for 1 h. Piperidine (0.22 mL, 2.19 mmol) was added, and the mixture was stirred for 1 h. Afterward, the mixture was partitioned between 1 M HCl and EtOAc, and the organic phase was filtered over silica. Subsequently, purification by column chromatography (CH/EA 1:1) afforded the product as a colorless solid.

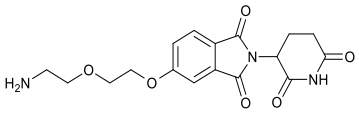
Yield: 531 mg (65% of th.).

^{1}H NMR (300 MHz, MeO*D*) δ [ppm] = 7.73 (d, *J* = 8.2 Hz, 1H), 7.22 (d, *J* = 2.2 Hz, 1H), 7.15 (dd, *J* = 8.2, 2.2 Hz, 1H), 5.24 (dd, *J* = 12.7, 5.3 Hz, 1H), 3.08 – 2.70 (m, 3H), 2.16 (dtd, *J* = 13.1, 5.1, 2.6 Hz, 1H), 2.03 (d, *J* = 4.8 Hz, 1H), 1.54 (s, 9H).

^{13}C NMR: (75 MHz, MeOD) δ [ppm] = 171.3, 168.7, 168.5, 165.1, 149.6, 135.6, 126.6, 123.2, 121.8, 111.2, 87.4, 50.4, 32.2, 28.7, 27.6, 22.8.

LC/MS: m/z calculated for $C_{18}H_{18}N_2O_7$ $[M - Boc+H]^+$: 275.1, found: 274.9.

General Procedure: A mixture of **59** (0.1 mmol, 1.0 eq.), Boc-NH-PEG$_n$-OTs (0.1 mmol, 1.0 eq.), and K_2CO_3 (0.3 mmol, 3.0 eq.) in DMF (1 mL) was agitated at 80 °C for 3 h. The solvent was evaporated, and the mixture was purified by RP flash chromatography to afford the desired intermediate. The intermediate residue was then resolved in DCM/TFA (2:1) and stirred at RT for 1 h. Evaporation and lyophilization gave the product.

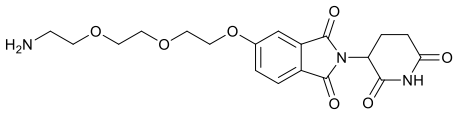


Compound **60**: Yield: 21 mg (44% of th.).

^{1}H NMR: (300 MHz, MeO*D*) δ [ppm] = 7.79 (d, *J* = 8.3 Hz, 1H), 7.40 (d, *J* = 2.3 Hz, 1H), 7.31 (dd, *J* = 8.3, 2.3 Hz, 1H), 5.09 (dd, *J* = 12.4, 5.4 Hz, 1H), 4.35 – 4.29 (m, 2H), 3.95 – 3.88 (m, 2H), 3.77 (dd, *J* = 5.6, 4.5 Hz, 2H), 3.14 (t, *J* = 5.0 Hz, 2H), 2.91 – 2.62 (m, 3H), 2.16 – 2.05 (m, 1H).

^{13}C NMR: (75 MHz, MeOD) δ [ppm] = 174.6, 171.5, 168.6, 168.5, 165.6, 135.7, 126.4, 125.1, 121.5, 110.2, 70.5, 69.6, 68.1, 50.6, 40.6, 32.2, 23.7.

LC/MS: m/z calculated for $C_{17}H_{19}N_3O_6$ $[M+H]^+$: 362.1, found: 362.0.

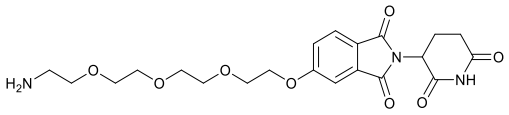


Compound **61**: Yield: 43 mg (83% of th.).

^{1}H NMR: (300 MHz, MeO*D*) δ [ppm] = 7.69 (d, *J* = 8.3 Hz, 1H), 7.32 (d, *J* = 2.3 Hz, 1H), 7.22 (dd, *J* = 8.3, 2.3 Hz, 1H), 4.99 (dd, *J* = 12.4, 5.4 Hz, 1H), 4.23 – 4.17 (m, 2H), 3.84 – 3.76 (m, 2H), 3.67 – 3.56 (m, 6H), 3.00 (t, *J* = 5.0 Hz, 2H), 2.84 – 2.52 (m, 3H), 2.04 (s, 1H), 1.92 (s, 1H), 1.18 (s, 1H).

^{13}C NMR: (75 MHz, MeOD) δ [ppm] = 174.6, 171.5, 168.6, 165.7, 135.7, 126.4, 125.0, 121.6, 110.2, 71.3, 70.6, 69.6, 68.2, 67.9, 50.6, 40.6, 32.2, 24.2, 23.7.

LC/MS: m/z calculated for $C_{19}H_{23}N_3O_7$ $[M+H]^+$: 406.2, found: 406.0.

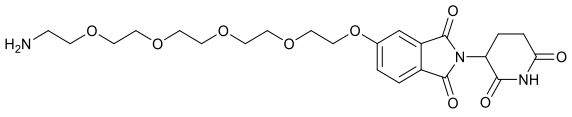


Compound **62**: Yield: 40 mg (71% of th.).

^{1}H NMR: (300 MHz, MeO*D*) δ [ppm] = 7.70 (d, *J* = 8.3 Hz, 1H), 7.33 (d, *J* = 2.2 Hz, 1H), 7.24 (dd, *J* = 8.3, 2.3 Hz, 1H), 5.01 (dd, *J* = 12.4, 5.4 Hz, 1H), 4.25 – 4.19 (m, 2H), 3.84 – 3.76 (m, 2H), 3.66 – 3.53 (m, 10H), 3.02 (t, *J* = 5.0 Hz, 2H), 2.86 – 2.54 (m, 3H), 2.09 – 1.99 (m, 1H).

^{13}C NMR: (75 MHz, MeOD) δ [ppm] = 174.6, 171.5, 168.6, 168.5, 165.8, 135.6, 126.4, 124.9, 121.6, 110.3, 71.6, 71.5, 71.4, 71.2, 70.5, 69.7, 67.8, 50.6, 40.6, 32.2, 23.7.

LC/MS: m/z calculated for $C_{21}H_{27}N_3O_8$ $[M+H]^+$: 450.2, found: 450.0.

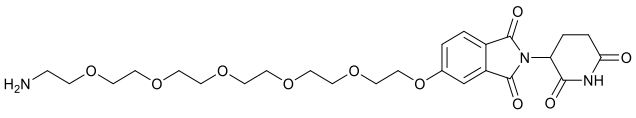


Compound **63**: Yield: 45 mg (74% of th.).

^{1}H NMR: (300 MHz, MeO*D*) δ [ppm] = 7.73 (d, *J* = 8.3 Hz, 1H), 7.35 (d, *J* = 2.2 Hz, 1H), 7.26 (dd, *J* = 8.3, 2.2 Hz, 1H), 5.03 (dd, *J* = 12.4, 5.4 Hz, 1H), 4.27 – 4.21 (m, 2H), 3.86 – 3.79 (m, 2H), 3.68 – 3.55 (m, 14H), 3.04 (t, *J* = 5.0 Hz, 2H), 2.89 – 2.55 (m, 3H), 2.06 (dtd, *J* = 12.7, 4.9, 2.1 Hz, 1H).

^{13}C NMR: (75 MHz, MeOD) δ [ppm] = 174.6, 171.5, 168.6, 168.5, 165.8, 135.7, 126.4, 125.0, 121.6, 110.3, 71.7, 71.4, 71.4, 71.3, 71.1, 70.5, 69.7, 67.8, 50.6, 40.6, 32.2, 23.7.

LC/MS: m/z calculated for $C_{23}H_{31}N_3O_9$ $[M+H]^+$: 494.2, found: 493.9.



Compound **64**: Yield: 53 mg (81% of th.).

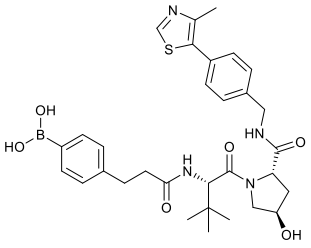
^{1}H NMR: (300 MHz, MeO*D*) δ [ppm] = 7.74 (d, *J* = 8.3 Hz, 1H), 7.38 (d, *J* = 2.2 Hz, 1H), 7.28 (dd, *J* = 8.3, 2.3 Hz, 1H), 5.04 (dd, *J* = 12.4, 5.4 Hz, 1H), 4.29 – 4.22 (m, 2H), 3.88 – 3.81 (m, 2H), 3.70 – 3.50 (m, 19H), 3.06 (t, *J* = 5.0 Hz, 2H), 2.89 – 2.57 (m, 3H), 2.11 – 2.02 (m, 1H).

^{13}C NMR: (75 MHz, MeOD) δ [ppm] = 174.6, 171.5, 168.6, 168.5, 165.7, 135.7, 126.4, 125.0, 121.5, 110.4, 71.6, 71.4, 71.3, 71.2, 70.8, 70.4, 69.6, 67.8, 50.6, 40.5, 32.2, 23.7.

LC/MS: m/z calculated for $C_{25}H_{35}N_3O_{10}$ $[M+H]^+$: 538.2, found: 538.0.

VHL-LH building blocks for Suzuki and Sonogashira reactions

General Procedure: VH032-amine (0.046–0.058 mmol, 1.0 eq.), TBTU (0.046–0.058 mmol, 1.0 eq.), and the respective carboxylic acid (0.046–0.058 mmol, 1.0 eq.) were solved in DMF (1 mL), and then DIPEA (0.14–0.17 mmol, 3.0 eq.) was added. The resulting suspension was stirred at RT for 16 h. The suspension was then concentrated under reduced pressure, purified by RP flash chromatography, and subsequently lyophilized.

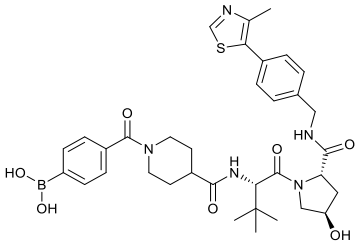


Compound **65**: Yield: 25 mg (71% of th.).

^{1}H NMR: (300 MHz, MeO*D*) δ [ppm] = 9.04 (s, 1H), 7.64 (d, *J* = 7.8 Hz, 1H), 7.44 (q, *J* = 8.3 Hz, 7H), 7.20 (d, *J* = 7.6 Hz, 2H), 4.63 – 4.44 (m, 5H), 4.34 (d, *J* = 15.6 Hz, 1H), 3.88 (d, *J* = 11.0 Hz, 1H), 3.76 (dd, *J* = 11.0, 3.9 Hz, 1H), 2.90 (t, *J* = 7.6 Hz, 2H), 2.59 (dp, *J* = 21.6, 7.6, 7.1 Hz, 2H), 2.48 (s, 4H), 2.28 – 1.95 (m, 3H), 0.94 (s, 9H).

^{13}C NMR: (75 MHz, MeOD) δ [ppm] = 178.6, 174.9, 174.5, 172.3, 153.5, 140.7, 130.9, 130.4, 129.1, 128.7, 71.1, 60.8, 59.1, 58.0, 48.6, 43.7, 38.9, 38.1, 36.5, 32.8, 32.8, 27.0, 15.4, 8.8.

LC/MS: m/z calculated for $C_{31}H_{39}BN_4O_6S$ $[M+H]^+$: 607.3, found: 607.0.

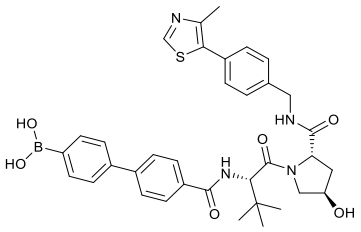


Compound **66**: Yield: 17 mg (43% of th.).

^{1}H NMR: (400 MHz, MeO*D*) δ [ppm] = 8.87 (d, *J* = 2.2 Hz, 1H), 7.82 (d, *J* = 7.7 Hz, 2H), 7.48 – 7.31 (m, 6H), 4.52 (s, 2H), 4.37 (s, 1H), 3.88 (d, *J* = 11.1 Hz, 1H), 3.84 – 3.67 (m, 2H), 2.91 (d, *J* = 12.5 Hz, 1H), 2.72 – 2.64 (m, 1H), 2.47 (d, *J* = 2.3 Hz, 3H), 2.22 (t, *J* = 10.4 Hz, 1H), 2.13 – 2.02 (m, 2H), 1.88 (d, *J* = 21.7 Hz, 1H), 1.70 (d, *J* = 21.3 Hz, 3H), 1.35 – 1.28 (m, 1H), 1.03 (s, 9H).

^{13}C NMR: (101 MHz, MeOD) δ [ppm] = 174.5, 172.7, 172.2, 152.9, 149.0, 140.3, 135.2, 133.4, 131.5, 130.4, 129.0, 126.7, 71.1, 60.8, 58.9, 58.0, 49.6, 49.3, 49.1, 48.9, 48.7, 43.7, 43.4, 38.9, 36.7, 27.0, 15.8.

LC/MS: m/z calculated for $C_{35}H_{44}BN_5O_7S$ $[M+H]^+$: 690.3, found: 690.3.

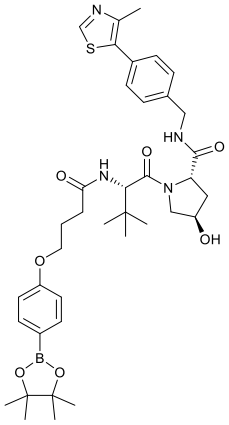


Compound **67**: Yield: 32 mg (quant.).

^{1}H NMR: (300 MHz, MeO*D*) δ [ppm] = 9.04 (s, 1H), 7.98 – 7.82 (m, 3H), 7.81 – 7.62 (m, 6H), 7.54 – 7.40 (m, 5H), 4.62 (dd, *J* = 16.4, 9.1 Hz, 3H), 4.37 (d, *J* = 15.6 Hz, 1H), 4.02 (d, *J* = 11.1 Hz, 1H), 3.90 (dd, *J* = 11.0, 3.8 Hz, 1H), 2.51 (s, 3H), 2.32 – 2.07 (m, 2H), 1.37 – 1.28 (m, 1H), 1.14 (s, 10H), 1.07 – 0.89 (m, 1H).

^{13}C NMR: (75 MHz, MeOD) δ [ppm] = 174.4, 172.4, 169.6, 153.2, 140.5, 131.2, 130.4, 129.1, 129.0, 128.1, 127.3, 71.1, 60.9, 59.4, 58.2, 57.5, 49.4, 49.1, 48.9, 43.7, 39.0, 37.3, 27.1, 15.6.

LC/MS: m/z calculated for $C_{35}H_{39}BN_4O_6S$ $[M+H]^+$: 655.3, found: 654.4.

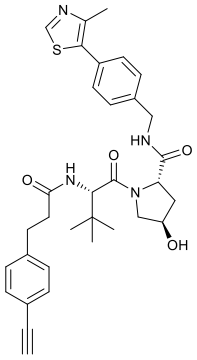


Compound **68**: Yield: 27 mg (65% of th.).

^{1}H NMR: (300 MHz, C*D*Cl$_3$) δ [ppm] = 7.67 – 7.60 (m, 3H), 7.24 – 7.16 (m, 2H), 6.82 – 6.73 (m, 3H), 6.25 (d, *J* = 8.7 Hz, 1H), 4.58 (t, *J* = 7.9 Hz, 1H), 4.51 – 4.41 (m, 3H), 4.23 (dd, *J* = 15.0, 5.2 Hz, 1H), 3.98 (d, *J* = 11.4 Hz, 1H), 3.89 (t, *J* = 6.0 Hz, 2H), 3.52 (dd, *J* = 11.4, 3.6 Hz, 1H), 2.46 – 2.39 (m, 4H), 2.32 (td, *J* = 7.5, 7.0, 4.9 Hz, 2H), 1.98 (p, *J* = 6.8 Hz, 3H), 1.23 (d, *J* = 1.6 Hz, 15H), 0.82 (s, 9H).

^{13}C NMR: (75 MHz, *C*DCl$_3$) δ [ppm] = 173.3, 171.9, 170.9, 161.5, 138.5, 136.7, 129.7, 128.3, 114.0, 83.7, 77.4, 70.2, 66.6, 58.7, 57.8, 56.9, 43.4, 36.1, 35.0, 32.8, 26.5, 25.2, 25.0, 15.9.

LC/MS: m/z calculated for $C_{38}H_{51}BN_4O_7S$ $[M+H]^+$: 719.4, found: 719.2.



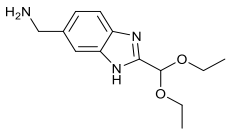
Compound **69**: Yield: 30 mg (88% of th.).

^{1}H NMR: (400 MHz, C*D*Cl$_3$) δ [ppm] = 9.37 (s, 1H), 7.38 (ddd, *J* = 16.8, 9.6, 5.7 Hz, 7H), 7.11 (d, *J* = 7.8 Hz, 2H), 6.35 (d, *J* = 8.7 Hz, 1H), 4.69 – 4.56 (m, 6H), 4.35 (dd, *J* = 15.4, 4.7 Hz, 1H), 4.10 (d, *J* = 11.2 Hz, 1H), 3.65 (dd, *J* = 11.4, 3.4 Hz, 1H), 3.03 (s, 1H), 2.92 (t, *J* = 7.2 Hz, 2H), 2.63 (s, 3H), 2.56 – 2.52 (m, 1H), 2.49 – 2.42 (m, 1H), 2.22 (dd, *J* = 13.6, 7.8 Hz, 1H), 0.88 (s, 9H).

^{13}C NMR: (101 MHz, *C*DCl$_3$) δ [ppm] = 173.2, 171.9, 171.1, 160.1, 159.7, 152.5, 143.8, 141.2, 140.2, 134.9, 132.6, 129.6, 128.8, 128.7, 128.5, 127.9, 127.0, 120.2, 116.6, 115.8, 113.8, 83.8, 70.3, 59.1, 57.9, 57.1, 43.3, 37.8, 36.4, 35.0, 31.6, 26.4, 14.0.

LC/MS: m/z calculated for $C_{33}H_{38}N_4O_4S$ $[M+H]^+$: 587.3, found: 586.3.

1st and 2nd generation METTL3 recruiter synthesis



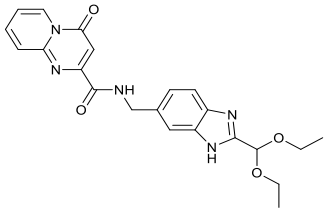
Compound **70**: To a solution of sodium ethoxide (437 mg, equals 19 mmol Na) in 10 mL of dry ethanol (1.9 eq.) *o*-phenylenediamine-5-carbonitrile (1.3 g, 10 mmol, 1.0 eq.) and ethyl diethoxyacetate (2.1 mL, 12 mmol, 1.2 eq.) were added. The mixture was heated in a sealed tube to 120 °C for 16 h, cooled to RT, and the solvent was removed in vacuo. The resulting residue was dissolved in water, neutralized with acetic acid, and extracted with ethyl acetate. Then, the combined organic phases were purified over a short silica column (CH/EA 1:1 +1% TEA) and concentrated under reduced pressure. This intermediate was converted without further characterization. To a solution of the carbonitrile intermediate (1.6 g) in methanol (10 mL), Raney Ni (200 mg, 3.4 mmol, 0.3 eq.) was added, followed by ammonia in methanol (7 M, 3 mL). The reaction solution was hydrogenated at 4 bar at RT for 4 h. The resulting mixture was filtered through a plug of silica. The raw product was purified by column chromatography (EA/MeOH 1:1 + 1% TEA).

Yield: 1.16 g (47% of th.).

^{1}H NMR: (300 MHz, C*D*Cl$_3$) δ [ppm] = 7.52 – 7.43 (m, 2H), 7.09 (dd, *J* = 8.3, 1.6 Hz, 1H), 5.68 (s, 1H), 3.87 (s, 2H), 3.72 – 3.53 (m, 4H), 3.39 (s, 3H), 1.16 (t, *J* = 7.1 Hz, 6H).

^{13}C NMR: (75 MHz, *C*DCl$_3$) δ = 151.8, 137.7, 137.3, 122.3, 97.2, 62.3, 49.8, 46.4, 15.0.

LC/MS: m/z calculated for $C_{13}H_{19}N_3O_2$ $[M+H]^+$: 250.2, found: 250.0.



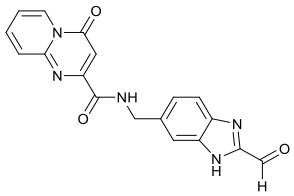
Compound **71**: A solution of 4-oxopyrido[1,2-a]pyrimidine-2-carboxylic acid hydrochloride (452 mg, 2 mmol, 1.0 eq.), TBTU (642 mg, 2 mmol, 1.0 eq.) and **70** (500 mg, 2 mmol, 1.0 eq.) in dry DMF (10 mL) was treated with DIPEA (1 mL, 6 mmol, 3.0 eq.). The suspension was stirred at RT for 16 h and concentrated in vacuo. The resulting residue was diluted with water and dichloromethane, and the organic layer was extracted with saturated $NaHCO_3$ solution and purified via column chromatography (DCM/MeOH 10:1 + 1% TEA). Evaporation gave the product as an off-white solid.

Yield: 472 mg (56% of th.).

^{1}H NMR: (300 MHz, C*D*Cl$_3$) δ [ppm] = 9.09 – 9.01 (m, 1H), 8.37 (s, 1H), 7.81 – 7.70 (m, 2H), 7.64 – 7.57 (m, 1H), 7.45 (d, *J* = 21.8 Hz, 1H), 7.31 (s, 1H), 7.21 – 7.14 (m, 1H), 5.74 (s, 1H), 4.75 (d, *J* = 6.0 Hz, 2H), 3.78 – 3.61 (m, 4H), 1.24 (t, *J* = 7.1 Hz, 6H).

^{13}C NMR: (75 MHz, *C*DCl$_3$) δ [ppm] = 163.0, 158.7, 153.6, 152.0, 150.6, 137.0, 127.7, 126.6, 116.3, 102.9, 97.0, 62.4, 46.1, 44.2, 15.2, 10.4.

LC/MS: m/z calculated for $C_{22}H_{23}N_5O_4$ [M+H]$^+$: 422.2, found: 422.1.



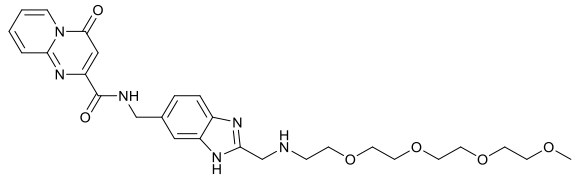
Compound **72**: **71** (230 mg, 0.55 mmol, 1.0 eq.) was solved in THF/water/conc. HCl (3+3+2 mL) and stirred at 80 °C for 3 h under an argon atmosphere. Evaporation and lyophilization afforded the dihydrochloride, which was suspended in DCM/MeOH/TEA (10:1:1), filtered over silica, and evaporated. The residue was washed with distilled water and lyophilized to yield the product as an off-white solid

Yield: 192 mg (quant.).

^{1}H NMR: (300 MHz, DMSO-d_6) δ [ppm] = 9.65 – 9.52 (m, 1H), 9.05 – 8.99 (m, 1H), 8.09 (ddd, *J* = 8.6, 6.7, 1.6 Hz, 1H), 7.79 (dt, *J* = 8.9, 1.2 Hz, 1H), 7.75 – 7.69 (m, 2H), 7.57 (dd, *J* = 8.7, 1.4 Hz, 1H), 7.47 (td, *J* = 6.9, 1.3 Hz, 1H), 6.90 (d, *J* = 4.2 Hz, 1H), 6.25 (s, 1H), 4.66 (s, 2H).

^{13}C NMR: (75 MHz, DMSO) δ [ppm] = 163.1, 157.9, 154.5, 153.5, 150.5, 138.8, 137.7, 130.9, 129.9, 127.5, 126.1, 126.0, 117.5, 114.1, 113.0, 101.0, 83.6, 8.4.

LC/MS: m/z calculated for $C_{18}H_{13}N_5O_3$ [M+H]$^+$: 348.1, found: 348.1.



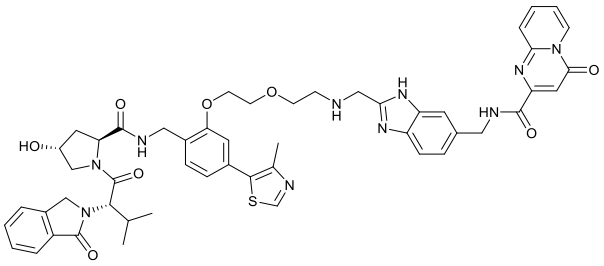
Compound **5**: OMe-PEG4-NH_2 (10.4 mg, 0.05 mmol, 1.0 eq.) and **72** (17.3 mg, 0.05 mmol, 1.0 eq.) were dissolved in dichloroethane (DCE, 1 mL), and AcOH (6 µL, 0.1 mmol, 2.0 eq.) was added to the reaction mixture. $NaBH(OAc)_3$ (21 mg, 0.1 mmol, 2.0 eq.) was added, and the mixture was incubated at 60 °C for 2 h. The reaction was quenched by the addition of MeOH (1 mL). Evaporation, purification by RP flash chromatography, and lyophilization afforded the product as a yellowish oil.

Yield: 26 mg (97% of th.).

LC/MS: m/z calculated for $C_{27}H_{34}N_6O_6$ $[M+H]^+$: 539.3, found: 538.9.

Purity (HPLC): 99%.

Synthesis of 1st generation PROTACs



Compound **11**: **43** (12.7 mg, 0.02 mmol, 1.0 eq.) and **72** (9 mg, 0.025 mmol, 1.3 eq.) were dissolved in dichloroethane (DCE, 1 mL), and AcOH (6 µL, 0.1 mmol, 2.0 eq.) was added to the reaction mixture. Then $NaBH(OAc)_3$ (21 mg, 0.1 mmol, 2.0 eq.) was added, and the mixture was incubated at 60 °C for 2 h. The reaction was quenched by the addition of MeOH (1 mL). Evaporation, purification by RP flash chromatography, and lyophilization afforded the product as a yellowish solid.

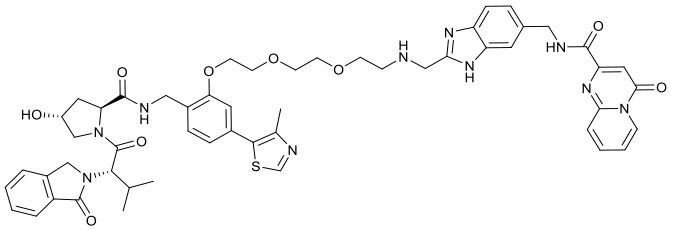
Yield: 10 mg (51% of th.).

^{1}H NMR: (600 MHz, MeO*D*) δ [ppm] = 9.00 (d, *J* = 7.2 Hz, 1H), 8.87 – 8.79 (m, 1H), 7.92 (ddd, *J* = 8.6, 6.8, 1.4 Hz, 1H), 7.74 (t, *J* = 9.0 Hz, 1H), 7.66 (dd, *J* = 24.8, 7.5 Hz, 1H), 7.57 (s, 1H), 7.52 (h, *J* = 7.7 Hz, 2H), 7.48 – 7.44 (m, 1H), 7.44 – 7.39 (m, 1H), 7.39 – 7.30 (m, 2H), 7.30 – 7.25 (m, 1H), 7.02 – 6.99 (m, 1H), 6.99 – 6.87 (m, 2H), 4.74 (d, *J* = 11.0 Hz, 1H), 4.66 (s, 2H), 4.57 – 4.41 (m, 5H), 4.41 – 4.25 (m, 3H), 4.23 – 4.10 (m, 2H), 3.94 – 3.82 (m, 4H), 3.79 (dd, *J* = 11.1, 3.9 Hz, 1H), 3.64 – 3.49 (m, 1H), 3.44 – 3.41 (m, 1H), 3.19 – 3.00 (m, 1H), 2.45 – 2.34 (m, 3H), 2.30 (dp, *J* = 17.6, 6.6 Hz, 1H), 2.15 – 2.10 (m, 1H), 1.96 (ddt, *J* = 13.5, 8.7, 4.3 Hz, 1H), 1.30 – 1.22 (m, 1H), 1.00 – 0.84 (m, 3H), 0.80 – 0.65 (m, 3H).

^{13}C NMR: (151 MHz, MeOD) δ [ppm] = 174.2, 170.9, 170.7, 165.4, 160.6, 157.8, 155.4, 153.0, 152.2, 149.1, 147.3, 143.7, 139.2, 135.4, 133.2, 133.0, 132.4, 129.9, 129.2, 128.5, 128.0, 127.7, 124.6, 124.6, 124.4, 124.4, 122.9, 118.4, 113.5, 102.5, 70.9, 70.8, 69.2, 67.4, 60.8, 60.1, 57.2, 45.1, 44.5, 39.4, 39.1, 30.1, 19.6, 19.0, 17.4, 17.3, 15.8.

LC/MS: m/z calculated for $C_{51}H_{54}N_{10}O_8S$ $[M+2H]^{2+}$: 484.2, found: 484.1.

Purity (HPLC): 97%.



Compound **12**: **44** (13.5 mg, 0.02 mmol, 1.0 eq.) and **72** (7 mg, 0.02 mmol, 1.0 eq.) were dissolved in HFIP (200 µL). One pearl of mol-sieve was added, and the mixture was stirred at 20 °C for 16 h. The reaction was diluted with DCE (1 mL), and $NaBH(OAc)_3$ (10 mg, 0.05 mmol, 2.5 eq.) was added and incubated at 20 °C for 3 h. The reaction was terminated by the addition of MeOH (1 mL). The evaporation of solvent, purification by RP flash chromatography, and lyophilization afforded the product as a yellowish solid

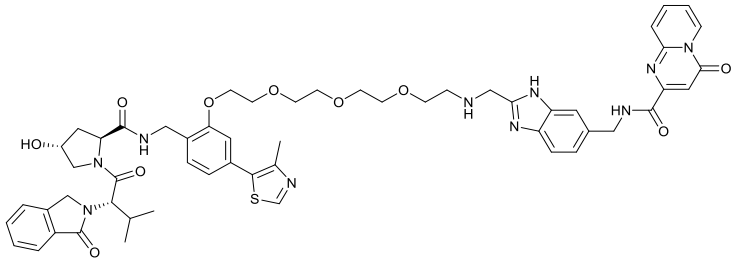
Yield: 6 mg (30% of th.).

^{1}H NMR (600 MHz, MeO*D*) δ [ppm] = 9.02 – 8.81 (m, 2H), 8.76 (d, *J* = 32.5 Hz, 1H), 7.89 (s, 1H), 7.71 (dd, *J* = 43.1, 7.6 Hz, 2H), 7.60 – 7.13 (m, 9H), 7.03 – 6.96 (m, 1H), 6.88 (s, 1H), 4.79 (dd, *J* = 19.5, 10.9 Hz, 1H), 4.69 – 4.30 (m, 8H), 4.28 – 3.99 (m, 5H), 3.98 – 3.93 (m, 1H), 3.93 – 3.77 (m, 3H), 3.76 – 3.55 (m, 5H), 3.16 – 2.95 (m, 2H), 2.44 (d, *J* = 17.6 Hz, 1H), 2.33 (d, *J* = 43.7 Hz, 3H), 2.20 – 2.12 (m, 1H), 2.06 – 1.89 (m, 2H), 1.32 – 1.21 (m, 1H), 0.99 (dt, *J* = 20.6, 10.9 Hz, 3H), 0.77 (dd, *J* = 37.2, 6.4 Hz, 3H).

^{13}C NMR (151 MHz, MeOD) δ [ppm] = 174.2, 174.1, 171.1, 170.9, 170.8, 165.3, 160.5, 157.9, 155.4, 152.9, 152.2, 149.2, 149.1, 143.8, 143.7, 139.1, 133.3, 133.2, 133.1, 133.0, 132.4, 130.0, 129.9, 129.3, 129.2, 128.5, 128.2, 128.1, 127.7, 124.4, 123.0, 122.8, 118.4, 113.7, 102.5, 71.8, 71.3, 70.8, 69.2, 67.9, 60.7, 60.1, 60.1, 57.3, 57.2, 40.7, 39.4, 39.2, 30.2, 19.7, 19.0, 16.0, 15.9.

LC/MS: m/z calculated for $C_{53}H_{58}N_{10}O_9S$ $[M+2H]^{2+}$: 506.2, found: 506.1.

Purity (HPLC): 91%.



Compound **13**: **45** (14.5 mg, 0.02 mmol, 1.0 eq.) and **72** (7 mg, 0.02 mmol, 1.0 eq.) were solved in HFIP (200 µL). One pearl of mol-sieve was added, and the mixture was stirred at 20 °C for 16 h and diluted with DCE (1 mL). To this reaction, $NaBH(OAc)_3$ (10 mg, 0.05 mmol, 2.5 eq.) was added, and the mixture was incubated at 20 °C for 3 h. The reaction was subsequently quenched by the addition of MeOH (1 mL). The evaporation of solvent, purification by RP flash chromatography, and lyophilization afforded the product as a yellowish solid.

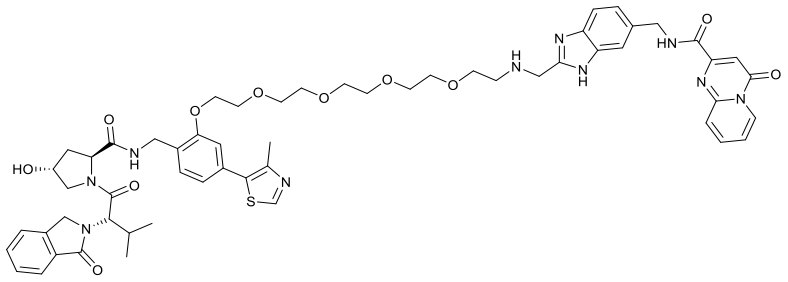
Yield: 2 mg (10% of th.).

^{1}H NMR: (600 MHz, MeO*D*) δ [ppm] = 8.98 (s, 1H), 8.82 (d, *J* = 32.5 Hz, 1H), 7.90 (d, *J* = 7.2 Hz, 1H), 7.76 – 7.67 (m, 2H), 7.59 – 7.37 (m, 5H), 7.36 – 7.27 (m, 2H), 7.20 (d, *J* = 26.1 Hz, 1H), 7.01 (d, *J* = 5.7 Hz, 1H), 6.90 (d, *J* = 7.4 Hz, 1H), 6.86 (s, 1H), 4.70 (s, 2H), 4.69 – 4.28 (m, 9H), 4.24 – 4.17 (m, 1H), 4.11 – 3.98 (m, 3H), 3.94 (d, *J* = 10.6 Hz, 1H), 3.89 – 3.69 (m, 4H), 3.67 – 3.45 (m, 7H), 3.14 – 3.03 (m, 1H), 2.87 (s, 1H), 2.46 – 2.28 (m, 4H), 2.15 (d, *J* = 7.3 Hz, 1H), 2.00 (d, *J* = 17.3 Hz, 1H), 1.36 – 1.22 (m, 2H), 1.00 (dd, *J* = 12.9, 6.2 Hz, 3H), 0.78 (dd, *J* = 22.7, 6.5 Hz, 3H).

^{13}C NMR: (151 MHz, MeOD) δ [ppm] = 170.9, 170.7, 170.7, 160.6, 158.0, 152.9, 152.2, 149.1, 143.8, 139.2, 133.3, 133.2, 132.4, 129.9, 129.9, 129.3, 129.2, 128.5, 128.2, 128.1, 127.8, 127.8, 124.5, 124.4, 122.8, 118.4, 113.7, 113.5, 102.5, 71.8, 71.7, 71.5, 71.5, 71.2, 70.8, 69.3, 67.8, 60.7, 60.1, 57.2, 44.6, 39.2, 30.2, 19.7, 19.0, 16.0, 15.9.

LC/MS: m/z calculated for $C_{55}H_{62}N_{10}O_{10}S$ $[M+2H]^{2+}$: 528.2, found: 528.1.

Purity (HPLC): 93%.



Compound **14**: **46** (15.3 mg, 0.02 mmol, 1.0 eq.) and **72** (7 mg, 0.02 mmol, 1.0 eq.) were solved in HFIP (200 µL). One pearl of mol sieve was added, and the mixture was stirred at 20 °C for 16 h and diluted with DCE (1 mL). To this reaction, $NaBH(OAc)_3$ (10 mg, 0.05 mmol, 2.5 eq.) was added, and the mixture was incubated at 20 °C for 3 h. The reaction was quenched by the addition of MeOH (1 mL). The evaporation of solvent, purification by RP flash chromatography, and lyophilization afforded the product as a yellowish solid.

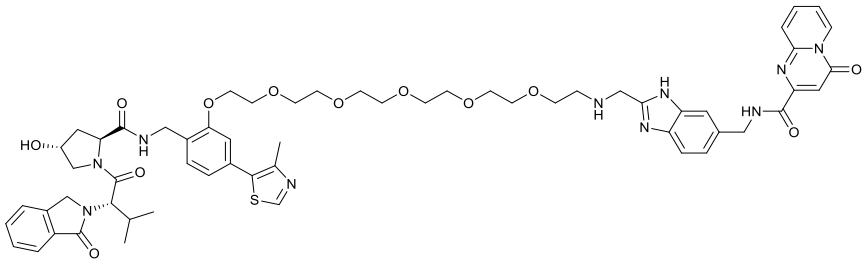
Yield: 4 mg (18% of th.).

^{1}H NMR: (600 MHz, MeO*D*) δ [ppm] = 8.97 (s, 1H), 8.85 – 8.75 (m, 1H), 7.89 (d, *J* = 6.3 Hz, 1H), 7.69 (td, *J* = 27.1, 6.3 Hz, 2H), 7.60 – 7.35 (m, 5H), 7.35 – 7.14 (m, 3H), 7.03 – 6.97 (m, 1H), 6.95 – 6.75 (m, 2H), 4.78 (d, *J* = 10.3 Hz, 1H), 4.70 – 4.14 (m, 9H), 4.05 (d, *J* = 19.3 Hz, 3H), 3.94 (d, *J* = 10.6 Hz, 1H), 3.88 – 3.70 (m, 3H), 3.65 – 3.42 (m, 9H), 3.39 (s, 1H), 3.30 (s, 1H), 3.15 – 3.00 (m, 1H), 2.77 (d, *J* = 68.3 Hz, 2H), 2.47 – 2.26 (m, 4H), 2.15 (s, 1H), 2.04 – 1.95 (m, 1H), 1.33 – 1.19 (m, 1H), 1.04 – 0.89 (m, 3H), 0.85 – 0.71 (m, 3H).

^{13}C NMR: (151 MHz, MeOD) δ [ppm] = 172.8, 169.5, 169.2, 163.9, 159.2, 156.6, 154.0, 151.5, 150.8, 147.7, 142.4, 137.8, 132.0, 131.9, 131.8, 131.5, 131.0, 128.6, 127.8, 127.1, 126.8, 126.4, 123.0, 123.0, 121.6, 121.4, 117.0, 112.4, 112.2, 101.1, 70.3, 70.1, 70.0, 69.9, 69.7, 69.4, 69.4, 68.0, 67.9, 66.5, 59.3, 58.7, 55.8, 43.2, 39.2, 38.1, 38.0, 37.8, 28.8, 24.7, 18.3, 18.3, 17.6, 14.6, 14.5.

LC/MS: m/z calculated for $C_{57}H_{66}N_{10}O_{11}S$ $[M+2H]^{2+}$: 550.2, found: 550.1.

Purity (HPLC): 95%.



Compound **15**: **47** (16.2 mg, 0.02 mmol, 1.0 eq.) and **72** (7 mg, 0.02 mmol, 1.0 eq.) were solved in HFIP (200 µL). One pearl of mol-sieve was added, and the mixture was stirred at 20 °C for 16 h and diluted with DCE (1 mL). Then $NaBH(OAc)_3$ (10 mg, 0.05 mmol, 2.5 eq.) was added, and the mixture was incubated at 20 °C for 3 h. The reaction was quenched by the addition of MeOH (1 mL). The evaporation of solvent, purification by RP flash chromatography, and lyophilization afforded the product as a yellowish solid.

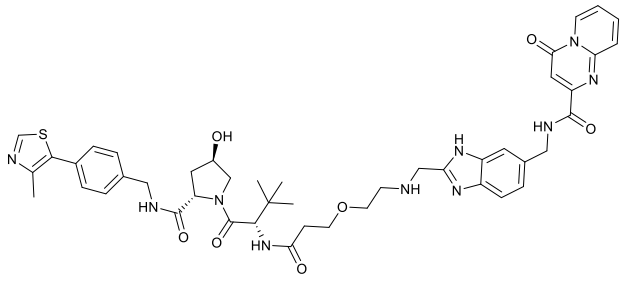
Yield: 4 mg (18% of th.).

^{1}H NMR: (600 MHz, MeO*D*) δ [ppm] = 8.98 (s, 1H), 8.82 (d, *J* = 28.3 Hz, 1H), 7.90 (s, 1H), 7.76 – 7.65 (m, 2H), 7.59 – 7.38 (m, 5H), 7.30 (dd, *J* = 33.1, 7.5 Hz, 2H), 7.22 (s, 1H), 7.02 (s, 1H), 6.96 – 6.83 (m, 2H), 4.78 (d, *J* = 10.6 Hz, 1H), 4.68 – 4.27 (m, 9H), 4.22 – 3.98 (m, 4H), 3.94 (d, *J* = 10.9 Hz, 1H), 3.90 – 3.69 (m, 4H), 3.67 – 3.41 (m, 14H), 3.29 (s, 2H), 2.79 (d, *J* = 77.2 Hz, 2H), 2.47 – 2.31 (m, 4H), 2.14 (d, *J* = 8.2 Hz, 1H), 2.04 – 1.97 (m, 1H), 1.32 – 1.22 (m, 1H), 1.00 (t, *J* = 6.5 Hz, 3H), 0.78 (dd, *J* = 15.8, 6.6 Hz, 3H).

^{13}C NMR: (151 MHz, MeOD) δ [ppm] = 174.2, 174.2, 170.9, 170.6, 165.3, 160.6, 158.0, 157.9, 155.4, 152.9, 152.2, 149.2, 149.1, 143.8, 139.2, 133.4, 133.3, 133.2, 132.9, 132.5, 130.0, 129.2, 128.5, 128.2, 127.8, 124.4, 122.8, 118.4, 113.6, 102.5, 71.7, 71.6, 71.5, 71.4, 71.3, 71.3, 71.2, 70.9, 70.8, 69.3, 67.9, 60.7, 60.1, 57.2, 49.6, 44.6, 40.5, 39.5, 39.4, 39.2, 30.2, 19.7, 19.0, 16.0, 15.9.

LC/MS: m/z calculated for $C_{59}H_{70}N_{10}O_{12}S$ $[M+2H]^{2+}$: 572.2, found: 572.2.

Purity (HPLC): 95%.



Compound **6**: **48** (22 mg, 0.04 mmol, 1.0 eq.), **72** (14 mg, 0.04 mmol, 1.0 eq.), and acetic acid (6 µL, 0.1 mmol, 2.5 eq.) were solved in HFIP (200 µL). One pearl of mol-sieve was added, and the mixture was stirred at 60 °C for 3 h and diluted with DCE (1 mL). $NaBH(OAc)_3$ (21 mg, 0.1 mmol, 2.5 eq.) was added, and the mixture was incubated for 24 h. The reaction was quenched by the addition of MeOH (1 mL). The evaporation of solvent, purification by RP flash chromatography, and lyophilization afforded the product.

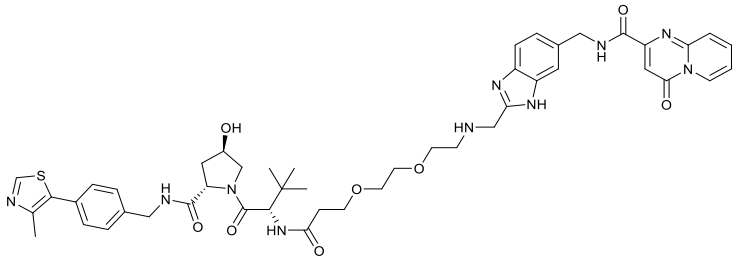
Yield: 8 mg (23% of th.).

^{1}H NMR: (600 MHz, DMSO-d_6) δ [ppm] = 9.42 (t, *J* = 6.5 Hz, 1H), 9.01 (dd, *J* = 7.2, 1.6 Hz, 1H), 8.98 (s, 1H), 8.59 (t, *J* = 6.1 Hz, 1H), 8.10 – 8.04 (m, 2H), 7.76 (d, *J* = 8.9 Hz, 1H), 7.60 – 7.55 (m, 2H), 7.45 (td, *J* = 6.9, 1.4 Hz, 1H), 7.39 (d, *J* = 8.1 Hz, 2H), 7.35 (d, *J* = 8.2 Hz, 2H), 7.27 (dd, *J* = 8.3, 1.6 Hz, 1H), 6.89 (s, 1H), 4.60 (d, *J* = 6.4 Hz, 2H), 4.50 (d, *J* = 9.3 Hz, 1H), 4.47 (s, 2H), 4.41 (dt, *J* = 16.3, 7.3 Hz, 2H), 4.33 (tt, *J* = 4.2, 2.3 Hz, 1H), 4.19 (dd, *J* = 15.9, 5.5 Hz, 1H), 2.61 – 2.55 (m, 1H), 2.42 (s, 4H), 2.03 (dd, *J* = 13.0, 8.0 Hz, 1H), 1.88 (ddd, *J* = 13.0, 8.9, 4.5 Hz, 1H), 0.89 (s, 9H).

^{13}C NMR: (151 MHz, DMSO) δ [ppm] = 172.0, 170.2, 169.6, 163.0, 158.4, 158.2, 158.0, 153.9, 151.6, 150.6, 147.8, 146.8, 139.5, 138.6, 133.8, 131.2, 129.7, 128.7, 127.5, 127.5, 126.2, 122.7, 117.4, 117.3, 115.3, 100.9, 69.0, 66.6, 65.2, 62.0, 58.8, 56.5, 56.5, 46.3, 43.7, 43.0, 41.7, 38.1, 35.4, 35.2, 26.4, 16.0, 15.1.

LC/MS: m/z calculated for $C_{45}H_{52}N_{10}O_7S$ $[M+2H]^{2+}$: 439.2, found: 439.1.

Purity (HPLC): 99%.



Compound **7**: **49** (11 mg, 0.02 mmol, 1.0 eq.) was solved in 0.5 mL DCE and 0.2 mL HFIP, then **72** (7 mg, 0.02 mmol, 1.0 eq.) was added and mixed until everything was solved. $Ti(O_iPr)_4$ (50 µL, 0.165 mmol, 8.0 eq.) was added and incubated at 30 °C for 8 h. After that, another portion $Ti(O_iPr)_4$ (50 µL, 0.165 mmol, 8.0 eq.) was added, and the mixture was incubated at 30 °C for 8 h. After the addition of 200 µL MeOH, the resulting solution was added to $NaBH_4$ (1 mg, 0.02 mmol, 1.0 eq.) and vortexed immediately. The solution was left at RT for 15 min, and then 10 µL TFA was added. Purification was done by flash chromatography and lyophilization to afford the product as an off-white solid.

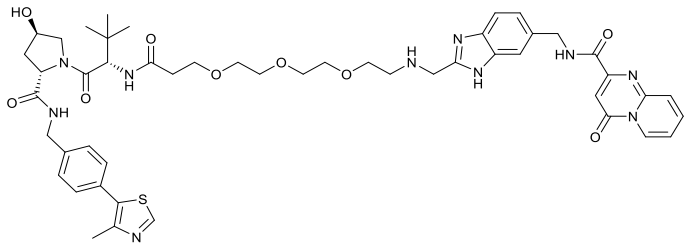
Yield: 9 mg (49% of th.).

^{1}H NMR: (600 MHz, MeO*D*) δ [ppm] = 8.99 (d, *J* = 7.0 Hz, 1H), 8.78 (s, 1H), 7.90 (t, *J* = 7.6 Hz, 1H), 7.73 (d, *J* = 8.8 Hz, 1H), 7.53 (s, 1H), 7.49 – 7.43 (m, 1H), 7.32 (t, *J* = 6.7 Hz, 3H), 7.27 (d, *J* = 8.1 Hz, 2H), 7.23 (d, *J* = 6.9 Hz, 1H), 7.00 (d, *J* = 12.9 Hz, 1H), 4.64 (s, 2H), 4.57 (s, 1H), 4.50 (t, *J* = 8.3 Hz, 1H), 4.43 – 4.36 (m, 2H), 4.26 (d, *J* = 15.4 Hz, 1H), 4.15 (s, 2H), 3.80 (d, *J* = 10.8 Hz, 1H), 3.71 – 3.63 (m, 3H), 3.57 (d, *J* = 35.0 Hz, 6H), 2.95 (s, 2H), 2.49 – 2.42 (m, 2H), 2.36 (s, 3H), 2.15 (dd, *J* = 12.8, 7.5 Hz, 1H), 1.99 (ddd, *J* = 13.2, 9.5, 3.7 Hz, 1H), 0.93 (s, 9H).

^{13}C NMR: (151 MHz, MeOD) δ [ppm] = 174.4, 173.8, 172.2, 165.3, 160.6, 155.4, 152.9, 152.2, 149.0, 140.2, 139.1, 134.6, 133.3, 131.5, 130.3, 128.9, 128.5, 127.8, 124.0, 118.4, 102.5, 71.3, 71.1, 68.3, 60.9, 59.0, 58.1, 44.6, 43.7, 39.0, 37.2, 36.8, 27.0, 21.9, 15.8.

LC/MS: m/z calculated for $C_{47}H_{56}N_{10}O_8S$ $[M+2H]^{2+}$: 461.2, found: 461.1.

Purity (HPLC): 95%.



Compound **8**: **50** (12 mg, 0.02 mmol, 1.0 eq.) was solved in 0.5 mL DCE and 0.2 mL HFIP, then **72** (7 mg, 0.02 mmol, 1.0 eq.) was added and mixed until everything was solved. $Ti(O_iPr)_4$ (50 µL, 0.165 mmol, 8.0 eq.) was added and incubated at 30 °C for 8 h. After that, another portion $Ti(O_iPr)_4$ (50 µL, 0.165 mmol, 8.0 eq.) was added and incubated at 30 °C for 8 h. After the addition of 200 µL MeOH, the resulting solution was added to $NaBH_4$ (1 mg, 0.02 mmol, 1.0 eq.) and vortexed immediately. The solution was left at RT for 15 min, and then 10 µL TFA was added. Purification was done by flash chromatography and subsequent lyophilization to afford the product as an off-white solid.

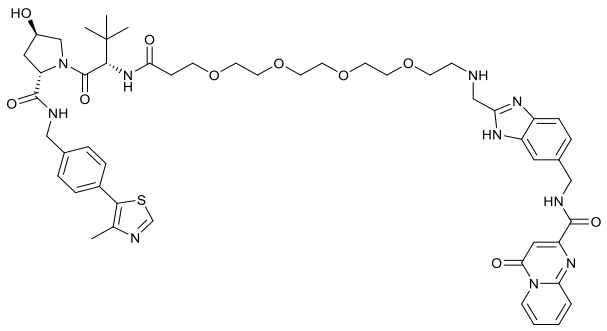
Yield: 8 mg (41% of th.).

^{1}H NMR: (600 MHz, Me*OD*) δ [ppm] = 9.00 (d, *J* = 7.0 Hz, 1H), 8.80 (s, 1H), 7.94 – 7.88 (m, 1H), 7.75 (d, *J* = 8.9 Hz, 1H), 7.53 (s, 1H), 7.47 (d, *J* = 7.8 Hz, 1H), 7.41 – 7.29 (m, 5H), 7.24 (d, *J* = 7.8 Hz, 1H), 7.03 (s, 1H), 4.65 (s, 2H), 4.56 (s, 1H), 4.53 – 4.48 (m, 1H), 4.45 (d, *J* = 15.7 Hz, 2H), 4.27 (d, *J* = 15.5 Hz, 1H), 4.14 (s, 2H), 3.81 (d, *J* = 10.9 Hz, 1H), 3.72 (dd, *J* = 10.9, 3.6 Hz, 1H), 3.68 – 3.47 (m, 12H), 2.94 (s, 2H), 2.45 (td, *J* = 13.4, 11.6, 5.5 Hz, 1H), 2.38 (s, 4H), 2.16 (dd, *J* = 12.9, 7.6 Hz, 1H), 2.01 (ddd, *J* = 16.2, 8.3, 3.6 Hz, 1H), 0.97 (d, *J* = 19.2 Hz, 9H).

^{13}C NMR: (151 MHz, MeOD) δ [ppm] = 174.5, 173.7, 172.1, 165.3, 160.6, 155.4, 152.9, 152.2, 149.0, 140.2, 139.1, 134.6, 133.4, 131.4, 130.3, 128.9, 128.5, 127.8, 124.0, 118.4, 102.5, 71.5, 71.4, 71.3, 71.2, 71.1, 68.2, 60.9, 59.0, 58.0, 44.6, 43.7, 39.0, 37.2, 36.8, 27.0, 21.9, 19.2, 15.8.

LC/MS: m/z calculated for $C_{49}H_{60}N_{10}O_9S$ $[M+2H]^{2+}$: 483.2, found: 483.1.

Purity (HPLC): 97%.



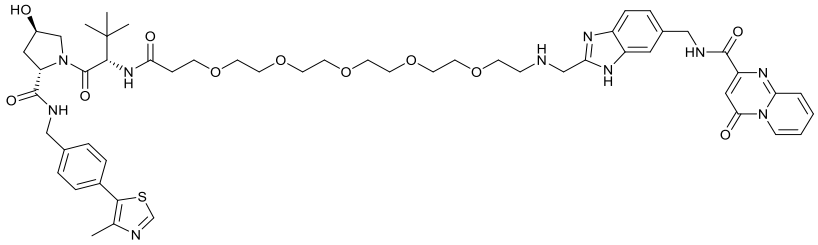
Compound **9**: **51** (13 mg, 0.02 mmol, 1.0 eq.) was solved in 0.5 mL DCE and 0.2 mL HFIP, then **72** (7 mg, 0.02 mmol, 1.0 eq.) was added and mixed until everything was solved. $Ti(O_iPr)_4$ (50 µL, 0.165 mmol, 8.0 eq.) was added, and the mixture was incubated at 30 °C for 8 h. After that, another portion $Ti(O_iPr)_4$ (50 µL, 0.165 mmol, 8.0 eq.) was added, and the mixture was incubated at 30 °C for 8 h. After the addition of 200 µL MeOH, the resulting solution was added to $NaBH_4$ (1 mg, 0.02 mmol, 1.0 eq.) and vortexed immediately. The solution was left at RT for 15 min, and then 10 µL TFA was added. Purification was done by flash chromatography and lyophilization to afford the product as an off-white solid.

Yield: 6 mg (30% of th.).

^{1}H NMR: (600 MHz, Me*OD*) δ [ppm] = 9.00 (d, *J* = 7.0 Hz, 1H), 8.80 (s, 1H), 7.94 – 7.89 (m, 1H), 7.75 (d, *J* = 8.9 Hz, 1H), 7.54 (s, 1H), 7.47 (d, *J* = 7.7 Hz, 1H), 7.40 – 7.30 (m, 5H), 7.24 (d, *J* = 8.0 Hz, 1H), 7.03 (d, *J* = 8.7 Hz, 1H), 4.66 (s, 2H), 4.56 (s, 1H), 4.53 – 4.41 (m, 4H), 4.30 – 4.25 (m, 1H), 4.15 (s, 2H), 3.81 (d, *J* = 11.1 Hz, 1H), 3.74 – 3.66 (m, 2H), 3.63 – 3.45 (m, 18H), 2.95 (s, 2H), 2.49 – 2.41 (m, 2H), 2.40 – 2.34 (m, 4H), 2.16 (dd, *J* = 12.9, 7.6 Hz, 1H), 2.01 (ddd, *J* = 16.9, 8.6, 4.0 Hz, 1H), 0.96 (s, 9H).

^{13}C NMR: (151 MHz, MeOD) δ [ppm] = 174.5, 173.7, 172.1, 165.3, 160.6, 155.4, 152.9, 152.2, 149.0, 140.2, 139.1, 134.6, 133.4, 131.4, 130.4, 130.3, 128.9, 128.5, 127.8, 123.9, 118.4, 102.5, 71.4, 71.3, 71.1, 70.8, 69.7, 68.2, 67.1, 60.9, 59.0, 58.0, 45.7, 44.6, 43.7, 40.5, 39.0, 37.2, 36.8, 27.0, 19.2, 15.9.

LC/MS: $C_{51}H_{64}N_{10}O_{10}S$ $[M+2H]^{2+}$: 502.1, found: 502.2.



Compound **10**: **52** (15 mg, 0.02 mmol, 1.0 eq.) was solved in 0.5 mL DCE and 0.2 mL HFIP, then **72** (7 mg, 0.02 mmol, 1.0 eq.) was added and mixed until everything was solved. $Ti(O_iPr)_4$ (50 µL, 0.165 mmol, 8.0 eq.) was added and incubated at 30 °C for 8 h. After that, another portion $Ti(O_iPr)_4$ (50 µL, 0.165 mmol, 8.0 eq.) was added, and the mixture was incubated at 30 °C for 8 h. After adding 200 µL MeOH, the resulting solution was added to $NaBH_4$ (1 mg, 0.02 mmol, 1.0 eq.) and vortexed immediately. The solution was left at RT for 15 min, and then 10 µL TFA was added. Purification was done by flash chromatography and lyophilization to afford the product as an off-white solid.

Yield: 3 mg (14% of th.).

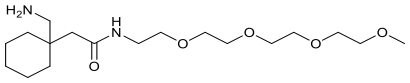
^{1}H NMR: (600 MHz, MeO*D*) δ [ppm] = 9.03 (d, *J* = 7.1 Hz, 1H), 8.81 (s, 1H), 7.95 – 7.91 (m, 1H), 7.77 (d, *J* = 8.9 Hz, 1H), 7.54 (s, 1H), 7.47 (d, *J* = 8.1 Hz, 1H), 7.42 – 7.30 (m, 5H), 7.24 (d, *J* = 8.2 Hz, 1H), 7.06 (s, 1H), 4.69 (d, *J* = 20.7 Hz, 2H), 4.59 (d, *J* = 10.1 Hz, 1H), 4.55 – 4.40 (m, 4H), 4.28 (d, *J* = 15.6 Hz, 1H), 4.05 (s, 1H), 3.85 – 3.81 (m, 1H), 3.78 – 3.45 (m, 20H), 2.83 (s, 1H), 2.51 – 2.45 (m, 1H), 2.41 – 2.36 (m, 3H), 2.16 (dd, *J* = 13.1, 7.4 Hz, 1H), 2.02 (ddd, *J* = 13.3, 9.3, 4.5 Hz, 1H), 1.31 – 1.22 (m, 2H), 0.98 (d, *J* = 13.0 Hz, 9H).

^{13}C NMR: (151 MHz, MeOD) δ [ppm] = 174.5, 173.7, 172.1, 165.3, 160.6, 155.5, 152.9, 140.3, 139.1, 133.4, 131.4, 130.4, 130.3, 128.9, 128.5, 127.8, 118.4, 102.6, 71.5, 71.3, 71.2, 71.1, 68.3, 60.8, 58.9, 58.0, 49.6, 44.6, 43.7, 39.0, 37.3, 36.8, 27.0, 15.9.

LC/MS: m/z calculated for $C_{53}H_{68}N_{10}O_{11}S$ $[M+2H]^{2+}$: 527.2, found: 527.1.

Purity (HPLC): 98%.

Synthesis of 2nd generation PROTACs



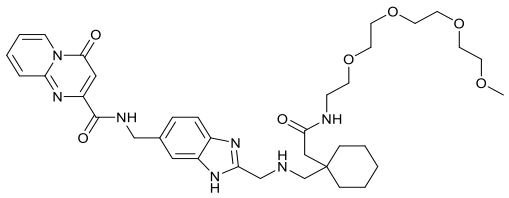
Compound **73**: A solution of OMe-PEG4-NH_2 (21 mg, 0.1 mmol, 1.0 eq.), TBTU (32 mg, 0.1 mmol, 1.0 eq.) and Boc-gabapentin (27 mg, 0.1 mmol, 1.0 eq.) in dry DMF (1 mL) was treated with DIPEA (52 µL, 0.3 mmol, 3.0 eq.), and the suspension was stirred at RT for 16 h. The suspension was concentrated in vacuo, and the resulting residue was purified by RP flash chromatography and lyophilized. The intermediate was resolved in DCM/TFA (1+1 mL) and stirred at RT for 30 min. Evaporation and lyophilization afforded the product as a colorless oil.

Yield: 31 mg (86% of th.).

^{1}H NMR: (300 MHz, MeO*D*) δ [ppm] = 3.62 – 3.45 (m, 15H), 3.35 (d, *J* = 5.3 Hz, 2H), 2.91 (s, 2H), 2.44 (s, 2H), 1.58 – 1.23 (m, 12H).

^{13}C NMR: (75 MHz, MeOD) δ [ppm] = 174.2, 72.9, 71.6, 71.5, 71.5, 71.3, 71.2, 70.4, 59.1, 44.1, 40.5, 36.5, 34.6, 26.7, 22.2.

LC/MS: m/z calculated for $C_{18}H_{36}N_2O_5$ $[M+H]^+$: 361.3, found: 361.1.



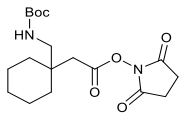
Compound **26**: **73** (7.2 mg, 0.02 mmol, 1.0 eq.) and **72** (7 mg, 0.02 mmol, 1.0 eq.) were dissolved in DCE/HFIP (500+100 µL) and $Ti(O_iPr)_4$ (50 µL, 0.165 mmol, 8.0 eq). The solution was stirred at RT for 16 h. Subsequently, $Ti(O_iPr)_4$ (50 µL, 0.165 mmol, 8.0 eq), MeOH (200 µL), and $NaBH_4$ (1 mg, 0.02 mmol, 1.0 eq.) were added. The reaction was incubated at RT for 30 min and quenched with TFA (10 µL). After evaporation and purification by RP flash chromatography, lyophilization afforded the product as a colorless solid.

Yield: 7 mg (51% of th.).

^{1}H NMR: (600 MHz, MeO*D*) δ [ppm] = 9.01 (d, *J* = 7.0 Hz, 1H), 7.93 (ddd, *J* = 8.4, 6.8, 1.3 Hz, 1H), 7.76 (d, *J* = 8.9 Hz, 1H), 7.53 (s, 1H), 7.48 (d, *J* = 7.2 Hz, 1H), 7.36 – 7.32 (m, 1H), 7.24 (d, *J* = 8.1 Hz, 1H), 7.03 (s, 1H), 4.65 (d, *J* = 15.8 Hz, 2H), 4.21 (s, 2H), 3.68 – 3.54 (m, 1H), 3.54 – 3.44 (m, 10H), 3.44 – 3.38 (m, 4H), 3.30 (d, *J* = 20.4 Hz, 3H), 2.83 (s, 2H), 2.38 (s, 2H), 1.40 (d, *J* = 51.7 Hz, 11H).

^{13}C NMR: (151 MHz, MeOD) δ [ppm] = 174.6, 165.3, 160.6, 155.4, 152.3, 139.2, 134.6, 128.5, 127.8, 124.0, 118.4, 102.5, 72.9, 71.5, 71.5, 71.5, 71.3, 71.2, 70.5, 59.1, 44.6, 40.4, 37.6, 35.3, 27.0, 23.8, 22.4.

LC/MS: m/z calculated for $C_{36}H_{49}N_7O_7$ $[M+H]^+$: 692.4, found: 692.2.



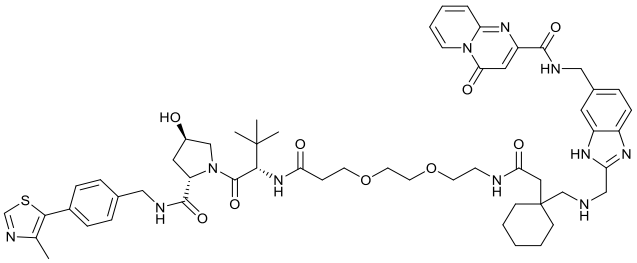
Compound **74**: Boc-gabapentin (700 mg, 2.6 mmol, 1.0 eq.) was dissolved in DCM (20 mL), and *N*-hydroxysuccinimide (300 mg, 2.6 mmol, 1.0 eq.), DMAP (5 mg, cat.), and DCC (500 mg, 2.45 mmol, 0.9 eq.) were added. The reaction was stirred at RT for 16 h, filtered over silica, and evaporated to give the product as a colorless oil.

Yield: 451 mg (47% of th.).

^{1}H NMR: (300 MHz, C*D*Cl$_3$) δ [ppm] = 5.24 (s, 1H), 3.15 (d, *J* = 6.8 Hz, 2H), 2.76 (s, 4H), 2.49 (s, 2H), 1.36 (s, 19H).

^{13}C NMR: (75 MHz, *C*DCl$_3$) δ [ppm] = 169.2, 167.1, 156.4, 79.0, 53.5, 46.6, 38.7, 37.4, 33.6, 28.3, 25.7, 25.6, 21.4.

LC/MS: m/z calculated for $C_{18}H_{28}N_2O_6$ [M - Boc+H]$^+$: 269.2, found: 269.0.



Compound **27**: **49** (11.8 mg, 0.02 mmol, 1.0 eq.) was dissolved in DMF (100 µL), DIPEA (10 µL, 0.06 mmol, 3.0 eq.), and **74** (7.3 mg, 0.02 mmol, 1.0 eq.) were added, and the mixture was stirred for at RT for 3 h. The solvent was evaporated, and the residue resolved in DCM/TFA (200+200 µL). The reaction was then stirred at RT for 30 min, the solvent evaporated, and the mix was purified by RP flash chromatography. The resulting intermediate (11.5 mg, 0.02 mmol, 1.0 eq.) was dissolved in DCE/HFIP (500+100 µL), and **72** (7 mg, 0.02 mmol, 1.0 eq.) and Ti(O$_i$Pr)$_4$ (50 µL, 0.165 mmol, 8.0 eq.) were added, and incubated at RT for 16 h. Subsequently, MeOH (200 µL) and $NaBH_4$ (1 mg, 0.02 mol, 1.0 eq.) were added at 0 °C, the reaction was incubated at RT for 30 min and quenched by the addition of 0.1% TFA (10 µL). The organic solvents were evaporated, and the residue was purified by RP flash chromatography.

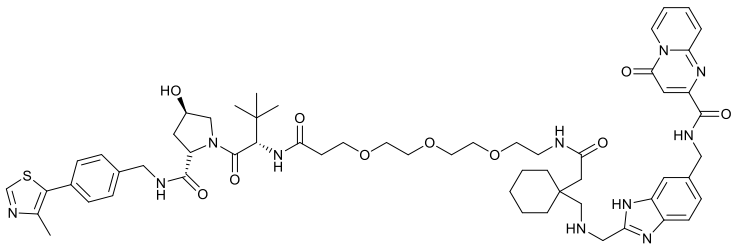
Yield: 4 mg (19% of th.).

^{1}H NMR: (400 MHz, MeO*D*) δ [ppm] = 9.09 (d, *J* = 7.2 Hz, 1H), 8.87 (s, 1H), 8.03 – 7.97 (m, 1H), 7.86 (dd, *J* = 20.5, 8.9 Hz, 2H), 7.72 – 7.57 (m, 2H), 7.51 – 7.34 (m, 6H), 7.09 (d, *J* = 17.4 Hz, 1H), 4.75 (s, 2H), 4.66 (d, *J* = 8.7 Hz, 1H), 4.60 – 4.49 (m, 5H), 4.35 (dd, *J* = 15.2, 4.9 Hz, 1H), 3.89 (d, *J* = 10.8 Hz, 1H), 3.80 (dd, *J* = 11.2, 3.8 Hz, 1H), 3.75 – 3.67 (m, 2H), 3.63 – 3.54 (m, 5H), 3.49 (t, *J* = 5.4 Hz, 2H), 3.26 – 3.19 (m, 3H), 2.56 (d, *J* = 11.8 Hz, 3H), 2.50 – 2.44 (m, 4H), 2.26 – 2.19 (m, 1H), 2.12 – 2.04 (m, 1H), 1.55 (s, 7H), 1.48 – 1.39 (m, 4H), 1.33 (t, *J* = 7.3 Hz, 3H), 1.04 (d, *J* = 9.5 Hz, 9H).

^{13}C NMR: (101 MHz, MeOD) δ [ppm] = 174.7, 174.4, 173.6, 172.2, 165.5, 160.6, 155.5, 152.9, 152.3, 140.2, 139.2, 131.5, 130.4, 130.3, 129.4, 129.0, 128.5, 127.8, 124.6, 118.7, 118.4, 102.6, 71.4, 71.2, 71.1, 70.4, 68.3, 60.9, 58.9, 58.0, 47.9, 45.8, 44.6, 43.7, 40.7, 39.0, 37.3, 37.0, 36.8, 34.8, 27.0, 26.7, 22.3, 21.9, 17.7, 17.5, 17.3, 17.1, 15.8, 9.2.

LC/MS: m/z calculated for $C_{56}H_{71}N_{11}O_9S$ [M+2H]$^{2+}$: 537.8, found: 537.7.

Purity (HPLC): 95%.



Compound **28**: **50** (15.8 mg, 0.025 mmol, 1.0 eq.) was dissolved in DMF (100 µL), DIPEA (10 µL, 0.06 mmol, 2.4 eq.), and **74** (9.1 mg, 0.025 mmol, 1.0 eq.) were added and the mixture was stirred at RT for 3 h. The solvent was evaporated, and the mixture was resolved in DCM/TFA (200+200 µL). The reaction was stirred at RT for 30 min, the solvent evaporated, and the mixture was purified by RP flash chromatography. The intermediate (12 mg, 0.02 mmol, 1.0 eq.) was dissolved in DCE/HFIP (500+100 µL), and **72** (7 mg, 0.02 mmol, 1.0 eq.) and $Ti(O_iPr)_4$ (50 µL, 0.165 mmol, 8.0 eq.) were added. This mixture was incubated at RT for 16 h. Subsequently, MeOH (200 µL) and $NaBH_4$ (1 mg, 0.02 mmol, 1.0 eq.) were added at 0 °C, the reaction was incubated at RT for 30 min and quenched by the addition of 0.1% TFA (10 µL). The organic solvents were evaporated, and the residue was purified by RP flash chromatography.

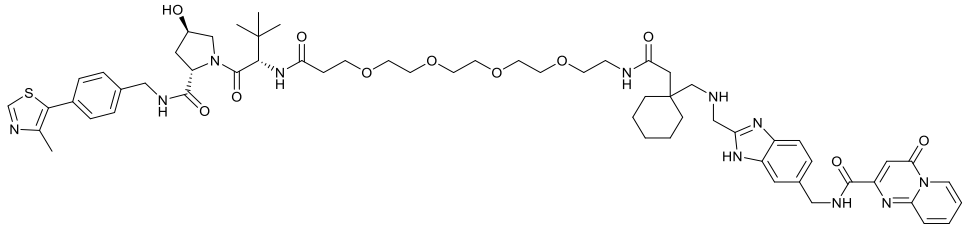
Yield: 3 mg (11% of th.).

^{1}H NMR: (400 MHz, MeO*D*) δ [ppm] = 9.10 (d, *J* = 6.6 Hz, 1H), 8.04 – 7.98 (m, 1H), 7.87 (dd, *J* = 18.4, 8.7 Hz, 2H), 7.68 (s, 1H), 7.62 (d, *J* = 8.2 Hz, 1H), 7.50 – 7.35 (m, 7H), 7.12 (s, 1H), 4.75 (s, 2H), 4.66 (d, *J* = 5.7 Hz, 1H), 4.56 (dd, *J* = 18.1, 9.7 Hz, 6H), 4.35 (d, *J* = 15.5 Hz, 1H), 3.89 (d, *J* = 11.2 Hz, 1H), 3.83 – 3.67 (m, 4H), 3.58 (dt, *J* = 13.7, 5.8 Hz, 12H), 3.48 (dt, *J* = 10.1, 5.4 Hz, 4H), 3.26 – 3.13 (m, 4H), 2.58 (q, *J* = 11.1, 9.1 Hz, 3H), 2.48 (d, *J* = 11.7 Hz, 4H), 2.26 – 2.17 (m, 2H), 2.13 – 2.05 (m, 1H), 1.88 – 1.81 (m, 1H), 1.75 – 1.69 (m, 1H), 1.61 (d, *J* = 5.7 Hz, 2H), 1.53 (d, *J* = 12.3 Hz, 9H), 1.44 (d, *J* = 6.3 Hz, 3H), 1.33 (t, *J* = 7.3 Hz, 3H), 1.04 (d, *J* = 6.7 Hz, 9H).

^{13}C NMR: (101 MHz, MeOD) δ [ppm] = 174.7, 174.5, 173.7, 172.2, 160.6, 140.3, 139.2, 135.5, 130.3, 129.0, 128.6, 127.8, 124.7, 118.4, 71.8, 71.6, 71.5, 71.3, 71.2, 71.0, 70.3, 68.3, 62.8, 60.9, 59.0, 58.0, 57.7, 57.5, 45.7, 45.6, 44.6, 43.7, 40.7, 39.0, 37.7, 37.3, 37.0, 36.8, 34.8, 30.8, 30.4, 28.1, 27.3, 27.0, 26.8, 26.7, 23.9, 17.5, 17.3, 17.1, 15.8, 9.2.

LC/MS: m/z calculated for $C_{58}H_{75}N_{11}O_{10}S$ $[M+2H]^{2+}$: 559.8, found: 559.7.

Purity (HPLC): 99%.



Compound **29**: **51** (24 mg, 0.035 mmol, 1.0 eq.) was dissolved in DMF (100 µL), DIPEA (10 µL, 0.06 mmol, 1.7 eq.), and **74** (13 mg, 0.035 mmol, 1.0 eq.) were added and the reaction was stirred at RT for 3 h. The solvent was evaporated, and the resulting residue was resolved in DCM/TFA (200+200 µL). The reaction was stirred at RT for 30 min, the solvent evaporated, and the residue purified by RP flash chromatography. The intermediate (21 mg, 0.03 mmol, 1.5 eq.) was dissolved in DCE/HFIP (500+100 µL), and **72** (7 mg, 0.02 mmol, 1.0 eq.) and $Ti(O_iPr)_4$ (50 µL, 0.165 mmol, 5.5 eq.) were added, and the mixture was incubated at RT for 16 h. Subsequently, MeOH (200 µL) and $NaBH_4$ (1 mg, 0.02 mmol, 1.0 eq.) were added at 0 °C, subsequently, the reaction was incubated at RT for 30 min and quenched by the addition of 0.1% TFA (10 µL). The organic solvents were evaporated, and the residue was purified by RP flash chromatography.

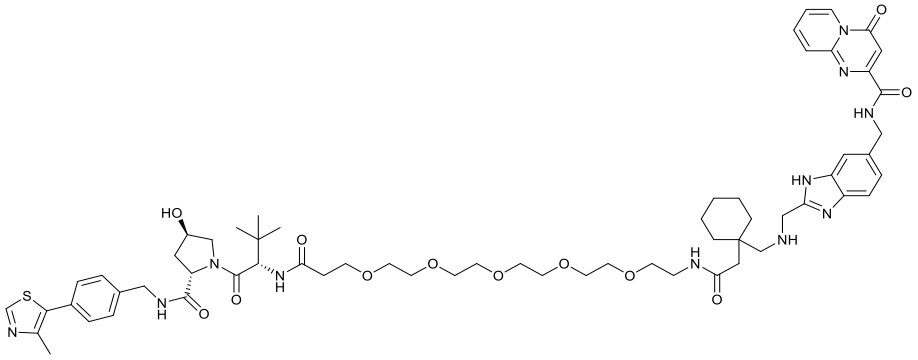
Yield: 4 mg (10% of th.).

^{1}H NMR: (400 MHz, MeO*D*) δ [ppm] = 9.10 (t, *J* = 6.8 Hz, 1H), 8.93 (s, 1H), 8.04 (dt, *J* = 24.3, 7.6 Hz, 1H), 7.87 (dd, *J* = 24.4, 8.8 Hz, 1H), 7.76 – 7.58 (m, 2H), 7.49 – 7.36 (m, 6H), 7.09 (d, *J* = 16.8 Hz, 1H), 4.75 (s, 2H), 4.65 (s, 1H), 4.60 – 4.47 (m, 5H), 4.35 (d, *J* = 15.5 Hz, 1H), 3.89 (d, *J* = 10.9 Hz, 1H), 3.79 (dd, *J* = 11.0, 3.7 Hz, 1H), 3.70 (dt, *J* = 9.7, 5.4 Hz, 2H), 3.64 – 3.55 (m, 13H), 3.48 (dq, *J* = 10.0, 5.7 Hz, 4H), 3.22 (d, *J* = 7.5 Hz, 2H), 2.58 (d, *J* = 9.2 Hz, 3H), 2.48 (d, *J* = 9.5 Hz, 3H), 2.21 (q, *J* = 10.1, 7.1 Hz, 1H), 2.08 (ddd, *J* = 13.1, 9.1, 4.3 Hz, 1H), 1.84 (dt, *J* = 14.3, 6.6 Hz, 1H), 1.71 (dt, *J* = 13.2, 6.4 Hz, 1H), 1.66 – 1.48 (m, 9H), 1.43 (d, *J* = 6.2 Hz, 3H), 1.32 (t, *J* = 7.3 Hz, 1H), 1.04 (d, *J* = 6.4 Hz, 9H).

^{13}C NMR: (101 MHz, MeOD) δ [ppm] = 174.5, 173.7, 172.2, 160.6, 140.3, 139.2, 130.3, 129.0, 128.6, 127.8, 124.8, 118.8, 118.4, 71.7, 71.6, 71.5, 71.4, 71.2, 71.1, 71.0, 70.3, 68.3, 62.8, 60.9, 59.0, 58.0, 45.6, 44.5, 43.7, 40.7, 39.0, 37.3, 37.0, 36.8, 34.8, 34.8, 30.8, 30.4, 28.1, 27.3, 27.1, 26.7, 22.2, 21.9, 15.8, 9.2.

LC/MS: m/z calculated for $C_{60}H_{79}N_{11}O_{11}S$ $[M+2H]^{2+}$: 581.8, found: 581.7.

Purity (HPLC): 95%.



Compound **30**: **52** (21 mg, 0.03 mmol, 1.0 eq.) was dissolved in DMF (100 µL), DIPEA (10 µL, 0.06 mmol, 2.0 eq.), and **74** (11 mg, 0.03 mmol, 1.0 eq.) were added and the mixture was stirred at RT for 3 h. The solvent was evaporated, and the resulting residue was resolved in DCM/TFA (200+200 µL). The reaction was stirred at RT for 30 min, evaporated, and purified by RP flash chromatography. The product (18 mg, 0.02 mmol, 1.0 eq.) was dissolved in DCE/HFIP (500+100 µL), and **72** (7 mg, 0.02 mmol, 1.0 eq.) and $Ti(O_iPr)_4$ (50 µL, 0.165 mmol, 8.0 eq.) were added, and incubated at RT for 16 h. Subsequently, MeOH (200 µL) and $NaBH_4$ (1 mg, 0.02 mmol, 1.0 eq.) were added at 0 °C, the reaction was incubated at RT for 30 min and quenched by the addition of 0.1% TFA (10 µL). The organic solvents were evaporated, and the residue was purified by RP flash chromatography.

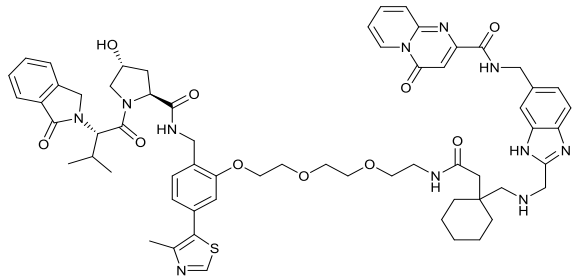
Yield: 4 mg (11% of th.).

^{1}H NMR: (400 MHz, MeO*D*) δ [ppm] = 9.16 – 8.82 (m, 2H), 8.01 (t, *J* = 7.3 Hz, 1H), 7.85 (d, *J* = 8.4 Hz, 1H), 7.74 – 7.59 (m, 2H), 7.43 (dt, *J* = 14.8, 7.8 Hz, 6H), 7.12 (s, 1H), 4.75 (s, 2H), 4.65 (s, 1H), 4.60 – 4.48 (m, 5H), 4.35 (d, *J* = 15.5 Hz, 1H), 3.89 (d, *J* = 10.7 Hz, 1H), 3.80 (dd, *J* = 11.0, 3.6 Hz, 1H), 3.70 (dt, *J* = 10.0, 5.8 Hz, 2H), 3.59 (dd, *J* = 11.6, 4.1 Hz, 17H), 3.48 (dq, *J* = 10.1, 5.3 Hz, 3H), 3.21 (s, 1H), 2.62 – 2.52 (m, 3H), 2.48 (d, *J* = 7.4 Hz, 3H), 2.21 (dd, *J* = 17.6, 10.2 Hz, 1H), 2.09 (td, *J* = 13.1, 11.0, 4.4 Hz, 1H), 1.85 (dt, *J* = 14.3, 6.7 Hz, 1H), 1.75 – 1.69 (m, 1H), 1.61 (s, 1H), 1.55 (s, 7H), 1.47 – 1.38 (m, 3H), 1.33 (t, *J* = 7.3 Hz, 1H), 1.04 (d, *J* = 6.1 Hz, 9H).

^{13}C NMR: (101 MHz, MeOD) δ [ppm] = 174.7, 174.5, 174.3, 173.7, 172.2, 160.6, 140.3, 139.2, 131.5, 130.4, 129.0, 128.6, 127.8, 124.7, 118.4, 71.7, 71.6, 71.6, 71.5, 71.4, 71.2, 71.1, 71.0, 70.3, 68.3, 62.8, 60.9, 59.0, 58.0, 50.0, 45.8, 45.7, 45.6, 44.6, 43.7, 40.7, 39.0, 37.7, 37.4, 37.0, 36.8, 36.5, 34.8, 34.8, 30.8, 30.4, 28.1, 27.3, 27.1, 26.8, 26.7, 23.9, 22.3.

LC/MS: m/z calculated for $C_{62}H_{83}N_{11}O_{12}S$ $[M+2H]^{2+}$: 603.8, found: 603.7.

Purity (HPLC): 96%.



Compound **31**: **44** (17.7 mg, 0.025 mmol, 1.0 eq.) was dissolved in DMF (500 µL), DIPEA (20 µL, 0.12 mmol, 4.8 eq.), and **74** (9.3 mg, 0.025 mmol, 1.0 eq.) were added and the mixture was stirred at RT for 3 h. The solvent was evaporated, and the resulting residue was resolved in DCM/TFA (200+200 µL). The reaction was stirred at RT for 30 min, the solvent evaporated, and the mixture was purified by RP flash chromatography. The residue (13 mg, 0.02 mmol, 1.0 eq.) was dissolved in DCE/HFIP (500+100 µL), and **72** (7 mg, 0.02 mmol, 1.0 eq.) and $Ti(O_iPr)_4$ (50 µL, 0.165 mmol, 8.0 eq.) were added. The reaction was incubated at RT for 16 h. Subsequently, MeOH (200 µL) and $NaBH_4$ (1 mg, 0.02 mmol, 1.0 eq.) were added at 0 °C. The reaction was incubated at RT for 30 min and quenched by the addition of 0.1% TFA (10 µL). The organic solvents were evaporated, and the residue was purified by RP flash chromatography.

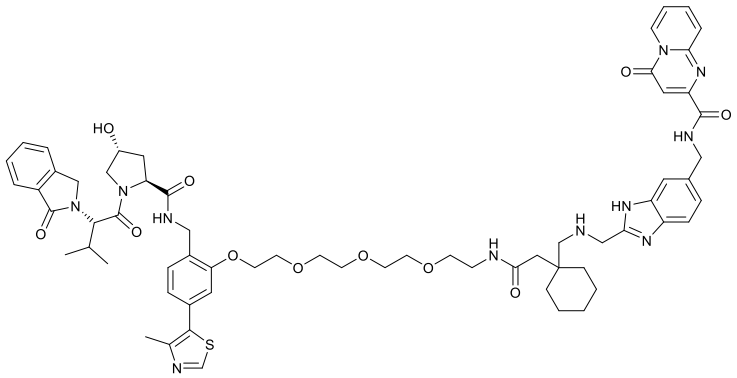
Yield: 5 mg (17% of th.).

^{1}H NMR: (400 MHz, MeO*D*) δ [ppm] = 9.06 (d, *J* = 7.1 Hz, 1H), 8.91 (s, 1H), 7.98 (t, *J* = 7.8 Hz, 1H), 7.78 (dd, *J* = 15.1, 8.1 Hz, 2H), 7.68 (s, 1H), 7.60 (t, *J* = 7.5 Hz, 2H), 7.54 (d, *J* = 7.5 Hz, 1H), 7.48 (t, *J* = 7.6 Hz, 1H), 7.40 (dt, *J* = 11.9, 8.1 Hz, 3H), 7.06 (d, *J* = 10.5 Hz, 1H), 7.02 (d, *J* = 3.9 Hz, 2H), 4.73 (s, 2H), 4.61 – 4.54 (m, 2H), 4.52 (d, *J* = 7.6 Hz, 3H), 4.46 (d, *J* = 3.4 Hz, 2H), 4.40 (d, *J* = 15.6 Hz, 1H), 4.19 (q, *J* = 4.3 Hz, 2H), 4.00 (d, *J* = 11.1 Hz, 1H), 3.88 (p, *J* = 4.4 Hz, 3H), 3.70 (t, *J* = 4.5 Hz, 2H), 3.62 – 3.55 (m, 3H), 3.48 (dd, *J* = 6.7, 4.2 Hz, 3H), 3.17 (s, 2H), 2.49 (d, *J* = 12.4 Hz, 5H), 2.24 – 2.18 (m, 1H), 2.05 (ddd, *J* = 13.3, 9.0, 4.5 Hz, 1H), 1.85 (p, *J* = 6.7 Hz, 1H), 1.75 – 1.64 (m, 1H), 1.62 (dd, *J* = 6.6, 4.0 Hz, 1H), 1.55 – 1.44 (m, 8H), 1.43 – 1.28 (m, 4H), 1.05 (d, *J* = 6.6 Hz, 3H), 0.83 (d, *J* = 6.6 Hz, 3H).

^{13}C NMR: (101 MHz, MeOD) δ [ppm] = 174.6, 174.1, 170.9, 170.7, 165.4, 160.6, 158.0, 143.8, 139.2, 135.6, 133.2, 132.9, 132.5, 130.0, 129.2, 128.5, 128.3, 127.7, 124.8, 124.4, 124.4, 122.9, 118.4, 116.5, 115.5, 113.7, 102.5, 71.8, 71.7, 71.2, 71.0, 70.8, 70.3, 69.3, 62.8, 60.7, 60.1, 58.7, 57.2, 45.6, 44.5, 40.7, 39.5, 39.1, 37.7, 36.9, 34.8, 34.7, 30.8, 30.4, 30.2, 28.1, 27.3, 26.7, 23.9, 22.2, 19.7, 19.0, 15.9.

LC/MS: m/z calculated for $C_{62}H_{73}N_{11}O_{10}S$ $[M+2H]^{2+}$: 582.8, found: 582.6.

Purity (HPLC): 95%.



Compound **32**: **45** (17 mg, 0.023 mmol, 1.0 eq.) was dissolved in DMF (500 µL), DIPEA (20 µL, 0.12 mmol, 5.2 eq.), and **74** (8.4 mg, 0.023 mmol, 1.0 eq.) were added and stirred at RT for 3 h. The solvent was evaporated, and the resulting residue resolved in DCM/TFA (200+200 µL). The reaction was stirred at RT for 30 min, the solvent evaporated, and the mix was purified by RP flash chromatography. The residue (11 mg, 0.013 mmol, 1.0 eq.) was dissolved in DCE/HFIP (500+100 µL), and **72** (7 mg, 0.02 mmol, 1.5 eq.) and $Ti(O_iPr)_4$ (50 µL, 0.165 mmol, 12.7 eq.) were added. The reaction was incubated at RT for 16 h. Subsequently, MeOH (200 µL) and $NaBH_4$ (1 mg, 0.02 mol, 1.5 eq.) were added at 0 °C. The reaction was incubated at RT for 30 min and quenched by the addition of 0.1% TFA (10 µL). The organic solvents were evaporated, and the residue was purified by RP flash chromatography.

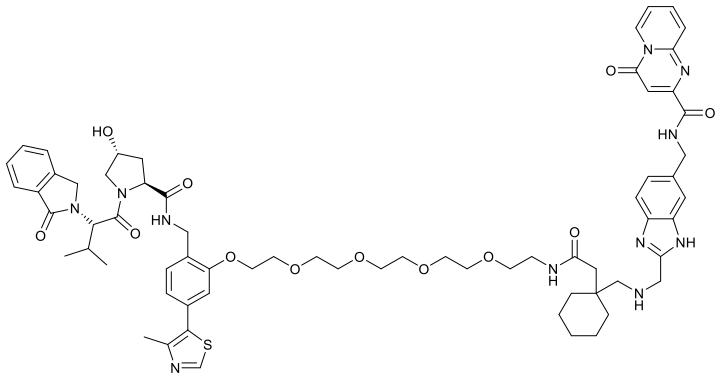
Yield: 4 mg (14% of th.).

^{1}H NMR: (400 MHz, MeO*D*) δ [ppm] = 9.06 (d, *J* = 7.1 Hz, 1H), 8.90 (s, 1H), 7.98 (t, *J* = 7.8 Hz, 1H), 7.79 (dd, *J* = 15.5, 8.3 Hz, 2H), 7.67 (s, 1H), 7.60 (dd, *J* = 8.1, 5.6 Hz, 2H), 7.55 (d, *J* = 7.6 Hz, 1H), 7.49 (t, *J* = 7.4 Hz, 1H), 7.39 (td, *J* = 9.3, 8.1, 4.3 Hz, 3H), 7.08 (s, 1H), 7.01 (d, *J* = 7.7 Hz, 2H), 4.74 (s, 2H), 4.62 (d, *J* = 18.0 Hz, 1H), 4.56 (d, *J* = 8.5 Hz, 1H), 4.52 (d, *J* = 5.6 Hz, 3H), 4.48 (d, *J* = 5.6 Hz, 2H), 4.41 (d, *J* = 15.6 Hz, 1H), 4.21 (q, *J* = 3.6 Hz, 2H), 3.99 (d, *J* = 11.0 Hz, 1H), 3.94 – 3.86 (m, 3H), 3.72 (dd, *J* = 5.6, 3.3 Hz, 2H), 3.64 (dd, *J* = 5.6, 3.5 Hz, 2H), 3.58 (dt, *J* = 9.5, 2.8 Hz, 3H), 3.51 (dd, *J* = 6.6, 3.3 Hz, 2H), 3.46 (dt, *J* = 10.4, 5.5 Hz, 3H), 3.18 (d, *J* = 4.9 Hz, 2H), 2.52 (d, *J* = 5.7 Hz, 2H), 2.48 (s, 3H), 2.25 – 2.18 (m, 1H), 2.07 (ddd, *J* = 13.5, 9.1, 4.6 Hz, 1H), 1.85 (p, *J* = 6.7 Hz, 1H), 1.75 – 1.67 (m, 1H), 1.61 (td, *J* = 6.7, 5.6, 3.4 Hz, 1H), 1.50 (dd, *J* = 17.8, 5.6 Hz, 8H), 1.43 – 1.32 (m, 3H), 1.05 (d, *J* = 6.5 Hz, 3H), 0.83 (d, *J* = 6.7 Hz, 3H).

^{13}C NMR: (101 MHz, MeOD) δ [ppm] = 174.6, 174.1, 170.9, 170.7, 165.4, 160.6, 158.0, 155.4, 143.8, 139.2, 135.6, 133.2, 132.9, 132.5, 130.0, 129.2, 128.5, 128.3, 127.8, 124.8, 124.4, 124.4, 122.8, 118.4, 116.5, 115.4, 113.7, 102.5, 71.8, 71.7, 71.6, 71.6, 71.2, 71.0, 70.8, 70.2, 69.4, 62.8, 60.7, 60.1, 57.2, 46.5, 45.6, 44.5, 40.7, 39.5, 39.1, 37.7, 37.0, 34.8, 30.8, 30.4, 30.2, 28.1, 27.3, 26.7, 22.2, 19.7, 19.0, 15.9.

LC/MS: m/z calculated for $C_{64}H_{77}N_{11}O_{11}S$ $[M+2H]^{2+}$: 604.8, found: 604.7.

Purity (HPLC): 95%.



Compound **33**: **46** (18.2 mg, 0.023 mmol, 1.0 eq.) was dissolved in DMF (500 µL), DIPEA (20 µL, 0.06 mmol, 2.6 eq.), and **74** (8.4 mg, 0.023 mmol, 1.0 eq.) were added and stirred at RT for 3 h. The solvent was evaporated, and the resulting residue was resolved in DCM/TFA (200+200 µL). The reaction was stirred at RT for 30 min, the solvent was evaporated, and the mixture was purified by RP flash chromatography. The residue (18 mg, 0.02 mmol, 1.0 eq.) was dissolved in DCE/HFIP (500+100 µL), and **72** (7 mg, 0.02 mmol, 1.0 eq.) and $Ti(O_iPr)_4$ (50 µL, 0.165 mmol, 8.0 eq.) were added. The reaction was incubated at RT for 16 h. Subsequently, MeOH (200 µL) and $NaBH_4$ (1 mg, 0.02 mmol, 1.0 eq.) were added at 0 °C. The reaction was incubated at RT for 30 min and quenched by the addition of 0.1% TFA (10 µL). The organic solvents were evaporated, and the residue was purified by RP flash chromatography.

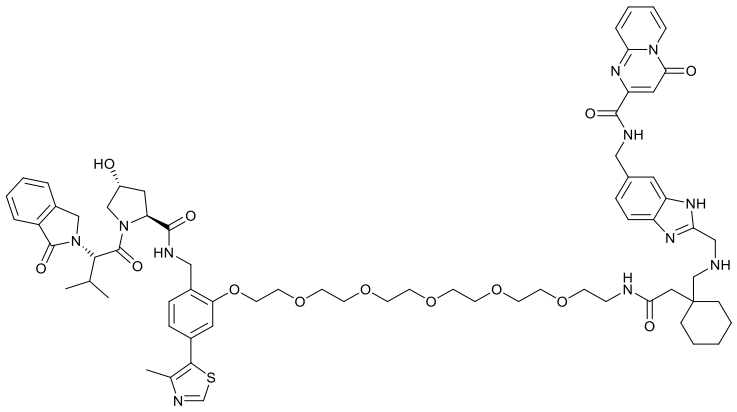
Yield: 3 mg (10% of th.).

^{1}H NMR: (400 MHz, MeO*D*) δ [ppm] = 9.07 (d, *J* = 7.2 Hz, 1H), 8.90 (s, 1H), 7.99 (t, *J* = 7.9 Hz, 1H), 7.79 (dd, *J* = 15.6, 8.2 Hz, 2H), 7.67 (s, 1H), 7.60 (dd, *J* = 7.9, 4.1 Hz, 2H), 7.55 (d, *J* = 7.6 Hz, 1H), 7.49 (t, *J* = 7.4 Hz, 1H), 7.45 – 7.35 (m, 3H), 7.08 (s, 1H), 7.01 (d, *J* = 7.4 Hz, 2H), 4.74 (s, 2H), 4.62 (d, *J* = 18.1 Hz, 1H), 4.56 (d, *J* = 8.5 Hz, 1H), 4.52 (d, *J* = 3.7 Hz, 3H), 4.48 (d, *J* = 5.8 Hz, 2H), 4.41 (d, *J* = 15.5 Hz, 1H), 4.21 (q, *J* = 3.8 Hz, 2H), 3.99 (d, *J* = 11.1 Hz, 1H), 3.89 (h, *J* = 4.4, 4.0 Hz, 3H), 3.75 – 3.70 (m, 2H), 3.65 (dd, *J* = 5.7, 3.2 Hz, 2H), 3.57 (ddd, *J* = 13.8, 9.0, 4.7 Hz, 7H), 3.53 – 3.44 (m, 5H), 3.19 (s, 2H), 2.53 (d, *J* = 9.5 Hz, 2H), 2.48 (s, 3H), 2.25 – 2.17 (m, 1H), 2.07 (ddd, *J* = 13.2, 8.9, 4.5 Hz, 1H), 1.85 (p, *J* = 6.7 Hz, 1H), 1.75 – 1.67 (m, 1H), 1.65 – 1.59 (m, 1H), 1.58 – 1.46 (m, 8H), 1.40 (d, *J* = 12.6 Hz, 3H), 1.05 (d, *J* = 6.4 Hz, 3H), 0.83 (d, *J* = 6.7 Hz, 3H).

^{13}C NMR: (101 MHz, MeOD) δ [ppm] = 174.6, 174.1, 170.9, 170.7, 165.4, 160.6, 158.1, 155.4, 143.8, 139.2, 135.6, 133.2, 132.9, 132.5, 130.0, 129.2, 128.5, 128.3, 127.8, 124.7, 124.4, 124.4, 122.8, 118.4, 116.5, 115.4, 113.7, 102.5, 71.8, 71.6, 71.5, 71.2, 71.0, 70.8, 70.3, 69.4, 62.8, 60.7, 60.1, 57.2, 45.7, 44.6, 40.7, 39.5, 39.1, 37.7, 37.0, 34.8, 30.8, 30.4, 30.2, 28.1, 27.3, 26.7, 22.2, 19.7, 19.0, 17.3, 15.9.

LC/MS: m/z calculated for $C_{66}H_{81}N_{11}O_{12}S$ $[M+2H]^{2+}$: 626.8, found: 626.6.

Purity (HPLC): 96%.



Compound **34**: **47** (25 mg, 0.040 mmol, 1.3 eq.) was dissolved in DMF (500 µL), DIPEA (20 µL, 0.06 mmol, 2.0 eq.), and **74** (11 mg, 0.030 mmol, 1.0 eq.) were added and stirred at RT for 3 h. The solvent was evaporated, and the resulting residue resolved in DCM/TFA (200+200 µL). The reaction was stirred at RT for 30 min. The solvent was evaporated and the mixture was purified by RP flash chromatography. The residue (14 mg, 0.02 mmol, 1.0 eq.) was dissolved in DCE/HFIP (500+100 µL), and **72** (7 mg, 0.02 mmol, 1.0 eq.) and $Ti(O_iPr)_4$ (50 µL, 0.165 mmol, 8.0 eq.) were added. The reaction was incubated at RT for 16 h. Subsequently, MeOH (200 µL) and $NaBH_4$ (1 mg, 0.02 mmol, 1.0 eq.) were added at 0 °C. The reaction was incubated at RT for 30 min and quenched by the addition of 0.1% TFA (10 µL). The organic solvents were evaporated, and the residue was purified by RP flash chromatography.

Yield: 3 mg (8% of th.).

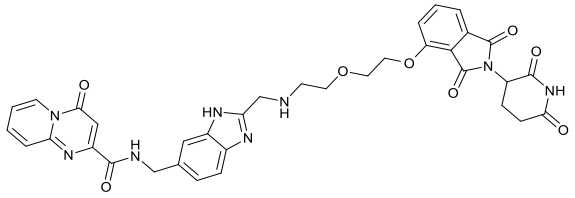
^{1}H NMR: (400 MHz, MeO*D*) δ [ppm] = 9.07 (d, *J* = 7.2 Hz, 1H), 8.91 (s, 1H), 7.99 (t, *J* = 7.7 Hz, 1H), 7.80 (dd, *J* = 16.6, 8.2 Hz, 2H), 7.68 (s, 1H), 7.64 – 7.54 (m, 3H), 7.49 (t, *J* = 7.4 Hz, 1H), 7.41 (dt, *J* = 12.7, 8.4 Hz, 3H), 7.09 (s, 1H), 7.07 – 6.96 (m, 2H), 4.74 (s, 2H), 4.63 (d, *J* = 18.0 Hz, 1H), 4.56 (d, *J* = 8.6 Hz, 1H), 4.52 (d, *J* = 3.5 Hz, 3H), 4.48 (d, *J* = 6.3 Hz, 2H), 4.42 (d, *J* = 15.5 Hz, 1H), 4.21 (q, *J* = 4.0 Hz, 2H), 3.99 (d, *J* = 10.9 Hz, 1H), 3.89 (q, *J* = 3.9 Hz, 3H), 3.72 (t, *J* = 4.2 Hz, 2H), 3.65 (p, *J* = 4.4 Hz, 3H), 3.57 (td, *J* = 13.0, 11.5, 4.7 Hz, 13H), 3.46 (d, *J* = 5.3 Hz, 2H), 3.19 (d, *J* = 10.7 Hz, 2H), 2.53 (d, *J* = 9.9 Hz, 2H), 2.47 (d, *J* = 10.9 Hz, 4H), 2.25 – 2.18 (m, 1H), 2.07 (ddd, *J* = 13.3, 8.9, 4.5 Hz, 1H), 1.78 (dq, *J* = 47.3, 7.2 Hz, 1H), 1.54 (s, 9H), 1.40 (dd, *J* = 14.9, 6.9 Hz, 3H), 1.06 (t, *J* = 5.8 Hz, 3H), 0.84 (d, *J* = 6.7 Hz, 3H).

^{13}C NMR: (101 MHz, MeOD) δ [ppm] = 174.6, 174.1, 170.9, 170.7, 165.4, 160.6, 158.1, 143.8, 139.2, 135.6, 133.2, 132.9, 132.5, 130.1, 129.2, 128.5, 128.3, 127.8, 124.7, 124.4, 124.4, 122.8, 118.4, 113.8, 102.5, 71.8, 71.6, 71.5, 71.5, 71.5, 71.2, 70.8, 70.3, 69.4, 60.7, 60.1, 57.2, 45.7, 44.6, 40.7, 39.5, 39.1, 37.7, 37.0, 34.8, 30.2, 26.7, 23.9, 22.2, 19.7, 19.0, 15.9.

LC/MS: m/z calculated for $C_{68}H_{85}N_{11}O_{13}S$ $[M+3H]^{3+}$: 432.9, found: 432.9.

Purity (HPLC): 95%.

Synthesis of CRBN-based PROTACs



Compound **16**: **54** (10.8 mg, 0.03 mmol, 1.0 eq.) and **72** (13.8 mg, 0.04 mmol, 1.3 eq.) were dissolved in DCE/ACN (1+0.2 mL), and AcOH (6 µL, 0.1 mmol, 3.3 eq.) was added. Subsequently, $NaBH(OAc)_3$ (21 mg, 0.1 mmol, 3.3 eq.) was added, and the mixture was incubated at 30 °C for 5 h. The reaction was quenched by the addition of MeOH (1 mL). The solvent was evaporated. Purification by RP flash chromatography and lyophilization afforded the product as a colorless solid.

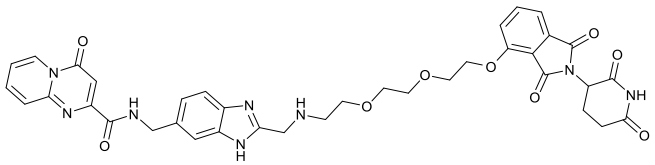
Yield: 7 mg (34% of th.).

^{1}H NMR: (600 MHz, Me*O*D) δ [ppm] = 9.03 (d, *J* = 7.0 Hz, 1H), 7.95 (ddd, *J* = 8.5, 6.7, 1.4 Hz, 1H), 7.79 (t, *J* = 8.2 Hz, 1H), 7.70 – 7.65 (m, 1H), 7.47 (s, 1H), 7.43 (d, *J* = 8.4 Hz, 1H), 7.40 – 7.30 (m, 3H), 7.24 (d, *J* = 8.3 Hz, 1H), 7.04 (s, 1H), 4.65 (s, 2H), 4.60 – 4.50 (m, 2H), 4.33 (t, *J* = 4.1 Hz, 2H), 4.03 – 3.89 (m, 4H), 3.50 – 3.37 (m, 2H), 2.60 (ddd, *J* = 18.5, 14.2, 5.1 Hz, 1H), 2.51 (d, *J* = 16.2 Hz, 1H), 2.42 – 2.32 (m, 1H), 1.80 – 1.72 (m, 1H), 1.33 – 1.22 (m, 1H).

^{13}C NMR: (151 MHz, MeOD) δ [ppm] = 174.4, 170.8, 168.3, 168.0, 165.4, 165.0, 160.7, 157.4, 155.4, 152.3, 139.2, 138.1, 134.8, 128.5, 127.8, 124.5, 120.3, 118.5, 116.8, 103.0, 102.5, 85.6, 70.3, 70.0, 67.6, 57.5, 56.2, 50.3, 45.2, 44.5, 32.1, 23.4.

LC/MS: m/z calculated for $C_{35}H_{32}N_8O_8$ $[M+H]^+$: 693.3, found: 693.1.

Purity (HPLC): 99%.



Compound **17**: **55** (8.0 mg, 0.02 mmol, 1.0 eq.) and **72** (7 mg, 0.02 mmol, 1.0 eq.) were dissolved in DCE/HFIP (500+100 µL) and $Ti(O_iPr)_4$ (50 µL, 0.165 mmol, 8.0 eq) and stirred at RT for 16 h. Subsequently, $Ti(O_iPr)_4$ (50 µL, 0.165 mmol, 8.0 eq.), MeOH (200 µL), and $NaBH_4$ (1 mg, 0.02 mmol, 1.0 eq.) were added, and the mixture was incubated at RT for 30 min. The reaction was quenched with TFA (10 µL), the solvent was evaporated, and the product was purified by RP flash chromatography. Lyophilization afforded the product as a colorless solid.

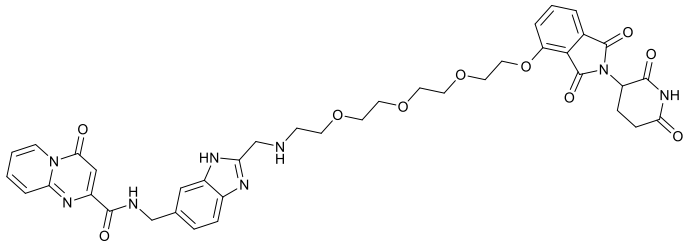
Yield: 7 mg (48% of th.).

^{1}H NMR: (600 MHz, Me*O*D) δ [ppm] = 9.00 (d, *J* = 7.0 Hz, 1H), 7.95 – 7.90 (m, 1H), 7.76 (d, *J* = 8.9 Hz, 1H), 7.54 (t, *J* = 7.9 Hz, 1H), 7.47 (s, 1H), 7.40 (d, *J* = 8.3 Hz, 1H), 7.34 (t, *J* = 6.9 Hz, 1H), 7.21 (t, *J* = 8.1 Hz, 3H), 7.03 (d, *J* = 5.7 Hz, 1H), 4.96 (d, *J* = 5.1 Hz, 1H), 4.64 (s, 2H), 4.25 (d, *J* = 21.4 Hz, 3H), 3.84 (s, 1H), 3.74 – 3.59 (m, 6H), 3.09 (s, 2H), 2.72 (td, *J* = 16.2, 14.0, 5.3 Hz, 1H), 2.64 – 2.52 (m, 2H), 2.00 (dd, *J* = 11.3, 6.2 Hz, 1H), 1.32 – 1.17 (m, 3H).

^{13}C NMR: (151 MHz, MeOD) δ [ppm] = 174.5, 171.7, 168.4, 167.5, 165.4, 160.6, 157.4, 155.4, 152.3, 139.2, 137.8, 134.8, 128.5, 127.8, 124.1, 120.4, 118.4, 117.8, 116.6, 102.5, 97.8, 71.9, 71.2, 70.3, 70.2, 68.7, 63.3, 50.4, 46.1, 44.5, 32.1, 23.6, 15.4.

LC/MS: m/z calculated for $C_{37}H_{36}N_8O_9$ $[M+H]^+$: 737.3, found: 737.1.

Purity (HPLC): 98%.



Compound **18**: **56** (8.8 mg, 0.02 mmol, 1.0 eq.) and **72** (7 mg, 0.02 mmol, 1.0 eq.) were dissolved in DCE/HFIP (500+100 µL) and $Ti(O_iPr)_4$ (50 µL, 0.165 mmol, 8.0 eq.) and stirred at RT for 16 h. Subsequently, $Ti(O_iPr)_4$ (50 µL, 0.165 mmol, 8.0 eq.), MeOH (200 µL), and $NaBH_4$ (1 mg, 0.02 mol, 1.0 eq.) were added, and the mixture was incubated at RT for 30 min. The reaction was quenched with TFA (10 µL), and the product was purified by RP flash chromatography. Lyophilization afforded the product as a colorless solid.

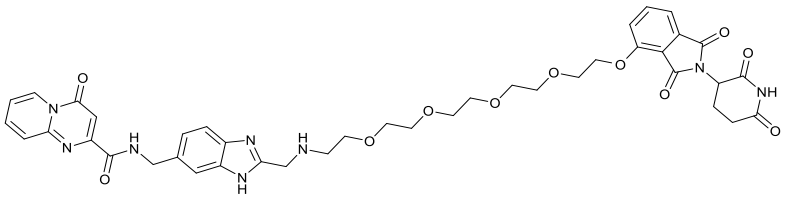
Yield: 4 mg (27% of th.).

^{1}H NMR: (600 MHz, Me*O*D) δ [ppm] = 9.01 (d, *J* = 7.0 Hz, 1H), 7.95 – 7.91 (m, 1H), 7.76 (d, *J* = 8.9 Hz, 1H), 7.56 – 7.48 (m, 2H), 7.43 (d, *J* = 8.4 Hz, 1H), 7.37 – 7.33 (m, 1H), 7.23 (d, *J* = 7.3 Hz, 2H), 7.16 (d, *J* = 8.5 Hz, 1H), 7.04 (s, 1H), 4.63 (d, *J* = 31.8 Hz, 3H), 4.29 (s, 1H), 4.17 (s, 2H), 3.78 (s, 1H), 3.70 – 3.55 (m, 7H), 3.08 (s, 2H), 2.80 – 2.69 (m, 2H), 2.67 – 2.51 (m, 3H), 2.05 – 1.93 (m, 2H), 1.24 (s, 1H).

^{13}C NMR: (151 MHz, MeOD) δ [ppm] = 184.3, 174.6, 171.6, 168.4, 167.5, 165.4, 160.6, 157.4, 155.5, 152.3, 139.2, 137.8, 134.8, 128.5, 127.8, 124.1, 120.4, 118.4, 117.9, 116.6, 102.5, 71.8, 71.5, 71.4, 71.0, 70.4, 70.2, 50.4, 44.5, 32.1, 23.7.

LC/MS: m/z calculated for $C_{39}H_{40}N_8O_{10}$ $[M+H]^+$: 781.3, found: 781.1.

Purity (HPLC): 95%.



Compound **19**: **57** (9.8 mg, 0.02 mmol, 1.0 eq.) and **72** (7 mg, 0.02 mmol, 1.0 eq.) were dissolved in DCE/HFIP (500+100 µL) and $Ti(O_iPr)_4$ (50 µL, 0.165 mmol, 8.0 eq.) and stirred at RT for 16 h. Subsequently, $Ti(O_iPr)_4$ (50 µL, 0.165 mmol, 8.0 eq.), MeOH (200 µL), and $NaBH_4$ (1 mg, 0.02 mmol, 1.0 eq.) were added, and the mixture was incubated at RT for 30 min. The reaction was quenched with TFA (10 µL), and the product was purified by RP flash chromatography. Lyophilization afforded the product as a colorless solid.

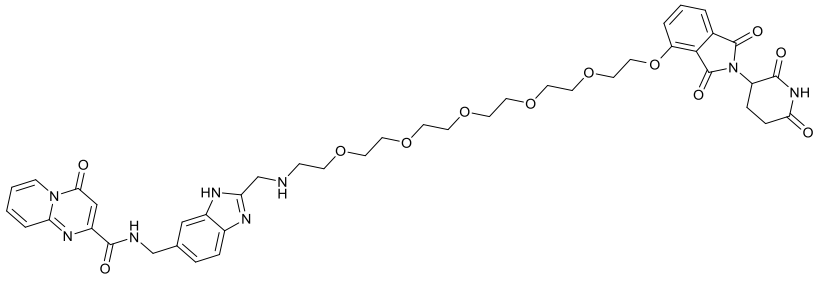
Yield: 6 mg (36% of th.).

^{1}H NMR: (600 MHz, Me*O*D) δ [ppm] = 8.98 (d, *J* = 7.0 Hz, 1H), 7.93 – 7.89 (m, 1H), 7.74 (d, *J* = 8.9 Hz, 1H), 7.58 – 7.54 (m, 1H), 7.52 (s, 1H), 7.44 (d, *J* = 8.2 Hz, 1H), 7.33 (t, *J* = 6.9 Hz, 1H), 7.24 (dd, *J* = 14.3, 7.8 Hz, 2H), 7.19 (d, *J* = 8.5 Hz, 1H), 7.01 (s, 1H), 4.98 (dd, *J* = 12.7, 5.4 Hz, 1H), 4.64 (s, 2H), 4.31 (s, 2H), 4.19 – 4.13 (m, 2H), 3.76 – 3.71 (m, 2H), 3.65 (s, 2H), 3.64 – 3.61 (m, 2H), 3.55 (s, 8H), 3.10 (s, 2H), 2.75 (ddd, *J* = 18.7, 13.9, 5.2 Hz, 1H), 2.67 – 2.55 (m, 2H), 2.06 – 2.00 (m, 1H), 1.32 – 1.20 (m, 1H).

^{13}C NMR: (151 MHz, MeOD) δ [ppm] = 174.6, 171.6, 168.4, 167.3, 165.3, 160.6, 157.5, 155.4, 152.2, 139.2, 137.8, 134.9, 134.8, 128.5, 127.8, 124.1, 120.5, 118.4, 118.0, 116.6, 102.5, 71.9, 71.5, 71.3, 71.3, 71.0, 70.4, 70.2, 68.5, 50.4, 46.0, 44.6, 32.1, 23.6.

LC/MS: m/z calculated for $C_{41}H_{44}N_8O_{11}$ $[M+H]^+$: 825.3, found: 825.1.

Purity (HPLC): 98%.



Compound **20**: **58** (10.6 mg, 0.02 mmol, 1.0 eq.) and **72** (7 mg, 0.02 mmol, 1.0 eq.) were dissolved in DCE/HFIP (500+100 µL) and $Ti(O_iPr)_4$ (50 µL, 0.165 mmol, 8.0 eq.) and stirred at RT for 16 h. Subsequently, $Ti(O_iPr)_4$ (50 µL, 0.165 mmol, 8.0 eq.), MeOH (200 µL), and $NaBH_4$ (1 mg, 0.02 mmol, 1.0 eq.) were added, and the mixture was incubated at RT for 30 min. The reaction was quenched with TFA (10 µL), the solvent was evaporated, and the product was purified by RP flash chromatography. Lyophilization afforded the product as a colorless solid.

Yield: 5 mg (29% of th.).

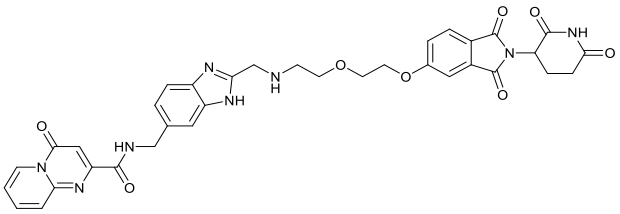
^{1}H NMR: (600 MHz, Me*O*D) δ [ppm] = 8.98 (d, *J* = 7.0 Hz, 1H), 7.95 – 7.89 (m, 1H), 7.74 (d, *J* = 8.6 Hz, 1H), 7.61 – 7.56 (m, 1H), 7.54 (d, *J* = 12.8 Hz, 1H), 7.44 (dd, *J* = 14.2, 5.6 Hz, 1H), 7.33 (t, *J* = 6.9 Hz, 1H), 7.23 (td, *J* = 21.2, 20.7, 7.3 Hz, 3H), 7.01 (s, 1H),

4.97 (dd, *J* = 12.7, 5.4 Hz, 1H), 4.65 (s, 2H), 4.36 – 4.24 (m, 2H), 4.15 (d, *J* = 37.7 Hz, 2H), 3.79 – 3.70 (m, 2H), 3.68 – 3.61 (m, 3H), 3.59 – 3.43 (m, 11H), 3.16 – 3.03 (m, 2H), 2.78 – 2.69 (m, 1H), 2.68 – 2.54 (m, 2H), 2.04 – 1.97 (m, 1H), 1.32 – 1.20 (m, 1H).

^{13}C NMR: (151 MHz, MeOD) δ [ppm] = 174.6, 171.5, 168.4, 167.3, 165.3, 160.6, 157.5, 155.4, 152.2, 139.2, 137.9, 134.9, 134.8, 128.5, 127.8, 124.1, 120.5, 118.4, 118.0, 116.6, 102.5, 71.9, 71.5, 71.4, 71.3, 71.2, 71.0, 70.4, 70.3, 68.6, 50.4, 46.1, 44.6, 32.1, 23.6, 19.2.

LC/MS: m/z calculated for $C_{43}H_{48}N_8O_{12}$ $[M+2H]^{2+}$: 435.2, found: 435.1.

Purity (HPLC): 94%.



Compound **21**: **60** (10.8 mg, 0.03 mmol, 1.0 eq.) and **72** (13.8 mg, 0.04 mmol, 1.3 eq.) were dissolved in DCE/ACN (1+0.2 mL), AcOH (6 µL, 0.1 mmol, 3.3 eq.) and $NaBH(OAc)_3$ (21 mg, 0.1 mmol, 3.3 eq.) were added and the reaction was incubated at 30 °C for 5 h. The reaction was quenched by the addition of MeOH (1 mL), the solvent was evaporated, and the product was purified by RP flash chromatography. Lyophilization afforded the product as a yellowish solid.

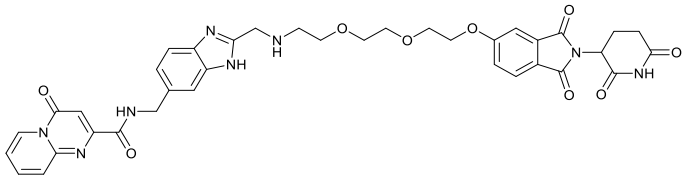
Yield: 9 mg (43% of th.).

^{1}H NMR: (600 MHz, MeO*D*) δ [ppm] = 8.98 (d, *J* = 7.0 Hz, 1H), 7.94 – 7.89 (m, 1H), 7.73 (d, *J* = 8.9 Hz, 1H), 7.62 (d, *J* = 8.3 Hz, 1H), 7.52 (s, 1H), 7.46 (d, *J* = 8.3 Hz, 1H), 7.33 (td, *J* = 7.0, 1.2 Hz, 1H), 7.29 – 7.22 (m, 2H), 7.16 (d, *J* = 7.4 Hz, 1H), 7.02 – 6.97 (m, 1H), 5.02 (dd, *J* = 12.8, 5.5 Hz, 1H), 4.63 (s, 2H), 4.48 (d, *J* = 16.4 Hz, 2H), 4.23 (s, 2H), 3.87 (dt, *J* = 17.0, 4.6 Hz, 3H), 3.29 (s, 9H), 2.79 (ddd, *J* = 17.3, 13.9, 5.2 Hz, 1H), 2.70 – 2.58 (m, 2H), 2.04 (dtd, *J* = 12.9, 6.1, 5.4, 3.1 Hz, 1H).

^{13}C NMR: (151 MHz, MeOD) δ [ppm] = 174.6, 171.5, 168.5, 168.4, 165.5, 165.3, 160.6, 155.3, 152.2, 139.3, 135.6, 135.2, 128.5, 127.7, 126.3, 125.0, 124.6, 124.2, 121.3, 118.5, 110.0, 102.5, 70.6, 69.5, 67.4, 57.5, 50.6, 49.9, 45.1, 44.6, 32.2, 23.7, 17.2.

LC/MS: m/z calculated for $C_{35}H_{32}N_8O_8$ $[M+H]^{+}$: 693.2, found: 693.1.

Purity (HPLC): 99%.



Compound **22**: **61** (8.0 mg, 0.02 mmol, 1.0 eq.) and **72** (7 mg, 0.02 mmol, 1.0 eq.) were dissolved in DCE/HFIP (500+100 µL) and $Ti(O_iPr)_4$ (50 µL, 0.165 mmol, 8.0 eq.) and the reaction was stirred at RT for 16 h. Subsequently, $Ti(O_iPr)_4$ (50 µL, 0.165 mmol, 8.0 eq.), MeOH (200 µL), and $NaBH_4$ (1 mg, 0.02 mmol, 1.0 eq.) were added, and the mixture was incubated at RT for 30 min. The reaction was quenched with TFA (10 µL), the solvent was evaporated, and the product was purified by RP flash chromatography. Lyophilization afforded the product as a colorless solid.

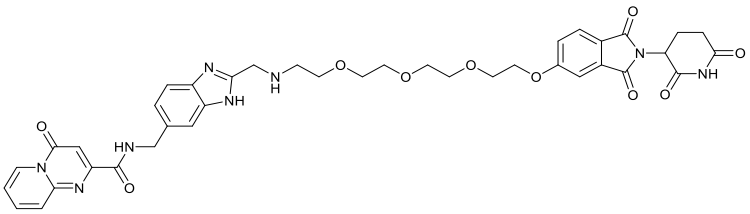
Yield: 13 mg (88% of th.).

^{1}H NMR: (600 MHz, Me*O*D) δ [ppm] = 9.00 (d, *J* = 7.0 Hz, 1H), 7.94 – 7.90 (m, 1H), 7.74 (d, *J* = 8.8 Hz, 1H), 7.55 – 7.50 (m, 2H), 7.43 (d, *J* = 8.0 Hz, 1H), 7.34 (t, *J* = 6.9 Hz, 1H), 7.23 (d, *J* = 8.1 Hz, 1H), 7.18 (s, 1H), 7.06 – 7.01 (m, 2H), 5.02 (dd, *J* = 12.9, 5.5 Hz, 1H), 4.63 (d, *J* = 30.9 Hz, 3H), 4.14 (d, *J* = 19.6 Hz, 3H), 3.79 (s, 2H), 3.67 – 3.59 (m, 5H), 2.99 (s, 2H), 2.80 (ddd, *J* = 19.3, 14.0, 5.2 Hz, 2H), 2.65 (dtd, *J* = 26.7, 13.3, 3.5 Hz, 3H), 2.08 – 2.03 (m, 1H), 1.30 – 1.23 (m, 2H).

^{13}C NMR: (151 MHz, MeOD) δ [ppm] = 174.6, 171.5, 168.5, 168.4, 165.5, 165.3, 160.6, 155.4, 152.2, 139.2, 135.5, 134.6, 128.5, 127.8, 126.1, 124.8, 124.0, 121.3, 118.4, 109.9, 102.5, 71.7, 71.3, 70.5, 69.6, 50.5, 44.6, 32.2, 23.7.

LC/MS: m/z calculated for $C_{37}H_{36}N_8O_9$ $[M+H]^+$: 737.3, found: 737.2.

Purity (HPLC): 99%.



Compound **23**: **62** (8.8 mg, 0.02 mmol, 1.0 eq.) and **72** (7 mg, 0.02 mmol, 1.0 eq.) were dissolved in DCE/HFIP (500+100 µL) and $Ti(O_iPr)_4$ (50 µL, 0.165 mmol, 8.0 eq.) and stirred at RT for 16 h. Subsequently, $Ti(O_iPr)_4$ (50 µL, 0.165 mmol, 8.0 eq.), MeOH (200 µL), and $NaBH_4$ (1 mg, 0.02 mmol, 1.0 eq.) were added and incubated at RT for 30 min. The reaction was quenched with TFA (10 µL), the solvent was evaporated, and the product was purified by RP flash chromatography. Lyophilization afforded the product as a colorless solid.

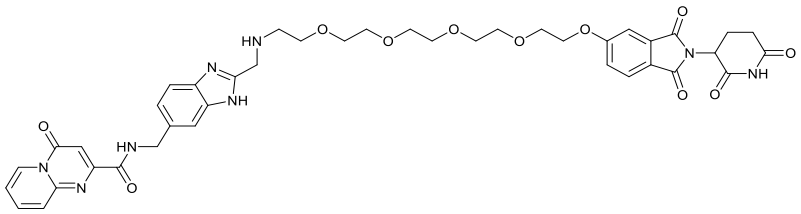
Yield: 6 mg (38% of th.).

^{1}H NMR: (600 MHz, Me*O*D) δ [ppm] = 8.99 (d, *J* = 7.0 Hz, 1H), 7.94 – 7.90 (m, 1H), 7.74 (d, *J* = 8.9 Hz, 1H), 7.57 – 7.51 (m, 2H), 7.45 (d, *J* = 8.1 Hz, 1H), 7.34 (t, *J* = 6.4 Hz, 1H), 7.24 (d, *J* = 8.3 Hz, 1H), 7.14 (s, 1H), 7.06 – 7.00 (m, 2H), 5.02 (dd, *J* = 12.8, 5.5 Hz, 1H), 4.62 (d, *J* = 30.6 Hz, 6H), 4.17 (s, 1H), 4.04 (d, *J* = 4.2 Hz, 1H), 3.72 – 3.66 (m, 2H), 3.63 – 3.53 (m, 8H), 3.29 (s, 1H), 2.97 (s, 1H), 2.79 (ddd, *J* = 18.0, 14.0, 5.3 Hz, 2H), 2.72 – 2.59 (m, 3H), 2.08 – 2.03 (m, 1H), 1.26 – 1.22 (m, 1H).

^{13}C NMR: (151 MHz, MeOD) δ [ppm] = 174.6, 171.5, 168.5, 168.5, 165.5, 165.3, 160.6, 155.4, 152.2, 139.2, 135.5, 128.5, 127.8, 126.1, 124.8, 124.0, 121.2, 118.4, 110.0, 102.5, 72.8, 71.7, 71.5, 71.5, 71.1, 70.5, 69.6, 50.5, 44.6, 32.2, 23.7, 19.1, 0.8.

LC/MS: m/z calculated for $C_{39}H_{40}N_8O_{10}$ $[M+H]^+$: 781.3, found: 781.2.

Purity (HPLC): 99%.



Compound **24**: **63** (9.8 mg, 0.02 mmol, 1.0 eq.) and **72** (7 mg, 0.02 mmol, 1.0 eq.) were dissolved in DCE/HFIP (500+100 µL) and $Ti(O_iPr)_4$ (50 µL, 0.165 mmol, 8.0 eq.) and stirred at RT for 16 h. Subsequently, $Ti(O_iPr)_4$ (50 µL, 0.165 mmol, 8.0 eq.), MeOH (200 µL), and $NaBH_4$ (1 mg, 0.02 mmol, 1.0 eq.) were added and incubated at RT for 30 min. The reaction was quenched with TFA (10 µL), the solvent was evaporated, and the product was purified by RP flash chromatography. Lyophilization afforded the product as a colorless solid.

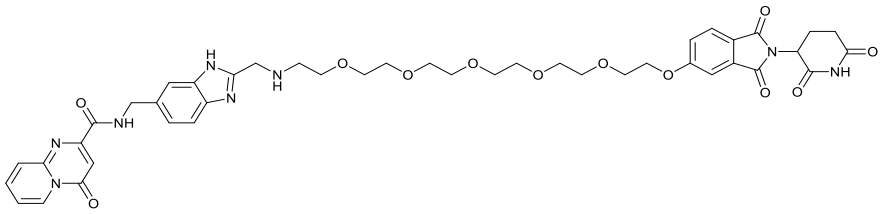
Yield: 4 mg (24% of th.).

^{1}H NMR: (600 MHz, MeO*D*) δ [ppm] = 9.06 (d, *J* = 7.0 Hz, 1H), 8.01 – 7.97 (m, 1H), 7.81 (t, *J* = 7.8 Hz, 1H), 7.67 (d, *J* = 8.3 Hz, 1H), 7.60 (s, 1H), 7.53 (d, *J* = 8.3 Hz, 1H), 7.42 – 7.39 (m, 1H), 7.31 (d, *J* = 8.2 Hz, 1H), 7.25 (s, 1H), 7.18 – 7.14 (m, 1H), 7.09 (s, 1H), 5.09 (dd, *J* = 12.9, 5.4 Hz, 1H), 4.73 (s, 2H), 4.19 (s, 1H), 4.15 – 4.13 (m, 1H), 3.78 – 3.71 (m, 3H), 3.70 – 3.58 (m, 14H), 2.97 (s, 2H), 2.91 – 2.82 (m, 2H), 2.79 – 2.67 (m, 3H), 2.16 – 2.10 (m, 1H), 1.35 – 1.30 (m, 1H).

^{13}C NMR: (151 MHz, MeOD) δ [ppm] = 174.6, 171.5, 168.5, 168.5, 165.6, 165.3, 160.6, 155.4, 152.2, 139.2, 135.5, 134.5, 128.5, 127.8, 126.2, 124.8, 123.9, 121.3, 118.4, 110.0, 102.5, 71.7, 71.5, 71.5, 71.5, 71.1, 70.4, 69.9, 69.6, 67.1, 50.5, 46.9, 44.6, 32.2, 23.7, 19.2.

LC/MS: m/z calculated for $C_{41}H_{44}N_8O_{11}$ $[M+H]^+$: 825.3, found: 825.1.

Purity (HPLC): 98%.



Compound **25**: **64** (10.6 mg, 0.02 mmol, 1.0 eq.) and **72** (7 mg, 0.02 mmol, 1.0 eq.) were dissolved in DCE/HFIP (500+ 100 µL) and $Ti(O_iPr)_4$ (50 µL, 0.165 mmol, 8.0 eq.) and stirred at RT for 16 h. Subsequently, $Ti(O_iPr)_4$ (50 µL, 0.165 mmol, 8.0 eq.), MeOH (200 µL), and $NaBH_4$ (1 mg, 0.02 mol, 1.0 eq.) were added and incubated at RT for 30 min. The reaction was quenched

with TFA (10 µL), the solvent was evaporated, and the product was purified by RP flash chromatography. Lyophilization afforded the product as a colorless solid.

Yield: 2 mg (12% of th.).

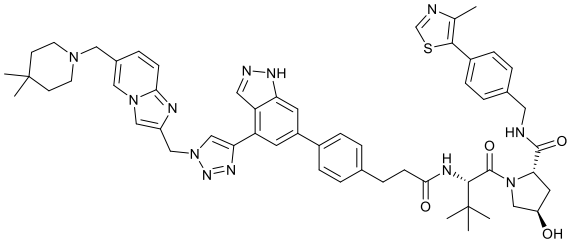
^{1}H NMR: (600 MHz, MeO*D*) δ [ppm] = 9.07 (d, *J* = 7.1 Hz, 1H), 8.02 – 7.98 (m, 1H), 7.82 (d, *J* = 9.4 Hz, 1H), 7.70 (d, *J* = 8.3 Hz, 1H), 7.62 (s, 1H), 7.55 (d, *J* = 8.3 Hz, 1H), 7.43 – 7.40 (m, 1H), 7.32 (d, *J* = 8.2 Hz, 1H), 7.29 (s, 1H), 7.20 (d, *J* = 7.3 Hz, 1H), 7.10 (s, 1H), 5.09 (dd, *J* = 12.8, 5.4 Hz, 1H), 4.74 (s, 1H), 4.67 (s, 1H), 4.36 – 4.32 (m, 1H), 4.24 (s, 1H), 4.18 (s, 1H), 3.95 – 3.90 (m, 1H), 3.80 – 3.78 (m, 1H), 3.74 – 3.56 (m, 14H), 3.37 (s, 3H), 3.25 – 3.20 (m, 1H), 3.03 (s, 1H), 2.92 – 2.83 (m, 2H), 2.80 – 2.67 (m, 3H), 2.16 – 2.11 (m, 1H), 2.06 (s, 1H), 1.34 (d, *J* = 6.6 Hz, 1H).

^{13}C NMR: (151 MHz, MeOD) δ [ppm] = 174.6, 171.5, 168.5, 168.5, 165.6, 160.6, 152.2, 139.2, 135.5, 128.5, 127.8, 126.2, 124.8, 121.4, 118.4, 110.1, 102.5, 71.7, 71.5, 71.5, 71.4, 71.4, 70.5, 69.6, 67.0, 50.6, 44.6, 32.2, 23.7, 19.2, 0.8.

LC/MS: m/z calculated for $C_{43}H_{48}N_8O_{12}$ $[M+2H]^{2+}$: 435.2, found: 435.1.

Purity (HPLC): 96%.

Synthesis of 3rd generation PROTACs



Compound **35**: **65** (6.7 mg, 0.011 mmol, 1.1 eq.), STM3006 (5 mg, 0.010 mmol, 1.0 eq.), potassium phosphate (4.3 mg, 0.02 mmol, 2.0 eq.), X-Phos (1 mg, 0.002 mmol, 0.2 eq.), and tris(dibenzylidenacetone)dipalladium (1 mg, 0.001 mmol, 0.1 eq.) were dissolved under argon atmosphere in 56 µL degassed water/ dioxane (1:4). The reaction was stirred at 110 °C for 1.5 h. The mixture was diluted with water, the solvents were evaporated, and the residue was purified with RP flash chromatography.

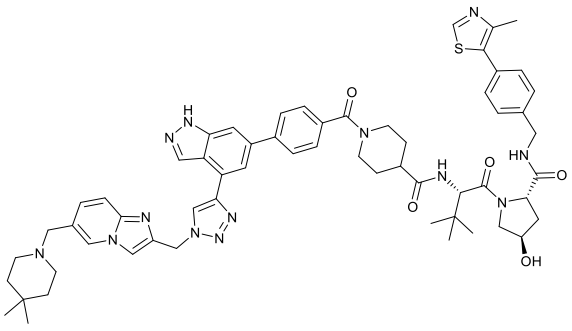
Yield: 4 mg (40% of th.).

^{1}H NMR: (600 MHz, DMSO-d_6) δ [ppm] = 8.98 (s, 2H), 8.59 (q, *J* = 6.2, 4.8 Hz, 2H), 8.44 (s, 1H), 8.03 – 7.97 (m, 2H), 7.90 (d, *J* = 1.4 Hz, 1H), 7.73 – 7.66 (m, 3H), 7.46 (d, *J* = 9.3 Hz, 1H), 7.42 (d, *J* = 8.1 Hz, 2H), 7.39 – 7.36 (m, 2H), 7.34 (d, *J* = 8.0 Hz, 2H), 7.20 (dd, *J* = 9.3, 1.7 Hz, 1H), 5.79 (d, *J* = 6.5 Hz, 2H), 5.18 (s, 2H), 4.56 (dd, *J* = 16.9, 9.4 Hz, 2H), 4.48 – 4.40 (m, 3H), 4.36 (s, 1H), 4.21 (dd, *J* = 15.9, 5.5 Hz, 2H), 3.69 – 3.65 (m, 2H), 3.43 (s, 2H), 2.90 – 2.83 (m, 2H), 2.67 – 2.60 (m, 2H), 2.44 (d, *J* = 3.5 Hz, 3H), 2.35 – 2.32 (m, 3H), 2.07 – 2.00 (m, 2H), 1.90 (ddd, *J* = 12.9, 8.7, 4.6 Hz, 2H), 1.30 (t, *J* = 5.5 Hz, 3H), 0.90 (d, *J* = 4.3 Hz, 7H), 0.87 (d, *J* = 4.7 Hz, 5H).

^{13}C NMR: (151 MHz, DMSO) δ [ppm] = 172.0, 171.3, 169.7, 163.7, 147.7, 145.8, 144.2, 141.4, 140.9, 140.5, 139.6, 138.6, 137.9, 131.2, 129.7, 129.1, 128.9, 128.7, 127.4, 127.3, 127.1, 125.6, 123.6, 123.2, 123.1, 118.7, 117.1, 116.2, 115.0, 111.6, 106.9, 68.9, 59.1, 58.8, 56.5, 56.4, 49.3, 48.0, 41.7, 40.1, 38.3, 38.0, 36.5, 35.3, 31.0, 28.3, 28.1, 26.4, 16.0.

LC/MS: m/z calculated for $C_{56}H_{64}N_{12}O_4S$ $[M+2H]^{2+}$: 501.2, found: 501.2.

Purity (HPLC): 97%.



Compound **36**: **66** (9.5 mg, 0.013 mmol, 1.0 eq.), STM3006 (6.7 mg, 0.013 mmol, 1.0 eq.), potassium phosphate (5.5 mg, 0.026 mmol, 2.0 eq.), X-Phos (1.2 mg, 0.003 mmol, 0.2 eq.), and tris(dibenzylidenacetone)dipalladium (2.3 mg, 0.003 mmol, 0.2 eq.) were dissolved under argon atmosphere in 112 µL degassed water/ dioxane (1:4). The reaction was stirred at 110 °C

for 2 h. The mixture was diluted with water, the solvents were evaporated, and the residue was purified with RP flash chromatography.

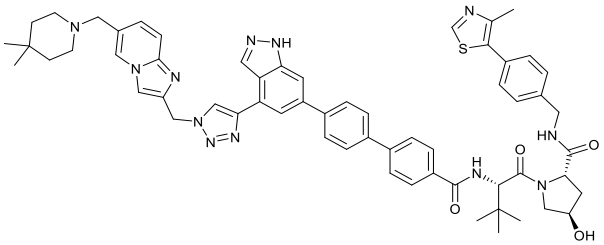
Yield: 4.5 mg (32% of th.).

^{1}H NMR: (400 MHz, DMSO-d_6) δ [ppm] = 8.98 (d, *J* = 3.6 Hz, 2H), 8.63 (s, 1H), 8.57 (t, *J* = 6.1 Hz, 1H), 8.44 (s, 1H), 7.99 (s, 1H), 7.95 (d, *J* = 1.4 Hz, 1H), 7.91 (d, *J* = 9.3 Hz, 1H), 7.88 (d, *J* = 1.8 Hz, 1H), 7.86 (d, *J* = 1.9 Hz, 1H), 7.75 (s, 1H), 7.51 (s, 1H), 7.49 (s, 1H), 7.48 – 7.42 (m, 2H), 7.41 (s, 1H), 7.38 (d, *J* = 8.4 Hz, 2H), 7.20 (dd, *J* = 9.3, 1.7 Hz, 1H), 5.80 (s, 2H), 5.14 (s, 1H), 4.54 (d, *J* = 9.3 Hz, 1H), 4.46 – 4.33 (m, 4H), 4.22 (dd, *J* = 15.9, 5.5 Hz, 1H), 3.71 – 3.59 (m, 4H), 2.71 (s, 2H), 2.44 (s, 3H), 2.35 (d, *J* = 4.0 Hz, 5H), 2.07 (s, 2H), 2.02 (d, *J* = 8.7 Hz, 1H), 1.94 – 1.86 (m, 1H), 1.55 (d, *J* = 12.5 Hz, 3H), 1.30 (t, *J* = 5.6 Hz, 4H), 0.94 (s, 10H), 0.87 (s, 6H).

^{13}C NMR: (101 MHz, DMSO) δ [ppm] = 173.7, 172.0, 169.7, 169.6, 168.8, 151.5, 151.5, 147.7, 145.8, 144.1, 141.3, 141.2, 140.5, 139.5, 137.8, 135.3, 131.2, 129.6, 128.6, 127.4, 127.3, 127.3, 125.6, 123.8, 123.2, 116.1, 111.6, 68.9, 59.1, 56.2, 50.0, 49.2, 41.7, 38.3, 37.9, 35.4, 28.2, 26.4, 19.1, 16.0, 1.2.

LC/MS: m/z calculated for $C_{60}H_{69}N_{13}O_5S$ $[M+2H]^{2+}$: 542.8, found: 542.7.

Purity (HPLC): 97%.



Compound **38**: **67** (7 mg, 0.011 mmol, 1.1 eq.), STM3006 (5 mg, 0.01 mmol, 1.0 eq.), potassium phosphate (4.3 mg, 0.02 mmol, 2.0 eq.), X-Phos (1 mg, 0.002 mmol, 0.2 eq.) and tris(dibenzylidenacetone)dipalladium (1 mg, 0.001 mmol, 0.1 eq.) were dissolved under argon atmosphere in 56 µL degassed water/ dioxane (1:4). The reaction was stirred at 110 °C for 1.5 h. The mixture was diluted with water, the solvents were evaporated, and the residue was purified with RP flash chromatography.

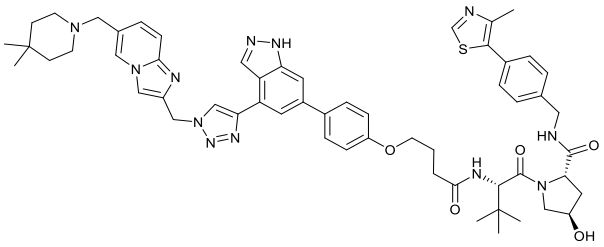
Yield: 3.7 mg (35% of th.).

^{1}H NMR: (400 MHz, DMSO-d_6) δ [ppm] = 9.00 (d, *J* = 6.7 Hz, 2H), 8.64 – 8.58 (m, 2H), 8.44 (s, 1H), 8.16 – 8.06 (m, 2H), 8.01 (s, 1H), 7.99 (s, 3H), 7.95 (s, 1H), 7.93 (s, 1H), 7.89 (s, 1H), 7.87 – 7.85 (m, 2H), 7.84 (s, 1H), 7.79 (s, 1H), 7.47 (d, *J* = 9.2 Hz, 1H), 7.42 (d, *J* = 2.9 Hz, 3H), 7.23 – 7.19 (m, 1H), 5.81 (s, 2H), 5.17 (d, *J* = 3.6 Hz, 1H), 4.81 (d, *J* = 9.1 Hz, 1H), 4.47 (q, *J* = 7.1, 6.1 Hz, 2H), 4.40 (dd, *J* = 8.3, 4.9 Hz, 2H), 4.25 (dd, *J* = 15.8, 5.6 Hz, 2H), 3.75 (d, *J* = 3.2 Hz, 2H), 3.45 (s, 3H), 2.45 (s, 2H), 2.07 (s, 3H), 1.31 (t, *J* = 5.6 Hz, 4H), 1.08 – 1.02 (m, 10H), 0.88 (s, 7H).

^{13}C NMR: (101 MHz, DMSO) δ [ppm] = 171.9, 169.5, 166.2, 158.4, 151.5, 147.8, 145.8, 142.3, 140.5, 139.9, 139.5, 133.0, 131.2, 129.7, 128.7, 128.5, 127.9, 127.5, 127.4, 126.3, 125.6, 123.7, 123.1, 116.1, 114.7, 68.9, 62.0, 59.1, 57.4, 49.2, 40.2, 38.2, 35.6, 28.2, 26.6, 25.5, 16.0, 1.2.

LC/MS: m/z calculated for $C_{60}H_{64}N_{12}O_4S$ $[M+2H]^{2+}$: 525.2, found: 525.2.

Purity (HPLC): 95%.



Compound **37**: **68** (15.8 mg, 0.022 mmol, 1.1 eq.), STM3006 (10 mg, 0.02 mmol, 1.0 eq.), potassium phosphate (8.4 mg, 0.04 mmol, 2.0 eq.), X-Phos (1 mg, 0.002 mmol, 0.1 eq.), and tris(dibenzylidenacetone)dipalladium (2 mg, 0.002 mmol, 0.1 eq.) were dissolved under argon atmosphere in 56 µL degassed water/ dioxane (1:4). The reaction was stirred at 110 °C for 1.5 h. The mixture was diluted with water, the solvents were evaporated, and the residue was purified with RP flash chromatography.

Yield: 5.6 mg (27% of th.).

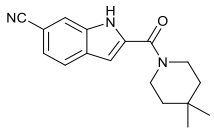
^{1}H NMR: (400 MHz, DMSO-d_6) δ [ppm] = 8.97 (d, *J* = 4.0 Hz, 1H), 8.57 (d, *J* = 5.0 Hz, 2H), 8.43 (s, 2H), 7.99 (d, *J* = 9.5 Hz, 2H), 7.87 (s, 1H), 7.72 (d, *J* = 8.4 Hz, 2H), 7.64 (s, 1H), 7.41 (dp, *J* = 16.7, 8.9 Hz, 5H), 7.20 (d, *J* = 9.5 Hz, 1H), 7.04 (d, *J* = 8.4 Hz, 2H), 5.79 (s, 2H), 4.57 (d, *J* = 9.3 Hz, 1H), 4.47 – 4.33 (m, 3H), 4.21 (dd, *J* = 15.9, 5.5 Hz, 1H), 4.02 (dt, *J* = 7.0, 4.2 Hz, 2H), 3.68 (d, *J* = 3.7 Hz, 1H), 2.44 (s, 3H), 2.34 (d, *J* = 7.0 Hz, 4H), 2.06 – 1.87 (m, 4H), 1.56 (td, *J* = 11.8, 10.1, 5.9 Hz, 3H), 1.30 (t, *J* = 5.8 Hz, 6H), 1.04 (d, *J* = 6.1 Hz, 2H), 0.94 (d, *J* = 6.0 Hz, 10H), 0.87 (s, 5H).

^{13}C NMR: (101 MHz, DMSO) δ [ppm] = 68.9, 67.1, 62.0, 59.1, 57.5, 56.5, 49.2, 41.6, 38.3, 38.0, 35.2, 32.3, 31.3, 28.2, 26.4, 26.3, 25.5, 23.1, 19.2, 15.9, 13.5.

LC/MS: m/z calculated for $C_{57}H_{66}N_{12}O_5S$ $[M+H]^+$: 1031.5, found: 1031.3.

Purity (HPLC): 99%.

Synthesis of 4th generation PROTACs



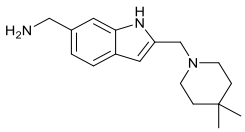
Compound **75**: Methyl 6-cyano-1*H*-indole-2-carboxylate (100 mg, 0.5 mmol, 1.0 eq.) was suspended in 1.5 mL methanol and 0.75 mL 1 M NaOH and stirred at RT for 4 h. The reaction mixture was acidified with 2 M HCl. Ethylacetat was added, and the solution was washed with water. The organic solvents were dried over Na_2SO_4 and evaporated. To this residue, TBTU (161 mg, 0.5 mmol, 1.0 eq.), DIPEA (219 µL, 1.250 mmol, 2.5 eq.), and 4,4-dimethylpiperidine hydrochloride (97 mg, 0.650 mmol, 1.3 eq.) were added in ethyl acetate (5 mL) and stirred at RT for 16 h. The organic solvents were evaporated, and the crude product was purified by RP flash chromatography.

Yield: 117 mg (83% of th.).

^{1}H NMR: (300 MHz, C*D*Cl$_3$) δ [ppm] = 11.14 (s, 1H), 7.78 – 7.76 (m, 1H), 7.70 – 7.66 (m, 1H), 7.30 (dd, *J* = 8.3, 1.4 Hz, 1H), 6.81 – 6.79 (m, 1H), 3.91 (s, 4H), 1.56 – 1.49 (m, 4H), 1.07 (s, 6H).

^{13}C NMR: (75 MHz, *C*DCl$_3$) δ [ppm] = 162.1, 134.9, 133.2, 130.3, 122.9, 122.6, 120.5, 117.4, 106.4, 105.0, 38.8, 29.5, 27.9.

LC/MS: m/z calculated for $C_{17}H_{19}N_3O$ $[M+H]^+$: 282.2, found: 282.1.



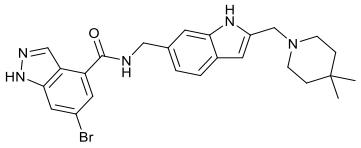
Compound **76**: **75** (195 mg, 0.695 mmol, 1.0 eq.) was dissolved in 1.5 mL anhydrous THF, and 1 M LAH (2.2 mL, 2.157 mmol, 3.1 eq.) in THF was added at 0 °C. The reaction was stirred at RT for 16 h before 1.5 mL of water and 1.5 mL of 1 M NaOH were added at 0 °C. The suspension was stirred for 10 min. The precipitate was removed by filtration and washed with THF. The organic solvents were evaporated, and the crude product was purified by RP flash chromatography.

Yield: 95 mg (50% of th.).

^{1}H NMR: (400 MHz, DMSO-d_6) δ [ppm] = 8.18 (s, 3H), 7.62 (d, *J* = 8.2 Hz, 1H), 7.54 (s, 1H), 7.13 (d, *J* = 8.2 Hz, 1H), 6.66 (d, *J* = 1.9 Hz, 1H), 4.51 (d, *J* = 4.0 Hz, 2H), 4.12 (q, *J* = 5.7 Hz, 2H), 3.25 (d, *J* = 12.6 Hz, 2H), 3.10 – 3.02 (m, 2H), 1.56 (q, *J* = 5.8, 3.9 Hz, 4H), 0.98 – 0.94 (m, 6H).

^{13}C NMR: (101 MHz, DMSO) δ [ppm] = 158.4, 158.1, 136.4, 128.3, 128.0, 127.5, 120.7, 120.6, 112.4, 105.3, 51.8, 48.0, 42.9, 34.8, 34.7, 30.9, 27.4, 25.5, 23.0.

LC/MS: m/z calculated for $C_{17}H_{25}N_3$ $[M+H]^+$: 272.2, found:271.0.



Compound **39**: **76** (40 mg, 0.147 mmol, 1.2 eq.), 6-bromo-1*H*-indazole-4-carboxylic acid (30 mg, 0.123 mmol, 1.0 eq.), TBTU (39 mg, 0.123 mmol, 1.0 eq.) and DIPEA (64 µL, 0.369 mmol, 3.0 eq.) were dissolved in ethyl acetate and stirred at RT for 16 h. The solvent was evaporated, and the crude product was purified with RP flash chromatography.

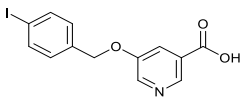
Yield: 8 mg (13% of th.).

^{1}H NMR: (400 MHz, Me*O*D) δ [ppm] = 8.54 (s, 1H), 8.37 (s, 1H), 7.91 (s, 1H), 7.88 – 7.81 (m, 1H), 7.71 (s, 1H), 7.56 (d, *J* = 8.2 Hz, 1H), 7.47 (s, 1H), 7.17 – 7.12 (m, 1H), 6.61 (s, 1H), 4.72 (s, 2H), 4.30 (s, 2H), 3.09 (dt, *J* = 7.9, 4.0 Hz, 4H), 1.61 (t, *J* = 5.9 Hz, 4H), 1.01 (s, 6H).

^{13}C NMR: (101 MHz, MeOD) δ [ppm] = 169.9, 168.3, 138.7, 134.7, 130.5, 129.3, 128.6, 127.2, 124.5, 121.8, 121.2, 121.1, 121.1, 120.9, 117.1, 111.5, 106.4, 54.7, 50.1, 45.0, 37.2, 28.8.

LC/MS: m/z calculated for $C_{25}H_{28}BrN_5O$ $[M+H]^+$: 494.2, found: 494.1.

Purity (HPLC): 99%.

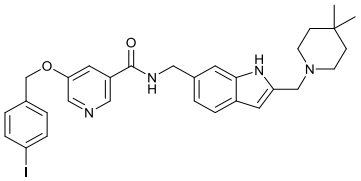


Compound **77**: Methyl 5-hydroxynicotinate (300 mg, 1.96 mmol, 1.0 eq.) was dissolved in 5 mL DMF, and NaH (156 mg, 6.5 mmol, 3.3 eq.) was added to the solution portion-wise at 0 °C. 1-(bromomethyl)-4-iodobenzene (582 mg, 1.96 mmol, 1.0 eq.) was dissolved in 1 mL DMF and added dropwise to the cooled solution. The reaction was stirred at RT for 16 h. Subsequently, the organic solvent was evaporated, and the residue was resolved in water and acidified with concentrated TFA. The precipitation was filtered and dried to afford the desired compound.

Yield: 485 mg (70% of th.).

^{1}H NMR: (300 MHz, DMSO-d_6) δ [ppm] = 8.68 (d, *J* = 1.4 Hz, 1H), 8.56 (d, *J* = 2.9 Hz, 1H), 7.83 – 7.74 (m, 4H), 7.27 (s, 3H), 5.23 (s, 2H).

LC/MS: m/z calculated for $C_{13}H_{10}INO_3$ $[M+H]^+$: 356.0, found: 356.0.

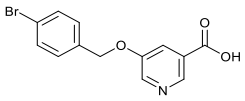


Compound **78**: **77** (7 mg, 0.02 mmol, 1.0 eq.), **76** (5.4 mg, 0.02 mmol, 1.0 eq.), HATU (7.6 mg, 0.02 mmol, 1.0 eq.), and DIPEA (14 µL, 0.08 mmol, 4.0 eq.) were dissolved in ethyl acetate and stirred at RT for 16 h. The solvent was evaporated, and the crude product was purified by RP flash chromatography.

Yield: 1.5 mg (12% of th.).

No NMR analytics available due to instability of this intermediate in NMR solvents.

LC/MS: m/z calculated for $C_{30}H_{33}IN_4O_2$ $[M+2H]^{2+}$: 305.1, found: 305.2.



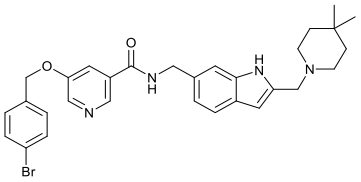
Compound **79**: Methyl 5-hydroxynicotinate (300 mg, 1.96 mmol, 1.0 eq.) was dissolved in 5 mL DMF, and NaH (156 mg, 6.5 mmol, 3.3 eq.) was added to the solution portion-wise at 0 °C. 1-(bromomethyl)-4-bromobenzene (488 mg, 1.96 mmol, 1.0 eq.) was dissolved in 1 mL DMF and added dropwise to the cooled solution. The reaction was stirred at RT for 16 h. Subsequently, the organic solvent was evaporated, and the crude product was purified via NP flash chromatography to afford the desired compound.

Yield: 200 mg (33% of th.).

^{1}H NMR: (300 MHz, MeO*D*) δ [ppm] = 8.81 (s, 1H), 8.60 (s, 1H), 8.16 (s, 1H), 7.62 – 7.57 (m, 2H), 7.44 (d, *J* = 8.0 Hz, 2H), 5.27 (s, 2H).

^{13}C NMR: (75 MHz, MeOD) δ [ppm] = 166.7, 141.8, 140.7, 136.4, 133.9, 132.9, 132.0, 130.8, 126.0, 123.3, 71.3.

LC/MS: m/z calculated for $C_{13}H_{10}BrNO_3$ $[M+H]^+$: 308.0, found: 307.9.



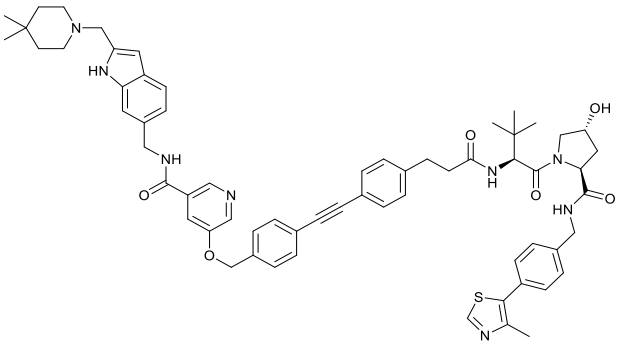
Compound **80**: **79** (40 mg, 0.13 mmol, 1.0 eq.) was dissolved in anhydrous DCM (4 mL). HATU (49 mg, 0.13 mmol, 1.0 eq.) and DIPEA (113 µL, 0.65 mmol, 5.0 eq.) were added at 0 °C. The reaction was stirred at 0 °C for 90 min before **76** (50 mg, 0.185 mmol, 1.4 eq.) dissolved in 2 mL DCM/DMF (1:1) was added at 0 °C. The reaction was stirred at RT for 16 h. The solvents were evaporated, and the crude product was purified with RP flash chromatography.

Yield: 42 mg (58% of th.).

^{1}H NMR: (400 MHz, DMSO-d_6) δ [ppm] = 9.18 (t, *J* = 5.9 Hz, 1H), 8.68 (s, 1H), 8.49 (d, *J* = 2.9 Hz, 1H), 7.88 – 7.85 (m, 1H), 7.64 – 7.58 (m, 3H), 7.46 – 7.42 (m, 3H), 7.31 (s, 1H), 7.00 – 6.94 (m, 1H), 6.30 (s, 1H), 5.23 (d, *J* = 11.8 Hz, 3H), 4.55 (d, *J* = 5.9 Hz, 2H), 3.77 (s, 2H), 2.05 – 1.89 (m, 1H), 1.37 (t, *J* = 5.6 Hz, 4H), 1.30 – 1.17 (m, 1H), 0.89 (s, 7H).

^{13}C NMR: (101 MHz, DMSO) δ [ppm] = 164.2, 163.1, 154.2, 142.6, 140.8, 140.6, 136.4, 135.7, 131.5, 130.6, 123.0, 129.9, 126.8, 121.3, 121.1, 119.8, 119.5, 119.0, 110.2, 69.0, 49.1, 43.3, 40.2, 28.0.

LC/MS: m/z calculated for $C_{30}H_{33}BrN_4O_2$ $[M+H]^+$: 561.2, found: 561.2.



Compound **40**: **69** (4.8 mg, 0.008 mmol, 1.0 eq.), **78** (5.0 mg, 0.008 mmol, 1.0 eq.), Tris(dibenzylidenaceton)dipaladium(0) (0.8 mg, 0.0008 mmol, 0.1 eq.), copper(I)iodide (0.3 mg, 0.0016 mmol, 0.2 eq.), and X-Phos (0.8 mg, 0.0016 mmol, 0.2 eq.) were dissolved in 0.5 mL degassed DMF/THF (1:1) and triethylamine (3.2 µL, 0.0024 mmol, 3.0 eq.). The reaction was stirred at 80 °C for 3 h. Subsequently, the organic solvents were evaporated, and the crude product was purified with RP flash chromatography.

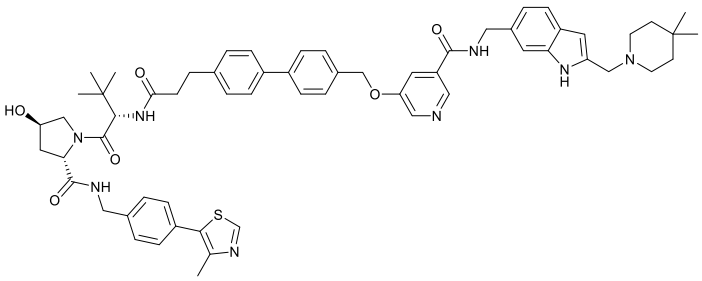
Yield: 0.6 mg (7% of th.).

^{1}H NMR: (600 MHz, DMSO-d_6) δ [ppm] = 10.91 (s, 1H), 9.21 – 9.18 (m, 1H), 8.98 (s, 1H), 8.69 (s, 1H), 8.61 – 8.58 (m, 1H), 8.51 (s, 1H), 8.00 (d, *J* = 9.5 Hz, 1H), 7.90 – 7.87 (m, 1H), 7.61 (d, *J* = 8.3 Hz, 1H), 7.57 (d, *J* = 8.2 Hz, 2H), 7.52 (d, *J* = 8.3 Hz, 2H), 7.46 – 7.37 (m, 6H), 7.28 (d, *J* = 7.9 Hz, 2H), 7.07 (d, *J* = 9.2 Hz, 1H), 6.95 – 6.92 (m, 1H), 6.21 (s, 1H), 5.27 (s, 2H), 5.18 – 5.16 (m, 1H), 4.55 (dd, *J* = 7.5, 4.1 Hz, 2H), 4.46 – 4.38 (m, 3H), 4.36 (s, 1H), 4.23 – 4.15 (m, 2H), 3.69 – 3.63 (m, 2H), 3.56 (s, 1H), 2.84 (ddt, *J* = 21.2, 14.6, 8.2 Hz, 3H), 2.61 (d, *J* = 22.3 Hz, 2H), 2.44 (s, 3H), 2.33 (s, 3H), 2.07 – 1.96 (m, 3H), 1.90 (ddd, *J* = 12.9, 9.5, 4.5 Hz, 2H), 1.33 – 1.29 (m, 3H), 1.27 – 1.22 (m, 2H), 0.89 (s, 5H), 0.87 (s, 6H).

^{13}C NMR: (151 MHz, DMSO) δ [ppm] = 172.0, 171.1, 169.6, 164.2, 154.3, 151.6, 147.8, 142.5, 140.8, 140.7, 139.6, 136.9, 136.6, 136.4, 131.5, 131.5, 131.3, 131.2, 129.7, 128.8, 128.7, 128.1, 127.4, 126.9, 119.8, 119.6, 119.3, 118.9, 110.1, 100.4, 69.3, 68.9, 68.8, 58.7, 56.5, 56.4, 55.6, 49.4, 43.3, 41.7, 40.1, 38.3, 38.0, 36.1, 35.3, 28.2, 26.4, 16.0.

LC/MS: m/z calculated for $C_{63}H_{70}N_8O_6S$ $[M+2H]^{2+}$: 534.3, found: 534.6.

Purity (HPLC): 97%.



Compound **41**: **65** (5.4 mg, 0.009 mmol, 1.1 eq.), **80** (5 mg, 0.008 mmol, 1.0 eq.), potassium phosphate (3.4 mg, 0.016 mmol, 2.0 eq.), X-Phos (1 mg, 0.002 mmol, 0.2 eq.), and tris(dibenzylidenacetone)dipalladium (1 mg, 0.001 mmol, 0.1 eq.) were dissolved under argon atmosphere in 120 µL degassed water/ dioxane (1:4). The reaction was stirred at 70 °C for 1.5 h. The mixture was diluted with water, and the mixture was directly purified by RP flash chromatography.

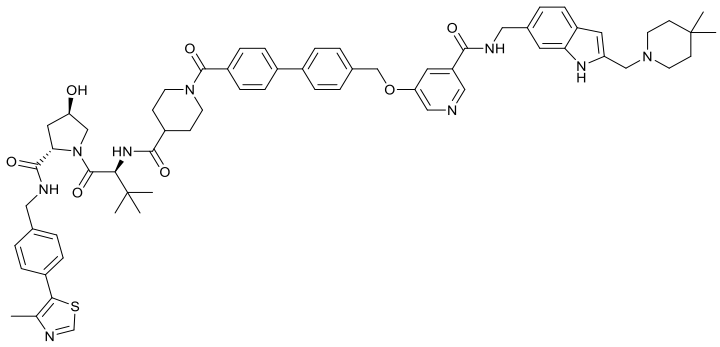
Yield: 2.4 mg (25% of th.).

^{1}H NMR: (600 MHz, DMSO-d_6) δ [ppm] = 9.21 (t, *J* = 6.0 Hz, 1H), 8.98 (s, 1H), 8.68 (dd, *J* = 4.2, 1.7 Hz, 1H), 8.59 (t, *J* = 6.1 Hz, 1H), 8.51 (d, *J* = 2.8 Hz, 1H), 7.99 (d, *J* = 9.4 Hz, 1H), 7.92 – 7.89 (m, 1H), 7.68 – 7.65 (m, 2H), 7.59 – 7.51 (m, 4H), 7.45 – 7.35 (m, 5H), 7.31 (d, *J* = 8.2 Hz, 2H), 6.98 – 6.92 (m, 2H), 6.25 (s, 2H), 5.27 (s, 2H), 5.17 (d, *J* = 3.5 Hz, 1H), 4.55 (dd, *J* = 7.7, 5.1 Hz, 3H), 4.43 (td, *J* = 9.2, 8.4, 5.2 Hz, 2H), 4.35 (d, *J* = 4.4 Hz, 1H), 4.21 (dd, *J* = 15.9, 5.5 Hz, 2H), 3.67 (d, *J* = 3.8 Hz, 3H), 2.86 (dq, *J* = 14.0, 6.2 Hz, 3H), 2.67 – 2.59 (m, 3H), 2.44 (s, 3H), 2.07 – 1.99 (m, 2H), 1.90 (ddd, *J* = 12.9, 8.8, 4.6 Hz, 2H), 1.34 (s, 3H), 1.26 – 1.22 (m, 3H), 1.15 (t, *J* = 6.4 Hz, 2H), 0.88 (d, *J* = 6.1 Hz, 11H).

^{13}C NMR: (151 MHz, DMSO) δ [ppm] = 172.0, 171.3, 169.7, 164.3, 163.2, 154.4, 151.5, 147.7, 140.8, 140.7, 140.7, 140.0, 139.6, 137.4, 136.4, 135.1, 131.2, 130.6, 129.7, 129.0, 128.7, 128.6, 128.0, 127.4, 126.8, 126.7, 126.6, 119.7, 110.2, 69.5, 68.9, 58.7, 56.5, 56.4, 49.2, 43.3, 41.7, 40.1, 38.0, 36.5, 35.3, 31.0, 26.4, 24.1, 16.0.

LC/MS: m/z calculated for $C_{61}H_{70}N_8O_6S$ $[M+2H]^{2+}$: 522.3, found: 523.0.

Purity (HPLC): 95%.



Compound **42**: **66** (6.2 mg, 0.009 mmol, 1.1 eq.), **80** (5 mg, 0.008 mmol, 1.0 eq.), potassium phosphate (3.4 mg, 0.016 mmol, 2.0 eq.), X-Phos (1 mg, 0.002 mmol, 0.2 eq.), and tris(dibenzylidenacetone)dipalladium (1 mg, 0.001 mmol, 0.1 eq.) were dissolved under argon atmosphere in 120 µL degassed water/ dioxane (1:4). The reaction was stirred at 70 °C for 1.5 h. The mixture was diluted with water and purified by RP flash chromatography.

Yield: 6.3 mg (70% of th.).

^{1}H NMR: (600 MHz, DMSO-d_6) δ [ppm] = 9.21 (t, *J* = 6.0 Hz, 2H), 8.98 (s, 1H), 8.69 – 8.67 (m, 1H), 8.59 (t, *J* = 6.1 Hz, 1H), 8.51 (d, *J* = 2.8 Hz, 1H), 7.99 (d, *J* = 9.4 Hz, 1H), 7.90 (dd, *J* = 2.9, 1.8 Hz, 1H), 7.68 – 7.65 (m, 2H), 7.58 – 7.52 (m, 4H), 7.43 – 7.36 (m, 5H), 7.31 (d, *J* = 8.2 Hz, 3H), 6.97 – 6.92 (m, 2H), 5.27 (s, 1H), 5.17 (d, *J* = 3.5 Hz, 1H), 4.55 (dd, *J* = 7.7, 5.1 Hz, 3H), 4.43 (td, *J* = 9.2, 8.4, 5.2 Hz, 3H), 4.35 (d, *J* = 4.4 Hz, 1H), 4.21 (dd, *J* = 15.9, 5.5 Hz, 2H), 3.67 (d, *J* = 3.8 Hz, 2H), 2.91 – 2.80 (m, 4H), 2.66 – 2.60 (m, 3H), 2.44 (s, 3H), 2.06 – 2.00 (m, 2H), 1.90 (ddd, *J* = 12.9, 8.8, 4.6 Hz, 2H), 1.34 (s, 4H), 1.25 – 1.19 (m, 4H), 1.15 (t, *J* = 6.4 Hz, 2H), 0.88 (d, *J* = 6.1 Hz, 14H).

^{13}C NMR: (151 MHz, DMSO) δ [ppm] = 172.0, 171.3, 169.7, 164.3, 163.2, 154.4, 151.5, 147.7, 140.8, 140.7, 140.0, 139.6, 137.4, 136.4, 135.1, 131.2, 130.6, 129.7, 129.0, 128.7, 128.6, 128.0, 127.4, 126.8, 126.7, 126.6, 119.7, 110.2, 69.5, 68.9, 58.7, 56.4, 49.2, 43.3, 41.7, 38.0, 36.5, 35.3, 31.0, 26.4, 24.1, 16.0.

LC/MS: m/z calculated for $C_{65}H_{75}N_9O_7S$ $[M+2H]^{2+}$: 563.8, found: 564.1.

Purity (HPLC): 97%.

“

5.2 Non-covalent Dyes in Microscale Thermophoresis for Studying RNA Ligand Interactions and Modifications

5.2.1 Context and Project Summary

Understanding and measuring biomolecular RNA interactions remains a significant challenge across multiple fields of medicinal research.[258,259] MST is a well-established and versatile method for quantifying molecular interactions, including those involving RNA.[260,261] Conventional MST protocols rely on covalent labeling of RNA with fluorescent dyes (e.g., Cy5 or fluorescein) at the 3′ or 5′ end, or at modified nucleosides.[261,262] In this study, members of the Sybr and Syto dye series were evaluated for their potential to non-covalently label RNA, enabling a more rapid mix-and-measure approach.

An initial screen of nine distinct dyes assessed RNA binding characteristics and dye-to-RNA stoichiometry, revealing a statistical 1:1 binding ratio in each case. The selected dyes were subsequently tested across a range of RNA molecules varying in length and secondary structure, focusing on reproducibility and photobleaching stability. Two dyes – Syto 59 (pico red channel in MST device) and SybrGold (nano blue channel in MST device) – became evident as the most suitable candidates for further application.

Subsequent experiments demonstrated the utility of these dyes in analyzing a diverse set of RNA-ligand interactions. First, six riboswitches, encompassing ligands of varying molecular size (from fluoride to cobalamin), were analyzed. In all cases, the K_D-values determined by the new method agreed with literature-reported values and those obtained via orthogonal biophysical techniques. The protocol was further tested for its capability to detect various RNA modifications. While larger or charge-altering modifications yielded pronounced changes in F_{norm}-values, smaller modifications such as methylation produced scarcely detectable F_{norm} shifts, with sensitivity dependent on the methylation site.

Lastly, the newly established protocol was applied as an enzymatic assay for METTL3/14 activity by monitoring m^6A modifications in RNA. Given the limited sensitivity of the method for detecting methylation, an antibody-based detection strategy was successfully employed. The K_M for SAM determined by MST was consistent with values obtained from the ^3H-incorporation assay, highlighting the applicability of the mix-and-measure approach in enzymatic studies involving RNA methylation.

This work has been published in: RSC Chemical Science (impact factor: 7.4).

Article reprinted (unmodified) with open access permission from *RSC Chem. Sci.,* **2023**, *14* (36), 9827–9837. ‘Non-covalent dyes in microscale thermophoresis for studying RNA ligand interactions and modifications.’ © The Authors. Published by The Royal Society of Chemistry. The work is licensed under CC BY 3.0 (https://creativecommons.org/licenses/by/3.0/).

The full version of the article, including the electronic Supplementary Information, can be accessed online at doi: 10.1039/d3sc02993j.

5.2.2 Contributions

Own contribution: ^{3}H-incorporation assay, SI writing.

Contributions from other authors: MST experiments, RNA preparation, PCR, *in vitro* transcription, and manuscript and SI writing and editing.

5.2.3 Publication

The following publication quoted within "" from page 278 to page 288 is the same as the manuscript cited on page 276.[263] "

Chemical Science

ROYAL SOCIETY OF CHEMISTRY

EDGE ARTICLE

View Article Online
View Journal | View Issue

Check for updates

Cite this: *Chem. Sci.*, 2023, **14**, 9827

All publication charges for this article have been paid for by the Royal Society of Chemistry

Non-covalent dyes in microscale thermophoresis for studying RNA ligand interactions and modifications†

Elisabeth Kallert, Malte Behrendt, Ariane Frey, Christian Kersten and Fabian Barthels *

Microscale Thermophoresis (MST) is a powerful biophysical technique that measures the mobility of biomolecules in response to a temperature gradient, making it useful for investigating the interactions between biological molecules. This study presents a novel methodology for studying RNA-containing samples using non-covalent nucleic acid-sensitive dyes in MST. This "mix-and-measure" protocol uses non-covalent dyes, such as those from the Syto or Sybr series, which lead to the statistical binding of one fluorophore per RNA oligo showing key advantages over traditional covalent labelling approaches. This new approach has been successfully used to study the binding of ligands to RNA molecules (*e.g.*, SAM- and $PreQ_1$ riboswitches) and the identification of modifications (*e.g.*, m^6A) in short RNA oligos which can be written by the RNA methyltransferase METTL3/14.

Received 12th June 2023
Accepted 27th August 2023

DOI: 10.1039/d3sc02993j

rsc.li/chemical-science

Open Access Article. Published on 29 August 2023. Downloaded on 10/23/2025 3:14:31 PM.
This article is licensed under a Creative Commons Attribution 3.0 Unported Licence.

Introduction

Understanding the molecular foundations of RNA biomolecular interactions is crucial for the study of their cellular involvement and the development of RNA-targeting therapeutics.[1,2] Microscale thermophoresis (MST) is a powerful biophysical technique for the study of the interactions between molecules such as proteins or nucleic acids with high sensitivity and specificity.[3,4] MST measures their mobility in response to a temperature gradient (usually 2–5 °C), and thus, the measured thermophoresis is dependent on the inherent properties of the biomolecule, such as its size, shape, and charge, while the origin is governed by the Soret coefficient.[5] In recent years, MST has been utilized in the study of RNA molecules, providing valuable insights into the dynamics and interactions of these intensively researched biomolecules.[6–8] The target RNA is commonly labelled with a covalent fluorescent reporter; subsequently, the sample is placed in a microliter-scale capillary, and a temperature gradient is applied by heating with an IR laser. Traditional MST methods for RNA studies rely on reporter dyes such as Cy5 or fluorescein, which are synthetically attached to the 3′- resp. 5′-ends, or to modified nucleosides.[6,8–11] While this is effective to prevent steric interaction of the fluorophore with the investigated biomolecular interface, it might also reduce the effect of local structural changes (T-jump effects) on the dyes' fluorescence.[12,13]

In this study, we present a novel MST-based methodology for the investigation of RNA-containing samples using nucleic acid-sensitive dyes, such as those from the Syto or Sybr series, which statistically bind to nucleic acids through non-covalent interaction.[14] It is important to note that most of these dyes do not significantly alter overall RNA stability which is a prerequisite for the study of biomolecular interactions.[15] To our knowledge, there is only one published study which has used non-covalent SybrGold labelling of DNA oligos using a non-microscale thermophoresis setup (microscope detection) to show that Sybr-DNA duplexes do not dissociate under common thermophoretic conditions.[16] In this previous study, however, no relation was made to applications in the recently popular MST experimental set-up nor to method development for nucleic acid analysis.

This led us to hypothesize that such nucleic acid dyes are also suitable for RNA labelling in MST experiments, and hence, we elaborated on the experimental scope, structure–activity relationships and practical applications for RNA–ligand and RNA-modification elucidation. Here, we report a "mix-and-measure" protocol that shows key advantages for relevant RNA-MST applications compared to covalent labelling approaches which are technically more challenging, time-consuming, and expensive (Fig. 1A). This approach thus pays homage to the dye-nitrilotriacetic acid (NTA) protocol developed for protein MST, which allows non-covalent labelling of proteins and has subsequently become more widely used than the original covalent maleimide- and NHS-labelling protocols.[17]

Institute of Pharmaceutical and Biomedical Sciences, Johannes Gutenberg-University of Mainz, Staudingerweg 5, 55128 Mainz, Germany. E-mail: barthels@uni-mainz.de

† Electronic supplementary information (ESI) available. See DOI: https://doi.org/10.1039/d3sc02993j

© 2023 The Author(s). Published by the Royal Society of Chemistry

View Article Online
Chemical Science Edge Article

Open Access Article. Published on 29 August 2023. Downloaded on 10/23/2025 3:14:31 PM.
This article is licensed under a Creative Commons Attribution 3.0 Unported Licence.

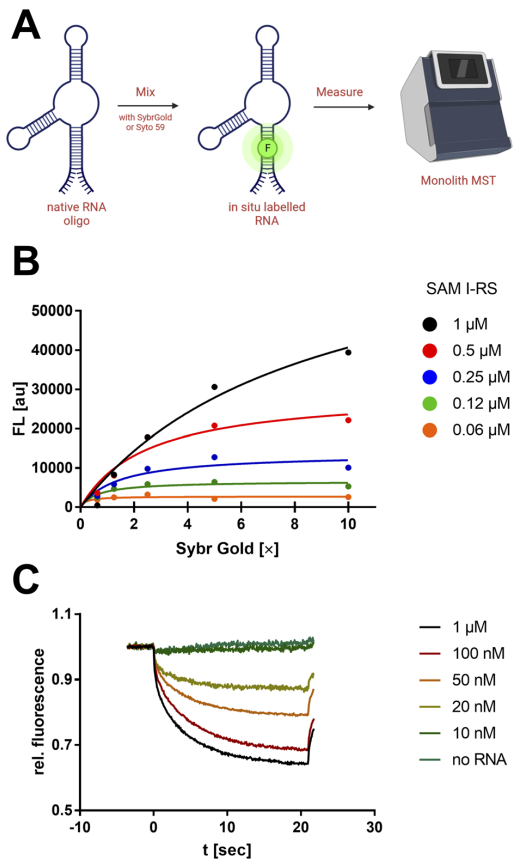


Fig. 1 Non-covalent nucleic acid dyes to study RNA by MST. (A) "Mix-and-measure" protocol for the thermophoretic analysis of native RNA oligos. (B) Fluorometric titration of SAM-I riboswitch with SybrGold. Samples were measured by a Tecan Spark 10 M plate reader ($\lambda_{ex/em}$: 490/550 nm). The apparent binding constant (Langmuir isotherm) was determined to be K_D = 85.3 nM. (C) RNA concentration-dependent MST curves with SybrGold (1×) and SAM-I riboswitch (variable concentration, blue laser, 8% excitation power). The apparent K_D from the F_{norm} (2 s) was 61.4 nM.

Results and discussion

Establishment of the non-covalent dye MST protocol

First, a qualitative working range of useful SybrGold and RNA concentrations was determined by fluorometry. With a sample matrix of RNA (62.5 nM–1 µM) and SybrGold (1×–10×) concentrations, the stoichiometry and apparent binding constant of the dye to the *S*-adenosylmethionine (SAM)-I riboswitch was determined (Fig. 1B).

It was found that 1× SybrGold produced sufficient fluorescence for MST (Monolith NT.115), and at such SybrGold concentrations, one fluorophore molecule is likely to bind statistically to the RNA of interest (K_D = 85.3 nM). Statistical 1 : 1 binding stoichiometry was concluded as a one-step binding event was observed to display the same apparent binding affinity independent of the RNA concentration. Hence, it was found that the minimum RNA concentration during MST was primarily limited by the binding affinity of SybrGold to the respective RNA sequence. For the SAM-I riboswitch, a significant thermophoretic response was saturated at an RNA concentration of approx. 100 nM, which was strongly distinguished from the unbound dye. F_{norm} (2 s): 0.75 *vs.* 0.96 (Fig. 1C).

As a next step, systematic investigations of structure–activity-relationships between fluorescent dyes and RNA in MST were performed. First, we investigated the effect of RNA length and its secondary structures on the MST characteristics, such as the initial fluorescence level and F_{norm}, using nine different dyes (Syto 17, Syto 59–64, SybrGold, and RiboGreen). For this purpose, we defined ten RNA categories containing each three RNA oligos which comprise different lengths and structural features (Table S1†). Across all dye and RNA combinations, MST mixtures were prepared as triplicates with 100 nM RNA and 1× dye. The mean initial fluorescence of different dyes was normalized by a concentration-dependent regression (Fig. S1†). In general, more complex RNA structures and longer oligonucleotide sequences resulted in higher absolute initial fluorescence (Fig. 2A). The central MST descriptor F_{norm} (2 s) was mostly between 0.75 and 0.90 across all combinations (Fig. 2C). Lower F_{norm} values (0.60–0.75) were eventually found for shorter RNA, however, a significant dependency on the dye or the category was not ascertained.

We found that shorter RNAs (<20 nt) exhibit more sensitive fluctuations in F_{norm}, suggesting that these are more susceptible to biological and chemical modifications (Fig. 2C). This can possibly be exploited to detect small changes in sequence or conditions for biological assay design. Depending on the dye, however, the standard error of the absolute fluorescence and F_{norm} was coincidently higher for these short RNAs. The standard deviation of the F_{norm} values (t = 2 s) was mostly <5‰ across all categories. An exception was the use of the dyes Syto 62 and RiboGreen. The data points in the dashed box of Fig. 2D are exclusively populated by RNA–dye combinations with Syto 62 or RiboGreen. For Syto 62, this may be due to the highly variable absolute fluorescence of the RNA–dye conjugates (Fig. 2B). The use of these two dyes might be not recommended for RNA-MST experiments.

After the broad analysis regarding the influence of RNA-dependent parameters on the initial fluorescence and F_{norm}, more detailed correlation studies with RNA descriptors (length, secondary structure, and base composition) were performed. The secondary structures of RNA oligos were predicted by the RNAfold web server.[18] By analyzing the relationship between F_{norm} and RNA length, we confirmed the trend shown in Fig. 2, wherein shorter RNAs (<20 nt) lead to a greater diversity of F_{norm} (Fig. S2A†). Notably, the F_{norm} parameters of the two blue dyes (SybrGold and RiboGreen) were generally lower than that of the red Syto dyes. High standard deviations (>5‰) were found only for Syto 62 and RiboGreen. As further correlation parameters, the proportion of hybridized bases (Fig. S2C†) and the secondary structural content were investigated (Fig. S2E†). Neither the analysis of the paired bases nor that of the

 © 2023 The Author(s). Published by the Royal Society of Chemistry

Open Access Article. Published on 29 August 2023. Downloaded on 10/23/2025 3:14:31 PM.
This article is licensed under a Creative Commons Attribution 3.0 Unported Licence.

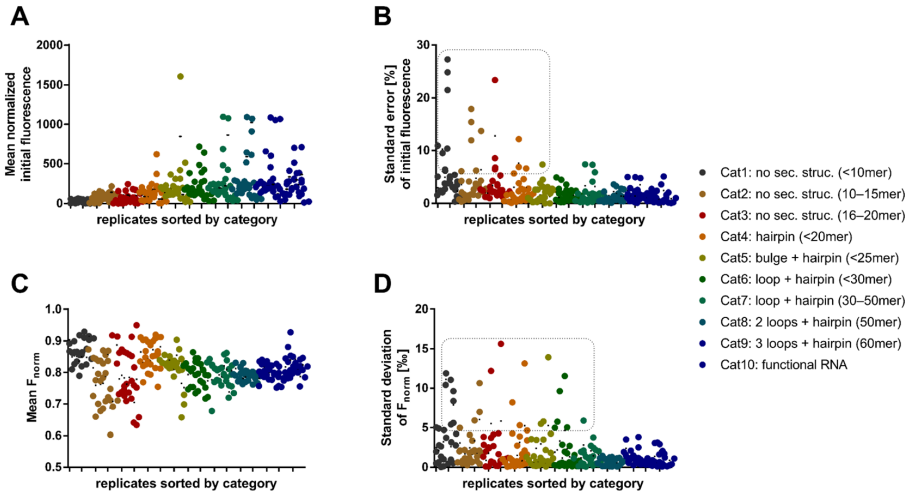


Fig. 2 Initial fluorescence and F_{norm} as RNA-dependent MST characteristics. (A) Mean normalized initial fluorescence of all dye combinations for each RNA oligo. (B) Relative standard error of the mean normalized initial fluorescence. For Syto 62 combinations with short RNAs (category 1–5) the error is >5% (dashed box). (C) The key MST descriptor F_{norm} ($t = 2$ s) displays mostly values between 0.75 and 0.90 across all categories and dyes. (D) Standard deviation of the F_{norm} values ($t = 2$ s).

loop/bulge content *vs.* F_{norm} yielded a significant correlation between the given quantities (Fig. S3†).

Another aspect of structure–activity relationships was the analysis of dye-dependent parameters on characteristics of thermophoresis curves described by the following descriptors (Fig. 3F): (1) slope of the pre-MST fluorescence traces (measure of dye photobleaching), (2) steady-state (t = 15–20 s) slope of thermophoresis traces (measure of the RNA–dye complex dissociation in the temperature gradient), (3) goodness (R^2) of the hyperbolic thermophoresis fit, (4) sum of the least squares error of a fluorescence–time curve triplicate (reproducibility of the whole MST experiment), (5) normalized initial fluorescence (measure for the brightness of the intrinsic dye fluorescence).

These results showed that Syto 60, 62, 63, and 64 exhibited increased susceptibility to photobleaching, with Syto 62 showing a particularly strong effect (Fig. 3A). In contrast, Syto 17, 59, and 61 as well as SybrGold and RiboGreen were mostly resistant to photobleaching. Furthermore, the dye–RNA complex of Syto 60, 62, and 63 seem to be prone to premature dissociation during thermophoresis, as a positive steady-state slope was observed for these dye combinations (Fig. 3B). We also found varying degrees of susceptibility to aggregation for Syto 17, 60, 62, and 63 during thermophoresis, while the other dyes were stable across all types of RNA samples. Regarding the reproducibility of an MST experiment triplicate, Syto 62 as well as Syto 60 and 63 led to significantly lower reproducibility compared to the other dyes (Fig. 3D). Lastly, Syto 59 is by far the brightest in terms of its intrinsic fluorescence compared to the other red dyes (Fig. 3E).

To summarize, we found that Syto 59 (red, pico channel) and SybrGold (blue, nano channel) are the most suitable (of the investigated) dyes for RNA-MST experiments, as they showed

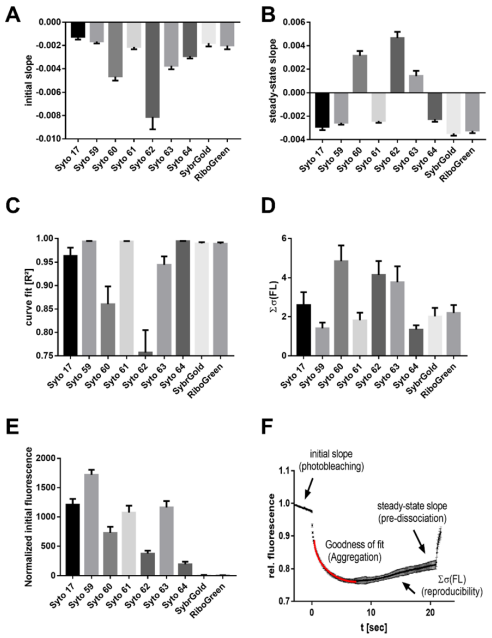


Fig. 3 Dye-dependent effects on the MST characteristics. (A) Initial slope indicating the photobleaching rate. (B) Steady-state (t = 15–20 s) slope showing the stability of dye–RNA complexes. (C) Goodness of the curve fit (R^2). (D) Dye-dependent reproducibility. (E) Normalized initial fluorescence. (F) Depiction of the MST curve descriptors analyzed in subfigures (A)–(D).

© 2023 The Author(s). Published by the Royal Society of Chemistry

Open Access Article. Published on 29 August 2023. Downloaded on 10/23/2025 3:14:31 PM.
This article is licensed under a Creative Commons Attribution 3.0 Unported Licence.

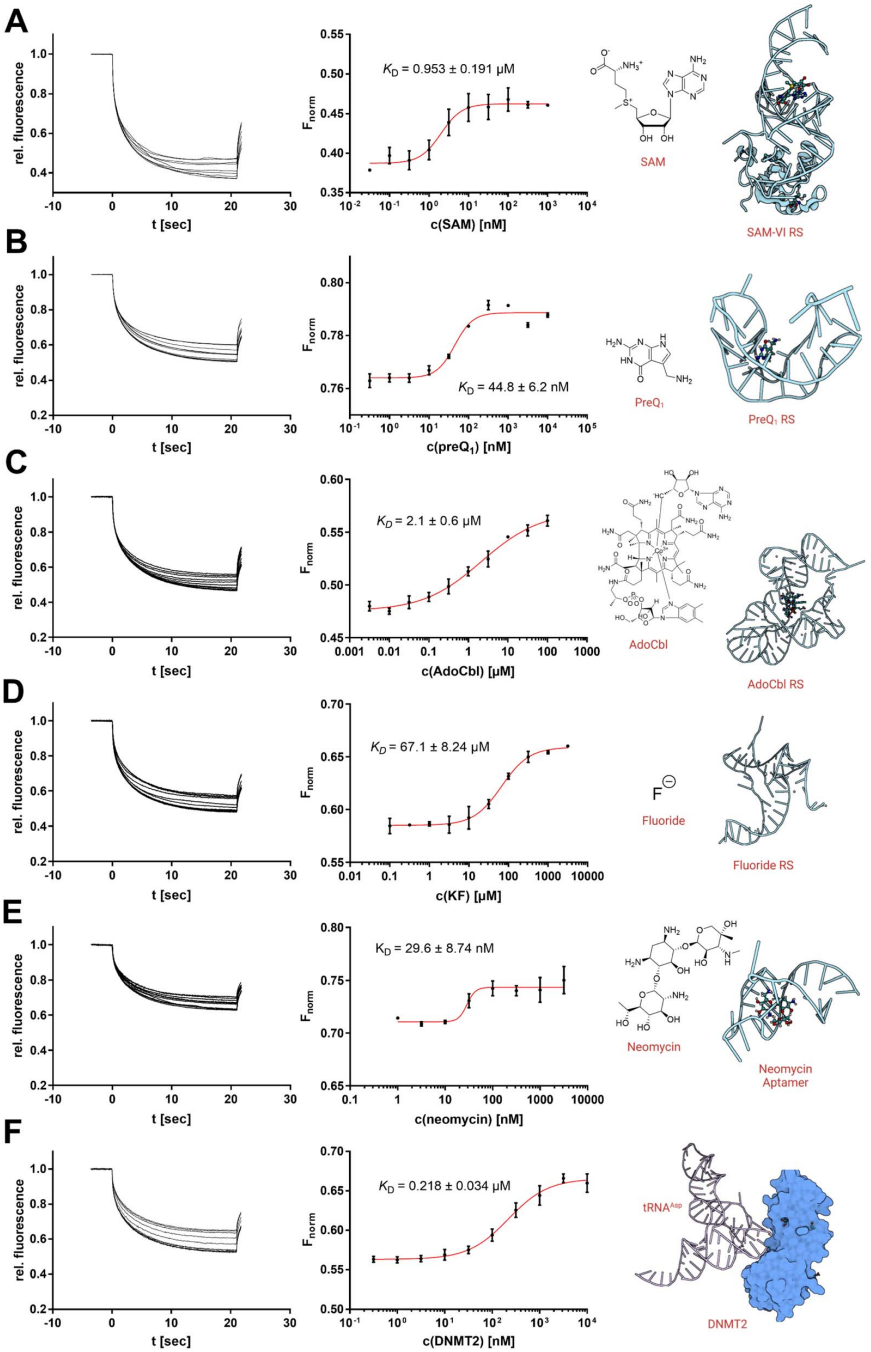


Fig. 4 Analysis of RNA–ligand binding by *in situ* labelling with SybrGold or Syto 59 (1×). Dissociation constants (K_D) were determined using a Boltzmann fit. (A) Interaction between SAM-VI RS and SAM (F_{norm} at 20 s, SybrGold). (B) PreQ$_1$ RS and the PreQ$_1$ ligand (F_{norm} at 1 s, SybrGold). (C) AdoCbl RS and the AdoCbl ligand (F_{norm} at 15 s, Syto 59). (D) Fluoride RS and the potassium fluoride ligand (F_{norm} at 5 s, Syto 59). (E) Neomycin aptamer and the neomycin ligand (F_{norm} at 5 s, Syto 59). (F) tRNA^{Asp} and DNMT2 (F_{norm} at 10 s, SybrGold).

 © 2023 The Author(s). Published by the Royal Society of Chemistry

Open Access Article. Published on 29 August 2023. Downloaded on 10/23/2025 3:14:31 PM.
This article is licensed under a Creative Commons Attribution 3.0 Unported Licence.

the best fluorescence benchmarks and highest reproducibility rates.

Investigation of RNA ligand binding

Targeting physiologically relevant RNA with small molecule drugs has become of increasing interest as a potential drug target over the last years.[1,19,20] Currently, the standard repertoire of bioanalytical techniques includes techniques such as nuclear magnetic resonance (NMR), surface plasmon resonance (SPR), and isothermal titration calorimetry (ITC).[21,22] However, in recent years, MST has probably become one of the most popular techniques for the characterization of RNA-small molecule interactions using covalently dye-labelled RNA targets.[6,8,10] Hence, we aimed to demonstrate four examples where the use of SybrGold and Syto 59 (Fig. 4 and S4†) showed comparable results to RNA ligand binding profiles as determined with orthogonal techniques.

Thus, we investigated three types of nucleotide-derived ligand riboswitch (RS) aptamer domains: the *T. tengcongensis* SAM-I RS, the *B. angulatum* SAM-VI RS, and the *T. tengcongensis* pre-queuosine 1 ($preQ_1$) RS, with their natural ligands SAM, *S*-adenosylhomocysteine (SAH), and $preQ_1$, respectively.[23–25] For the SAM-I RS, our MST data yielded a $K_D = 157$ nM for SAM and $K_D = 137$ μM for SAH agreeing with previously reported values obtained by ITC measurements.[26] For the SAM-VI RS, our MST results for SAM ($K_D = 953$ nM) and SAH ($K_D = 10$ μM) were also consistent with our covalently Cy5-labelled MST experiments (Fig. S5†) and literature reports.[27,28] Similarly, our results showed that $preQ_1$ binds the $preQ_1$ RS with an apparent $K_{D,app}$ of 44.8 nM.

While this value is in the same order of magnitude as our previously reported Cy5-labelled RNA affinity (Fig. S5†), it should be noted that high-affinity ligands (<50 nM) will result in tight-binding to the RNA receptor ([RNA] = 100 nM) and thus imply some scope limitation of this presented protocol.[6,8] For the existing protocols using a covalently labelled RNA target, however, this mostly represents the same technical limitation.

As a next step, we investigated three additional RS aptamer domains against chemically more diverse chemotypes of ligands: a marine metagenome AdoCbl RS, the *T. petrophila* fluoride anion RS, and a synthetic neomycin aptamer.[29–31] The AdoCbl RS naturally binds different variants of the cobalamin co-factor family, which are exceptionally large ligands with a molecular weight of >1000 Da. Our MST experiments using an env8 mutant AdoCbl RS with Syto 59 labelling determined a K_D value of 2.1 μM with adenosylcobalamin (AdoCbl) as a ligand, which is in agreement with the literature.[29] Thus, the non-covalent RNA-MST method is also suitable for non-typically large ligands and their riboswitches.

Next, we studied the opposite case; a riboswitch that is able to bind very small ligands. Aptamers against the smallest known ligands are fluoride anion aptamers. The study of the *T. petrophila* fluoride anion RS showed that this protocol is also useful for such applications if ligand binding results in a substantial conformational change of the aptamer. Hence, non-covalent RNA-MST experiments with Syto 59 ($K_D = 67.1$ μM) are in the same order as dissociation constants determined by ITC experiments in the literature.[30]

As a final example, we examined a neomycin-binding aptamer of synthetic origin. The apparent binding affinity of neomycin to the 27-mer RNA oligo could be determined by $K_{D,app}$ of 29.6 nM.[31]

Of note, the titration of *in situ* labelled RNA samples with their natural ligands mostly does not lead to a change in the fluorescence intensity by displacement of the dye with the ligand (see MST capillary scans in Fig. S8†). In this regard, an RNA target usually has just one ligand binding resp. interaction site but possibly several dye binding sites, some of which overlap with the ligand binding site and some of which do not. If we choose the concentrations of RNA (100 nM) and dyes (1×) such that statistically at most 1 dye molecule is bound per RNA (Fig. 1B), there will be functional, fluorescent RNA molecules in solution that we can (a) address with the ligand resp. interaction and (b) measure their altered thermophoresis behaviour. For the very short $preQ_1$ riboswitch or the neomycin aptamer (both 27 nt), however, we quantified a slight effect on the initial fluorescence at higher ligand concentrations which supports our model of statistical labelling, since for such a short RNA receptor there are fewer opportunities for dye binding that do not overlap with the ligand binding site (Fig. S8A&G†).

Furthermore, we also investigated a macromolecular interaction of RNA with an endogenous protein–ligand. The $tRNA^{Asp}$ represents the physiological substrate of the RNA methyltransferase DNMT2.[32] Using SybrGold, we were able to determine a dissociation constant of this macromolecular interaction ($K_D = 0.218$ μM) similar to a value determined by fluorescence polarization.[33]

Investigation of RNA nucleobase modifications

The development of methods for the detection and quantification of RNA modifications such as nucleobase methylation is a recent topic of research due to their physiological relevance and disease involvement.[34] Currently, the gold standard repertoire of bioanalytical techniques includes mass spectrometric, radiometric, and sequencing methods.[35] Due to the simple and fast preparation of an MST experiment, the development of an MST protocol for the quantification of RNA modifications might offer practical advantages. Thus, the two most promising fluorescent dyes (SybrGold & Syto 59) were harnessed to test for the detection of specific RNA nucleoside modifications.

First, as a proof of concept, two variously modified model RNA oligos AUUAACCUUUUAA (Fig. 5) and CCA-CAACCAUGGUGAGCAA (Fig. 6 and S6†) were investigated for changes in their F_{norm} parameters in dependence on specific RNA modifications. In summary, these model experiments showed that larger or charge-altering RNA modifications (*e.g.*, 5-taurinomethyl-2-thiourididylation) have a more pronounced effect on F_{norm} than single nucleoside methylations (*e.g.*, 6-methyladenine, or 2′-*O*-methylation), which often resulted in scarcely detectable F_{norm} shifts (Fig. 5, 6, and S6†).

In the first step, the influence of different physiologically relevant modifications such as pseudouridylation (ψ), 5-uridine

View Article Online

Open Access Article. Published on 29 August 2023. Downloaded on 10/23/2025 3:14:31 PM. This article is licensed under a Creative Commons Attribution 3.0 Unported Licence.

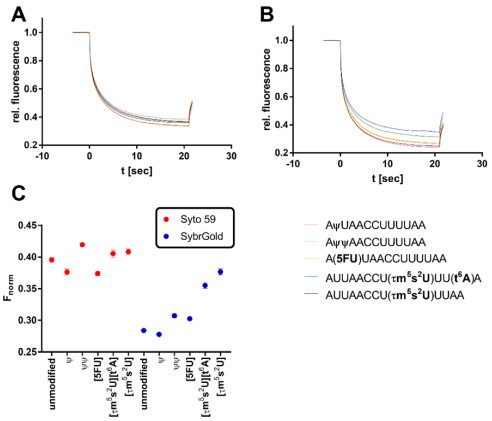


Fig. 5 Analysis of various modifications of the model oligo AUUAACCUUUAA (100 nM) by MST. (A) Thermophoresis curves for the usage of Syto 59 as a reporter dye. (B) Thermophoresis curves for the usage of SybrGold as a reporter dye. (C) MST response (F_{norm} at 10 s) of the modified oligos in comparison to their unmodified analogues.

fluorination (5FU), 5-taurinomethyl-2-thiouridiylation (τm^5s^2U), and threonylcarbamoyladenosylation (t^6A) on the short non-structured model oligonucleotide AUUAACCUUAA as a fragment of the hmt-tRNA^{Lys} was investigated.[36]

Significant divergences were found between the two dyes SybrGold and Syto 59 in the differential analysis of the F_{norm} values. While Syto 59 showed only slight changes in F_{norm} values depending on the modifications (Fig. 5A), significant increases in F_{norm} values were measurable when SybrGold was used, especially for the two oligos with the 5-taurinomethyl-2-thiouridiylation (Fig. 5B). A more systematic investigation of a second model oligonucleotide (CCACAACCAUGGUGAGCAA) was conducted. This is a generically designed oligo that has a hairpin with three regions (stem, loop, tail). The hypothesis was to show at which position RNA methylations have a particular effect on the MST shift For this purpose, the adenine positions of the unmodified parent oligo were systematically methylated either at the N^1 or N^6 position of an adenine base (Fig. 6), or the 2′-OH group of ribose was methylated (Fig. S6†).

In contrast to the results shown in Fig. 5, the detection of adenine methylation with Syto 59 led to more sensitive changes in F_{norm} values than with SybrGold (Fig. 6C). In particular, m^1A

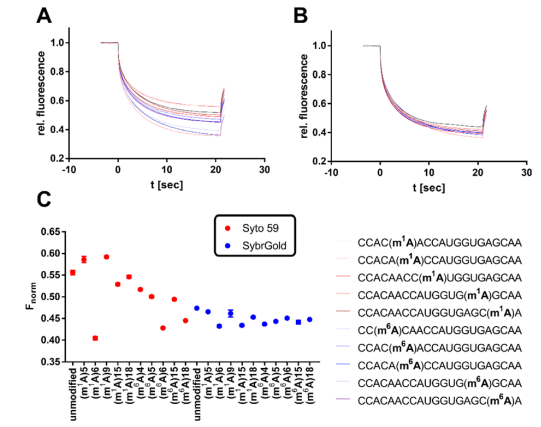


Fig. 6 Analysis of various modifications of the model oligo CCACAACCAUGGUGAGCAA (100 nM) by MST. (A) Thermophoresis curves for the usage of Syto 59 as a reporter dye. (B) Thermophoresis curves for the usage of SybrGold as a reporter dye. (C) MST response (F_{norm} at 10 s) of the modified oligos in comparison to their unmodified analogues.

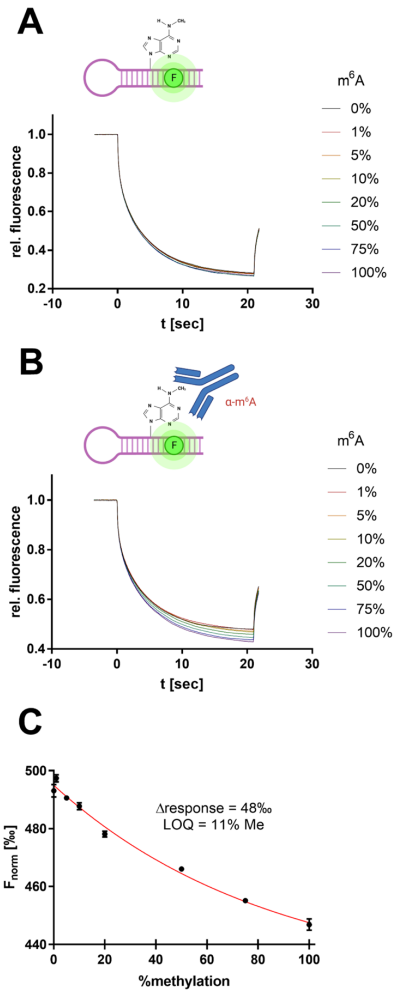


Fig. 7 Antibody-assisted detection of RNA m^6A modification by SybrGold MST. (A) MST traces for METTL3/14 substrate methylation levels (total RNA: 100 nM). (B) Same reaction mixture as in (A) but supplemented with 600 nM anti-m^6A antibody clone 9B7.[40] (C) MST response (F_{norm} at 10 s) as a function of substrate methylation derived from (B). The limit of quantitation (LOQ) was defined by 3σ around F_{norm} = 0%.

© 2023 The Author(s). Published by the Royal Society of Chemistry

View Article Online
Edge Article Chemical Science

Open Access Article. Published on 29 August 2023. Downloaded on 10/23/2025 3:14:31 PM.
This article is licensed under a Creative Commons Attribution 3.0 Unported Licence.

or m^{6}A methylation of the 6th adenine base resulted in significantly altered F_{norm} values compared to the unmodified oligo indicating that local influences of RNA modification either affect the binding of the fluorophore or these modifications modulate the global topology resp. folding of the RNA and thus lead to an altered thermophoresis behaviour. The detection of ribose methylation followed a similar trend, however, with this form of modification leading to generally lower changes in F_{norm} values (Fig. S6C†).

Development of an MST-based METTL3/14 enzyme assay

To derive a relevant biotechnological application from this model concept, an MST-based enzyme assay was developed for the RNA methyltransferase METTL3/14 allowing the tracking of the enzymatic insertion of a single methyl group to an RNA substrate. METTL3/14, which has recently become popular as a potential drug target, is an RNA methyltransferase that transfers a methyl group from SAM to the N^6 atom of an adenine base found in a GGACU motif.[37] Thus, we focused on the development of an enzymatic assay that can follow the 6-methyladenine (m^{6}A) methylation of the METTL3/14 substrate oligo AACUUAAUGUUUGCAUUGG(m^{6}A)CUUGAGUUA.

MST offers the potential to evaluate turnover rates of enzymatic reactions, especially in cases in which no direct detection *via* fluorescence reporter exists.[38,39] Therefore, we sought to determine the intrinsic difference of the substrate's m^{6}A modification in thermophoresis behaviour. For this purpose, we simulated different m^{6}A methylation levels from 0–100% by

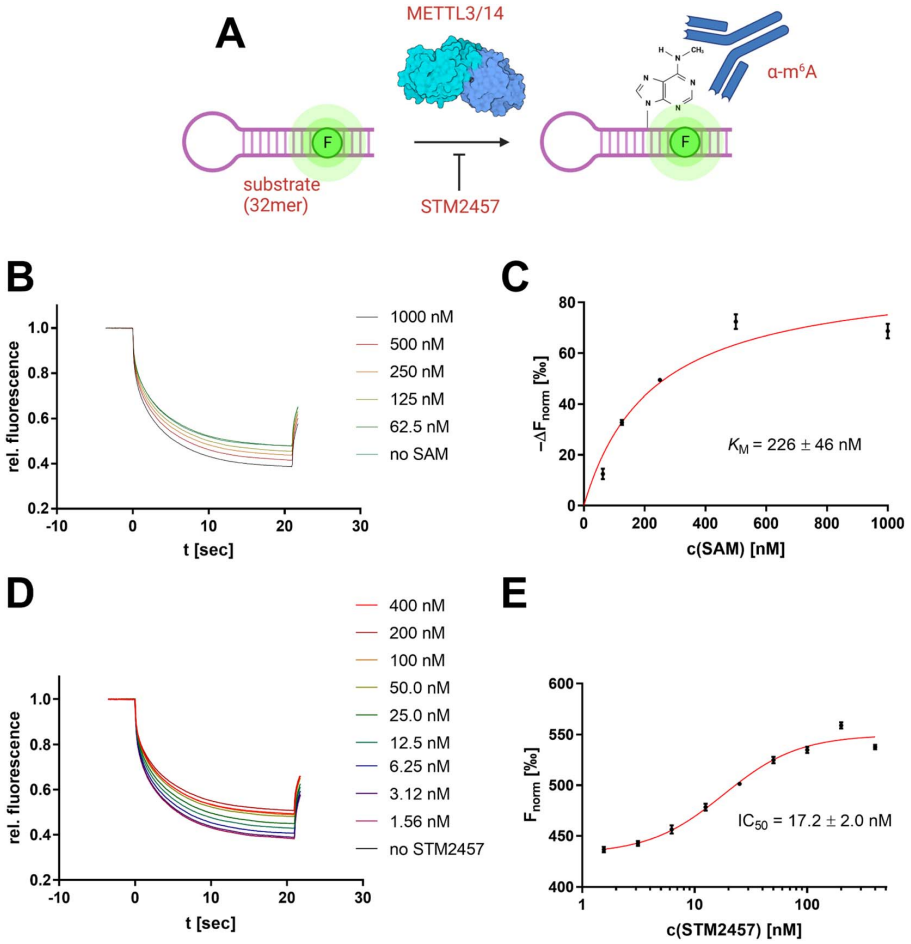


Fig. 8 Development of an MST-based METTL3/14 assay. (A) Illustration of the assay concept: a 32mer METTL3/14 substrate oligo is converted enzymatically which can be detected using an anti-m^{6}A antibody and SybrGold MST. (B) Enzymatic substrate methylation with varying concentrations of SAM as cofactor. After 2 h of incubation time, the crude reaction mixture was supplemented with the anti-m^{6}A antibody and analyzed by SybrGold MST. (C) Michaelis–Menten plot of the MST response (F_{norm} at 10 s) *vs.* the SAM concentration. A K_M value (226 nM) was calculated by non-linear regression. (D) MST curves of the enzymatic substrate methylation in the presence of STM2457 as METTL3/14 inhibitor. (E) Determination of the STM2457 IC_{50} value by dose–response fit of F_{norm} *vs.* [STM2457].

© 2023 The Author(s). Published by the Royal Society of Chemistry

View Article Online
Chemical Science Edge Article

Open Access Article. Published on 29 August 2023. Downloaded on 10/23/2025 3:14:31 PM.
This article is licensed under a Creative Commons Attribution 3.0 Unported Licence.

mixing the synthetic substrate oligo with its methylated analogue at a total RNA concentration of 100 nM (Fig. 7A).

However, the use of 1× SybrGold and Syto 59 as a reporter dye resulted in very little intrinsic difference between the unmethylated and methylated oligos' F_{norm} values ($\Delta = 5‰$), so discrimination was not sufficient for the evaluation of enzymatic turnover. Therefore, we harnessed an antibody-coupled approach to amplify the F_{norm} discrimination signal. The addition of an m^{6}A-specific antibody (9B7 clone, 600 nM) resulted in a 10-fold dispersion ($\Delta = 48‰$, LOQ = 11% methylation) of the RNA oligos' F_{norm} (Fig. 7B and C).[40] This concept thus resembles an immuno-MST assay which has been previously described for non-RNA substrates but in this form claims novelty as an RNA methyltransferase assay.[41,42]

In this regard, the RNA substrate (120 nM), METTL3/14 enzyme (10 nM), and a variable concentration of the cofactor SAM (0–1000 nM) were incubated for 2 h at room temperature. Subsequently, the reaction was added with the anti-m^{6}A antibody (600 nM) and mounted in MST capillaries as a crude reaction mixture without further purification of the RNA substrate (Fig. 8A). The resulting thermophoresis curves showed a dependence of the F_{norm} response on the concentration of the SAM cofactor (Fig. 8B), which can be attributed to a different methylation content of the RNA substrate. The differential analysis of this F_{norm} shift at different SAM concentrations agreed with the calibration of the m^{6}A content (Fig. 7C) and indicated near quantitative methylation at the highest SAM concentration of 1 μM (Fig. 8C). The initial addition of SAH (10 μM) as a known inhibitor of methylation reaction yielded no shifts of the F_{norm} values (Fig. S7A†), confirming the effective inhibition of the enzyme and the overall assay concept. Michaelis–Menten regression of this differential methylation content (ΔF_{norm}) allowed the determination of an apparent K_M value for SAM of 226 nM which is in agreement with a ^{3}H-based enzyme assay (Fig. S7B†) and literature reports.[43]

To demonstrate the usefulness of the developed METTL3/14 assay for drug discovery applications, we also performed an inhibition experiment with the known literature inhibitor STM2457 (Fig. 8C), which revealed an apparent inhibition constant IC_{50} of 17.2 nM in agreement with the literature-determined value.[44]

Conclusions

In conclusion, we could show that the use of non-covalent nucleic acid dyes is suitable to determine some RNA modifications by a simple "mix-and-measure" protocol. Comparing *in situ* labelled RNA samples with orthogonal ligand binding assays, we found that the usage of non-covalent dyes mostly does not alter ligand binding of the RNA molecules, and hence, this new protocol might result in a wide range of opportunities for research applications on the function of RNA molecules. Meanwhile, small modifications that do not significantly affect F_{norm} could be enhanced by the use of a modification-specific antibody, as shown for the METTL3/14 assay, allowing the detection of minimal chemical modifications such as single-site methylation of larger RNA molecules. We hope to have laid the first step for the development of further RNA-immuno-MST assays and for numerous studies in this field.

Experimental section

DNA/RNA oligos

DNA/RNA oligos except for the ones prepared by *in vitro* transcription (IVT, see below) were purchased in HPLC-purified quality (for oligo sequences and manufacturers see Tables S1 and S2†). All experiments were performed under RNase-avoiding conditions. The concentrations of RNA, DNA, and enzymes were determined by a ThermoScientific NanoDrop2000.

RNA preparation

PCR. The DNA templates for the IVT were amplified using PCR. The PCR reaction mixture contained 10 nM of template DNA, 2 μM of each forward and reverse primer, 400 μM dNTP Mix (NEB), 3 mM $MgCl_2$, 0.05 U μL^{-1} Q5 High-Fidelity DNA Polymerase (NEB) and 1× Q5 reaction buffer (NEB) in a final volume of 200 μL. The reaction was performed using a ^{3}Prime thermal cycler with the following cycling conditions: initial denaturation (95 °C, 30 s), followed by 30 cycles of denaturation (95 °C, 30 s), annealing (temperature depends on the primer sequence and was determined by NEB T_M calculator, 30 s) and extension (72 °C, 45 s), and a final extension (72 °C, 2 min). The PCR product homogeneity was checked on a 0.4% agarose gel to confirm the size and purity.

***In vitro* transcription (IVT).** The crude PCR products were used as templates for *in vitro* transcription using the T7 polymerase system. The IVT reaction mixture contained 400 μL PCR product (without further purification), 5 mM of each NTP, 5 mM DTT, 2.5 μg mL^{-1} BSA, $MgCl_2$ (concentration depends on RNA type and was determined before using micro reactions with different $MgCl_2$ concentrations), 50 U mL^{-1} T7 RNA polymerase (ThermoFisher) and 1× reaction buffer (ThermoFisher) in a final volume of 1 mL. The reaction was incubated at 37 °C for 2 hours, and then, another aliquot of T7 RNA polymerase was added and incubated for 4 hours at 37 °C.

RNA extraction and purification. The formed pyrophosphate was removed by centrifugation at 14 000 g for 5 min directly after transcription and the cleared supernatant was transferred to a micro reaction tube for further sample processing. To remove the PCR- and IVT enzymes, a phenol/chloroform extraction was performed twice using ROTI® phenol/chloroform/isoamyl alcohol (Carl Roth) and the standard protocol from the supplier. For a better gel resolution, the extracted samples were desalted using Zeba spin desalting columns (ThermoFisher) following the standard protocol from the supplier. Furthermore, ethanol precipitation was applied to remove chloroform residues and concentrate the RNA. For this, the samples were mixed with 2.5× volume ethanol, 0.1× volume 3 M NaOAc (pH 4.7), and 1 μL glycogen (20 g L^{-1}, ThermoFisher), cooled at −80 °C for 2 hours, then centrifuged for 45 min at 4 °C and 16 000 g. The pellet was washed twice with

 © 2023 The Author(s). Published by the Royal Society of Chemistry

Open Access Article. Published on 29 August 2023. Downloaded on 10/23/2025 3:14:31 PM.
This article is licensed under a Creative Commons Attribution 3.0 Unported Licence.

75% ice-cold ethanol and centrifuged again for 10 min at 4 °C and 16 000 g. The air-dried pellet was redissolved in a small volume of RNase-free water and an equal volume of 2× gel loading buffer (2× TBE, 67% formamide) was added.

For the purification of RNA, a native polyacrylamide gel electrophoresis was utilized. A 10% acrylamide gel solution was prepared using the ROTIPHORESE® DNA sequencing system and 10× TBE buffer. After sample loading, the electrophoresis separation was performed at 15 W until the dye markers of the ladder showed sufficient resolution in the separation range of interest. The RNA was visualized by UV shadowing (254 nm), extracted by cutting out the bands of interest, and the excised parts were aliquoted into small pieces and frozen at −20 °C for 30 min. The frozen sample bands were extracted overnight at 15 °C in a 0.3 M NaOAc (pH 4.7) solution and the samples were centrifuged for 10 min at room temperature and 10 000 g, the supernatant and the gel residues were added into 0.45 μm Nanosep (Pall corporation) tubes and centrifuged again for 10 min and 10 000 g. The flow-through was precipitated with ethanol as described above. The pellet was redissolved in RNase-free water and stored until usage at −20 °C. The RNA product homogeneity was checked on a native 10% polyacrylamide gel to confirm the size and purity.

Setup of a standard mix-and-measure RNA-MST experiment (non-covalent dyes)

The reaction mixtures used for a typical MST experiment contained 100 nM of the investigated RNA and 1× of the respective dye both dissolved in MST buffer (50 mM Tris–HCl pH 7.5, 100 mM KCl, and 25 mM $MgCl_2$) and supplemented with ligands or additives if needed. Previous to the measurement, the RNA stock solution was heated for 5 min at 75 °C and then cooled down to room temperature in the heating block.

MST experiments were carried out using a Monolith NT.115 instrument (NanoTemper Technologies) using Monolith standard capillaries. The instrument was calibrated according to the manufacturer's instructions. The laser type was chosen dye-dependently (NanoBlue laser for SybrGold and RiboGreen and PicoRed laser for Syto dyes). General settings were applied for all MST experiments as follows: manual temperature control: 25 °C, fluorescence measurement before MST: 4 s, MST (IR laser) on: 20 s, fluorescence after MST: 2 s, delay: 25 s. The laser power was adjusted to optimize the signal-to-noise ratio and the fluorescence signal. LED and MST power settings were chosen individually for each sample by adjusting the LED power to yield fluorescence signals of at least 300 units (blue laser) or 3000 units (red laser) and the MST power to achieve an appropriate thermophoretic response (standard setting: medium MST power). MST measurements were analyzed using the NT analysis software (version 1.5.41) and exported for statistical analysis and plotting in GraphPad Prism 7.01.

Advice for the establishment of new RNA–ligand assay systems

We recommend the following procedure for assaying new RNA targets: initially, the new experimental setup should be tested with 100 nM RNA and 1× SybrGold (for NanoBlue devices) or 1× Syto 59 (for PicoRed devices). Initial assays include four controls consisting of 100 nM RNA, 1× dye, and a known reference ligand ($c = 10\times K_D$) in a buffer that has been shown to be appropriate for the biological function of the RNA: (1) +RNA/+dye/+ligand, (2) +RNA/+dye/−ligand, (3) −RNA/+dye/−ligand, (4) −RNA/+dye/+ligand. Samples 3 and 4 should not show a significant thermophoresis curve due to the absence of RNA. Sample 1 should optimally result in an MST shift compared to Sample 2 as a function of reference ligand concentration.

If a ligand-dependent MST shift is not achieved with this initial setup, we recommend the following steps with the same assay setup: (1) variation of RNA dyes as described above, (2) variation of RNA concentration, (3) variation of thermophoresis settings (laser power, temperature, *etc.*).

MST experiments with 5′-Cy5-labelled RNA

MST experiments were performed on a Monolith NT.115 using standard uncoated capillaries. The 5′-Cy5-labelled RNA was heated to 75 °C for 5 min and cooled to room temperature for 60 min. The Cy5-labelled $PreQ_1$ RS and SAM-VI RS were diluted to 20 nM in MST buffer (50 mM Tris–HCl pH 7.5, 100 mM KCl, and 25 mM $MgCl_2$) and supplemented with ligands in appropriate concentrations. Data acquisition was performed identically to the setup of the non-covalently labelled MST experiments (*vide supra*). MST measurements were analyzed using the NT analysis software (version 1.5.41) and exported for statistical analysis and plotting in GraphPad Prism 7.01.

METTL3/14 MST assay (K_M & IC_{50}) determination

MST-based METTL3/14 assays were carried out by mixing the RNA substrate AACUUAAUGUUGCAUUGGACUUGAGUUA (Iba, final: 120 nM), the METTL3/14 enzyme (Biomol, final: 10 nM) and a variable concentration of the cofactor *S*-adenosylmethionine (Sigma Aldrich, final: 0–1000 nM) in 50 μL of assay buffer (20 mM Tris pH 7.5, 1 mM DTT, 0.01% Triton X-100, 50 mM KCl and 0.25 mM $MgCl_2$). After an incubation period of 2 h at room temperature, the reaction was quenched by the addition of SAH (Sigma Aldrich, final: 10 μM, $K_I = 260$ nM), added with the anti-m^6A antibody (clone 9B7, final: 600 nM), SybrGold (final: 1×), and mounted in MST capillaries in triplicates. The laser power was adjusted to 20% for the LED laser and "high" for MST laser. MST measurements were analyzed using the NT analysis software (version 1.5.41) and exported for statistical analysis and plotting in GraphPad Prism 7.01. The decrease in F_{norm} *vs.* [SAM] is a measure of the activity of the enzyme, and thus, the MST traces follow the Michaelis–Menten equation which was used for enzyme kinetic analysis: $v_0 = (v_{max} \times [S]/K_M + [S])$, where v_0 is the initial reaction rate, at a given substrate concentration [S]. v_{max} is the maximum reaction rate, while K_M indicates [S] at which the conversion rate is half-maximal.

To determine the IC_{50} value of the reference inhibitor STM2457, the assay was performed as described above with the following adaptations. 500 nM SAM was used as substrate. STM2457 was added as DMSO stock (final DMSO conc.: 3%).

© 2023 The Author(s). Published by the Royal Society of Chemistry

View Article Online
Chemical Science Edge Article

Open Access Article. Published on 29 August 2023. Downloaded on 10/23/2025 3:14:31 PM.
This article is licensed under a Creative Commons Attribution 3.0 Unported Licence.

The enzyme reactions were incubated for 60 min at room temperature and quenched with SAH (10 μM). F_{norm} values *vs.* [STM2457] were evaluated using a 4-parameter Hill equation to determine an IC_{50} value: $y(F_{norm}) = \text{bottom} + ([\text{STM2457}]^{slope}) \times (\text{top} - \text{bottom})/([\text{STM2457}]^{slope} + IC_{50}^{slope})$.

METTL3/14 tritium-based assay

The radiometric METTL3/14 assay was carried out as described previously by mixing the RNA substrate AACUUAAUGUUGCAUUGGACUUGAGUUA (Iba, final: 200 nM), the METTL3/14 enzyme (Biomol, final: 20 nM) and a variable concentration of the cofactor ^{3}H-SAM (Hartmann Analytics 15 Ci mmol^{-1}, final: 0–1000 nM) in 10 μL of assay buffer (20 mM HEPES pH 7.5, 50 mM KCl, 250 μM $MgCl_2$, 1 mM DTT, 0.01% Tween-20).[43] The reactions were started by the addition of the cofactor ^{3}H-SAM and were carried out at room temperature for 30 min. Aliquots of 8 μL were taken from the reaction mixture and spotted on Whatman glass microfiber filters (GF/C, 25 mm, Cytiva). The RNA was precipitated on the filters in 5% ice-cold TCA (Sigma Aldrich) for 35 min. The filters were washed twice with 5% TCA at room temperature for 20 and 10 min and once in EtOH for 10 min. After drying, the filters were transferred into scintillation vials and 3 mL of Gold MV liquid scintillation cocktail (PerkinElmer) was added. Scintillation was measured on a scintillation counter (TriCarb Liquid Scintillation Analyzer 4810TR) with a measurement time of 1 min. Statistical analysis and plotting were performed in GraphPad Prism 7.01 as described above.

Data availability

The datasets supporting this article have been uploaded as part of the ESI.†

Author contributions

Elisabeth Kallert: formal analysis, methodology, validation, writing—original draft. Malte Behrendt: methodology, validation. Ariane Frey: methodology, formal analysis. Christian Kersten: conceptualization, writing—review & editing. Fabian Barthels: conceptualization, visualization, writing—review & editing.

Conflicts of interest

There are no conflicts to declare.

Acknowledgements

Financial support by the German Research Foundation (DFG) in the framework of the Transregio Collaborative Research Center RMAP (TRR319 RMaP) is gratefully acknowledged. We thank Prof. Mark Helm (University of Mainz) for providing various RNA oligos and Prof. Gunter Meister (University of Regensburg) for providing the anti-m^{6}A antibody. The figures in this article were created with **https://www.biorender.com/**.

Notes and references

1 J. L. Childs-Disney, X. Yang, Q. M. R. Gibaut, Y. Tong, R. T. Batey and M. D. Disney, *Nat. Rev. Drug Discovery*, 2022, **21**, 736–762.
2 A. L. Garner, *ACS Med. Chem. Lett.*, 2023, **14**, 251–259.
3 M. Jerabek-Willemsen, C. J. Wienken, D. Braun, P. Baaske and S. Duhr, *Assay Drug Dev. Technol.*, 2011, **9**, 342–353.
4 S. E. Deeb, A. Al-Harrasi, A. Khan, M. Al-Broumi, G. Al-Thani, M. Alomairi, P. Elumalai, R. A. Sayed and A. E. Ibrahim, *Methods Appl. Fluoresc.*, 2022, **10**, 042001.
5 S. Duhr and D. Braun, *Proc. Natl. Acad. Sci. U.S.A.*, 2006, **103**, 19678–19682.
6 M. H. Moon, T. A. Hilimire, A. M. Sanders and J. S. Schneekloth, *Biochemistry*, 2018, **57**, 4638–4643.
7 D. Jacob, K. Thüring, A. Galliot, V. Marchand, A. Galvanin, A. Ciftci, K. Scharmann, M. Stock, J.-Y. Roignant, S. A. Leidel, Y. Motorin, R. Schaffrath, R. Klassen and M. Helm, *Angew. Chem., Int. Ed.*, 2019, **58**, 9565–9569.
8 E. Kallert, T. R. Fischer, S. Schneider, M. Grimm, M. Helm and C. Kersten, *J. Chem. Inf. Model.*, 2022, **62**, 4134–4148.
9 S. Balaratnam, C. Rhodes, D. D. Bume, C. Connelly, C. C. Lai, J. A. Kelley, K. Yazdani, P. J. Homan, D. Incarnato, T. Numata and J. S. Schneekloth Jr, *Nat. Commun.*, 2021, **12**, 5856.
10 C. Entzian and T. Schubert, *Methods*, 2016, **97**, 27–34.
11 A. Chramiec-Głąbik, M. Rawski, S. Glatt and T.-Y. Lin, in *RNA–Protein Complexes and Interactions: Methods and Protocols*, ed. R.-J. Lin, Springer US, New York, NY, 2023, pp. 29–53.
12 M. Jerabek-Willemsen, T. André, R. Wanner, H. M. Roth, S. Duhr, P. Baaske and D. Breitsprecher, *J. Mol. Struct.*, 2014, **1077**, 101–113.
13 S. A. I. Seidel, P. M. Dijkman, W. A. Lea, G. van den Bogaart, M. Jerabek-Willemsen, A. Lazic, J. S. Joseph, P. Srinivasan, P. Baaske, A. Simeonov, I. Katritch, F. A. Melo, J. E. Ladbury, G. Schreiber, A. Watts, D. Braun and S. Duhr, *Methods*, 2013, **59**, 301–315.
14 P. J. Kolbeck, W. Vanderlinden, G. Gemmecker, C. Gebhardt, M. Lehmann, A. Lak, T. Nicolaus, T. Cordes and J. Lipfert, *Nucleic Acids Res.*, 2021, **49**, 5143–5158.
15 R. Silvers, H. Keller, H. Schwalbe and M. Hengesbach, *ChemBioChem*, 2015, **16**, 1109–1114.
16 Y. T. Maeda, T. Tlusty and A. Libchaber, *Proc. Natl. Acad. Sci. U.S.A.*, 2012, **109**, 17972–17977.
17 T. Bartoschik, S. Galinec, C. Kleusch, K. Walkiewicz, D. Breitsprecher, S. Weigert, Y. A. Muller, C. You, J. Piehler, T. Vercruysse, D. Daelemans and N. Tschammer, *Sci. Rep.*, 2018, **8**, 4977.
18 A. R. Gruber, R. Lorenz, S. H. Bernhart, R. Neuböck and I. L. Hofacker, *Nucleic Acids Res.*, 2008, **36**, W70–W74.
19 C. M. Connelly, M. H. Moon and J. S. Schneekloth, *Cell Chem. Biol.*, 2016, **23**, 1077–1090.
20 K. E. Deigan and A. R. Ferré-D'Amaré, *Acc. Chem. Res.*, 2011, **44**, 1329–1338.
21 B. D. Blakeley, S. M. Deporter, U. Mohan, R. Burai, B. S. Tolbert and B. R. Mc Naughton, *Tetrahedron*, 2012, **68**, 8837–8855.

© 2023 The Author(s). Published by the Royal Society of Chemistry

Open Access Article. Published on 29 August 2023. Downloaded on 10/23/2025 3:14:31 PM.
This article is licensed under a Creative Commons Attribution 3.0 Unported Licence.

22 C. P. Jones, G. Piszczek and A. R. Ferré-D'Amaré, *Methods Mol. Biol.*, 2019, **1964**, 75–87.
23 R. T. Batey, *Wiley Interdiscip. Rev.: RNA*, 2011, **2**, 299–311.
24 A. Serganov, *Curr. Opin. Struct. Biol.*, 2009, **19**, 251–259.
25 R. R. Breaker, *Biochemistry*, 2022, **61**, 137–149.
26 R. K. Montange, E. Mondragón, D. van Tyne, A. D. Garst, P. Ceres and R. T. Batey, *J. Mol. Biol.*, 2010, **396**, 761–772.
27 A. Sun, C. Gasser, F. Li, H. Chen, S. Mair, O. Krasheninina, R. Micura and A. Ren, *Nat. Commun.*, 2019, **10**, 5728.
28 C. M. Connelly, T. Numata, R. E. Boer, M. H. Moon, R. S. Sinniah, J. J. Barchi, A. R. Ferré-D'Amaré and J. S. Schneekloth, *Nat. Commun.*, 2019, **10**, 1501.
29 J. T. Polaski, S. M. Webster, J. E. Johnson and R. T. Batey, *J. Biol. Chem.*, 2017, **292**, 11650–11658.
30 A. Ren, K. R. Rajashankar and D. J. Patel, *Nature*, 2012, **486**, 85–89.
31 H. Gustmann, A.-L. J. Segler, D. B. Gophane, A. J. Reuss, C. Grünewald, M. Braun, J. E. Weigand, S. T. Sigurdsson and J. Wachtveitl, *Nucleic Acids Res.*, 2019, **47**, 15–28.
32 A. Jeltsch, A. Ehrenhofer-Murray, T. P. Jurkowski, F. Lyko, G. Reuter, S. Ankri, W. Nellen, M. Schaefer and M. Helm, *RNA Biol.*, 2017, **14**, 1108–1123.
33 S. Johannsson, P. Neumann, A. Wulf, L. M. Welp, H.-D. Gerber, M. Krull, U. Diederichsen, H. Urlaub and R. Ficner, *Sci. Rep.*, 2018, **8**, 8880.
34 N. Jonkhout, J. Tran, M. A. Smith, N. Schonrock, J. S. Mattick and E. M. Novoa, *RNA*, 2017, **23**, 1754–1769.
35 M. Helm, M. C. Schmidt-Dengler, M. Weber and Y. Motorin, *Adv. Biol.*, 2021, **5**, 2100866.
36 Y. Motorin and M. Helm, *Biochemistry*, 2010, **49**, 4934–4944.
37 F. Fiorentino, M. Menna, D. Rotili, S. Valente and A. Mai, *J. Med. Chem.*, 2023, **66**, 1654–1677.
38 H. Yu and Q. Zhao, *Anal. Chem.*, 2023, **95**, 2152–2156.
39 A. Topf, P. Franz and G. Tsiavaliaris, *BioTechniques*, 2017, **63**, 187–190.
40 F. Weichmann, R. Hett, A. Schepers, T. Ito-Kureha, A. Flatley, K. Slama, F. D. Hastert, N. B. Angstman, M. C. Cardoso, J. König, S. Hüttelmaier, C. Dieterich, S. Canzar, M. Helm, V. Heissmeyer, R. Feederle and G. Meister, *RNA*, 2020, **26**, 1489–1506.
41 C. J. Wienken, P. Baaske, U. Rothbauer, D. Braun and S. Duhr, *Nat. Commun.*, 2010, **1**, 100.
42 S. Lippok, S. A. I. Seidel, S. Duhr, K. Uhland, H.-P. Holthoff, D. Jenne and D. Braun, *Anal. Chem.*, 2012, **84**, 3523–3530.
43 S. M. Buker, Z. A. Gurard-Levin, B. D. Wheeler, M. D. Scholle, A. W. Case, J. L. Hirsch, S. Ribich, R. A. Copeland and P. A. Boriack-Sjodin, *SLAS Discovery*, 2020, **25**, 361–371.
44 E. Yankova, W. Blackaby, M. Albertella, J. Rak, E. De Braekeleer, G. Tsagkogeorga, E. S. Pilka, D. Aspris, D. Leggate, A. G. Hendrick, N. A. Webster, B. Andrews, R. Fosbeary, P. Guest, N. Irigoyen, M. Eleftheriou, M. Gozdecka, J. M. L. Dias, A. J. Bannister, B. Vick, I. Jeremias, G. S. Vassiliou, O. Rausch, K. Tzelepis and T. Kouzarides, *Nature*, 2021, **593**, 597–601.

“

5.2.4 Supporting Information

The following supporting information quoted within "" from page 289 to page 297 is the same as the manuscript cited on page 276.[263] "

Electronic Supplementary Material (ESI) for Chemical Science.
This journal is © The Royal Society of Chemistry 2023

Non-covalent Dyes in Microscale Thermophoresis for Studying RNA Ligand Interactions and Modifications

Elisabeth Kallert,[a] Malte Behrendt,[a] Ariane Frey,[a] Christian Kersten,[a] Fabian Barthels*[a]

[a] E. Kallert, M. Behrendt, A. Frey, Dr. C. Kersten, Dr. F. Barthels
Institute of Pharmaceutical and Biomedical Sciences
Johannes Gutenberg-University of Mainz
Staudingerweg 5, 55128 Mainz, Germany
E-mail: barthels@uni-mainz.de

RNA and DNA oligo sequences

Table S1. Oligos used for RNA-MST experiments. **Category 1**: no structure, <10mer; **category 2**: no structure, 10–15mer; **category 3**: no structure, 16–20mer; **category 4**: hairpin, 16–20mer; **category 5**: bulge/internal loop + hairpin, 21–25mer; **category 6**: internal loop + hairpin, 26–30mer; **category 7**: bulge + internal loop + hairpin(s), 31–50mer; **category 8**: 2 internal loops + 1 hairpin, 50mer; **category 9**: 3 internal loops + 1 hairpin, 60mer; **category 10**: various functional RNA.

OligoID	Cat.	RNA sequence	Manufacturer
MH993	1	GUUAUUC	Iba
MH996	1	UUUUAUUUU	Biomers
MH474	1	GGUACCCAA	Iba
MH122	2	ACAGCUAUCCAUUG	Iba
MH847	2	UCUGAGGGUCCAGGG	Biomers
MH268	2	CCCGGUAAUCGCAUA	Salifu
MH266	3	AAACUUAAAACUUUACUGU	Salifu
MH907	3	ACAAGAAGGGUUUGAUCAUC	Iba
MH272	3	AGAAAUAUGUCUGAUAAA	Salifu
MH355	4	CGCGGGAGACCGGGGUUCGA	Dharmacon
MH261	4	GCUUGAAACCAGCUUUGGG	Salifu
MH1428	4	GGAUCCUCUAGAGUCGACCU	Idt
MH515	5	GGUGGGGUUCCCGAGCGGCCAAAG	Iba
MH499	5	GUUCGAUCCACAGAAUUCGCACCA	Biomers
MH649	5	GGUUCGAUUCCCCGACGGGGAGCCA	Iba
MH857	6	UCUAGAGGAUCCCGGGUACCGAGCUC	Biomers
MH876	6	UGCCGCCCGUCUUGAAACACGGACCAAGGA	Iba
MH1145	6	AACUUAAUGUUUUUGCAUUGGACUUUGAGUUA	Iba
MH761	7	GGCGUGUAGGAUAUUAAAUCAUACCAGAUCGCGG	Iba
MH646	7	UCCUCGUUAGUAUAGUGGUGAGUAUCCCCGCCUAUAUC	Iba
MH566	7	GUCACGCGGGAGACCGGGGUUCGAUUCCCCGACGGGGAGCCA	Iba
MH723	8	CCGCGAUCUGGAGAGGUGAAGAAUACGACCACCUACAAGAAGGACACGCC	Iba
MH721	8	CCGCGAUCUGGAGAGGUGAAGAAUACGACCACCUAAGAAGGACACGCC	Iba
MH762	8	CCGCGAUCUGGAGAGGUGAAGAAUUCGACCACCUACCAGAAGGACACGCC	Iba
MH950	9	CGGAGCCAGCGAGUCUAACCUUGGCCGAGAGGUCUUGGUAAUCUUGUGAAACUC CGUCGU	Iba

MH952	9	GGCCUCAGGAUCUGCUUAGAGAAGGGGGCAACUCCAUCUCAGAGCGGAGAAUUUGGACAA	Iba
MH953	9	UCUUGGAUUUAUUGAAGACUAACUACUGCGAAAGCAUUUGCCAAGGACGUUUUCAUUAAU	Iba
tRNA^{Asp}	10	UCCUCGUUAGUAUAGUGGUGAGUAUCCCCGCCUGUCACGCGGGAGACCGGGGUUCGAUUCCCCGACGGGGAG	In house IVT
PreQ$_1$ RS (*Thermoanaerobacter tengcongensis*)	10	GGAGAGGUUCUAGCUACACCUCUAUAAAAAACUAA	biomers
SAM-I RS (*Thermoanaerobacter tengcongensis*)	10	GGCUUAUCAAGAGAGGGGGAGCGACUGGCGCGAAGAACCCCGGCAACCAGAAAUGGUGCCAAUUCCUGCAGCGGAAACGUUGAAAGAUGAGCCG	In house IVT
SAM-VI RS (*Bifidobacterium angulatum*)	–	GGCAUUGUGCCUCGCAUUGCACUCCGCGGGGCGAUAAGUCCUGAAAAGGGAUGUC	In house IVT
Cy5-PreQ$_1$ RS (*Bacillus subtilis*)	–	Cy5-AGAGGUUCUAGCUACACCCUCUAUAAAAAACUAA	Eurofins Genomics
Cy5-SAM-VI RS (*Bifidobacterium angulatum*)	–	Cy5-GGCAUUGUGCCUCGCAUUGCACUCCGCGGGGCGAUAAGUCCUGAAAAGGGAUGUC	Eurofins Genomics
AdoCbl riboswitch (Marine metagenome *env8* 4WJvar)	–	GGCCUGAAAGCGUGGUGGGGAAGUGACGUGAAAAUUCGUCCAGAUUACUUGAUACGGUUAUACUCCGAGUGCCACCCAGGCCAUACAACGAGCAAGGAGACUC	GenScript
Fluoride riboswitch (*Thermotoga petrophila*)	–	GGGCGAUGAGGCCCGCCCAAACUGCCCUGAAAAGGGCUGAUGGCCUCUACUG	GenScript
Neomycin aptamer (synthetic)	–	GGCUGCUUGUCCUUUAAUGGUCCAGUC	GenScript
METTL3/14 substrate	–	AACUUAAUGUUGCAUUGGACUUGAGUUA	Iba

Table S2. DNA templates and primers used for PCR and IVT.

OligoID	description	DNA sequence	Manufacturer
MH53	Universal forward primer	CGCGCGAAGCTTAATACGACTCACTATA	IDT
EK0004	Reverse primer SAM-I RS	CGGCTCATCTTTCAACGTTTCCG	IDT
EK0010	Reverse primer SAM-VI RS	GACATCCCTTTTCAGGACTTATCGCCCCG	IDT
MH1102	Reverse primer $tRNA^{Asp}$	TGGCGGGCCGTCG	Iba
EK0003	Template SAM-I RS	CGGCTCATCTTTCAACGTTTCCGCTGCAGGAATTGGCACCATTTCTGGTTGCCGGGGTTCTTC GCGCCAGTCGCTCCCCCTCTCTTGATAAGCCTATAGTGAGTCGTATTA	IDT
EK0009	Template SAM-VI RS	GACATCCCTTTTCAGGACTTATCGCCCCGCGGAGTGCAATGCGAGGCACAATGCCTATAGT GAGTCGTATTA	IDT
MH1101	Template $tRNA^{Asp}$	TGGCGGGCCGTCGGGGAATCGAACCCCGGTCTCCCGCGTGACAGGCGGGGATACTCACCA CTATACTAACGACCCTATAGTGAGTCGTATT	Iba

Supplementary Figures

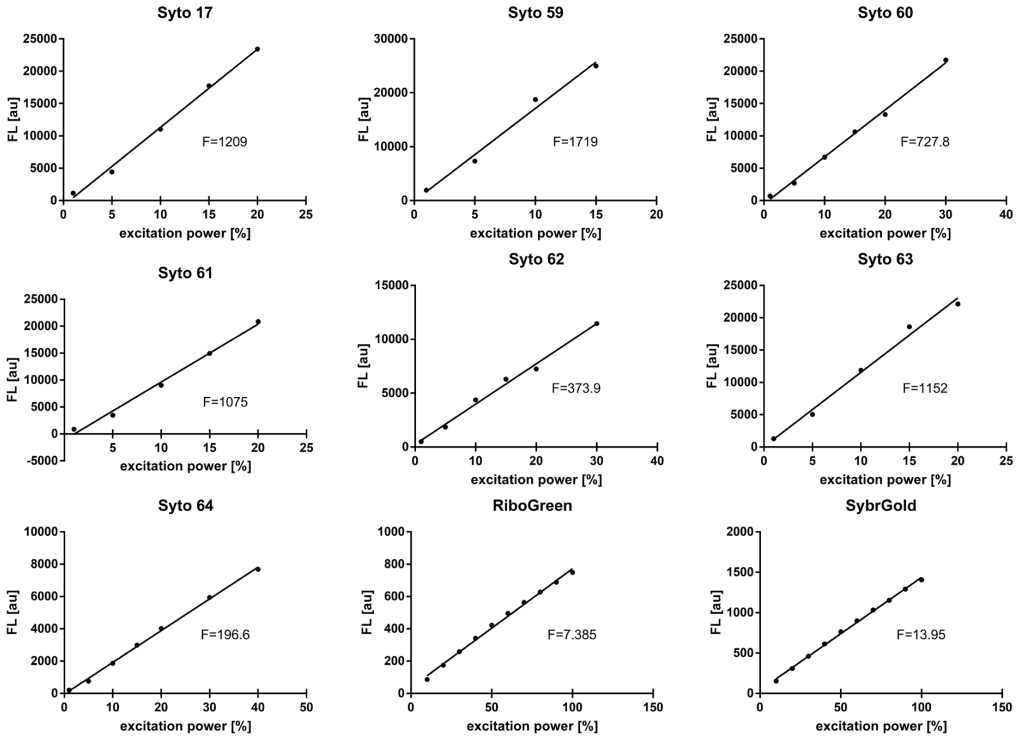


Figure S1. Regression plots for dye fluorescence normalization. Each dye (1×) was mixed with 100 nM of MH646 as RNA model oligonucleotide (UCCUCGUUAGUAUAGUGGUGAGUAUCCCCGCCUAUAUC). The initial fluorescence intensity as a function of the excitation power was determined pre-MST with either the NanoBlue laser for SybrGold and RiboGreen or the PicoRed laser for the Syto dyes. Linear regression yielded a slope-derived sensitivity factor (F) for the normalization of fluorescence intensity during structure-activity-relationship experiments.

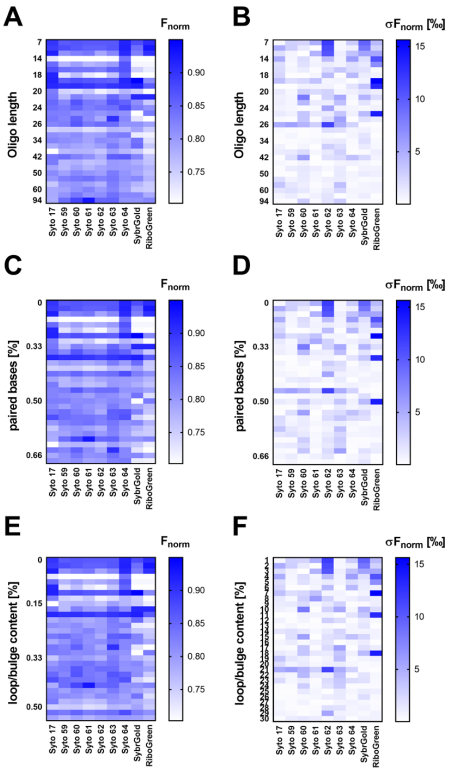


Figure S2. Structural RNA-dependent effects on F_{norm}. (**A**) Correlation between oligo length and F_{norm}. (**B**) Correlation between oligo length and σF_{norm}. (**C**) Correlation between hybridized base content and F_{norm}. (**D**) Correlation between hybridized base content and σF_{norm}. (**E**) Correlation between loop/bulge content and F_{norm}. (**F**) Correlation between loop/bulge content and σF_{norm}.

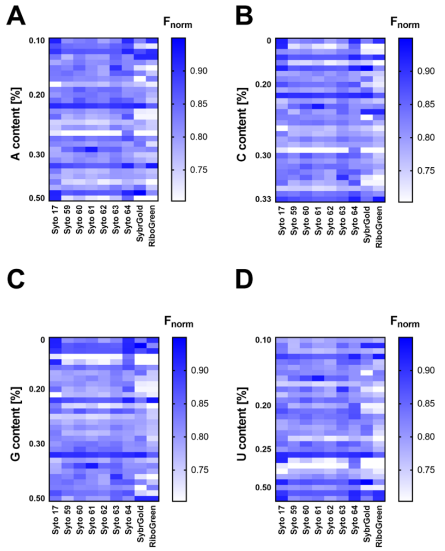


Figure S3. RNA sequence-dependent effects on F_{norm}. (**A**) Correlation between adenine content and F_{norm}. (**B**) Correlation between cytosine content and F_{norm}. (**C**) Correlation between guanine content and F_{norm}. (**D**) Correlation between uridine content and F_{norm}.

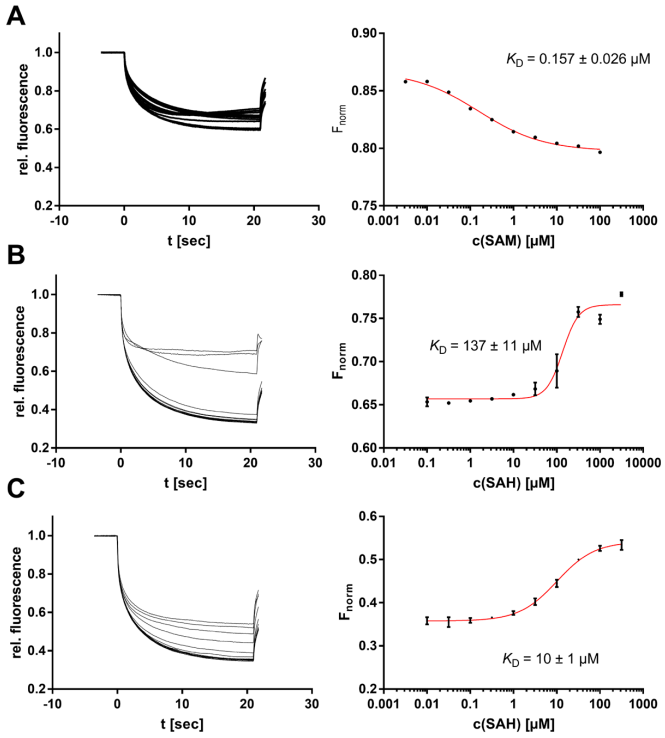


Figure S4. Analysis of RNA-ligand interaction by in situ labelling with SybrGold (1×). (**A**) Interaction between SAM-I RS and SAM (F_{norm} at 1 s). (**B**) SAM-I RS and SAH (F_{norm} at 1 s). (**C**) SAM-VI RS and SAH (F_{norm} at 15 s).

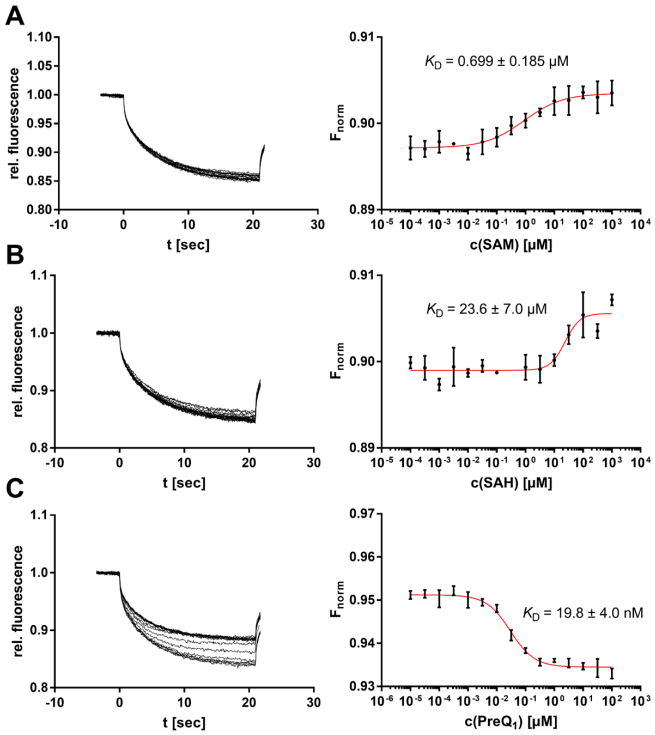


Figure S5. Analysis of RNA-ligand interaction by Cy5-labelled RNA-MST (**A**) Interaction between SAM-VI RS and SAM (F_{norm} at 5 s). (**B**) SAM-VI RS and SAH (F_{norm} at 5 s). (**C**) $PreQ_1$ RS and $PreQ_1$ (F_{norm} at 1 s).

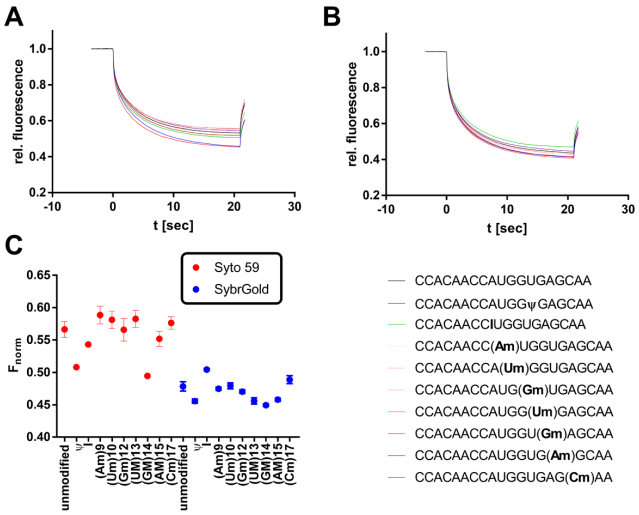


Figure S6. Analysis of various modifications of the model oligo CCACAACCAUGGUGAGCAA (100 nM) by MST. (**A**) Thermophoresis curves for the usage of Syto 59 as a reporter dye. (**B**) Thermophoresis curves for the usage of SybrGold as a reporter dye. (**C**) MST response (F_{norm} at 10 s) of the modified oligos in comparison to their unmodified analogues.

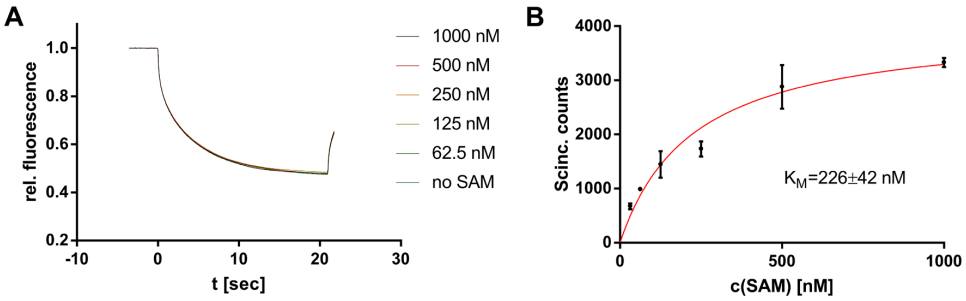


Figure S7. Supplementary data for the establishment of the METTL3/14 assay. (**A**) Thermophoresis curves for the METTL3/14 reaction inhibited by the initial addition of SAH (10 µM). Enzymatic substrate methylation with varying concentrations of SAM as the cofactor. After 2 h of incubation time, the crude reaction mixture was supplemented with the anti-m^{6}A antibody and analyzed by SybrGold MST. (**B**) Tritium-based METTL3/14 methyltransferase assay. The Michaelis-Menten plot was derived from radiometric analysis of ^{3}H incorporation into RNA substrate AACUUAAUGUUUGCAUUGGACUUGAGUUA. A K_M value (226 nM) was calculated by non-linear regression (Michaelis Menten).

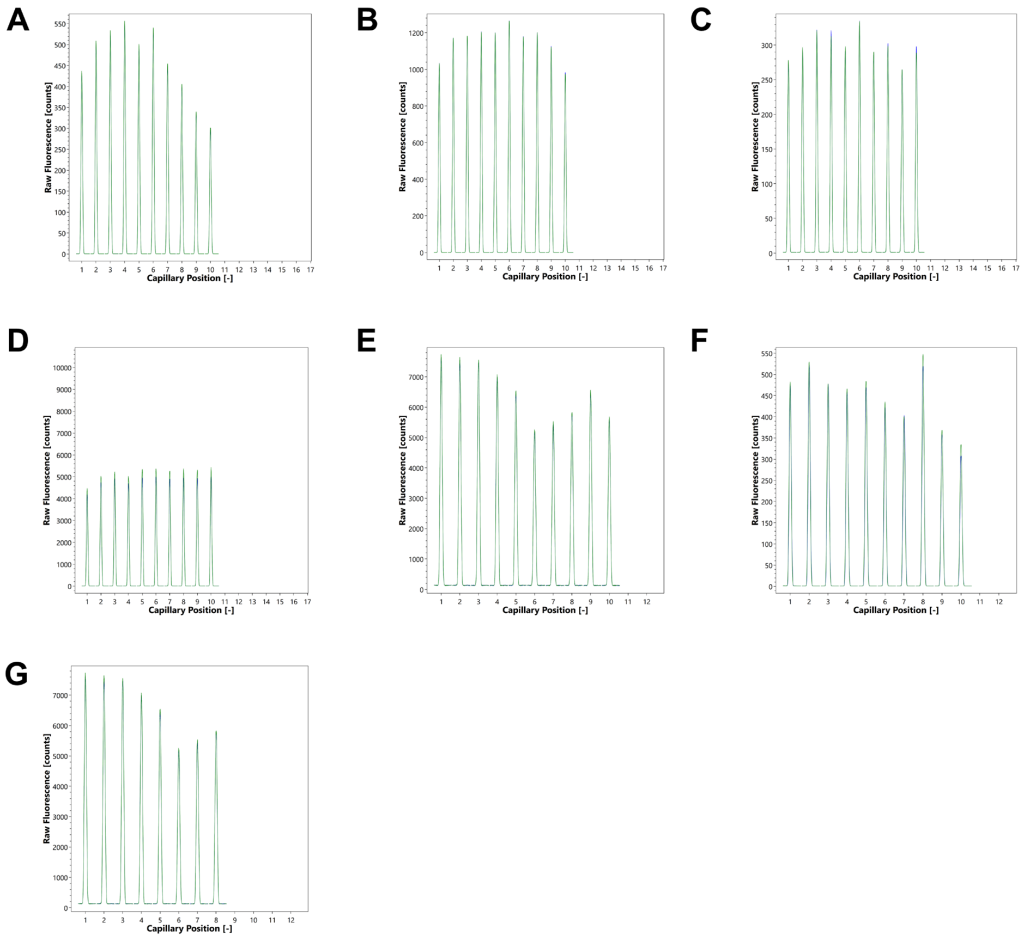


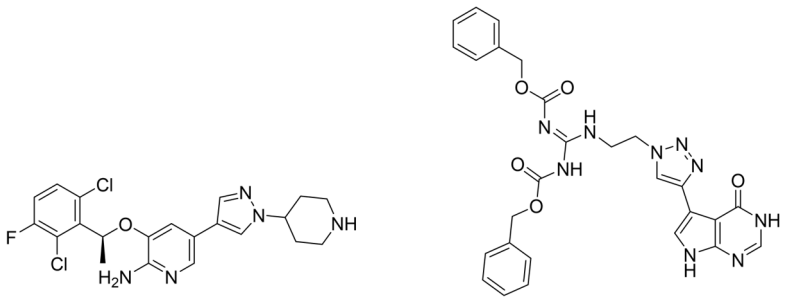
Figure S8. Capillary scans of RNA-ligand interaction samples for the assessment of dye displacement by ligand binding. Capillary scans are presented with increasing concentration corresponding to the MST curves in Figure 4 and Figure S4. (**A**) $PreQ_1$ RS vs. $PreQ_1$. (**B**) SAM-I RS vs. SAM. (**C**) SAM-VI RS vs. SAM. (**D**) Fluoride RS vs. potassium fluoride. (**E**) AdoCbl RS vs. adenosyl cobalamin. (**F**) DNMT2 vs. tRNA. (**G**) Neomycin aptamer vs. neomycin.

“

6 Summary & Outlook

This thesis demonstrates the use of diverse chemical libraries in the field of medicinal chemistry of RNA Mtases and explores strategies for screening large libraries against these targets. In addition, new modalities, including PROTACs, were successfully implemented for this enzyme class.

In detail, in **Project 1**, two D2B strategies were employed for various RNA Mtases to identify fluorescent tracers and inhibitors. In both studies, the well-established CuAAC reaction, widely used in D2B strategies, was utilized. The first part of the project, including fluorescent tracer development, provides the basis for an HTS against METTL1, identifying (*S*)-crizotinib (**19**, K_D = 138 µM) as an inhibitor. In the second part, a newly developed tracer was used to screen a 320-member triazole library synthesized in a well-plate format without prior purification against *S. aureus* TrmD. These efforts resulted in the identification of an inhibitor employing a prodrug strategy that exhibited antibacterial efficacy against *S. aureus*.



19
K_D (METTL1) = 138 µM

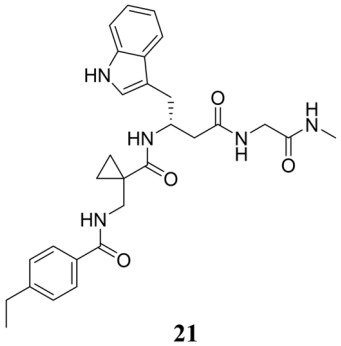
20
MBC (*S. aureus*) = 12.5 µM

Figure 18. Chemical structure of (*S*)-crizotinib (**19**) and the prodrug (**20**) developed for targeting *S. aureus* TrmD.

As an **outlook for Project 1,** the fluorescent tracers discovered in this project can be employed in future HTS campaigns for additional RNA Mtases. Furthermore, the identified inhibitor, (*S*)-crizotinib, offers potential for further optimization regarding affinity and selectivity. Obtaining the X-ray co-crystal structure with METTL1 could provide valuable insights into the binding mode and guide chemical modifications to improve affinity.

The X-ray structure of TrmD analyzed in the second part of the project also provides a basis for further affinity optimization. In addition, the prodrug strategy could be expanded and further investigated for *S. aureus* TrmD and its homologs. Notably, X-ray crystallography revealed a previously untargeted unique cysteine residue (Cys104) within the TrmD binding pocket, presenting an opportunity to develop covalent inhibitors for TrmD.

In **Project 2**, implementation of the DELopen platform provided by Wuxi AppTec yielded five novel and selective binders for DNMT2, of which only three peptidomimetics demonstrated inhibitory efficacy against DNMT2. X-ray analysis of a peptidomimetic DEL hit revealed a structural rearrangement of a flexible loop that blocks the SAM binding pocket, resulting in DNMT2 inhibition. Based on these findings, a SAR study was conducted, affording a lead compound with low micromolar affinity. Cellular investigations demonstrated a significant reduction in m^5C modifications of tRNA and a synergistic effect with doxorubicin regarding cell viability. Lastly, a pull-down displacement assay showed that none of the tested DNMT2 interaction proteins (NonO and eIF4E) bind to the discovered binding pocket.

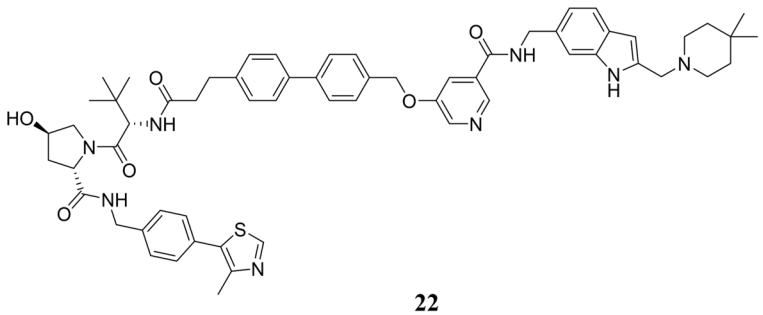


21
K_D (DNMT2) = 10.2 µM

Figure 19. Chemical structure of the most promising peptidomimetic DEL hit, which exhibited low micromolar affinity and high selectivity for DNMT2.

As an **outlook for Project 2,** the pull-down displacement assay could be extended to additional known DNMT2-interacting proteins to explore the possibility of a regulatory binding pocket. Moreover, the information obtained from the X-ray structure enables a more comprehensive inhibitor-design study that could also target the tRNA-binding pocket. Although the triazine-containing compounds did not exhibit inhibitory activity, they may serve as binding moieties for PROTAC approaches targeting DNMT2. Therefore, obtaining an X-ray co-crystal structure of these compounds would be valuable for elucidating their binding mode and identifying potential exit vectors for PROTAC development.

Project 3 was divided into two parts. During the first part, four sequential generations of METTL3-targeting PROTACs resulted in the discovery of AF 151, utilizing an inhibitor previously developed by Storm Therapeutics as a POI ligand. The PROTAC exhibited similar DC_{50}-values as the previously discovered WD6305, but with a major improvement compared to the parent compound STM2457 regarding cellular m^1A reduction in RNA and cell viability of cancer cells. In the second part of the project, a mix-and-measure protocol was established to investigate RNA interactions and modifications. The method was proven with six different riboswitches and their respective ligands, and as a functional assay for METTL3/14, detecting the m^6A modification in RNA.



22
AF 151
DC_{50} (METTL3) = 430 nM

Figure 20. Chemical structure of the METTL3-targeting PROTAC AF 151, obtained through optimization over four successive generations.

As an **outlook for Project 3**, the developed mix-and-measure protocol provides a versatile tool for studying RNA interactions and modification. It can facilitate the discovery of novel RNA-binding ligands and can support the identification and characterization of RNA Mtase inhibitors.

In summary, this thesis establishes a foundation for future drug discovery efforts targeting diverse RNA Mtases. Two novel screening methodologies – based on fluorescent tracer and non-covalent RNA dyes – were developed, enabling more efficient characterization and identification of inhibitors and ligands. Moreover, application of the D2B strategy to *S. aureus* yielded the first prodrugs with demonstrable antibacterial activity against *S. aureus* TrmD, thereby confirming its druggability. This finding provides a basis for future TrmD-targeting campaigns aimed at developing novel antibacterial agents. In addition, DEL screening revealed a previously uncharacterized allosteric binding pocket in DNMT2 and led to the identification of the first selective, cell-permeable DNMT2 inhibitors. The discovery of this new allosteric site offers a promising entry point for the rational design of novel selective DNMT2 inhibitors.

7 Bibliography

(1) Saletore, Y.; Meyer, K.; Korlach, J.; Vilfan, I. D.; Jaffrey, S.; Mason, C. E. The Birth of the Epitranscriptome: Deciphering the Function of RNA Modifications. *Genome Biol.* **2012**, *13* (10), 175. https://doi.org/10.1186/gb-2012-13-10-175.

(2) Schaefer, M.; Kapoor, U.; Jantsch, M. F. Understanding RNA Modifications: The Promises and Technological Bottlenecks of the 'Epitranscriptome.' *Open Biol.* **2017**, *7* (5), 170077. https://doi.org/10.1098/rsob.170077.

(3) Fischer, T. R.; Meidner, L.; Schwickert, M.; Weber, M.; ´Zimmermann, R. A.; Kersten, C.; Schirmeister, T.; Helm, M. Chemical Biology and Medicinal Chemistry of RNA Methyltransferases | Nucleic Acids Research | Oxford Academic. *Nucleic Acids Res.* **2022**, *50* (8), 4216–4245. https://doi.org/10.1093/nar/gkac224.

(4) Cappannini, A.; Ray, A.; Purta, E.; Mukherjee, S.; Boccaletto, P.; Moafinejad, S. N.; Lechner, A.; Barchet, C.; Klaholz, B. P.; Stefaniak, F.; Bujnicki, J. M. MODOMICS: A Database of RNA Modifications and Related Information. 2023 Update. *Nucleic Acids Res.* **2024**, *52* (D1), D239–D244. https://doi.org/10.1093/nar/gkad1083.

(5) McCown, P. J.; Ruszkowska, A.; Kunkler, C. N.; Breger, K.; Hulewicz, J. P.; Wang, M. C.; Springer, N. A.; Brown, J. A. Naturally Occurring Modified Ribonucleosides. *WIREs RNA* **2020**, *11* (5), e1595. https://doi.org/10.1002/wrna.1595.

(6) Davis, F. F.; Allen, F. W. Ribonucleic Acids from Yeast Which Contain a Fifth Nucleotide. *J. Biol. Chem.* **1957**, *227* (2), 907–915.

(7) Penzo, M.; Guerrieri, A.; Zacchini, F.; Treré, D.; Montanaro, L. RNA Pseudouridylation in Physiology and Medicine: For Better and for Worse. *Genes* **2017**, *8* (11), 301. https://doi.org/10.3390/genes8110301.

(8) Menezes, M. R.; Balzeau, J.; Hagan, J. P. 3′ RNA Uridylation in Epitranscriptomics, Gene Regulation, and Disease. *Front. Mol. Biosci.* **2018**, *5*, 61. https://doi.org/10.3389/fmolb.2018.00061.

(9) Barbieri, I.; Kouzarides, T. Role of RNA Modifications in Cancer. *Nat. Rev. Cancer* **2020**, *20* (6), 303–322. https://doi.org/10.1038/s41568-020-0253-2.

(10) Bass, B. L.; Weintraub, H. An Unwinding Activity That Covalently Modifies Its Double-Stranded RNA Substrate. *Cell* **1988**, *55* (6), 1089–1098. https://doi.org/10.1016/0092-8674(88)90253-X.

(11) Yang, B.; Wang, J.-Q.; Tan, Y.; Yuan, R.; Chen, Z.-S.; Zou, C. RNA Methylation and Cancer Treatment. *Pharmacol. Res.* **2021**, *174*, 105937. https://doi.org/10.1016/j.phrs.2021.105937.

(12) Blanco, S.; Kurowski, A.; Nichols, J.; Watt, F. M.; Benitah, S. A.; Frye, M. The RNA–Methyltransferase Misu (NSun2) Poises Epidermal Stem Cells to Differentiate. *PLoS Genet.* **2011**, *7* (12), e1002403. https://doi.org/10.1371/journal.pgen.1002403.

(13) Blanco, S.; Dietmann, S.; Flores, J. V.; Hussain, S.; Kutter, C.; Humphreys, P.; Lukk, M.; Lombard, P.; Treps, L.; Popis, M.; Kellner, S.; Hölter, S. M.; Garrett, L.; Wurst, W.; Becker, L.; Klopstock, T.; Fuchs, H.; Gailus-Durner, V.; Hrabě De Angelis, M.; Káradóttir, R. T.; Helm, M.; Ule, J.; Gleeson, J. G.; Odom, D. T.; Frye, M. Aberrant Methylation of t RNA s Links Cellular Stress to Neuro-developmental Disorders. *EMBO J.* **2014**, *33* (18), 2020–2039. https://doi.org/10.15252/embj.201489282.

(14) Schubert, H. L.; Blumenthal, R. M.; Cheng, X. Many Paths to Methyltransfer: A Chronicle of Convergence. *Trends Biochem. Sci.* **2003**, *28* (6), 329–335. https://doi.org/10.1016/S0968-0004(03)00090-2.

(15) Cantoni, G. L. Biological Methylation: Selected Aspects. *Annu. Rev. Biochem.* **1975**, *44* (1), 435–451. https://doi.org/10.1146/annurev.bi.44.070175.002251.

(16) Sun, Q.; Huang, M.; Wei, Y. Diversity of the Reaction Mechanisms of SAM-Dependent Enzymes - ScienceDirect. *Acta Pharm. Sin. B* **2021**, *11* (3), 632–650. https://doi.org/10.1016/j.apsb.2020.08.011.

(17) Dong, A.; Yoder, J. A.; Zhang, X.; Zhou, L.; Bestor, T. H.; Cheng, X. Structure of Human DNMT2, an Enigmatic DNA Methyltransferase Homolog That Displays Denaturant-Resistant Binding to DNA. *Nucleic Acids Res.* **2001**, *29* (2), 439–448. https://doi.org/10.1093/nar/29.2.439.

(18) Li, J.; Wang, L.; Hahn, Q.; Nowak, R. P.; Viennet, T.; Orellana, E. A.; Roy Burman, S. S.; Yue, H.; Hunkeler, M.; Fontana, P.; Wu, H.; Arthanari, H.; Fischer, E. S.; Gregory, R. I. Structural Basis of Regulated m7G tRNA Modification by METTL1–WDR4. *Nature* **2023**, *613* (7943), 391–397. https://doi.org/10.1038/s41586-022-05566-4.

(19) Śledź, P.; Jinek, M. Structural Insights into the Molecular Mechanism of the m6A Writer Complex. *eLife* **2016**, *5*, e18434. https://doi.org/10.7554/eLife.18434.

(20) Strassler, S. E.; Bowles, I. E.; Dey, D.; Jackman, J. E.; Conn, G. L. Tied up in Knots: Untangling Substrate Recognition by the SPOUT Methyltransferases - Journal of Biological Chemistry. *J. Biol. Chem.* **2022**, *298* (10), 102393. https://doi.org/10.1016/j.jbc.2022.102393.

(21) Dixon, M. M.; Huang, S.; Matthews, R. G.; Ludwig, M. The Structure of the C-Terminal Domain of Methionine Synthase: Presenting S-Adenosylmethionine for Reductive Methylation of B12. *Structure* **1996**, *4* (11), 1263–1275. https://doi.org/10.1016/S0969-2126(96)00135-9.

(22) Schubert, H. L.; Wilson, K. S.; Raux, E.; Woodcock, S. C.; Warren, M. J. The X-Ray Structure of a Cobalamin Biosynthetic Enzyme, Cobalt-Precorrin-4 Methyltransferase. *Nat. Struct. Biol.* **1998**, *5* (7), 585–592. https://doi.org/10.1038/846.

(23) Tkaczuk, K. L.; Dunin-Horkawicz, S.; Purta, E.; Bujnicki, J. M. Structural and Evolutionary Bioinformatics of the SPOUT Superfamily of Methyltransferases. *BMC Bioinformatics* **2007**, *8* (1), 73. https://doi.org/10.1186/1471-2105-8-73.

(24) Michel, G.; Sauvé, V.; Larocque, R.; Li, Y.; Matte, A.; Cygler, M. The Structure of the RlmB 23S rRNA Methyltransferase Reveals a New Methyltransferase Fold with a Unique Knot. *Structure* **2002**, *10* (10), 1303–1315. https://doi.org/10.1016/S0969-2126(02)00852-3.

(25) Xiao, B.; Jing, C.; Wilson, J. R.; Walker, P. A.; Vasisht, N.; Kelly, G.; Howell, S.; Taylor, I. A.; Blackburn, G. M.; Gamblin, S. J. Structure and Catalytic Mechanism of the Human Histone Methyltransferase SET7/9. *Nature* **2003**, *421* (6923), 652–656. https://doi.org/10.1038/nature01378.

(26) Li, M.; Tao, Z.; Zhao, Y.; Li, L.; Zheng, J.; Li, Z.; Chen, X. 5-Methylcytosine RNA Methyltransferases and Their Potential Roles in Cancer. *J. Transl. Med.* **2022**, *20* (1), 214. https://doi.org/10.1186/s12967-022-03427-2.

(27) Tuorto, F.; Liebers, R.; Musch, T.; Schaefer, M.; Hofmann, S.; Kellner, S.; Frye, M.; Helm, M.; Stoecklin, G.; Lyko, F. RNA Cytosine Methylation by Dnmt2 and NSun2 Promotes tRNA Stability and Protein Synthesis. *Nat. Struct. Mol. Biol.* **2012**, *19* (9), 900–905. https://doi.org/10.1038/nsmb.2357.

(28) Heissenberger, C.; Liendl, L.; Nagelreiter, F.; Gonskikh, Y.; Yang, G.; Stelzer, E. M.; Krammer, T. L.; Micutkova, L.; Vogt, S.; Kreil, D. P.; Sekot, G.; Siena, E.; Poser, I.; Harreither, E.; Linder, A.; Ehret, V.; Helbich, T. H.; Grillari-Voglauer, R.; Jansen-Dürr, P.; Koš, M.; Polacek, N.; Grillari, J.; Schosserer, M. Loss of the Ribosomal RNA Methyltransferase NSUN5 Impairs Global Protein Synthesis and Normal Growth. *Nucleic Acids Res.* **2019**, *47* (22), 11807–11825. https://doi.org/10.1093/nar/gkz1043.

(29) Sajini, A. A.; Choudhury, N. R.; Wagner, R. E.; Bornelöv, S.; Selmi, T.; Spanos, C.; Dietmann, S.; Rappsilber, J.; Michlewski, G.; Frye, M. Loss of 5-Methylcytosine Alters the Biogenesis of Vault-Derived Small RNAs to Coordinate Epidermal Differentiation. *Nat. Commun.* **2019**, *10* (1), 2550. https://doi.org/10.1038/s41467-019-10020-7.

(30) Xing, J.; Yi, J.; Cai, X.; Tang, H.; Liu, Z.; Zhang, X.; Martindale, J. L.; Yang, X.; Jiang, B.; Gorospe, M.; Wang, W. NSun2 Promotes Cell Growth via Elevating Cyclin-Dependent Kinase 1 Translation. *Mol. Cell. Biol.* **2015**, *35* (23), 4043–4052. https://doi.org/10.1128/MCB.00742-15.

(31) Schaefer, M.; Pollex, T.; Hanna, K.; Tuorto, F.; Meusburger, M.; Helm, M.; Lyko, F. RNA Methylation by Dnmt2 Protects Transfer RNAs against Stress-Induced Cleavage. *Genes Dev.* **2010**, *24* (15), 1590–1595. https://doi.org/10.1101/gad.586710.

(32) Oerum, S.; Meynier, V.; Catala, M.; Tisné, C. A Comprehensive Review of m6A/m6Am RNA Methyltransferase Structures. *Nucleic Acids Res.* **2021**, *49* (13), 7239–7255. https://doi.org/10.1093/nar/gkab378.

(33) Schwartz, S.; Mumbach, M. R.; Jovanovic, M.; Wang, T.; Maciag, K.; Bushkin, G. G.; Mertins, P.; Ter-Ovanesyan, D.; Habib, N.; Cacchiarelli, D.; Sanjana, N. E.; Freinkman, E.; Pacold, M. E.; Satija, R.; Mikkelsen, T. S.; Hacohen, N.; Zhang, F.; Carr, S. A.; Lander, E. S.; Regev, A.

Perturbation of m6A Writers Reveals Two Distinct Classes of mRNA Methylation at Internal and 5′ Sites. *Cell Rep.* **2014**, *8* (1), 284–296. https://doi.org/10.1016/j.celrep.2014.05.048.

(34) Yang, Y.; Hsu, P. J.; Chen, Y.-S.; Yang, Y.-G. Dynamic Transcriptomic m6A Decoration: Writers, Erasers, Readers and Functions in RNA Metabolism. *Cell Res.* **2018**, *28* (6), 616–624. https://doi.org/10.1038/s41422-018-0040-8.

(35) Huang, H.; Weng, H.; Sun, W.; Qin, X.; Shi, H.; Wu, H.; Zhao, B. S.; Mesquita, A.; Liu, C.; Yuan, C. L.; Hu, Y.-C.; Hüttelmaier, S.; Skibbe, J. R.; Su, R.; Deng, X.; Dong, L.; Sun, M.; Li, C.; Nachtergaele, S.; Wang, Y.; Hu, C.; Ferchen, K.; Greis, K. D.; Jiang, X.; Wei, M.; Qu, L.; Guan, J.-L.; He, C.; Yang, J.; Chen, J. Recognition of RNA N6-Methyladenosine by IGF2BP Proteins Enhances mRNA Stability and Translation. *Nat. Cell Biol.* **2018**, *20* (3), 285–295. https://doi.org/10.1038/s41556-018-0045-z.

(36) Liu, N.; Zhou, K. I.; Parisien, M.; Dai, Q.; Diatchenko, L.; Pan, T. N 6-Methyladenosine Alters RNA Structure to Regulate Binding of a Low-Complexity Protein. *Nucleic Acids Res.* **2017**, *45* (10), 6051–6063. https://doi.org/10.1093/nar/gkx141.

(37) Liu, N.; Dai, Q.; Zheng, G.; He, C.; Parisien, M.; Pan, T. N6-Methyladenosine-Dependent RNA Structural Switches Regulate RNA–Protein Interactions. *Nature* **2015**, *518* (7540), 560–564. https://doi.org/10.1038/nature14234.

(38) Li, H.; Zhong, Y.; Cao, G.; Shi, H.; Liu, Y.; Li, L.; Yin, P.; Chen, J.; Xiao, Z.; Du, B. METTL3 Promotes Cell Cycle Progression via m^6 A/YTHDF1-Dependent Regulation of *CDC25B* Translation. *Int. J. Biol. Sci.* **2022**, *18* (8), 3223–3236. https://doi.org/10.7150/ijbs.70335.

(39) Li, J.; Zhang, H.; Wang, H. N1-Methyladenosine Modification in Cancer Biology: Current Status and Future Perspectives. *Comput. Struct. Biotechnol. J.* **2022**, *20*, 6578–6585. https://doi.org/10.1016/j.csbj.2022.11.045.

(40) Liu, F.; Clark, W.; Luo, G.; Wang, X.; Fu, Y.; Wei, J.; Wang, X.; Hao, Z.; Dai, Q.; Zheng, G.; Ma, H.; Han, D.; Evans, M.; Klungland, A.; Pan, T.; He, C. ALKBH1-Mediated tRNA Demethylation Regulates Translation. *Cell* **2016**, *167* (3), 816-828.e16. https://doi.org/10.1016/j.cell.2016.09.038.

(41) Zhang, X.; Zhu, W.-Y.; Shen, S.-Y.; Shen, J.-H.; Chen, X.-D. Biological Roles of RNA m7G Modification and Its Implications in Cancer. *Biol. Direct* **2023**, *18* (1), 58. https://doi.org/10.1186/s13062-023-00414-5.

(42) Malbec, L.; Zhang, T.; Chen, Y.-S.; Zhang, Y.; Sun, B.-F.; Shi, B.-Y.; Zhao, Y.-L.; Yang, Y.; Yang, Y.-G. Dynamic Methylome of Internal mRNA N7-Methylguanosine and Its Regulatory Role in Translation. *Cell Res.* **2019**, *29* (11), 927–941. https://doi.org/10.1038/s41422-019-0230-z.

(43) Muthukrishnan, S.; Both, G. W.; Furuichi, Y.; Shatkin, A. J. 5′-Terminal 7-Methylguanosine in Eukaryotic mRNA Is Required for Translation. *Nature* **1975**, *255* (5503), 33–37. https://doi.org/10.1038/255033a0.

(44) Björk, G. R.; Wikström, P. M.; Byström, A. S. Prevention of Translational Frameshifting by the Modified Nucleoside 1-Methylguanosine. *Science* **1989**, *244* (4907), 986–989. https://doi.org/10.1126/science.2471265.

(45) Kirchner, S.; Ignatova, Z. Emerging Roles of tRNA in Adaptive Translation, Signalling Dynamics and Disease. *Nat. Rev. Genet.* **2015**, *16* (2), 98–112. https://doi.org/10.1038/nrg3861.

(46) Ofir-Rosenfeld, Y.; Vasiliauskaitė, L.; Saunders, C.; Sapetschnig, A.; Tsagkogeorga, G.; Albertella, M.; Carkill, M.; Self-Fordham, J.; Holz, J. B.; Rausch, O. STC-15, an Oral Small Molecule Inhibitor of the RNA Methyltransferase METTL3, Inhibits Tumour Growth through Activation of Anti-Cancer Immune Responses Associated with Increased Interferon Signalling, and Synergises with T Cell Checkpoint Blockade. *Eur. J. Cancer* **2022**, *174*, S123. https://doi.org/10.1016/S0959-8049(22)01128-5.

(47) Papadopoulos, K. P.; Ahnert, J. R.; Ofir-Rosenfeld, Y.; Holz, J.-B.; Team, S.-22101 S. Phase 1 Dose Escalation and Cohort Expansion Study Evaluating Safety, PK, PD and Clinical Activity of STC-15, a METTL-3 Inhibitor, in Patients with Advanced Malignancies. *J. Clin. Oncol.* **2024**. https://doi.org/10.1200/JCO.2024.42.16_suppl.2586.

(48) Goll, M. G.; Kirpekar, F.; Maggert, K. A.; Yoder, J. A.; Hsieh, C.-L.; Zhang, X.; Golic, K. G.; Jacobsen, S. E.; Bestor, T. H. Methylation of $tRNA^{Asp}$ by the DNA Methyltransferase Homolog Dnmt2. *Science* **2006**, *311* (5759), 395–398. https://doi.org/10.1126/science.1120976.

(49) Jeltsch, A.; Ehrenhofer-Murray, A.; Jurkowski, T. P.; Lyko, F.; Reuter, G.; Ankri, S.; Nellen, W.; Schaefer, M.; Helm, M. Mechanism and Biological Role of Dnmt2 in Nucleic Acid Methylation. *RNA Biol.* **2017**, *14* (9), 1108–1123. https://doi.org/10.1080/15476286.2016.1191737.

(50) Müller, S.; Windhof, I. M.; Maximov, V.; Jurkowski, T.; Jeltsch, A.; Förstner, K. U.; Sharma, C. M.; Gräf, R.; Nellen, W. Target Recognition, RNA Methylation Activity and Transcriptional Regulation of the Dictyostelium Discoideum Dnmt2-Homologue (DnmA). *Nucleic Acids Res.* **2013**, *41* (18), 8615–8627. https://doi.org/10.1093/nar/gkt634.

(51) Schaefer, M.; Lyko, F. Solving the Dnmt2 Enigma. *Chromosoma* **2010**, *119* (1), 35–40. https://doi.org/10.1007/s00412-009-0240-6.

(52) Goll, M. G.; Bestor, T. H. EUKARYOTIC CYTOSINE METHYLTRANSFERASES. *Annu. Rev. Biochem.* **2005**, *74* (1), 481–514. https://doi.org/10.1146/annurev.biochem.74.010904.153721.

(53) Shanmugam, R.; Aklujkar, M.; Schäfer, M.; Reinhardt, R.; Nickel, O.; Reuter, G.; Lovley, D. R.; Ehrenhofer-Murray, A.; Nellen, W.; Ankri, S.; Helm, M.; Jurkowski, T. P.; Jeltsch, A. The Dnmt2 RNA Methyltransferase Homolog of Geobacter Sulfurreducens Specifically Methylates tRNA-Glu. *Nucleic Acids Res.* **2014**, *42* (10), 6487–6496. https://doi.org/10.1093/nar/gku256.

(54) Jeltsch, A. Beyond Watson and Crick: DNA Methylation and Molecular Enzymology of DNA Methyltransferases. *ChemBioChem* **2002**, *3* (4), 274–293. https://doi.org/10.1002/1439-7633(20020402)3:4<274::AID-CBIC274>3.0.CO;2-S.

(55) Santi, D. V.; Norment, A.; Garrett, C. E. Covalent Bond Formation between a DNA-Cytosine Methyltransferase and DNA Containing 5-Azacytosine. *Proc. Natl. Acad. Sci.* **1984**, *81* (22), 6993–6997. https://doi.org/10.1073/pnas.81.22.6993.

(56) Lyko, F. The DNA Methyltransferase Family: A Versatile Toolkit for Epigenetic Regulation. *Nat. Rev. Genet.* **2018**, *19* (2), 81–92. https://doi.org/10.1038/nrg.2017.80.

(57) Schaefer, M.; Steringer, J. P.; Lyko, F. The Drosophila Cytosine-5 Methyltransferase Dnmt2 Is Associated with the Nuclear Matrix and Can Access DNA during Mitosis. *PloS One* **2008**, *3* (1), e1414. https://doi.org/10.1371/journal.pone.0001414.

(58) Rashad, S.; Niizuma, K.; Tominaga, T. tRNA Cleavage: A New Insight. *Neural Regen. Res.* **2019**, *15* (1), 47–52. https://doi.org/10.4103/1673-5374.264447.

(59) Thompson, D. M.; Parker, R. Stressing Out over tRNA Cleavage. *Cell* **2009**, *138* (2), 215–219. https://doi.org/10.1016/j.cell.2009.07.001.

(60) Park, J.; Ahn, S. H.; Shin, M. G.; Kim, H. K.; Chang, S. tRNA-Derived Small RNAs: Novel Epigenetic Regulators. *Cancers* **2020**, *12* (10), 2773. https://doi.org/10.3390/cancers12102773.

(61) Sobala, A.; Hutvagner, G. Small RNAs Derived from the 5′ End of tRNA Can Inhibit Protein Translation in Human Cells. *RNA Biol.* **2013**, *10* (4), 553–563. https://doi.org/10.4161/rna.24285.

(62) Gebetsberger, J.; Wyss, L.; Mleczko, A. M.; Reuther, J.; Polacek, N. A tRNA-Derived Fragment Competes with mRNA for Ribosome Binding and Regulates Translation during Stress. *RNA Biol.* **2017**, *14* (10), 1364–1373. https://doi.org/10.1080/15476286.2016.1257470.

(63) Tuorto, F.; Herbst, F.; Alerasool, N.; Bender, S.; Popp, O.; Federico, G.; Reitter, S.; Liebers, R.; Stoecklin, G.; Gröne, H.; Dittmar, G.; Glimm, H.; Lyko, F. The tRNA Methyltransferase Dnmt2 Is Required for Accurate Polypeptide Synthesis during Haematopoiesis. *EMBO J.* **2015**, *34* (18), 2350–2362. https://doi.org/10.15252/embj.201591382.

(64) Shanmugam, R.; Fierer, J.; Kaiser, S.; Helm, M.; Jurkowski, T. P.; Jeltsch, A. Cytosine Methylation of tRNA-Asp by DNMT2 Has a Role in Translation of Proteins Containing Poly-Asp Sequences. *Cell Discov.* **2015**, *1*, 15010. https://doi.org/10.1038/celldisc.2015.10.

(65) Forbes, S. A.; Beare, D.; Gunasekaran, P.; Leung, K.; Bindal, N.; Boutselakis, H.; Ding, M.; Bamford, S.; Cole, C.; Ward, S.; Kok, C. Y.; Jia, M.; De, T.; Teague, J. W.; Stratton, M. R.; McDermott, U.; Campbell, P. J. COSMIC: Exploring the World's Knowledge of Somatic Mutations in Human Cancer. *Nucleic Acids Res.* **2015**, *43* (Database issue), D805–D811. https://doi.org/10.1093/nar/gku1075.

(66) Tzelepi, V.; Logotheti, S.; Efstathiou, E.; Troncoso, P.; Aparicio, A.; Sakellakis, M.; Hoang, A.; Perimenis, P.; Melachrinou, M.; Logothetis, C.; Zolota, V. Epigenetics and Prostate Cancer: Defining the Timing of DNA Methyltransferase Deregulation during Prostate Cancer

Progression. *Pathology (Phila.)* **2020**, *52* (2), 218–227. https://doi.org/10.1016/j.pathol.2019.10.006.

(67) Lewinska, A.; Adamczyk-Grochala, J.; Wnuk, M. TRDMT1-Mediated RNA C-5 Methylation as a Novel Target in Anticancer Therapy. *Biochim. Biophys. Acta BBA - Rev. Cancer* **2023**, *1878* (6), 188964. https://doi.org/10.1016/j.bbcan.2023.188964.

(68) Bloniarz, D.; Adamczyk-Grochala, J.; Lewinska, A.; Wnuk, M. The Lack of Functional DNMT2/TRDMT1 Gene Modulates Cancer Cell Responses during Drug-Induced Senescence. *Aging* **2021**, *13* (12), 15833–15874. https://doi.org/10.18632/aging.203203.

(69) Chen, H.; Yang, H.; Zhu, X.; Yadav, T.; Ouyang, J.; Truesdell, S. S.; Tan, J.; Wang, Y.; Duan, M.; Wei, L.; Zou, L.; Levine, A. S.; Vasudevan, S.; Lan, L. m5C Modification of mRNA Serves a DNA Damage Code to Promote Homologous Recombination. *Nat. Commun.* **2020**, *11* (1), 2834. https://doi.org/10.1038/s41467-020-16722-7.

(70) Zhu, X.; Wang, X.; Yan, W.; Yang, H.; Xiang, Y.; Lv, F.; Shi, Y.; Li, H.; Lan, L. Ubiquitination-Mediated Degradation of TRDMT1 Regulates Homologous Recombination and Therapeutic Response. *NAR Cancer* **2021**, *3* (1), zcab010. https://doi.org/10.1093/narcan/zcab010.

(71) Lewinska, A.; Adamczyk-Grochala, J.; Kwasniewicz, E.; Deregowska, A.; Semik, E.; Zabek, T.; Wnuk, M. Reduced Levels of Methyltransferase DNMT2 Sensitize Human Fibroblasts to Oxidative Stress and DNA Damage That Is Accompanied by Changes in Proliferation-Related miRNA Expression. *Redox Biol.* **2017**, *14*, 20–34. https://doi.org/10.1016/j.redox.2017.08.012.

(72) Zhang, Y.; Zhang, X.; Shi, J.; Tuorto, F.; Li, X.; Liu, Y.; Liebers, R.; Zhang, L.; Qu, Y.; Qian, J.; Pahima, M.; Liu, Y.; Yan, M.; Cao, Z.; Lei, X.; Cao, Y.; Peng, H.; Liu, S.; Wang, Y.; Zheng, H.; Woolsey, R.; Quilici, D.; Zhai, Q.; Li, L.; Zhou, T.; Yan, W.; Lyko, F.; Zhang, Y.; Zhou, Q.; Duan, E.; Chen, Q. Dnmt2 Mediates Intergenerational Transmission of Paternally Acquired Metabolic Disorders through Sperm Small Non-Coding RNAs. *Nat. Cell Biol.* **2018**, *20* (5), 535–540. https://doi.org/10.1038/s41556-018-0087-2.

(73) Grandjean, V.; Fourré, S.; De Abreu, D. A. F.; Derieppe, M.-A.; Remy, J.-J.; Rassoulzadegan, M. RNA-Mediated Paternal Heredity of Diet-Induced Obesity and Metabolic Disorders. *Sci. Rep.* **2015**, *5* (1), 18193. https://doi.org/10.1038/srep18193.

(74) Schwickert, M.; Zimmermann, R. A.; Habeck, T.; Hoba, S. N.; Nidoieva, Z.; Fischer, T. R.; Stark, M. M.; Kersten, C.; Lermyte, F.; Helm, M.; Schirmeister, T. Covalent S-Adenosylhomocysteine-Based DNA Methyltransferase 2 Inhibitors with a New Type of Aryl Warhead. *ACS Med. Chem. Lett.* **2023**, *14* (6), 777–787. https://doi.org/10.1021/acsmedchemlett.3c00062.

(75) Schwickert, M.; Fischer, T. R.; Zimmermann, R. A.; Hoba, S. N.; Meidner, J. L.; Weber, M.; Weber, M.; Stark, M. M.; Koch, J.; Jung, N.; Kersten, C.; Windbergs, M.; Lyko, F.; Helm, M.; Schirmeister, T. Discovery of Inhibitors of DNA Methyltransferase 2, an Epitranscriptomic Modulator and Potential Target for Cancer Treatment. *J. Med. Chem.* **2022**, *65* (14), 9750–9788. https://doi.org/10.1021/acs.jmedchem.2c00388.

(76) Zimmermann, R. A.; Fischer, T. R.; Schwickert, M.; Nidoieva, Z.; Schirmeister, T.; Kersten, C. Chemical Space Virtual Screening against Hard-to-Drug RNA Methyltransferases DNMT2 and NSUN6. *Int. J. Mol. Sci.* **2023**, *24* (7), 6109. https://doi.org/10.3390/ijms24076109.

(77) Björk, G. R.; Jacobsson, K.; Nilsson, K.; Johansson, M. J. O.; Byström, A. S.; Persson, O. P. A Primordial tRNA Modification Required for the Evolution of Life? *EMBO J.* **2001**, *20* (1–2), 231–239. https://doi.org/10.1093/emboj/20.1.231.

(78) Christian, T.; Evilia, C.; Williams, S.; Hou, Y.-M. Distinct Origins of tRNA(m1G37) Methyltransferase. *J. Mol. Biol.* **2004**, *339* (4), 707–719. https://doi.org/10.1016/j.jmb.2004.04.025.

(79) Byström, A. S.; Björk, G. R. Chromosomal Location and Cloning of the Gene (trmD) Responsible for the Synthesis of tRNA (m1G) Methyltransferase in Escherichia Coli K-12. *Mol. Gen. Genet. MGG* **1982**, *188* (3), 440–446. https://doi.org/10.1007/bf00330046.

(80) Lahoud, G.; Goto-Ito, S.; Yoshida, K.; Ito, T.; Yokoyama, S.; Hou, Y.-M. Differentiating Analogous tRNA Methyltransferases by Fragments of the Methyl Donor. *RNA* **2011**, *17* (7), 1236–1246. https://doi.org/10.1261/rna.2706011.

(81) Ito, T.; Masuda, I.; Yoshida, K.; Goto-Ito, S.; Sekine, S.; Suh, S. W.; Hou, Y.-M.; Yokoyama, S. Structural Basis for Methyl-Donor-Dependent and Sequence-Specific Binding to tRNA

Substrates by Knotted Methyltransferase TrmD. *Proc. Natl. Acad. Sci. U. S. A.* **2015**, *112* (31), E4197-4205. https://doi.org/10.1073/pnas.1422981112.

(82) Ahn, H. J.; Kim, H.; Yoon, H.; Lee, B. I.; Suh, S. W.; Yang, J. K. Crystal Structure of tRNA(m1G37)Methyltransferase: Insights into tRNA Recognition. *EMBO J.* **2003**, *22* (11), 2593–2603. https://doi.org/10.1093/emboj/cdg269.

(83) Hou, Y.-M.; Matsubara, R.; Takase, R.; Masuda, I.; Sulkowska, J. I. TrmD: A Methyl Transferase for tRNA Methylation With m1G37. *The Enzymes* **2017**, *41*, 89–115. https://doi.org/10.1016/bs.enz.2017.03.003.

(84) Elkins, P. A.; Watts, J. M.; Zalacain, M.; van Thiel, A.; Vitazka, P. R.; Redlak, M.; Andraos-Selim, C.; Rastinejad, F.; Holmes, W. M. Insights into Catalysis by a Knotted TrmD tRNA Methyltransferase. *J. Mol. Biol.* **2003**, *333* (5), 931–949. https://doi.org/10.1016/j.jmb.2003.09.011.

(85) Sakaguchi, R.; Lahoud, G.; Christian, T.; Gamper, H.; Hou, Y.-M. A Divalent Metal Ion-Dependent N(1)-Methyl Transfer to G37-tRNA. *Chem. Biol.* **2014**, *21* (10), 1351–1360. https://doi.org/10.1016/j.chembiol.2014.07.023.

(86) Marintchev, A.; Wagner, G. Translation Initiation: Structures, Mechanisms and Evolution. *Q. Rev. Biophys.* **2004**, *37* (3–4), 197–284. https://doi.org/10.1017/S0033583505004026.

(87) Jørgensen, F.; Kurland, C. G. Processivity Errors of Gene Expression in Escherichia Coli. *J. Mol. Biol.* **1990**, *215* (4), 511–521. https://doi.org/10.1016/S0022-2836(05)80164-0.

(88) Gamper, H. B.; Masuda, I.; Frenkel-Morgenstern, M.; Hou, Y.-M. The UGG Isoacceptor of tRNAPro Is Naturally Prone to Frameshifts. *Int. J. Mol. Sci.* **2015**, *16* (7), 14866–14883. https://doi.org/10.3390/ijms160714866.

(89) Gamper, H. B.; Masuda, I.; Frenkel-Morgenstern, M.; Hou, Y.-M. Maintenance of Protein Synthesis Reading Frame by EF-P and m1G37-tRNA. *Nat. Commun.* **2015**, *6* (1), 7226. https://doi.org/10.1038/ncomms8226.

(90) Forsyth, R. A.; Haselbeck, R. J.; Ohlsen, K. L.; Yamamoto, R. T.; Xu, H.; Trawick, J. D.; Wall, D.; Wang, L.; Brown-Driver, V.; Froelich, J. M.; C, K. G.; King, P.; McCarthy, M.; Malone, C.; Misiner, B.; Robbins, D.; Tan, Z.; Zhu Zy, Z.; Carr, G.; Mosca, D. A.; Zamudio, C.; Foulkes, J. G.; Zyskind, J. W. A Genome-Wide Strategy for the Identification of Essential Genes in Staphylococcus Aureus. *Mol. Microbiol.* **2002**, *43* (6), 1387–1400. https://doi.org/10.1046/j.1365-2958.2002.02832.x.

(91) Baba, T.; Ara, T.; Hasegawa, M.; Takai, Y.; Okumura, Y.; Baba, M.; Datsenko, K. A.; Tomita, M.; Wanner, B. L.; Mori, H. Construction of Escherichia Coli K-12 in-Frame, Single-Gene Knockout Mutants: The Keio Collection. *Mol. Syst. Biol.* **2006**, *2*, 2006.0008. https://doi.org/10.1038/msb4100050.

(92) Gerdes, S. Y.; Scholle, M. D.; Campbell, J. W.; Balázsi, G.; Ravasz, E.; Daugherty, M. D.; Somera, A. L.; Kyrpides, N. C.; Anderson, I.; Gelfand, M. S.; Bhattacharya, A.; Kapatral, V.; D'Souza, M.; Baev, M. V.; Grechkin, Y.; Mseeh, F.; Fonstein, M. Y.; Overbeek, R.; Barabási, A.-L.; Oltvai, Z. N.; Osterman, A. L. Experimental Determination and System Level Analysis of Essential Genes in Escherichia Coli MG1655. *J. Bacteriol.* **2003**, *185* (19), 5673–5684. https://doi.org/10.1128/JB.185.19.5673-5684.2003.

(93) Thanassi, J. A.; Hartman-Neumann, S. L.; Dougherty, T. J.; Dougherty, B. A.; Pucci, M. J. Identification of 113 Conserved Essential Genes Using a High-Throughput Gene Disruption System in Streptococcus Pneumoniae. *Nucleic Acids Res.* **2002**, *30* (14), 3152–3162. https://doi.org/10.1093/nar/gkf418.

(94) White, T. A.; Kell, D. B. Comparative Genomic Assessment of Novel Broad-Spectrum Targets for Antibacterial Drugs. *Comp. Funct. Genomics* **2004**, *5* (4), 304–327. https://doi.org/10.1002/cfg.411.

(95) Goto-Ito, S.; Ito, T.; Ishii, R.; Muto, Y.; Bessho, Y.; Yokoyama, S. Crystal Structure of Archaeal tRNA(m1G37)Methyltransferase aTrm5. *Proteins Struct. Funct. Bioinforma.* **2008**, *72* (4), 1274–1289. https://doi.org/10.1002/prot.22019.

(96) Klevens, R. M. Invasive Methicillin-Resistant Staphylococcus Aureus Infections in the United States. *JAMA* **2007**, *298* (15), 1763. https://doi.org/10.1001/jama.298.15.1763.

(97) Cheung, G. Y. C.; Bae, J. S.; Otto, M. Pathogenicity and Virulence of *Staphylococcus Aureus*. *Virulence* **2021**, *12* (1), 547–569. https://doi.org/10.1080/21505594.2021.1878688.

(98) Tong, S. Y. C.; Davis, J. S.; Eichenberger, E.; Holland, T. L.; Fowler, V. G. Staphylococcus Aureus Infections: Epidemiology, Pathophysiology, Clinical Manifestations, and Management. *Clin. Microbiol. Rev.* **2015**, *28* (3), 603–661. https://doi.org/10.1128/cmr.00134-14.

(99) Lowy, F. D. Antimicrobial Resistance: The Example of Staphylococcus Aureus. *J. Clin. Invest.* **2003**, *111* (9), 1265–1273. https://doi.org/10.1172/jci18535.

(100) Lowy, F. D. Staphylococcus Aureus Infections. *N. Engl. J. Med.* **1998**, *339* (8), 520–532. https://doi.org/10.1056/nejm199808203390806.

(101) Rasigade, J.-P.; Dumitrescu, O.; Lina, G. New Epidemiology of Staphylococcus Aureus Infections. *Clin. Microbiol. Infect.* **2014**, *20* (7), 587–588. https://doi.org/10.1111/1469-0691.12718.

(102) Kourtis, A. P.; Hatfield, K.; Baggs, J.; Mu, Y.; See, I.; Epson, E.; Nadle, J.; Kainer, M. A.; Dumyati, G.; Petit, S.; Ray, S. M.; Emerging Infections Program MRSA author group; Ham, D.; Capers, C.; Ewing, H.; Coffin, N.; McDonald, L. C.; Jernigan, J.; Cardo, D. Vital Signs: Epidemiology and Recent Trends in Methicillin-Resistant and in Methicillin-Susceptible Staphylococcus Aureus Bloodstream Infections — United States. *MMWR Morb. Mortal. Wkly. Rep.* **2019**, *68* (9), 214–219. https://doi.org/10.15585/mmwr.mm6809e1.

(103) Whitehouse, A. J.; Thomas, S. E.; Brown, K. P.; Fanourakis, A.; Chan, D. S.-H.; Libardo, M. D. J.; Mendes, V.; Boshoff, H. I. M.; Floto, R. A.; Abell, C.; Blundell, T. L.; Coyne, A. G. Development of Inhibitors against Mycobacterium Abscessus tRNA (m1G37) Methyltransferase (TrmD) Using Fragment-Based Approaches. *J. Med. Chem.* **2019**, *62* (15), 7210–7232. https://doi.org/10.1021/acs.jmedchem.9b00809.

(104) Wilkinson, A. J.; Ooi, N.; Finlayson, J.; Lee, V. E.; Lyth, D.; Maskew, K. S.; Newman, R.; Orr, D.; Ansell, K.; Birchall, K.; Canning, P.; Coombs, P.; Fusani, L.; McIver, E.; Pisco, J.; Ireland, P. M.; Jenkins, C.; Norville, I. H.; Southern, S. J.; Cowan, R.; Hall, G.; Kettleborough, C.; Savage, V. J.; Cooper, I. R. Evaluating the Druggability of TrmD, a Potential Antibacterial Target, through Design and Microbiological Profiling of a Series of Potent TrmD Inhibitors. *Bioorg. Med. Chem. Lett.* **2023**, *90*, 129331. https://doi.org/10.1016/j.bmcl.2023.129331.

(105) Thomas, S. E.; Whitehouse, A. J.; Brown, K.; Burbaud, S.; Belardinelli, J. M.; Sangen, J.; Lahiri, R.; Libardo, M. D. J.; Gupta, P.; Malhotra, S.; Boshoff, H. I. M.; Jackson, M.; Abell, C.; Coyne, A. G.; Blundell, T. L.; Floto, R. A.; Mendes, V. Fragment-Based Discovery of a New Class of Inhibitors Targeting Mycobacterial tRNA Modification. *Nucleic Acids Res.* **2020**, *48* (14), 8099–8112. https://doi.org/10.1093/nar/gkaa539.

(106) Hill, P. J.; Abibi, A.; Albert, R.; Andrews, B.; Gagnon, M. M.; Gao, N.; Grebe, T.; Hajec, L. I.; Huang, J.; Livchak, S.; Lahiri, S. D.; McKinney, D. C.; Thresher, J.; Wang, H.; Olivier, N.; Buurman, E. T. Selective Inhibitors of Bacterial T-RNA-(N1G37) Methyltransferase (TrmD) That Demonstrate Novel Ordering of the Lid Domain. *J. Med. Chem.* **2013**, *56* (18), 7278–7288. https://doi.org/10.1021/jm400718n.

(107) Qi, Y.-N.; Liu, Z.; Hong, L.-L.; Li, P.; Ling, Z.-Q. Methyltransferase-like Proteins in Cancer Biology and Potential Therapeutic Targeting. *J. Hematol. Oncol.J Hematol Oncol* **2023**, *16* (1). https://doi.org/10.1186/s13045-023-01477-7.

(108) Liu, J.; Yue, Y.; Han, D.; Wang, X.; Fu, Y.; Zhang, L.; Jia, G.; Yu, M.; Lu, Z.; Deng, X.; Dai, Q.; Chen, W.; He, C. A METTL3–METTL14 Complex Mediates Mammalian Nuclear RNA N6-Adenosine Methylation. *Nat. Chem. Biol.* **2014**, *10* (2), 93–95. https://doi.org/10.1038/nchembio.1432.

(109) Warda, A. S.; Kretschmer, J.; Hackert, P.; Lenz, C.; Urlaub, H.; Höbartner, C.; Sloan, K. E.; Bohnsack, M. T. Human METTL16 Is a 6-methyladenosine (m6A) Methyltransferase That Targets pre-mRNAs and Various Non-coding RNAs. *EMBO Rep.* **2017**, *18* (11), 2004–2014. https://doi.org/10.15252/embr.201744940.

(110) Chen, H.; Liu, Q.; Yu, D.; Natchiar, K.; Zhou, C.; Hsu, C.; Hsu, P.-H.; Zhang, X.; Klaholz, B.; Gregory, R. I.; Cheng, X.; Shi, Y. METTL5, an 18S rRNA-Specific m^6A Methyltransferase, Modulates Expression of Stress Response Genes. Cold Spring Harbor Laboratory April 28, 2020. https://doi.org/10.1101/2020.04.27.064162.

(111) Xu, L.; Liu, X.; Sheng, N.; Oo, K. S.; Liang, J.; Chionh, Y. H.; Xu, J.; Ye, F.; Gao, Y.-G.; Dedon, P. C.; Fu, X.-Y. Three Distinct 3-Methylcytidine (m3C) Methyltransferases Modify tRNA and mRNA in Mice and Humans. *J. Biol. Chem.* **2017**, *292* (35), 14695–14703. https://doi.org/10.1074/jbc.m117.798298.

(112) Mao, X.-L.; Li, Z.-H.; Huang, M.-H.; Wang, J.-T.; Zhou, J.-B.; Li, Q.-R.; Xu, H.; Wang, X.-J.; Zhou, X.-L. Mutually Exclusive Substrate Selection Strategy by Human m3C RNA Transferases METTL2A and METTL6. *Nucleic Acids Res.* **2021**, *49* (14), 8309–8323. https://doi.org/10.1093/nar/gkab603.

(113) Alexandrov, A.; Martzen, M. R.; Phizicky, E. M. Two Proteins That Form a Complex Are Required for 7-Methylguanosine Modification of Yeast tRNA. *RNA* **2002**, *8* (10), 1253–1266. https://doi.org/10.1017/s1355838202024019.

(114) Haute, L. V.; Hendrick, A. G.; D'Souza, A. R.; Powell, C. A.; Rebelo-Guiomar, P.; Harbour, M. E.; Ding, S.; Fearnley, I. M.; Andrews, B.; Minczuk, M. METTL15 Introduces N4-Methylcytidine into Human Mitochondrial 12S rRNA and Is Required for Mitoribosome Biogenesis. *Nucleic Acids Res.* **2019**, *47* (19), 10267–10281. https://doi.org/10.1093/nar/gkz735.

(115) He, J.; Hao, F.; Song, S.; Zhang, J.; Zhou, H.; Zhang, J.; Li, Y. METTL Family in Health and Disease. *Mol. Biomed.* **2024**, *5* (1). https://doi.org/10.1186/s43556-024-00194-y.

(116) Tomikawa, C. 7-Methylguanosine Modifications in Transfer RNA (tRNA). *Int. J. Mol. Sci.* **2018**, *19* (12), 4080. https://doi.org/10.3390/ijms19124080.

(117) Chen, J.; Zhou, Q.; Li, S.; Ling, R.; Zhao, Y.; Chen, D.; Wang, A.; Cao, Y. Metabolic Reprogramming Driven by METTL1-Mediated tRNA m7G Modification Promotes Acquired Anlotinib Resistance in Oral Squamous Cell Carcinoma. *Transl. Res.* **2024**, *268*, 28–39. https://doi.org/10.1016/j.trsl.2024.01.009.

(118) Alexandrov, A.; Grayhack, E. J.; Phizicky, E. M. tRNA m^7 G Methyltransferase Trm8p/Trm82p: Evidence Linking Activity to a Growth Phenotype and Implicating Trm82p in Maintaining Levels of Active Trm8p. *RNA* **2005**, *11* (5), 821–830. https://doi.org/10.1261/rna.2030705.

(119) Pandolfini, L.; Barbieri, I.; Bannister, A. J.; Hendrick, A.; Andrews, B.; Webster, N.; Murat, P.; Mach, P.; Brandi, R.; Robson, S. C.; Migliori, V.; Alendar, A.; d'Onofrio, M.; Balasubramanian, S.; Kouzarides, T. METTL1 Promotes Let-7 MicroRNA Processing via m7G Methylation. *Mol. Cell* **2019**, *74* (6), 1278-1290.e9. https://doi.org/10.1016/j.molcel.2019.03.040.

(120) Dong, R.; Wang, C.; Tang, B.; Cheng, Y.; Peng, X.; Yang, X.; Ni, B.; Li, J. WDR4 Promotes HCC Pathogenesis through N7-Methylguanosine by Regulating and Interacting with METTL1. *Cell. Signal.* **2024**, *118*, 111145. https://doi.org/10.1016/j.cellsig.2024.111145.

(121) Zhang, L.-S.; Liu, C.; Ma, H.; Dai, Q.; Sun, H.-L.; Luo, G.; Zhang, Z.; Zhang, L.; Hu, L.; Dong, X.; He, C. Transcriptome-Wide Mapping of Internal N7-Methylguanosine Methylome in Mammalian mRNA. *Mol. Cell* **2019**, *74* (6), 1304-1316.e8. https://doi.org/10.1016/j.molcel.2019.03.036.

(122) Ruiz-Arroyo, V. M.; Raj, R.; Babu, K.; Onolbaatar, O.; Roberts, P. H.; Nam, Y. Structures and Mechanisms of tRNA Methylation by METTL1–WDR4. *Nature* **2023**, *613* (7943), 383–390. https://doi.org/10.1038/s41586-022-05565-5.

(123) Cartlidge, R. A.; Knebel, A.; Peggie, M.; Alexandrov, A.; Phizicky, E. M.; Cohen, P. The tRNA Methylase METTL1 Is Phosphorylated and Inactivated by PKB and RSK in Vitro and in Cells. *EMBO J.* **2005**, *24* (9), 1696–1705. https://doi.org/10.1038/sj.emboj.7600648.

(124) Meyer, M. B.; Pike, J. W. Genomic Mechanisms Controlling Renal Vitamin D Metabolism. *J. Steroid Biochem. Mol. Biol.* **2023**, *228*, 106252. https://doi.org/10.1016/j.jsbmb.2023.106252.

(125) Pike, J. W.; Lee, S. M.; Benkusky, N. A.; Meyer, M. B. Genomic Mechanisms Governing Mineral Homeostasis and the Regulation and Maintenance of Vitamin D Metabolism. *JBMR Plus* **2021**, *5* (1). https://doi.org/10.1002/jbm4.10433.

(126) Deng, Y.; Zhou, Z.; Ji, W.; Lin, S.; Wang, M. METTL1-Mediated m7G Methylation Maintains Pluripotency in Human Stem Cells and Limits Mesoderm Differentiation and Vascular Development. *Stem Cell Res. Ther.* **2020**, *11* (1). https://doi.org/10.1186/s13287-020-01814-4.

(127) Chen, X.-Z.; Li, X.-M.; Xu, S.-J.; Hu, S.; Wang, T.; Li, R.-F.; Liu, C.-Y.; Xue, J.-Q.; Zhou, L.-Y.; Wang, Y.-H.; Li, P.-F.; Wang, K. TMEM11 Regulates Cardiomyocyte Proliferation and Cardiac Repair via METTL1-Mediated m7G Methylation of ATF5 mRNA. *Cell Death Differ.* **2023**, *30* (7), 1786–1798. https://doi.org/10.1038/s41418-023-01179-0.

(128) Chen, Z.; Zhu, W.; Zhu, S.; Sun, K.; Liao, J.; Liu, H.; Dai, Z.; Han, H.; Ren, X.; Yang, Q.; Zheng, S.; Peng, B.; Peng, S.; Kuang, M.; Lin, S. METTL1 Promotes Hepatocarcinogenesis via m^7G tRNA Modification-dependent Translation Control. *Clin. Transl. Med.* **2021**, *11* (12). https://doi.org/10.1002/ctm2.661.

(129) Zeng, X.; Liao, G.; Li, S.; Liu, H.; Zhao, X.; Li, S.; Lei, K.; Zhu, S.; Chen, Z.; Zhao, Y.; Ren, X.; Su, T.; Cheng, A. S.; Peng, S.; Lin, S.; Wang, J.; Chen, S.; Kuang, M. Eliminating METTL1-mediated Accumulation of PMN-MDSCs Prevents Hepatocellular Carcinoma Recurrence after Radiofrequency Ablation. *Hepatology* **2023**, *77* (4), 1122–1138. https://doi.org/10.1002/hep.32585.

(130) Ying, X.; Liu, B.; Yuan, Z.; Huang, Y.; Chen, C.; Jiang, X.; Zhang, H.; Qi, D.; Yang, S.; Lin, S.; Luo, J.; Ji, W. METTL1-m^{7}G-EGFR/EFEMP1 Axis Promotes the Bladder Cancer Development. *Clin. Transl. Med.* **2021**, *11* (12). https://doi.org/10.1002/ctm2.675.

(131) Chen, J.; Li, K.; Chen, J.; Wang, X.; Ling, R.; Cheng, M.; Chen, Z.; Chen, F.; He, Q.; Li, S.; Zhang, C.; Jiang, Y.; Chen, Q.; Wang, A.; Chen, D. Aberrant Translation Regulated by METTL1/WDR4-mediated tRNA N7-methylguanosine Modification Drives Head and Neck Squamous Cell Carcinoma Progression. *Cancer Commun.* **2022**, *42* (3), 223–244. https://doi.org/10.1002/cac2.12273.

(132) Zeng, Z.; Zhang, X.; Jiang, C.-Q.; Zhang, Y.-G.; Wu, X.; Li, J.; Tang, S.; Li, L.; Gu, L.-J.; Xie, X.-Y.; Jiang, Y.-A. Identifying Novel Therapeutic Targets in Gastric Cancer Using Genome-Wide CRISPR-Cas9 Screening. *Oncogene* **2022**, *41* (14), 2069–2078. https://doi.org/10.1038/s41388-022-02177-1.

(133) Orellana, E. A.; Liu, Q.; Yankova, E.; Pirouz, M.; De Braekeleer, E.; Zhang, W.; Lim, J.; Aspris, D.; Sendinc, E.; Garyfallos, D. A.; Gu, M.; Ali, R.; Gutierrez, A.; Mikutis, S.; Bernardes, G. J. L.; Fischer, E. S.; Bradley, A.; Vassiliou, G. S.; Slack, F. J.; Tzelepis, K.; Gregory, R. I. METTL1-Mediated m7G Modification of Arg-TCT tRNA Drives Oncogenic Transformation. *Mol. Cell* **2021**, *81* (16), 3323-3338.e14. https://doi.org/10.1016/j.molcel.2021.06.031.

(134) Dai, Z.; Liu, H.; Liao, J.; Huang, C.; Ren, X.; Zhu, W.; Zhu, S.; Peng, B.; Li, S.; Lai, J.; Liang, L.; Xu, L.; Peng, S.; Lin, S.; Kuang, M. N7-Methylguanosine tRNA Modification Enhances Oncogenic mRNA Translation and Promotes Intrahepatic Cholangiocarcinoma Progression. *Mol. Cell* **2021**, *81* (16), 3339-3355.e8. https://doi.org/10.1016/j.molcel.2021.07.003.

(135) Nai, F.; Flores Espinoza, M. P.; Invernizzi, A.; Vargas-Rosales, P. A.; Bobileva, O.; Herok, M.; Caflisch, A. Small-Molecule Inhibitors of the m7G-RNA Writer METTL1. *ACS Bio Med Chem Au* **2024**, *4* (2), 100–110. https://doi.org/10.1021/acsbiomedchemau.3c00030.

(136) Sarah Joanne Bucknell; Elizabeth Jane Thomas; Frederick Arthur Brookfield; Lisa Marie Frost; Lee james Bowles; Samuel Titus Mckee; James Patrick Martin; Angela Glen. Inhibitory Compounds. WO2025/104443 A1, May 22, 2025.

(137) Jiang, X.; Liu, B.; Nie, Z.; Duan, L.; Xiong, Q.; Jin, Z.; Yang, C.; Chen, Y. The Role of m6A Modification in the Biological Functions and Diseases. *Signal Transduct. Target. Ther.* **2021**, *6* (1), 74. https://doi.org/10.1038/s41392-020-00450-x.

(138) Zeng, C.; Huang, W.; Li, Y.; Weng, H. Roles of METTL3 in Cancer: Mechanisms and Therapeutic Targeting. *J. Hematol. Oncol.J Hematol Oncol* **2020**, *13* (1), 117. https://doi.org/10.1186/s13045-020-00951-w.

(139) Ping, X.-L.; Sun, B.-F.; Wang, L.; Xiao, W.; Yang, X.; Wang, W.-J.; Adhikari, S.; Shi, Y.; Lv, Y.; Chen, Y.-S.; Zhao, X.; Li, A.; Yang, Y.; Dahal, U.; Lou, X.-M.; Liu, X.; Huang, J.; Yuan, W.-P.; Zhu, X.-F.; Cheng, T.; Zhao, Y.-L.; Wang, X.; Danielsen, J. M. R.; Liu, F.; Yang, Y.-G. Mammalian WTAP Is a Regulatory Subunit of the RNA N6-Methyladenosine Methyltransferase. *Cell Res.* **2014**, *24* (2), 177–189. https://doi.org/10.1038/cr.2014.3.

(140) Wang, X.; Feng, J.; Xue, Y.; Guan, Z.; Zhang, D.; Liu, Z.; Gong, Z.; Wang, Q.; Huang, J.; Tang, C.; Zou, T.; Yin, P. Structural Basis of N6-Adenosine Methylation by the METTL3–METTL14 Complex. *Nature* **2016**, *534* (7608), 575–578. https://doi.org/10.1038/nature18298.

(141) Corbeski, I.; Vargas-Rosales, P. A.; Bedi, R. K.; Deng, J.; Coelho, D.; Braud, E.; Iannazzo, L.; Li, Y.; Huang, D.; Ethève-Quelquejeu, M.; Cui, Q.; Caflisch, A. The Catalytic Mechanism of the RNA Methyltransferase METTL3. *eLife* **2024**, *12*, RP92537. https://doi.org/10.7554/eLife.92537.3.

(142) Liu, S.; Zhuo, L.; Wang, J.; Zhang, Q.; Li, Q.; Li, G.; Yan, L.; Jin, T.; Pan, T.; Sui, X.; Lv, Q.; Xie, T. METTL3 Plays Multiple Functions in Biological Processes. *Am. J. Cancer Res.* **2020**, *10* (6), 1631–1646.

(143) Yao, Y.; Bi, Z.; Wu, R.; Zhao, Y.; Liu, Y.; Liu, Q.; Wang, Y.; Wang, X. METTL3 Inhibits BMSC Adipogenic Differentiation by Targeting the JAK1/STAT5/C/EBPβ Pathway *via* an m^6 A-

YTHDF2–Dependent Manner. *FASEB J.* **2019**, *33* (6), 7529–7544. https://doi.org/10.1096/fj.201802644R.

(144) Tian, C.; Huang, Y.; Li, Q.; Feng, Z.; Xu, Q. Mettl3 Regulates Osteogenic Differentiation and Alternative Splicing of Vegfa in Bone Marrow Mesenchymal Stem Cells. *Int. J. Mol. Sci.* **2019**, *20* (3), 551. https://doi.org/10.3390/ijms20030551.

(145) Miao, W.; Chen, J.; Jia, L.; Ma, J.; Song, D. The m6A Methyltransferase METTL3 Promotes Osteosarcoma Progression by Regulating the m6A Level of LEF1. *Biochem. Biophys. Res. Commun.* **2019**, *516* (3), 719–725. https://doi.org/10.1016/j.bbrc.2019.06.128.

(146) Feng, Z.; Li, Q.; Meng, R.; Yi, B.; Xu, Q. METTL 3 Regulates Alternative Splicing of MyD88 upon the Lipopolysaccharide-induced Inflammatory Response in Human Dental Pulp Cells. *J. Cell. Mol. Med.* **2018**, *22* (5), 2558–2568. https://doi.org/10.1111/jcmm.13491.

(147) Kobayashi, M.; Ohsugi, M.; Sasako, T.; Awazawa, M.; Umehara, T.; Iwane, A.; Kobayashi, N.; Okazaki, Y.; Kubota, N.; Suzuki, R.; Waki, H.; Horiuchi, K.; Hamakubo, T.; Kodama, T.; Aoe, S.; Tobe, K.; Kadowaki, T.; Ueki, K. The RNA Methyltransferase Complex of WTAP, METTL3, and METTL14 Regulates Mitotic Clonal Expansion in Adipogenesis. *Mol. Cell. Biol.* **2018**, *38* (16), e00116-18. https://doi.org/10.1128/MCB.00116-18.

(148) Liu, Q.; Zhao, Y.; Wu, R.; Jiang, Q.; Cai, M.; Bi, Z.; Liu, Y.; Yao, Y.; Feng, J.; Wang, Y.; Wang, X. ZFP217 Regulates Adipogenesis by Controlling Mitotic Clonal Expansion in a METTL3-m^6A Dependent Manner. *RNA Biol.* **2019**, *16* (12), 1785–1793. https://doi.org/10.1080/15476286.2019.1658508.

(149) Aguilo, F.; Zhang, F.; Sancho, A.; Fidalgo, M.; Di Cecilia, S.; Vashisht, A.; Lee, D.-F.; Chen, C.-H.; Rengasamy, M.; Andino, B.; Jahouh, F.; Roman, A.; Krig, S. R.; Wang, R.; Zhang, W.; Wohlschlegel, J. A.; Wang, J.; Walsh, M. J. Coordination of m 6 A mRNA Methylation and Gene Transcription by ZFP217 Regulates Pluripotency and Reprogramming. *Cell Stem Cell* **2015**, *17* (6), 689–704. https://doi.org/10.1016/j.stem.2015.09.005.

(150) Hess, M. E.; Hess, S.; Meyer, K. D.; Verhagen, L. A. W.; Koch, L.; Brönneke, H. S.; Dietrich, M. O.; Jordan, S. D.; Saletore, Y.; Elemento, O.; Belgardt, B. F.; Franz, T.; Horvath, T. L.; Rüther, U.; Jaffrey, S. R.; Kloppenburg, P.; Brüning, J. C. The Fat Mass and Obesity Associated Gene (Fto) Regulates Activity of the Dopaminergic Midbrain Circuitry. *Nat. Neurosci.* **2013**, *16* (8), 1042–1048. https://doi.org/10.1038/nn.3449.

(151) Xu, K.; Yang, Y.; Feng, G.-H.; Sun, B.-F.; Chen, J.-Q.; Li, Y.-F.; Chen, Y.-S.; Zhang, X.-X.; Wang, C.-X.; Jiang, L.-Y.; Liu, C.; Zhang, Z.-Y.; Wang, X.-J.; Zhou, Q.; Yang, Y.-G.; Li, W. Mettl3-Mediated m6A Regulates Spermatogonial Differentiation and Meiosis Initiation. *Cell Res.* **2017**, *27* (9), 1100–1114. https://doi.org/10.1038/cr.2017.100.

(152) Zhang, J.; Bai, R.; Li, M.; Ye, H.; Wu, C.; Wang, C.; Li, S.; Tan, L.; Mai, D.; Li, G.; Pan, L.; Zheng, Y.; Su, J.; Ye, Y.; Fu, Z.; Zheng, S.; Zuo, Z.; Liu, Z.; Zhao, Q.; Che, X.; Xie, D.; Jia, W.; Zeng, M.-S.; Tan, W.; Chen, R.; Xu, R.-H.; Zheng, J.; Lin, D. Excessive miR-25-3p Maturation via N6-Methyladenosine Stimulated by Cigarette Smoke Promotes Pancreatic Cancer Progression. *Nat. Commun.* **2019**, *10* (1), 1858. https://doi.org/10.1038/s41467-019-09712-x.

(153) Li, T.; Hu, P.-S.; Zuo, Z.; Lin, J.-F.; Li, X.; Wu, Q.-N.; Chen, Z.-H.; Zeng, Z.-L.; Wang, F.; Zheng, J.; Chen, D.; Li, B.; Kang, T.-B.; Xie, D.; Lin, D.; Ju, H.-Q.; Xu, R.-H. METTL3 Facilitates Tumor Progression via an m6A-IGF2BP2-Dependent Mechanism in Colorectal Carcinoma. *Mol. Cancer* **2019**, *18* (1), 112. https://doi.org/10.1186/s12943-019-1038-7.

(154) Wei, W.; Huo, B.; Shi, X. miR-600 Inhibits Lung Cancer via Downregulating the Expression of METTL3. *Cancer Manag. Res.* **2019**, *Volume 11*, 1177–1187. https://doi.org/10.2147/CMAR.S181058.

(155) Barbieri, I.; Tzelepis, K.; Pandolfini, L.; Shi, J.; Millán-Zambrano, G.; Robson, S. C.; Aspris, D.; Migliori, V.; Bannister, A. J.; Han, N.; De Braekeleer, E.; Ponstingl, H.; Hendrick, A.; Vakoc, C. R.; Vassiliou, G. S.; Kouzarides, T. Promoter-Bound METTL3 Maintains Myeloid Leukaemia by m6A-Dependent Translation Control. *Nature* **2017**, *552* (7683), 126–131. https://doi.org/10.1038/nature24678.

(156) Chen, M.; Wei, L.; Law, C.; Tsang, F. H.; Shen, J.; Cheng, C. L.; Tsang, L.; Ho, D. W.; Chiu, D. K.; Lee, J. M.; Wong, C. C.; Ng, I. O.; Wong, C. RNA N6-methyladenosine Methyltransferase-like 3 Promotes Liver Cancer Progression through YTHDF2-dependent Posttranscriptional Silencing of SOCS2. *Hepatology* **2018**, *67* (6), 2254–2270. https://doi.org/10.1002/hep.29683.

(157) Taketo, K.; Konno, M.; Asai, A.; Koseki, J.; Toratani, M.; Satoh, T.; Doki, Y.; Mori, M.; Ishii, H.; Ogawa, K. The Epitranscriptome m6A Writer METTL3 Promotes Chemo- and Radioresistance in Pancreatic Cancer Cells. *Int. J. Oncol.* **2017**. https://doi.org/10.3892/ijo.2017.4219.

(158) Xia, T.; Wu, X.; Cao, M.; Zhang, P.; Shi, G.; Zhang, J.; Lu, Z.; Wu, P.; Cai, B.; Miao, Y.; Jiang, K. The RNA m6A Methyltransferase METTL3 Promotes Pancreatic Cancer Cell Proliferation and Invasion. *Pathol. - Res. Pract.* **2019**, *215* (11), 152666. https://doi.org/10.1016/j.prp.2019.152666.

(159) Lin, S.; Liu, J.; Jiang, W.; Wang, P.; Sun, C.; Wang, X.; Chen, Y.; Wang, H. METTL3 Promotes the Proliferation and Mobility of Gastric Cancer Cells. *Open Med.* **2019**, *14* (1), 25–31. https://doi.org/10.1515/med-2019-0005.

(160) Li, X.; Tang, J.; Huang, W.; Wang, F.; Li, P.; Qin, C.; Qin, Z.; Zou, Q.; Wei, J.; Hua, L.; Yang, H.; Wang, Z. The M6A Methyltransferase METTL3: Acting as a Tumor Suppressor in Renal Cell Carcinoma. *Oncotarget* **2017**, *8* (56), 96103–96116. https://doi.org/10.18632/oncotarget.21726.

(161) Vu, L. P.; Pickering, B. F.; Cheng, Y.; Zaccara, S.; Nguyen, D.; Minuesa, G.; Chou, T.; Chow, A.; Saletore, Y.; MacKay, M.; Schulman, J.; Famulare, C.; Patel, M.; Klimek, V. M.; Garrett-Bakelman, F. E.; Melnick, A.; Carroll, M.; Mason, C. E.; Jaffrey, S. R.; Kharas, M. G. The N6-Methyladenosine (m6A)-Forming Enzyme METTL3 Controls Myeloid Differentiation of Normal Hematopoietic and Leukemia Cells. *Nat. Med.* **2017**, *23* (11), 1369–1376. https://doi.org/10.1038/nm.4416.

(162) Haan, S. SOCS2 Physiological and Pathological Functions. *Front. Biosci.* **2016**, *8* (1), 189–204. https://doi.org/10.2741/e760.

(163) Franke, T. F.; Yang, S.-I.; Chan, T. O.; Datta, K.; Kazlauskas, A.; Morrison, D. K.; Kaplan, D. R.; Tsichlis, P. N. The Protein Kinase Encoded by the Akt Proto-Oncogene Is a Target of the PDGF-Activated Phosphatidylinositol 3-Kinase. *Cell* **1995**, *81* (5), 727–736. https://doi.org/10.1016/0092-8674(95)90534-0.

(164) Lee, J.; Kim, S.; Jin, M. S.; Kim, Y. Discovery of Substituted Indole Derivatives as Allosteric Inhibitors of M^6 A-RNA Methyltransferase, METTL3 -14 Complex. *Drug Dev. Res.* **2022**, ddr.21910. https://doi.org/10.1002/ddr.21910.

(165) Bedi, R. K.; Huang, D.; Eberle, S. A.; Wiedmer, L.; Śledź, P.; Caflisch, A. Small-Molecule Inhibitors of METTL3, the Major Human Epitranscriptomic Writer. *ChemMedChem* **2020**, *15* (9), 744–748. https://doi.org/10.1002/cmdc.202000011.

(166) Yankova, E.; Blackaby, W.; Albertella, M.; Rak, J.; De Braekeleer, E.; Tsagkogeorga, G.; Pilka, E. S.; Aspris, D.; Leggate, D.; Hendrick, A. G.; Webster, N. A.; Andrews, B.; Fosbeary, R.; Guest, P.; Irigoyen, N.; Eleftheriou, M.; Gozdecka, M.; Dias, J. M. L.; Bannister, A. J.; Vick, B.; Jeremias, I.; Vassiliou, G. S.; Rausch, O.; Tzelepis, K.; Kouzarides, T. Small-Molecule Inhibition of METTL3 as a Strategy against Myeloid Leukaemia. *Nature* **2021**, *593* (7860), 597–601. https://doi.org/10.1038/s41586-021-03536-w.

(167) Du, Y.; Yuan, Y.; Xu, L.; Zhao, F.; Wang, W.; Xu, Y.; Tian, X. Discovery of METTL3 Small Molecule Inhibitors by Virtual Screening of Natural Products. *Front. Pharmacol.* **2022**, *13*, 878135. https://doi.org/10.3389/fphar.2022.878135.

(168) Guirguis, A. A.; Ofir-Rosenfeld, Y.; Knezevic, K.; Blackaby, W.; Hardick, D.; Chan, Y.-C.; Motazedian, A.; Gillespie, A.; Vassiliadis, D.; Lam, E. Y. N.; Tran, K.; Andrews, B.; Harbour, M. E.; Vasiliauskaite, L.; Saunders, C. J.; Tsagkogeorga, G.; Azevedo, A.; Obacz, J.; Pilka, E. S.; Carkill, M.; MacPherson, L.; Wainwright, E. N.; Liddicoat, B.; Blyth, B. J.; Albertella, M. R.; Rausch, O.; Dawson, M. A. Inhibition of METTL3 Results in a Cell-Intrinsic Interferon Response That Enhances Antitumor Immunity. *Cancer Discov.* **2023**, *13* (10), 2228–2247. https://doi.org/10.1158/2159-8290.CD-23-0007.

(169) Dolbois, A.; Bedi, R. K.; Bochenkova, E.; Müller, A.; Moroz-Omori, E. V.; Huang, D.; Caflisch, A. 1,4,9-Triazaspiro[5.5]Undecan-2-One Derivatives as Potent and Selective METTL3 Inhibitors. *J. Med. Chem.* **2021**, *64* (17), 12738–12760. https://doi.org/10.1021/acs.jmedchem.1c00773.

(170) Leung, D.; Abbenante, G.; Fairlie, D. P. Protease Inhibitors: Current Status and Future Prospects. *J. Med. Chem.* **2000**, *43* (3), 305–341. https://doi.org/10.1021/jm990412m.

(171) Smyth, T. P. Substrate Variants versus Transition State Analogues as Noncovalent Reversible Enzyme Inhibitors. *Bioorg. Med. Chem.* **2004**, *12* (15), 4081–4088. https://doi.org/10.1016/j.bmc.2004.05.041.
(172) Schramm, V. L. Transition States, Analogues, and Drug Development. *ACS Chem. Biol.* **2013**, *8* (1), 71–81. https://doi.org/10.1021/cb300631k.
(173) West, M. L.; Fairlie, D. P. Targeting HIV-1 Protease: A Test of Drug-Design Methodologies. *Trends Pharmacol. Sci.* **1995**, *16* (2), 67–75. https://doi.org/10.1016/S0165-6147(00)88980-4.
(174) Ealick, S. E.; Babu, Y. S.; Bugg, C. E.; Erion, M. D.; Guida, W. C.; Montgomery, J. A.; Secrist, J. A. Application of Crystallographic and Modeling Methods in the Design of Purine Nucleoside Phosphorylase Inhibitors. *Proc. Natl. Acad. Sci.* **1991**, *88* (24), 11540–11544. https://doi.org/10.1073/pnas.88.24.11540.
(175) Kicska, G. A.; Long, L.; Hörig, H.; Fairchild, C.; Tyler, P. C.; Furneaux, R. H.; Schramm, V. L.; Kaufman, H. L. Immucillin H, a Powerful Transition-State Analog Inhibitor of Purine Nucleoside Phosphorylase, Selectively Inhibits Human T Lymphocytes. *Proc. Natl. Acad. Sci.* **2001**, *98* (8), 4593–4598. https://doi.org/10.1073/pnas.071050798.
(176) Miles, R. W.; Tyler, P. C.; Furneaux, R. H.; Bagdassarian, C. K.; Schramm, V. L. One-Third-the-Sites Transition-State Inhibitors for Purine Nucleoside Phosphorylase. *Biochemistry* **1998**, *37* (24), 8615–8621. https://doi.org/10.1021/bi980658d.
(177) Grillo, M. A.; Colombatto, S. S-Adenosylmethionine and Its Products. *Amino Acids* **2008**, *34* (2), 187–193. https://doi.org/10.1007/s00726-007-0500-9.
(178) Loenen, W. A. M. S-Adenosylmethionine: Jack of All Trades and Master of Everything? *Biochem. Soc. Trans.* **2006**, *34* (2), 330. https://doi.org/10.1042/BST20060330.
(179) Fontecave, M.; Atta, M.; Mulliez, E. S-Adenosylmethionine: Nothing Goes to Waste. *Trends Biochem. Sci.* **2004**, *29* (5), 243–249. https://doi.org/10.1016/j.tibs.2004.03.007.
(180) Petrossian, T. C.; Clarke, S. G. Uncovering the Human Methyltransferasome. *Mol. Cell. Proteomics* **2011**, *10* (1), M110.000976. https://doi.org/10.1074/mcp.M110.000976.
(181) Rudenko, A. Yu.; Mariasina, S. S.; Sergiev, P. V.; Polshakov, V. I. Analogs of S-Adenosyl-L-Methionine in Studies of Methyltransferases. *Mol. Biol.* **2022**, *56* (2), 229–250. https://doi.org/10.1134/S002689332202011X.
(182) Pugh, C. S.; Borchardt, R. T.; Stone, H. O. Sinefungin, a Potent Inhibitor of Virion mRNA(Guanine-7-)-Methyltransferase, mRNA(Nucleoside-2'-)-Methyltransferase, and Viral Multiplication. *J. Biol. Chem.* **1978**, *253* (12), 4075–4077. https://doi.org/10.1016/S0021-9258(17)34682-3.
(183) Cornelissen, N. V.; Michailidou, F.; Muttach, F.; Rau, K.; Rentmeister, A. Nucleoside-Modified AdoMet Analogues for Differential Methyltransferase Targeting. *Chem. Commun.* **2020**, *56* (14), 2115–2118. https://doi.org/10.1039/C9CC07807J.
(184) Daigle, S. R.; Olhava, E. J.; Therkelsen, C. A.; Majer, C. R.; Sneeringer, C. J.; Song, J.; Johnston, L. D.; Scott, M. P.; Smith, J. J.; Xiao, Y.; Jin, L.; Kuntz, K. W.; Chesworth, R.; Moyer, M. P.; Bernt, K. M.; Tseng, J.-C.; Kung, A. L.; Armstrong, S. A.; Copeland, R. A.; Richon, V. M.; Pollock, R. M. Selective Killing of Mixed Lineage Leukemia Cells by a Potent Small-Molecule DOT1L Inhibitor. *Cancer Cell* **2011**, *20* (1), 53–65. https://doi.org/10.1016/j.ccr.2011.06.009.
(185) Feng, Q.; Wang, H.; Ng, H. H.; Erdjument-Bromage, H.; Tempst, P.; Struhl, K.; Zhang, Y. Methylation of H3-Lysine 79 Is Mediated by a New Family of HMTases without a SET Domain. *Curr. Biol.* **2002**, *12* (12), 1052–1058. https://doi.org/10.1016/S0960-9822(02)00901-6.
(186) Bouvet, M.; Debarnot, C.; Imbert, I.; Selisko, B.; Snijder, E. J.; Canard, B.; Decroly, E. In Vitro Reconstitution of SARS-Coronavirus mRNA Cap Methylation. *PLoS Pathog.* **2010**, *6* (4), e1000863. https://doi.org/10.1371/journal.ppat.1000863.
(187) Decroly, E.; Ferron, F.; Lescar, J.; Canard, B. Conventional and Unconventional Mechanisms for Capping Viral mRNA. *Nat. Rev. Microbiol.* **2012**, *10* (1), 51–65. https://doi.org/10.1038/nrmicro2675.
(188) Bobiļeva, O.; Bobrovs, R.; Kaņepe, I.; Patetko, L.; Kalniņš, G.; Šišovs, M.; Bula, A. L.; Grīnberga, S.; Borodušķis, M.; Ramata-Stunda, A.; Rostoks, N.; Jirgensons, A.; Tārs, K.; Jaudzems, K. Potent SARS-CoV-2 mRNA Cap Methyltransferase Inhibitors by Bioisosteric Replacement of Methionine in SAM Cosubstrate. *ACS Med. Chem. Lett.* **2021**, *12* (7), 1102–1107. https://doi.org/10.1021/acsmedchemlett.1c00140.

(189) Jung, J.; Kim, L. J. Y.; Wang, X.; Wu, Q.; Sanvoranart, T.; Hubert, C. G.; Prager, B. C.; Wallace, L. C.; Jin, X.; Mack, S. C.; Rich, J. N. Nicotinamide Metabolism Regulates Glioblastoma Stem Cell Maintenance. *JCI Insight* **2017**, *2* (10), e90019. https://doi.org/10.1172/jci.insight.90019.

(190) Fedorowicz, A.; Mateuszuk, Ł.; Kopec, G.; Skórka, T.; Kutryb-Zając, B.; Zakrzewska, A.; Walczak, M.; Jakubowski, A.; Łomnicka, M.; Słomińska, E.; Chlopicki, S. Activation of the Nicotinamide N-Methyltransferase (NNMT)-1-Methylnicotinamide (MNA) Pathway in Pulmonary Hypertension. *Respir. Res.* **2016**, *17* (1), 108. https://doi.org/10.1186/s12931-016-0423-7.

(191) Palanichamy, K.; Kanji, S.; Gordon, N.; Thirumoorthy, K.; Jacob, J. R.; Litzenberg, K. T.; Patel, D.; Chakravarti, A. NNMT Silencing Activates Tumor Suppressor PP2A, Inactivates Oncogenic STKs, and Inhibits Tumor Forming Ability. *Clin. Cancer Res.* **2017**, *23* (9), 2325–2334. https://doi.org/10.1158/1078-0432.CCR-16-1323.

(192) Gao, Y.; Van Haren, M. J.; Moret, E. E.; Rood, J. J. M.; Sartini, D.; Salvucci, A.; Emanuelli, M.; Craveur, P.; Babault, N.; Jin, J.; Martin, N. I. Bisubstrate Inhibitors of Nicotinamide *N* -Methyltransferase (NNMT) with Enhanced Activity. *J. Med. Chem.* **2019**, *62* (14), 6597–6614. https://doi.org/10.1021/acs.jmedchem.9b00413.

(193) Mahmoodi, N.; Harijan, R. K.; Schramm, V. L. Transition-State Analogues of Phenylethanolamine *N* -Methyltransferase. *J. Am. Chem. Soc.* **2020**, *142* (33), 14222–14233. https://doi.org/10.1021/jacs.0c05446.

(194) Kirshner, N.; Goodall, McC. The Formation of Adrenaline from Noradrenaline. *Biochim. Biophys. Acta* **1957**, *24*, 658–659. https://doi.org/10.1016/0006-3002(57)90271-8.

(195) Ghai, R.; Falconer, R. J.; Collins, B. M. Applications of Isothermal Titration Calorimetry in Pure and Applied Research—Survey of the Literature from 2010. *J. Mol. Recognit.* **2012**, *25* (1), 32–52. https://doi.org/10.1002/jmr.1167.

(196) Vuignier, K.; Schappler, J.; Veuthey, J.-L.; Carrupt, P.-A.; Martel, S. Drug–Protein Binding: A Critical Review of Analytical Tools. *Anal. Bioanal. Chem.* **2010**, *398* (1), 53–66. https://doi.org/10.1007/s00216-010-3737-1.

(197) Ladbury, J. E. Calorimetry as a Tool for Understanding Biomolecular Interactions and an Aid to Drug Design. *Biochem. Soc. Trans.* **2010**, *38* (4), 888–893. https://doi.org/10.1042/BST0380888.

(198) Roselin, L. S.; Lin, M.; Lin, P.; Chang, Y.; Chen, W. Recent Trends and Some Applications of Isothermal Titration Calorimetry in Biotechnology. *Biotechnol. J.* **2010**, *5* (1), 85–98. https://doi.org/10.1002/biot.200900092.

(199) Kellner, S.; Burhenne, J.; Helm, M. Detection of RNA Modifications. *RNA Biol.* **2010**, *7* (2), 237–247. https://doi.org/10.4161/rna.7.2.11468.

(200) Pomerantz, S. C.; McCloskey, J. A. [44] Analysis of RNA Hydrolyzates by Liquid Chromatography-Mass Spectrometry. In *Methods in Enzymology*; Elsevier, 1990; Vol. 193, pp 796–824. https://doi.org/10.1016/0076-6879(90)93452-Q.

(201) Haag, S.; Sloan, K. E.; Höbartner, C.; Bohnsack, M. T. In Vitro Assays for RNA Methyltransferase Activity. In *RNA Methylation*; Lusser, A., Ed.; Methods in Molecular Biology; Springer New York: New York, NY, 2017; Vol. 1562, pp 259–268. https://doi.org/10.1007/978-1-4939-6807-7_17.

(202) Salyan, M. E. K.; Pedicord, D. L.; Bergeron, L.; Mintier, G. A.; Hunihan, L.; Kuit, K.; Balanda, L. A.; Robertson, B. J.; Feder, J. N.; Westphal, R.; Shipkova, P. A.; Blat, Y. A General Liquid Chromatography/Mass Spectroscopy-Based Assay for Detection and Quantitation of Methyltransferase Activity. *Anal. Biochem.* **2006**, *349* (1), 112–117. https://doi.org/10.1016/j.ab.2005.10.040.

(203) Li, S.; Gu, X. J.; Hao, Q.; Fan, H.; Li, L.; Zhou, S.; Zhao, K.; Chan, H. M.; Wang, Y. K. A Liquid Chromatography/Mass Spectrometry-Based Generic Detection Method for Biochemical Assay and Hit Discovery of Histone Methyltransferases. *Anal. Biochem.* **2013**, *443* (2), 214–221. https://doi.org/10.1016/j.ab.2013.08.029.

(204) Melnyk, S.; Pogribna, M.; Pogribny, I. P.; Yi, P.; James, S. J. Measurement of Plasma and Intracellular S-Adenosylmethionine and S-Adenosylhomocysteine Utilizing Coulometric Electrochemical Detection: Alterations with Plasma Homocysteine and Pyridoxal 5'-Phosphate Concentrations. *Clin. Chem.* **2000**, *46* (2), 265–272.

(205) Inniss, N. L.; Kozic, J.; Li, F.; Rosas-Lemus, M.; Minasov, G.; Rybáček, J.; Zhu, Y.; Pohl, R.; Shuvalova, L.; Rulíšek, L.; Brunzelle, J. S.; Bednárová, L.; Štefek, M.; Kormaník, J. M.; Andris,

E.; Šebestík, J.; Li, A. S. M.; Brown, P. J.; Schmitz, U.; Saikatendu, K.; Chang, E.; Nencka, R.; Vedadi, M.; Satchell, K. J. F. Discovery of a Druggable, Cryptic Pocket in SARS-CoV-2 Nsp16 Using Allosteric Inhibitors. *ACS Infect. Dis.* **2023**, *9* (10), 1918–1931. https://doi.org/10.1021/acsinfecdis.3c00203.

(206) Hayrapetyan, A.; Grosjean, H.; Helm, M. Effect of a Quaternary Pentamine on RNA Stabilization and Enzymatic Methylation. *bchm* **2009**, *390* (9), 851–861. https://doi.org/10.1515/BC.2009.096.

(207) Motorin, Y.; Burhenne, J.; Teimer, R.; Koynov, K.; Willnow, S.; Weinhold, E.; Helm, M. Expanding the Chemical Scope of RNA:Methyltransferases to Site-Specific Alkynylation of RNA for Click Labeling. *Nucleic Acids Res.* **2011**, *39* (5), 1943–1952. https://doi.org/10.1093/nar/gkq825.

(208) Brulé, H.; Elliott, M.; Redlak, M.; Zehner, Z. E.; Holmes, W. M. Isolation and Characterization of the Human tRNA-(N^1 G37) Methyltransferase (TRM5) and Comparison to the *Escherichia Coli* TrmD Protein. *Biochemistry* **2004**, *43* (28), 9243–9255. https://doi.org/10.1021/bi049671q.

(209) Tovy, A.; Hofmann, B.; Helm, M.; Ankri, S. In Vitro tRNA Methylation Assay with the Entamoeba Histolytica DNA and tRNA Methyltransferase Dnmt2 (Ehmeth) Enzyme. *J. Vis. Exp.* **2010**, No. 44, 2390. https://doi.org/10.3791/2390.

(210) Nidoieva, Z.; Sabin, M. O.; Dewald, T.; Weldert, A. C.; Hoba, S. N.; Helm, M.; Barthels, F. A Microscale Thermophoresis-Based Enzymatic RNA Methyltransferase Assay Enables the Discovery of DNMT2 Inhibitors. *Commun. Chem.* **2025**, *8* (1), 32. https://doi.org/10.1038/s42004-025-01439-9.

(211) Zimmermann, R. A.; Schwickert, M.; Meidner, J. L.; Nidoieva, Z.; Helm, M.; Schirmeister, T. An Optimized Microscale Thermophoresis Method for High-Throughput Screening of DNA Methyltransferase 2 Ligands. *ACS Pharmacol. Transl. Sci.* **2022**, *5* (11), 1079–1085. https://doi.org/10.1021/acsptsci.2c00175.

(212) Sakamoto, K. M.; Kim, K. B.; Kumagai, A.; Mercurio, F.; Crews, C. M.; Deshaies, R. J. Protacs: Chimeric Molecules That Target Proteins to the Skp1–Cullin–F Box Complex for Ubiquitination and Degradation. *Proc. Natl. Acad. Sci.* **2001**, *98* (15), 8554–8559. https://doi.org/10.1073/pnas.141230798.

(213) Pettersson, M.; Crews, C. M. PROteolysis TArgeting Chimeras (PROTACs) — Past, Present and Future. *Drug Discov. Today Technol.* **2019**, *31*, 15–27. https://doi.org/10.1016/j.ddtec.2019.01.002.

(214) Toure, M.; Crews, C. M. Small-Molecule PROTACS: New Approaches to Protein Degradation. *Angew. Chem. Int. Ed.* **2016**, *55* (6), 1966–1973. https://doi.org/10.1002/anie.201507978.

(215) An, S.; Fu, L. Small-Molecule PROTACs: An Emerging and Promising Approach for the Development of Targeted Therapy Drugs. *EBioMedicine* **2018**, *36*, 553–562. https://doi.org/10.1016/j.ebiom.2018.09.005.

(216) Adjei, A. A. What Is the Right Dose? The Elusive Optimal Biologic Dose in Phase I Clinical Trials. *J. Clin. Oncol.* **2006**, *24* (25), 4054–4055. https://doi.org/10.1200/JCO.2006.07.4658.

(217) Cao, C.; He, M.; Wang, L.; He, Y.; Rao, Y. Chemistries of Bifunctional PROTAC Degraders. *Chem. Soc. Rev.* **2022**, *51* (16), 7066–7114. https://doi.org/10.1039/D2CS00220E.

(218) Bondeson, D. P.; Mares, A.; Smith, I. E. D.; Ko, E.; Campos, S.; Miah, A. H.; Mulholland, K. E.; Routly, N.; Buckley, D. L.; Gustafson, J. L.; Zinn, N.; Grandi, P.; Shimamura, S.; Bergamini, G.; Faelth-Savitski, M.; Bantscheff, M.; Cox, C.; Gordon, D. A.; Willard, R. R.; Flanagan, J. J.; Casillas, L. N.; Votta, B. J.; Den Besten, W.; Famm, K.; Kruidenier, L.; Carter, P. S.; Harling, J. D.; Churcher, I.; Crews, C. M. Catalytic in Vivo Protein Knockdown by Small-Molecule PROTACs. *Nat. Chem. Biol.* **2015**, *11* (8), 611–617. https://doi.org/10.1038/nchembio.1858.

(219) Lu, J.; Qian, Y.; Altieri, M.; Dong, H.; Wang, J.; Raina, K.; Hines, J.; Winkler, J. D.; Crew, A. P.; Coleman, K.; Crews, C. M. Hijacking the E3 Ubiquitin Ligase Cereblon to Efficiently Target BRD4. *Chem. Biol.* **2015**, *22* (6), 755–763. https://doi.org/10.1016/j.chembiol.2015.05.009.

(220) Itoh, Y.; Ishikawa, M.; Naito, M.; Hashimoto, Y. Protein Knockdown Using Methyl Bestatin−Ligand Hybrid Molecules: Design and Synthesis of Inducers of Ubiquitination-Mediated Degradation of Cellular Retinoic Acid-Binding Proteins. *J. Am. Chem. Soc.* **2010**, *132* (16), 5820–5826. https://doi.org/10.1021/ja100691p.

(221) Schneekloth, A. R.; Pucheault, M.; Tae, H. S.; Crews, C. M. Targeted Intracellular Protein Degradation Induced by a Small Molecule: En Route to Chemical Proteomics. *Bioorg. Med. Chem. Lett.* **2008**, *18* (22), 5904–5908. https://doi.org/10.1016/j.bmcl.2008.07.114.

(222) Roy, R. D.; Rosenmund, C.; Stefan, M. I. Cooperative Binding Mitigates the High-Dose Hook Effect. *BMC Syst. Biol.* **2017**, *11* (1), 74. https://doi.org/10.1186/s12918-017-0447-8.

(223) Zorba, A.; Nguyen, C.; Xu, Y.; Starr, J.; Borzilleri, K.; Smith, J.; Zhu, H.; Farley, K. A.; Ding, W.; Schiemer, J.; Feng, X.; Chang, J. S.; Uccello, D. P.; Young, J. A.; Garcia-Irrizary, C. N.; Czabaniuk, L.; Schuff, B.; Oliver, R.; Montgomery, J.; Hayward, M. M.; Coe, J.; Chen, J.; Niosi, M.; Luthra, S.; Shah, J. C.; El-Kattan, A.; Qiu, X.; West, G. M.; Noe, M. C.; Shanmugasundaram, V.; Gilbert, A. M.; Brown, M. F.; Calabrese, M. F. Delineating the Role of Cooperativity in the Design of Potent PROTACs for BTK. *Proc. Natl. Acad. Sci.* **2018**, *115* (31). https://doi.org/10.1073/pnas.1803662115.

(224) Vetma, V.; O'Connor, S.; Ciulli, A. Development of PROTAC Degrader Drugs for Cancer. *Annu. Rev. Cancer Biol.* **2025**, *9* (1), 119–140. https://doi.org/10.1146/annurev-cancerbio-061824-105806.

(225) Gough, S. M.; Flanagan, J. J.; Teh, J.; Andreoli, M.; Rousseau, E.; Pannone, M.; Bookbinder, M.; Willard, R.; Davenport, K.; Bortolon, E.; Cadelina, G.; Gordon, D.; Pizzano, J.; Macaluso, J.; Soto, L.; Corradi, J.; Digianantonio, K.; Drulyte, I.; Morgan, A.; Quinn, C.; Békés, M.; Ferraro, C.; Chen, X.; Wang, G.; Dong, H.; Wang, J.; Langley, D. R.; Houston, J.; Gedrich, R.; Taylor, I. C. Oral Estrogen Receptor PROTAC Vepdegestrant (ARV-471) Is Highly Efficacious as Monotherapy and in Combination with CDK4/6 or PI3K/mTOR Pathway Inhibitors in Preclinical ER+ Breast Cancer Models. *Clin. Cancer Res.* **2024**, *30* (16), 3549–3563. https://doi.org/10.1158/1078-0432.CCR-23-3465.

(226) Hamilton, E. P.; Ma, C.; De Laurentiis, M.; Iwata, H.; Hurvitz, S. A.; Wander, S. A.; Danso, M.; Lu, D. R.; Perkins Smith, J.; Liu, Y.; Tran, L.; Anderson, S.; Campone, M. VERITAC-2: A Phase III Study of Vepdegestrant, a PROTAC ER Degrader, versus Fulvestrant in ER+/HER2- Advanced Breast Cancer. *Future Oncol.* **2024**, *20* (32), 2447–2455. https://doi.org/10.1080/14796694.2024.2377530.

(227) *Arvinas and Pfizer Announce Positive Topline Results from Phase 3 VERITAC-2 Clinical Trial*. Pfizer. https://www.pfizer.com/news/press-release/press-release-detail/arvinas-and-pfizer-announce-positive-topline-results-phase (accessed 2025-01-24).

(228) Zengerle, M.; Chan, K.-H.; Ciulli, A. Selective Small Molecule Induced Degradation of the BET Bromodomain Protein BRD4. *ACS Chem. Biol.* **2015**, *10* (8), 1770–1777. https://doi.org/10.1021/acschembio.5b00216.

(229) Brenner, S.; Lerner, R. A. Encoded Combinatorial Chemistry. *Proc. Natl. Acad. Sci.* **1992**, *89* (12), 5381–5383. https://doi.org/10.1073/pnas.89.12.5381.

(230) Gironda-Martínez, A.; Donckele, E. J.; Samain, F.; Neri, D. DNA-Encoded Chemical Libraries: A Comprehensive Review with Succesful Stories and Future Challenges. *ACS Pharmacol. Transl. Sci.* **2021**, *4* (4), 1265–1279. https://doi.org/10.1021/acsptsci.1c00118.

(231) Flood, D. T.; Kingston, C.; Vantourout, J. C.; Dawson, P. E.; Baran, P. S. DNA Encoded Libraries: A Visitor's Guide. *Isr. J. Chem.* **2020**, *60* (3–4), 268–280. https://doi.org/10.1002/ijch.201900133.

(232) Collie, G. W.; Clark, M. A.; Keefe, A. D.; Madin, A.; Read, J. A.; Rivers, E. L.; Zhang, Y. Screening Ultra-Large Encoded Compound Libraries Leads to Novel Protein–Ligand Interactions and High Selectivity. *J. Med. Chem.* **2024**, *67* (2), 864–884. https://doi.org/10.1021/acs.jmedchem.3c01861.

(233) Castañón, J.; Román, J. P.; Jessop, T. C.; De Blas, J.; Haro, R. Design and Development of a Technology Platform for DNA-Encoded Library Production and Affinity Selection. *SLAS Discov.* **2018**, *23* (5), 387–396. https://doi.org/10.1177/2472555217752091.

(234) Conole, D.; H Hunter, J.; J Waring, M. The Maturation of DNA Encoded Libraries: Opportunities for New Users. *Future Med. Chem.* **2021**, *13* (2), 173–191. https://doi.org/10.4155/fmc-2020-0285.

(235) Ma, P.; Zhang, S.; Huang, Q.; Gu, Y.; Zhou, Z.; Hou, W.; Yi, W.; Xu, H. Evolution of Chemistry and Selection Technology for DNA-Encoded Library. *Acta Pharm. Sin. B* **2024**, *14* (2), 492–516. https://doi.org/10.1016/j.apsb.2023.10.001.

(236) Wang, X.; Sun, H.; Liu, J.; Dai, D.; Zhang, M.; Zhou, H.; Zhong, W.; Lu, X. Ruthenium-Promoted C–H Activation Reactions between DNA-Conjugated Acrylamide and Aromatic Acids. *Org. Lett.* **2018**, *20* (16), 4764–4768. https://doi.org/10.1021/acs.orglett.8b01837.

(237) Kölmel, D. K.; Loach, R. P.; Knauber, T.; Flanagan, M. E. Employing Photoredox Catalysis for DNA-Encoded Chemistry: Decarboxylative Alkylation of α-Amino Acids. *ChemMedChem* **2018**, *13* (20), 2159–2165. https://doi.org/10.1002/cmdc.201800492.

(238) Badir, S. O.; Sim, J.; Billings, K.; Csakai, A.; Zhang, X.; Dong, W.; Molander, G. A. Multifunctional Building Blocks Compatible with Photoredox-Mediated Alkylation for DNA-Encoded Library Synthesis. *Org. Lett.* **2020**, *22* (3), 1046–1051. https://doi.org/10.1021/acs.orglett.9b04568.

(239) Thomas, B.; Lu, X.; Birmingham, W. R.; Huang, K.; Both, P.; Reyes Martinez, J. E.; Young, R. J.; Davie, C. P.; Flitsch, S. L. Application of Biocatalysis to on-DNA Carbohydrate Library Synthesis. *ChemBioChem* **2017**, *18* (9), 858–863. https://doi.org/10.1002/cbic.201600678.

(240) Kunig, V. B. K.; Ehrt, C.; Dömling, A.; Brunschweiger, A. Isocyanide Multicomponent Reactions on Solid-Phase-Coupled DNA Oligonucleotides for Encoded Library Synthesis. *Org. Lett.* **2019**, *21* (18), 7238–7243. https://doi.org/10.1021/acs.orglett.9b02448.

(241) Zhang, Y.; Clark, M. A. Design Concepts for DNA-Encoded Library Synthesis. *Bioorg. Med. Chem.* **2021**, *41*, 116189. https://doi.org/10.1016/j.bmc.2021.116189.

(242) Collie, G. W.; Barlind, L.; Bazzaz, S.; Börjesson, U.; Dale, I. L.; Disch, J. S.; Habeshian, S.; Jetson, R.; Khurana, P.; Madin, A.; Michaelides, I. N.; Peng, L.; Snijder, A.; Stubbs, C. J. Discovery of a Selective C-MET Inhibitor with a Novel Binding Mode. *Bioorg. Med. Chem. Lett.* **2022**, *75*, 128948. https://doi.org/10.1016/j.bmcl.2022.128948.

(243) Veerman, J. J. N.; Bruseker, Y. B.; Damen, E.; Heijne, E. H.; Van Bruggen, W.; Hekking, K. F. W.; Winkel, R.; Hupp, C. D.; Keefe, A. D.; Liu, J.; Thomson, H. A.; Zhang, Y.; Cuozzo, J. W.; McRiner, A. J.; Mulvihill, M. J.; Van Rijnsbergen, P.; Zech, B.; Renzetti, L. M.; Babiss, L.; Müller, G. Discovery of 2,4-1 *H* -Imidazole Carboxamides as Potent and Selective TAK1 Inhibitors. *ACS Med. Chem. Lett.* **2021**, *12* (4), 555–562. https://doi.org/10.1021/acsmedchemlett.0c00547.

(244) Cuozzo, J. W.; Centrella, P. A.; Gikunju, D.; Habeshian, S.; Hupp, C. D.; Keefe, A. D.; Sigel, E. A.; Soutter, H. H.; Thomson, H. A.; Zhang, Y.; Clark, M. A. Discovery of a Potent BTK Inhibitor with a Novel Binding Mode by Using Parallel Selections with a DNA-Encoded Chemical Library. *ChemBioChem* **2017**, *18* (9), 864–871. https://doi.org/10.1002/cbic.201600573.

(245) Harris, P. A.; King, B. W.; Bandyopadhyay, D.; Berger, S. B.; Campobasso, N.; Capriotti, C. A.; Cox, J. A.; Dare, L.; Dong, X.; Finger, J. N.; Grady, L. C.; Hoffman, S. J.; Jeong, J. U.; Kang, J.; Kasparcova, V.; Lakdawala, A. S.; Lehr, R.; McNulty, D. E.; Nagilla, R.; Ouellette, M. T.; Pao, C. S.; Rendina, A. R.; Schaeffer, M. C.; Summerfield, J. D.; Swift, B. A.; Totoritis, R. D.; Ward, P.; Zhang, A.; Zhang, D.; Marquis, R. W.; Bertin, J.; Gough, P. J. DNA-Encoded Library Screening Identifies Benzo[*b*][1,4]Oxazepin-4-Ones as Highly Potent and Monoselective Receptor Interacting Protein 1 Kinase Inhibitors. *J. Med. Chem.* **2016**, *59* (5), 2163–2178. https://doi.org/10.1021/acs.jmedchem.5b01898.

(246) Nissink, J. W. M.; Bazzaz, S.; Blackett, C.; Clark, M. A.; Collingwood, O.; Disch, J. S.; Gikunju, D.; Goldberg, K.; Guilinger, J. P.; Hardaker, E.; Hennessy, E. J.; Jetson, R.; Keefe, A. D.; McCoull, W.; McMurray, L.; Olszewski, A.; Overman, R.; Pflug, A.; Preston, M.; Rawlins, P. B.; Rivers, E.; Schimpl, M.; Smith, P.; Truman, C.; Underwood, E.; Warwicker, J.; Winter-Holt, J.; Woodcock, S.; Zhang, Y. Generating Selective Leads for Mer Kinase Inhibitors—Example of a Comprehensive Lead-Generation Strategy. *J. Med. Chem.* **2021**, *64* (6), 3165–3184. https://doi.org/10.1021/acs.jmedchem.0c01904.

(247) Cuozzo, J. W.; Clark, M. A.; Keefe, A. D.; Kohlmann, A.; Mulvihill, M.; Ni, H.; Renzetti, L. M.; Resnicow, D. I.; Ruebsam, F.; Sigel, E. A.; Thomson, H. A.; Wang, C.; Xie, Z.; Zhang, Y. Novel Autotaxin Inhibitor for the Treatment of Idiopathic Pulmonary Fibrosis: A Clinical Candidate Discovered Using DNA-Encoded Chemistry. *J. Med. Chem.* **2020**, *63* (14), 7840–7856. https://doi.org/10.1021/acs.jmedchem.0c00688.

(248) Rianjongdee, F.; Atkinson, S. J.; Chung, C.; Grandi, P.; Gray, J. R. J.; Kaushansky, L. J.; Medeiros, P.; Messenger, C.; Phillipou, A.; Preston, A.; Prinjha, R. K.; Rioja, I.; Satz, A. L.; Taylor, S.; Wall, I. D.; Watson, R. J.; Yao, G.; Demont, E. H. Discovery of a Highly Selective

BET BD2 Inhibitor from a DNA-Encoded Library Technology Screening Hit. *J. Med. Chem.* **2021**, *64* (15), 10806–10833. https://doi.org/10.1021/acs.jmedchem.1c00412.

(249) Encinas, L.; O'Keefe, H.; Neu, M.; Remuiñán, M. J.; Patel, A. M.; Guardia, A.; Davie, C. P.; Pérez-Macías, N.; Yang, H.; Convery, M. A.; Messer, J. A.; Pérez-Herrán, E.; Centrella, P. A.; Álvarez-Gómez, D.; Clark, M. A.; Huss, S.; O'Donovan, G. K.; Ortega-Muro, F.; McDowell, W.; Castañeda, P.; Arico-Muendel, C. C.; Pajk, S.; Rullás, J.; Angulo-Barturen, I.; Álvarez-Ruíz, E.; Mendoza-Losana, A.; Ballell Pages, L.; Castro-Pichel, J.; Evindar, G. Encoded Library Technology as a Source of Hits for the Discovery and Lead Optimization of a Potent and Selective Class of Bactericidal Direct Inhibitors of *Mycobacterium Tuberculosis* InhA. *J. Med. Chem.* **2014**, *57* (4), 1276–1288. https://doi.org/10.1021/jm401326j.

(250) Fernández-Montalván, A. E.; Berger, M.; Kuropka, B.; Koo, S. J.; Badock, V.; Weiske, J.; Puetter, V.; Holton, S. J.; Stöckigt, D.; Ter Laak, A.; Centrella, P. A.; Clark, M. A.; Dumelin, C. E.; Sigel, E. A.; Soutter, H. H.; Troast, D. M.; Zhang, Y.; Cuozzo, J. W.; Keefe, A. D.; Roche, D.; Rodeschini, V.; Chaikuad, A.; Díaz-Sáez, L.; Bennett, J. M.; Fedorov, O.; Huber, K. V. M.; Hübner, J.; Weinmann, H.; Hartung, I. V.; Gorjánácz, M. Isoform-Selective ATAD2 Chemical Probe with Novel Chemical Structure and Unusual Mode of Action. *ACS Chem. Biol.* **2017**, *12* (11), 2730–2736. https://doi.org/10.1021/acschembio.7b00708.

(251) Gehrtz, P.; Marom, S.; Bührmann, M.; Hardick, J.; Kleinbölting, S.; Shraga, A.; Dubiella, C.; Gabizon, R.; Wiese, J. N.; Müller, M. P.; Cohen, G.; Babaev, I.; Shurrush, K.; Avram, L.; Resnick, E.; Barr, H.; Rauh, D.; London, N. Optimization of Covalent MKK7 Inhibitors *via* Crude Nanomole-Scale Libraries. *J. Med. Chem.* **2022**, *65* (15), 10341–10356. https://doi.org/10.1021/acs.jmedchem.1c02206.

(252) Meidner, J. L.; Frey, A. F.; Zimmermann, R. A.; Sabin, M. O.; Nidoieva, Z.; Weldert, A. C.; Hoba, S. N.; Krone, M. W.; Barthels, F. Nanomole Scale Screening of Fluorescent RNA-Methyltransferase Probes Enables the Discovery of METTL1 Inhibitors. *Angew. Chem. Int. Ed Engl.* **2024**, *63* (48), e202403792. https://doi.org/10.1002/anie.202403792.

(253) Zhong, W.; Pasunooti, K. K.; Balamkundu, S.; Wong, Y. H.; Nah, Q.; Gadi, V.; Gnanakalai, S.; Chionh, Y. H.; McBee, M. E.; Gopal, P.; Lim, S. H.; Olivier, N.; Buurman, E. T.; Dick, T.; Liu, C. F.; Lescar, J.; Dedon, P. C. Thienopyrimidinone Derivatives That Inhibit Bacterial tRNA (Guanine37-N^1)-Methyltransferase (TrmD) by Restructuring the Active Site with a Tyrosine-Flipping Mechanism. *J. Med. Chem.* **2019**, *62* (17), 7788–7805. https://doi.org/10.1021/acs.jmedchem.9b00582.

(254) Hübner, A. F.; Weldert, A. C.; Marciniak, T.; Hof, F.; Beck, V. S.; Carien, S.; Mulartschyk, S. N.; Wolf, E.; Ziebuhr, W.; Barthels, F. Nanoscale Direct-to-Biology Optimization and Structural Insights into Selective *S. Aureus* TrmD Inhibitors. *J. Med. Chem.* **2025**, *68* (24), 26246–26262. https://doi.org/10.1021/acs.jmedchem.5c02323.

(255) Frey, A. F.; Schwan, M.; Weldert, A. C.; Kadenbach, V.; Kopp, J.; Nidoieva, Z.; Zimmermann, R. A.; Gleue, L.; Zimmer, C.; Jörg, M.; Friedland, K.; Helm, M.; Sinning, I.; Barthels, F. DNA-Encoded Library Screening Uncovers Potent DNMT2 Inhibitors Targeting a Cryptic Allosteric Binding Site. *iScience* **2025**, 113300. https://doi.org/10.1016/j.isci.2025.113300.

(256) Li, K.; Crews, C. M. PROTACs: Past, Present and Future. *Chem. Soc. Rev.* **2022**, *51* (12), 5214–5236. https://doi.org/10.1039/D2CS00193D.

(257) Weldert, A. C.; Frey, A. F.; Krone, M. W.; Krähe, F.; Kuhn, H.; Kersten, C.; Barthels, F. Structure-Guided Design of a Methyltransferase-like 3 (METTL3) Proteolysis Targeting Chimera (PROTAC) Incorporating an Indole–Nicotinamide Chemotype. *RSC Med. Chem.* https://doi.org/10.1039/d5md00359h.

(258) Garner, A. L. Contemporary Progress and Opportunities in RNA-Targeted Drug Discovery. *ACS Med. Chem. Lett.* **2023**, *14* (3), 251–259. https://doi.org/10.1021/acsmedchemlett.3c00020.

(259) Childs-Disney, J. L.; Yang, X.; Gibaut, Q. M. R.; Tong, Y.; Batey, R. T.; Disney, M. D. Targeting RNA Structures with Small Molecules. *Nat. Rev. Drug Discov.* **2022**, *21* (10), 736–762. https://doi.org/10.1038/s41573-022-00521-4.

(260) Jerabek-Willemsen, M.; Wienken, C. J.; Braun, D.; Baaske, P.; Duhr, S. Molecular Interaction Studies Using Microscale Thermophoresis. *ASSAY Drug Dev. Technol.* **2011**, *9* (4), 342–353. https://doi.org/10.1089/adt.2011.0380.

(261) Moon, M. H.; Hilimire, T. A.; Sanders, A. M.; Schneekloth, J. S. Measuring RNA–Ligand Interactions with Microscale Thermophoresis. *Biochemistry* **2018**, *57* (31), 4638–4643. https://doi.org/10.1021/acs.biochem.7b01141.
(262) Entzian, C.; Schubert, T. Studying Small Molecule–Aptamer Interactions Using MicroScale Thermophoresis (MST). *Methods* **2016**, *97*, 27–34. https://doi.org/10.1016/j.ymeth.2015.08.023.
(263) Kallert, E.; Behrendt, M.; Frey, A.; Kersten, C.; Barthels, F. Non-Covalent Dyes in Microscale Thermophoresis for Studying RNA Ligand Interactions and Modifications. *Chem. Sci.* **2023**, *14* (36), 9827–9837. https://doi.org/10.1039/d3sc02993j.

8 Curriculum Vitae

Personal Data

Name	Ariane Felicitas Hübner (born Frey)
Birthdate	03.04.1996
Address	[redacted]
Email	ariane.frey@web.de

Education & Scientific Experience

2022–2026 **University of Mainz,** Doctoral studies

- Supervisor: [redacted] & Dr. Fabian Barthels
  Nanoscale Libraries and Novel Drug Modalities for Targeting RNA Methyltransferases

2017–2022 **University of Mainz,** M.Sc. Biomedicinal Chemistry

02/22–07/22 **Research visit,** [redacted] (Centro de Investigación Príncipe Felipe, Valencia, Spain)
Development of chromophore-based Polypeptide Platforms for theranostic purposes in neurodegenerative disorders

05/21–12/21 **Master's thesis,** [redacted] (Johannes Gutenberg University of Mainz)
Synthese und Testung von uPA Inhibitoren mit Argininmimetika als P1-Aminosäure

01/21–04/21 **Research visit,** [redacted] (Johannes Gutenberg University of Mainz)
Synthese und Testung von Matriptasenhibitoren zur Verwendung von Thermodynamik- und Kinetikstudien

2015–2017 **University of Mainz,** B.Sc. Biomedicinal Chemistry

01/17–04/17 **Bachelor thesis,** [redacted] (University Medical Center of the Johannes Gutenberg University Mainz)
Dermcidin - ein neuroprotektiver Faktor?

2006–2015 [redacted], A levels (Abitur)